UNIVERSITEIT
GENT

Bronnen, modi en effecten van vloeistofstromingen aan de zeebodem.
Sources, modes and effects of seabed fluid flow.

Davy Depreiter

RCMG

Universiteit Gent
Faculteit Wetenschappen
Vakgroep Geologie en Bodemkunde

RCMG - Marine Geology
Vakgroep Geologie-Bodemkunde
UNIVERSITEIT GENT
Krijgslaan 281-S8 B-9000 GENT (BELGIUM)
Tel. 09-264 45 87 - Fax 09-264 49 67

1387

Bronnen, modi en effecten van vloeistofstromingen aan de zeebodem.

Sources, modes and effects of seabed fluid flow.

Davy Depreiter

RCMG

Universiteit Gent
Faculteit Wetenschappen
Vakgroep Geologie en Bodemkunde

Bronnen, modi en effecten van vloeistofstromingen aan de zeebodem.

Sources, modes and effects of seabed fluid flow.

Davy Depreiter

Promotor: Prof. Dr. Jean-Pierre Henriet

Universiteit Gent
Faculteit Wetenschappen
Vakgroep Geologie en Bodemkunde

Krijgslaan 281 S8
B-9000 Gent

Tel.: +32-9-264.45.85
Fax.: +32-9-331.49.67

RCMG

Proefschrift voorgelegd
tot het behalen van de graad van
Doctor in de Wetenschappen, Geologie
Academiejaar 2008-2009

Acknowledgements - Dankbetuigingen

Bij het tot stand komen van dit werk, zijn heel wat mensen direct en indirect betrokken geweest. Ik wens iedereen te bedanken voor de kansen, richting en steun die ze me gegeven hebben. Jullie zijn met zoveel dat het niet mogelijk is om al jullie namen hier neer te schrijven, en ik zou er zeker enkele vergeten... Toch wil ik enkele mensen met een speciaal woordje bedanken...:

In the making of this work, many people have been involved directly and indirectly. I want to thank them all for the chances, directions and support they have given me during this period. So many have been involved that it is impossible to write all your names here (I would forget some of you, I'm afraid). But still, a few of these people, I would like to thank with a special word...:

Jean-Pierre Henriet, je hebt mij in 2002 de Golf van Cadiz op gestuurd aan boord van de "Professor Logachev", mijn eerste kennismaking met marien geologisch en geofysisch onderzoek. Dat was de kans die je me gaf toen ik in de loop van de eerste licentie kwam vragen naar licentiaatsthesisonderwerpen in verband met geofysica en planetaire geologie. Na een jaar seismiek van in de Golf van Cadiz te bestuderen, was ik gebeten om er meer mee te gaan doen. Dit was het startpunt van een fantastisch leerpad waarlangs ik vrijheid, vertrouwen, steun, vorming en inspiratie kreeg en je opende deuren waar nodig. Er is zoveel om op te noemen maar veel te weinig woorden om een gepaste 'dank u' te zeggen... Toch, bij deze wil ik je bedanken voor de afgelopen jaren en alvast uitkijken naar de jaren die nog komen...

Crisogono Vasconcelos, I met you onboard the R/V "Professor Logachev" in 2002. Geomicrobiology was a new world to me. You invited me to visit your Geomicrobiology Lab in Zürich at the end of that summer. I looked at microbes emitting light after they were stained with fluorescent die, I extracted DNA from rocks,... A year later, I came back to Zürich for a semester of Erasmus studentship at the ETH. More recently, our paths have crossed in the frameworks of different projects and you have remained as supporting as always, even though I didn't take that one opportunity... I am grateful for all you learned me, for inspiration and for Friday beers. I also want to thank you for your and Gisèles hospitality in Zürich (and Davos).

Judy McKenzie, you have supported and inspired me in my work and in writing and presenting IODP proposals. You have opened doors that have given me many chances and influenced me in many ways. Thank you very much.

I enrolled in the "Microbial evolution and ecology" course at the University of Zürich learning all about microbes and what they do with chemistry and rocks,... Kurt Hanselmann, Thomas Horath and Munti Yuhana, thank you all for the inspiration and knowledge you gave me.

I was granted the participation in the 2004 "Geobiology" summer course at the University of Southern California, sponsored by the Agouron Institute, organized on Catalina Island and in Canada. Twenty young researchers and tens of instructors from all over the world mixed their knowledge of geology, geochemistry, microbiology, genetics, modeling,... I am grateful that I was part of it.

Yuri Podlachikov, thank you for learning about the infinite possibilities of finite element modeling.

The scientists and crews onboard R/V Belgica, R/V Pelagia and R/V Charles Darwin, thank you for the wonderful weeks offshore, exploring the seafloor in the Gulf of Cadiz and other places.

Dit hele verhaal zou niet mogelijk geweest zijn zonder een bron van inkomsten. IWT Vlaanderen heeft me gedurende vier jaar voorzien van een beurs en een budget om te spenderen aan het onderzoek. Bedankt voor deze uitzonderlijke steun.

Alle collega's en vrienden aan het RCMG, dank jullie voor het delen in de vreugde en perikelen die deel uitmaken van een doctoraatsonderzoek. Het uitwisselen van kleine of grote ideeën zette me telkens een stapje verder in de goede richting, dus zonder jullie zou dit werk ook niet geworden zijn wat het is. Anneleen, vier jaar of langer bureaumaatjes zijn. Je enthousiasme en spirit hebben me vaak moed gegeven. Bedankt hiervoor!

Mijn ouders, schoonouders, broers en zussen... Jullie hebben dit verhaal van de eerste minuut meegemaakt. Je hebt niet altijd gehoord waarmee ik precies mee bezig was en toch heb ik altijd steun, vertrouwen en bewondering gekregen. Bedankt voor alle schouderkloppen. Papa en mama, bedankt voor alle kansen die ik gekregen heb, jaren geleden. Zonder jullie steun vanaf het begin was er geen sprake van dit alles...

Lieve Débra... Je hebt me door alle ups and downs heen, immens veel moed, steun, vertrouwen en geloof gegeven. Je hebt soms op me moeten wachten als ik van huis was, maar het weerzien was altijd veel intenser dan het weggaan. Ook al waren sommige keuzes moeilijk, ik ben blij met de keuzes die we gemaakt hebben. Na wat zoeken, hebben we ons nestje gevonden. Nu bouwen we samen verder aan ons verhaal. Bedankt voor al wat je tot nu toe gegeven hebt... zonder jou was het nooit gelukt.

Lieve kleine Sen... Je bent het mooiste geschenk dat ik ooit in mijn leven gekregen heb. Jij en je mama zijn het dierbaarste wat ik heb...

Davy Depreiter,
25/05/2009, Lokeren

Contents

List of Figures

List of Tables

Part I

Generalities

Chapter 1

Introduction

In this introductory chapter, the nature and significance of seabed fluid flow and mud volcanism is addressed. The aim and outline, as well as the project framework of this work is explained.

1.1 Seabed fluid flow and mud volcanoes

The seabed is the interface between the oceanic and the sedimentary environment. Each of these environments is characterized by its own chemical and physical equilibria and dynamic processes or transitions between equilibria. The seabed hence represents the transition between different sets of equilibria and processes.

Seabed fluid flow is a process in which fluids are transferred from the sedimentary to the oceanic environment, and vice versa (Judd and Hovland, 2007). The fluid itself also carries chemical compounds, heat, etc. and therefore, seabed fluid flow also transfers chemicals and heat from one environment to the other environment. Seabed fluid flow can occur under different forms, e.g. as gas bubbles escaping from the sediments, as hydrothermal fluids escaping from mineralized chimneys at oceanic spreading axes, as fresh water escaping near shore from aquifers, as liquid mud extruded from a mud volcano crater, ... Seabed fluid flow has consequences for geochemical, mineralogical and biological processes: e.g. convective transport can strongly enhance microbial activity in near-surface sediments due to the increased supply of electron donors. Some of these processes lead to formation of minerals which thus can be regarded as products of seabed fluid flow (e.g. authigenic carbonate crusts in sediments).

The drivers of seabed fluid flow are diverse. Most often, fluids escaping from the seafloor are related to subsurface temperature, density and pressure differences, e.g. due to the thermal expansion of seawater in the warm basalts of ocean ridges, due to the generation of gas in sediments, due to differential loading of a buried sediment body, ... Compaction of sediments increasing with burial depth leads to a decrease in pore volume and results in ascending fluid flow as well. Fluids can also enter the sedimentary environment, e.g. on a beach where seawater is flushed into sands, or generated by a thermal or density-driven convective cell in the sediments. Depending on the driver, and many other environmental parameters, seabed fluid flow occurs in many modes: diffuse versus focused, slow versus fast, liquid versus gaseous, ...

A specific type of (seabed) fluid flow comprises the process of mud volcanism. Mud volcanoes are structures that are formed at the surface by extrusion of fluids, mud and rock clasts of variable size. The extruded material is called mud breccia and flows out of the crater. Before extrusion, the mud breccia has been transported upwards from a source layer through a feeder pipe. The clay fraction of the mud breccia is derived from liquefied, undercompacted muds of the source layer and clay deposits above the source layer. The rock clasts are derived from strata surrounding the feeder pipe. The nature and origin of the fluid phase is a combination of pore fluids from sediment compaction, biogenic methane from organic matter decomposition, lateral fluid influx along permeable layers or fault planes, deep-sourced thermogenic methane and other hydrocarbons, hydrothermal fluids, fluids from undercompacted and/or overpressured layers (Kopf, 2002). The mud breccia piles up as a more or less steep

(mostly depending on fluid content and viscosity) elevated structure. More fluid mud can form far-extending mud flows around the mud volcano body. Mud volcanoes can be classified by their morphology (e.g. Kopf, 2002), discriminating flat, fluid examples (mud pies), typical cone-shaped structures (mud volcanoes *s.s.*), rigid dome-shaped structures (mud domes) or depressions in which mud is rising (mud pools).

The geographic occurrence of mud volcanoes is related to geological settings that favour the generation of undercompacted or overpressured sedimentary strata. The process of overpressure creation and its consequences will be discussed in chapters 6. Judd and Hovland (2007) give an extensive overview of the occurrence of seabed fluid flow in general, while Milkov (2000), Dimitrov (2002b) and Kopf (2002) give overviews of the occurrence of mud volcanoes.

Over 900 onshore and 800 offshore mud volcanoes have been identified at this moment. Most of the mud volcanoes occur in regions with active tectonic plate margins or where accretionary wedges are being formed. A brief overview of the world-wide occurrence of mud volcanoes has to indicate the significance of mud volcanism.

At the westernmost end of the Alpine orogenic belt, the Gulf of Cadiz boast over 30 mud volcanoes on the lower slope. The first mud volcanoes where discovered in 1999 (Gardner, 1999, 2001). The mud volcanoes are organized in different fields, depending on their location and geological setting. More information about this region is given in Chapter 2. On the other side of the Gibraltar Strait, in the Alboran Sea, different mud volcanoes are known as well (Sautkin et al., 2003). The central part of the Adriatic Sea has different sites where seeps and mud diapirs are present, as well as small mud volcanoes (Hovland, 1989; Colantoni et al., 1998; Curzi, 1998) together with cemented carbonate sediments. In Greece, mud volcanoes are found associated to hydrothermal venting (related to the Hellenic back-arc, on and around many of the Greek Islands, Dando et al. (1999)). Similarly, hydrothermally related mud volcanoes are observed on the south flank of the Etna volcano (Sicily). The Mediterranean Ridge, an accretionary wedge in the eastern Mediterranean, is known to feature mud volcanoes since a few decades ((e.g. Kenyon et al., 1982; Limonov et al., 1996; Mascle et al., 1999). The mud volcanoes form a long continuous belt, named the "Mediterranean Ridge mud diapiric belt". Many of these mud volcanoes are active. More recently, large-scale mud volcanism, pockmarks and carbonate cemented sediment occurrences were discovered on the Nile Delta and Fan (Dupre et al., 2007). The Black Sea has high concentrations of methane in the deep waters. At the seafloor, seeps, mud volcanoes and gas hydrates are found widespread on the continental shelf, slope and in deeper parts.

In Asia, mud volcanism is known from the Makran coast (Iran-Pakistan) along with other seabed fluid flow features (e.g. Rad et al., 1996; Wiedicke et al., 2001) and India (Rao et al., 2001). The South China Sea is known for widespread mud volcanism and other seabed fluid flow processes: offshore Brunei (Van Rensbergen and Morley, 2001), offshore Vietnam (Traynor and Sladen, 1997), Hong Kong and Taiwan (Chow et al., 2001). In southeast Asia,

mud volcanoes are known from the Banda Arc (Barber et al., 1986), and other fluid flow features in the Timor Sea. The Hikurangi margin, off New Zealand has ubiquitous gas hydrates (Lewis and Marshall, 1996; Pecher et al., 2003; Barnes et al., 2009; Klaucke et al., 2009; Jones et al., 2009) and gas seeps have been reported at different places.

One of the most studied mud volcanoes (in terms of geology, geophysics, geochemistry, microbiology) is the Håkon Mosby mud volcano offshore Norway (Vogt et al., 1999). It is associated with the Senja fracture zone. The mud volcano is rather small, although it is well known for its gas hydrate occurrence away from the mud volcano center and microbial mats with different habitats depending on geochemical parameters.

Along the continental margin of Africa, many seabed fluid flow features are known, including mud volcanoes which have been observed on the Niger Delta and Fan where fluid escape is related to undercompacted sediments, generation of gas and migration along lystric faults (Hovland et al., 1997).

In other parts of the world, including the Western Pacific, offshore Alaska, the west-coast of the USA, fluid flow processes are as widespread as in the other regions. Specifically for mud volcanism, Central America is a very active region, with Costa Rica, the Barbados area and the Gulf of Mexico in general.

1.2 Aim and outline

The general goal of this work is to contribute to the study of the migration and expulsion of fluids. It was chosen to approach "fluid flow" from a multidisciplinary point of view and at different scales. The aim is to obtain an understanding of different fluid flow processes that mostly, but not exclusively, pertain to mud volcanism. The processes looked at, include drivers of fluid flow (which are the cause of the fluid flow) and fluid flow effects (processes that arise as a consequence of the fluid flow). The fluid flow itself can happen at different scales, velocities and with different thermal or chemical properties. This variability can be seen as different modes of fluid flow. The study area on which will be focused, is the El Arraich mud volcano field, on the Moroccan Atlantic continental margin, as a part of the Gulf of Cadiz.

The Gulf of Cadiz is characterized by an accretionary wedge type body west of Gibraltar. Above this complex geological structure, many fluid expulsion related seabed features have been identified along the Iberian and Moroccan continental margin (Baraza and Ercilla, 1996; Gardner, 2001; Somoza et al., 2003; Pinheiro et al., 2003). The presence of methane in the mud volcano sediments also gave evidence of recent activity (Mazurenko et al., 2003). Rock clasts in the sediments were used to build an offshore stratigraphy for a small part of the Gulf of Cadiz (Ovsyannikov et al., 2003). Flinch et al. (1996) indicated the presence of rotated blocks as parts of the accretionary wedge below the Moroccan continental margin. Mud volcanoes, found in the El Arraiche mud volcano field, will be shown to largely coincide with the position

of the crests of these rotated blocks. A first aim of this work is to describe the environment in which these mud volcanoes occur and to evaluate the co-occurrence of these deep subseafloor structures, the mud volcanoes and other fluid expulsion features at the seafloor.

At different sites in the Gulf of Cadiz, carbonate precipitates were observed and sampled (e.g. Diaz-del Rio et al., 2003; Akhmanov et al., 2003). These carbonate "crusts" and "chimneys" all occur in areas of present or past fluid and gas emission at the seafloor; some of these are within mud volcano craters. A second aim of this work is to describe these carbonate precipitates to unveil the nature and origin of the parental fluids that migrate towards the seafloor surface and identify the processes that lead to their formation.

Finally, to put the observations and results in a more general framework, different numerical experiments will be done to evaluate the potential of different fluid flow drivers on seabed fluid flow, mud volcano activity and the effects on thermal and geochemical processes.

Within the El Arraiche mud volcano field, cold-water coral mounds have been discovered. Although these features are not directly related to mud volcanism, fluid migration may play a role in their genesis and/or evolution. Therefore, attention will be given to these structures within this work. The structure, nature, origin and growth of cold-water coral mounds are a heavily studied and debated subject. The research on the NE Atlantic margins has culminated in the drilling of large cold-water coral mounds offshore Ireland (Ferdelman et al., 2006). New and unexpected observations have only fuelled the debate and has raised new questions. Within this work, it will be shown how a specific type of fluid flow can influence the internal diagenetic and geochemical environment in cold-water coral mounds. Due to the lack of detailed data derived from the study area, an excursion will be made to the Challenger Mound off southwest Ireland to illustrate the possible consequences of this fluid flow process.

1.3   Project framework

The work here presented frames in and has been supported by different (inter)national projects:

EC FP5 'Research and Training Network' EURODOM (2002-2005). Eurodom is a consortium of projects involved in the research of margin slope stability around Europe. Determining factors for slope instabilities, slope failure, fluid migration pathways and the occurrence of cold water coral reefs are main research subjects.

EC FP6 'Integrated Project' HERMES (2005-2009). HERMES brings together expertise in many fields of research in order to identify and explain relationships between biodiversity and ecosystem functioning. HERMES study sites extend from the Arctic to the Black Sea and include biodiversity hotspots such as cold seeps, cold-water coral mounds and reefs, canyons and anoxic environments, and communities found on open slopes. These important systems require urgent study because of their possible biological fragility, unique genetic resources, global relevance to carbon cycling and susceptibility to global change and human impact.

ESF EUROMARGINS MoundForce (2003-2006). The MoundForce project has started in response to the question about the origin and growth of deep water coral reefs. The goal is to determine a set of environmental conditions for their origin and growth. The hypotheses about the link between these structures and hydrocarbons was tested. Tectonic, sedimentological, oceanographic and biological studies were included in the project.

ESF EUROMARGINS MVSeis (2003-2006). The MVSeis project studies the crustal structure, the stratigraphy and sediment dynamics, the tectonic setting and the detailed geometry of fluid migration pathways related to mud volcano activity in the Golf of Cadiz. Attention was given to the possible relation to deep structures in the accretionary wedge structure and the location of mud volcano fields.

ESF EURODIVERSITY Microsystems (2006-2008). MICROSYSTEMS proposes to turn the Pen Duick mounds off Morocco, into a natural laboratory through the following actions and experiments: a) Biotope exploration and characterization of biodiversity through geophysical and video imaging, targeted microbiological profiling, evaluation of present and past oceanic conditions; b) Microbial diversity census and evaluation of the functional link microbes-metazoans through metazoan species analysis, biogeochemical and molecular fingerprinting, laboratory culturing, fauna-microbe interactions analysis, evaluation of microbially mediated processes of carbonate precipitation; and c) Assessment of the impact of biodiversity changes through the development of a reactor technology to simulate and assess the functionality of the micro-ecological niches and the impact of environmental changes.

FWO project GeNesis (2003-2008). The GeNesis project aims to explain the genesis of cold water coral reefs. Within this project, the technology of the Renard Centre of Marine Geology has been further developed, including high-resolution seismic methods and video-controlled seafloor sampling.

Chapter 2

Geological Background of the Ibero-Maghrebian Domain

This chapter gives an overview of the geographic, oceanographic and geological background of the study area in the largest sense, i.e., the Gulf of Cadiz and the Betic-Rif Arc mountain belt. The chapter provides a regional framework and context for the observations, interpretations and discussions presented in the subsequent chapters.

The geomorphology of the Gulf of Cadiz, with canyon systems, lobe-shaped bodies on the seafloor, an arcuate mountain belt, hints a complex geological history.

The oceanography of the area has the same degree of complexity: the area is characterized by different water masses that well up, sink, branch or mix.

The geological appearance of the present-day is the work of geological forces during hundreds of millions of years. However, most of it was determined during the Atlantic rifting and spreading and the Alpine orogeny. At present, a debate about different key elements in the Gulf of Cadiz geology persists...

2.1   Geography

The large-scale study area comprises the Gulf of Cadiz, a part of the eastern Atlantic Ocean located between 9 - 6° W and 34 - 37° N (Fig. 2.1). The Gulf of Cadiz straddles the African-Eurasian continental boundary and connects to the Mediterranean Sea through the Strait of Gibraltar. The shelf fringing the continents is about 30 - 40 km wide off Morocco and up to 50 km off Spain. Further offshore, the seafloor gradually plunges westwards to depths of about 4000 m. Outside the Gulf of Cadiz, the Seine Abyssal Plain and Horseshoe Abyssal Plain reach depths of 5000 m and deeper.

Along the northern part of the shelf edge, off Spain and Portugal, multiple large canyon systems have developed. The central part of the Gulf features lobe-shaped topographies with irregular, strongly accidented surfaces, fault related linear features and singular circular to ellipsoid elevations. The geomorphology alone hints a complex geological structure and history. The southern part of the Gulf of Cadiz is characterized by a large depression: the Rharb Valley Canyon.

One of the most striking features observed onshore is the presence of an orogenic belt that spans southern Spain and northern Morocco: the Betic-Rif Arc. Altitudes of over 1000 meter are reached only a few tens of kilometers onshore. North and south of the Betic-Rif Arc appear large plains: the Guadalquivir Basin in Spain, and the Rharb Basin in Morocco.

The Gulf of Cadiz has been an important trading area since the middle ages, and evidences of cultural influences in both directions. Major cities where this history can be found include Cadiz, Faro, Tanger, Rabat, along with many additional coastal cities and villages with rich histories of trading and fishery activities.

2.2   Oceanography

The oceanographic situation in the Gulf of Cadiz is relevant for understanding sedimentation patterns, the occurrence of sedimentation patterns, the erosion capacity of the currents, seawater flow directions, etc. Some of these parameters will be useful further in this work. Here, an overview of the main oceanic currents in the Gulf of Cadiz will be given (Fig. 2.2).

One of the most important factors influencing the current patterns in the Gulf of Cadiz is the exchange of waters with the Mediterranean Sea through the Strait of Gibraltar (e.g., Villanueva and Gutierrezmas, 1994; Hernandez-Molina et al., 2006). The exchange consists of the warm and highly saline Mediterranean Outflow Water (or Mediterranean Undercurrent) near the bottom, and the less saline and cooler Atlantic Inflow Water at the surface.

The Atlantic Inflow Water is derived from the North Atlantic Surface Water which in turn is related to the Gulf Stream: it is a branch that runs along the western coast of the Iberian peninsula towards the south and continues towards the Canary Islands. Near Cape San Vicente, one branch of this current enters the Gulf of Cadiz and runs along the Iberian shelf
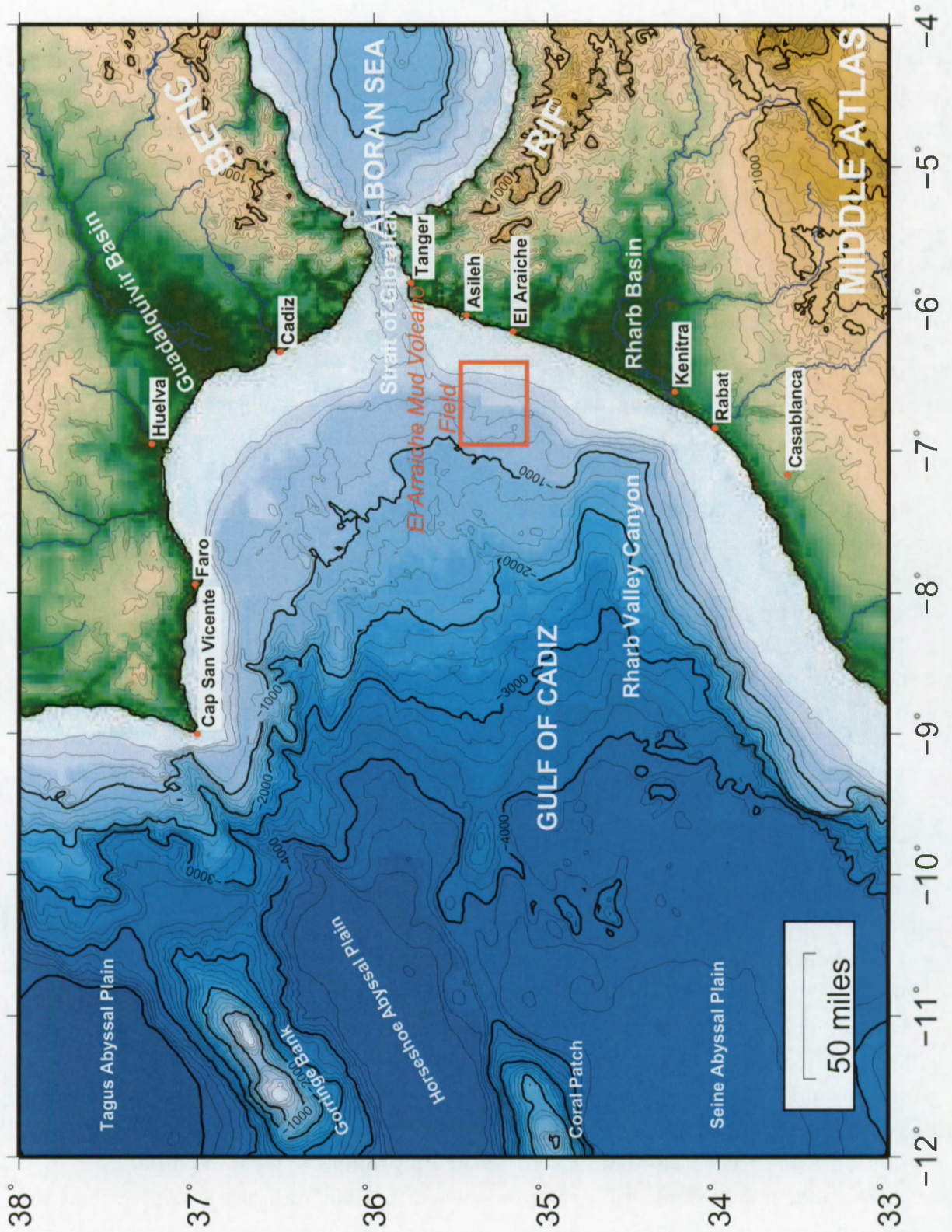
Figure 2.1: *Geography of the Gulf of Cadiz area. See section 2.1.*

towards the Strait of Gibraltar (Hernandez-Molina et al., 2006). Part of this current enters the Strait (the Atlantic Inflow Water), while another part runs further along the Moroccan margin and forms large eddies in the Gulf of Cadiz (Stevenson, 1977; Villanueva and Gutierrezmas, 1994; Carton et al., 2002).

Below these surface waters, the Mediterranean Outflow Water (MOW) enters the Gulf of Cadiz and splits into different branches: the Mediterranean upper water (MU) runs along the upper Iberian slope up to Cape San Vicente; the Mediterranean lower water (ML) is more saline and constitutes the principle part of the MOW. The ML is divided in different branches (the intermediate branch, the principal branch and the southern branch). The intermediate branch moves northwestward, the principle branch is located south of the Guadalquivir Bank in the Guadalquivir Channel, the southern branch plunges steeply towards the southwest. In total, three large MOW pathways can be identified (Hernandez-Molina et al., 2006): towards the north along the Iberian margin, to the west from Cape San Vincente and to the southwest as far as the Canary Islands, and then to the west.

The North Atlantic Deep Water (NADW) is a cold southward flowing water mass that is generated in the northern Atlantic. A part of the MOW mixes with the NADW and flows further southwards along the western part of the Atlantic Ocean.

Near-surface shoreward currents exist in the southern Gulf of Cadiz, being most intense during winter and spring months, and recirculation runs southwards as a jet (Machin et al., 2006). Coastal upwelling of cold water in the southernmost part of the Gulf of Cadiz is related to this current pattern. Pelegri et al. (2005) illustrate the coastal jet and upwelling north of the Cape Ghir region as well as further south, near the Canary Islands.

Apart from the warm Mediterranean Outflow Water, pulses of cool water originate in the Strait of Gibraltar due to tidally induced (La Violette and Lacombe, 1988) or wind in-duced (Folkard et al., 1997) upwelling; these cool waters also flow along the Moroccan coast in southward direction.

In 2005, during the 'MoundForce 2004' cruise with RV Pelagia (Mienis et al., 2004), a strong semi-diurnal tidal current component was observed in the El Arraiche study area. Current velocities up to 25 cm.s^{-1} were recorded.

2.3 Geology

The Gulf of Cadiz is located at the westernmost extension of the Alpine deformation front between Eurasia and Africa. The area is also part of the Atlantic Ocean, and therefore the rifting and spreading of this ocean, and the activity of related transform faults have played a role in the shaping of the Gulf of Cadiz. Nowadays, the main features of the area include the presence of an orogenic belt (the Betic-Rif Chain) with large foreland basins (Guadalquivir and Rharb basins), the presence of an accretionary wedge-like body ('nappe prérifaine'), with some mass wasting features ('olistostrome of the Gulf of Cadiz'), and the possibility of past
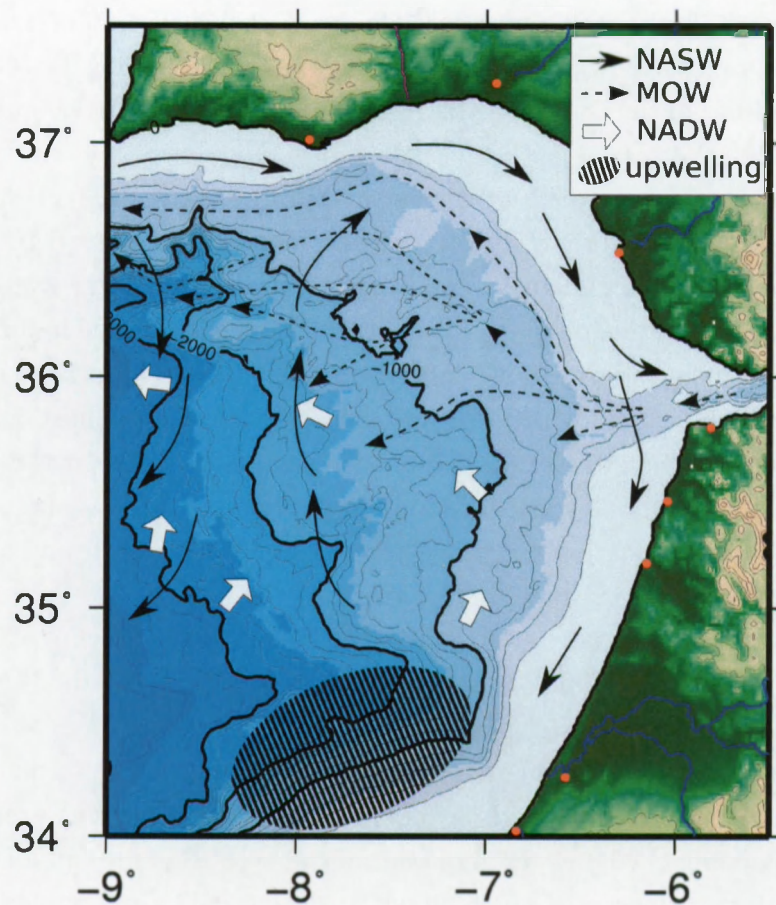
Figure 2.2: Oceanography of the Gulf of Cadiz area showing the main current patterns in the area, based on Villanueva and Gutierrezmas (1994); Carton et al. (2002); Pelegri et al. (2005); Hernandez-Molina et al. (2006). NASW: North Atlantic Surface Water; MOW: Mediterranean Outflow Water; NADW: North Atlantic Deep Water.

or present subduction processes under the Strait of Gibraltar. All of these elements together render a complex overall picture.

In this section an overview of the tectonic evolution of the area will be given, based on elements available in literature. The debate of the true nature of the Gulf of Cadiz will be addressed, as well as the large-scale stratigraphy.

2.3.1 Regional tectonic evolution

The origin and evolution of the Atlantic Ocean and the convergence of the Eurasian and African continents are key items to understand the Gulf of Cadiz geology.

Seafloor spreading started in the Central Atlantic (bounded on the north side by the Gloria Transform Fault) around 180 million years ago (Ma) (Middle Jurassic) and somewhat later, around 140 Ma (Lower Cretaceous), in the southernmost part of the North Atlantic (Ziegler
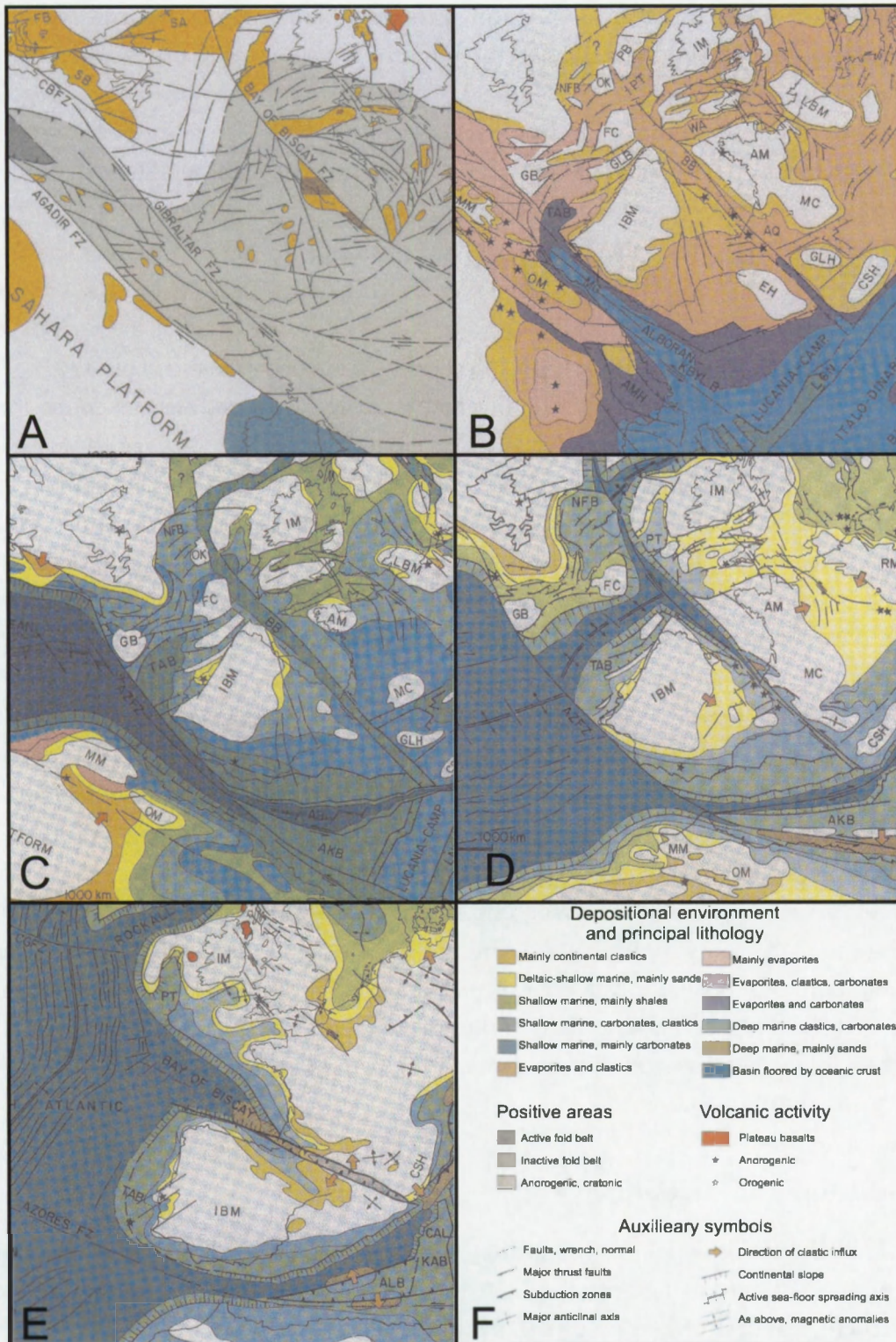
Figure 2.3: *Paleotectonic-paleogeographic maps to illustrate the regional tectonic evolution, after Ziegler and van Hoorn (1989). A: Perm – Carboniferous. B: Late Triassic. C: Late Jurassic. D: Aptian – Albian. E: Paleocene. F: Legend. See text in section 2.3.1 for details.*

and van Hoorn, 1989) (Figure 2.3A,B,C). Rifting processes earlier in the Mesozoic were related to tensional stresses, while the actual break-up patterns were related to pre-existing Paleozoic fault zones (Pique and Laville, 1996) (Figure 2.3A). By early Jurassic times, the spreading of the westernmost Tethys (Figure 2.3B) had resulted in the separation of the northern African and Iberian margins, potentially extending up to the Gorringe Bank region (see Maldonado et al., 1999, and references therein).

The separation of Eurasia and North America initiated 118 Ma ago (Lower Cretaceous) north of the Azores-Gibraltar Fracture Zone (AGFZ) (Figure 2.3C,D). At this time, transform faults were active in the Gulf of Cadiz and a triple junction occurred in the vicinity of the Gorringe bank, separating North America, Africa and Iberia (Maldonado et al., 1999). During a long period (84 – $\sim$ 40 Ma), Iberia was attached to Africa as spreading was more active in the northern North Atlantic. During the Late Cretaceous and earliest Tertiary, the crustal separation had been achieved in all parts of the North Atlantic and the new continental margins became mostly inactive (Ziegler and van Hoorn, 1989), except for transform faults related to differential spreading at the oceanic axes. The progressive closing of oceanic basins in the central and western Tethys and the westward movement of the Alpine deformation front into the western Mediterranean area was caused by the northward drift of Africa. This process also changed the stress patterns in the whole Atlantic area (Figure 2.3E).

During Eocene-Oligocene times, the Pyrenean orogeny took place (collision of Iberia and Eurasia) and, according to Ziegler and van Hoorn (1989), the internal parts of the western Mediterranean were emplaced (Betic and Rif chain) yielding important shortening in the area. Between the mid-Oligocene and Late Miocene, about 200 km of shortening would have occurred in N-S direction in the Gulf of Cadiz and Alboran Sea (Dewey et al., 1989), followed by 50 km of NW-directed oblique convergence from Late Miocene until present.

During the Quaternary, uplift has occurred in the Gibraltar area, evidenced by exposed Pleistocene marine deposits; in the area of the Rharb basin however, subsidence has been observed (Cadet et al., 1977). The current-day general stress pattern shows N-S to NW-SE directed horizontal compression (Buforn et al., 1995), corresponding to the continued convergence of Africa and Eurasia.

2.3.2   Structure and stratigraphy

It was said in the introduction of this section that the overall structure of the Gulf of Cadiz area is complex. Therefore, it is appropriate to break up the description in a number of topics: onland structure and stratigraphy of the Betic-Rif orogen and foreland basins (Rharb and Guadalquivir), structure and stratigraphy of the offshore domain (the accretionary wedge, possible subduction and the mass wasting nappe or olistostrome), the presence and role of salt in the offshore domain and finally the presence of fluid migration pathways and mud volcanoes. From this topical break-up, it is already evident that the study of the region in

the past has often been divided in two fields: the shore-based approach of classical structural geology and stratigraphy, in contrast to the offshore, mostly geophysical, approach. Both have led to different, even opposing understandings of the region. Most of this discussion concentrates on the nature of the plate convergence, ranging from different types of collision mechanisms to opposing directions of supposed ongoing subduction.

The Betic-Rif orogen and foreland basins (Rharb and Guadalquivir)   The Betic-Rif orogen is the westernmost part of the Alpine orogenic belt. It is discontinuous with the western Alps due to the opening of Mediterranean basins (Durand-Delga, 1980). Michard et al. (2002) provides a very comprehensive review of the tectonic and structural history of the orogen and the Alboran Sea. They cite different models to explain the origin of the Betic-Rif orogen, divided in three categories:

- Models of collisional orogeny unrelated to any subduction zone;

- Models involving a single, NW-dipping subduction zone, extending from the Betic-Rif transect to the northern Apennines;

- Models involving a Cretaceous-Eocene, E-dipping subduction zone (Alpine subduction), followed by an Oligocene-Neogene NW-dipping subduction (Maghrebide-Apenninic subduction) with a microcontinent in between.

However, Michard et al. (2002) recognize a composite orocline including a deformed, exotic terrane (the Alboran Terrane, part of the Alkapeca microcontinent before deformation; Figures 2.4A and 2.5A) which was thrust onto two different plates (Iberia and Africa; for a reconstruction, see Platt et al. (2003)) and now form the most internal zones of the mountain chain. SE-dipping subduction of the Iberian margin (Early Cretaceous – Eocene; Figures 2.4B and 2.5B) is followed by Late Eocene – Oligocene NW-dipping subduction of the African margin (Figures 2.4C and 2.5C). Tomographic inversion indeed shows the existence of high-velocity bodies in the upper mantle beneath the Rif and Alboran Sea region, although Seber et al. (1996) attribute this to a previously thickened and then delaminated lithosphere, rather than "simple subduction". As a result of this, the thickened Alboran Terrane undergoes rifting and collapse (Figures 2.4D and 2.5D). Towards the external parts of the orogen, an accretionary prism is formed and thrust over the flexural foreland. Evidence of flexural extension in Morocco is found at the transition from the Rharb to Mamora Basin, a zone with Hercynian wrench-faults reactivated as normal faults, yielding large differences in thickness of sedimentary basin infill, and dates as syn- to post-thrust of the Rif nappes (Zouhri et al., 2002). In a later paper, Chalouan and Michard (2004) refine this model, mostly in terms of age constraints, and define the area as a subduction-subduction-transform fault triple junction. This is achieved by the merging of the two subduction zones west of the Alboran Terrane with the Azores-Gibraltar transform fault.

The units of the Betic-Rif chain are, as shown above, closely related to the geodynamic evolution, and include (e.g., Durand-Delga, 1972; Bouillin et al., 1986):

- the Internal Zones; compressional, overthrusted nappes consisting of Triassic (and older) basement and sedimentary rocks that have undergone metamorphism of Alpine origin; nappes of Paleozoic deposits partly covered by younger formations, not affected by metamorphism; Mesozoic metamorphic and Paleogene carbonate units; they represent a paleo-continental margin;

- the Flyschs or Median Zones, consisting of three groups: Cretaceous-Paleogene arkosic sediments, fine-grained Aptian-Albian sediments and Oligocene-Early Miocene flysch deposits, covering older units;

- the External Zones: in the External Rif these are mainly Cretaceous formations, with similarities to the youngest flysch unit, and also gypsiferous Trias to Upper Miocene sediments; they are thought to be a palaeogeographic transition to the Atlasic domain; in the Subbetic the deposits of the Jurassic and Cretaceous are mainly carbonates.

Chalouan et al. (2001) elaborate somewhat more on the evolution of the External Zones. Until the Late Tortonian, contraction is ongoing in the External Zones (formation of the accretionary wedge). During the late Tortonian and early Pliocene, subsidence and mild extension occurs as a result of flexural bending of the North African margin, concurrent with gravitational collapse of the accretionary wedge (referred to as a tectonic-sedimentary prism by Chalouan et al. (2001)). This happened not only in the western part of the Rif, but gravity driven nappes occur all around the Rif belt (Frizon de Lamotte, 1987). Crespo-Blanc and Frizon de Lamotte (2006) stress that the Betic and Rif external domains are, despite their major similarities, in fact very different: the thick-skinned structure in the External Rif versus the thin-skinned in the Subbetic domain. The stacking in the External Rif predates the stacking in the Subbetic; metamorphism is only occurring in part of the External Rif. Later in the Pliocene, the External Zone and its foredeep are subject to contraction again, with creation of reverse faulting. It is caused, according to Chalouan et al. (2001), by the bending of subducting slab and/or deep-seated mantle processes in the Alboran Sea. Flinch et al. (1996) show however that not all faults in the external Western Rif and Rharb Basin are related to thrust sheets, but rather to mixed extensional-compressional 'satellite' basins. This will be discussed within the offshore domain below. Also Cirac et al. (1993) noted that extension is still ongoing at present in the Rharb basin.

Structure and stratigraphy of the offshore domain (the accretionary wedge, possible subduction and the mass wasting nappe or olistostrome) The geodynamic evolution of the offshore domain is completely different from the onshore and Alboran domain. First of all, the origin is closely related to Atlantic rifting and spreading (see section 2.3.1). In the Gulf
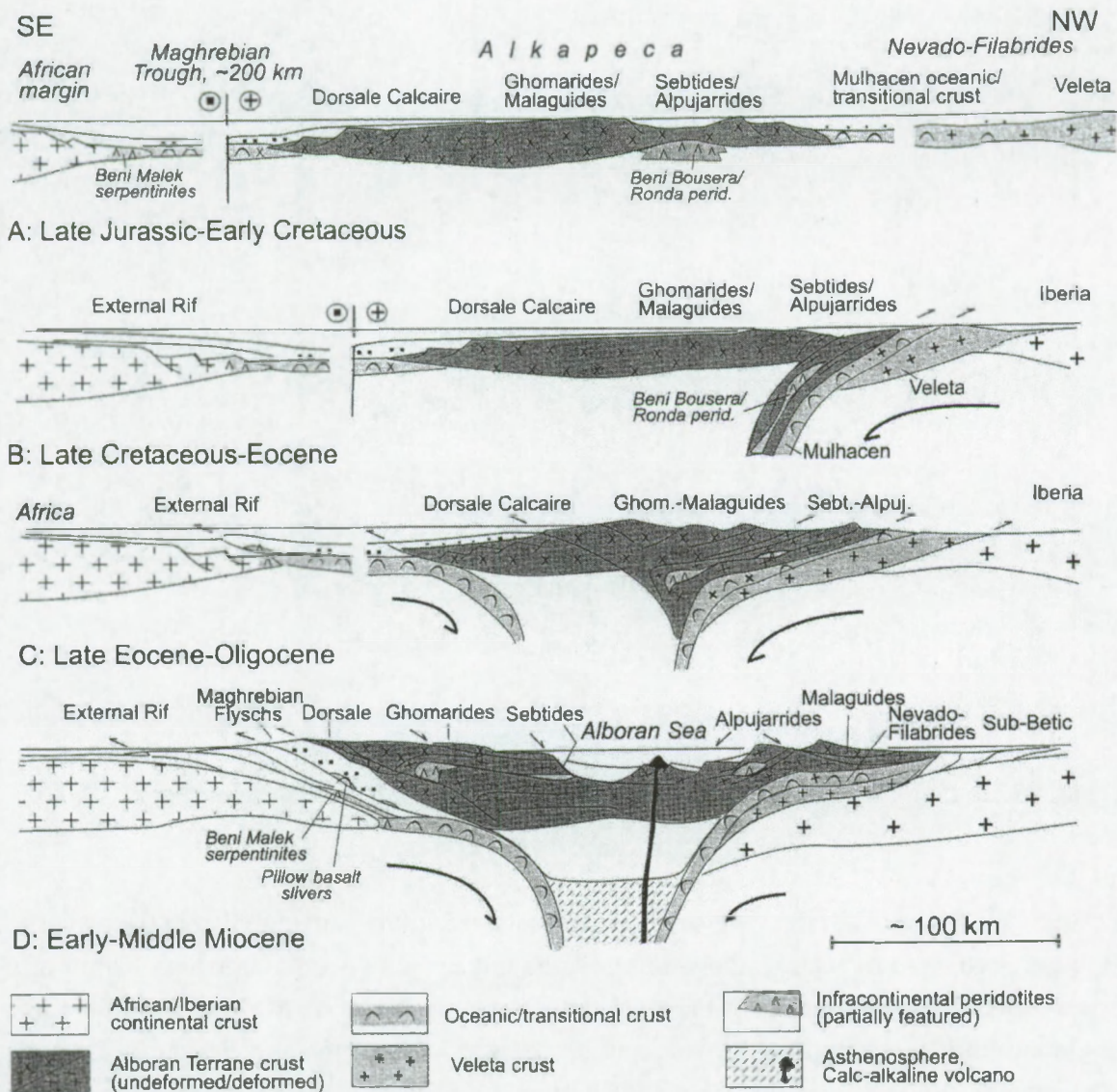
Figure 2.4: Different stages of the Betic-Rif orogeny in NW-SE transect between the Iberian and African margin, east of Gibraltar (Michard et al., 2002). In figure 2.5, the locations of these transects can be found.
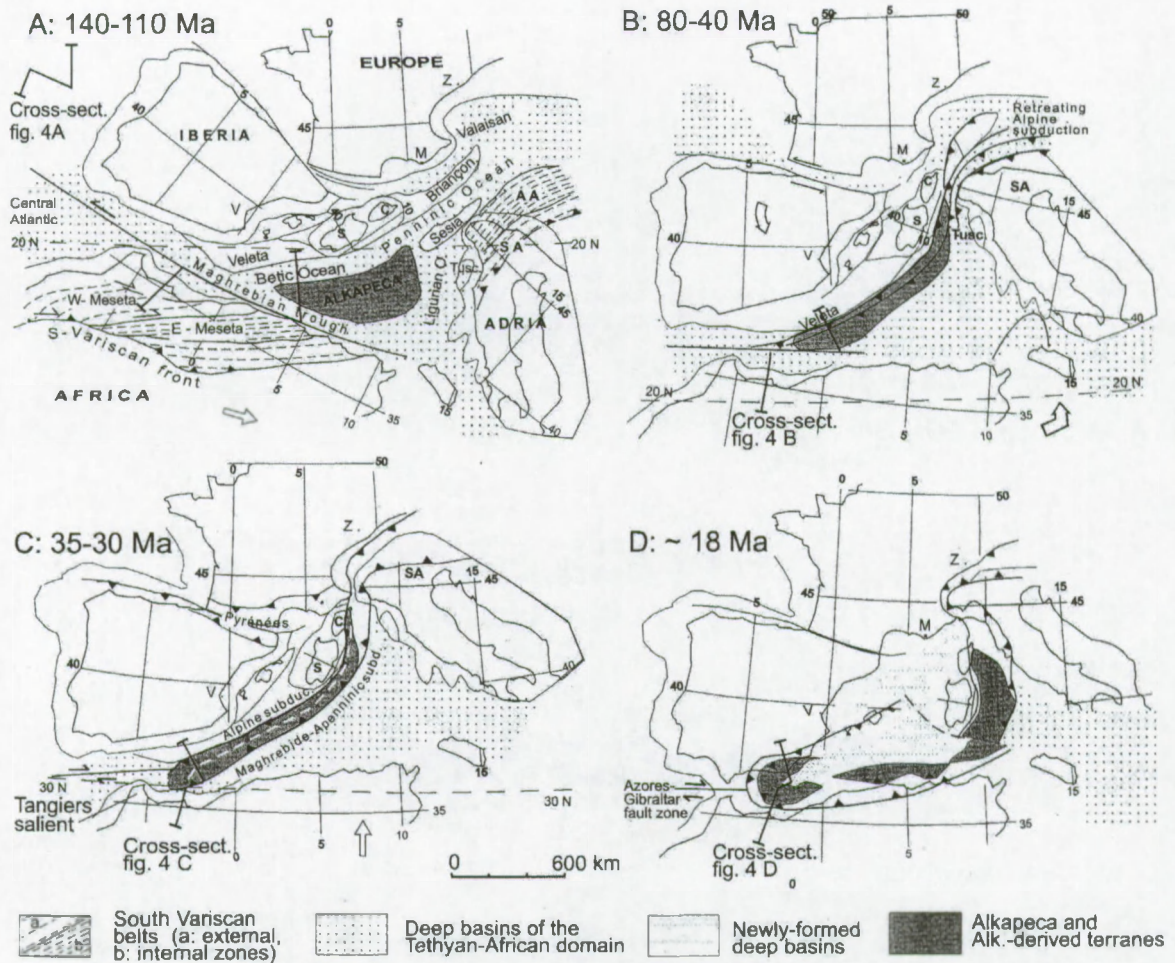
Figure 2.5: *Different stages of the Betic-Rif orogenic in plan view (Michard et al., 2002).*

of Cadiz, the Azores-Gibraltar transform runs westward to the Gorringe Bank (Tortella et al., 1997) but is covered by a large allochtonous sedimentary body over a large area. Other transects, perpendicular to the Betic-Rif arcuate chain but more directed towards the Gulf of Cadiz (Chalouan and Michard, 2004; Cavazza et al., 2004; Crespo-Blanc and Frizon de Lamotte, 2006), clearly show the accretionary wedge nature of this body. A seismic study of the crustal structure in the Gulf of Cadiz shows that its present configuration is the result of three main events (Gonzalez-Ferrnandez et al., 2001): extensional processes involving rifting and oceanic spreading from the Triassic breakup of Pangea until the Late Cretaceous; the relative westward movement of the Alboran domain producing the Betic-Rif chain and its foreland basins and emplacement of the accretionary wedge; and finally, during the Tortonian, the formation of the chaotic mass wasting nappe in the Gulf of Cadiz. The resulting crustal thickness in the center and westernmost part of the Gulf of Cadiz is reported as about 20 km. In the northeast, the thickness is about 27 km. The crustal thinning is more pronounced in N-S direction than

in E-W direction. Zeyen et al. (2005) give a more detailed model of the crustal structure based on gravity data. They report a crustal thickness of 30 km beneath the Iberian Peninsula to less than 23 km in the central part of the Gulf of Cadiz and then remains about 25 km in southern direction until the External Rif front, from where it increases to 38 km thickness beneath the northern border of the High Atlas. Zeyen et al. (2005) also report a lithospheric thickening under the Gulf of Cadiz, where the very thick lithospheric mantle, with the Moho at depths of 160 to 190 km, is interpreted as a consequence of a SW trending lithospheric slab extending from the Betics to the Gulf of Cadiz and the Gharb Basin. Such a subduction feature was not reported in onshore studies (see above) or other offshore studies. However, Gutscher et al. (2002) also favour subduction in the Gulf of Cadiz, not SW trending but directed towards the Alboran Sea. According to these authors, this is the most simple explanation for the 'seemingly contradictory observations from the complex Rif-Betic region'. Slab rollback toward the west causes extension and subsidence in the Alboran Sea. They also attribute the 1755 earthquake that destroyed Lisbon to this subduction, suggesting that the subduction is an ongoing process.

It can at least be said that consensus has more or less been reached about the nature and origin of the mass wasting body in the Gulf of Cadiz. The earliest reports date from the early 1970s (Beck, 1972; Mulder, 1973) and one of the earliest datings of the event set the age to Middle to Late Miocene (Auzende et al., 1981). Torelli et al. (1997) report the detailed first three-dimensional geometry of the mass wasting body in the Gulf of Cadiz. They discriminate a western part from an eastern part, identifying the former as a gravity deposit (debris flows, olistotromes) and the latter as a tectonic melange corresponding to the south-verging accretionary prism as the submarine extension of the Rif. Other studies have revealed more details. The northern and central part of the Gulf of Cadiz can be divided in three main areas (Bonnin et al., 1975; Auzende et al., 1981; Maestro et al., 2003; Medialdea et al., 2004): a) the eastern domain corresponds to the offshore extension of the Betic-Rifean external front and is characterized by salt and shale nappes, later affected by extensional collapse. This structure is part of the pre-Messinian orogenic wedge and include the units of the Flysch Trough, the External Betics and Rifean areas and a diapiric zone consisting of Triassic salts and Middle Miocene plastic clays and shales. b) The central domain between the Betic-Rifean front and the abyssal plain consists of allochtonous masses emplaced during the Tortonian (7.1 – 11.2 Ma (million years)) by gravitational and tectonic instability. c) The westernmost domain corresponds to the abyssal plains, where the toe of the allochtonous body is found. This domain is characterized by thrust faulting. Figures 2.6 and 2.7 illustrate this differentiation.

Only few sources discuss the structure of the NW Moroccan offshore area. Flinch et al. (1996) interprets the overall structure of the SW Iberian and NW Moroccan margin as that of an accretionary prism, emplaced in response to a westward motion of the Alboran domain during the Miocene (based on the timing of deformation) and assumes east-ward dipping subduction of normal to transitional continental crust. These authors divide the sedimentary
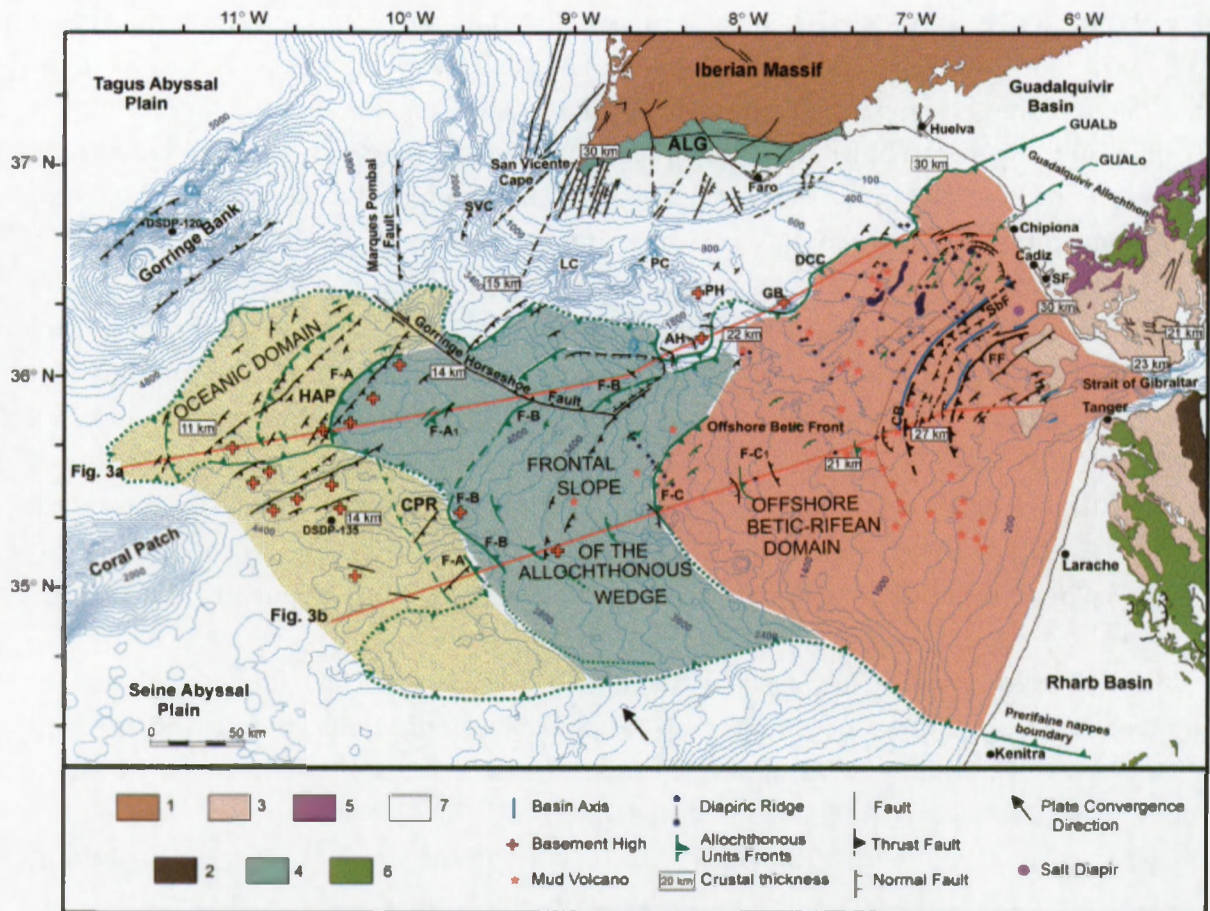
Figure 2.6: Structure of the Gulf of Cadiz accretionary wedge / allochtonous nappes, after Medialdea et al. (2004)

prism in four tectonostratigraphic units: a) the Hercynian basement, consisting of metamorphic and igneous Palaeozoic rocks, overlain unconformably by b) the Infra-Nappe, consisting of some Triassic shaly and evaporitic deposits in halfgrabens and Cretaceous to Lower and Middle Miocene sediments, c) the Prerifaine Nappe (the accretionary wedge) which consists of Triassic to Miocene sediments, but the stratigraphy is obscured by complex deformation, and d) the Supra-Nappe, seaward prograding Upper Miocene to Holocene siliciclastics.

Furthermore, Flinch et al. (1996) recognizes four structural domains in the NW Moroccan offshore area (figure 2.8): a) the offshore Tanger-Asilah fold and thrust belt: this is the most internal part of the accretionary wedge, with west-vergent folds and thrusts with NNW-SSE strikes (which is parallel to the axis of the Gibraltar Arc). b) The offshore Larache extensional zone: the westward extending thrusts and folds from the offshore Tanger-Asilah fold and thrust belt are here transected by NW-SE trending SW-dipping low-angle lystric normal faults. The extensional basins are bounded by anastomising lystric faults that sole out into a basal low-angle detachment which offsets the top of the accretionary wedge. The result is
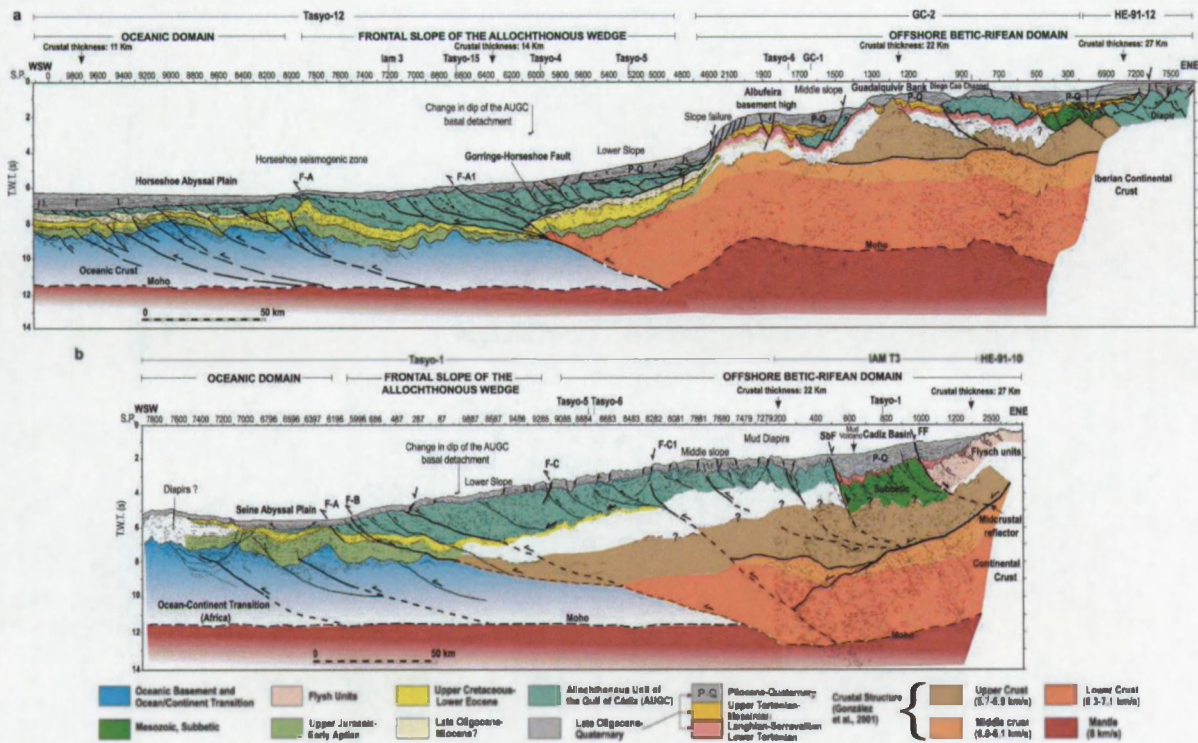
Figure 2.7: Structure of the Gulf of Cadiz accretionary wedge / allochtonous nappes, after Medialdea et al. (2004). Location of the profiles correspond to '3a' and '3b' in figure 2.6.

the presence of extensional horses. E-W oriented sections show strongly rotated blocks on the hanging wall of the low-angle extensional detachments. The overlying sediments show significant growth. E-W oriented shale ridges are present in the central part of this area and are caused by shale withdrawal induced by extensional displacement. c) The offshore Rharb frontal imbricates – an extensional-compressional zone: this is the frontal part of the accretionary complex located west of the Rharb basin and the northernmost portion of the Rif foredeep. There is a combination of compressional and extensional elements, with NW-SE strikes. d) The foredeep, offshore Rabat, where the Infra-Nappe units plunge beneath the accretionary wedge. Some vertical faults are related to the flexural extension caused by the tectonic loading of the wedge.

The seismic stratigraphy of the Gulf of Cadiz is presented in detail by Maldonado et al. (1999). The basement of the Gulf of Cadiz is made up of Palaeozoic rocks derived from the Hercynian orogeny. The identification of the Mesozoic and lower Cenozoic units are based on wells and multi-channel seismics from the northernmost part of the Gulf of Cadiz. These units are present in half-graben structures related to the Atlantic rifting and were affected by inversion during the Neogene compression. Triassic evaporites have acted as detachment planes (see above) for the formation of the Neogene mass wasting body. Two main Triassic

(a)   (b)
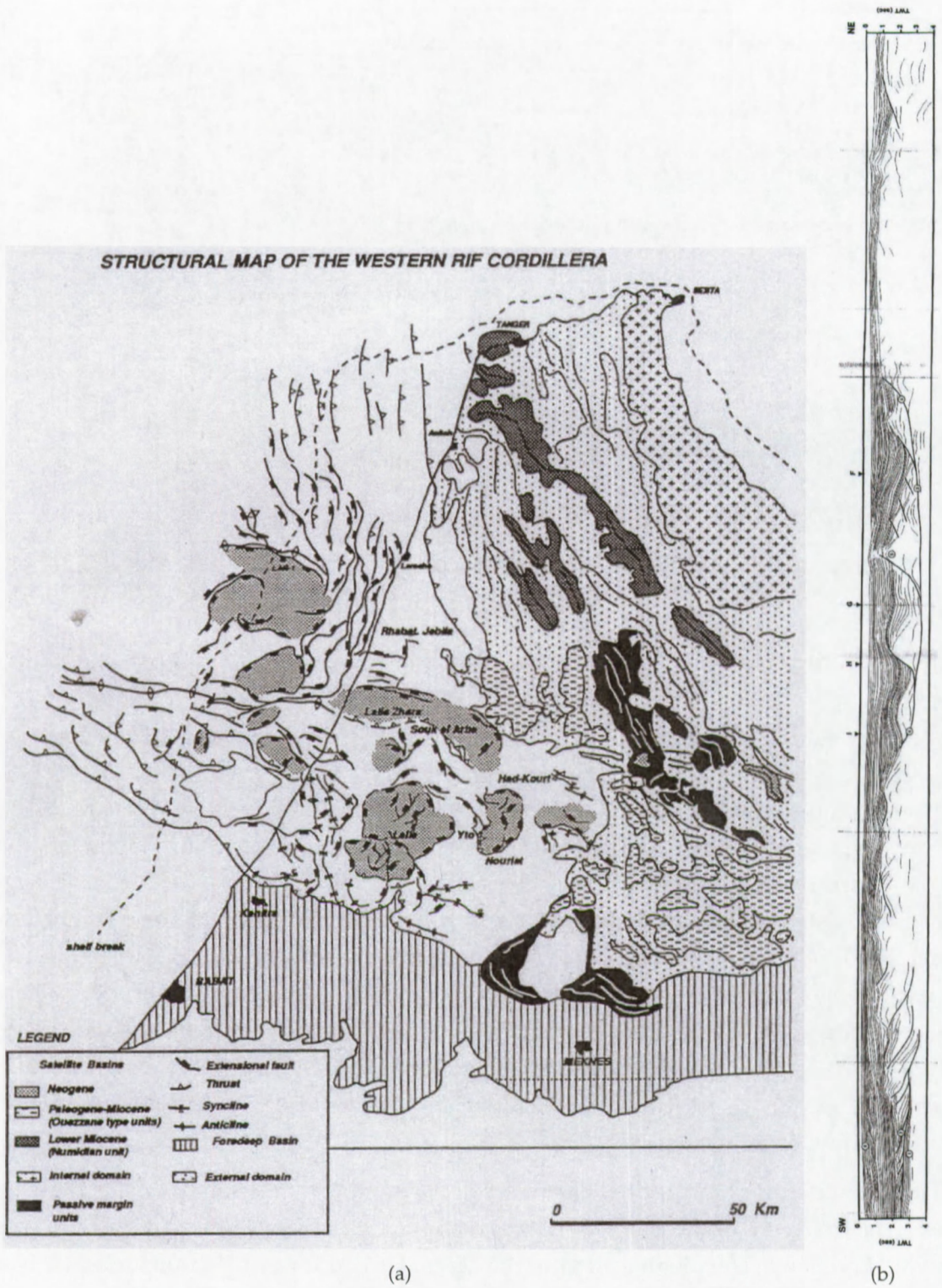
Figure 2.8: *Structural features of the on- and offshore NW Morocco (a) with a transect over the upper slope (b). Figures after Flinch et al. (1996)*

units are present showing a typical Germanic-type facies: a lower siliciclastic unit and an upper evaporitic unit (salts, gypsum and shallow water carbonates). The upper unit is the source of many diapiric structures. The Lower to Middle Jurassic is represented by tilted blocks detached from the Upper Triassic unit and was part of the carbonate platform along the southern Iberian margin in the Tethys domain. The Upper Jurassic and Lower Creatceous unit is interpreted as a sequence of synrift carbonate fans, debris aprons and slope facies filling the half-grabens. The middle Cretaceous has a strong seismic basal unconformity with variable seismic facies depending on the location. Silts and shales have been encountered in drill holes as well as polygenic conglomerates, indicating slope facies interbedded with footwall fans, grading upwards into aggrading slope and basin deposits. The Upper Cretaceous to uppermost Eocene represents the final episode of an extensional and passive margin evolution. The unit is absent at many places. Upper Oligocene to Lower Miocene units are a prograding to aggrading carbonate shelf platform developed over the entire margin. The top of the unit is a regional unconformity that acted as paleoslope for the generation of the Upper Miocene turbidite system, while basinwards, it is found below the mid-Miocene mass wasting body.

The Neogene and Quaternary are characterized by seven main stratigraphic units, differentiated on the basis of their relationship to the mass wasting body. Unit M1 is the pre-olistotrome unit (Langhian-Serravalian and lower Tortonian). It is overlain by the olistostrome in a large part of the Gulf of Cadiz. The unit is generally progradational to aggradational and consists of marly clays, fine-grained limestones and green clays with pyrite and glauconite. The overpressured ductile marly clays may account for marl diapirism that occurred in the central part of the Gulf of Cadiz. The syn-olistostrome unit M2 (upper Tortonian) is well recognized near the front of the olistostrome and on top of the olistostrome where small depressions are present. The unit consists of plastic grey clays with abundant glauconite and pyrite. The next unit is the olistostrome unit, which has a chaotic seismic facies. Internal angular unconformities are due to wedge-shape thrusting. Overthrusting occurred as well in the body. Backthrusting and extension is observed at the back of the olistostrome. It is believed that over- and backthrusting are coeval processes. The position of the olistostrome is governed by the previous morphology. Unit M3 (Messinian) covers the olistostrome and fills the lows in the relief. The lithology consists of clays and fine-grained sand lenses that are known as gas fields in the northern Gulf of Cadiz.

The Lower Pliocene unit P1 has a basin-wide erosional unconformity as a base. It has parallel, continuous and high-amplitude reflections. The unit consists of hemipelagic clays with some interbedded sandy clay turbiditic deposits. In the deeper parts of the basins, deep-sea fans are present. The Upper Pliocene unit P2 has an aggradational to onlapping lower boundary, while the top is subhorizontal. The internal seismic facies is more transparent, with discontinuous reflectors at the bottom, and with higher amplitude, interfingered reflectors at the top. The unit consists of hemipelagic clays, turbidite sands and current-drift deposits. The
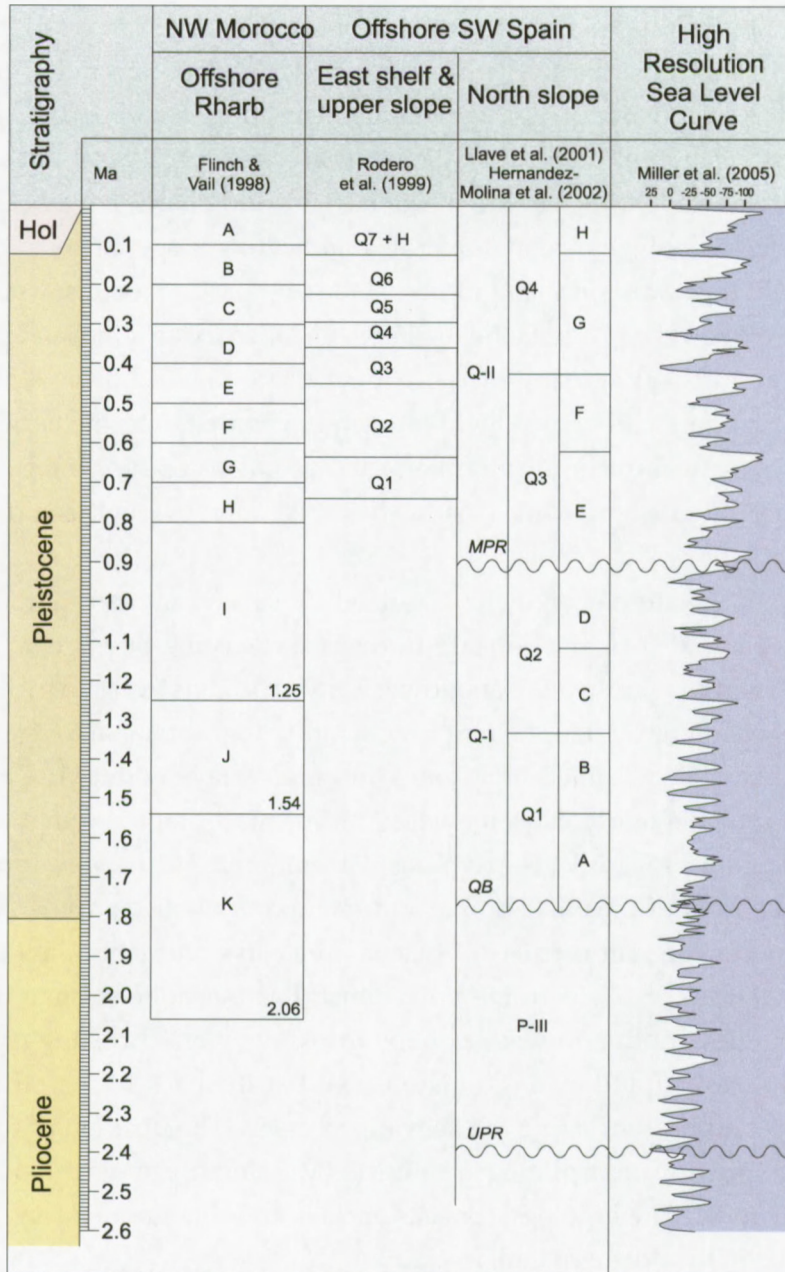
Figure 2.9: Compilation of the stratigraphic units of the Pliocene and Quaternary based on different literature sources. MPR = Mid-Pleistocene Revolution. QB = Quaternary Boundary; UPR = Upper Pliocene Revolution.

lower boundary of the Upper Pliocene - Quaternary (Unit P/Q) is a basin-wide unconformity. The basal reflectors onlap and prograde basinwards. The facies and thickness variations are controlled by the structure of the margin, the sediment sources and the Plio-Quaternary eu-static sea-level fluctuations (see also Rodero et al., 1999). This is an interesting property since this could allow correlation with the data off NW Morocco. The Mediterranean Outflow Water is responsible for the development of drift deposits and erosional surfaces (Nelson et al., 1999).

In the northern part of the Gulf of Cadiz (the Faro-Albufeira contourite system) Llave et al. (2001) identified two third-order eustatic cycles (QI, QII) in the Quaternary sedimentary record, consisting of eight fourth-order cycles. QI is an aggradational depositional sequence, while QII is a progradational depositional sequence. The boundary between both is inter-preted as being the sea-level fall of the Mid Pleistocene Revolution (MPR) around 900-920 ka (thousands of years) ago. The two last fourth-order sea-level cycles from the Late Pleistocene - Holocene (180 ka) were recognized on the shelf and slope off Cadiz, in the northeastern part of the Gulf of Cadiz (Somoza et al., 1997).

Flinch and Vail (1998) identified nine Pleistocene fourth order glacio-eustatic cycles in the sequence stratigraphic analysis on seismic data of the shelf and slope south off the Rharb (south of the EA field). The Upper Miocene units are described as anoxic pyrite bearing marls with occasional sand and siltstone beds. The Lower and Middle Pliocene units bear witness of continued pelagic sedimentation. The Upper Pliocene units bear evidence of a strong transgressive period, with a strong landward shift of the system. Hence this unit is not reported in the offshore. The Pleistocene is characterized by mud dominated prograding sequences, changing to an aggrading progradation in the Late Pleistocene. In the study area off Larache, data from one well (LAR-1) is present, which is reproduced by Flinch (1993). The well is located in the stratified Upper Miocene to Pleistocene sediments and only reports of lithology and Globorotalia biozones are given. The lithology corresponds largely to the above description. The Pleistocene has additional coquinas and sandstone levels, which could be turbiditic in origin.

Cirac et al. (1993) had recognized anticlinal structures with large radius curvatures and series of small normal faults on seismic data on the shelf off Larache to Kenitra. The folding structures have axes that run E-W and continue on land (e.g. the Lalla Zohra anticline, south of Moulay Bou Selham). The normal faults break the anticlines up in steps, and with that, resemble structures on the northern edge of the Rharb Basin on land related to subsidence. Morley (1992) describes the structure of the onshore Larache-Acilah area. At this location, the thrust nappes transition to a chaotic melange below the post-nappe deposits offshore.

Fluid migration and mud volcanism Fluid migration in continental margins and accre-tionary wedges is a process with importance for geohazards (slope stability, earthquake trig-gering, ...), geochemistry (redox processes, cementation and dissolution of minerals, ...), geother-

mics (stability of subsurface gas hydrates), fossil energy (production, storage and leakage of hydrocarbons), etc...

The structural nature of the Gulf of Cadiz, with its plate boundaries, Betic-Rif orogen, accretionary wedge and mass wasting body evidently results in the high abundance of faults and fractures. Therefore, the hydrogeological situation of the area is difficult to study as a whole, yet different parts of it have been addressed in literature, although mostly related to mud volcanism, hydrocarbon seepage at the seafloor and to slope stability.

Mud volcanoes in the Gulf of Cadiz were first discovered in 1999 (Gardner, 2000, 2001) and by now, over 30 mud volcanoes have been identified (Pinheiro et al., 2003; Somoza et al., 2003, e.g.). The Guadalquivir Diapiric Ridge (GDR) mud volcano field and the Tasyo mud volcano field are related to diapiric ridge development and to lateral compressional stress generated at the front of thrust anticlines within the olistostrome/accretionary wedge body (Somoza et al., 2003). The Deep Portuguese Margin (DPM) (Pinheiro et al., 2003) field is situated in the distal part of the olistostrome body at depths between 2 km and 3.2 km. So far, three mud volcanoes were identified in this field. The Spanish-Moroccan (SPM) field lies at depths between 600 and 1200 meter within the accretionary prism but outside the olistostrome unit area. The El Arraiche (EA) mud volcano field, offshore the city Larache, is the south-eastern continuation of the Spanish-Moroccan field (Van Rensbergen et al., 2005b). More recent studies have addressed the geochemical and microbial environment in these mud volcanoes (Stadnitskaia et al., 2006; Niemann et al., 2006; Hensen et al., 2007; Stadnitskaia et al., 2008). In chapter 4, mud volcanoes will be discussed in more detail.

Other fluid escape related features, such as carbonate hardgrounds and carbonate chimneys, were observed on many locations in the northern part Gulf of Cadiz (e.g., Diaz-del Rio et al., 2003; Somoza et al., 2003; Leon et al., 2006). Diaz-del Rio et al. (2003) were the first to report authigenic carbonates of ankerite, ferrous dolomite and calcite composition, associated with iron oxides. The carbon isotopic composition indicated mixed biogenic and thermogenic methane in parent fluid. The close association of dolomite micrite and iron oxides was interpreted as indicative for the formation under the influence of anaerobic methane oxidation consortia (Boetius et al., 2000). Somoza et al. (2003) had reported chimneys with calcitic and ferrous dolomitic composition, derived from the Hesperides mud volcano (Iberian margin).

Lee and Baraza (1999) performed a geotechnical study of a part of the northern slope of the Gulf of Cadiz and concluded that the studied part is stable under static loading, but that seismic activity or storm waves may cause destabilization resulting in slope failure. Furthermore, the presence of gas and subsurface overpressure may increase the risk. Mulder et al. (2003) conclude from geomorphological data that the entire upper slope area off southwestern Spain is an unstable contouritic levee, where sediment deformation and destabilization is not unlikely under tectonic activity. Earthquake activity is not uncommon in the Gulf of Cadiz (Fonseca, 2005).
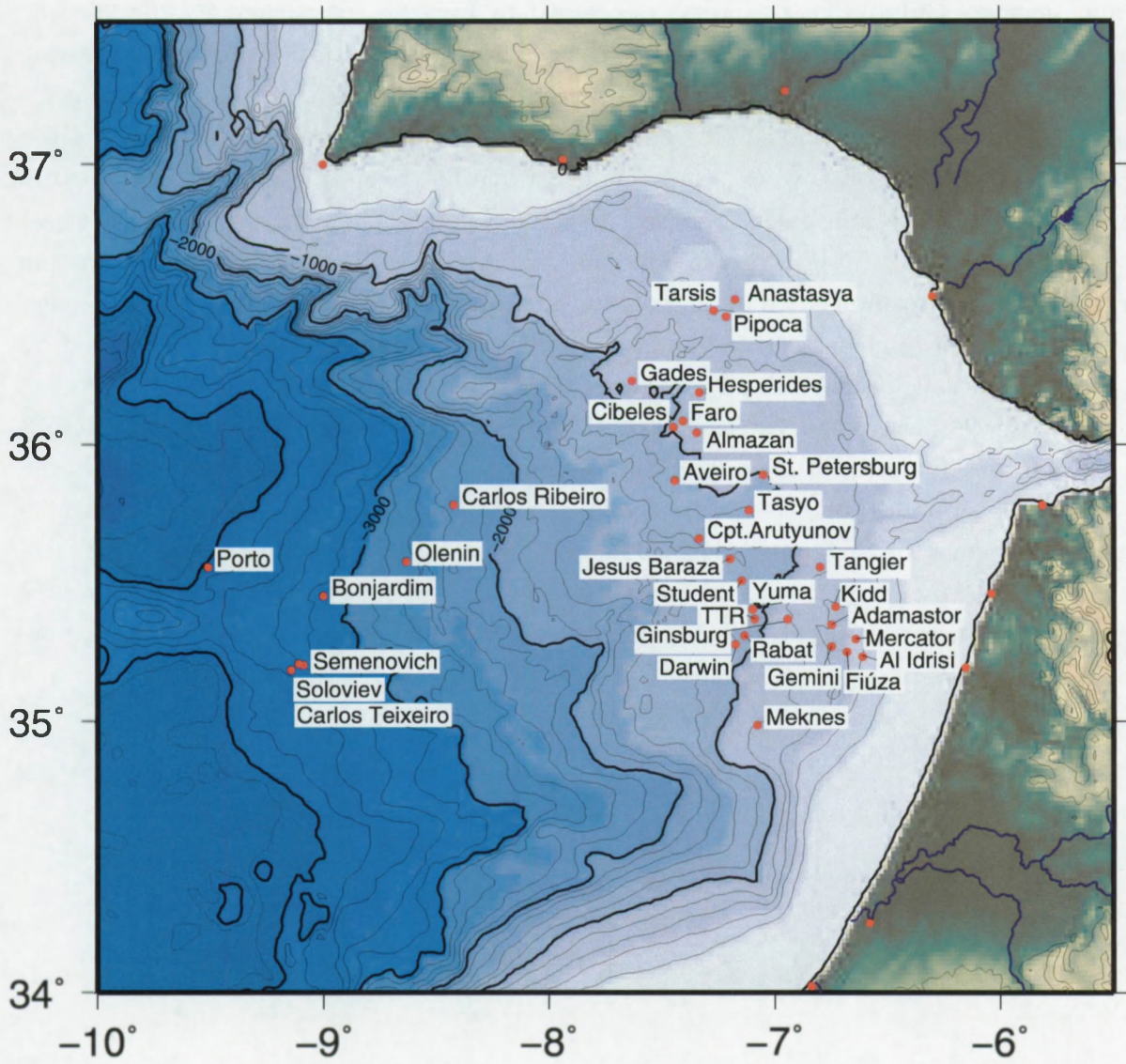
Figure 2.10: *Mud volcanoes in the Gulf of Cadiz. Compiled from references in text and during cruises.*

Salt deposits   A last factor that could be important in this study, is the presence of salt in the subsurface. The buoyancy of salt leads to the formation of salt domes, diapirs and walls in the subsurface. These features typically pierce the overburden, can relate to fault structures and influence subsurface fluid flow. It can also act as a seal for hydrocarbon migration.

Maestro et al. (2003) and Medialdea et al. (2004) show the presence of salt and shale diapirs in the northern Gulf of Cadiz. The salt deposits date from the Triassic and Middle Miocene and have played a key role in the large-scale slope failure (i.e., the creation of the mass wasting nappe). They show the presence of 'down-to-basin' lystric growth faults that merge into the top salt. The faults accommodate the gliding of the overburden along the salt and/or shale detachments. Further oceanwards, contractional structures are encountered, while transform faults connect the upslope extensional and downslope contractional features. Reports of salt on the upper slope off NW Morocco have not been found. In the past few years, gypsum crystals have been sampled in the crater of Mercator mud volcano (in the study area), together with anomalously high salt concentrations in pore waters (Hensen et al., 2007). This gives an indication that salt sheets, walls or diapirs likely exist in the subsurface.

Flinch (1993) describes Triassic shales and evaporites intermixed with Upper Cretaceous marls, forming the 'marnes à gypse' onshore Morocco, in the External Rif and Rharb basin. In the south-central Rif, Triassic breccia levels were found in wells, representing the basal detachment of mass wasting units, which could be equivalent, at least in function, to what Maestro et al. (2003) reports in the North of the Gulf of Cadiz. This shows that passive margin-type allochtonous (because of intermixed or brecciated nature) evaporites were emplaced before the Neogene compression and collapse.

Chapter 3

Methodology

As previously stated in the introduction, a multi-disciplinary approach is used to better understand fluid flow processes in sediments. Here, the different techniques used in this study will briefly be presented.

3.1 Geophysical data

Visualizing the subsurface in a way relevant to stratigraphy and structures (Chapter 4) can be achieved by seismic reflection methods. These methods are based on emitting an acoustic pulse and recording the echo of that pulse. The acoustic pulse is reflected at geological surfaces, e.g. stratigraphic (lithologic) boundaries. To be more precise, the reflection occurs at a surface where the acoustic impedance changes. The acoustic impedance Z [kg.m^{-2}.s^{-1}] is defined as

$$Z = \rho\, v_{\text{sed}} \tag{3.1}$$

with ρ [kg.m^{-3}] the density of the rock or sediment and v_{sed} [m.s^{-1}] the acoustic velocity in that rock or sediment. So, a change in impedance can be caused by a change in density or acoustic velocity. After being reflected, the signal is recorded and processed to be ready for interpretation.

The acoustic source mainly used in this study is a multi-electrode sparker. With this tool, an acoustic pulse is created by an strong electric discharge (a spark), between the tips of the electrodes and a shielded mass. The waveform of the acoustic pulse is high-frequent and thus allows to make a high-resolution image of the subsurface. Alternative sources used comprised a sleeve air gun with lower output frequency than the sparker, as well as a chirp echosounder yielding a very high frequency (supplied by Ifremer, Brest, France). The recording was done with a single channel streamer, consisting of 4 groups of 2 hydrophones in a zero-offset configuration.

The incoming signals undergo electronic band-pass filtering to eliminate high-frequent noise and low-frequent ship and electrical noise. The data are recorded in Elics format in a Delph Seismic system (Triton Elics Inc.) and transformed to the SEG-Y standard format. The post-processing of the seismic data recorded in 2002 was done on a Sun Ultra II Workstation (200 MHz UltraSparc-I processor, 256 MB RAM) with SunOS 5.6. Data acquired in 2005 and 2007 were processed on a Dell Precision 360 (Intel Pentium 4 3GHz, 2 GB RAM) with Red Hat Linux (kernel 2.4.21-15EL). The data were processed in two steps. First a static signal shift was attributed to compensate for swell. Second, the actual signal processing was done to enhance the signal for interpretation purposes. This includes bandpass filtering, deconvolution and signal amplification. The detailed processing parameters are reproduced in Appendix A.

Other data used in the study include multibeam bathymetry and side scan sonar imagery. Multibeam bathymetric sounding is a technique used to produce a 3D elevation model of the seafloor. It is based on the emission and reception of acoustic pulses by an array of transducers. It is capable of determining the depth of the seafloor under and sideways of the ship. Side scan sonar imagery is also an acoustic technique. It uses a tool that is towed a certain distance above the sea floor. It emits a signal and records the backscatter sideways. Because

of the low elevation of the source, highs and lows in topography will reflect variable amounts of acoustic energy, which leads to the creation of shadows. Besides this, sediment properties can also affect the backscattered signal. The result is that the data retrieved can be used to identify morphologies on the seafloor, topographic features, and (near-)surface sedimentary properties. These data were available in processed form, so the processing will not be discussed.

3.2 Mineralogical and geochemical methods

Different techniques were used for the investigation of authigenic carbonates (Chapter 5).

X-Ray Diffraction (XRD) analysis of selected samples was performed on bulk mill powdered samples ($0.2 - 0.5$ cm^3). XRD analysis was executed with a Philips PW 2236/20 with Co-Kα radiation (0.05 Å step size, $15 - 78$ degree angles, operated at 45 kV, 30 mA). XRD analysis allows the identification of minerals present in the sample (qualitative).

The same powders (23 sub-samples) were used for bulk geochemical analysis. Apart from deducing general trends in the data, the goal of these analyses was also to seek trends between variables within single specimens to assess whether conclusions could be made about the growth of carbonate crusts and chimneys.

Atomic absorption spectroscopy (AAS) measurements were carried out on Varian AA6 and AA-1475 atomic absorption spectrometers. 1 gram of bulk material of each sample was dissolved using 1N HCl. The insoluble residue (IR) after sample preparation is reported in weight percent of the bulk sample. The elemental contents of Ca, Mg, Fe, Al are reported in weight percent of the soluble part (SP; equation 3.2). Mn, Sr, Na, K, Zn and Pb are reported in ppm (of the soluble part).

$$SP = (1 - IR) * 100 \tag{3.2}$$

This data presentation was chosen because of the large overall variation in IR content (9.51% - 29.80%; Table 5.1), which variably affects the relative contents of elements in different samples and therefore makes the between-sample comparison of the elemental contents difficult. By normalizing all geochemical parameters to the soluble part, this effect is compensated for. There were no strong correlations between K or Al and other variables; this could indicate that there is no significant co-elution of elements from non-carbonate components such as clays. The mole fractions are calculated based on the most abundant divalent ions only (Ca, Mg, Fe, Mn, Sr).

Stable carbon and oxygen isotope analysis was done on small sub-samples taken with a hand-held micro-drill. All data represent bulk analysis as individual cements are too small in volume to be sampled separately. The analyses were done at the University of Erlangen, Germany. Carbonate powders were first treated with 100% phosphoric acid (density < 1.9

g.cm^{-3}, (Wachter and Hayes, 1985)) at 75 °C using a Kiel III on-line carbonate preparation line. The liberated CO_2 gas was then analyzed with a ThermoFinnigan 252 mass spectrometer. The Sol II isotope standard was used. Reproducibility is better than ±0.13 ‰ for $\delta^{13}C$ and ±0.08 ‰ for $\delta^{18}O$. All reported numbers are relative to the V-PDB standard, except indicated otherwise.

Thin sections of crusts and chimneys were examined, using conventional transmitted light microscopy. Samples were impregnated with blue epoxy to visualize the porosity distribution. All thin sections were half stained with an Alizarin Red S – potassium-ferricyanide mixture (Dickson, 1966) to reveal carbonate mineralogy and the presence of ferroan phases. For cathodoluminescence examination, an cold cathode luminescence instrument (K.U. Leuven) was used. Samples were studied for the existence of measurable fluid inclusions — unfortunately none were suited for analysis.

3.3 Numerical methods

3.3.1 The finite element method

Many physical processes can be expressed as (partial) differential equations (PDEs). These are equations that express the change of a magnitude with respect to a certain variable, mostly spatial or temporal (e.g., Farlow, 1993). Solving these PDEs is a specific discipline of mathematics. Designing an analytic solution for most PDEs is impossible — only for the most simple PDEs exact solutions are known. Therefore, PDEs are solved using numerical methods to obtain approximate solutions. The two most used methods for numerically solving PDEs are the finite difference method (FDM) and finite element method (FEM).

Both methods try to obtain solutions for the given PDE in discrete points (most commonly in space), instead of an analytical continuous solution. The collection of the discrete points is called a grid or mesh. There are very advanced methods for building meshes because the quality of the mesh is important for the quality of the final PDE solution. On the other hand, the resolution of the mesh is also limited by computing power. For this work, the best computer available for solving PDEs was a machine with 4 Xeon processors at 2.4 GHz each and 6 GB of high-speed Random Access Memory (RAM) available. During the work, all meshes were scaled so that all operations could be executed within the available memory space. This prevents swapping operations between RAM and hard disk. Doing so, the resolution of the mesh was still sufficiently high to obtain smooth solutions.

Besides the governing PDEs, there are boundary conditions to be taken into consideration. The boundary conditions are those conditions that are imposed on the edges of the mesh. For instance, if the temperature in the subsurface is modeled, an imposed boundary conditions could be the temperature at the seafloor, or a constant heat flux as lower boundary.

The finite element method solves a set of PDEs by applying different steps. First, a mesh is created, consisting of a number of elements. Each element is bound by a number of nodes. Next, within each element, the solution of a PDE variable is approximated by a linear combination of the solutions of the variable at the element nodes. For an unknown scalar u at a given position in the element, this is

$$u \approx \sum N_a \tilde{u}_a \tag{3.3}$$

where $\tilde{u}_a$ are the variables for each of the element nodes and N_a are the coefficients of the linear combination which are called shape functions. These shape functions are a function of the local coordinates. With this numerical discretization, referred to as the Galerkin method, the differentiation of the PDE variables is now transformed into a differentiation of the shape functions. Equation 3.3 is back substituted in the governing PDE and leads to a formulation of the PDE in terms of the nodal values $\tilde{u}_a$. This substitution also leads to an error, or the residual, since equation 3.3 was an approximation. However, the Galerkin weighted residual method says that the weighted average of this residual is required to vanish over the domain of the equation (e.g., Zienkiewicz et al., 2005). The residuals are multiplied with the shape functions and integrated over the domain and equalled to zero. Finally, the result is a set of linear algebraic equations: one equation for each element and variable. The form of this is

$$[K][u] = [f] \tag{3.4}$$

with $[K]$ the matrix containing the coefficients of the linear combinations (the stiffness matrix), $[u]$ the row matrix containing the unknowns of each node, and $[f]$ the row matrix derived from the independent source terms of the original PDEs. Different approaches for solving the set of equations exist: direct (involving elimination and substitution) and iterative methods (involving the minimizing of a solution residual). Solver algorithm design constitutes an intense field of research in mathematics. The solution of this calculation yields a value for each parameter in each node; for each point in between the nodes, the linear combination (equation 3.3) — hence the PDE is numerically solved. For an in-depth description of the Finite Element Method, please refer to Smith and Griffiths (2004) and Zienkiewicz et al. (2005)

In this work, all PDEs are solved through this finite element method. Initially this choice was made because mathematically, the FEM approach is more exact than the FDM approach. In the FEM approach, the PDE solution is being approximated, while in the FDM method, the PDEs themselves are approximated which therefore already introduces an error before the solution step has started. The Finite Element Method therefore results in more robust quality of the the approximation between mesh points compared to the Finite Difference Method.

Initially, a self-written code was used to solve simple PDE problems, but as the problems became more complex, not only in terms of coupled equations, but mostly in size of the prob-

lem (i.e. mesh resolution, requiring more adequate meshing and refining algorithms), the software package Comsol Multiphysics[1] was used.

3.3.2 Subsurface fluid flow modeling

The ability of fluids to flow through a porous material, e.g. pore waters through a sediment, can be described by Darcy's Law:

$$Q = -KA\frac{dh}{dl} \tag{3.5}$$

with Q [$m^3.s^{-1}$] the total discharge of fluid through a cross-section, A [m^2]. $\frac{dh}{dl}$ [dimensionless] is the hydraulic gradient which expresses the change in hydraulic head dh [m] over a distance dl [m]. Because a fluid flows from regions with a high hydraulic head to regions with a low hydraulic head, a negative sign is present in the equation. K [$m.s^{-1}$], the hydraulic conductivity, expresses how fast a fluid can move through a porous material. The hydraulic conductivity is a material constant, but also depends on the fluid viscosity and the specific weight of the fluid, or

$$K = k_i\frac{\gamma}{\mu} \tag{3.6}$$

where γ [$kg.m^{-2}.s^{-2}$] is the specific weight ($\gamma = \rho_f g$, with ρ_f [$kg.m^{-3}$] the fluid density and g [$m.s^{-2}$] the gravitational acceleration), μ [$kg.m^{-1}.s^{-1}$] is the dynamic fluid viscosity and k_i [m^2] is the intrinsic permeability depending on the porous material alone.

The Darcian flux q [$m.s^{-1}$] is the discharge per unit area, or the amount of fluid flowing through a unit cross-sectional area, and therefore

$$q = \frac{Q}{A} = -K\frac{dh}{dl} \tag{3.7}$$

The hydraulic head, or total head h [m] is composed of the pressure head and elevation head. The pressure head h_p [m] is derived from the pressure p [Pa] measured at a certain depth in a fluid column, or $h_p(z) = p(z)/(\rho_f g)$. The elevation head $D(z)$ [m] is the elevation of a certain point above a certain reference level z_0, or $D(z) = z - z_0$. In this work, calculations were done in function of pressure p and in a two-dimensional framework and therefore the one-dimensional equation 3.7 is converted to

$$q = -K\nabla\left[\frac{p(z)}{\rho_f g} + D(z)\right] \tag{3.8}$$

---

[1]Information available from http://www.comsol.com

or with the datum level set to zero, $z_0 = 0$,

$$q = -K\nabla \left[\frac{p(z)}{\rho_f g} + z \right] \tag{3.9}$$

Conservation of mass requires that the difference of mass (= fluid) inflow and outflow in any infinitesimal box equals the change in mass storage with time, or

$$\frac{\partial(\Theta\rho_f)}{\partial t} + \nabla(\rho_f q) = 0 \tag{3.10}$$

with Θ the porosity (dimensionless). The first term is an expression for the change in mass storage with time: the mass storage change can be achieved by altering the fluid density or porosity of the sediment. The fluid density change is related to the compressibility of the fluid, and the sediment porosity change is related to the compressibility of the solid matrix. The first term of equation 3.10 can be expanded (chain rule) as

$$\frac{\partial(\Theta\rho_f)}{\partial t} = \rho_f \frac{\partial\Theta}{\partial t} + \Theta \frac{\partial\rho_f}{\partial t} \tag{3.11}$$

The isothermal fluid compressibility β [Pa^{-1}] describes the decrease in volume with increasing pore fluid pressure, per unit volume, or the increase in density with increasing pressure, or

$$\beta = \frac{-1}{V_w} \frac{\partial V_w}{\partial p} = \frac{1}{\rho_f} \frac{\partial\rho_f}{\partial p} \text{ which can be expanded as} \tag{3.12}$$

$$\beta = \frac{1}{\rho_f} \frac{\partial t}{\partial p} \frac{\partial\rho_f}{\partial t} \text{ which can be rearranged as} \tag{3.13}$$

$$\frac{\partial\rho_f}{\partial t} = \rho_f \beta \frac{\partial p}{\partial t} \tag{3.14}$$

in which V_w [m^3] is the fluid volume and t [s] the time.

The soil compressibility coefficient α [Pa^{-1}] (Bear, 1972) is defined as the decrease in volume of the soil under increasing effective stress, or

$$\alpha = \frac{-1}{V_b} \frac{\partial V_b}{\partial \sigma_e} \text{ leading to} \tag{3.15}$$

$$\alpha \frac{\partial\sigma_e}{\partial t} = \frac{-1}{V_b} \frac{\partial V_b}{\partial t} \tag{3.16}$$

with V_b [m^3] the bulk volume, σ_e [Pa] the effective stress. Next, an important assumption is that the solid volume V_s [m^3] is constant, or $V_s = (1 - \Theta)V_b =$ constant. Differentiating over time leads to

$$\frac{\partial V_s}{\partial t} = \frac{\partial[(1 - \Theta)V_b]}{\partial t} = (1 - \Theta)\frac{\partial V_b}{\partial t} - V_b\frac{\partial\Theta}{\partial t} = 0 \tag{3.17}$$

which can be rearranged as a function that expresses that the bulk volume change is solely due to porosity change:

$$\frac{\partial V_b}{\partial t} = \frac{V_b}{1 - \Theta} \frac{\partial \Theta}{\partial t} \qquad (3.18)$$

The compressibility of water at 25 °C is 4.4×10^{-10} Pa^{-1} and assumed constant. Ranges of compressibility are compiled in table 3.1.

Combining equations 3.16 and 3.18 results in

$$\alpha \frac{\partial \sigma_e}{\partial t} = \frac{-1}{1 - \Theta} \frac{\partial \Theta}{\partial t} \qquad (3.19)$$

which expresses that an increase in effective stress will result in a decrease of porosity. Substitution of the total stress σ, defined as the sum of effective stress and pore pressure, $\sigma = \sigma_e + p$, into the last equation gives

$$\frac{\partial \Theta}{\partial t} = -(1 - \Theta)\alpha \left(\frac{\partial \sigma}{\partial t} - \frac{\partial p}{\partial t} \right) \qquad (3.20)$$

Because the total stress is constant, $\frac{\partial \sigma}{\partial t} = 0$ and thus

$$\frac{\partial \Theta}{\partial t} = \alpha(1 - \Theta)\frac{\partial p}{\partial t} \qquad (3.21)$$

Now the equations 3.9, 3.14 and 3.21 can be used for substitutions in equation 3.10 (taking

Table 3.1: *Range of values of compressibility*

	Compressibility, α [Pa^{-1}]	Source
Clay	$10^{-6} - 10^{-8}$	a
Sand	$10^{-7} - 10^{-9}$	a
Gravel	$10^{-8} - 10^{-10}$	a
Plastic Clay	$2 \times 10^{-6} - 2.6 \times 10^{-7}$	b
Stiff Clay	$2.6 \times 10^{-7} - 1.3 \times 10^{-7}$	b
Medium-hard Clay	$1.3 \times 10^{-7} - 6.9 \times 10^{-8}$	b
Loose Sand	$10^{-7} - 5.2 \times 10^{-8}$	b
Dense Sand	$2 \times 10^{-8} - 1.3 \times 10^{-8}$	b
Dense, Sandy Gravel	$10^{-8} - 5.2 \times 10^{-9}$	b
Water at 25 °C	4.8×10^{-10}	b
Water at 25 °C	4.4×10^{-10}	a

a) Freeze and Cherry (1979)
b) Schwartz and Zhang (2003), modified after Domenico and Mifflin (1965)

in account the expansion in equation 3.11), resulting in

$$\rho_f(\alpha(1 - \Theta) + \beta\Theta)\frac{\partial p}{\partial t} - \nabla\rho_f\left[K\nabla(\frac{p}{\rho_f g} + z)\right] = 0 \tag{3.22}$$

and after rearrangements in

$$S_s\frac{\partial p}{\partial t} = \nabla\left[\frac{K}{\rho_f g}\left(\nabla p + \rho_f g \nabla z\right)\right] \tag{3.23}$$

assuming that the solid volume does not change over time (a consequence of equation 3.17). Equation 3.23 will be the governing equation for time-dependent fluid flow in porous media, applied in the models further in this work. S_s [Pa^{-1}] is the specific storage of the aquifer, here defined as[2]

$$S_s = \alpha(1 - \Theta) + \beta\Theta \tag{3.24}$$

A simplification to equation 3.23 can be made in case a steady state (i.e. constant over time) situation is regarded. In such a case, pressure does not change over time, so the first term of the equation may be omitted, resulting in

$$\nabla\left[\frac{K}{\rho_f g}(\nabla p + \rho g \nabla z)\right] = 0 \tag{3.25}$$

3.3.3 Turbulence modeling

The Navier-Stokes equations describe the flow of an incompressible Newtonian fluid (a fluid with constant density and with a linear stress – strain rate curve, the proportionality constant being the viscosity) in terms of pressure and velocity. The equation in vector formulation expressed as forces, is written as

$$\rho_f\frac{\partial \mathbf{v}}{\partial t} - \mu\nabla^2\mathbf{v} + \rho_f\mathbf{v}\cdot\nabla\mathbf{v} + \nabla p = \mathbf{f} \tag{3.26}$$

with ρ [kg.m^{-3}] the density of the fluid, $\mathbf{v}$ [m.s^{-1}] the velocity vector, t [s] the time, p [Pa] the pressure, μ [Pa.s] the dynamic viscosity of the fluid (assumed constant) and $\mathbf{f}$ [N] the body forces, e.g. the gravity force. In this equation, the first term expresses the unsteady acceleration, or the velocity change over time, the second term represents the viscous stresses in the fluid leading to a loss in momentum, the third term is the convective acceleration, i.e. the velocity change in space, the fourth term is the pressure gradient force, and the last term is any additional body force. An additional equation is the mass continuity equation, stating that no mass can be created or destroyed within a volume. Because we keep density as a

---

[2]Sometimes, the specific storage is defined as $S_s = \gamma(\alpha(1 - \Theta) + \beta\Theta)$ with γ the specific weight of the fluid. However, here we use a different form as it is present in the Comsol Multiphysics software.

constant, the mass continuity simplifies to a volume conservation equation, or

$$\nabla \cdot \mathbf{v} = 0 \tag{3.27}$$

A constant temperature is a necessary assumption to let this be valid.

If turbulence appears in the flow, too much computational effort is required to resolve the turbulence at all scales. At small scales, eddies in the current transport momentum at random. To describe this, the momentum equations are averaged in time or space, which, depending on the model, adds new unknowns. In engineering and oceanography, an often used turbulence model is the K-Epsilon Turbulence model. In this model, in addition to velocity and pressure, the turbulent kinetic energy k [kg.m^2.s^{-2}] and the energy dissipation ϵ [kg.m^2.s^{-3}] appear as new variables. These new variables relate to the kinetic energy of the eddies that appear in the turbulent flow. The new set of equations is written as

$$\rho_f \frac{\partial \mathbf{v}}{\partial t} - (\mu + \rho_f C_\mu \frac{k^2}{\epsilon}) \nabla^2 \mathbf{v} + \rho_f \mathbf{v} \cdot \nabla \mathbf{v} + \nabla p = \mathbf{f} \tag{3.28}$$

$$\nabla \cdot \mathbf{v} = 0 \tag{3.29}$$

$$\rho_f \frac{\partial k}{\partial t} - (\mu + \rho_f \frac{C_\mu}{\sigma_k}) \frac{k^2}{\epsilon} \nabla^2 k + \rho_f \mathbf{v} \cdot \nabla k = \rho_f C_\mu \frac{k^2}{2\epsilon} \nabla^2 \mathbf{v} - \rho_f \epsilon \tag{3.30}$$

$$\rho_f \frac{\partial \epsilon}{\partial t} - (\mu + \rho_f \frac{C_\mu}{\sigma_\epsilon}) \frac{k^2}{\epsilon} \nabla^2 \epsilon + \rho_f \mathbf{v} \cdot \nabla k = \rho_f C_{\epsilon 1} \frac{k}{2} \nabla^2 \mathbf{v} - \rho_f C_{\epsilon 2} \frac{\epsilon^2}{k} \tag{3.31}$$

The first equation is similar to the Navier Stokes equation (eq. 3.26), except that the viscous stress term is now expanded with the turbulent viscosity term $\rho_f C_\mu \frac{k^2}{\epsilon}$, which indicates that momentum is lost not only by the viscosity of the fluid itself, but also by the turbulence. The third and fourth equation are equations for the turbulence kinetic energy k and dissipation rate of the turbulence energy, $\epsilon = 0.09$. C_μ, $C_{\epsilon 1} = 1.44$,$C_{\epsilon 2} = 1.92$, $\sigma_k = 0.9$ and $\sigma_\epsilon = 1.3$ are experimentally defined constants. This model is valid for turbulent transport at high Reynolds numbers. For all details of the turbulence model, please refer to the Comsol Multiphysics software documentation or see Wilcox (1998).

3.3.4 General transport equations

When a fluid is flowing, it can transport chemicals, heat, etc. There are two important transport means: advection and diffusion. Advective transport describes the movement of an item ξ along with the flow of the fluid. The amount transported thus depends on the amount present in the fluid itself (the concentration) and the fluid velocity, or, $\mathcal{J}_c = c_\xi \mathbf{u}$ where $\mathcal{J}_c$ [ξ.m^{-2}.s^{-1}] is a flux, c_ξ [ξ.m^{-3}] a concentration or density and $\mathbf{u}$ [m.s^{-1}] the fluid velocity. Diffusive transport describes the movement of an item down the concentration gradient. It is unrelated to fluid flow, but occurs when the concentration of an item is higher at one location than at another. When such a situation occurs, transport will occur in the direction

of the lowest concentration, until equilibrium has been established. The amount transported through time thus depends on the concentration gradient and the capability of the item to diffuse through the fluid. This is written as $\mathcal{J}_d = -D\nabla c_\xi$ where $\mathcal{J}_d$ [ξ.m^{-2}.s^{-1}] is a mass flux, D [m^2.s^{-1}] the diffusivity of the medium, expressing the ease of diffusion and ∇c_ξ [ξ.m^{-4}] is the concentration gradient. The total mass flux of a certain quantity through the medium is the sum $\mathcal{J} = \mathcal{J}_d + \mathcal{J}_c$.

A general transport equation is a partial differential equation that describes transport phenomena, this includes advective and diffusive transport defined above, but also reactions or processes that destroy or create a given item, and changes in concentration of the item through time. The general form of the equation is

$$\frac{\partial \xi}{\partial t} + \nabla \cdot \mathcal{J}(t, x, \xi, \nabla\xi, ...) = \mathcal{R}(t, x, \xi) \tag{3.32}$$

The first term expresses the change of a quantity ξ through time. The second term is the divergence a flux. The flux can be a function of time, location, the quantity ξ or its gradient $\nabla\xi$. The last term is the reaction term and adds or removes the quantity ξ.

In the next sections, this general form will be adapted for heat transport and chemical transport.

3.3.4.1 Heat flow equations

In chapter 6, heat flow will be discussed. The heat flux is defined as the flow of energy through a unit area per unit time. Diffusive heat transport, or, more common, heat conduction, is described by Fourier's Law. It describes the heat conduction as proportional to the negative temperature gradient. The proportionality factor is know as the thermal conductivity of the material. Mathematically, this is expressed as

$$J_{c,q} = -k\nabla T \tag{3.33}$$

with $J_{c,q}$ [W.m^{-2}] the conductive heat flux, k [W.m^{-1}.K^{-1}] the thermal conductivity, and ∇T [K.m^{-1}] the temperature gradient. The heat flux caused by advection, is defined by the flow velocity and the temperature of the flowing medium, or

$$J_{a,q} = T\mathbf{v} \tag{3.34}$$

with $J_{a,q}$ [W.m^{-2}] the advective heat flux, T [K] the temperature of the fluid and $\mathbf{v}$ the velocity of the fluid [m.s^{-1}].

When these flux equations are substituted in equation 3.32 and the assumption is made that no heat is created (e.g. radiogenically) which leads to $\mathcal{R} = 0$, then the governing heat

flow equation describing the temperature change in a body over time, is obtained, or

$$\frac{\partial T}{\partial t} = -k\nabla^2 T + T\nabla \cdot \mathbf{v} \tag{3.35}$$

3.3.4.2 Chemical transport and reaction equations

Chemical transport or mass transport describes the transport phenomena of chemical compounds in a medium. In this work, the transport and reaction of methane and sulfate will be used to simulate the depth at which methane oxidation coupled to sulfate reduction could occur (see Chapters 6 and 7). The goal of this is to simulate at which depth the process of microbially mediated anaerobic oxidation of methane (AOM) could occur (Hinrichs et al., 1999).

According to the equations in section 3.3.4, the diffusive and advective flux of methane resp. sulfate will be

$$J_{d,\mathrm{CH_4}} = -D_{\mathrm{CH_4}}\nabla[\mathrm{CH_4}] \quad , \text{resp. } J_{d,\mathrm{SO_4}} = -D_{\mathrm{SO_4}}\nabla[\mathrm{SO_4}] \tag{3.36}$$

$$J_{c,\mathrm{CH_4}} = [\mathrm{CH_4}]\mathbf{v} \quad , \text{resp. } J_{c,\mathrm{SO_4}} = [\mathrm{SO_4}]\mathbf{v} \tag{3.37}$$

with $[\mathrm{SO_4}]$ resp. $[\mathrm{CH_4}]$ the concentration of sulfate resp. methane $[\mathrm{mol.m^{-3}}]$, $D_{\mathrm{SO_4}}$ resp. $D_{\mathrm{CH_4}}$ their respective diffusivities. With these equations substituted into equation 3.32, we obtain the governing equations for the chemical transport and reaction.

The governing steady state equations will be, assuming constant diffusivities for methane and sulfate,

$$-D_{\mathrm{CH_4}}\nabla^2[\mathrm{CH_4}] = R - \mathbf{v} \cdot \nabla[\mathrm{CH_4}] \tag{3.38}$$

$$-D_{\mathrm{SO_4}}\nabla^2[\mathrm{SO_4}] = R - \mathbf{v} \cdot \nabla[\mathrm{SO_4}] \tag{3.39}$$

$\mathbf{v}$ is moved outside the divergence operator because of mass conservation or continuity

$$\nabla \cdot (\rho\mathbf{v}) = 0 \tag{3.40}$$

The diffusivities are kept constant in the model, therefore they also appear in front of the Laplacian operator. R symbolizes the reaction of $\mathrm{CH_4}$ and $\mathrm{SO_4}$, defined as

$$R = -C_r[\mathrm{SO_4}][\mathrm{CH_4}] \tag{3.41}$$

with C_r a reaction constant which controls the width of the potential reaction zone, the overlap of sulfate and methane profiles. In the models, it is typically chosen to generate a narrow reaction zone, however wide enough to prevent numerical instabilities. A second order reaction equation will thus define a depth range where reaction is taken place. The reactivity will

be zero where any of the concentrations of both reactants is zero; it will be small where both concentrations are small but non-zero; a maximum will exist in between. This simulates the natural requirement that both reactants are present. Although the situation in nature is much more complex than this, a second-order reaction as model approach is closer to reality than first-order or zero-order reaction equations that were used in older studies.

Finally, the governing equations in case of transient models will be

$$\frac{\partial[\mathrm{CH_4}]}{\partial t} - D_{\mathrm{CH_4}}\nabla^2[\mathrm{CH_4}] = R - \mathbf{v} \cdot \nabla[\mathrm{CH_4}] \tag{3.42}$$

$$\frac{\partial[\mathrm{SO_4}]}{\partial t} - D_{\mathrm{SO_4}}\nabla^2[\mathrm{SO_4}] = R - \mathbf{v} \cdot \nabla[\mathrm{SO_4}] \tag{3.43}$$

Part II

Evidence for past and present fluid flow

Chapter 4

Geophysical evidence of fluid flow: the El Arraiche mud volcano field

The goal of this chapter is to (1) provide a seismostratigraphic and shallow structural framework of the study area and (2) provide geophysical evidence for active of past fluid flow, mainly by identifying the past mud volcano activity periods based on the recognition of large mud flows.

4.1 Surface and shallow subsurface structures of the El Arraiche mud volcano field

4.1.1 Surface structure

The surface morphology and structure of the El Arraiche mud volcano (MV) field is best described with multibeam bathymetric data and side-scan sonar data. A map based on multibeam data, shown in figure 4.1, gives an overview of the main seafloor structures. The most prominent features are the large circular structures that rise 25 to 250 meters above the seafloor. The muddy sediments containing brecciated clasts and retrieved from the center area of these structures, were interpreted as mud volcanic mud breccia, transported from deeper units (Ovsyannikov et al., 2003) towards the surface. The sediment samples often contain large amounts of gas. Therefore, it was concluded that these seafloor structures are mud volcanoes (Kenyon et al., 1999, 2000, 2003).

The largest mud volcano is Al Idrisi[1] MV. The structure covers an area of more than 20 km^2 and is about 250 meter high. It is one of the largest known submarine mud volcanoes in the world. Down the slope, some smaller mud volcanoes are present: Mercator[2] MV, Fiúza[3] MV, Gemini[4] MV, Kidd[5] MV and Adamastor[6] MV. The smallest mud volcanoes are Lazarillo de Tormes[7] MV and Don Quichote[8] MV.

The Al Idrisi mud volcano (Figure 4.2) covers an area of 23.6 km^2. The deepest point, in the northern moat, is situated 440 m below sea level (bsl) and the highest point is located at 197 m bsl. The diameter of the structure is 4.5 to 6 km. The slopes of the mud volcano flanks range between 4 and 10 degrees. At the surface of the mud volcano, multiple individual mud flows can be identified. These mudflows run radially from the crater edge down the slope and end near or in the moat as a lobe shaped body. The crater of the mud volcano has a diameter of 1.35 km. Inside the crater, a small mud dome structure is present.

The Mercator MV (Figure 4.3) is located on the south slope of a NW-SE trending ridge structure (Vernadsky[9] Ridge). The mud volcano is 140 m high at its south side, and only 50

---

[1] Abu Abd Allah Muhammad al-Idrisi, 1100-1166, Moroccan cartographer.

[2] Gerardus Mercator, 1512-1594, Flemish cartographer.

[3] Armando Fiúza, 1938-2001, Portuguese oceanographer.

[4] The name of this mud volcano reflects the presence of two craters.

[5] Robert Kidd, 1947 - 1996, British marine geoscientist.

[6] Adamastor is a mythological character in the poem "Os Lusiadas" by the Portuguese poet Luis Vaz de Camoes (1524-1580). Adamastor represents the natural forces the Portuguese navigators have to fight.

[7] "The life of Lazarillo de Tormes and of his fortunes and adversities" is a 16th century novella by an anonymous author about the main characters rising from poverty. It was banned in Spain, until a censored version was allowed in 1574. The version that circulated in Europe was the Antwerp version (1557).

[8] Don Quichote is the main character from the novel "El ingenioso hidalgo don Quijote de la Mancha" written by the Spanish author Miguel de Cervantes Saavedra. The name is given to the mud volcano to symbolize its small size in comparison to the surrounding 'giant' mud volcanoes, in analogy to Don Quichote fighting the windmills which he believes are cruel giants.

[9] Vladimir Ivanovich Vernadsky, 1863 - 1945, Soviet mineralogist and geochemist. Vernadsky's best known
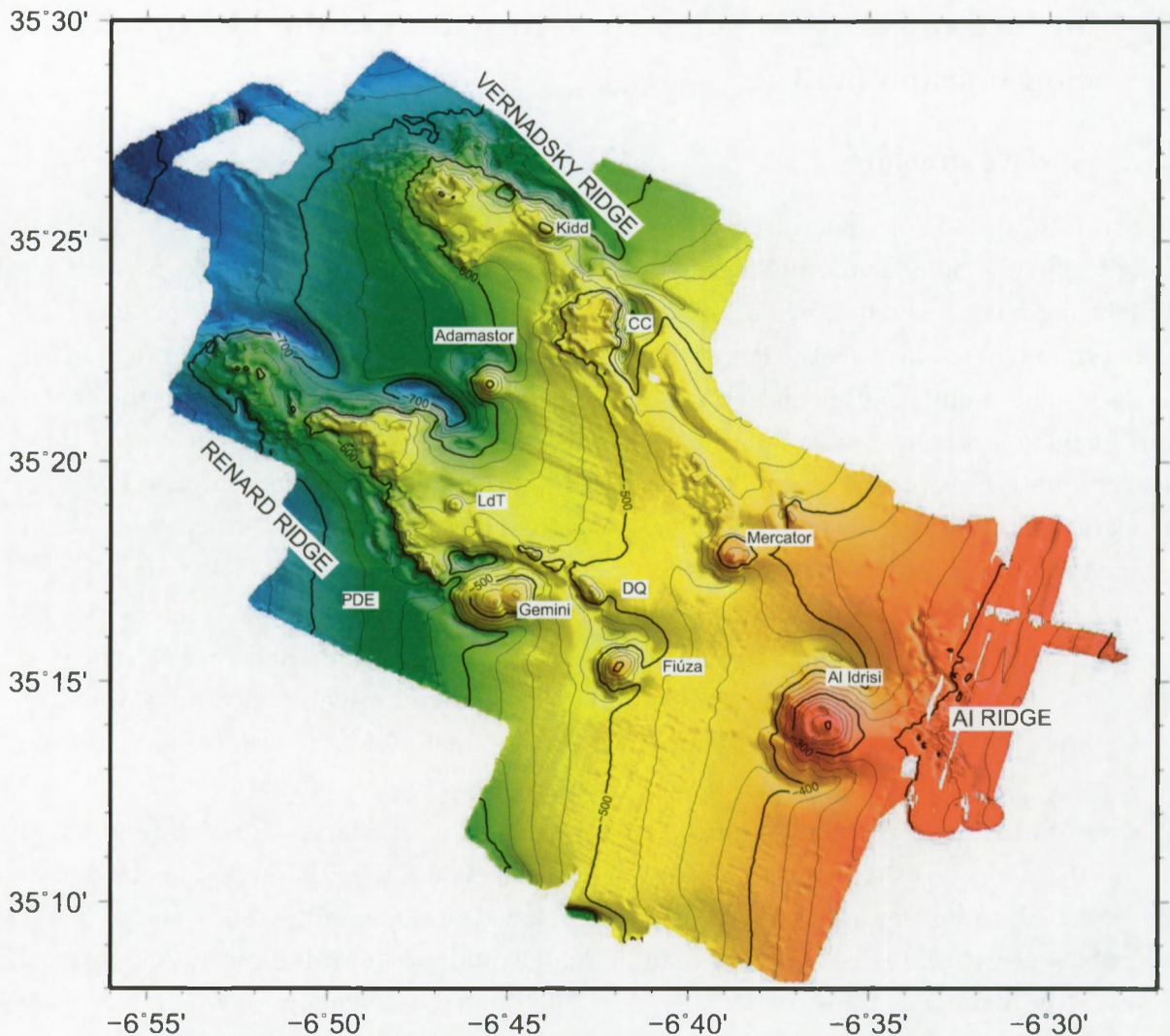
Figure 4.1: *Bathymetric map of the El Arraiche mud volcano field with names of the main features. DQ = Don Quichote MV, LdT = Lazarillo de Tormes MV, PDE = Pen Duick Escarpment, CC = Conger Cliff, AI Ridge = Al Idrisi Ridge.*

meter at its north side. The structure covers about 5 km^2. The deepest point of the moat is about 490 m bsl, while the top is situated at a depth of 350 m bsl. The diameter of the structure is 2.5 km at the base. The top consists of a dome structure of about 1 km diameter; no crater is observed. The flank morphology of the mud volcano displays a stepped terrace shape. This is also observed on the side-scan sonar data. On the west side, a large mud flow lobe runs down to a large crescent shaped moat. This moat is about 20 m deep and encircles the mud volcano at the east and south side. The side-scan sonar illustrates the presence of many lobe-shaped featurs around the center of the mud volcano.

work is "Biosfera" in which he pioneers the view that life is the most important geological force shaping the earth. He is deemed founding father of geochemistry, geobiology and other interdisciplinary geosciences.
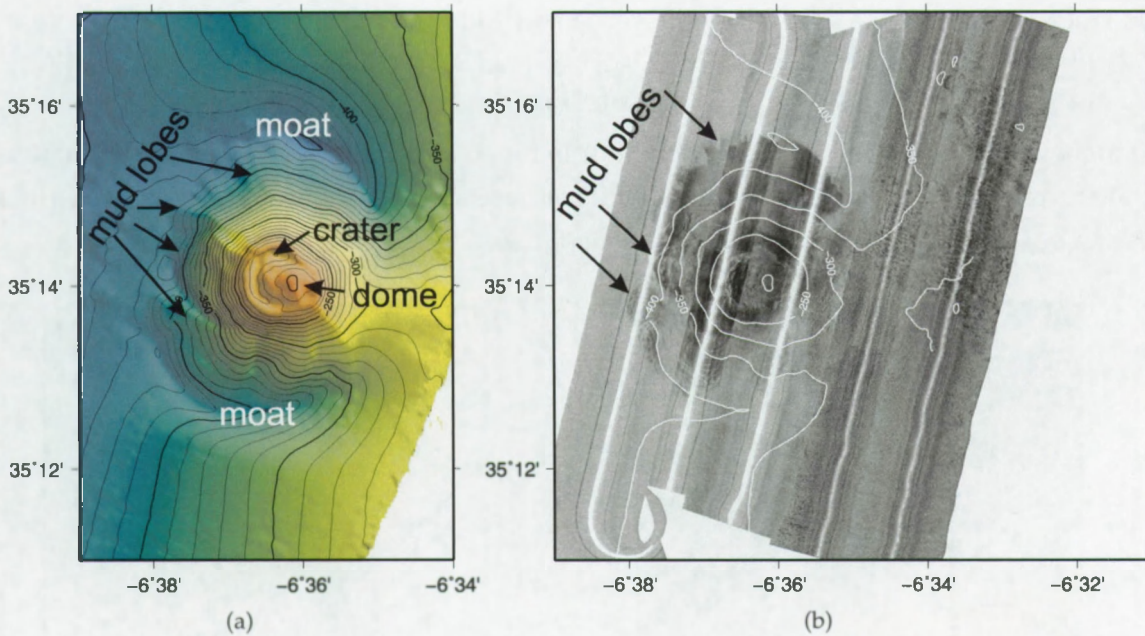
Figure 4.2: *Bathymetry and surface morphology of Al Idrisi mud volcano. a) multibeam bathymetry showing the crater depression with dome inside it, large crescent moats on north and south side, and lobe structures on the flanks. b) Side-scan sonar imagery showing featuring highly reflective mud lobes on the north slope.*
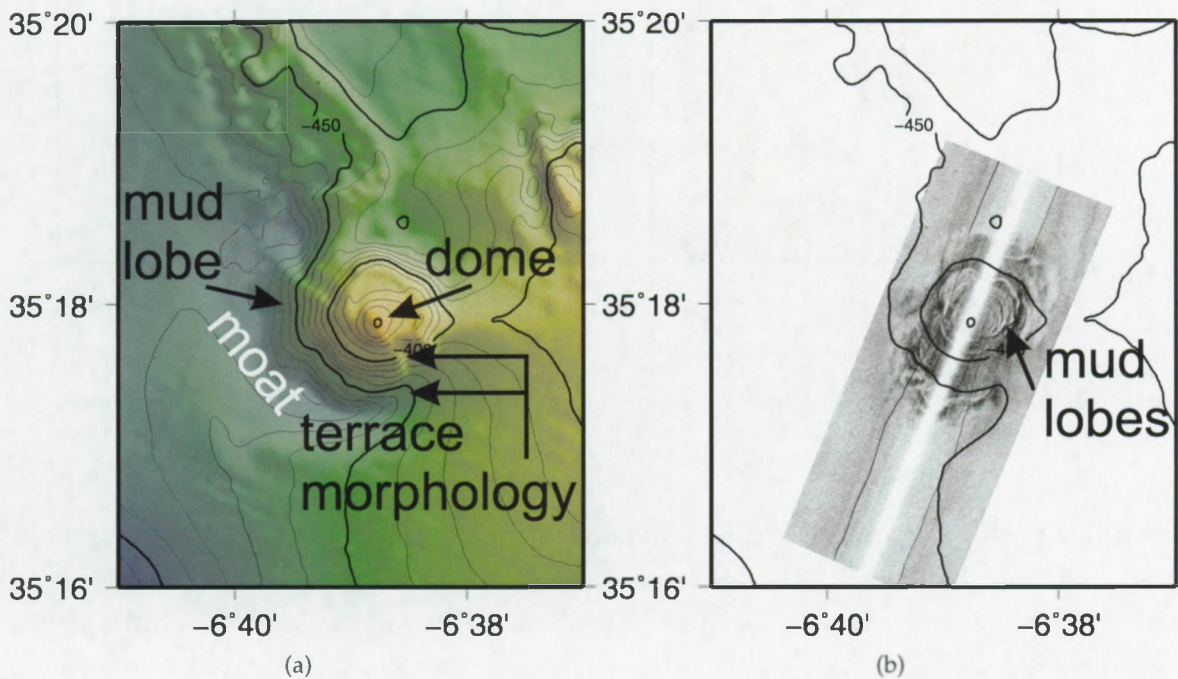
Figure 4.3: *Bathymetry and surface morphology of Mercator mud volcano. a) multibeam bathymetry showing the stepped terrace morphology and central dome. b) side-scan sonar image showing a high number of mud lobes around the central dome.*

Further northwest, also situated on the Vernadsky Ridge, a second mud volcano is present. The Kidd MV (Figure 4.4), about 4 km^2 in surface area, is situated on the north flank of the ridge and is asymmetrical in shape, just like the Mercator mud volcano. Its south side is only 60 m high, while at the south side, the height from top to moat is about 180 meter. The bathymetric morphology does not reveal much of its surface structure, although some individual lobes can be identified which could be large mud flows.
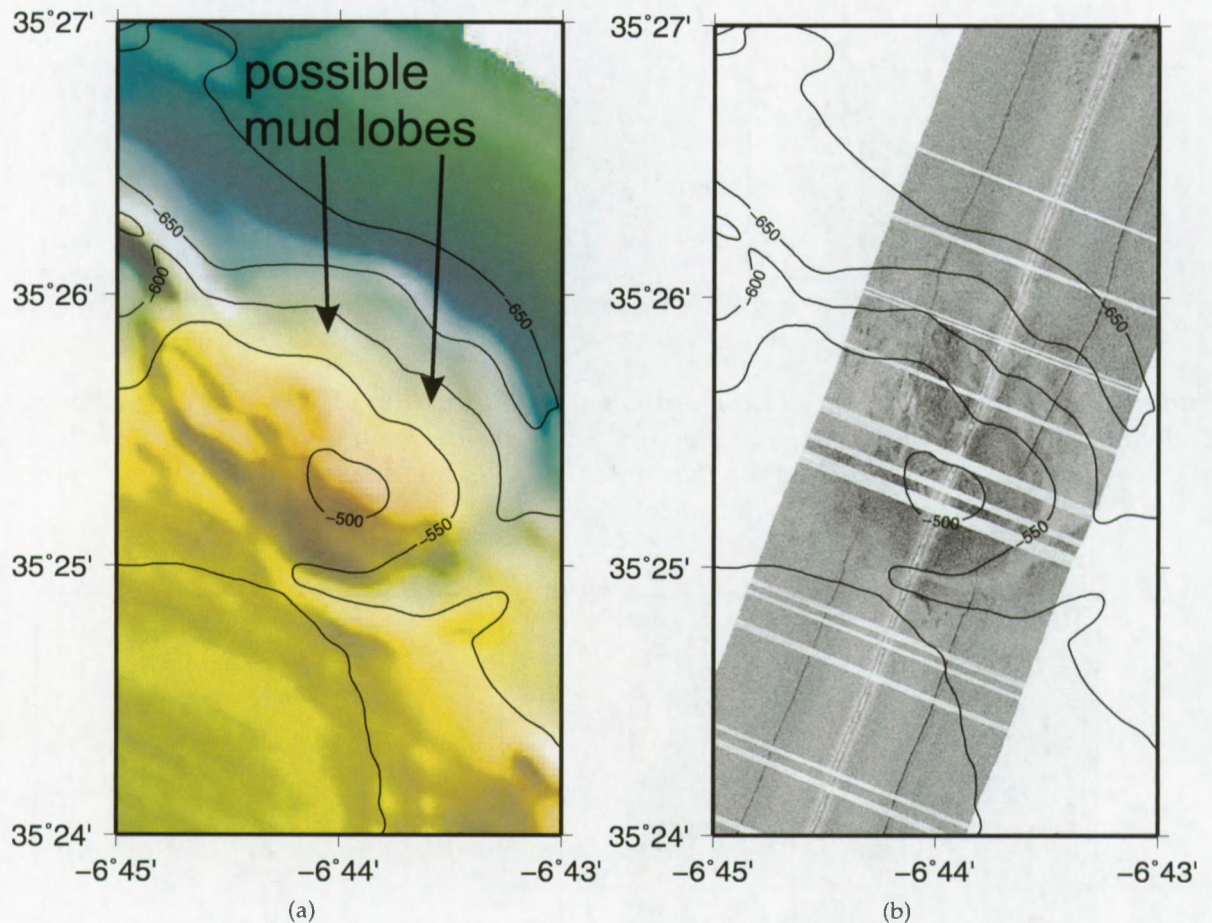
Figure 4.4: Bathymetry and surface morphology of Kidd MV. a) multibeam bathymetry. b) side-scan sonar image.

South of the Kidd mud volcano and unrelated to any ridge structure, the Adamastor mud volcano is found (Figure 4.5). The surface it occupies is about 5 km^2. It is surrounded by a small crescent shaped moat with a depth of about 20 m at the northwest side. At the southwest side, a very deep moat is present, although this moat is rather related to the ridge structure further south (Renard[10] Ridge). Adamastor mud volcano is about 160 m high and has a

---

[10] Alphonse-François Renard, 1842-1903, Belgian mineralogist and petrographer. He was professor of geology at Ghent University as of 1888 and co-author of the "Report on Deepsea Deposits" (1891) after the first Antarctica expedition of H.M.S. Challenger, known for the first description of manganese and phosphate nodules.

conical shape. Surface detail is scarce both on bathymetric and side-scan sonar data; only on the bathymetry, on the northwest side a lobe structure hinting a mud flow structure is present. A crater is not present at the top of the mud volcano.
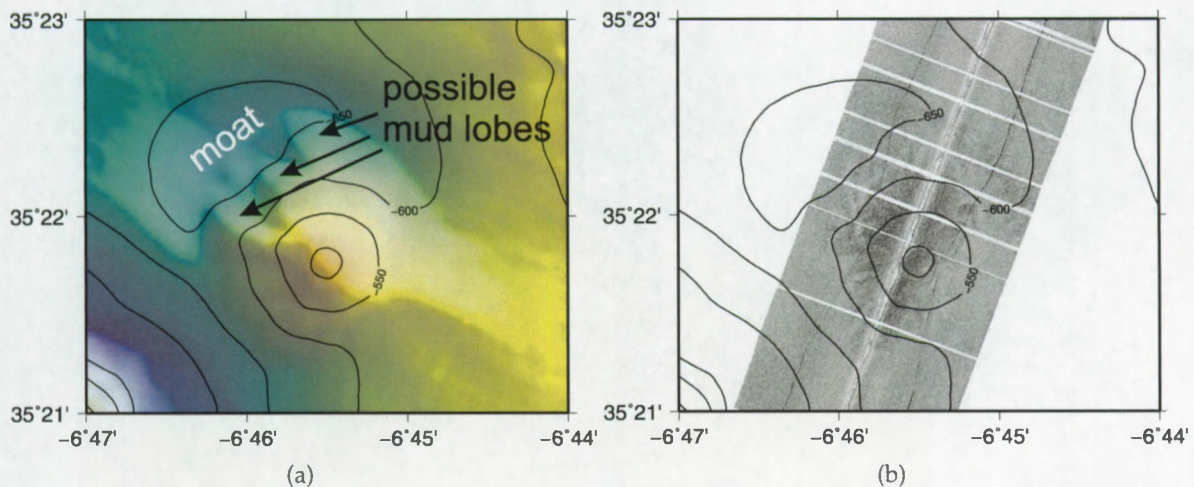
Figure 4.5: *Bathymetry and surface morphology of Adamastor MV. a) multibeam bathymetry. b) side-scan sonar image.*

A large ridge trending NW-SE is found further south: Renard Ridge (Figure 4.6). There are several mud volcanoes associated to this ridge. At the eastern side, the Fiúza mud volcano is found at a depth of 520 m bsl and the top is situated at 390 m bsl. A horse-shoe shaped moat structure of 20 to 40 m deep is found on the north, west and south side of the mud volcano. A crater is not present on the top, but on the flanks, several lobe shaped bodies running from top to moat are seen and are interpreted as large mud flows. The slope angle varies between 6 and 10 degrees. On the northwest side of the mud volcano, the moat widens in a small depression and continues in a small moat south of an elongate structure standing out of the surrounding seafloor about 60 m. The structure has no characteristic surface features except for the high reflectivity in the sonar data. From seismic data (see further, section 4.1.2) it appears however that this is a mud volcano. To the west, some smaller structures are present, with similar high reflectivity.

Gemini mud volcano is built up of two individual cones without any crater. On the north, west and south sides of the mud volcano, deep moats have developed. The northern moat seems to be situated between two converging arcuate ridge crests and may therefore, at least partly, be structurally controlled. The two cones both top at a water depth of 423 m. The west cone is higher however, due to the occurrence of the moat on the west side. The height ranges, depending on where it is measured, between 170-250 (west cone) and 117-169 m (east cone). The surface area of the complete structure is 11.1 km². The slopes of the cones are less steep than the other craters, varying between 2 and 4°.

Lazarillo de Tormes mud volcano is a small structure (surface area 0.5 km²) of 40 m high.
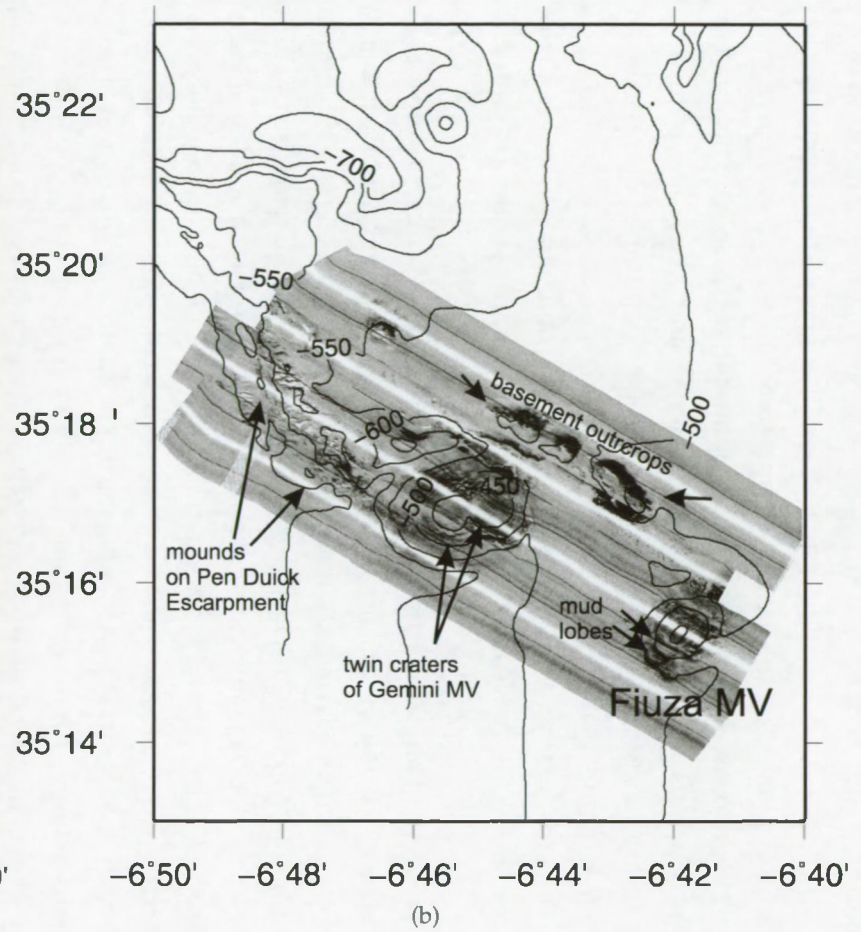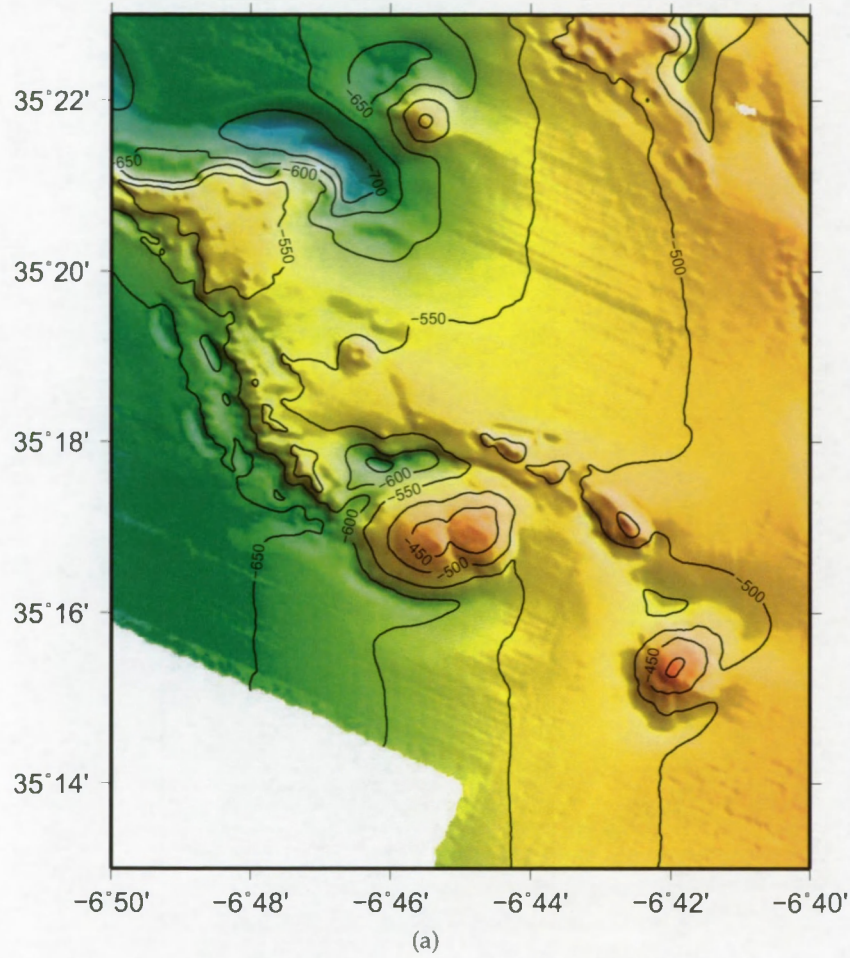
Figure 4.6: *The Pen Duick Escarpment, Gemini mud volcano and Fiúza mud volcano. a) multibeam bathymetry. b) side-scan sonar image.*
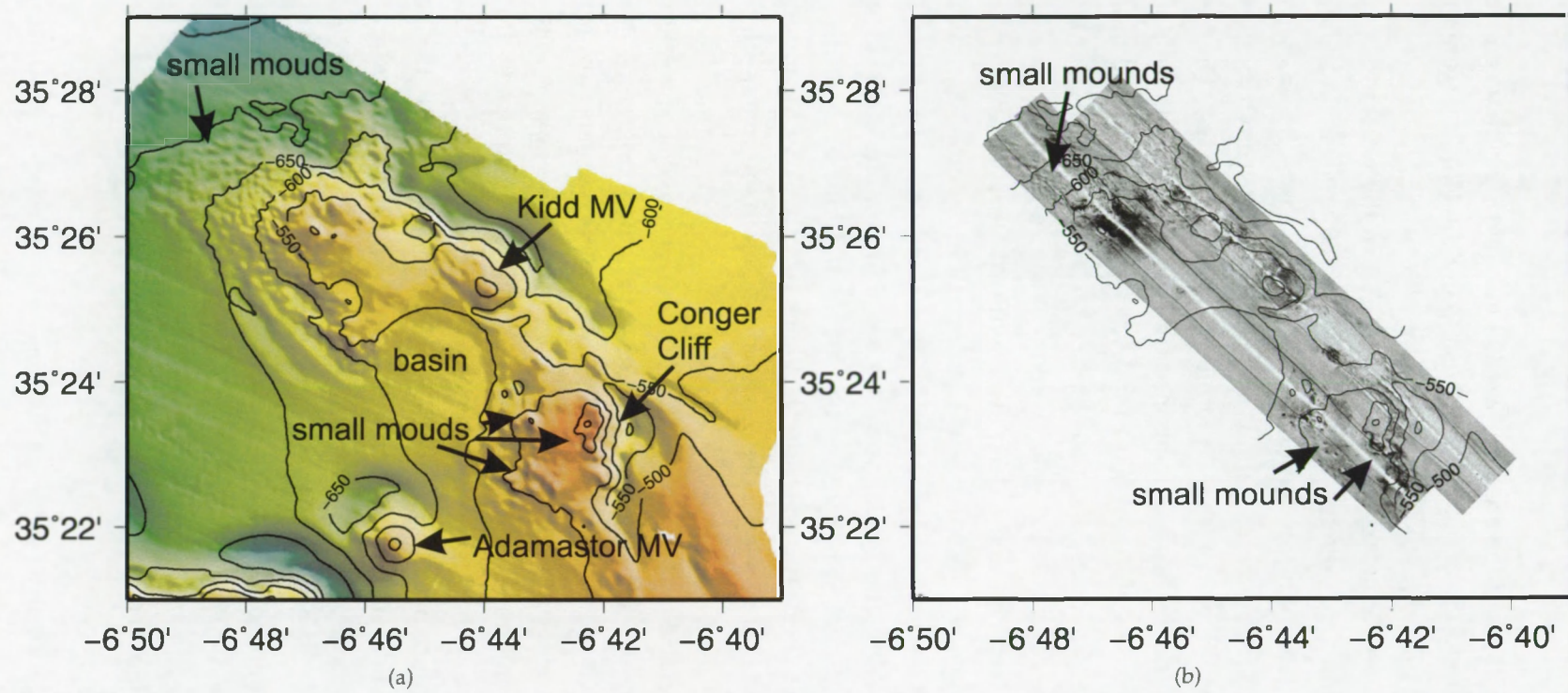
Figure 4.7: *Bathymetry and surface morphology of Vernadsky Ridge. On the NW side of the ridge, many small elevations reflect the presence of small coral patches. On the side-scan imagery, they appear as faint shadows. a) Multibeam bathymetry. b) side-scan sonar image.*

It has a small crater depression in the center. No other surface features can be discerned.

Important structural features of the area are two 30 km long ridges that run from NW to SE. The ridges stand out up to 150 m high with respect to the surrounding seafloor and are 5 to 10 km wide. The top of the ridges plunge towards the NW.

The northern ridge is the Vernadsky Ridge (Figure 4.7). On the westernmost part of the data, small hill-like structures are present, with diameters of 100 to 400 m and a height of less than 10 m. From video and sampling observations (Foubert et al., 2008), it is known that in this region patches of mostly dead cold water corals are present. They seem to occur in a depth range between 800 and 660 m bsl, on the westernmost part of the ridge. On the side-scan sonar data these patches are observed as faint shadows. Along the north side of this area, a deep moat is present, passing north of Kidd mud volcano. South of Kidd mud volcano, the ridge seems to be less prominent and makes place for a small basin. However, east of this small basin, the ridge re-appears as an elevated plateau topped with small elevations. The east side features a steep cliff and a deep moat, with an elevation difference of 180 m. This area was video-surveyed by ROV Genesis (Cadipor III expedition, 06/2007). The cliff appeared to consist of a carbonate-like basement hardrock with large cavernous holes. The cliff was named Conger Cliff, after the large conger eel hiding in one of the crevasses. On the top of the cliff, the elevations appeared to be patches and hills of dead deep-sea coral rubble. Further southwest, the Vernadsky ridge becomes less visible in the topography, but it is clear that along the ridge crest a large depression exists, up to the area north of Mercator mud volcano.

The Renard Ridge (Figure 4.6) is found south of Vernadsky Ridge. The westernmost part of the ridge is a low elevated plateau (40-60 m high) with some topographic irregularities. Along the north side of the ridge, a wide and shallow moat is present. Towards the east, the ridge becomes higher, and more accidented. Ridge crest sections appear to be arcuate in shape. Northwest of Gemini mud volcano, a 7 km long arcuate ridge topped with small hill-shaped features is present. This ridge section, Pen Duick[11] Escarpment, has been observed and sampled in detail because of the occurrence of small mounds of mostly dead cold water corals. In some of the mounds, shallow methane gas fronts have been observed and anaerobic methane oxidation is an active process, influencing the stability of the carbonate framework of dead corals (Maignien et al., 2007; Foubert et al., 2008).

East of the Al Idrisi mud volcano, a ridge structure (Al Idrisi Ridge) is appearing from under the mud volcano body (Figure 4.2). Further east and north, the seafloor is very irregular with small hill-like features of a few meters high and a few tens of meters in diameter. Sampling during the Cadipor II cruise revealed the presence of dead cold water coral patches (Foubert et al., 2008).

---

[11] 36' yacht built since 1898 by Gridiron and Workers at Carrigaloe near Crosshaven in Ireland and made famous by the sailor Eric Tabarly.
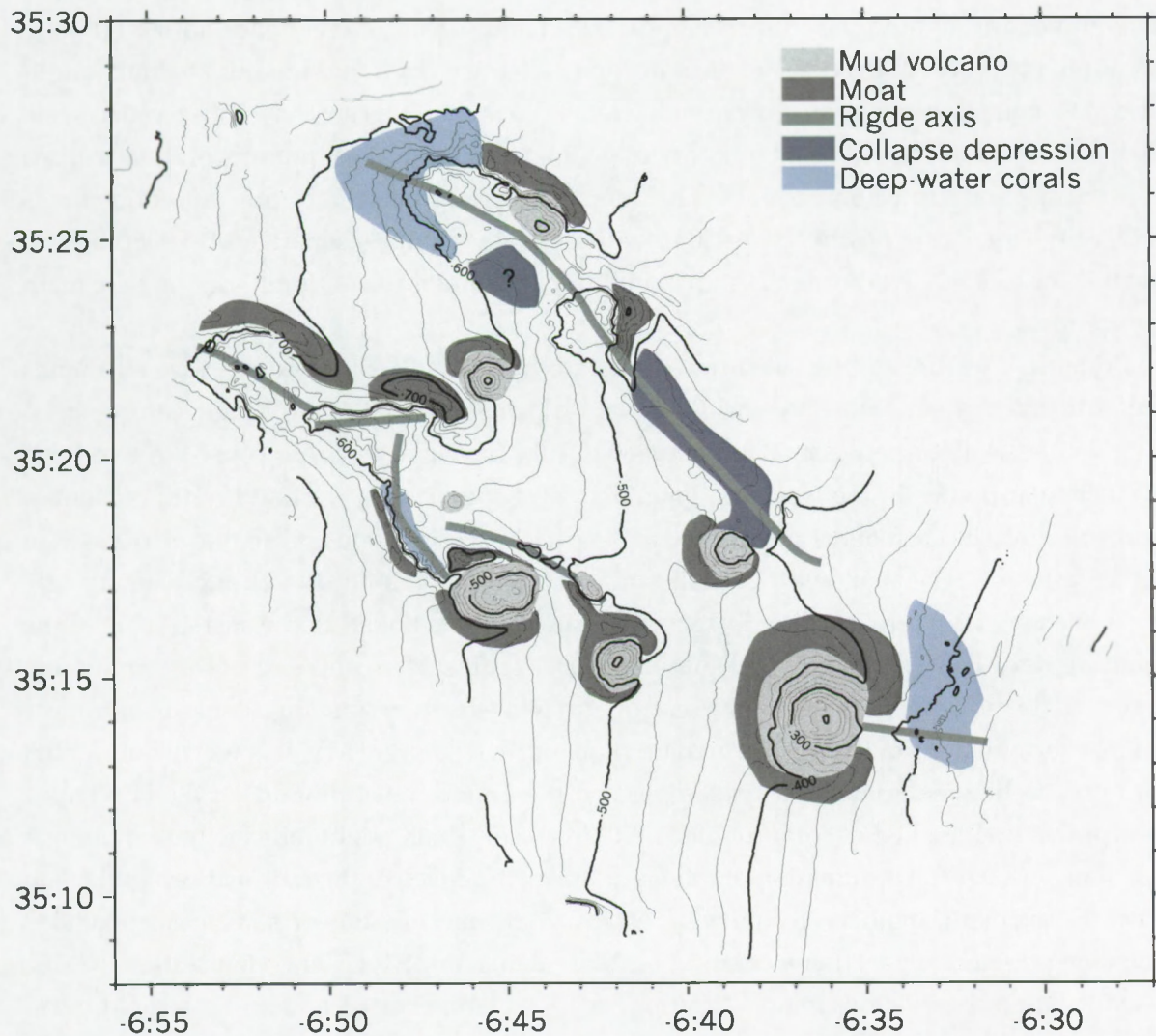
Figure 4.8: *Structural and morphological features inferred from multibeam bathymetry and side-scan sonar images.*

The different features have been compiled in a map (figure 4.8) that illustrates the close association between structural ridges and mud volcanoes. It also shows the dominance of erosional moats on the south and north side of mud volcanoes which could indicate a strong W-E tot NW-SE directed current component.

4.1.2   Shallow subsurface structure

The seismic data allow to recognize structural features like faults and fractures, folding structures and diapiric structures. One specific reflector in the data has been chosen as an 'acoustic basement'. It is not a basement reflection in the meaning of a Paleo- or Mesozoic hardrock on which younger sedimentary units are deposited. Here it is meant as a reflector which can

be identified throughout the entire seismic data set and serves as a reference horizon (Figure 4.9). At many places in the data set the reflection is characterized by a medium to high amplitude. At some places it has an erosive character and onlap on this surface is observed as well. Therefore, it is interpreted as a boundary of geological significance in terms of (relative) sea level change and/or tectonic events. The depth[12] map (Figure 4.10) of this reflection allows to identify large-scale positive structural features such as ridges, separated by deep basins. The thickness of the overburden is shown in figure 4.11 and is useful for identifying the main depocentres.

Prominent features of the subsurface structures are the NW-SE trending ridge structures (Fig. 4.10): Vernadsky Ridge, Renard Ridge and Al Idrisi Ridge. Renard Ridge features steep slopes at the seafloor between 500 m and 800 m bsl. The ridge seems to consist of two large quasi-circular bodies in the west and long arcuate shaped ridges west and north of Gemini mud volcano. The crest of the ridge is 700 m deep at the western end and shallows to less than 500 m eastward. The shallowest point is situated east of Gemini mud volcano. Gemini MV, Don Quichote MV and Lazarillo de Torres MV are closedly linked to the eastern part of the Renard Ridge. The Gemini is found south of a large fault surface and east of the termination of an arcuate escarpment (Pen Duick Escarpment) while the two small mud volcanoes appear near the terminations of the second arcuate ridge north of Gemini MV. It is worth noting that mud breccia like material has been sampled on the easternmost 'mound' of the Pen Duick Escarpment under a bed of coral rubble (TTR-16 cruise) which might indicate mud mobilization along or near the termination of the scarp fault. Moreover, at the terminations of the Pen Duick Escarpment, methane fronts were observed at much shallower subsurface positions than along the center part (pers. comm. Lois Maignien, LabMET, UGent; Hans Pirlet, RCMG, UGent). These observations may indicate a (genetic) relation between the ridge structure and the occurrence of the mud volcanoes. The terminations of the small arcuate ridges may represent highly fractured or deformed zones and thus form places of preferential upward fluid flow (Sibson and Scott, 1998) — especially where two ridges link or intersect — compared to the central parts of these ridges, and compared to the western part of the Renard Ridge where these smaller arcuate ridges do not seem to occur.

The base reflector could not entirely be mapped around the Vernadsky Ridge, therefore only part of it is covered. The Vernadsky Ridge is wider and less steep than the Renard Ridge. The crest of the ridge plunges to the northwest: in the west, the crest is situated at a depth of 500 m bsl and at 400 mbsl north of Mercator. Further east, it converges with the Al Idrisi Ridge. In contrast to the Renard Ridge, a large collapse depression can be observed in the area between Kidd MV and Mercator MV. The crestal depression is bound on both sides by sets of normal faults. At one specific site, the Conger Cliff, a topographic difference of nearly 150 m exists, although this is enhanced by erosion activity. The western part of the Vernadsky Ridge

---

[12]To convert the two-way travel time of the seismic data, to depth in meters, a seismic velocity model was developed, as shown in Appendix B.
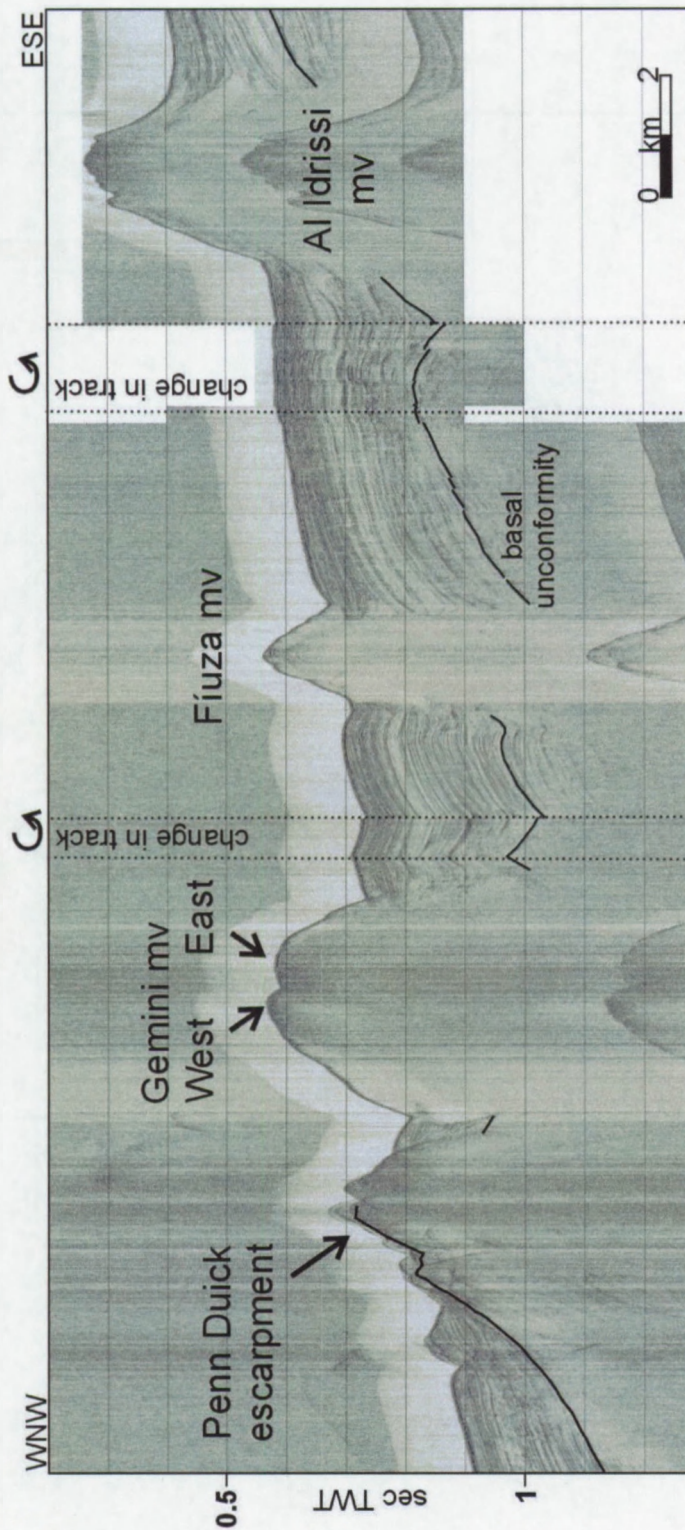
Figure 4.9: High resolution seismic line traversing the El Arraiche mud volcano field illustrating the reference reflector (horizon picked in black).
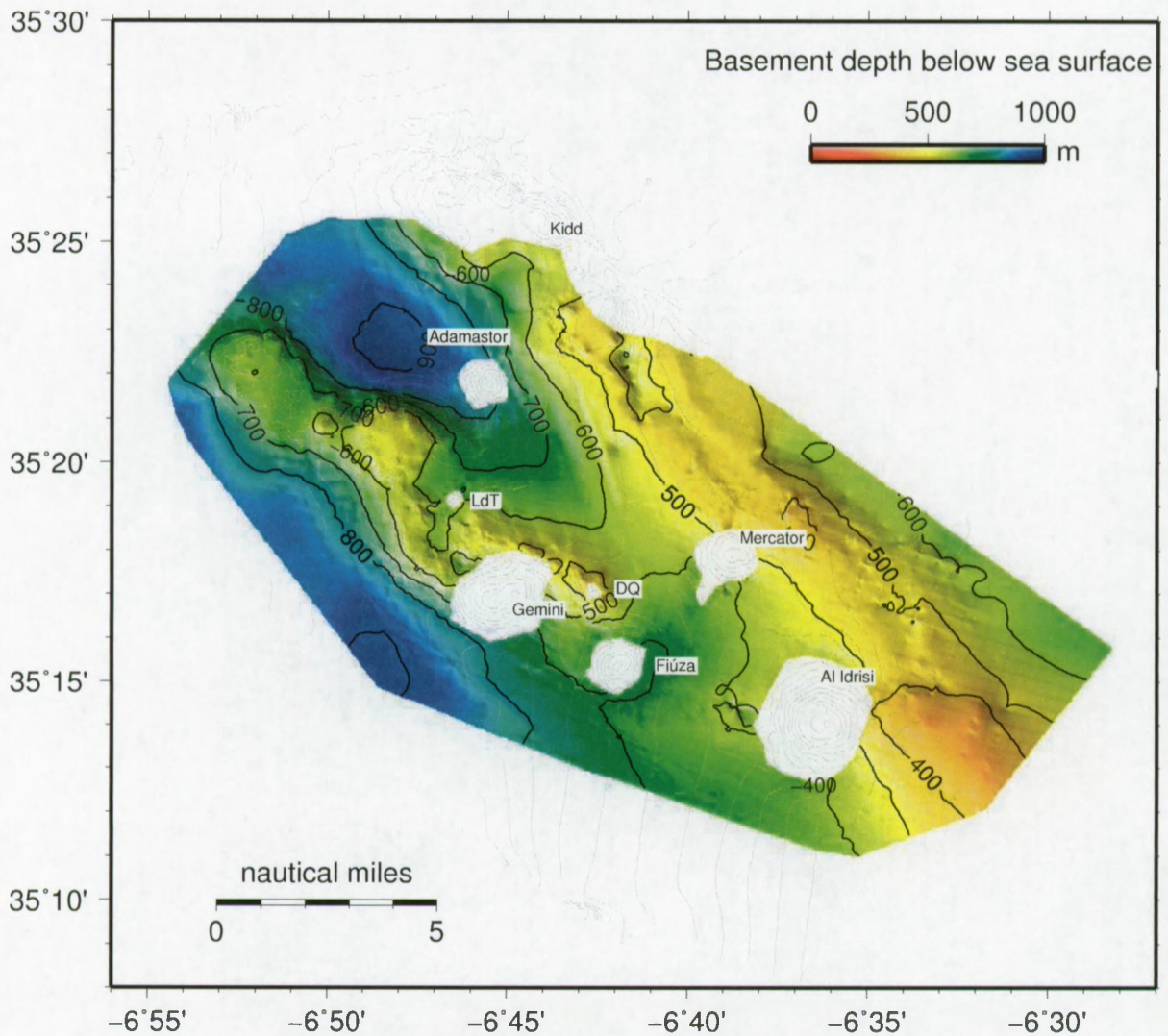
Figure 4.10: *Basement (reference reflector) map, depth (m) below the sea surface based on seismic data. The large-scale ridges are separated by deep intra-ridge basins. This map also shows the close association between ridges and mud volcanoes. The velocity model used for time to depth correction can be found in Appendix B*
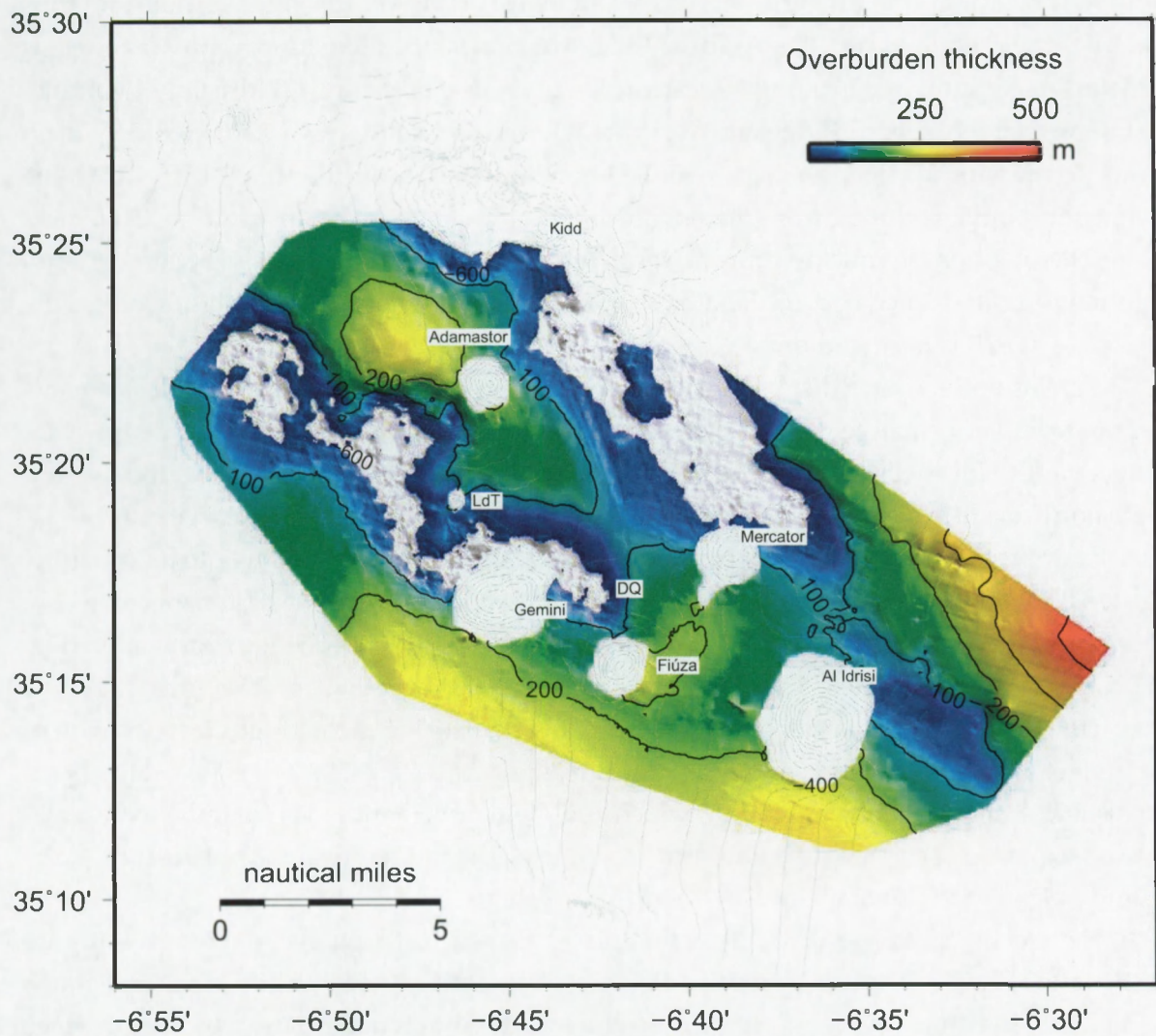
Figure 4.11: *Thickness of the sediments overlaying the reference reflector. Grayish-white areas indicate that the ridges are close to or at the seafloor (< 10 m depth). The velocity model used for time to depth correction can be found in Appendix B*

not entirely covered in seismic data, but the multibeam bathymetric data hints the existence of quasi-circular domes similar to the ones observed on the western side of Renard Ridge.

The highest position of the ridge crests is found east of Al Idrisi mud volcano, at a depth of 380 m bsl. At this location, a less pronounced E-W trending ridge structure converges with the major NW-SE trending Vernadsky Ridge, northeast of Al Idrisi MV. The former structure is the Al Idrisi Ridge and can be observed east and west of the Al Idrisi mud volcano and thus underlies the mud volcano. The Al Idrisi Ridge has a weak positive topography (a few tens of meters maximum) and is plunges westward between the Fiúza and Al Idrisi mud volcano.

In between the Renard Ridge and Vernadsky Ridge and south of Vernadsky Ridge, deep basins occur, with the deepest point over 900 m below the sea surface (Fig. 4.10, 4.11). The sedimentary infill, counting from the reference reflection, in these basins is up to 250 meters thick. The overburden quickly thins towards the ridge axis and becomes very thin or zero. Especially in the deeper part of the area, below 400-500 m, the ridge crest crops out at the seafloor, where it is partly eroded.

The crests of the ridges display many normal faults (Figure 4.13A-D) with displacements varying from very small (e.g. west of Al Idrisi MV) to very large (e.g. north of Gemini MV, Conger Cliff). Northwest of Mercator MV a large collapse depression is visible at the seafloor while northeast of Al Idrisi the seafloor is highly irregular due to small displacements.

Seismic profiles over the central part of the Vernadsky Ridge give insight into its structure. Figure 4.13A shows the outcropping and eroded low-amplitude acoustic basement being covered by younger sequences. Correlation of the seismic data around the ridge culmination (Fig. 4.13A, between 3500 and 4000 m along profile distance) indicates that a large normal fault had been active in the past. This has created an offset of about 400 m at the ridge crest (location of the Conger Cliff). Northwards of the large normal fault (between 4000 and 6000 m along profile distance), smaller faults are found, which could either be antithetics from the main fault, or a consequence of collapse of a antiform crest after sediment removal in the subsurface due to mud volcano activity of the nearby Kidd mud volcano.

In the vicinity of this structurally active place, acoustic diffractions are observed (figure 4.13B, at 2500 and 4000 m along profile distance). Some diffractions clearly stand out above the seafloor and thus can be interpreted as (sidewards) diffractions caused by the presence of mound structures. The seismic data retrieved at the northern part of the Vernadsky Ridge are densely populated by acoustic diffractions (figure 4.13C). The diffraction height runs up to 50 m and their width up to 200 m. These diffractions are again interpreted as mound diffractions, indicating that nearly the whole seabed is covered with mound build-ups and mound patches. Structural basement highs are separating small intraridge basins. These are likely to be fault-controlled.

A very high-resolution deep-tow chirp seismic profile along the crest of PDE (figure 4.14) shows the mounds as rounded cone shaped features, with a height up to 60 m. No internal structures are observed. On some parts of the profile, mostly between 1500 and 4000 m along
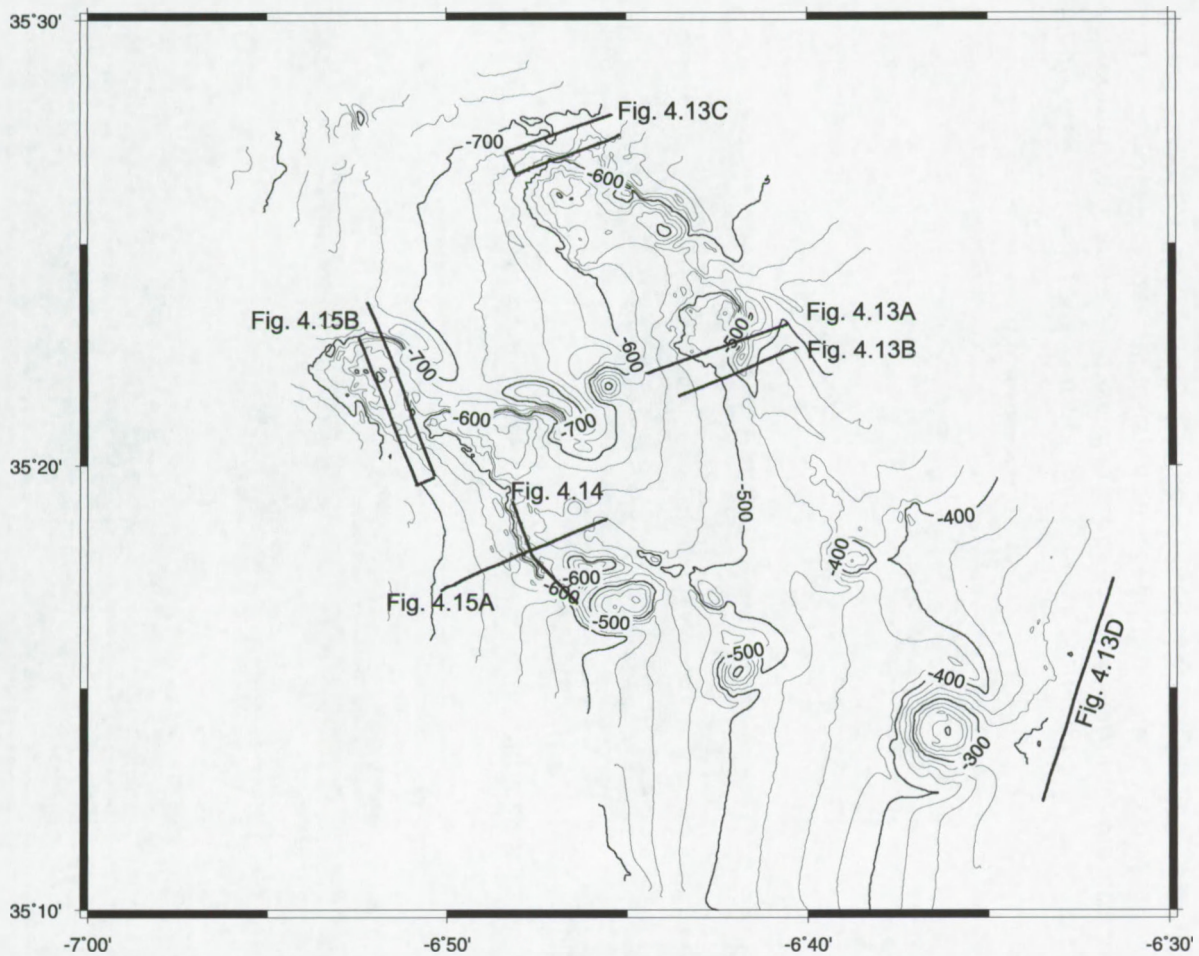
Figure 4.12: Location of seismic profiles in figures 4.13, 4.14 and 4.15

the distance axis, subsurface reflections are recorded. Generally, the subsurface has a low amplitude. An erosive surface below the mounds can be observed and is interpreted as the mound base.

A profile perpendicular to the PDE shows medium to high amplitude sequences, covering a low-amplitude unit (figure 4.15A). The low-amplitude body has a very steep SW dipping slope beneath the escarpment. Northwards, NE dipping reflections are observed in the low-amplitude unit. The low-amplitude structural acoustic basement, which is part of Renard Ridge, is eroded and crops out at the seafloor. Diffractions at and above the outcropping basement are indicative for the occurrence of elevated mound structures. A small mound-like low-amplitude body occurs in the high amplitude sequences that cover the basement. Other profiles near the PDE also indicated the presence of small mound-like features in the sedimentary sequences (figure 4.16). Reflections are draping the features, indicating that they are real physical structures. The small mounded features only occur upslope a set of small normal faults associated with gas blanking and bright spots. A direct relation between the
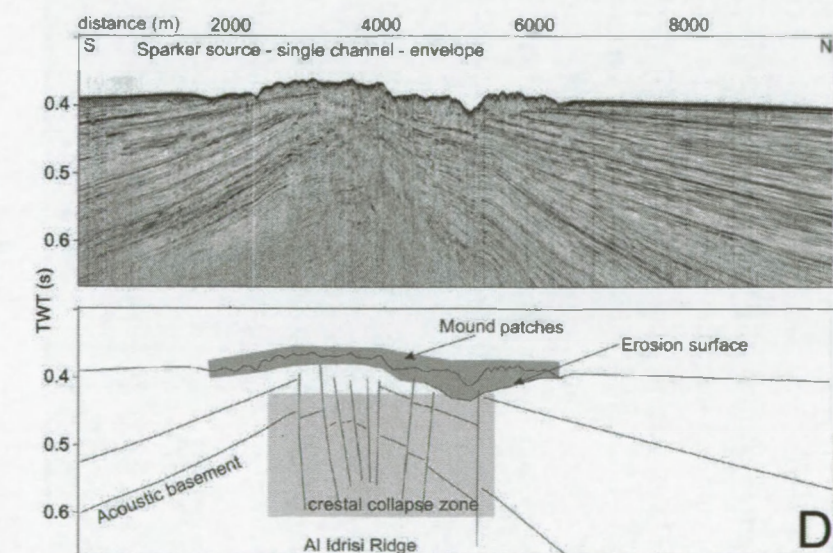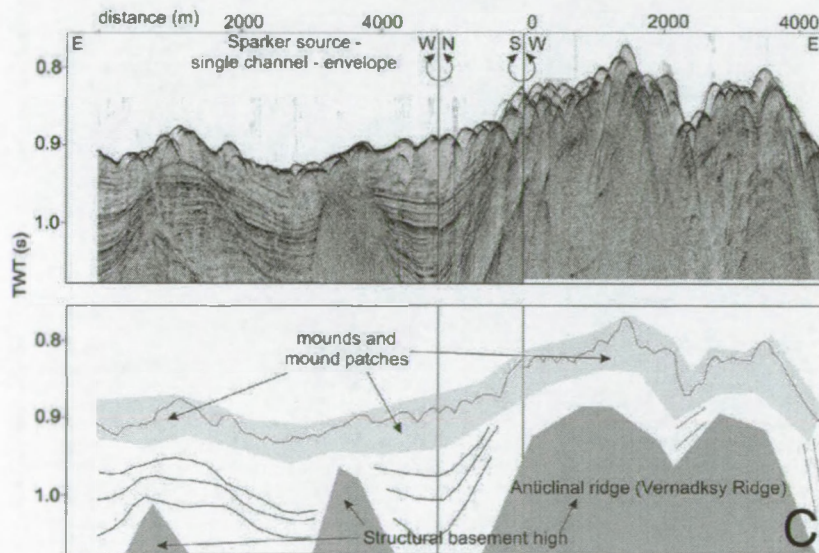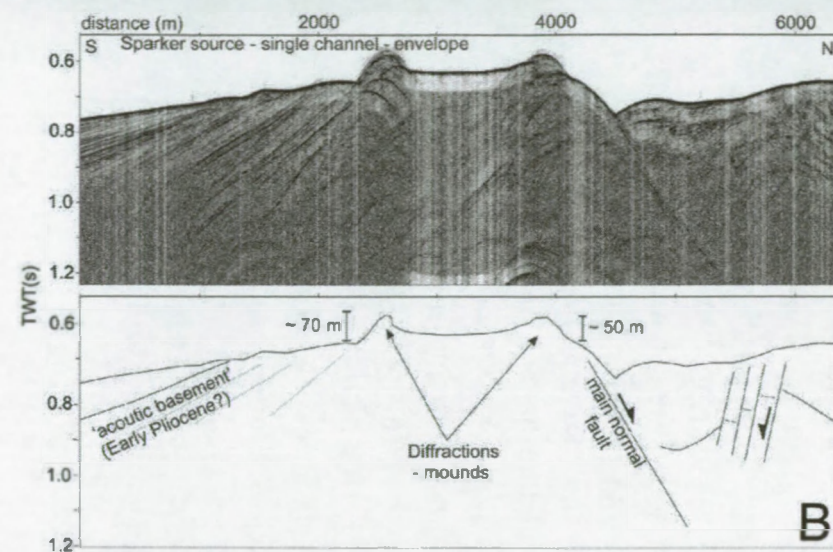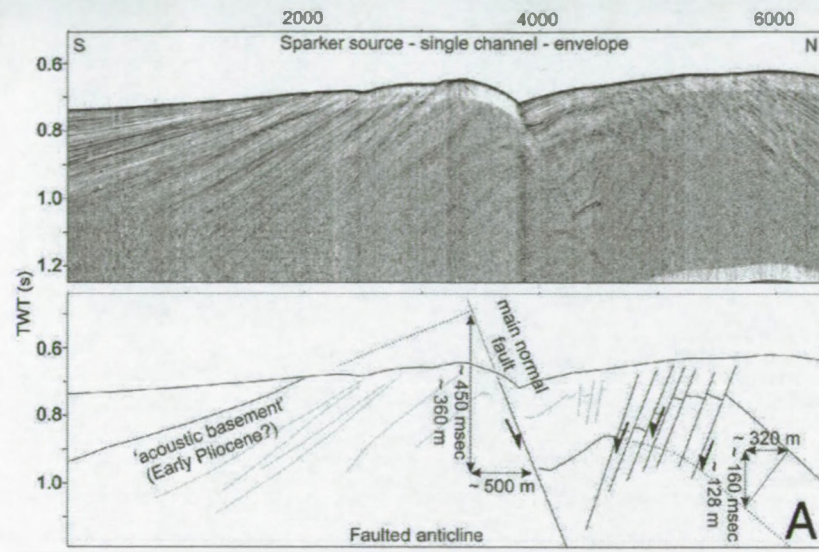
Figure 4.13: *(A) Sparker seismic profile over the central part of Vernadsky Ridge, showing the outcropping acoustic basement as well as a normal fault and a set of smaller faults giving insight into the structure of the ridge. (B) Sparker seismic profile over the central part of Vernadsky Ridge, representing a set of diffractions on top of the basement, which can be interpreted as mound structures. (C) Set of seismic profiles over the northern part of Vernadsky Ridge, showing the dense population of different mounds and mound patches and the structural basement highs separated by small intraridge basins. (D) Sparker seismic profile, representing the Al Idrisi Ridge and a set of small mound-like features on the sediments burying the ridge.*
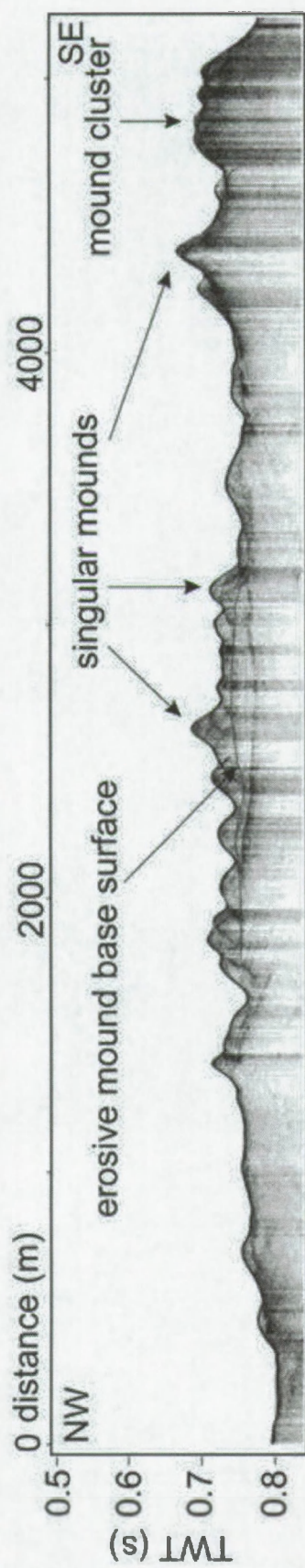
Figure 4.14: *CHIRP seismic profile over Pen Duick Escarpment indicating the singular mounds topping the cliff and the erosive mound base surface).*
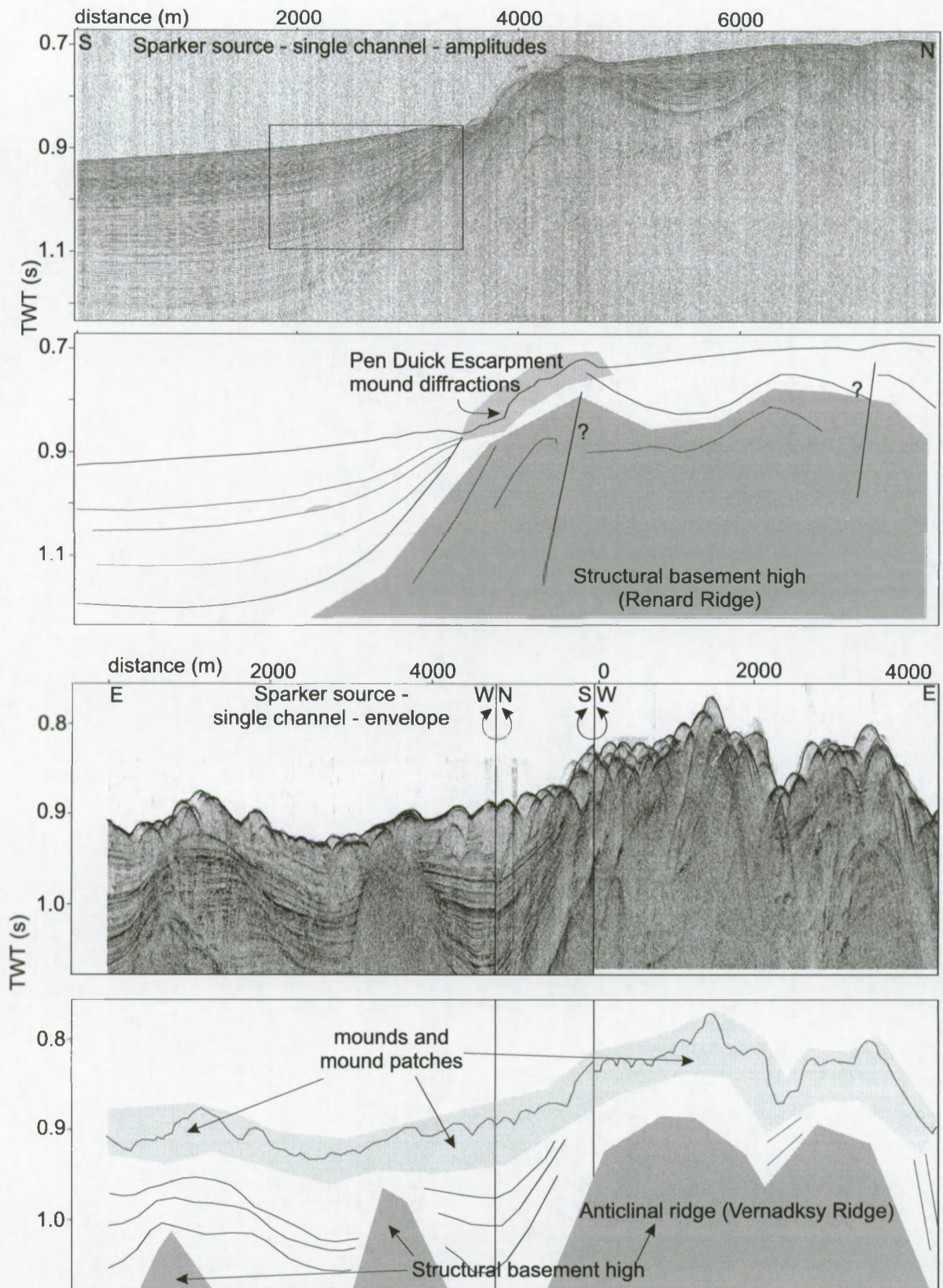
Figure 4.15: *(A) Sparker seismic profile perpendicular to the PDE, showing the mound diffractions on the escarpment. The box indicates the location of the detail in figure 4.16 (B) Set of Sparker seismic profiles over Renard Ridge. The structural basement, two faults and mound structures can be recognized on the profiles.*
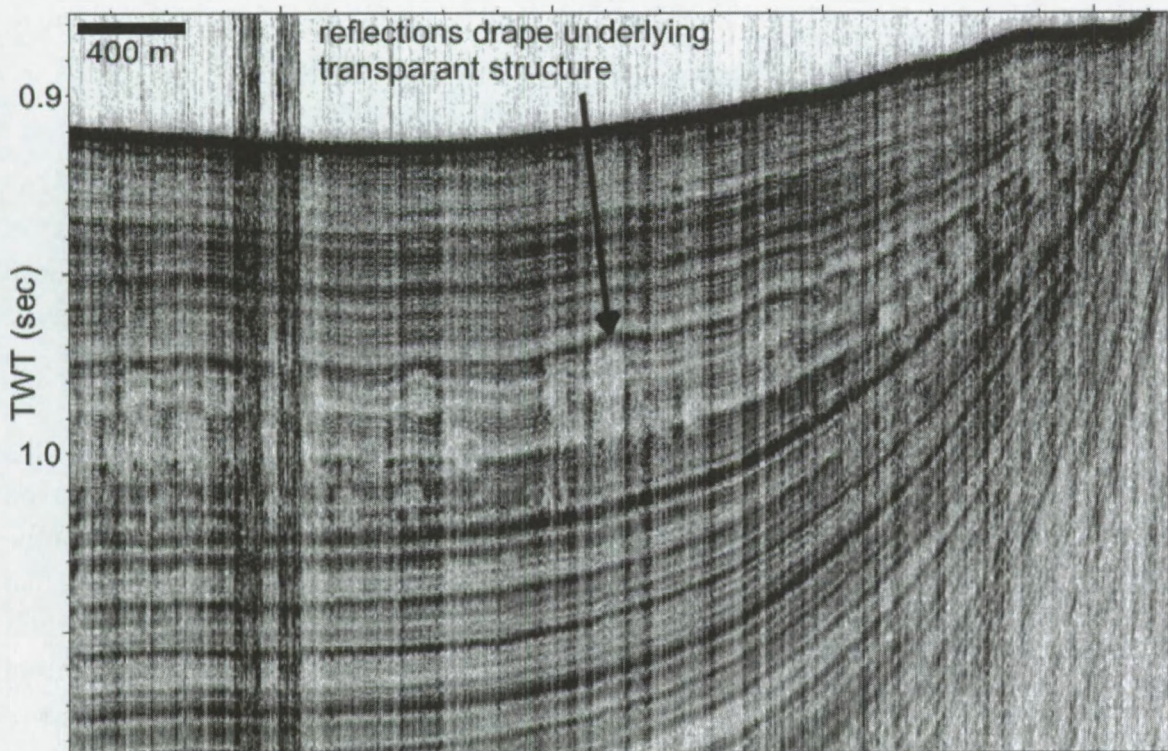
Figure 4.16: *Some small buried mounded features occurring in the sediments at the foot of the escarpment.*

two observations is speculative. The features may be interpreted as small buried mounds and could be an indication of the onset of mound growth in the area.

A set of seismic profiles, jointly shown in figure 4.15B, shows the occurrence of many mounded features at the culminations of the low-amplitude acoustic basement. The presence of at least two large normal faults can be inferred from the data. A first fault occurs at the northern side of the ridge and dips towards the north. The basement is present near or at the surface. On top of the ridge, elevated features are indicating the presence of mound structures. Further southwards, a second normal fault with a large offset again disrupts the seafloor. A large set of diffractions is again interpreted as the presence of mounds on top of the outcropping basement. The height of the mounds reaches several tens of meters.

The Al Idrisi ridge appears on seismic data as an anticline that is buried below the sedimentary sequences. The crest of the low-amplitude basement, culminating at less than 100 m below the seafloor, is highly fractured and may have collapsed in response to sediment withdrawal by mud volcano activity. Several bright spots indicate the presence of gas in the sediments at shallow positions. Mound-like features with a low-amplitude and chaotic internal facies are topping the anticline culmination area at the seafloor. Below the chaotic facies, an erosive surface is present (figure 4.13D). The chaotic mounded features can be interpreted

as small coral patches, what is confirmed by sampling. The erosive surface is interpreted as the base of the mounds.

4.1.3   Possible relation to deep structures

Flinch (1993) indicates the presence of large rotated blocks of Miocene deposits that offset the top of the accretionary wedge (Figure 2.8). These blocks slid and rotated along deep lystric faults, resulting in a ridge-basin-ridge morphology; the ridges corresponding to the culminating parts of the rotated blocks. The basins in between these crests developed and filled during the Plio-Pleistocene.

The location of the Vernadsky Ridge, Renard Ridge and Al Idrisi Ridge coincide with the locations of the westernmost ridges indicated by Flinch (1993). Therefore, it may be assumed that in the Flinch model, the seafloor ridges correspond to or reflect the upper edges of the buried rotated blocks. The large lystric faults are then evident fluid migration pathways that enable depressuring of the accretionary wedge sediments. The extrusion of fluids and mud at the seafloor resulted over time in the growth of large mud volcanoes. The observed crestal depressions and normal faults could then be explained by collapse due to mass loss compensation.

This model leaves some observations unanswered. First, the large ridges are in fact built up by multiple short pieces of arcuate, even anastomizing smaller ridges. This is best illustrated in the Renard Ridge. This would require the existence of many small blocks that have rotated in different directions and over different angles. The Flinch model does not account for this. Second, the large quasi-circular features on the west side of Vernadsky and Renard Ridge cannot be explained by the presence of rotated blocks, so an alternative explanation needs to be considered.

The presence of the large mud volcanoes indicates mobilisation of massive amounts of mud breccia towards the surface. Large amounts of overpressured mud does not only give rise to mud volcano activity, but also to diaprism. Diapiric structures are found to lie under mud volcanoes (Hedberg, 1974), e.g. in the northern part of the Gulf of Cadiz (Fernandez-Puga et al., 2007) in eastern Indonesia (Barber et al., 1986), on the Mediterranean Ridge (Camerlenghi et al., 1992, 1995; Kopf et al., 2000), deepwater Nigeria (Graue, 2000), the Gulf of Mexico (Sassen et al., 2003), the Makran margin (Schluter et al., 2002), offshore Brunei (Van Rensbergen and Morley, 2001), Barbados complex (Sumner and Westbrook, 2001), the South and East China Sea (Xie et al., 2003; Yin et al., 2003), etc. The mechanism of diapirism preceding mud volcanism, or worded differently, mud volcanism as a surface expression of diapirism, seems to be an ubiquitous process. The large gypsum crystals and brines observed at the Mercator mud volcano crater may even indicate the combination of salt and mud diapirism. Hensen et al. (2007) suggested a shallow salt source at the latter location.

Anastomizing ridges are often observed in areas where subsurface salt mobilisation is ac-

tive (C. Berndt, National Oceanography Centre Southamtpon, 2007, pers. comm.). Vendeville and Jackson (1992) show typical linear diapiric walls parallel to and closely associated with extensional graben systems. Additionally, the profiles presented by Vendeville and Jackson (1992) and Hudec and Jackson (2006), but also in many other studies including those from the Gulf of Mexico (Seni, 1992), the Cascadia Margin (McNeill et al., 1997), offshore Israel (Gradmann et al., 2005), in the Pyrenees (McClay et al., 2004) and offshore Angola (Duval et al., 1992; Lundin, 1992) are nearly identical to the line drawings presented by Flinch (1993) and Flinch et al. (1996). In all these profiles, lystric faults extend into ridge-like structures at the seafloor, while beneath these features, large triangular-shaped bodies are present. Flinch attributes these triangular bodies (that appeared chaotic in the seismic data, Flinch (1993)) to parts of the accretionary wedge complex, which consists of a chaotic mix of sediments. However, in all the forementioned studies, these are identified as (partly) isolated asymmetric pockets of salt. Bally (1981) defined these ridge-like asymmetric features, where a short steep scarp slope is in normal fault contact with the cover, as *salt rollers*. In a model of halokinesis, the quasi circular structures associated to the ridges (described above) could also be small diapiric bodies of mud and/or salt.

The presence of salt sheets beneath the Plio-Pleistocene deposits indeed facilitate slope instability, leading to features like the mass wasting nappe of the Gulf of Cadiz (Maestro et al., 2003). Although there is no data available in this study to prove or disprove a situation in which halokineses actually controls the region, morphological and geochemical (Hensen et al., 2007) data suggest the presence a salt body in the subsurface. Together with the similarity between the interpretative drawings made by Flinch (1993) and multiple examples in literature, the case for extensional tectonics combined with halokinesis and mud mobilisation as tectonic-structural setting for the El Arraich mud volcano field becomes a possibility.

4.2 Shallow stratigraphy of the El Arraiche mud volcano field

4.2.1 Description

4.2.1.1 General

The low-amplitude, parallel to slightly divergent reflections of the 'seismic basement' (below the reference horizon) are characterized by the presence of three anticlinal ridge structures of which the ridge crests are often strongly eroded. The depth of the crests is between 700 and 350 msec below sea surface. Both the Vernadsky Ridge and Renard Ridge are outcrops of these ridges and trend NW-SE. A more E-W oriented ridge is completely buried and is located under the Al Idrisi mud volcano. The ridge is shallowly buried at the mud volcano's east side (90 meters below seafloor) and the westward dipping crest deepens to 135 mbsf in the westernmost part of the Al Idrisi seismic grid. Between the Fiúza, Al Idrisi and Gemini MV, the top of the basement deepens to 1050 msec ($\sim$ 900 m) and forms a central basin. Also south of the Renard Ridge, between the Renard and Vernadsky Ridges and north of Vernadsky Ridge, the basins deepen strongly. The deepest parts are encountered southwest of Gemini MV with depths down to 1200 msec below sea surface. The basement is covered by concordant to onlapping units with higher amplitude; together with the strong erosion at the ridge crests rendering the interface an obvious unconformity. The sedimentary cover is absent or very thin at the ridge crests north of Gemini and Mercator mud volcanoes and east of Al Idrisi mud volcano. In the basins however, thicknesses over 400 msec (about 360 m) are observed. Unfortunately, it was impossible to correlate all units and subunits north of the Gemini mud volcano and Mercator mud volcano.

The sedimentary cover above the refrence horizon mostly consist of parallel, continuous reflectors with variable amplitudes. Small internal unconformities were observed and served to subdivide the strata in different units. In general, the tops and bottoms of the units are continuous and parallel, although erosional truncation is observed. Onlap is observed in a few cases and mostly corresponds to units that cover a pre-existing positive topography, e.g. an extruded mud flow or a ridge structure. Since the units are situated on the upper slope, the general reflector configuration suggests that the units are progradational-aggradational wedges. This corresponds to the general sedimentary setting of the Gulf of Cadiz and NW Africa since the Plio-Pleistocene (Flinch and Vail, 1998; Maldonado et al., 1999; Hernandez-Molina et al., 2003).

Three large units were recognized and could be divided in smaller subunits. Unit 1 is built up by continuous parallel to slightly divergent reflections with low to intermediate amplitude. Small internal unconformities occur mostly near the ridge crests and are used to divide the unit in three subunits. Subunit 1a covers the basement. It is conform in the basins and shows onlap against the ridge flanks. The configuration is mostly parallel but shows some divergence towards the depocentres. The subunits 1b and 1c have slightly higher amplitudes
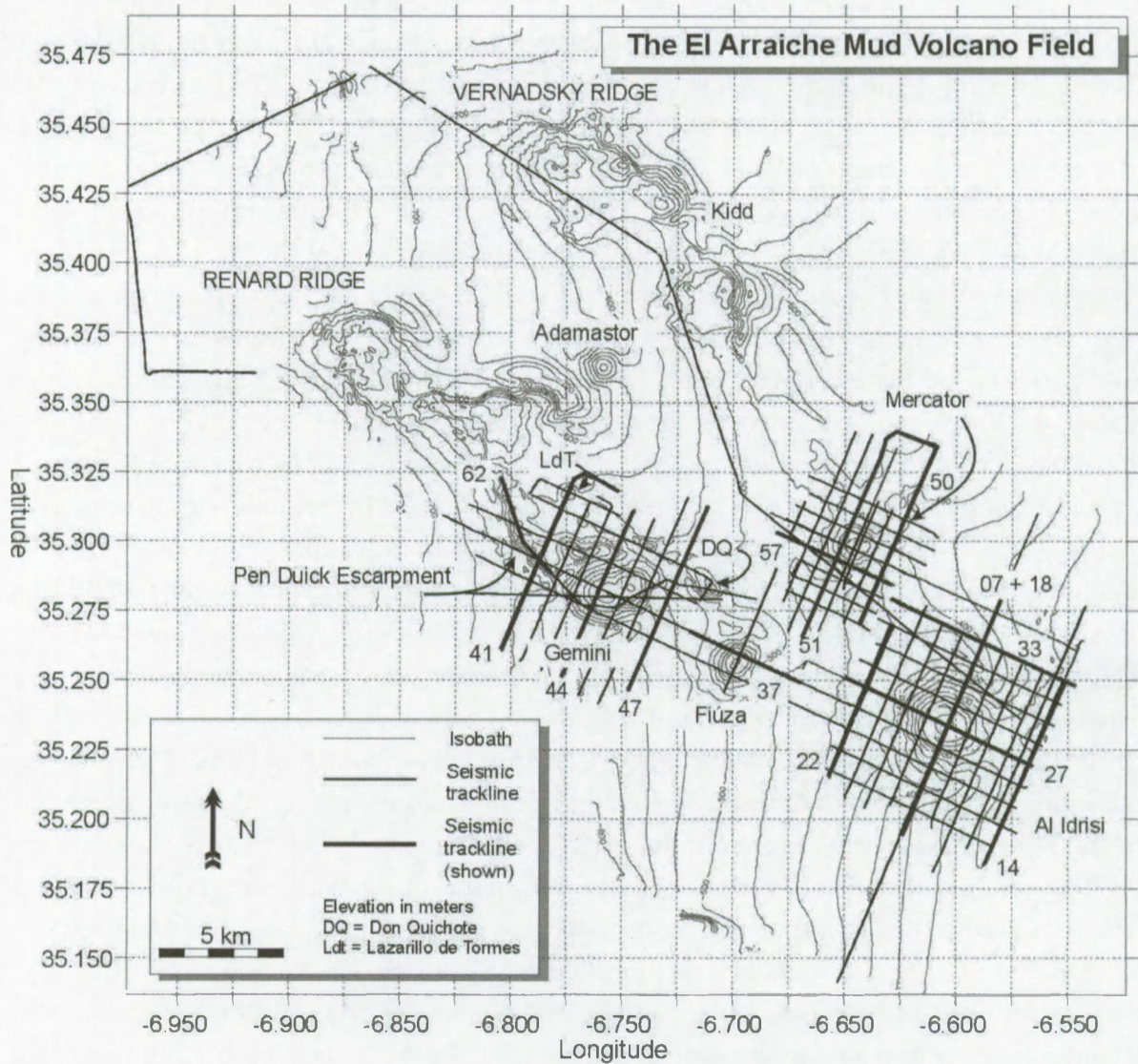
Figure 4.17: *Locatio of seismic profiles presented in figures 4.18 to 4.24. Bathymetry map of the El Arraiche Mud Volcano field. Contour spacing : 25 m.*

than subunit 1a. The subunits 1b and 1c show onlap against subunit 1a and the ridges. The units thicken towards the depocenters but have in general a parallel reflector configuration. Strong erosion of the top of unit 1 exists, e.g. north of the Al Idrisi mud volcano, although this is a result of erosional moat formation around the Al Idrisi mud volcano. Otherwise, the top of the unit is concordant.

Unit 2 is characterized by reflectors with low to intermediate amplitudes that are parallel to divergent (due to basinward thickening). The top and bottom of the unit is mostly concordant except near the ridge crests and around the mud volcanoes (due to the presence of erosional moats). Unit 2 is subdivided in 2 subunits that strongly thicken towards the depocentres.

Unit 3 is subdivided in 5 subunits based on small internal unconformities. The lower subunits (3a, 3b, 3c) consist of parallel medium to high amplitude reflections that onlap slightly near the ridge crests. These units appear to have a more aggradational than progradational character because they remain more isopachous compared to the underlying subunits. The two upper subunits, 3d and 3e, have high amplitudes and mostly parralel reflections and also appear more aggrading in nature. The base of these units is often onlapping.

4.2.1.2   Al Idrisi mud volcano (Figures 4.18, 4.19, 4.20)

The top of the basement is eroded at the north side of the mud volcano and dips slightly towards the centre of the MV at its east side. At the north side of the mud volcano, unit 1 onlaps the eroded basement, and dips towards the center of the MV (Fig. 4.18, lower image). At the south side of the mud volcano, erosion is not observed, but unit 1 also slightly dips towards the center of the MV. Subunit 1a covers the basement around Al Idrisi MV, except at the Al Idrisi ridge crest at the east side of the mud volcano, with onlap near the ridge crests. The internal configuration is parallel, with a low amplitude. Subunit 1b and 1c, locally onlapping subunit 1a and the Al Idrisi Ridge, have slightly higher amplitudes than subunit 1a. The internal configuration of subunit 1b is parallel, and subunit 1c is rather divergent (Fig. 4.19, upper image). The top of subunit 1c is often stronlgy eroded near the top of the ridges (Fig. 4.20, upper image). Unit 2 is divergent south of the mud volcano, while at the north side, the unit dips towards the center of the mud volcano (Fig. 4.18). The unit has a low amplitude and continuous seismic facies. Subunits 3a, 3b and 3c are parallel and with a medium to high amplitude (Fig. 4.19). Subunit 3d is divergent, subunit 3e onlaps strongly at the south side of the ridge, and has a parallel to divergent reflector configuration.

The oldest mudflow extruded by the Al Idrisi MV is observed in subunit 1b, it is a small mudflow caught in a shallow moat-like feature. Unit 2 is characterized by the presence of many mud flows at all sides of the mud volcano (Fig. 4.20). Only one small mudflow is present at the base of subunit 3a. No mud flows are observed in subunits 3b, 3c. The two youngest units, 3d and 3e, contain many mudflows again (Fig. 4.18, 4.20).
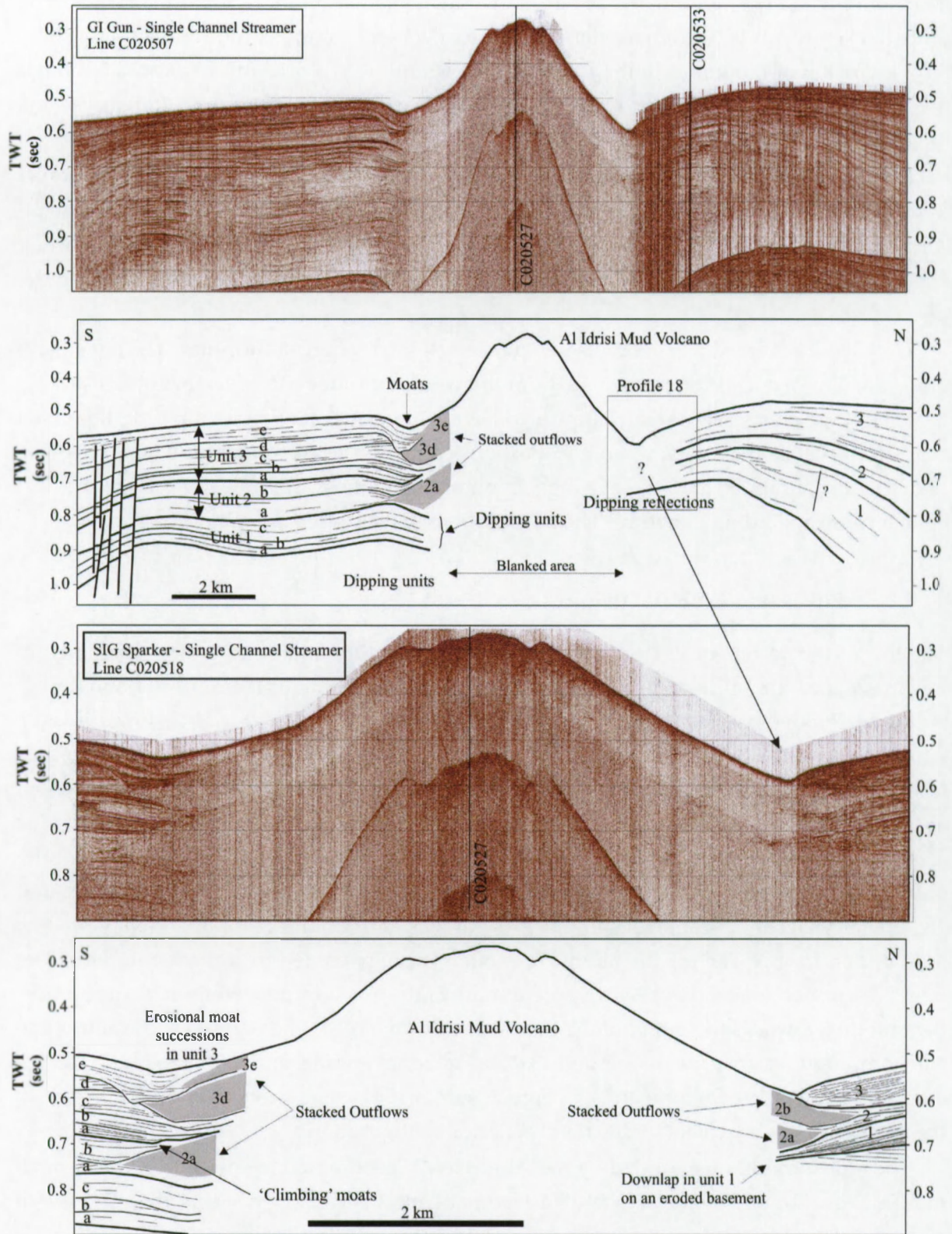
Figure 4.18: *Two N-S directed seismic profiles through Al Idrisi MV.*

Moats around the mud volcano are present at the south and north side. Subunits 3d and 3e are very deeply incised by moats with depths of over 100 m (Fig. 4.18). Ersional moats are also present at the south side in subunits 2a through 3c. There is a continuous alternation of deposition and erosional moat formation, strongest in unit 3. Specifically at the south side of the mud volcano, it can be observed how a mud flow deposition shifts the deepest point of a moat outwards from the center of the mud volcano. After deposition, this point climbs back towards the center of the mud volcano, while sediments onlap the youngest mudflow.

4.2.1.3   Mercator mud volcano (Figures 4.21, 4.22)

The Mercator mud volcano is located on south flank of the Vernadsky Ridge. The NW-SE trending ridge culminates near the mud volcano and plunges towards the east to merge with the Al Idrisi Ridge northeast of the Al Idrisi mud volcano. The crest is subject to heavy collapse creating offset ramps of over 25 m north of the Mercator MV (Fig. 4.21, upper image). The faults run parallel with the anticlinal ridge crestline. Just north of the Mercator mud volcano, a heavily faulted and collapsed area is present with curved normal faults disappearing under the mud volcano. Accousic blanking as well as bright spots are associated with these faults (Fig. 4.21, upper image). South of the Mercator MV, the ridge flank contains a depression. A small buried mud volcano is present at this depression as well (Fig. 4.21, upper image).

The top of the basement is eroded near the ridge crest, especially in areas where it is not covered by younger sediments, e.g. northeast of the mud volcano (Fig. 4.21, lower image). Diffraction hyperboles at ridge crests are present at some locations, where small mounded features are observed on the multibeam bathymetric data. The basement and unit 1 are faulted at the west side of the Mercator MV, and faulted, eroded and dipping towads the center of the mud volcano at the east side. Units 1 and 2 onlap against the basement at the Vernadsky Ridge culmination (Fig. 4.21, lower image). The internal configuration of subunit 1a is slightly divergent to parallel, subunits 1b has a parallel and 1c a slightly divergent reflector configuration with higher amplitudes than subunit 1a. Subunit 2a has high amplitudes, subunit 2b low amplitudes. Moat erosion is present at the base of unit 2, and also at the east side at the base of subunit 2. Subunits 3a, 3b and 3c are parallel, first onlap and then drape the underlying topography and cover the existing mud flows completely. The amplitude of these subunits is medium to low. Units 3d and 3e have higher amplitude and display som divergence perpendicular to the ridges.

The oldest mud flow is situated in unit 1, at the north side of the mud volcano where no detailed stratigraphy was tied. Large mudflows then are present at the base of unit 2, within subunits 2a and 2b. Subunits 3a, 3b and 3c contain no mudflows, subunits 3d and 3e contain many large mudflows again (Fig. 4.21, upper image; Fig. 4.22).

Moats are present at the south side, as well as the southwest and southeast side of the mud
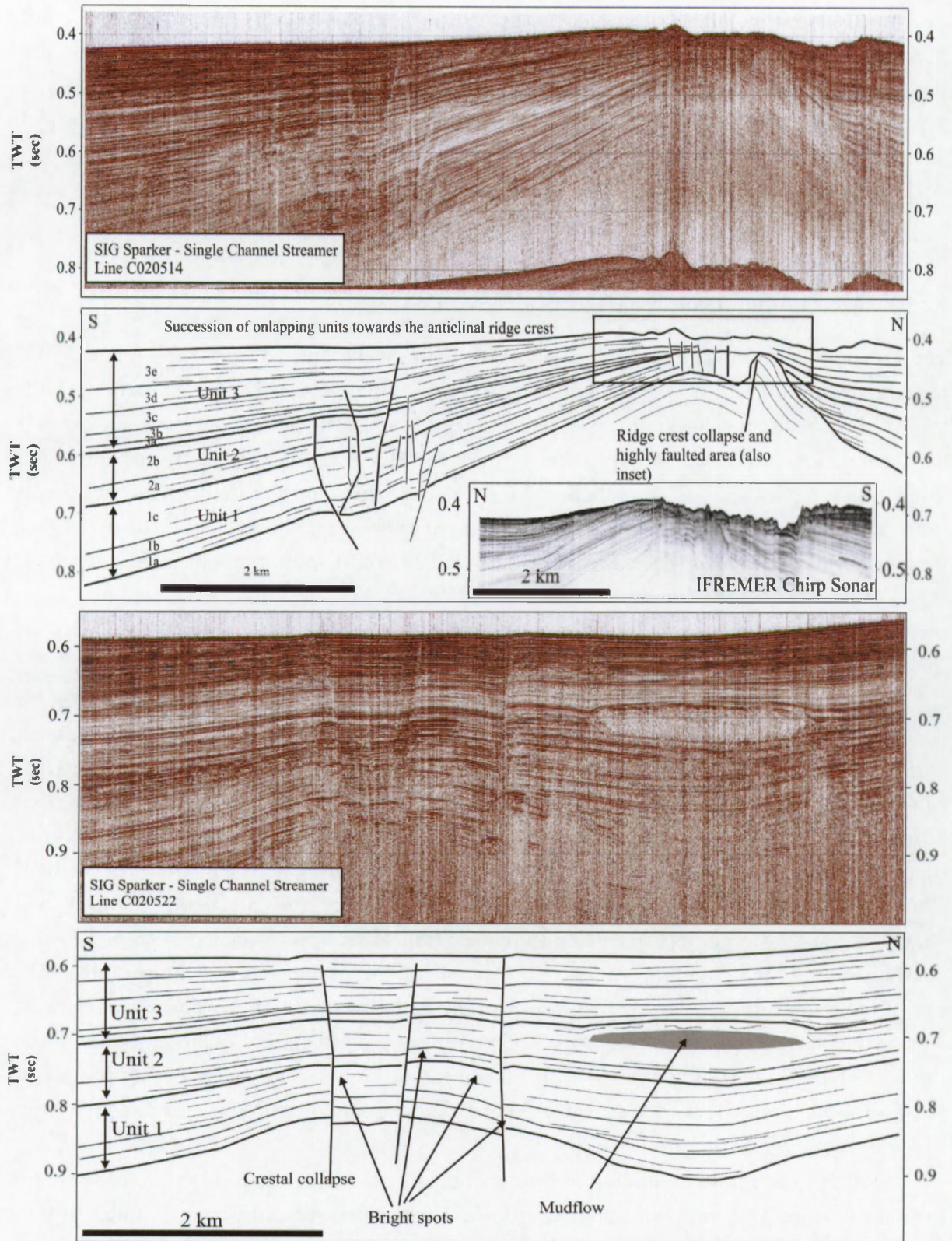
Figure 4.19: Two N-S directed seismic profiles. Top: east of Al Idrisi MV; Bottom: west of Al Idrisi MV.

volcano. The oldest moats are present at the base of subunit 1c, which can be best observed at the southeast side of the mud volcnano (Fig. 4.22). A large mudflow fills a moat at the base of unit 2. This deep moat exists throughout unit 2, slowly becoming less deep as it fills with sediments. At the southwest side, the deepest point of the moat shift towards the mud volcano as depth decreases and the underlying mudflow gets buried. At the southeast side, a mudflow in subunit 2b shifts the deepest point of the moat outwards. The seismic reflections suggest a continuous deposition with existence of a moat until subunit 3d. With the moat shifting further towards the mud volcano. In subunit 3d, new mudflows appear and shift the deepest moat locations outwards again. The maximum distance between the inner- and outermost moat occurence is over 250 meters. The deepest moats are found at the south side of the mud volcano. The moat at the present seafloor is over 40 meters deep.

4.2.1.4   Gemini mud volcano (Figure 4.23), Figure 4.24, lower image)

The Gemini mud volcano is located at a large scarp structure (Fig. 4.23, upper image) at the easternmost extension of the Renard Ridge. North of the mud volcano, a large erosive scarp is present, with a deep moat present in between both (Fig. 4.23, lower image). West of the Gemini mud volcano, the Pen Duick Escarpment extends northwestwards. The basement crops out at the seafloor north (Figure 4.23) and east (Figure 4.24, lower image) of the Gemini mud volcano. South of the mud volcano, it is deeply buried (400 msec twt below the seafloor). Seismic blanking and the occurrence of bright spots along small normal faults is widespread in the area around the Renard Ridge.

The top of the basement is strongly eroded at the ridge crests. It crops out at the seafloor. The basement generally has a low amplitude parallel seismic facies, but below the ridge crest, the signal is chaotic or blanked. The thickness of the cover runs up to over 400 msec twt in the southernmost part of the dataset. Unfortunately, it was impossible to correlate all units and subunits north of the Renard Ridge. Unit 1 is built up by parallel to divergent reflections, with onlap at the base of subunit 1a. The amplitude of the reflections is low (1a) to intermediate (1b, 1c). The top of subunit 1b is locally eroded at the east side of the Gemini mud volcano, maybe as a sign of initial moat formation. Unit 2 is has a parallel to divergent reflector configuration perpendicular to Renard Ridge. The amplitude of the reflections is of a low to intermediate strength. The lower part of unit 3 has a parallel (3a - 3c) to slightly divergent (3d, 3e) reflection configuration. The amplitudes vary from intermediate to high.

The Gemini MV blanks a lot of the underlying strata, so it is not as easy to recognize the mud flows interfingering with the normal deposits as in the case of the Al Idrisi and Mercator MVs. The only clear mudflows occur in subunit 3d at the south side of the mud volcano (Fig. 4.23, lower image) and in subunits 2b, 3d and 3e at the east side. The unit 1 is pushed upwards near the mud volcano and overlies a transparant area. This could be a deep and old mudflow, but no other indications are present to support this.
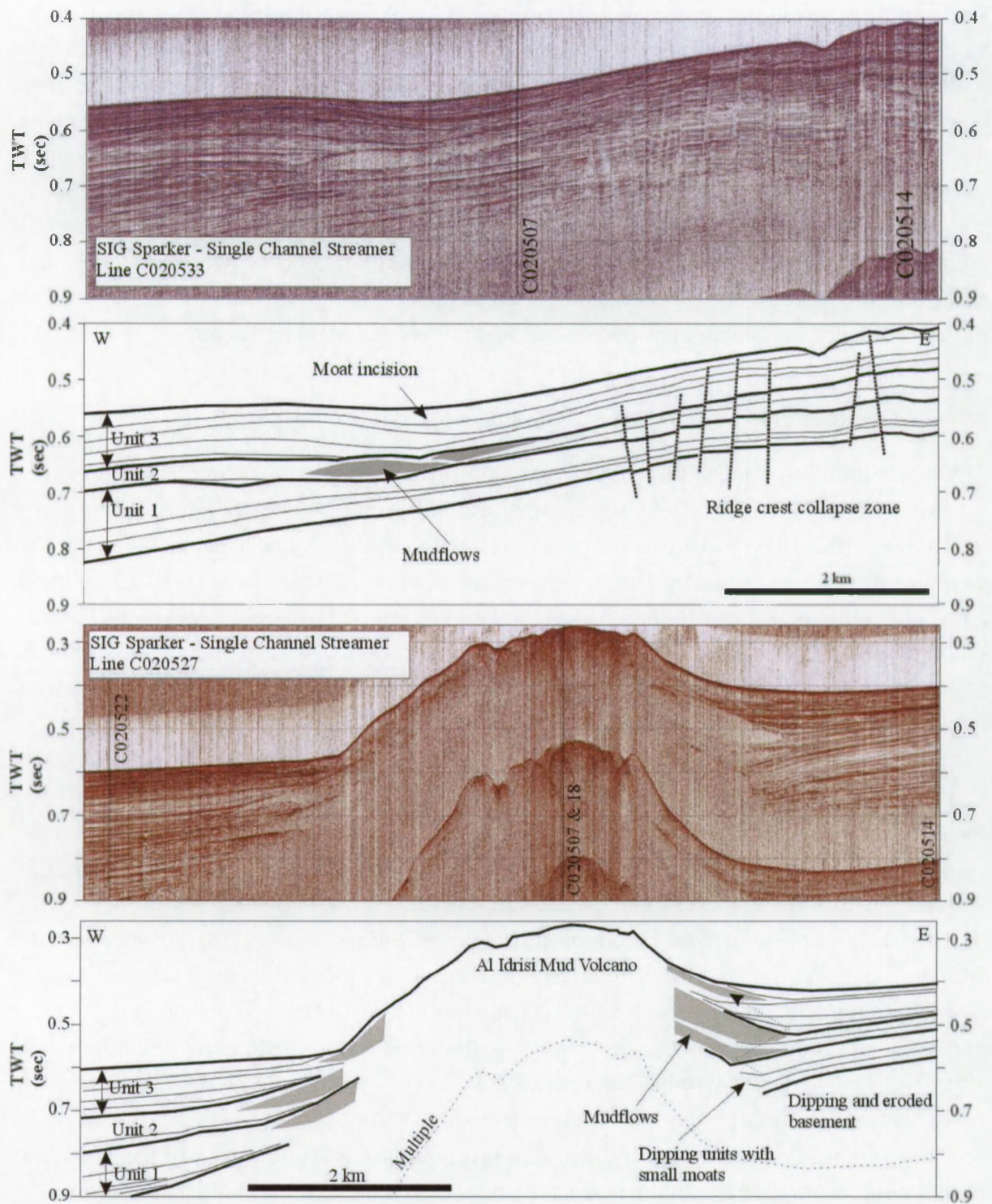
Figure 4.20: *Two E-W directed seismic profiles. Top: north of Al Idrisi MV; Bottom: over Al Idrisi MV.*

Erosional moats are observed starting from 2b and exist throughout subunit 3e. The moat-like structure north of Gemini MV has probably gotten its magnitude due to a combination of erosion and fault offset.

4.2.1.5 Fiúza mud volcano (Figure 4.24, lower image)

Only three seismic lines have been interpreted over the FiÃžza MV; not all sides of the mud volcano gave information on the activity of this MV, only the east and west side.

The basement east and west of Fiúza MV slightly dips towards the mud volcano. Also the reflections of unit 1 display a dip. The amplitudes of the units vary from low – intermediate for unit 1, to low (unit 2) to intermediate-high (unit 1).

Mud flows are present in subunits 1c, 2a, the top of 2b or the base of 3a, 3d and 3e. Again no mudflows are observed in subunits 3b and 3c. At the west side of Fiúza, onlap of normal deposits on a mudflow is very well visible in unit 2a, with infill of a moat in front of the mudflow.

4.2.1.6 Anomalous internal reflections in mud volcanoes

The Mercator and Fiuza mud volcanoes both show an anomalous but coherent subbottom reflection, indicated as H event (Figures 4.21, 4.22, 4.25). The depth of the H event varies from 0 msec near the mud volcano crater to over 50 msec further away. The presence of any coherent signal is unexpected since mud volcanoes are mainly built up by an extruded mud-supported breccia, hence lacking any internal structure. Only a chaotic seismic facies is expected. The depth of this event was mapped over the Mercator mud volcano, a seismic grid over the Fiúza MV is not present. The seismic signal shows that the H event has an inverse polarity in regard to the seafloor reflection (see figure 4.26). The H event only occurs within the mud volcano body and does not extend into the layered hemipelagic sedimentary environment around the mud volcanoes. Hence it is not a crosscutting reflection. Away from the crater, the reflection is parallel to the seafloor, where it forms a bottom simulating reflector (BSR) at a depth of about 50 milliseconds below the seafloor. The H event shallows toward the center of the mud volcano and intercepts with the seafloor reflection at the edge of the crater (Figures 4.25 and 4.27).

4.2.2 Stratigraphy

Flinch and Vail (1998) interpreted 11 stratigraphic units south of the study area of which 8 postdate the Mid-Pleistocene Revolution (MPR; 900 ka) (see also figure 2.9). The last units correspond to 4th order sea-level fluctuations. Llave et al. (2001) and Hernandez-Molina et al. (2003) show that prograding-aggrading wedges on the shelf and slope of the northern Gulf of Cadiz are in fact tied to asymmetric 3th and 4th-order climatic and sea-level cycles of 200
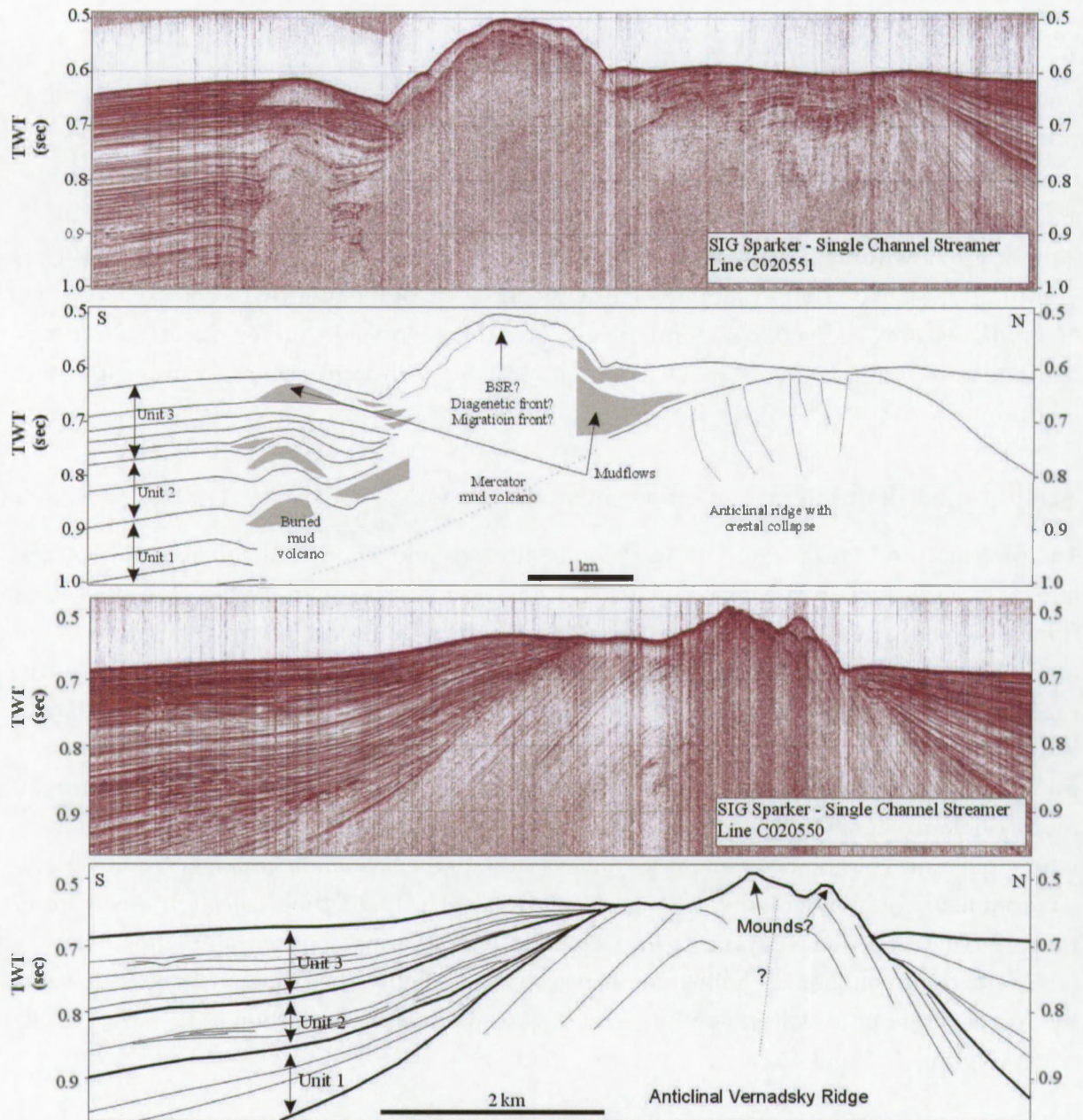
Figure 4.21: *Two N-S directed seismic profiles. Top: over Vernadsky ridge, Mercator MV and buried MV; Bottom: over Verndasky ridge, east of Mercator MV.*
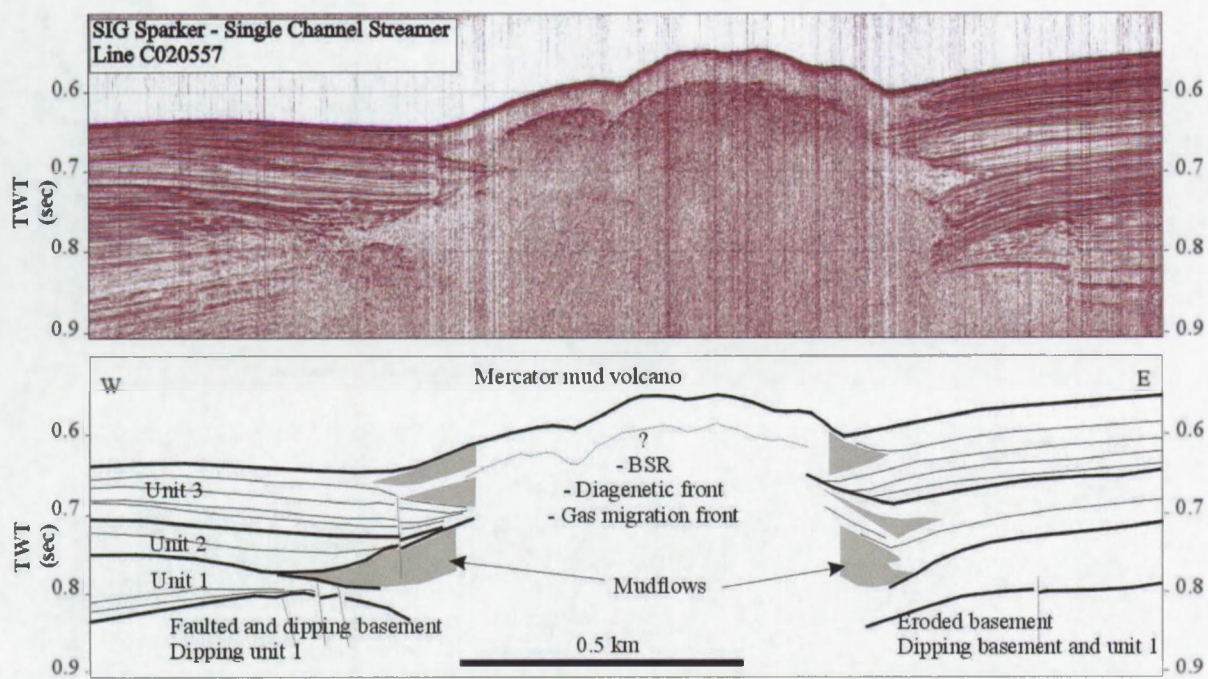
Figure 4.22: E-W directed seismic profile over Mercator MV.
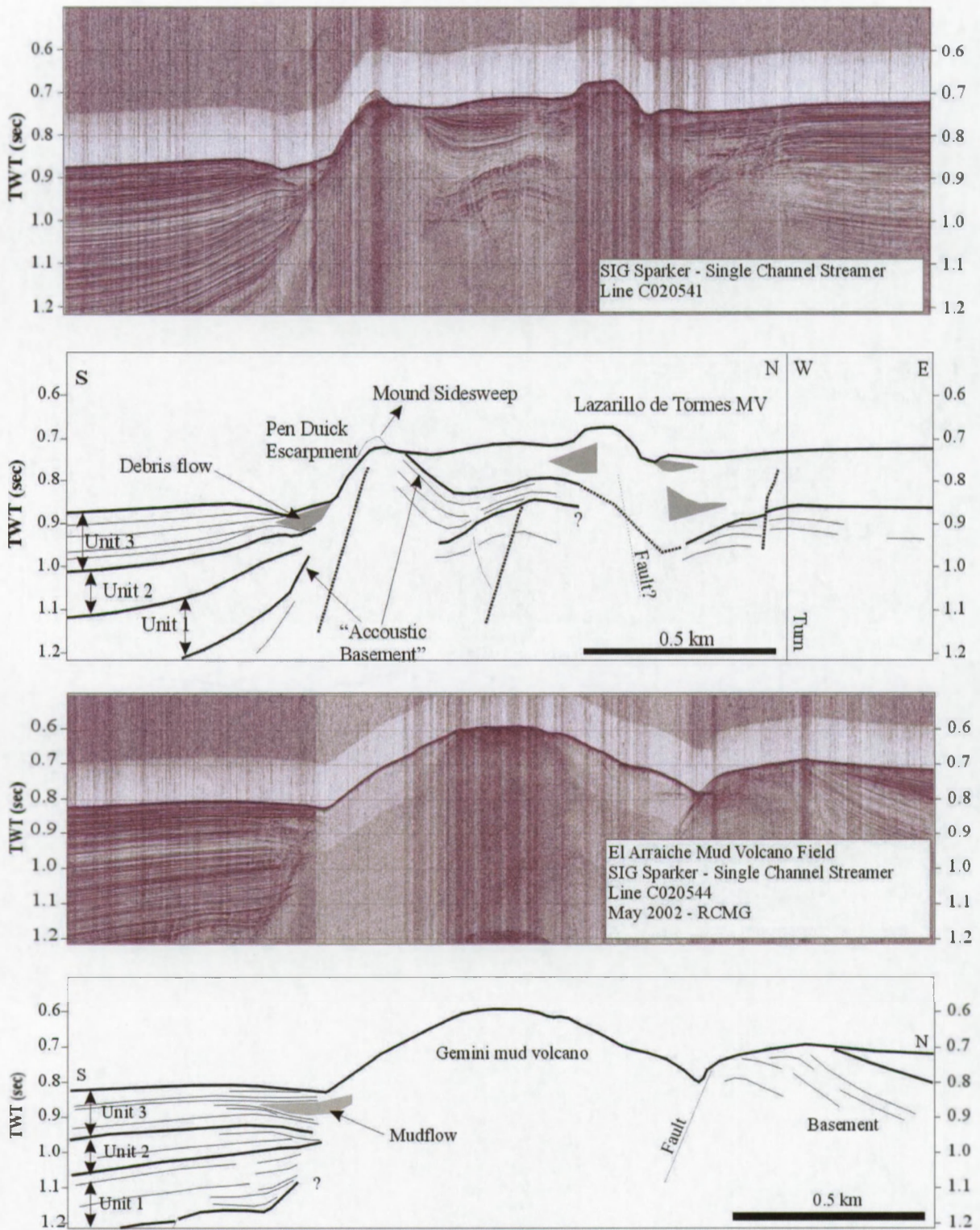
Figure 4.23: *Two N-S directed seismic profiles. Top: over Renard ridge and Pen Duick Escarpment; Bottom: over Gemini MV.*

ka duration which postdate the Quaternary Discontinuity (1.6 Ma; QD). The only source of chronostratigraphic information in the area is the LAR-1 drill hole (Flinch, 1993) which is just outside the El Arraiche mud volcano field and cannot easily be tied into our dataset.

Nevertheless, the stratigraphic units identified in the dataset may be related to sea level fluctuations. Small unconformities may represent boundaries of different prograding clino-forms and aggradational layers of one or more stratigraphic sequences in response to third and fourth order sea-level cycles. In total, 10 subunits were identified. With a 100.000 year sea-level cycle (orbital inclination in the Milankovic cycle setting the pace for the ice ages) for the Late Pleistocene (after the MPR), 9 of these units would fit in the post-MPR period. This would also mean that in the depocentres, up to 250 m of sediment would have been deposited in less than 1 Ma, or 25 cm per 1000 years. Alternatively, the MPR corresponds to a boundary between units 1-2 or 2-3 which have also stronger erosive features. The reference reflector, often characterized by strong erosion, could then correspond to the QD. With the available data, it is impossible to be conclusive about the chronostratigraphic framework. However, within the proposed IODP Drilling project IODP Pre-692 "Mud volcanoes as a window into the deep biosphere" (Depreiter et al., 2006), drilling in the sedimentary sequence, mud flows and mud volcanoes are projected and would allow to address this question.

4.2.3   Mud flows, mud volcano activity and moats

4.2.3.1   Mud flows, expressions of mud volcano activity

On seismic profiles, mud flows once deposited at the foot of a mud volcano, interfinger with hemipelagic sediments. The mud flows are characterized by a chaotic signal since no internal structure is present. The lower boundary of the mud flow often is hard to define since the reflections of the covered strata are rendered discontinuous and with lowered amplitude. However, the reflection on which the mud flow is lying can be identified by tracking the mud flow shape towards the point where it thins to a single reflection. By this means it was possible to locate the stratigraphic position of the mudflow and thus compare the occurrences of mud flows from different mud volcanoes in a stratigraphic section. Based on the amount of mud flows interfingering with the hemipelagic sediments at a certain stratigraphic depth, the periods of activity of the mud volcanoes can also be reconstructed.

Correlation of the mud flow events between the different mud volcanoes showed that mud extrusion events did not occur exactly simultaneously. However, on a larger time scale, i.e. at the level of subunits, mud volcano activity is strikingly in concert (Figure 4.28). Moast of the mudflows occurred in subunits 1c, 2a, 2b, 3d and 3e while no or little mudflows where observed in the other subunits.

The occurrence at different depths of the mud flows within the sedimentary units around the mud volcanoes, indicates that the mud volcanoes are long-lived structures with activity at several moments in geological history. The activity is concentrated in certain subunits,
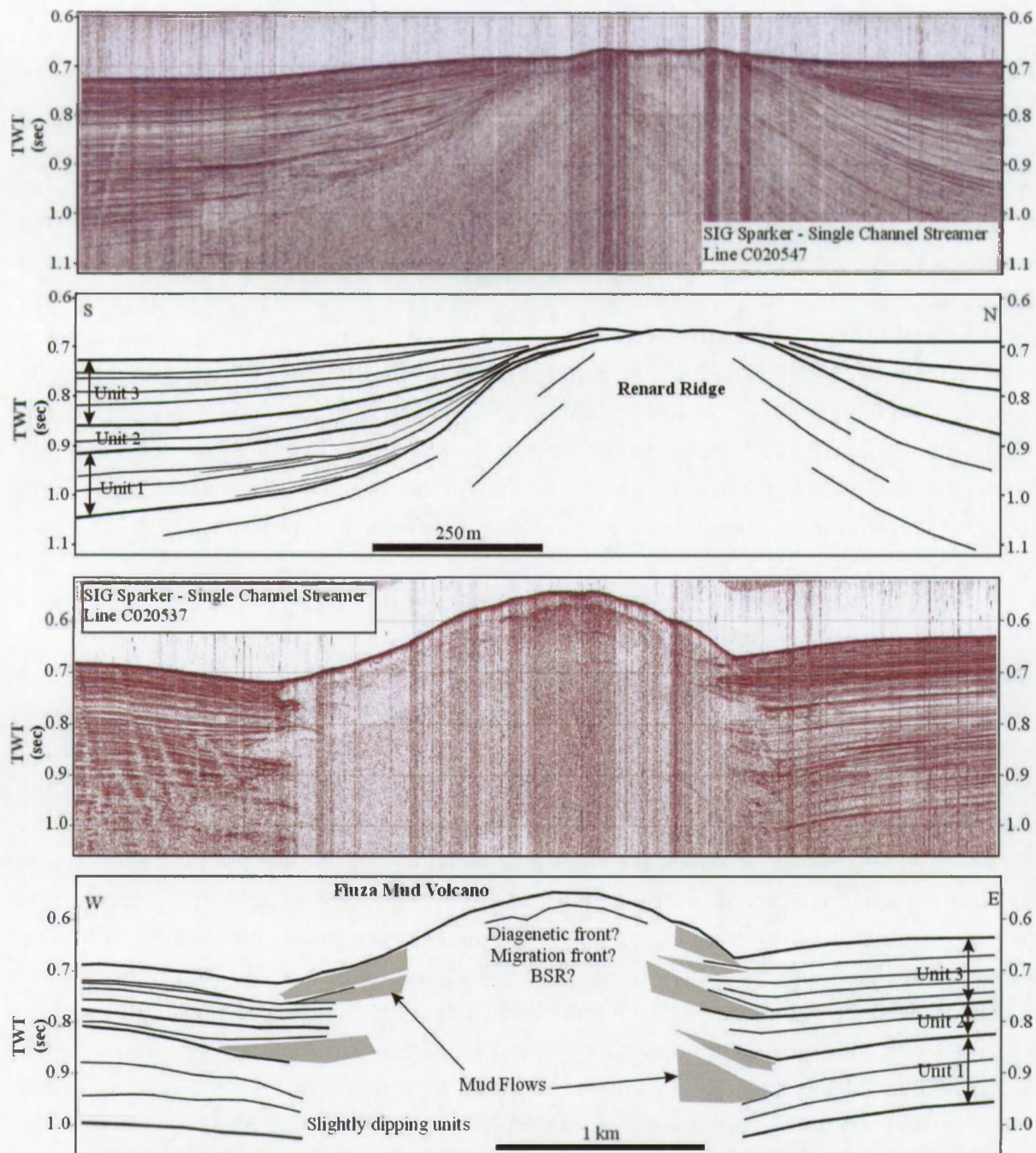
Figure 4.24: *Top: N-S directed seismic profile over Renard rigde east of Gemini MV; Bottom: E-W directed seismic profile over Fiúza MV.*
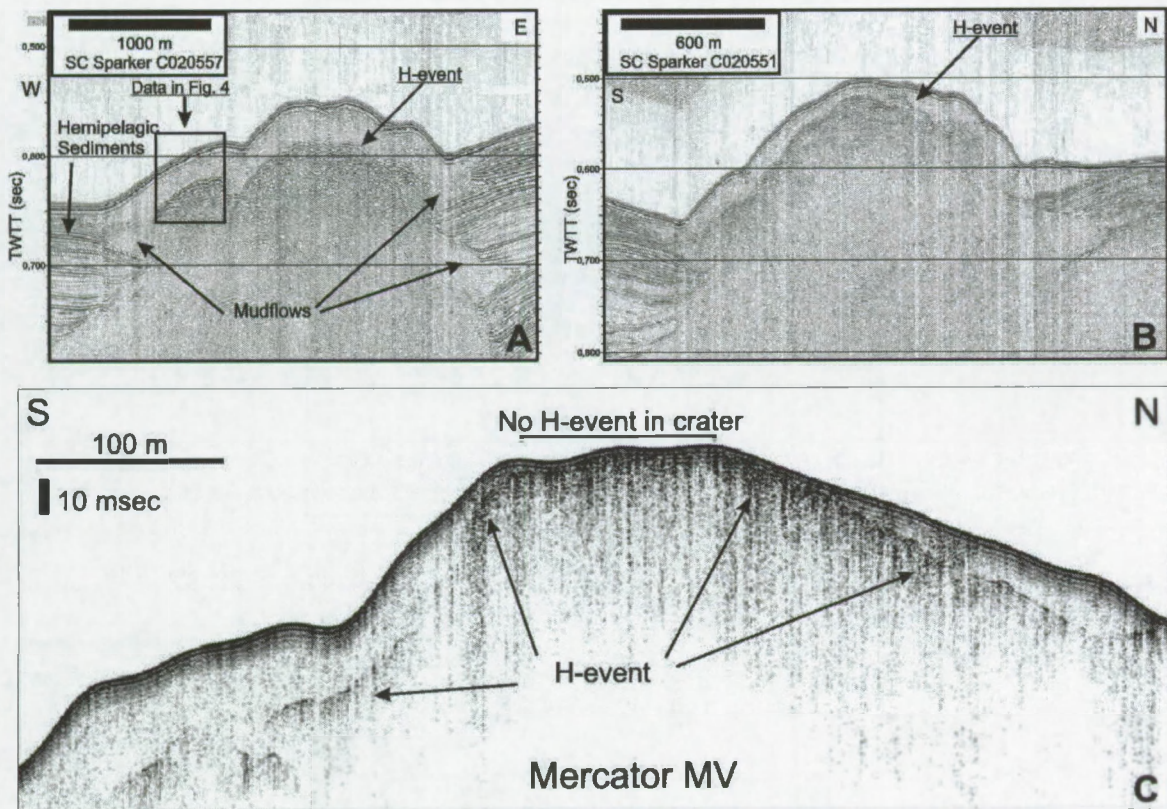
Figure 4.25: *(A and B) High-resolution sparker and (C) very high resolution chirp sonar (courtesy Ifremer) seismic lines over Mercator MV. The stratified seismic facies at the sides of Mercator MV (Figures A and B) represents hemipelagic sediments. The mud volcano itself has no internal structure; therefore a chaotic to transparent facies is observed. The unexpected H event reflector is visible on all profiles, Figure A is a profile far away from the crater and therefore the event occurs deepest. Figure B is a profile that passes next to the crater; therefore the H event is shallower near the crater than elsewhere. Figure C line crosses the crater and shows the H event intercepting the seafloor reflection.*

whereas other subunits are barren of any mudflow, for all mud volcanoes. This could mean that there is an internal or external trigger that activates the mud volcanoes at certain times. As this doesn't happen exactly simultaneously, internal or external short-lived events (e.g. earthquakes) may be excluded from the trigger list. However, a long-lived process that influences overpressure in the deep subsurface, may trigger mud volcanism, albeit at slightly different times between the different mud volcanoes. In chapter 6, such processes will be explored.
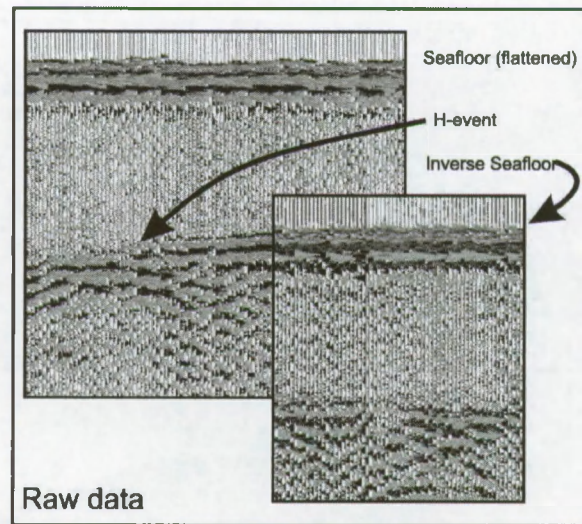
Figure 4.26: *Inverse seismic polarity of the H event with regard to the seafloor.*
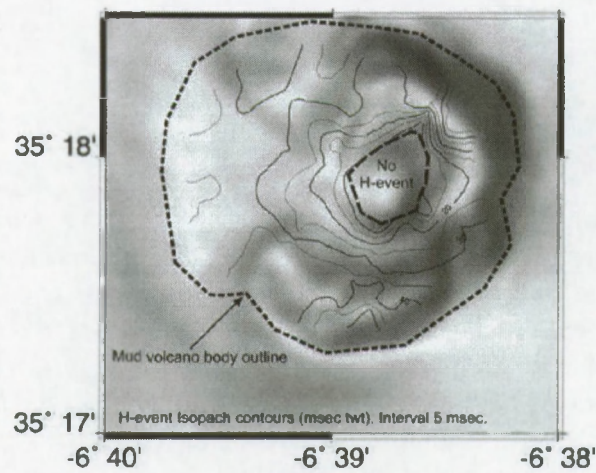
Figure 4.27: *Subbottom depth of the H event in the Mercator mud volcano in two-way travel time. The concentric shallowing of the H event toward the crater is shown by the contours. Background figure is a shaded relief map of the Mercator mud volcano (illuminated from west).*

4.2.3.2   Erosional moats

The mud volcanoes are surrounded by erosional moats, as can be observed on the bathymetry map. The seismic profiles also reveal the presence of moats throughout the mud volcanic history.

The influence of a large mud volcano edifice — as any other positive feature at the seafloor — on the bottom water current pattern is such that erosional moats are to be created. The presence or absence of erosional moats around the mud volcanoes thus can be taken as an

	MUDFLOWS				DIPPING UNITS			
	AL IDRISI	MERCATOR	GEMINI	FIUZA	AL IDRISI	MERCATOR	GEMINI	FIUZA
	N W S E	W S E	S E	W E	N W S E	W S E	E S	W E

Figure 4.28: Compilation of occurrence of mud flows and dipping units around mudvolcanoes.

indicator for the timing of the appearance of the mud volcano body.

The presence of deep moats around the Al Idrisi MV is not restricted to the present. Unit 2a shows a moat in front of a large mudflow south of the mud volcano. This moats exists during the deposition of units 2b through 3c. Units 3d and 3e are very deeply incising with moats of more than 100 meter deep. Also at the north side of the mud volcano, the alteration of deposition and moat formation is shown to be a very dynamic system, especially in unit 3. At the south side, we observe how due to a mud flow deposition, the deepest point of a moat is shifted outwards from the center of the mud volcano and how this points climbs afterwards towards the center of the mud volcano, covering the youngest mud flows. East and west of the Al Idrisi MV, the moats are absent due to the presence of the anticlinal ridge, rendering the surface topography elevated.

The erosive surface at the base of subunit 1b, east side of the Mercator MV, is not considered to be a moat. The youngest moat is rather thought to be the base of unit 2, in front of the large mud flow deposited at the base of this unit. The moat shape continues to exist during the deposition of subunit 2b until the deepest point is shifted outwards due to the infilling of the moat by a mudflow. Hereby, the moat depth decreases during deposition of unit 2b and the deepest point of the moat climbs back towards the center of the mud volcano. The seismic reflections suggest a consecutive deposition and erosion during the deposition through unit 3d. Then again, a mudflow shifts the deepest point outward. The current moat is located more inwards again after the deposition of unit 1e. At the west side, unit 1c is eroded by the base of unit 2a, successively covered by a large mudflow. The moat shifts towards the center of the mud volcano throughout the deposition of unit 2 and 3a-d however the moats become less pronounced. Erosion becomes stronger in unit 3e and mudflows also shift the deepest point of the moat outward to its current position.

At the south side of this mud volcano, moats are present in units 2 and 3 with contin-

uous alteration of deposition and erosion. Generally, they are much deeper than the moats observed east and west of the mud volcano, above the ridge flanks, indicating a stronger current. The moat at the current surface is over 40 meter deep.

South of Pen Duick Escarpment and Gemini mud volcano, moats are observed starting from subunit 2b and exist throughout unit 3. The moat-like structure north of Gemini MV will not be regarded, since it is unlikely that currents alone can be taken responsible or a moat of these dimensions: it is suggested that most of the depression is caused by a fault extending from the Pen Duick Escarpment towards the east, while the offset is diminishing in the same direction. Subsequently, the current between the fault surface and the Gemini MV must have further deepened the depression.

The location of the moats around the mud volcanoes shows that (1) the moats shift in and outwards after the extrusion of mud flows and that (2) moats are often deeper just before and after mud flow deposits and shallower when it is climbing towards the centre of the mud volcano. Next to this, (3) the moats are always arc- to horseshoe-shaped and directed in an E-W direction. For the older moats in unit 1c – 2, one could suggest that this is controlled by the anticlinal ridge orientation. For unit 3 this seems less likely, since — especially for the Al Idrisi MV — the ridge topography is smoothed by the sedimentary cover.

Moat formation in the El Arraiche mud volcano field is clearly evident from unit 2. Precedingly, either no strong current is present to form moats, either no large mud volcanoes are present to divert the bottom currents. The appearance of the moats must indicate that a mud volcano body was present at that time. The moats appear shortly after the occurrence of the first small mudflows and hereby add proof for the timing of origin of the mud volcanoes.

The arc-shaped moats throughout the seismic section, are always directed in an E-W direction and flank the mud volcanoes at their north and south side. One could argue that currents are steered by the topography of the ridge structures in an initial stage. However, this does not hold for the youngest units since the infilling of the basins smoothens topography. As indicated in chapter 2, tidal currents are known to run up- and down the slope. It is likely that these strong currents are mostly responsible for the moat formation.

4.2.3.3 Downward bending reflections around mud volcanoes

Downward bending of reflections around mud volcanoes has been reported multiple times. Various interpretations have been given to this aspect: Somoza et al. (2003) attribute the bending reflections recognized around mud volcanoes of the Gulf of Cadiz to collapse depressions and observe that they often correspond with discontinuities in the contourite sequence. Wiedicke et al. (2001) describe the downward bending of reflections next to a mud mound at the front of the Makran accretionary complex. This feature may be generated by compensatory marginal subsidence related to the extrusion of mud and not by erosion, since the depression at the surface is non-erosive. Graue (2000) attributes concentric faults and dip-

ping sections around mud volcanoes in deep-water Nigeria to caldera collapse. However, Dimitrov (2002b) allocates the downward dip to a 'pull down' effect of the reflections around to the feeder because the mud breccia is characterized by a lower sound velocity than the host sediments.

On the herein described seismic dataset, we observed different features: (i) dipping reflections of unit 1 (oldest unit) and the basement at the north side of the Al Idrisi MV (figure 4.18) and normal faults west and an obvious collapse depression west of the mud volcano; (ii) dipping reflections of the basement and unit 1 east and west of Mercator MV (figure 4.22), with basement erosion at the west side and associated normal faulting at the east side. Also a large collapse zone north of the mud volcano and a possible collapse south of it with a small buried mud volcano related to it are observed. (iii) The Pen Duick Escarpment – Gemini MV (figure 4.24) area is much more complex: two large normal faults closely related to the mud volcano suggest large-scale collapse in this area. Based on these observations on the high resolution seismics, we conclude that the downward bending of reflections at the level of the basement and the oldest units (1a, 1b) is caused by basement collapse as a response to the activity of the mud volcano. The removal of sediment beneath the mud volcanoes creates a mass deficit which has to be compensated. This is thought to be creating the central collapse zone. Associated with the bending reflections, normal faults are often observed and are in support of the collapse event. Since normal faults often run up towards the seafloor, it seems that collapse is an ongoing process and could be an indication that the mud volcanic activity has not finished yet.

4.3 Geophysical evidence of fluid flow in the El Arraiche mud volcano field

The geophysical data presented in this chapter has delivered evidence for past and present fluid flow on a large scale.

On the basis of multibeam and side-scan sonar data, supported up with literature references of seafloor sampling data, we can indicate the presence of 8 mud volcanoes of various sizes. In the introdution (Chapter 1), mud volcanoes were introduced as prime indicators of large-scale fluid flow because they are the consequence of the extrusion of large amounts of mud, rock clasts and fluid at the seafloor. Indeed, the largest mud volcano, Al Idrisi MV, is a cone shaped structure of about 200 meter high and 5 km in diameter which means that about 1.3 km^3 mud and rock clasts has been extruded from the subsurface. Lobe shaped bodies and high-reflectivity patches on the slopes of the mud volcanoes hint mud flow bodies near or at the surface of the mud volcanoes. These features indicate rather recent activity of these mud volcanoes.

Seismic data yielded insight in the subsurface environment around the mud volcanoes.

It was noted that most of the mud volcanoes are associated with large ridge structures that are crosscut by many faults. The occurrence blanking or bright spots associated with some of these faults hint the presence of gas in the sediments. Around the mud volcanoes, many mudflows were observed extending to deep levels in the sedimentary record. This observation evidences the long-lived nature of the mud volcanoes and the recurrent periods of activity. It can even be said that a certain internal or external trigger of mud volcano activity is suspected, albeit not exactly simultaneously between the mud volcanoes.

In the next chapter, a closer look will be taken to carbonate crusts and chimney structures that have formed in several environments related to these mud volcanoes. Samples have been extracted from mud volcano craters and sedimentary environments such as Pen Duick Escarpment. Geochemical and mineralogical analysis of these carbonate samples should give more insights in the fluids that are flowing through the sediments, and in the processes involved in the formation of the crusts.

Chapter 5

Geochemical and petrological evidence of fluid flow: carbonate crusts and chimneys

This chapter contains the results of the study of carbonate chimneys and crusts from the Gulf of Cadiz. The data will be interpreted and discussed in order to obtain evidence of fluid flow and information about the parental fluids and processes leading to carbonate precipitation.

5.1   Introduction to authigenic carbonates

Authigenic carbonates are formed in sediments where carbonate is oversaturated and alkalinity is sufficiently high. One cause of carbonate oversaturation, relevant to fluid flow in oceanic sediments, is the oxidation of migrating methane bearing fluids and free gas ('cold seeps'). In the upper meters of the sedimentary column, hydrocarbons undergo microbial oxidation, e.g., anaerobic oxidation of methane (AOM) coupled to sulfate reduction (Hinrichs et al., 1999; Boetius et al., 2000) (equation 5.1).

$$SO_4^{2-} + CH_4 \longrightarrow HCO_3^- + HS^- + H_2O \qquad\qquad (5.1)$$
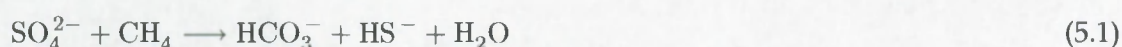
As a consequence of this reaction, alkalinity in the sediment pore water increases and promotes the precipitation of carbonate minerals (e.g., Ritger et al., 1987; Aharon and Fu, 2000; Peckmann and Thiel, 2004). Alternatively, though depending on the saturation state of the pore waters, authigenic carbonate in marine settings can also be formed driven by diffusion or advection of bicarbonate from seawater into the sediments (e.g., Allouc, 1990) or by dissolution of carbonate phases more soluble than the newly precipitating cements (e.g., Mullins et al., 1985).

Carbon stable isotope analysis is used to elucidate the source of the carbon atoms present in the carbonate. The carbon present in biogenic (created by microbial activity) and thermogenic (created by thermal cracking of organic matter) methane is isotopically lighter (biogenic methane: -110 ‰ – thermogenic methane: -25 to -35‰[1]; Roberts and Aharon, 1994; Whiticar, 1999) than carbon present in seawater[2] ($\Sigma CO_2 \sim 0$‰; Bickert and Wefer, 1999). Organic matter in recent sediments is also isotopically light (-10 to -30‰; Faure, 1986). Oxygen stable isotope ratios[3] can give indications about the fluid source and the temperature of carbonate precipitation.

In this chapter, the results of petrographic and geochemical analyses of a set of carbonate crusts and chimneys retrieved from margins in the Gulf of Cadiz (Fig. 5.1) are reported. The samples are taken from a span of environments (also see section 5.2): mud volcanoes on the Moroccan margin (Meknes MV, Kidd MV), Hesperides MV on the Iberian margin, Pen Duick Escarpment and an erosional sedimentary environment west of the Strait of Gibraltar (herein referred to as the Mediterranean Outflow Area). The parental fluids and genetic processes of the different samples are discussed and the data is interpreted in terms of modes of fluid flow

---

[1]Carbon and oxygen isotopic data of carbonate minerals is reported with respect to the Vienna Pee Dee Belemnite (V-PDB) standard unless otherwise indicated. See chapter 3 for more information.

[2]Marine total inorganic carbon

[3]Oxygen isotopic data of fluids is reported with respect to the Vienna Standard Mean Ocean Water (V-SMOW) standard unless otherwise indicated. See chapter 3 for more information.

in which the petrographic characteristics of the samples function as a key to fluid flow and its genesis.

5.2 Sampling sites

Carbonate crust and chimney samples were retrieved from four different locations by seafloor dredging and boxcoring. Representative samples were selected for further analysis.

Moroccan margin mud volcanoes   Samples from two mud volcanoes on the Moroccan margin were retrieved, i.e. Kidd MV and Meknes MV.

The Kidd MV is located at a depth of 550 m on the north flank of the Vernadsky Ridge (for more details, see 4.1) in the El Arraiche mud volcano field. The samples are retrieved from the crater area. Cores retrieved during cruise TTR-14 onboard R/V Professor Logachev emanated a strong hydrogen sulfide smell. By tv-guided grab sampling, a large amount of carbonate-cemented mud breccia and small chimney structures were sampled together with large clasts, dominated by bedded sandstones and porous carbonate rocks.

The Meknes MV is located at a water depth of 700 m and is a 50 m high sub-circular dome-like structure with a conical shape and a flat top. The slopes of the structure are about 7.7 degrees and its diameter is about 1100 m. Cores retrieved during cruise TTR-14 in the center mud volcano crater, showed the presence of mud breccia at and near the seafloor. The absence of a hemipelagic sediment drape may indicate recent activity. TV-guided grab sampling recovered an assemblage of small cm-sized brittle carbonate crusts and bedded sand- and claystones.

Pen Duick Escarpment (PDE)   Piston and gravity coring indicated active fluid migration through the sediments and mounds (Maignien et al., 2007; Foubert et al., 2008). At several places across the 5 km long escarpment, carbonate-cemented sediments are present. Carbonate crusts were sampled from the sediment surface by video-guided grab sampling near the northeast side of a carbonate mound on the Pen Duick Escarpment (Foubert et al., 2008), as well as by boxcoring on the southwest slope of the same mound. The analyzed samples used in this work were sampled by tv-guided grab sampling during TTR-12 cruise onboard R/V Professor Logachev and from a boxcore taken during the 2004 Hermes cruise onboard R/V Pelagia.

Mediterranean Outflow Area (MOA)   The Mediterrean Outflow Water has strongly eroded the seafloor west of Tanger (Morocco), resulting in seafloor channels. The southern border of one of these is bound by a steep cliff of about 75 m high with a slope of 13 degrees. The flanks and plateau-like top of the ridges were characterized by patches of high backscatter on side scan sonar records (TTR-14 cruise, data not shown). Seafloor dredging on these locations at
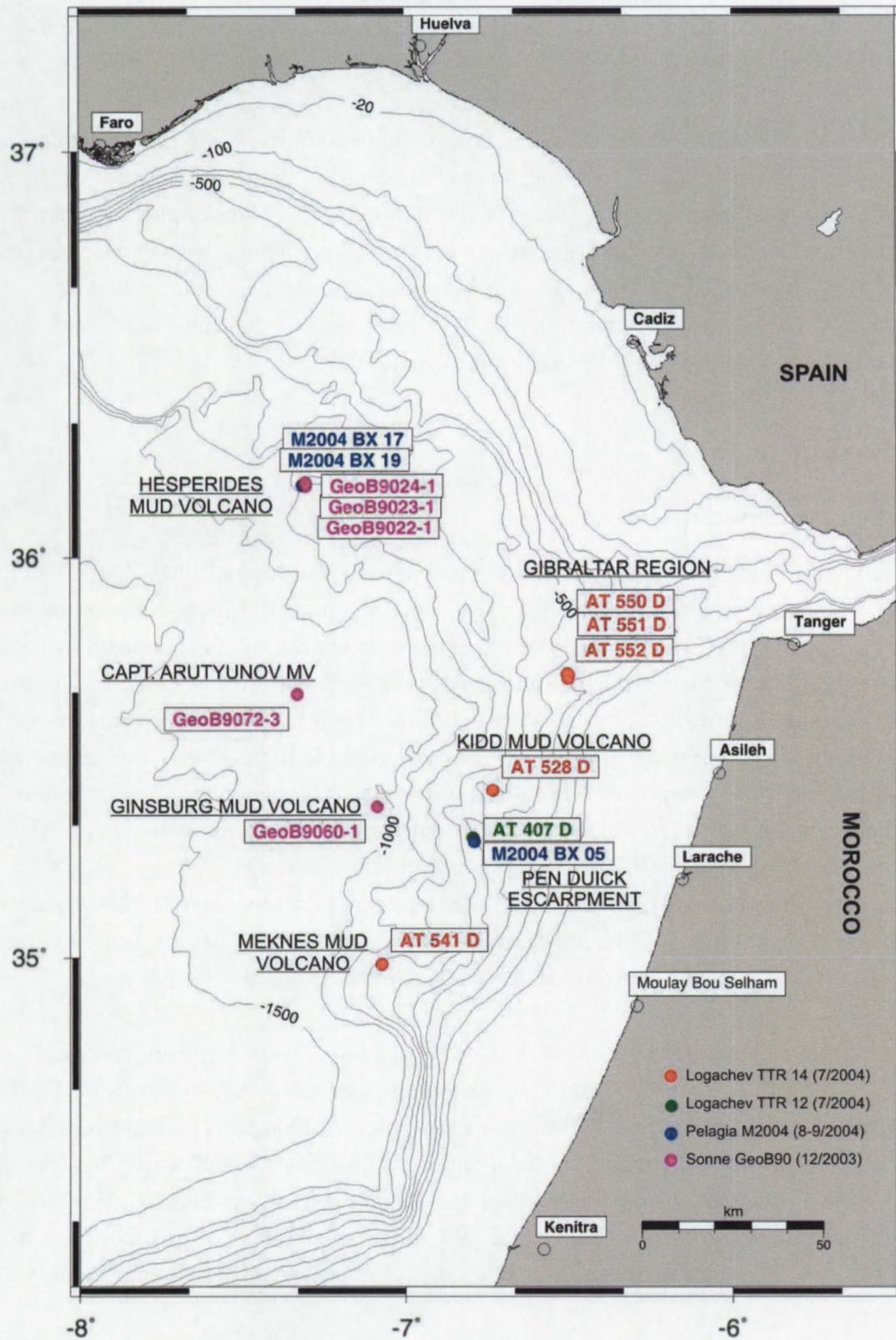
Figure 5.1: Locations in the Gulf of Cadiz where carbonate chimneys and crusts were sampled.

a depth of about 400m has yielded an assemblage of massive dark brownish dm- to m-sized chimneys and crusts.

Hesperides MV (HMV)   With the goal of comparing the source fluids and formation processes of the authigenic carbonates from the northwest Moroccan margin, a set of slices of carbonate chimneys from the Hesperides MV were analyzed. The samples were retrieved during Sonne cruise SO175 in 2003 and from a boxcore taken during the 2004 Hermes cruise onboard R/V Pelagia. Hesperides MV is a large complex mud volcano in the Tasyo field (Somoza et al., 2003) on the Iberian margin. It is composed of multiple cones, with a total diameter of 3 km and a height of 150 m (Somoza et al., 2003).

5.3   Results

5.3.1   Petrography and XRD analyses

Moroccan mud volcanoes   The carbonate crusts retrieved from Kidd MV (Fig. 5.2A) are variable in size and have an irregular shape. Most specimens are large (up to several decimeters across), well lithified mud breccia with a light brown to gray colour, colonized by benthic organisms (corals, bryozoans, sponges) and partly degraded by boring organisms. These contrast with cm-sized, more brittle and soft gray nodular crusts with a smooth surface. In one case, partly dissolved coral debris is completely embedded in lithified very fine, brittle, gray lime mud. Visible rock fragments (clay- and siltstone) and biogenous fragments (corals, bivalve shells) are embedded within the crusts. In general, the crusts feature many voids, cracks and fractures which have been filled by cements and sediments.

The crusts from Meknes MV (Fig. 5.2B) are up to a decimeter large (largest diameter), brittle, gray, nodular crusts. Visible rock fragments included in the crusts are mm-sized pieces of silt- and claystone, next to biogenous debris like coral fragments.

In transmitted light, the crusts from Kidd MV display a chaotic texture consisting of a muddy aragonite (based on XRD results, see below) micrite matrix ($\sim$ 50%, Fig. 5.2C, D), floating micritic peloids ($\sim$ 5-10%, Fig. 5.2D) and a small amount of bioclasts (pelagic foraminifera, < 1%). Accessory minerals include variable amounts of detrital mono- and polycrystalline quartz, authigenic pyrite, iron oxihydroxides, detrital feldspar and calcite. The grayish parts of the crusts contain pyrite and cloudy iron oxihydroxides, while the brownish parts of the crusts only contain oxihydroxides. The remaining volume consists of circumgranular voids, cracks and fractures.

Throughout the crust, many generations of cracks and fractures are present, which are often filled by washed-in rock fragments (e.g. siltstones, $\sim$ 10%) and incompletely cemented by acicular to fibrous aragonite fans (up to 20%, Fig. 5.2E). Circumgranular voids often occur
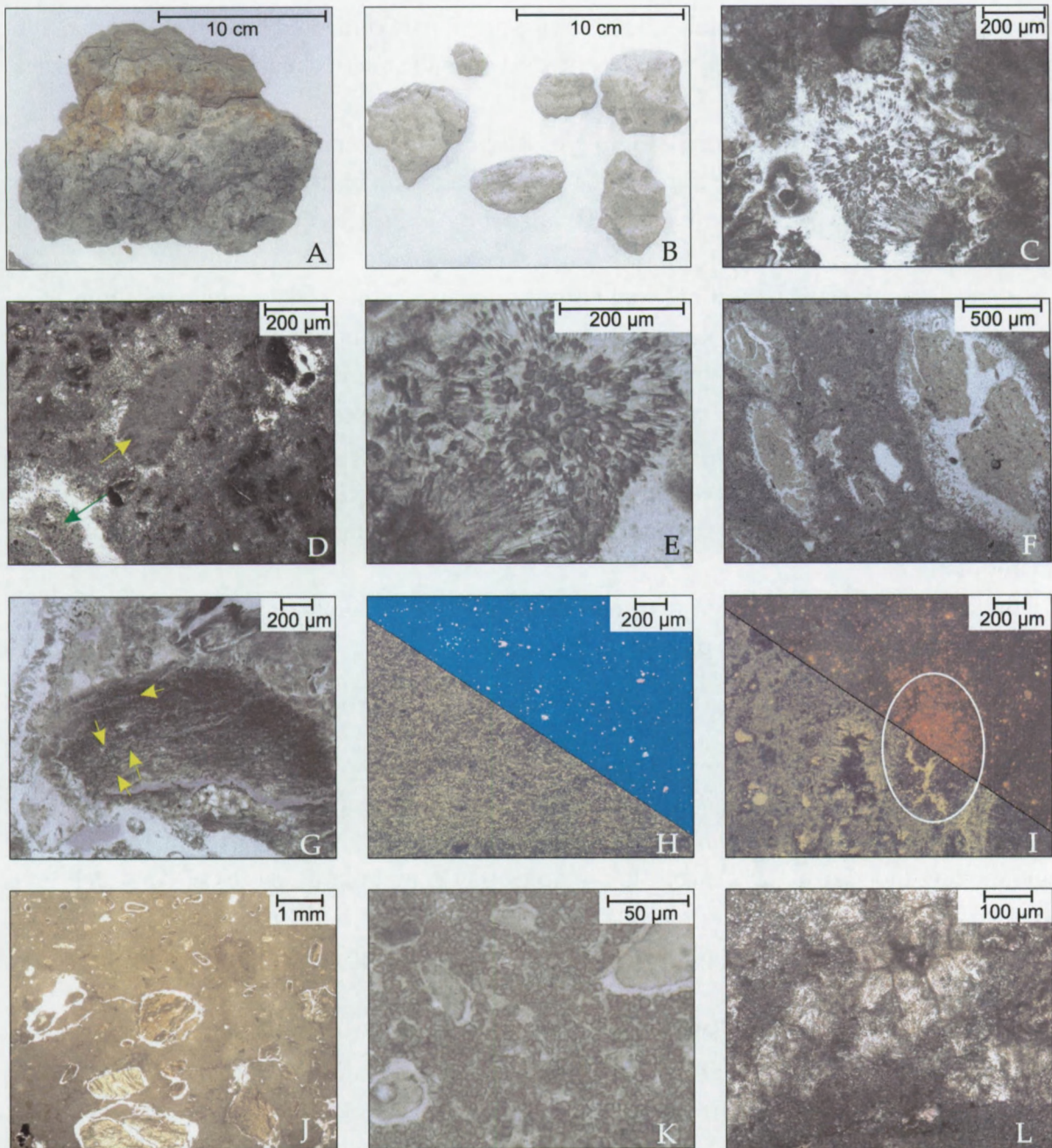
Figure 5.2: Petrography of Moroccan mud volcano crusts. A, C-I: Kidd mud volcano crusts. B, J-L: Meknes mud volcano crusts. A) Lithified mud breccia crust. B) Small calcitic crusts. C) Texture of the Kidd mud volcano crusts. Brownish micrite matrix and aragonite botryoids incompletely fill the porosity created by fractures. Unstained section. D) Aragonite micrite matrix of mud breccia crusts with peloid (yellow arrow) included in fine crystalline aragonite that has precipitated in a circumgranular void around the peloid. Small black spots in the lower left of the image are pyrite crystals (green arrow). E) Aragonite botryoids that are found in fractures and voids. F) Rock fragments with circumgranular void, incompletely cemented by clear aragonite needles. G) Finely laminated feature of uncertain origin. Small black dots in the structure are small pyrite crystals (yellow arrows). Diffuse light. Continued on next page

around rock fragments and peloids. These voids are mostly cemented by fibrous to prismatic aragonite (Fig. 5.2F). The cements grows outward from the micritic matrix towards the center of the voids and cracks.

Banded structures of uncertain origin are also present within the matrix (Fig. 5.2G): they consist of finely laminated structures that are associated with high amounts of pyrite and are therefore believed to be organic (e.g. fossil plant debris) or bacterially-mediated (e.g. bacterial mats).

Some aragonite fans have a radaxial fibrous appearance that contains ghosts of thin acicular crystals. Therefore, these seem to be recrystallized, although the original texture is still visible. Bioclasts cemented in the matrix however are unaltered. Cold cathode luminescence microscopy indicates that all aragonite phases are non-luminescent. Thus, there are few signs of matrix recrystallization of the crusts. However, within the matrix, small (micron-sized) red luminescent crystals are present (Fig. 5.2H). In some areas, large clusters of micron sized bright-red luminescent crystals are present (Fig. 5.2I); This may indicate the formation of microdolomite.

Bulk XRD analysis indicated that the main carbonate mineralogy is aragonite, while no other carbonate minerals were detected (Fig. 5.3A).

In general, the crusts from Kidd MV can be described as (fossiliferous) intrapelmicrites (classification after Folk, 1959).

The small nodular crusts from Meknes MV consist of a fine gray microsparitic matrix (Fig. 5.2J) which is made up of equant non-ferrous calcite crystals (Fig. 5.2K). Allochems (micritic peloids, few bioclasts ($< 1\%$ except for samples that contain large pieces of coral debris)), accessory minerals (quartz) and rock clasts (quartzite, siltite, up to 1 mm in size) float in the matrix. In some samples, void filling fibrous aragonite is overgrown by microsparitic cement (Fig. 5.2L).

The crusts have a high intercrystalline microporosity (40%). Small amounts of microdolomite crystals have been formed in fine cracks and circumgranular dissolution voids. Patches of microdolomite occur dispersed in the matrix, resembling the microdolomite that was observed in incompletely filled voids and cracks. Therefore, these patches of micro-

Figure 5.2: Continued - H) Transmitted light (lower left) and CCL (upper right) image of the matrix of the Kidd mud volcano crusts. The matrix is non-luminescent apart from small crystals with bright red luminescence. CCL image taken at 7.54 kV, ~ 280 µA, 120 seconds exposure. I) Transmitted light and CCL image of microdolomite formed in void, with bright red luminescence. CCL image taken at 9.7 kV, ~ 250 µA, 120 seconds exposure. J) Texture of the Meknes mud volcano crusts. K) Detail of the matrix in diffuse light to enhance the granular appearance of the calcite microspar. L) Granular calcite growing over previously formed aragonite fans.

dolomite may correspond to completely filled (dissolution) voids. A few larger euhedral dolomite crystals ($\sim$10 μm) are found in the matrix. Framboidal pyrite ($<$ 2%) has been observed as dispersed clumps in the matrix. They sometimes are partly oxidized.

All carbonate phases in the samples from Meknes MV are non-luminescent, except for the euhedral dolomite crystals that have a bright red luminescence. Bulk XRD analysis confirms that the main carbonate mineralogy is high-Mg calcite (with 11 mol% $MgCO_3$ based on the [104] value (Fig. 5.3A), Lumsden (1979)).
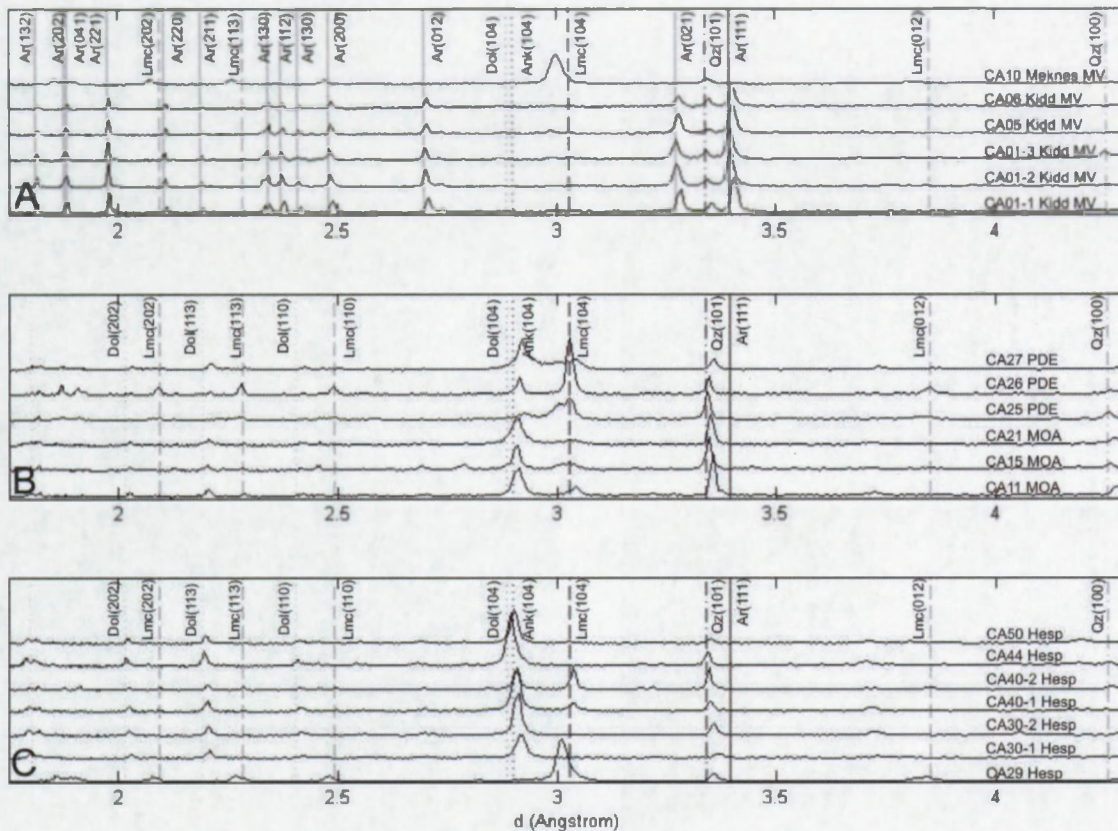
Figure 5.3: *X-ray diffractograms of carbonate crusts and chimneys (bulk). A: Moroccan mud volcano crusts. B: Pen Duick Escarpment and MOA samples. C: Crusts (CA29, CA30) and chimneys (CA40, CA44, CA50) from Hesperides MV. The numbers "CA" refer to individual sample specimens. PDE = Pen Duick Escarpment; MOA = Mediterranean Outflow Area; Hesp = Hesperides MV.*

Pen Duick Escarpment The sampled crusts consist of grayish to brownish lithified (silty) mud (Fig. 5.4A), with variable inclusions of large bioclasts (visible bivalve shells, coral and crinoid stalk fragments, gastropods) to mm-sized bioclast debris. The crusts display bioerosion traces. Remains of biota that had attached to the surface, such as bryozoans, corals and bivalves, are found on the surface of the crusts. One sample was found at 20 cm depth in
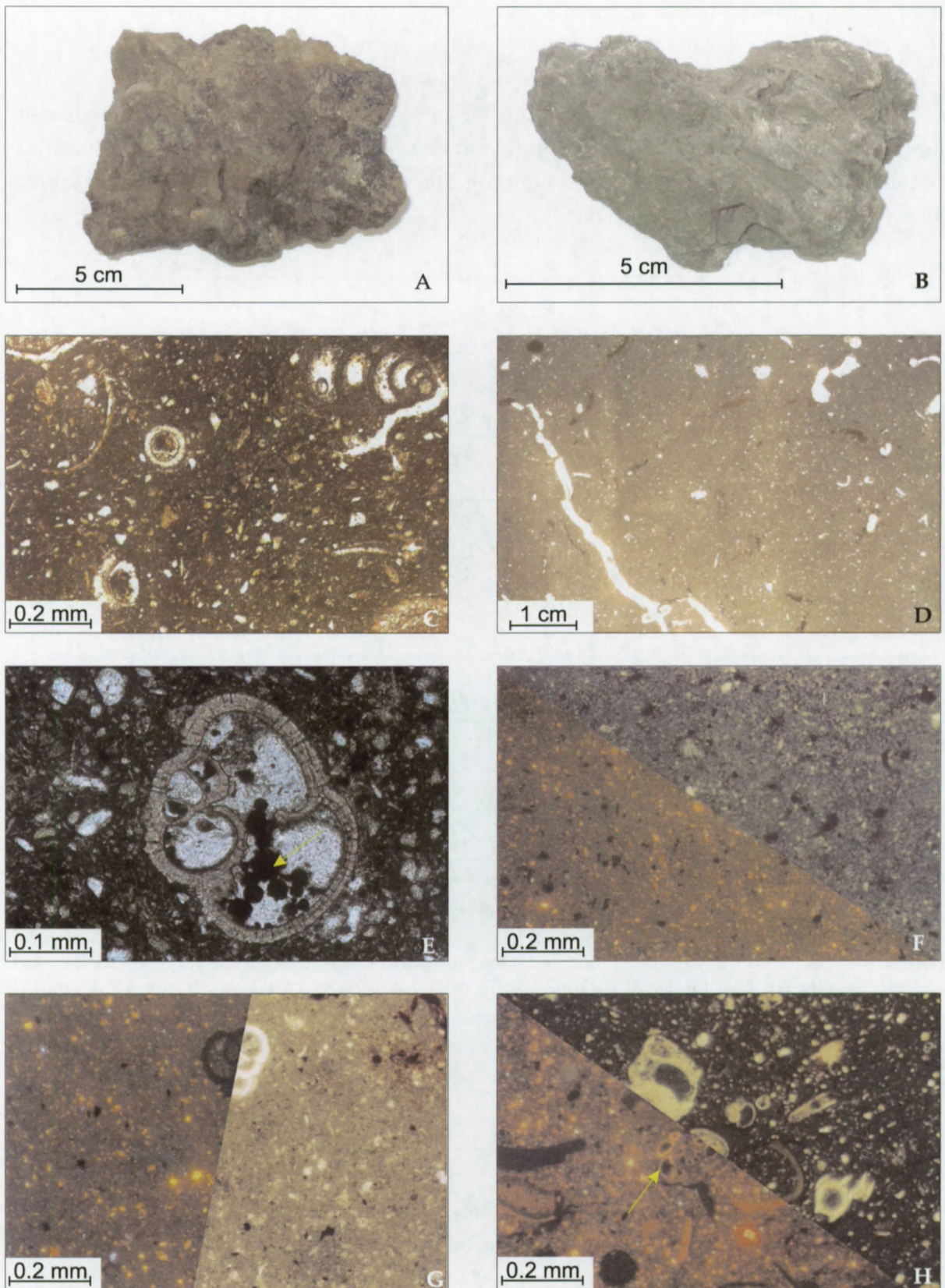
Figure 5.4: Petrography of Pen Duick Escarpment crusts. Continued on next page.

olive-grayish clay in a boxcore on the southwest slope of the carbonate mound. This crust consisted of less well lithified mud (Fig. 5.4B) including a partly dissolved deep-water coral fragment. No bio-erosion traces were observed.

In thin section, the crusts are mud-supported fossil-bearing micritic limestones (wacke-stones (Fig. 5.4C) to mudstones (Fig. 5.4D). The non-carbonate constituents include detrital quartz and feldspar, iron oxihydroxides clusters resulting from pyrite oxidation, and glau-conite. Fossil content includes bivalve shell debris, echinoderm spikes, planktonic forams, bryozoans and undeterminable debris. The crust sampled from the subsurface contained pyrite clusters. The fossil content is not recrystallized (Fig. 5.4E), although micritization (Fig. 5.4C) has occurred in some cases, as well as dissolution of some bivalve shells. Fossil shells are mostly non-luminescent, in contrast to the red luminescent matrix (CL, Fig. 5.4F-H). Some bivalve and foraminifera shells have a dull orange-red luminescent outline (Fig. 5.4H) (a cou-ple of tens of microns wide) at the inner side of the chambers. Some bivalve shells are dull red luminescent. Many micron-sized, crimson red dull luminescent 'spots' are present in the matrix. Sometimes, these 'spots' form large clusters. Some larger luminescent crystals (up to 0.2 mm) have bright orange interiors, with less bright red outer rims. These 'spots' and clusters may be microdolomite crystals.

Results from bulk XRD analysis indicate variable carbonate mineralogy. The wackestone mainly consists of low-Mg and high-Mg calcite (12 mol% $MgCO_3$ based on Lumsden (1979); Fig. 5.3B), with some dolomite, while the mudstones consists of dolomite and low-Mg calcite. The mudstone sampled from the subsurface displays a strong low-Mg calcite peak. Deep-water coral fragments present in the sample may have caused this signal, if the aragonite skeleton were previously replaced by calcite.

Mediterranean Outflow Area   The carbonate crusts and chimneys from the Mediterranean Outflow Area, west of Tanger (Fig. 5.1), consist of carbonate-cemented sandstones. The crusts are weakly to very well lithified yellowish-brown portions of sandy host sediment with a

---

Figure 5.4: Continued - A. Carbonate crust sampled at the seafloor on the Pen Duick Es-carpment. B. Carbonate crust sampled 20 cm below the seafloor in olive-gray mud. C. Typ-ical matrix of carbonate wackestone from the PDE, with dissolved and micritized bioclasts. D. Typical matrix of carbonate mudstone, with cracks and voids. E. Detail of an unaltered foraminifera shell in a stained thin section. Pyrite is present inside the foraminifera shell (yel-low arrow). F-G: Tranmitted light (upper right) and cold cathodoluminescence image (lower left; 9.50 kV, 220ÎijA, 120 sec) of carbonate crust. The matrix is dull red-orange luminescent, with many small (crimson) red crystals present. H: Tranmitted light (upper right) and cold cathodoluminescence image (lower left; 9.50 kV, 220ÎijA, 120 sec) of carbonate crust with lu-minescent and non-luminescent bioclasts. The bioclast in the center of the image has a red luminescent rim along the inner parts of the shell (yellow arrow).
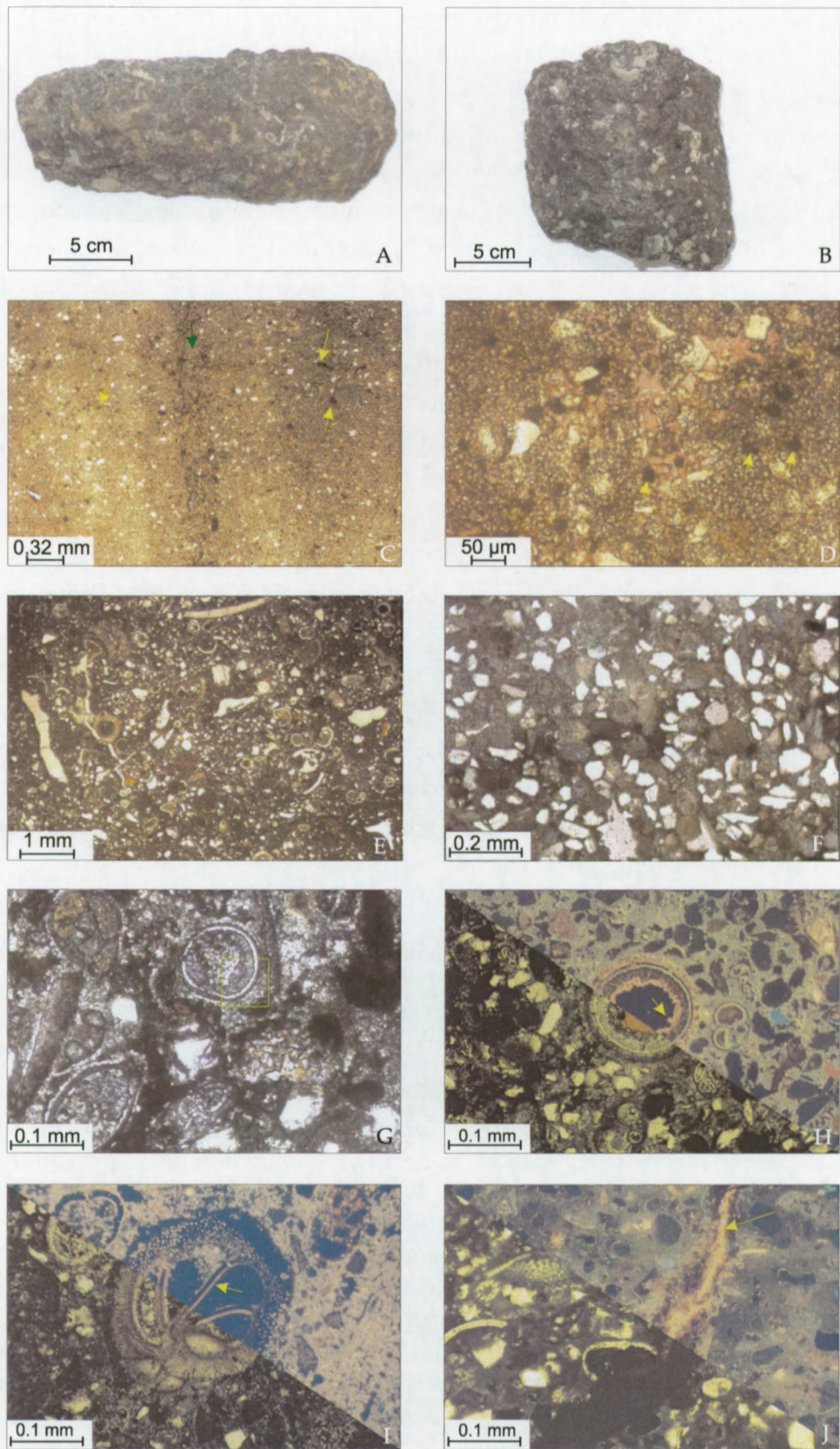
Figure 5.5: *Petrography of Mediterranean Outflow Area crusts. Continued.*

dark brown to blackish outer coating (Fig. 5.5A). The samples have sizes up to 10 cm thick and 15 cm long. Most of the crusts have been colonized and bored by benthic organisms (e.g. bryozoans and corals). The single carbonate chimney fragment that was analyzed (Fig. 5.5B), was 15 cm high and 10 cm in diameter with a central open conduit of 2 cm wide. Its outer appearance was similar to the massive black coloured crusts.

Thin sections show micritic matrix-supported fossiliferous cemented sand and silt (mud- to wackestones; Fig. 5.5 C-J), with other detrital components like (oxidized) glauconite ($\sim$ 2%), feldspar, detrital calcite and dolomite grains. The matrix/cement is a brownish dolomite-ankerite micrite to microsparite (20-60%) with an orange-brown dull luminescence. Brown clouds of iron oxihydroxides (Fig. 5.5D) are present which may explain the overall brownish colour of the micrite matrix/cement (Fig. 5.5E). Quartz and glauconite grains are locally armoured with a fine rim of clear authigenic dolomite. Both the in- and outside of foraminifera tests and also fine fractures, record different additional cement phases (Fig. 5.5G-I). Inside foraminifera tests three different cement zonations were observed, i.e. (1) a fine, clear, unstained, blocky dolomite rim is present in most foraminifera tests. It has an orange-brownish luminescence which is similar to the matrix luminescence. The phase also fills the perforations in the foraminifera tests; (2) further inside, a blue stained dolomite phase is often present. This phase has a micritic to fibrous appearance and a dark red luminescence, with low to medium intensity; (3) the innermost phase is made up of a clear, blocky, unstained dolomite phase with bright orange-red luminescence. Not all phases occur in each foraminifera test. The foraminifera tests themselve are not recrystallized and are not luminescent.

In cemented fractures, the earliest dolomite phase consists of euhedral dolomite crystals with a brownish luminescence of low intensity. Faint zonations can be observed. The subsequent cement phase, along the center of the fracture, consists of bright red luminescent microdolomite (Fig. 5.5J). The remaining porosity of the crusts and chimney is low (< 5%) and consists of incompletely cemented biomolds and uncemented fine fractures.

Figure 5.5: Continued - A. Carbonate crust sample. B. Carbonate chimney sample. C. Overview of carbonate mudstone matrix with partly oxidezed pyrite clusters (yellow arrows). Pyrite concentration running in a band from top to bottom in the center of the image (green arrow). D. Detail of matrix, showing the microsparitic nature with interparticular pore space and partly oxidized pyrite clusters (yellow arrows). E. Overview of carbonate wackestone with high amount of bioclasts. Stained thin section. F. Overview of carbonate cemented wackestone. Stained thin section. Diffuse light. G. Detailed view of late cement phases (yellow box; explanation: see text). Stained thin section. H. Transmitted light (lower left) and CCL (upper right) image of matrix and late cement phases in foraminifera shell (yellow arrow). I. Transmitted light (lower left) and CCL (upper right) image of matrix and late cement phases in foraminifera shell (yellow arrow). J. Transmitted light (lower left) and CCL (upper right) image of matrix and dolomite phase in fracture (yellow arrow).

Bulk XRD analyses (Fig. 5.3B) indicate that the main carbonate mineral present in the sample is an ankerite-dolomite phase. The [104] spacing of this phase is between 2.906 and 2.914 Å, well above the values for stoeichiometric dolomite (2.886 Å) and ankerite (2.901 Å), which cannot easily be explained. The [101] peak of quartz is strong in all samples.

Hesperides mud volcano The carbonate chimneys sampled at the Hesperides MV have a huge diversity in sizes, ranging from a few centimeters to decimeters wide, and with lengths up to one meter. The shapes are very diverse (Fig. 5.6A): straight, bended, or helical, with singular columns, branching shapes, with cemented or open conduits, with or without nodule protuberances. This diversity of carbonate chimney morphology is not uncommon, and was already described for other samples from the Gulf of Cadiz (Diaz-del Rio et al., 2003).

From different samples, slices were cut for further analysis (Fig. 5.6B, 5.6C). The chimney slices were all made perpendicular to the vertical axis, which allows investigating possible lateral changes from the central conduit towards the outer edge of the structure.

Most of the samples have a brownish colour with a 1 millimeter thick, dark brown to blackish outer coating. Most of the slices are transected by cracks, mostly sub-concentric, although radial cracks occur. One sample is a small grayish chimney slice, with dark gray coloured concentric 'bands' around the cemented conduit. The outer edge is light brown coloured.

In thin section, the samples are made up of an orange-brown micritic to microsparitic carbonate mud matrix with floating grains (variable amounts of quartz, feldspar, clastic carbonates, pyrite, glauconite; Fig. 5.6D) and bioclasts (mainly micritized foraminifera, in some cases completely dissolved, Fig. 5.6E). The matrix is dull orange luminescent (Fig. 5.6F, 5.6G). The distribution of the allochems is heterogenous due to bioturbation. Burrows contain no or little allochems (Fig. 5.6D). The chimneys can be classified as carbonate mud- to wackestones.

Many cracks of different width crosscut the samples. The wide cracks ($\sim$ 0.2 mm and wider) are often filled with material similar to the surrounding material. Sometimes, the colour is less brownish but rather gray, however, heavy extensive iron oxihyroxide staining sometimes colours the infill dark brown. The fine cracks are clear in appearance, and filled by microsparitic carbonate. This latter phase often has a brighter orange luminescence than the rest of the matrix.

Fine-grained pyrite occurs throughout the matrix of some samples (Fig 5.6H, I), often surrounded by patches of iron oxihydroxides, which are possibly a product of pyrite oxidation. In some cases, pyrite oxidation is complete and lumps of iron oxihydroxides remain. Pyrite is also associated with some of the cracks (Fig. 5.6J). Euhedral microdolomite ($< 5\mu$m) is observed within small cavities in some samples, as well as inside foraminifera tests, associated with iron oxihydroxides.

Only some of the thin sections reflect the concentric nature of the chimney structures. In a single sample, the conduit infill consisted of bioclastic and peloidal carbonate cemented by
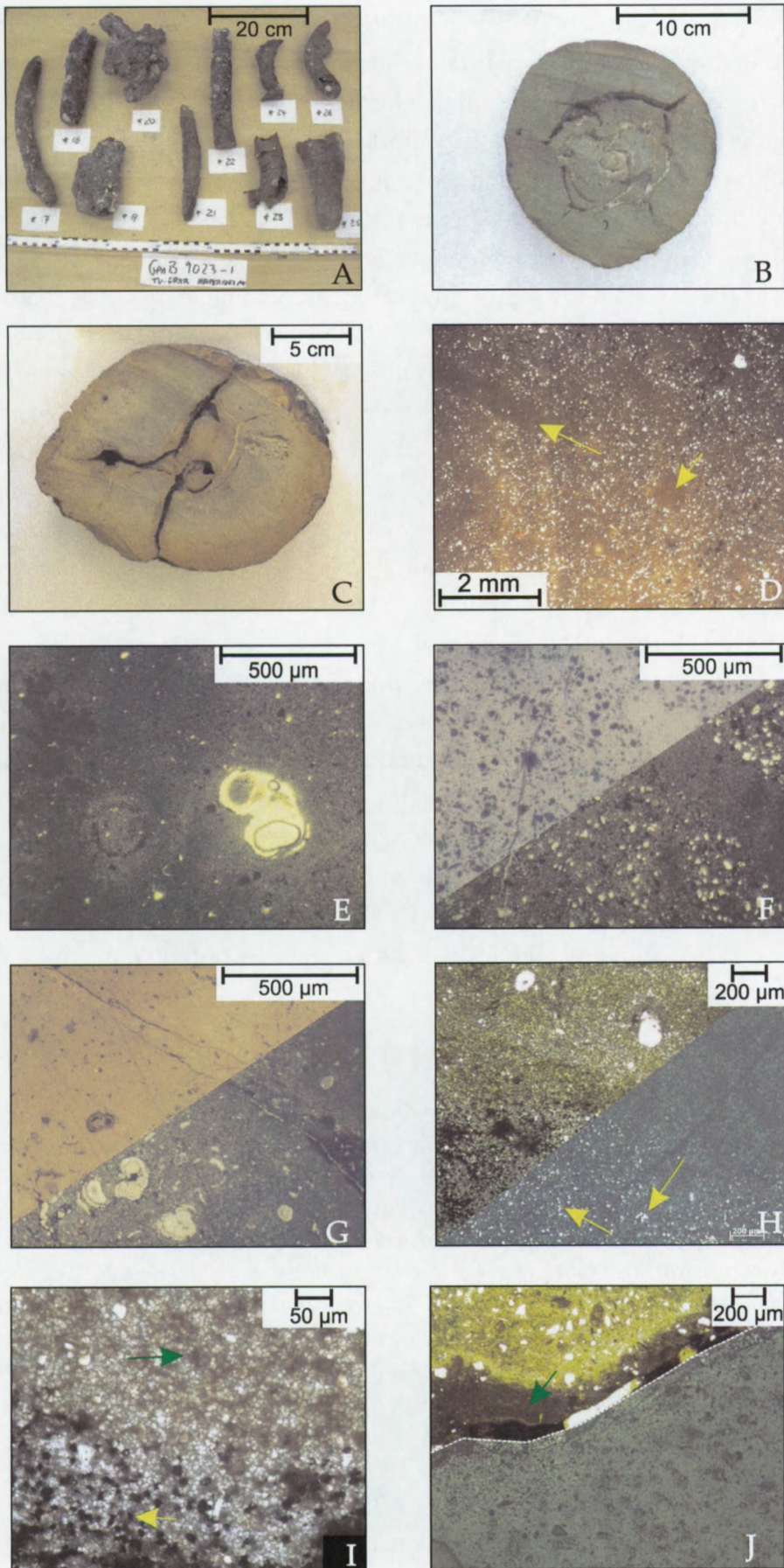
Figure 5.6: *Petrography of Hesperides mud volcano chimneys. Continued on next page.*

microsparitic carbonate, with a high amount of allochems (mostly quartz grains). The conduit area is surrounded by a clear microsparitic carbonate with some dissolution voids (porosity decreases outwards), and a lower amount of allochems. Further outwards, there is an abrupt change to a darker, cloudy micrite with few allochems.

The small grayish chimney has a matrix similar to the other (brownish) samples: it consists of micritic to microsparitic carbonate, with floating allochems, and few bioclasts. The matrix is similarly dull orange-yellow luminescent. Etching with an Alizarin Red-S and K-ferricyanide mix did not stain the sample, indicating a dolomite matrix. The main difference is that in this sample, the pyrite content is very high (5-10%, estimate). The dark gray bands (visible on hand specimen) are actually concentric areas containing even higher amounts of pyrite (20%, estimate). Fine cracks can be observed running parallel to these bands, with an elevated pyrite concentration along these cracks. Under high magnification (50x), it can be seen how the pyrite is starting to oxidize, rendering the matrix brownish. At and near the edge of the sample, pyrite is completely absent, and the matrix has a yellowish to brownish colour due to the presence of iron oxihydroxide clouds (Fig. 5.6H, I). XRD of the samples (Fig. 3C) indicates that the main carbonate mineralogy is dolomite-ankerite. Samples with a high fossil content have a clear low-Mg calcite peak.

The carbonate crusts from the Hesperides mud volcano site are very diverse both in size and appearance (Fig. 5.7A, B, C). Dimensions range from large blocks of multiple decimeters across to small crusts of 10 centimeters wide and one centimeter thick. The macroscopic texture ranges from porous homogenous brown, gray and white coloured crusts with a smooth outer surface that is variably stained by iron oxihydroxides, to brecciated cemented crusts with an uneven and burrowed outer surface with visible cemented bioclasts like coral and bryozoan fragments.

The microscopic texture has a high diversity as well. A porous gray coloured carbon-

Figure 5.6: Continued - A: Carbonate chimney samples; note the diversity in size and shapes. The outer rim of the samples is coated blackish brown by iron oxihydroxides. B-C: Slices through chimney samples used for further analysis with concentric (B) and radial (C) cracks. D: Typical view of chimney matrix in plain transmitted light with bioturbation traces (yellow arrows) where allochems are mostly absent. E: Chimney matrix in plain transmitted light with dissolved bioclast. F: Transmitted light (lower right) and CCL (upper right) image of dull orange luminescent matrix. G: Transmitted light (lower right) and CCL (upper right) image of dull orange luminescent matrix and non-luminescent bioclasts. H: Transmitted light (upper left) and epiluminescent (lower right) image of matrix with variable amount of pyrite (yellow arrows), reflecting the light. I: Detail of transition in crust from reduced (lower part containing high amounts of pyrite; yellow arrow) to oxidized part (upper part, no pyrite but only remaining iron oxyhydroxides; green arrow). J: Dark staining of matrix (green arrow) by iron oxihydroxides that have migrated along and finally completely filled a fracture. Upper half is transmitted light, lower half is epiluminescent light.
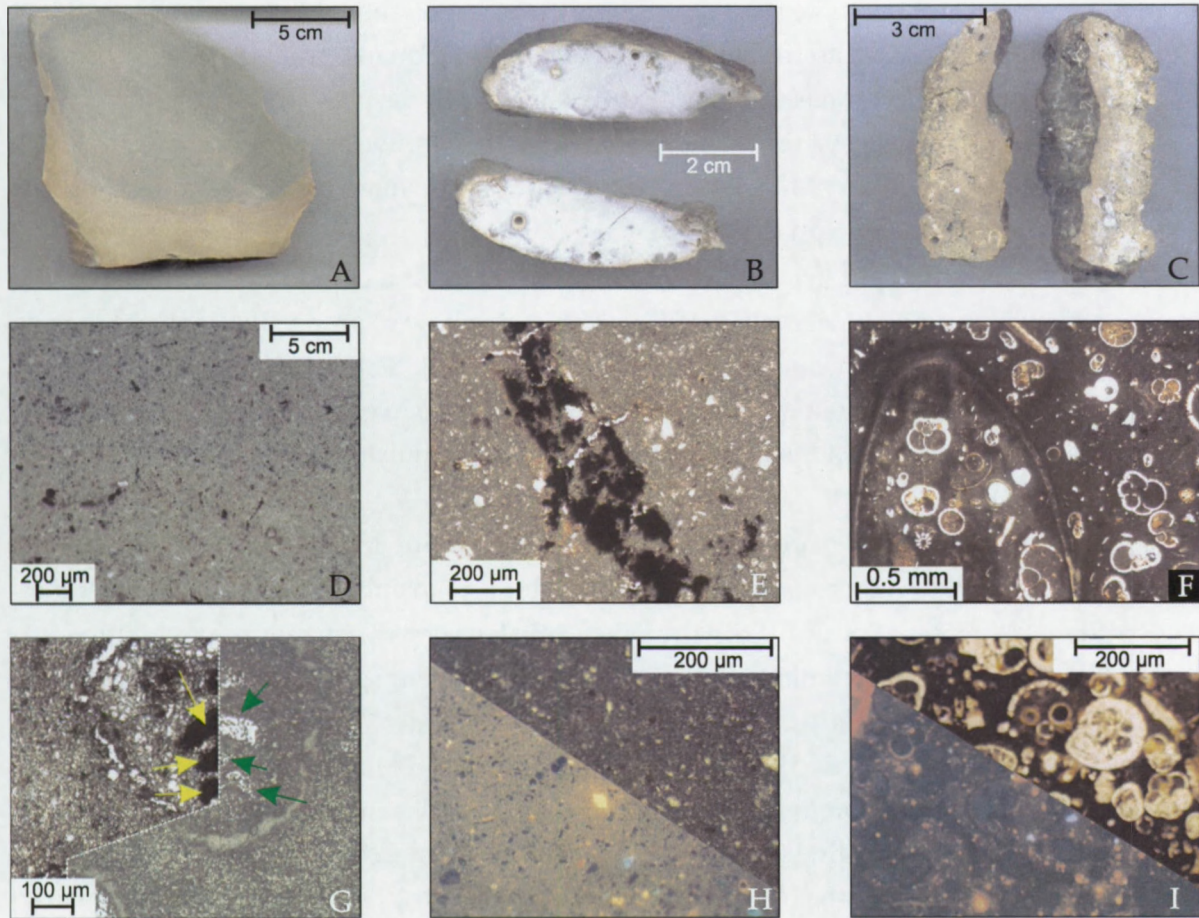
Figure 5.7: Petrography of Hesperides mud volcano crusts. A: Carbonate mudstone with redox zonation: parly reduced (gray), partly oxidized (brownish). The boundary is rather sharp. B: Whitish-gray carbonate wackestone with dark outer rim, stained by iron oxihydroxides. C: Fossiliferous carbonate wackestone with the outside also stained by iron oxihydroxides. D: Detail of the matrix of A in transmitted light, showing the transition from the oxidized part (lower half of image) to the reduced part. E: Detail of the matrix of B with concentration of pyrite precipitated in small cavities. F: Detail of the matrix of C, with dark staining by iron oxihydroxides and many unaltered bioclasts. G: Detail of the matrix of A in transmitted light (left side) and epiluminescence (right side) showing the presence of light reflecting pyrite (yellow arrows: pyrite appears opaque in transmitted light; green arrows: pyrite reflecting light) in the foram tests. H: Detail of the matrix of B in transmitted light (upper right) and CCL (lower left) showing the dull orange luminescent matrix, with red luminescent dolomite crystals. I: Detail of the matrix of C in transmitted light (upper right, similar to F), and CCL (lower left) image. Fossils are non-luminescent although a fine dull red luminescent overgrowth on the in- and outside of the shells is present

ate crust consists of carbonate mudstone (Fig. 5.7D) (micrite to microsparite, with a dull yellow-brown luminescence) in which fossil shells (foraminifera tests) have been selectively dissolved, generating biomoldic porosity. The tests of the dissolved foraminifera are filled with pyrite (Fig. 5.7G). Most abundant allochems are floating quartz grains ($< 5\%$). A brownish coloured part of the crust has a similar texture, apart from the presence of iron oxihydroxides derived from (partial) pyrite oxidation. The transition between the reduced (gray) and oxidized (brown) zone is very sharp. XRD indicated that the main carbonate mineralogy is dolomite. No other carbonate phases are detected (Fig. 5.3C).

A different white to light gray coloured sample consists of a cloudy micrite matrix with floating quartz grains and bioclasts (Fig. 5.7E). The dull yellow to orange luminescent matrix contains dispersed pyrite which is partly oxidized (Fig. 5.7H). Staining of the fossils indicate that the original calcite mineralogy has been preserved, which may indicate that no recrystallization has occurred in this sample. High-Mg calcite was the only carbonate mineral detected by XRD (Fig. 5.3).

A porous, dark brown crust with eroded outer surface due to boring activities of biota, consists of a lithified fossiliferous ooze (Fig. 5.7F). Bioclasts include foram shells (sometimes filled with matrix material or iron oxihydroxides), bivalve shell fragments, crinoid fragments and echinoid spines. The foraminifera were identified as recent species (pers. comm. David Van Rooij, RCMG, Ghent Univ.). The micritic matrix is rendered dark brown by iron oxihydroxides. The aomunt of detrital components is low ($< 10\%$) and consists of quartz and feldspar. Dolomite of uncertain nature is present. Small cracks in the crust often are associated with pyrite and iron oxihydroxides. Fossils are non-luminescent although a fine dull red luminescent overgrowth on the in- and outside of the shells is present (Fig. 5.7I). The matrix itself is dull crimson red, with dispersed bright red spots.

5.3.2 Bulk geochemistry (AAS)

Generalities The results of the analysis on the carbonate samples are given in table 5.1. The details of the analysis were given in chapter 3.

Mg/Ca versus Sr/Ca ratios are plotted in Fig. 5.8A, and indicates 3 fields: low Mg/Ca - high Sr/Ca (corresponding to the aragonite cemented samples), low-medium Mg/Ca - low Sr/Ca (the high-Mg calcite cemented samples) and high Mg/Ca - low Sr/Ca (the dolomite-ankerite cemented samples). The plots in Fig. 5.8 and Fig. 5.9 visualize various couples of geochemical parameters, differentiating between samples from Hesperides MV and the Moroccan margin (incl. PDE, MOA, Meknes MV and Kidd MV).

Calculation of the cross-correlation coefficients for the complete geochemical dataset (Table 5.2) gives some first indications about possible trends between different measured variables. The correlation coefficient R is a measure of the quality of a linear curve fitted to the dataset. The significance of the correlation coefficient R is expressed as p-values for testing the

Sample	% I.R.	% Ca	% Mg	% Fe	ppm Mn	ppm Sr	Recalculated to (100-IR)%				
							% Al	ppm Na	ppm K	ppm Zn	ppm Pb
Kidd MV & Meknes MV											
1A	23,02	26,72	0,57	0,90	165	4110	0,91	5555	2599	26	32
1B	14,72	26,16	0,33	0,64	125	4550	0,57	3085	1883	19	25
5	11,30	26,07	0,50	0,78	80	4864	0,65	2623	1569	20	28
6	16,15	25,22	1,03	0,70	114	4958	0,78	3549	2458	21	35
10	16,73	24,60	3,15	0,85	178	1543	0,79	3379	2111	29	35
Mediterranean Outflow Area											
11A	18,12	19,53	6,19	4,47	396	630	1,27	2248	4267	48	31
11B	18,96	18,90	8,05	3,00	392	642	0,96	1621	3027	37	36
11C	23,00	19,66	7,95	2,62	371	638	1,08	1523	3574	36	32
11D	16,73	18,28	7,21	4,79	422	622	1,16	1894	3841	47	30
15A	21,03	19,74	5,32	6,96	618	710	1,11	2767	3523	48	37
15B	20,54	19,72	5,49	6,44	605	686	1,06	2546	3276	45	26
15C	19,28	19,49	5,67	6,57	546	695	1,07	2807	3335	56	31
15D	22,89	19,48	6,73	7,07	573	529	0,91	1835	2752	51	27
15E	21,30	19,76	6,11	6,90	593	626	0,98	2339	3003	48	23
15F	14,78	18,90	4,60	7,52	583	731	1,10	3111	3614	66	29
21A	13,88	18,59	6,79	7,73	922	565	1,16	1714	4193	62	29
21B	17,36	18,54	7,59	5,31	813	513	1,05	1321	3475	42	35
21C	16,96	18,05	7,72	4,80	672	513	1,13	1413	3851	40	25
21D	14,70	17,66	6,98	8,04	593	633	1,09	2158	3820	72	34
22	29,80	20,26	6,57	5,00	480	699	1,21	1996	2990	63	27
PDE											
25	23,88	24,86	3,90	2,04	204	761	1,10	2692	2919	43	25
26	15,40	24,08	3,40	1,04	235	722	0,89	3086	2758	33	25
27	12,39	21,64	7,23	1,02	131	739	0,73	1685	2249	25	24
Hesperides MV											
29	21,02	25,10	3,22	0,91	230	1392	0,89	4487	3068	38	32
30A	12,45	17,32	9,83	2,89	434	427	1,14	2750	3822	43	29
30B	13,03	17,64	9,95	1,81	459	435	1,14	2442	3780	29	24
30C	15,77	18,31	10,45	0,82	437	452	1,06	2137	3339	33	30
40A	12,02	18,77	8,89	3,13	361	491	0,82	2253	2582	50	28
40B	12,31	19,31	8,99	2,34	427	466	0,73	2168	2247	33	24
40C	12,20	17,45	7,65	2,88	600	448	0,74	2374	2210	39	21
40D	19,48	19,36	5,84	3,17	517	760	0,97	2059	2860	53	26
44A	12,71	17,08	8,55	7,25	700	598	1,05	2132	3460	49	24
44B	13,69	16,94	9,83	4,36	935	558	0,93	1499	2738	25	21
44C	13,04	16,70	9,68	4,76	963	537	0,78	1418	2231	26	29
44D	9,52	17,74	8,41	6,44	834	521	0,82	1452	2545	44	23
50A	9,51	16,23	8,16	7,91	1058	473	0,85	1856	2810	64	23
50B	10,45	17,37	9,13	4,90	1156	472	1,06	1648	3638	37	23
50C	10,71	17,29	9,02	4,84	1058	472	1,03	1744	3516	35	20
50D	10,99	17,26	8,24	6,12	1001	471	0,93	1704	3024	52	20
50E	9,55	17,14	6,72	9,09	911	573	1,02	2527	3339	65	23

Table 5.1: Results from AAS analyses.
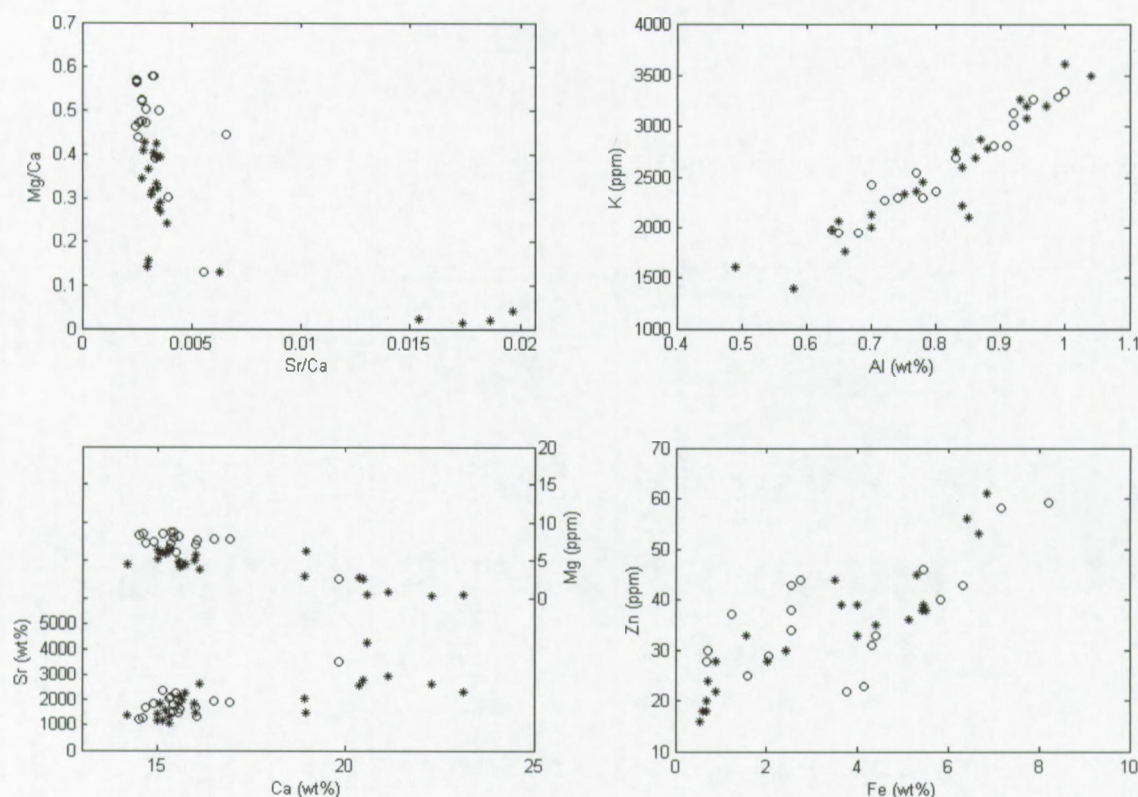
***Figure 5.8**: Plots of different geochemical parameters for crusts and chimneys from the Gulf of Cadiz. * = Samples from the Moroccan margin; o= samples from the Hesperides MV.*

H_0 hypothesis of no correlation ($R = 0$). The best correlations (R closest to -1 or 1) with high significance (p < 0.05, H_0: R=0) are found between Al and K (R=0.95), Ca and Sr (R=0.82), Fe and Zn (R=0.81), Ca and Mg (R=-0.80). Other significant but less good correlations were found between Ca and Fe (R=-0.64), Ca and Mn (R=-0.67), Mg and Mn (R=0.66), Fe and Mn (R=0.71), Mg and Sr (R=-0.75), Ca and Na (R=0.67), Mg and Na (R=-0.67). Other correlations were less significant (see table 5.2).

A principal component analysis (PCA) with varimax rotation was performed on the dataset. The two first principal components (PC's) explain 69.9% of the total variance in the dataset. PC1 corresponds with relatively high contributions from Ca and Sr, and low contributions from Fe, Mn, Mg, Zn, Al and K. PC2 corresponds to relatively high contributions from Pb, K, Al, Na, and Zn, and relatively low contribution from Mg. When the data are projected in PC-space (PC1, PC2; Fig. 5.10), it appears that the samples from the Moroccan mud volcanoes, as well as the Pen Duick Escarpment are positively determined by principle component 1 (PC1). Most of the samples from the Mediterranean outflow area (MOA) and the Hesperides MV have a negative score for PC1, but are spread over a wide range for PC2. It appears that on average, the MOA samples have a lower PC2 score than the Hesperides MV samples. The

Table 5.2: *Cross-correlation coefficients between variable pairs of overall dataset (n=40; H_0: R=0; p<0.05).*

Mg	Fe	Al	Na	K	Mn	Sr	Zn	Pb	
-0,796	-0,643	-0,633	0,674	-0,588	-0,674	**0,820**	-0,568	0,175	**Ca**
	0,354	0,463	-0,669	0,481	0,664	-0,752	0,285	-0,214	**Mg**
		0,473	-0,385	0,500	0,706	-0,483	**0,811**	-0,162	**Fe**
			-0,294	**0,946**	0,434	-0,565	0,537	0,078	**Al**
				-0,265	-0,531	0,572	-0,225	0,215	**Na**
					0,472	-0,526	0,537	0,116	**K**
						-0,508	0,483	-0,269	**Mn**
							-0,521	0,244	**Sr**
								-0,024	**Zn**
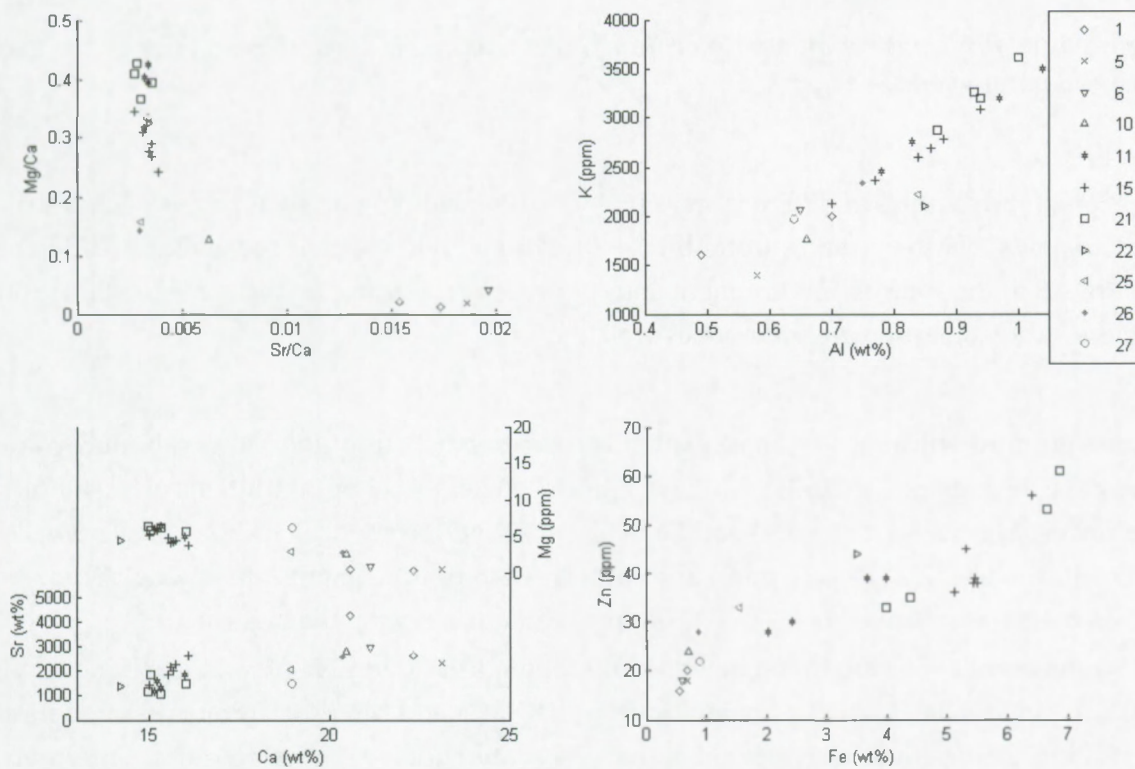
Figure 5.9: *Geochemical data plots for individual samples derived from the Moroccan margin. The numbers in the legend refer to individual sample specimens corresponding to the numbers in table 5.1*
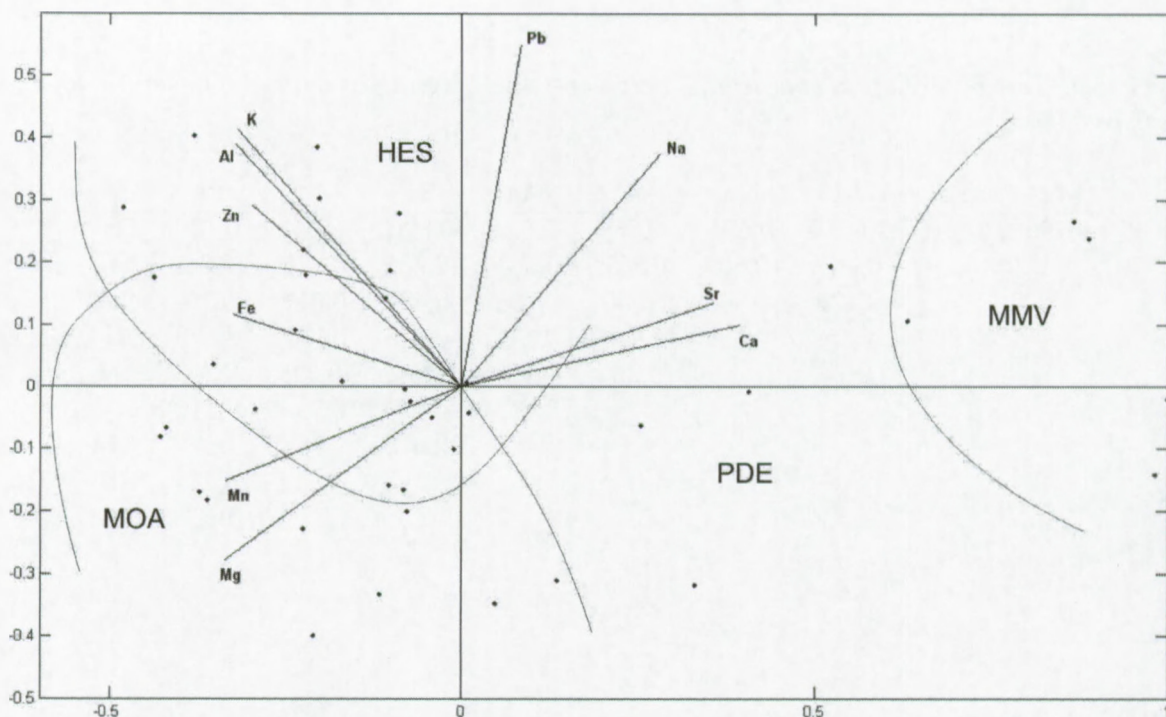
Figure 5.10: *Principal component plot (horizontal axis: PC1; vertical axis: PC2) of the geochemical parameters. See text.*

division of the samples in different areas (Fig. 5.10) coinciding with their provenance is striking. It shows that the samples from different locations/settings are geochemically different, and thus that the sources, environment and/or processes, leading to carbonate precipitation, at these various location are different as well.

Moroccan mud volcanoes The cemented carbonate crusts from the Moroccan mud volcanoes have the highest Ca (20.48 – 23.12 wt%) and Sr (1285 – 4314 ppm) contents of all samples, and lowest Mg (0.28 – 2.62 wt%) and Fe (0.55 – 0.71 wt%) content. K (1392 – 2061 ppm), Al (0.49 – 0.70 wt%), Zn (14 – 24 ppm) and Mn (71 – 148 ppm) contents are among the lowest within the dataset, while Na (2327 – 4276 ppm) content is among the highest.

Strong correlations are found between the contents of IR and Na (R = 0.97), Sr and Zn (R = -0.92), Mn and Sr (R = 0.91), Mg and Sr (R = -0.89), Ca and Mn (R = -0.85). Although these correlation coefficients are significant at the 95% confidence level, caution during interpretation is necessary because of the small sample size (N = 5). Correlations between K and Al resp. Fe and Zn are weak (R^2 = 0.47 respectively 0.59). The cemented mud breccia samples have the highest Sr/Ca ratios, varying between 2.87×10^{-3} and 8.99×10^{-3}; the Mg/Ca ratios are the lowest within the dataset (varying between 0.035 and 0.232). This corresponds to the aragonite (Kidd MV) and calcite (Meknes MV) mineralogy of these samples.

Pen Duick Escarpment   Only three samples from Pen Duick Escarpment were analysed by AAS. The samples have an intermediate to high insoluble residue (12.39 – 23.88 wt%), high Ca (18.92 – 20.37 wt%) and low to intermediate Mg (2.88 – 6.33 wt%) and low Fe (0.88 – 1.55 wt%), Mn (115 – 199 ppm) and Sr (579 – 647 ppm) contents. Sr/Ca ratios are low (1.37×10^{-3} – 1.56×10^{-3}), and Mg/Ca are rather high (0.233 – 0.551).

Mediterranean Outflow Area   In general, the Ca (14.99 – 16.11 wt%), Sr (408 – 623 ppm) and Na (1092 – 2651 ppm) contents are lower than in the samples described in the previous sections. Mg (3.92 – 6.62 wt%), Fe (2.02 – 6.86 wt%), Mn (286 – 794 ppm), Al (0.7 – 1.04 wt%), K (2122 – 3611 ppm) and Zn (28 – 61 ppm) contents are intermediate to high compared to the complete dataset.

K and Al are strongly correlated (R = 0.99; N = 15), as well as Sr and Na (R = 0.86). IR and K (R = -0.81), Mg and Na (R = -0.82), Fe and Zn (R = 0.80) are less well correlated, but still significant at the 95% confidence level. The carbonate crusts have intermediate to high Mg/Ca ratios (0.401 – 0.705) and low Sr/Ca ratios (1.24×10^{-3} – 1.77×10^{-3}).

In the analyzed chimney specimen, a concentric pattern of geochemical parameters was observed. The observed pattern shows that the samples near the conduit of the chimney have a lower content in Fe, Zn, Na and Sr (to a lesser extent) than the samples more towards the outside. The content in Mg was observed to be higher in the center than on the outside. The Ca content did not display such a trend.

Hesperides mud volcano   Slices of 3 different carbonate chimneys and 2 carbonate crust were analyzed, with in total 18 measurements.

For the chimney samples, the Ca (14,52 – 16.93 wt%) and Sr (393 – 612 ppm) contents are similar to the MOA samples. The Mg (4.70 – 8.48 wt%) contents are among the highest of all samples, while Fe (2.05 – 8.22 wt%), Mn (318 – 1035 ppm), Al (0.64 – 0.95 wt%), K (1940 – 3258 ppm) and Na (1233 – 2286 ppm) have a rather high range.

K and Al are strongly correlated (R=0.97). Other correlations are rather weak (R>0.7 or R<-0.7 and significant at 95% level): Ca and Na (R=0.74), IR and Sr (R=0.74), IR and Fe (R=-0.71), Mg and Sr (R=-0.71), Fe and Mn (R=0.70) Ca and Mg (R=-0.70). The correlation between Fe and Zn is even weaker (R=0.67). The carbonate chimneys have high Mg/Ca ratios (0.497 – 0.956) and low Sr/Ca ratios (1.11×10^{-3} – 1.8×10^{-3}).

The chemical parameters of the carbonate crusts have values that largely fall within the ranges of the chimney samples, except for the whitish high-Mg calcite sample, which has higher Ca, Sr and Na contents, and lower Mg, Fe, Mn contents. Consistently with the mineralogy, the Mg/Ca ratio is lower and the Sr/Ca ratio is higher compared to the dolomite chimney samples.

Within the chimney samples, concentric chemical patterns are not as clear as for the MOA samples. One sample has strong lithological differences between the outside and the conduit

area of the chimney: the outer sample is stained by iron oxihydroxides, the middle sample is rather grayish, and the two innermost samples partly corroded or dissolved. The most prominent trends are a decrease in Mg content from the out- to inside, and an increase of Fe in the same direction.

5.3.3 Bulk stable isotopes (carbon, oxygen)

The crusts from the Moroccan mud volcanoes have $\delta^{13}C$ values in the range of -30 to -19 ‰ and $\delta^{18}O$ values between +2 to +5 ‰. The samples from the Pen Duick Escarpment fall within this broad range as well. The MOA samples also have comparable $\delta^{18}O$ values. However, due to variable bioclast content, $\delta^{13}C$ ranges from -25 to -5 ‰. The least depleted carbon isotope compositions corresponded to samples with high bioclast contents.

The samples from the Hesperides mud volcano have heavier oxygen compositions, with $\delta^{18}O$ between +4.3 and +7‰. The carbon isotope composition has a very broad range, with $\delta^{13}C$ between -15 and -50 ‰. The crust samples form a small subcluster within the broad range that are characterized by $\delta^{13}C$ values around -35 ‰ and the heaviest oxygen compositions, with $\delta^{18}O$ between +5.5 and +7 ‰. The $\delta^{13}C$ and $\delta^{18}O$ values are plotted in Fig. 5.11. In Fig. 5.12, the theoretical precipitation temperature corresponding with the $\delta^{18}O$ values of the different samples is plotted (see also section 5.4.1), in function of the fractionation factor of the corresponding mineralogy and supposing that $\delta^{18}O$ of seawater is +0.5 to +1.5 ‰V-SMOW[4] (Diaz-del Rio et al., 2003).

5.4 Interpretation and discussion

5.4.1 Parental fluids of carbonate crusts and chimneys

Moroccan margin mud volcanoes Aragonite formation is typically linked to oxic conditions at or near the seafloor (Longman, 1980; Hovland et al., 1987; Matsumoto, 1990). The high sulfate availability at or near the seafloor favours aragonite over calcite or dolomite precipitation. The aragonite micrite and the aragonite botryoids of the carbonate crusts from the **Kidd mud volcano** are indicative of rapid cementation induced at many nucleation sites under high carbonate oversaturation conditions, close to or even at the seafloor (Given and Wilkinson, 1985; Burton, 1993).

The presence of framboidal pyrite can be explained by oxidation of organic matter or hydrocarbons coupled to sulfate reduction (implying anoxic conditions). The strong smell of hydrogen sulfide during sampling is an indication of ongoing sulfate reduction. The produced sulfide is precipitated with ferrous iron as pyrite minerals. Clouds of small microdolomite crystals observed in these samples, may be produced in sites were sulfate levels have decreased sufficiently.

---

[4]Oxygen isotope composition of fluids is expressed against the Vienna Standard Mean Ocean Water standard.
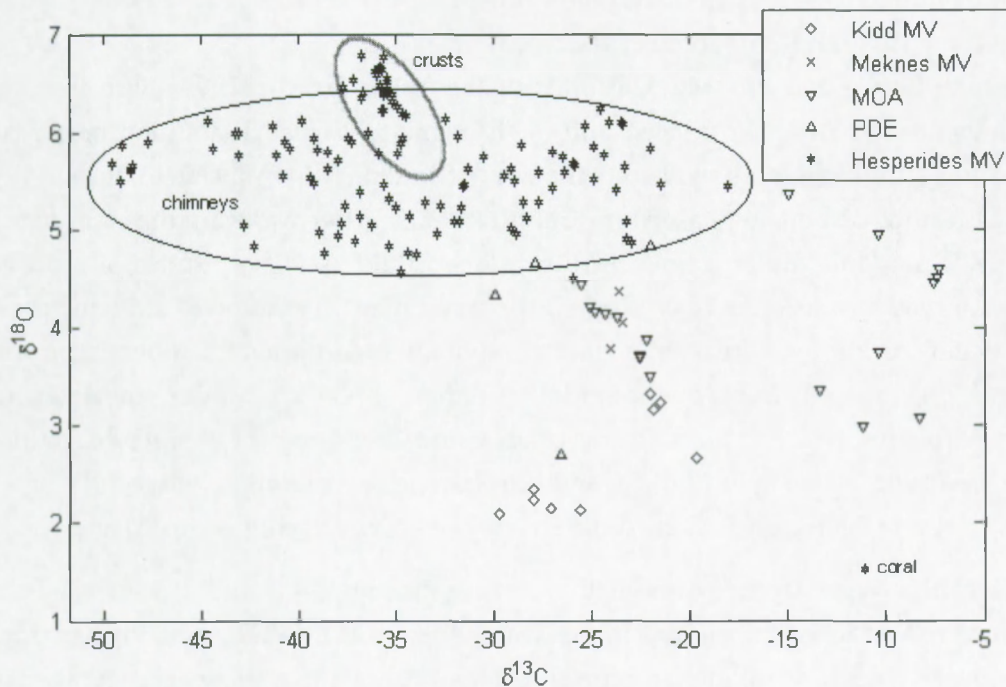
Figure 5.11: Stable isotope plot (oxygen, carbon) of the different samples in function of their provenance. Strong clustering is observed.

Naehr et al. (2000) interpret the co-occurrence of aragonite and pyrite in samples from the Blake Ridge Diapir as a product of precipitation very close to the sediment-water interface in an oxygen depleted environment where the generation of bicarbonate by anaerobic methane oxidation resulted in oversaturation with respect to aragonite. However, pyrite is not observed in close association with acicular aragonite in the Moroccan Margin samples, which could indicate that their origins are not coeval.

Therefore, we propose that the pyrite and microdolomite, and possibly the aragonite micrite matrix formed under conditions where sulfate is reduced (coupled to anaerobic methane oxidation), in contrast to the the acicular aragonite crystals that formed in voids and cracks under oxic conditions. This bears evidence of the temporal fluctuation of the position of the oxic-anoxic boundary in the upper sediments.

Considering the brecciated appearance of the carbonate crusts, this fluctuation may well be linked to sediment overturning controlled by mud volcano activity. The presence of different generations of cracks and fractures, filled with aragonite crystals, bear evidence of repeated episodes of cementation, (re)fracturing and recementation. This concurs with the fact that the crater of a mud volcano is a dynamic environment: here, brecciation may occur when pressure build-up of trapped gases in the mud volcano plumbing system exceeds the strength of the cemented or lithified mud breccia, and break up the crusts by vigorous ascent. Kidd

MV is surrounded by highly fluidized mud flow deposits, which are additional evidence for such past activity (Van Rensbergen et al., 2005a).

The high Sr/Ca and low Mg/Ca ratios of the crusts are consistent with the aragonite mineralogy. K and Al are correlated and likely relate to partial dissolution or corrosion of clays during sample dissolution despite the use of diluted HCl (1N). Due to the absence of an identified ferrous carbonate phase, it is doubtful that Fe is derived from the carbonate phase. Fe (and Zn) may initially be advected during deep fluid ascent (episodes of mud volcano activity), or may have been derived from the host sediment in relation to reducing conditions during water/rock interactions. In a sulfate reduction environment, Zn-bearing pyrite may have been precipitated. Subsequent oxidation under aerobic conditions could generate Fe-Zn-oxyhydroxides, which could be a source of Fe and Zn during the sample dissolution. The strong correlation between Fe and Zn, and the absence of correlation between Fe or Zn with K or Al, suggests that Fe and Zn are not derived from clays, in contrast to Al and K.

The bulk oxygen isotope composition of most the samples from Kidd MV can be a result of precipitation in equilibrium with seawater (Fig. 5.12), taking aragonite fractionation (Grossman and Ku, 1986) into account. It can be assumed that seawater $\delta^{18}O$ lies between 0.5 and 1.5‰ (Diaz-del Rio et al., 2003) and seawater temperature between 13 and 15°C.

For some samples however, either a heavier fluid oxygen composition or a higher precipitation temperature (up to 17°C) would be needed to explain the observed oxygen isotope composition. Considering the setting of a mud volcano crater, a temperature increase of a couple of degrees near the seafloor can be achieved during mud volcano activity involving ascending fluids. Alternatively, the increase in $\delta^{18}O$ may be caused by clay dehydratation: ^{18}O is expelled from smectite as it is transformed into illite. Hensen et al. (2007) identified this process as the major fluid source in different mud volcanoes in the Gulf of Cadiz. A third possibility is that ^{18}O-rich waters were derived from destabilized gas hydrates, as a consequence of mud volcano activity. Gas hydrate stability is possible in mud volcanoes in this area (Depreiter et al., 2005). Upon gas hydrate destabilization, a large amount of hydrocarbon gas (mainly methane) and ^{18}O-rich water is released. If these hydrates previously formed in equilibrium with seawater (taking into account fractionation factors for gas hydrate formation; Davidson et al., 1983; Matsumoto and Borowski, 2000), then the observed $\delta^{18}O$ signature can also be explained by decomposition of these hydrates.

The carbon isotopic composition indicates variable mixing between a depleted carbon source ($\sim$ -30‰ or less), and a less depleted source, such as a marine organic carbon source ($\sim$ -20‰), or dissolved inorganic carbon derived from seawater ($\sim$ 0‰). Since very depleted carbon (e.g. derived from microbial methane (-50‰ and less) has not been encountered and considering that the crusts are derived from a mud volcano crater, thermogenic methane, marine OM and marine DIC are deemed to be the most likely carbon sources contributing to the total carbon pool.
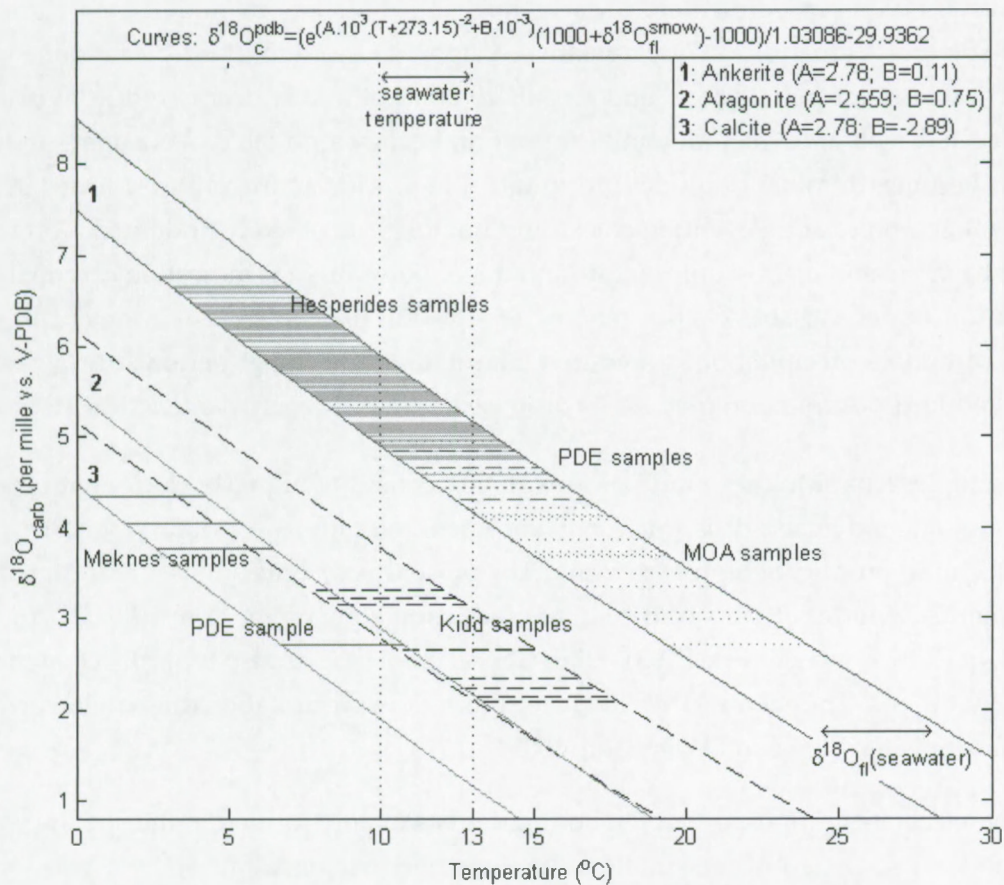
Figure 5.12: *Relation between oxygen stable isotope composition, mineralogy and precipitation temperature. The curves on the graph represent the stable oxygen isotope composition of the carbonate samples in function of the precipitation temperature, the mineralogy and the stable oxygen isotope composition of the parental fluid. The curve is described by the function shown on top of the graph. For each mineralogy, different parameters are used (listed in the upper right corner of the graph). Therefore, different mineralogies lead to slightly differently shaped curves. For each mineralogy, two curves are plotted: the upper one using a stable oxygen isotope composition of the fluid of 1.5‰, the lower one using 0.5 ‰. These values concur with the seawater oxygen isotope composition range as published by Diaz-del Rio et al. (2003). Each horizontal line represents the oxygen isotope composition of an individual sample. For each sample, the horizontal is plotted between the two curves of the corresponding main carbonate mineralogy. In the horizontal axis, the precipitation temperature range can be read, supposing a seawater fluid composition. The seawater temperature range is plotted by two vertical range. If the precipitation temperature of the sample lays within the seawater temperature range and the seawater oxygen composition range, then the sample may have been formed in equilibrium with seawater, near or at seafloor temperature conditions. If the sample temperature range is left of the seawater temperature range, then the carbonate was formed at a lower temperature, or the parental fluid had a higher oxygen isotope signature. If the samples plot at the right of the seawater temperature range, then either they formed at an elevated temperature or from heavy oxygen depleted source. The specific samples and locations are discussed in the text.*

The observed synsedimentary to early diagenetic brecciation and recementation of the carbonate crusts are indicative of a relatively vigorous ascent of fluids. Aragonite micrite likely forms in an initial stage, and as sulfate concentrations decrease due to oxidation of advected methane, microdolomite formation becomes possible. As sulfate reduction locally becomes dominant, sulfides precipitate. Large acicular aragonite is formed in a later stage (after a brecciation event) in cracks and fractures, most likely under oxic conditions.

The macro- and microscopic texture and mineralogy are thus indicating carbonate crust formation under variable circumstances: an episodically violent environment in which rapid carbonate precipitation is favoured, alternating with quiet periods during which a more reduced precipitation prevails, is proposed as a likely early diagenetic setting.

The samples from **Meknes mud volcano** mainly consist of high-Mg calcite with presence of microdolomite crystals. It is unclear if the microdolomite is a primary product or is a recrystallization product of high-Mg calcite. The presence of pyrite suggests a local reducing environment. Reported depths of the sulfate reduction zone range from 10 to 30 cm below the seafloor (Bileva and Blinova, 2003). High-Mg calcite (HMC) is also typically created under suboxic conditions. The equant HMC likely reflects a slow precipitation due to a lower supply rate of bicarbonate (Given and Wilkinson, 1985).

Therefore, it is proposed that the nodular crusts mainly formed in the shallow subsurface, in the upper part of the sulfate reduction zone, where sulfate activity was too high for dolomite to form, alternating with periodes of stronger sulfate depletion during which microdolomite could form.

The oxygen isotope composition of the Meknes MV samples can be a result of precipitation in equilibrium with seawater with a temperature of 0.5 to 6 °C, taking the calcite fractionation factor (Friedman and O'Neill, 1977) into account. However, this temperature is at least 5 degrees too low for this sampling location. The $\delta^{18}O$ of the parental fluid was heavier than seawater ($\sim 2.5 - 3‰$ V-SMOW) if precipitation occurred under present-day oceanographic conditions (10°C). Thus, involvement of ^{18}O enriched water, such as derived from the destabilization of gas hydrates, or clay transformations cannot be excluded (see discussion above). Although we cannot be conclusive of the exact fluid source, the oxygen source is a non-marine (deep-sourced) pore fluid.

The carbon isotope compositions of these crusts vary around -23 to -24‰. Similar carbon sources as for the Kidd MV samples can be proposed, although the mixing of the different sources must have led to a larger uniformity in Meknes MV than in Kidd MV.

From these individual observations and interpretations, it is suggested that the nodular crusts from Meknes mud volcano formed during a period of mud volcano inactivity, whilst a slow supply of bicarbonate from the oxidation of thermogenic methane. The influence of

marine organic matter oxidation is less likely due to the non-marine signal of the $\delta^{18}O$: a source of ^{18}O enriched water is inferred, although we cannot be conclusive about its nature.

Pen Duick Escarpment   The carbonate crusts, sampled at the seafloor, consist of micritic mud- to wackestones. XRD analyses indicate the predominance of dolomite in the mudstones and the presence of some dolomite in the wackestone. The red luminescent micritic matrix may also support the presence of Mn in the carbonate micrite, reflecting suboxic precipitation conditions. The broad dolomite [104] diffraction peak in the wackestone sample, may indicate the non-stoechiometric nature of the dolomite. Whether this relates to the alteration of a high-Mg calcite precursor is however unclear. In the mudstone sample, high-Mg calcite is absent. There, the dolomite micrite may have completely replaced a high-Mg calcite precursor, or may be authigenic in origin. Dispersed bright red luminescent phases, precipitated on bioclast substrates, were observed. Also, microdolomite crystals in the matrix were observed in cathodoluminescence microscopy, either as single bright red luminescent crystals, or as complete clusters. As reported in literature, the formation of dolomite micrite and microdolomite need a low-sulfate environment that can only be attained through sulfate reduction in the marine environment. If sufficient iron is present in the system, pyrite can precipitate. Iron oxihydroxides observed in the matrix, are likely products of pyrite oxidation.

The $\delta^{18}O$ composition indicates that the carbonates precipitated in equilibrium with seawater. The carbon stable isotope composition, ranging between -20 and -30‰ does not indicate biogenic methane as a major source of carbon. Thermogenic methane and organic matter, are likely the most important sources of depleted carbon.

Based on this information, it is proposed that the Pen Duick Escarpment crusts were formed in or below the sulfate reduction zone (coupled to methane and organic matter oxidation) through the formation of a dolomite micrite, which may reflect a high-Mg calcite precursor. Pyrite precipitated as co-product. In a later stage, this pyrite oxidized to a variable degree in an oxidizing environment, which led to the formation of iron oxihydroxides. This means that either the oxidizing agents penetrated the subsurface to a deeper level, or the crusts moved closer to the seabed — something that can be attained through erosion of the sediment above the crusts.

The observed dissolution of fossils may actually be related to the process of pyrite oxidation which generates large amounts of acid, which in turn can locally promote carbonate

dissolution through the following reactions:

$$2\,FeS_2 + 7\,O_2 + 2\,H_2O \longrightarrow 2\,Fe^{2+} + 4\,SO_4^{2-} + 4\,H^+ \qquad \text{(Reaction with oxygen)}$$

$$4\,Fe^{2+} + O_2 + 4\,H^+ \longrightarrow 4\,Fe^{3+} + 2\,H_2O \qquad \text{(Ferrous to ferric iron)}$$

$$4\,Fe^{3+} + 12\,H_2O \longrightarrow 4\,Fe(OH)_3 + 12\,H^+ \qquad \text{(Hydrolysis)}$$

$$FeS_2 + 14\,Fe^{3+} + 8\,H_2O \longrightarrow 15\,Fe^{2+} + 2\,SO_4^{2-} + 16\,H^+ \quad \text{(Reaction of ferric iron and pyrite)}$$
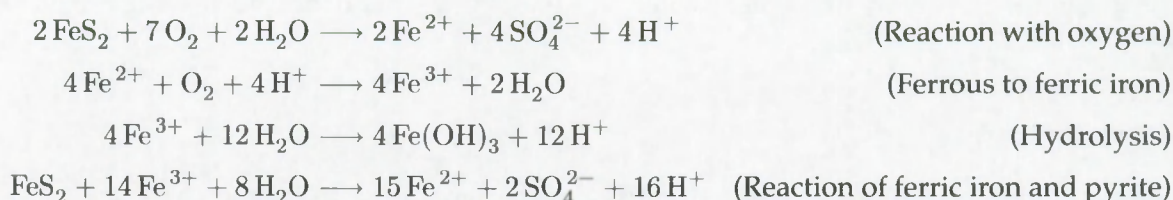
In an individual crust sampled from a shallow subsurface position, dolomitization is less pronounced than in seafloor samples. Included coral fragments are partially dissolved, and other bioclasts have undergone micritisation. XRD indicates low-Mg calcite next to a small amount of dolomite as main carbonate components. High-Mg calcite is not observed. The crust itself was less well lithified and brittle and may represent an earlier stage of the other crusts, with ongoing authigenic dolomite micrite formation that is lithifying the mud. The dissolution of the coral fragment may be due, rather than to pyrite oxidation since no pyrite or iron oxihydroxides are observed in the sample, to local acid generated through organic matter oxidation coupled to sulphate reduction:

$$SO_4^{2-} + 2 <CH_2O> \longrightarrow 2\,HCO_3^- + H_2S \rightleftharpoons 2\,HCO_3^- + H^+ + HS^-$$
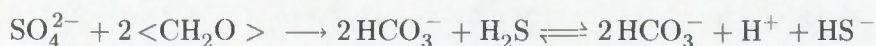
This could indicate that sulfate reduction both happens coupled to organic matter oxidation and thermogenic methane oxidation. A small amount of acid generation is enough to undersaturate and dissolve aragonite (Walter and Burton, 1990; Tribble, 1993). Since sulfate reduction coupled to methane oxidation does not generate acidity,

$$SO_4^{2-} + CH_4 \longrightarrow HCO_3^- + HS^- + H_2O$$

dolomite precipitation is promoted due to the increase of total alkalinity. Alternatively, the dissolution could be a result of oxic organic matter oxidation,

$$CH_2O + O_2 \longrightarrow CO_2 + H_2O \rightleftharpoons HCO_3^- + H^+$$
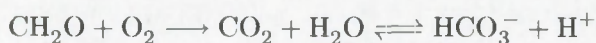
which also creates acidity.

Mediterranean Outflow Area The carbonate crusts and chimneys from the Mediterranean Outflow Area, mainly consist of matrix-supported lithified sandstone with dolomite/ankerite micrite as matrix component. The luminescence of the matrix is dull yellow-brown, which coincides with a low Mg – high Fe ankerite phase as reflected in the bulk geochemical data. On average, the MOA samples have a higher Fe content and lower Mg content than the samples from Hesperides MV (see section 5.3.2), which also have an ankerite matrix.

There is evidence of multiple episodes of carbonate precipitation, or changing chemistry

during precipitation. Bioclasts, fine fractures and detrital quartz and glauconite often contain a fine rim of clear, unstained, authigenic blocky dolomite, often with euhedral crystal shapes. Its luminescence is similar to that of the matrix. Later dolomite phases have a dull to bright red-orange luminescence, respectively corresponding to a blueish stained and unstained dolomite phase, both indicating a change from a ferrous dolomite/ankerite to non-ferrous dolomite. This could mean that the ferrous iron present in the pore fluids became depleted during dolomite/ankerite precipitation, or that the pore fluid became less reduced, which caused an increase in Mn^{2+} concentration, relative to Fe^{2+}. Since bioclasts are not recrystallized, the ankerite/dolomite matrix must be formed through selective replacement of a less stable micrite.

The bulk Fe, Zn and Mn contents of the samples are significantly higher than in the crusts from Pen Duick Escarpment or the Moroccan mud volcanoes. This can be caused by the ankerite matrix, but also by the presence of glauconite and/or iron oxihydroxides in the samples. However, the absence of a correlation between these elements and Al or K suggests that glauconite is not the source of Fe in the data. The influence of iron oxihydroxides cannot be excluded on the basis of these data alone although the weak correlation between Zn and Fe could mean that iron oxihydroxides (that scavenge a.o. Zn) were only weakly or moderately leached during analysis. A strong Zn and Fe correlation would indicate the opposite. Furthermore, the cold-cathode luminescence data indicates that ferrous dolomite or ankerite is indeed present in the samples.

The stable oxygen isotope composition ($\delta^{18}O_c$ = +2.98 to +5.36‰) suggests a precipitation between seawater temperature and slightly elevated temperatures (up to about 22°C). These latter temperatures could be explained by either a precipitation at a depth up to $\sim$ 150 m (based on a surface temperature of 13°C and a geothermal gradient : 60 mK/m (a typical background value for the North Atlantic Ocean; Sclater et al., 1980)), or by the ascent of deep warm fluids towards the seafloor. The presence of the dolomite matrix and absence of aragonitic phases (as observed in the crusts sampled in the mud volcanoes) hints formation in reduced conditions. A position very close is therefore excluded. Given the matrix-supported texture of the samples, and the fact that not all samples require a warm fluid to explain the oxygen isotope composition (mixing between seawater temperature (13°C) and a warmer temperature (22°C)), we conclude that the hypothesis of ascending warm fluid is more likely to explain the observations than precipitation at great depths. Also, formation at great depths ($\sim$ 150 m) would make it difficult to expose the samples at the seafloor after a period of erosion. The formation environment of the samples can be summarized as within the zone where sulfate is reduced, influenced by warm ascending fluids, but still close enough to the seafloor to allow post-formation exhumation.

The carbon stable isotope composition from the carbonate crusts are somewhat depleted in heavy carbon (-7 to -15‰), and the samples from the carbonate chimney a little more depleted (-22 to -25‰). The least depleted samples are those with a high bioclast content, leading

to a mixed signal between that of the matrix and bioclasts. Therefore, we infer variable mixing between carbon derived from bioclasts ($\sim 0‰$), organic matter (-20‰) and thermogenic methane (-20 to -30‰). Admixture of biogenic methane may have been possible, but only in small amounts. We infer the oxidation of thermogenic methane as a source because the oxidation of organic matter alone would not easily explain the presence of an extensive field of carbonate crusts and chimneys. Furthermore, the need for the advection of warm fluids or the destabilization of gas hydrates supports the likelihood of methane presence in the system.

Hesperides mud volcano The carbonate chimneys have open conduits, allowing seawater to make direct contact with the carbonates from the outside and inside after the exhumation of the chimneys from their host sediment. The areas that are most in contact with seawater do show a higher Fe, Zn, Na and Sr and a lower Mn, Mg content. This observation was also made in the MOA samples.

The carbonate chimneys from the Hesperides mud volcano are carbonate mud- to wacke-stones with a microsparitic matrix with a dull orange-red luminescence which is interpreted as ankerite or ferrous dolomite. This is supported by the XRD data.

Iron oxihydroxides have coloured the chimneys brownish and accumulations are sometimes present along fine cracks. These oxihydroxides are most probably derived from partial oxidation of pyrite, a sign of sea-bottom exposure of the samples. Pyrite is still ubiquitous in the matrix. Bioclasts in the samples are not recrystallized which may indicate that the Fe-dolomite/ankerite is precipitated directly from the pore fluids and not a product of replacement.

Later Fe-dolomite/ankerite phases, precipitated in fine cracks, have a brighter luminescence which could indicate a lower iron content in the parental fluid.

Although the matrix of most of the chimneys has a homogenous appearance, some samples possess a concentric pattern. In such cases, the central conduit is filled with coarse detrital material (bioclasts, quartz grains) and cemented later than the surrounding parts of the chimney. This could indicate that the formation of chimneys is linked to a rather vigorous fluid expulsion capable of locally winnowing or maybe even removing the host sediment from the conduit, before it became completely buried in the sediment, hence suggesting a formation at or near the seafloor.

The $\delta^{18}O$ and $\delta^{13}C$ values of the carbonate chimneys are very variable: +4.5 to +6.5‰, respectively -17 to -50‰. Most of the samples have $\delta^{13}C$ between -25 and -45‰. The variation within samples is most likely due to the variable inclusion of bioclastic material in the bulk sample that was analyzed. Still, the values clearly indicate a mixture of different carbon sources: i.e. microbially generated methane as a source of very depleted carbon is required, next to one or more heavier carbon sources, organic matter, bioclastic material and possibly marine DIC. The oxygen is enriched in ^{18}O and this cannot entirely be explained by fractionation during precipitation in equilibrium with seawater. Therefore, a heavy oxygen source is

needed to explain all observations. Similarly to the observations from the other locations, it is very difficult to be conclusive about this source, but gas hydrate stabilisation (also suggested in earlier work by citetSomoza2003, Diaz-del-Rio2003) or clay dehydration are the most likely candidates.

The carbonate crusts from Hesperides mud volcano are much more diverse in nature than the chimneys. First of all, the mineralogy of the crusts can be high-Mg calcite, dolomite or ankerite. The high-Mg calcite crusts possibly formed in a zone where the sulfate concentration was high enough to prevent authigenic dolomite formation. High amounts of pyrite (as also reflected by the existence of iron oxihydroxides) in the high-Mg calcite crusts hint that sulfate reduction was ongoing and sulfides precipitated as pyrite. Most likely, the crusts were formed near the seafloor, which is supported by the high interparticular space in these samples. Cementation in a deeply buried site with sulfate advection from a deep brine source would result in a more compacted host sediment, and hence in a packstone instead of a mud-to wackestone. The dolomite/ankerite samples are petrographically similar to the carbonate chimneys. Hence, we suppose that they were formed under similar conditions, except that the precipitation occurred from diffuse gas present in the pore fluids instead of related to a focused flow.

Isotopically, the crusts have a much lower variation in both $\delta^{13}C$ and $\delta^{18}O$ than the chimneys but similar conclusions can be made as for the carbonate chimneys from this location.

Some crusts and chimneys display extensive pyrite oxidation, iron oxihydroxides deposits, surface boring by benthic organisms (e.g. boring clams) and surface colonization by sessile organisms (corals, bryozoans). All these features indicate that these chimneys and crusts must have been laying on the seafloor for a time that allows colonization and bio-erosion, as well as chemical oxidation by seawater.

5.4.2 Modes of fluid flow

Above, different morphological, geochemical and petrographical characteristics of carbonate crusts and chimneys that were derived from different environments were described. The variability in these characteristics can be used as a key to propose different settings and modes of fluid flow as well as related processes that are found in the Gulf of Cadiz: focused versus diffuse flow, strong versus weak flow, slow versus fast mineralization, next to variations in potential parental fluids.

Carbonate chimneys that feature an open central conduit, are prime indicators of focused fluid flow. The process of channeling the fluid along a path with a small cross-section (the conduit opening is often not wider than a few centimeters) cannot easily be explained by one process. A possibility is that the fluid flow is focused along small-scale fractures, sedimentary heterogeneities and possibly even burrows that were filled with coarser material than the surrounding sediment. All these features have a local enhanced permeability which facilitates fluid flow at that site. Alternatively, a diffuse gas cloud reaching saturation will lead to bubble

generation, and create an upward stream of gas bubbles. Yet also in this case, preferential flow paths may be similar to these mentioned above. Through migration or advection of methane, carbonate could get precipitated well above the regional sulfate-methane transition zone, even in near-surface sediments. Subsequent erosive processes can easily exhume the carbonate chimneys from the surrounding sediments.

Slabs of carbonate crusts do not witness a focused fluid flow. The cementation of the sediments rather happens from dissolved methane in pore waters or diffuse gas clouds in the pores. From the morphologies, there is no apparent preferential fluid flow direction.

It was possible to differentiate rapidly cemented aragonite micrite crusts from the Kidd mud volcano crater versus slowly cemented crusts built up of equant high-Mg calcite at the Meknes mud volcano crater. The difference in mineralogy was attributed to a difference in carbonate supply (Given and Wilkinson, 1985) which is related to fluid flow velocity and the concentration of carbonate ions in the fluid. High carbonate concentration in mud volcano settings can be achieved by advection of deep-sourced CO_2 or by fast microbial oxidation of large amounts of CH_4 (inferring high microbial activity). High fluid flow velocities may be generated in different ways, but in mud volcano craters, it will most likeyl be related to mud volcano activity. The multiple fracturing episodes of the crusts from the Kidd mud volcano further supported violent and repetitive sediment breakup by mud volcano activity.

Crusts and chimneys in which the main carbonate phase consisted of dolomite (or ankerite) were interpreted as being formed deeper in the sediments, where sulfate was depleted through coupling with anaerobic oxidation of methane (AOM). It is evident that the depth of the AOM front itself is related to the strength of upward fluid flow: strong upward fluid flow will result in a shallower AOM zone than when upward fluid flow is absent or weak. In this approach, the formation of dolomite crusts and chimneys are indicative of a less strong fluid flow. The resulting crusts and chimneys can only be exhumed through erosion or overturning the sedimentary column through e.g. mud volcano activity.

5.5 Geochemical and petrological evidence of fluid flow

The different environments and processes involved in the formation of the carbonate crusts and chimneys are represented in figure 5.13.

The lithified mud breccia crusts sampled from Kidd mud volcano on the Moroccan margin have been formed in two modes: an aerobic mode during which aragonite is precipitated in voids and fractures, and an anaerobic mode, linked to sulfate reduction during which pyrite and microdolomite formed. These two modes alternated, which is evidenced by different phases of fracturing and cementing. The parental fluid is thought to be deep-sourced because of the mud volcano setting and isotopic indications for the oxidation of thermogenic methane. Small amounts of biogenic methane cannot be excluded, but very depleted carbonate samples
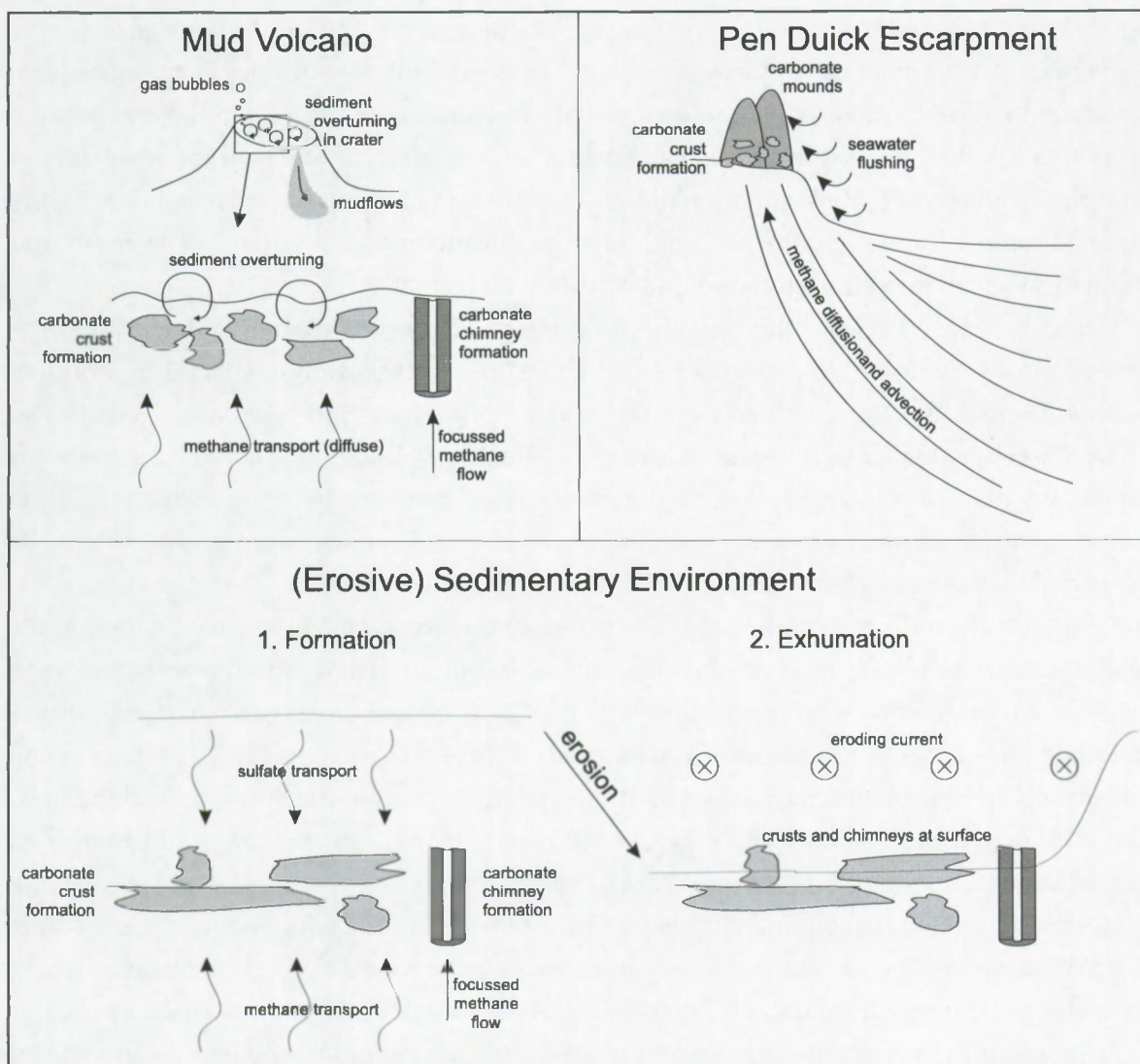
Figure 5.13: *General model for carbonate chimney and crust formation in function of setting.*

have not been encountered; therefore biogenic methane would not be a mojor carbon source. Heavy oxygen is interpreted as derived from gas hydrate destabilization or clay dehydration.

The nodular crusts from Meknes mud volcano have a high-Mg calcite mineralogy, and microdolomite and pyrite is present. All this suggests a formation under reducing conditions, within the sulfate reduction zone. Geochemical and isotopic data bear evidence of similar fluids involved as for the Kidd mud volcano.

The dolomitic crusts from Pen Duick Escarpment are pieces of lithified host sediment with variable inclusion of allochems and bioclasts. The formation of the crusts is linked to the seepage and oxidation of thermogenic methane, coupled to sulphate reduction, as evidenced by pyrite (and iron oxihydroxide) occurrence. Bioclast dissolution is thought to be a late product of pyrite oxidation which creates acidity.

The carbonate crusts and chimneys from the Mediterranean Outflow Area are Fe-dolomite – ankerite micrite cemented sandstones with evidence of multiple episodes of carbonate precipitation in small bioclasts, fine fractures and around allochems, after an initial cementation event that lithified the sediment. Recrystallization of bioclasts and other components did not take place, however. The precipitation of these samples must have taken place under slightly elevated temperatures, or influenced by the destabilization of gas hydrates. The crusts and chimneys were exhumed from the sediment after their formation.

The carbonate crusts and chimneys from the Hesperides mud volcano on the Iberian margin are mostly Fe-dolomite / ankerite cemented mud- to wackestones, stained by iron oxihydroxides that likely are derived from the oxidation of pyrite. High-Mg calcite crusts also occur. There is evidence of different phases of carbonate precipitation. The samples from this site are the only ones in which microbial methane is inferred as one of the dominant carbon sources, apart from other sources. Here also, heavy oxygen isotope compositions can only be explained by inferring gas hydrate stabilization or clay dehydration.

These results indicate a high variability in environments of carbonate precipitation in the Gulf of Cadiz: mud volcanoes, carbonate mound and fault-related environments and sedimentary environments. Carbonate chimneys versus carbonate crusts bear evidence of precipitation in a focused fluid flow versus a more diffuse gas-charged fluid. Differences in mineralogy have provided indications about the relative speed of precipitation and the position with regard to the subsurface geochemical zonation. Carbon and oxygen isotopic data has revealed the existence of different types of parental fluid components that are involved in the formation of these crusts and chimneys: seawater versus fluids derived from gas hydrate destabilization or clay dehydration as oxygen sources; thermogenic versus biogenic methane, but also possibly organic matter and marine dissolved inorganic carbon as carbon sources.

This and previous chapter has brought evidence for the migration and expulsion of fluids within the El Arraiche mud volcano field. In the next part, numerical modeling exercises will be done to evaluate the significance and effects of fluid flow on the geothermal and geochemical field. Different drivers of fluid will be regarded, as they often act at different scales and thus with different consequences.

Part III

Modeling the drivers and effects of fluid flow

Chapter 6

Internal drivers of fluid flow

The approach of this part of the study is to numerically model the fluid flow process and its consequences on a thermal and geochemical field. At the end of this and the next chapter, you will find case studies where this approach is used to better understand and predict natural phenomena or test hypotheses that are relevant to better understanding the fluid flow processes in the El Arraiche mud volcano field on the NW Moroccan margin.

6.1 Introduction

A fluid can be defined as a material that instantly deforms under an applied shear stress of any magnitude - a fluid has no rigidity. A fluid in equilibrium is not subject to an applied shear stress. As a consequence of this[1], any point at a given height in a column of fluid is in equilibrium, the fluid pressure is the same (Pascal's Law).

If the (pressure) equilibrium in a fluid column is disrupted, the fluid will flow to reach a new equilibrium. Therefore, fluid flow is a mechanism caused by a driving force – a **fluid flow driver**. The pressure difference over a certain distance will make fluid flow from the high pressure area to the low pressure area. The force responsible is the pressure gradient force F_{pgf}, defined as

$$F_{\mathrm{pgf}} = \frac{1}{\rho}\frac{\Delta P}{\Delta x} \qquad\qquad (6.1)$$

In this equation, ρ [kg m^{-3}] is the density of the moving fluid, ΔP [Pa] the pressure difference between two points and Δx [m] the distance between these two points.

In this and the next chapter, two groups of fluid flow drivers will be explored: internal drivers and external drivers. **Internal drivers** are defined here as a force or pressure gradient that is created inside the sediment body. Internal drivers include density differences and deeply generated overpressure due to dehydration processes and thermal cracking of hydrocarbons. **External drivers** rather depend on a force or pressure gradient created outside the sedimentary environment, for instance tides and currents. Although the generated pressure gradients get transferred into the sediment, the drivers are referred to as external, as the "cause" of the fluid flow is outside the sediment.

Because fluid flow drivers are very diverse in kind, not all can be regarded in detail. Large-scale sediment and fluid mobilization related to the genesis and activity of mud volcanoes will be regarded in detail when discussing the internal fluid flow drivers; eustacy, tides and seafloor currents will be discussed as external fluid flow drivers. The significance of these drivers will be evaluated in terms of magnitude of the pressure gradient and the fluid flow that is generated. Also, the consequences for the thermal and geochemical field will be analyzed. This will lead to a comparison of internal and external drivers of subsurface fluid flow, while trying to identify the scale at and situation in which either is important or negligible.

The approach of this part of the study is to numerically model the fluid flow process and its consequences on a thermal and geochemical field. At the end of this and the next chapter, you will find case studies where this approach is used to better understand and predict natural phenomena or test hypotheses that are relevant to better understanding the fluid flow processes in the El Arraiche mud volcano field on the NW Moroccan margin.

---

[1] For a derivation, see Faber (1995, p. 4-6)

6.2   Internal fluid flow drivers: an overview

Internal fluid flow drivers that generate a pressure gradient inside a basin or sediment body can have different origins, but density differences and overpressuring are the most important in geological processes.

Density differences   As the density of a material is defined by the ratio of its unit mass per unit volume, changing the density of a fluid can be achieved in two ways: either the mass of a unit volume of fluid is changed, or the volume of a unit mass is changed. The former involves a mechanism which does not affect volume change or does so in a negligible way. For instance, by dissolving an amount of salt in fresh water (the volume changes slightly, but the mass changes at a greater rate; the net effect is that the density has increased). The latter, changing the volume of a unit mass, can be achieved as the result of thermal expansion. During the heating of a fluid, it will thermally expand, requiring a greater volume. Hence, in a unit volume, a smaller amount of fluid (mass) will be present, and the net effect is a density decrease.

There are ample geological processes where density differences drive fluid flow (Judd and Hovland, 2007). Mantle convection is mainly driven by thermal expansion of mantle material at great depth, causing upward flow. Cold and dense mantle material near the surface will sink. The result is the creation of convection cells. Salt diapirism is a mechanism where salt bodies pierce the overburden and migrate upwards because they have a lower density than overburden sediments. Petroleum is lighter than water as well, and can be found leaking at the seafloor (e.g. Gulf of Mexico). Freshwater has a lower density than saline water. This density difference drives fresh water springs found for instance in Scandinavian Fjords.

Overpressure   During burial of sediments, pore space decreases and pore fluids are evacuated. However, under certain conditions, especially in very fine-grained sediments, this pore fluid removal is ineffective and pore fluids become 'locked' inside the pores. This phenomenon, called *undercompaction*, or *disequilibrium compaction*, typically happens under conditions of (1) rapid sedimentation and burial during which the burial rate outpaces the compaction rate because sediment permeability is too low, and (2) tectonic compression, a situation in which buried sedimentary bodies with low permeability are subject to additional pressure due to tectonic convergence. Also, permeable strata may be sealed by low permeability strata, e.g. clays.

As the fluids are trapped, increasing the burial will increase the fluid pressure above the normal hydrostatic pressure. The hydrostatic pressure is the pressure caused by the above laying water column,

$$P_h = \rho_w g h \tag{6.2}$$

with P_h [Pa] the hydrostatic pressure, ρ_w [kg.m^{-3}] the fluid density, g [m.s^{-2}] the gravitational acceleration and h [m] the height of the overlying water column. When undercompaction occurs, the effective pore pressure will be

$$P = P_h + P_e \tag{6.3}$$

where P_e [Pa] is the excess pressure or overpressure caused by the weight of the overburden sediment. Such a situation is illustrated in figure 6.1.

Alternatively, the generation or inflow of gas or oil in a sealed permeable layer, will also increase the pore pressure. Because gas or oil has a lower density than water, it floats on top of the water in the reservoir layer. Because of the lower density, the pressure gradient in a oil and gas column will be lower than in water; hence the pore pressure in the oil and gas bearing zone will be higher than when no oil or gas would be present. This is illustrated in figure 6.2.
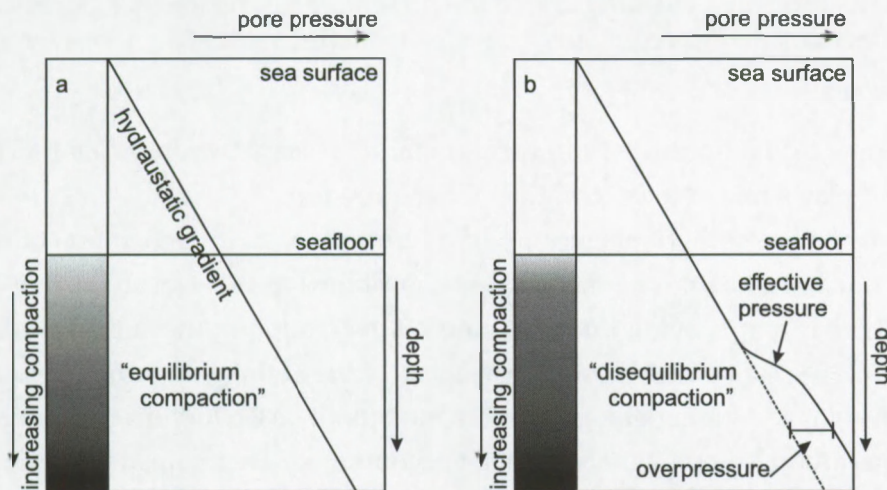
Figure 6.1: *Overpressure due to disequilibrium compaction. a) equilibrium compaction and pressure profile; b) disequilibrium compaction and pressure profile.*

Other Other drivers of fluid flow in sedimentary environments that will not be discussed in this work include groundwater discharge controlled by topography and overpressure generation due to the (formation and) dissolution of gas hydrates (Judd and Hovland, 2007).

6.3 Overpressure and sediment buoyancy on the northwest Moroccan margin

The occurrence of large mud volcanoes on the northwest Moroccan margin conveys of the presence of overpressure in the subsurface. The size of the mud volcanoes (see Chapter 4) alone implicates the mobilization of very large amounts of sediments towards and extrusion
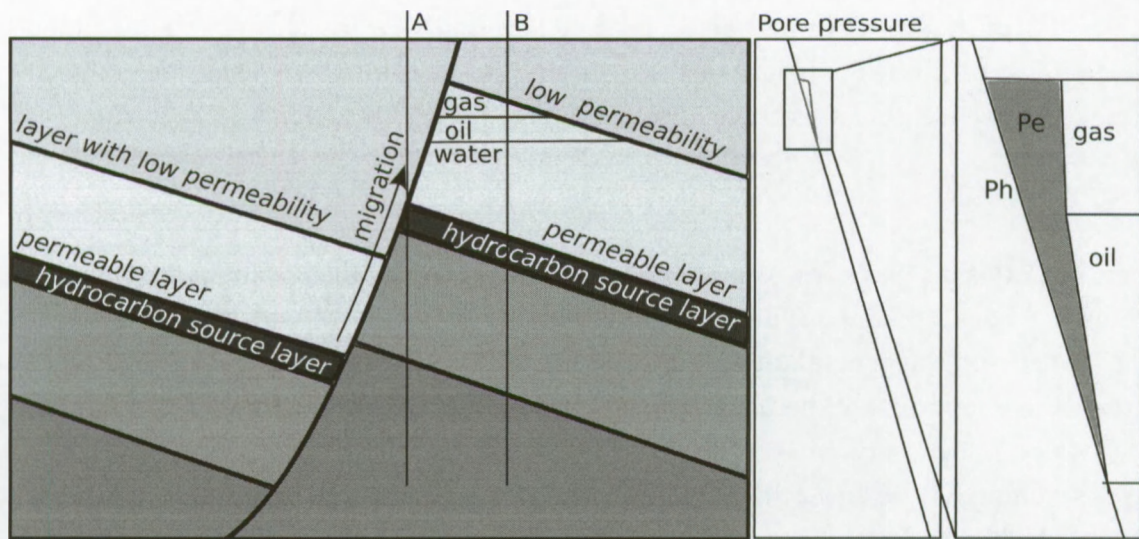
Figure 6.2: *Overpressure generated due to the presence of an oil and gas pocket. Due to the lower densities of oil and gas compared to water, the pore pressure increases locally.*

at the seafloor. On the northwest Moroccan margin, at least two important factors can be identified that play a role in the generation of overpressure.

The first factor is the thermal cracking of hydrocarbons, with generation of oil and gas. In section 6.2, it was shown how this process contributes to the overpressuring of a buried sediment. There is ample evidence of gas and oil generation in the subsurface in this area (Chapters 4, 5). The stable carbon isotope analysis of the authigenic carbonates gave insight in the carbon source. Although biogenic methane cannot be excluded as a source of carbon, very depleted carbon isotope signals were not encountered. Therefore, it was esteemed more likely that thermogenic methane was a more important carbon source in the area. Additionally, Stadnitskaia et al. (2006) reported on hydrocarbon gas compositions from different mud volcanoes in the Gulf of Cadiz. The mud volcanoes from the El Arraiche mud volcano field were not included in this study, but the results from 3 nearby mud volcanoes (Ginsburg MV, Yuma MV and Rabat MV) can at least be used as indicators. It was shown that the C_{2+} content of the sampled gases is low (3 %). Together with stable isotope data, the composition was characteristic for a thermogenic gas field. The gases were identified as mature gases (Bernard Index < 1.2 %), derived from a mixture of type II and type III kerogens (Table 6.1). Mud clasts sampled from Yuma mud volcano were dated from the middle Eocene to late Miocene (Ovsyannikov et al., 2003), corresponding to the age of the accretionary wedge sediments (Maldonado et al., 1999). Kerogen studies of these clasts showed general immaturity (Kozlova et al., 2008). Together with the mature characteristics of the sampled gases, this may plead for the existence of deeper, similar kerogen deposits present in the gas generation window. This would imply the possible migration and redeposition of migrated thermogenic gas within the olistostrome and/or even within the Pliocene-Quaternary sediments on the

Kerogen Types and Gas Wetness

Kerogen is the insoluble portion of organic matter present in sedimentary rocks. The soluble part is known as bitumen. Under high temperatures (due to burial), kerogen can be transformed in hydrocarbon gas and oil. There are different types of kerogen:

Type I
Type I kerogen has a high hydrogen:carbon (H:C) ratio (> 1.25) due to it's low content of aromatic structures. It is often referred to as lacustrine kerogen since its main component is lacustrine algae. This type of kerogen thus forms in anoxic lakes or under specific anoxic marine conditions, hence it has a rather low occurrence. It typically produces liquid hydrocarbons.

Type II
Type II kerogen has a lower H:C ratio (< 1.25) and is derived from terrestrial plants and marine algae with high lipid content. It typically produces a mix of gas and oil. Sometimes, this kerogen contains high amounts of sulphur.

Type III
Kerogen type III has the lowest H:C ratio (< 1) due to the high abundance of ring and aromatic compounds derived from non-lipid plant-derived material such as cellulose, terpenes and phenolic compounds from plants. This kerogen typically produces methane and coal.

Type IV
Type IV kerogen mostly is decomposed organic matter consisting of polycyclic aromatic hydrocarbons, and hence has a very low H:C ratio (< 0.5). It has no hydrocarbon potential.

Gas wetness is used to describe the compositional variations in hydrocarbon gases. Dry gas is defined as CH_4, or abbreviated as C_1. Wet gas is defined as C_{2-4}, so all gases containing 2 to 4 carbon atoms. The gas wetness index is then the ratio of C_1 and the sum of all gas, C_{1-4}: $\frac{C_1}{C_{1-4}}$. The Bernard Index is a similar ratio, defined as $\frac{C_1}{C_{2+3}}$.

Table 6.1: Kerogen Types and Gas Wetness

Moroccan margin (Stadnitskaia et al., 2006).

A second factor for overpressuring on the northwest Moroccan margin is the dehydration of clays. During transformation of smectite to illite, large amounts of H_2O are set free, and the result is an increase in fluid volume. The H_2O can be discriminated from seawater on the basis of hydrogen and oxygen stable isotopes (Sheppard and Gilg, 1996). Hensen et al. (2007) reported this type of H_2O in the crater of Captain Arutyunov MV, corresponding to earlier reports of Yuma and Ginsburg MV (Mazurenko et al., 2003). Hensen et al. (2007) inferred a

fluid source of approximately 5 km, which comprises the lower sedimentary units deposited on the basement. For this calculation, an average thermal gradient of 30°C per km was supposed. At a higher regional thermal gradient, e.g. 60°C, as used in Depreiter et al. (2005), the dehydration process would occur at much shallower locations. Anyway, Hensen et al. (2007) conclude that the release of freshwater at greater depth is the quantitatively dominant process of fluid formation in this area.

Thermal cracking of kerogen, with generation of oil and gas, together with formation of fresh water from clay dehydration have a great overpressuring potential. The different literature sources that address the source of overpressured mud in the Gulf of Cadiz are unable to pinpoint a precise location (e.g., Stadnitskaia et al., 2006; Hensen et al., 2007; Ovsyannikov et al., 2003) which is mostly due to the chaotic nature of the accretionary wedge: any stratigraphic correlation is missing. Small limestone clasts indicated that the mud volcano feeder system probably roots in or below Upper Cretaceous to Miocene rocks (Akhmanov et al., 2003; Ovsyannikov et al., 2003).

The overpressured mud is piercing the overburden, at least partly controlled by structural features (see Chapter 4) and is thought to form intrusive bodies (Chapter 2), and drive mud volcano formation and activity. However, a second material must be taken into account: salt. It has become apparent rather recently that salt diapirism is occurring, at least under Mercator mud volcano. Evidence for this was found in the presence of large gypsum crystals sampled in cores sampled during cruise TTR-15 (2005) onboard R/V Logachev, and during FP6 Hermes cruise M1/3 onboard R/V MS Merian (2006). The salt itself most likely of Triassic origin (Haeckel et al., 2007), although the crystals might be reprecipitated at a shallower location. During the latter cruise, geochemical evidence was found for halite dissolution (chloride enrichment up to 5.3 M, about 9 times the seawater Cl concentration). Li an B concentrations indicated a deep fluid source, related to mineral dewatering reactions; supported by a radiogenic $^{87}Sr/^{86}Sr$ pore water signal of 0.7106 (Haeckel et al., 2007). Upward advection rates were calculated, yielding fluid flow rates of about 6 cm per year at the top of the mud volcanoes, towards 0.3 cm at the rim of the crater.

The growth anticline underlying the Mercator mud volcano can be explained by sediment buoyancy. The precise nature of the diapiric material is unknown, but with the presented data, it is acceptable to infer a mixed system of overpressured mud and salt.

6.4   Modeling the effects of internally driven fluid flow

In mud volcano craters, it is evident that fluid flow can be episodically strong, mobilizing sediment from great depths and extruding it at the seafloor. Yet, a mud volcano does not display vigorous activity at all times. For instance, Haeckel et al. (2007) inferred an upward fluid flow of 0.3 to 6 cm per year in Mercator mud volcano at present. Not only mud volcano craters (and the inferred feeder pipe), but also fault zones can be important fluid flow zones.

In this section, the importance and significance for geochemistry and geothermics will be discussed in such settings.

6.4.1   Geothermal effects

The temperature in sediments is governed in the first place by the temperature at the sediment surface, the local geothermal gradient and the depth at which the temperature is measured. However, upward fluid flow will affect the temperature as well because of heat advection. The extent of the temperature change will depend on the strength of the fluid flow.

Using the model for heat flow in porous media, introduced in chapter 3, a set of model runs were executed to quantify the effect of upward fluid flow on the temperature profile in sediments. Standard model parameters include a surface temperature of 10°C (a typical value at the El Arraiche mud volcano field), a sediment column depth of 1 km, a regional thermal gradient of 0.06 $K.m^{-1}$, which is a normal background value for the North Atlantic Ocean (Sclater et al., 1980). The thermal conductivity, heat capacity and density of the fluid and solid were set to 0.529 $W.m^{-1}.K^{-1}$, resp. 2.5 $W.m^{-1}.K^{-1}$; 4181 $J.kg^{-1}.K^{-1}$ resp. 1000 $J.kg^{-1}.K^{-1}$; 1000 $kg.m^{-3}$ resp. 2700 kg/m^{-3}. The source fluid temperature is controlled by the geothermal gradient and the surface temperature (i.e., the no-flow situation). Different runs were executed to quantify the role of various parameters:

1. The *fluid flow velocity* was varied from 0 mm per year, to 10 m per year.

2. The model was run with different *porosity* profiles: one model used a constant 75% porosity, an other used the porosity model described by Spinelli et al. (2004) as porosity $n = 0.909z^{-0.073}$. For analytical reasons, the function was implemented as:

$$n(z) = \begin{cases} 0.909 & (z \le 1\text{m}) \\ 0.909z^{-0.073} & (z > 1\text{m}) \end{cases} \qquad (6.4)$$

   and results in a profile as shown in figure 6.3

3. The model was run in *transient mode* to evaluate the evolution of the temperature profile over time under different fluid flow velocities after a hypothetical strong 'eruptive' fluid flow event which created a constant temperature profile.

4. *Different fluid source depths* were simulated by changing the column length.

Fluid flow velocity effects   The effect of fluid flow velocity is highly variable. The temperature profile for low fluid flow velocities (in the order of less than 1 mm per year) is insignificant because it offsets the temperature curve only slightly, or not at all (figure 6.4a). This
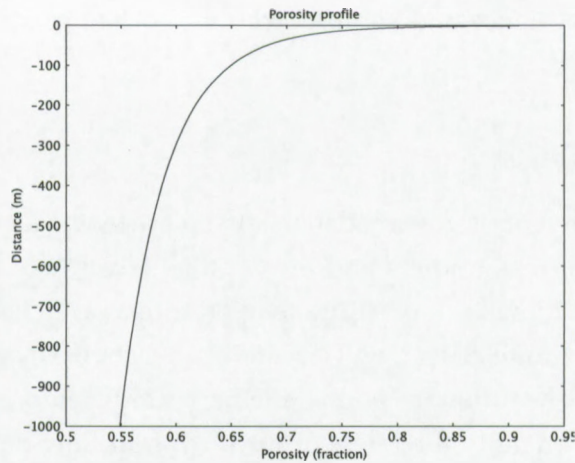
Figure 6.3: Porosity profile based on Spinelli et al. (2004).

means that the advective heat flux is (significantly) lower than the conductive heat flux. For these flow velocities, the thermal gradient remains more or less constant (figure 6.4b).

The magnitude of the advective heat flux $J_a = \rho c T v$ is in the order of $10^3 \times 4.181 \times 10^3 \times 3 \times 10^2 \times v = 1.25 \times 10^9 \times v$, which is much smaller than the conductive heat flux (Figure 6.5). For example, for $v < 1\text{mm.y}^{-1} = 3.17 \times 10^{-11} \text{m.s}^{-1}$, the advective heat flux becomes $J_a < 4 \times 10^{-2}$ W.m^{-2}. The conductive heat flux $J_c = k \frac{\partial T}{\partial x}$ will be in the order of $1.025 \times 0.06 = 6.15 \times 10^{-2}$ W.m^{-2} which is effectively higher than the advective heat flux J_a (Figure 6.5b).

For higher fluid flow velocities, the temperature profile is curved upwards (Figure 6.4a), which means that the upward advective transport of heat becomes more significant. At greater depth, the thermal gradient (Figure 6.4b) becomes smaller than average (even zero where a constant temperature profile occurs), and therefore the conductive heat flux becomes (much) smaller than the advective heat flux (Figure 6.6). Near the surface however, where the temperature is strongly influenced by the constant surface temperature. The thermal gradient becomes larger than deeper in the sediments. Thus the conductive heat transport will become more important again, albeit still smaller than the advective heat flux.

> This numerical experiment shows that the upward fluid flow in sediments has a major impact on the geothermal profile near the seafloor. Geothermal measurements over a short depth profile near the seafloor will not represent the geothermal situation deeper in the sediments. Such measurements can lead to over-estimation of the geothermal gradient. The effect of fluid flow should always be considered during the interpretation of such data.

Porosity effects   The main consequences of the decreasing porosity with depth is the changing effective thermal conductivity and a change in fluid flow velocity[2]. The effective thermal

---

[2]In this model exercise, it is assumed that permeability and porosity have a linear relationship.
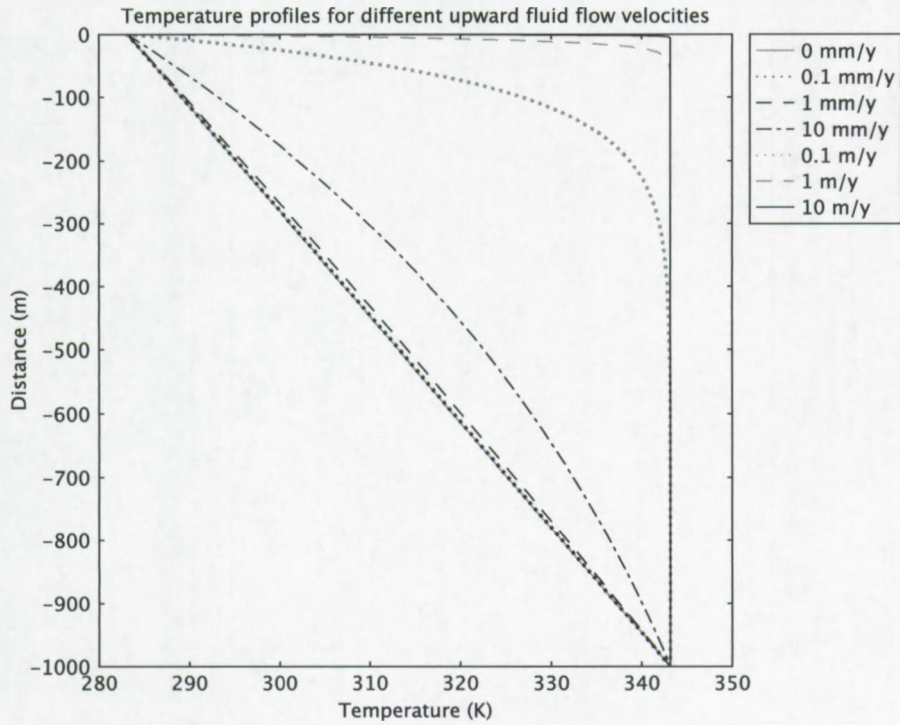
(a)
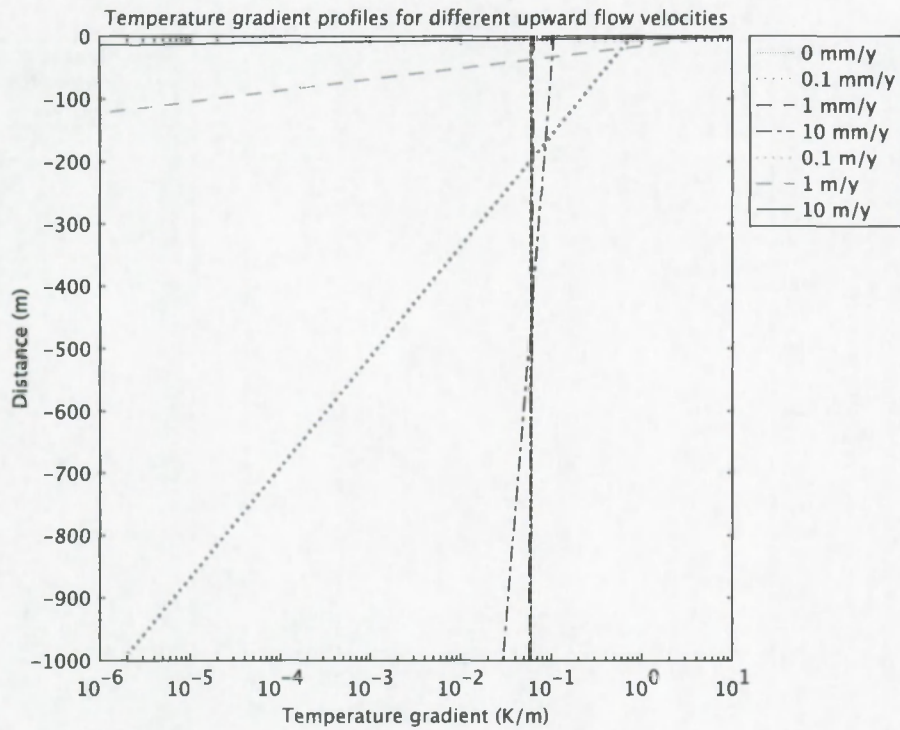
(b)

Figure 6.4: *Temperature (a) and thermal gradient (b) profiles under different fluid flow velocities for a constant porosity profile (0.75).*
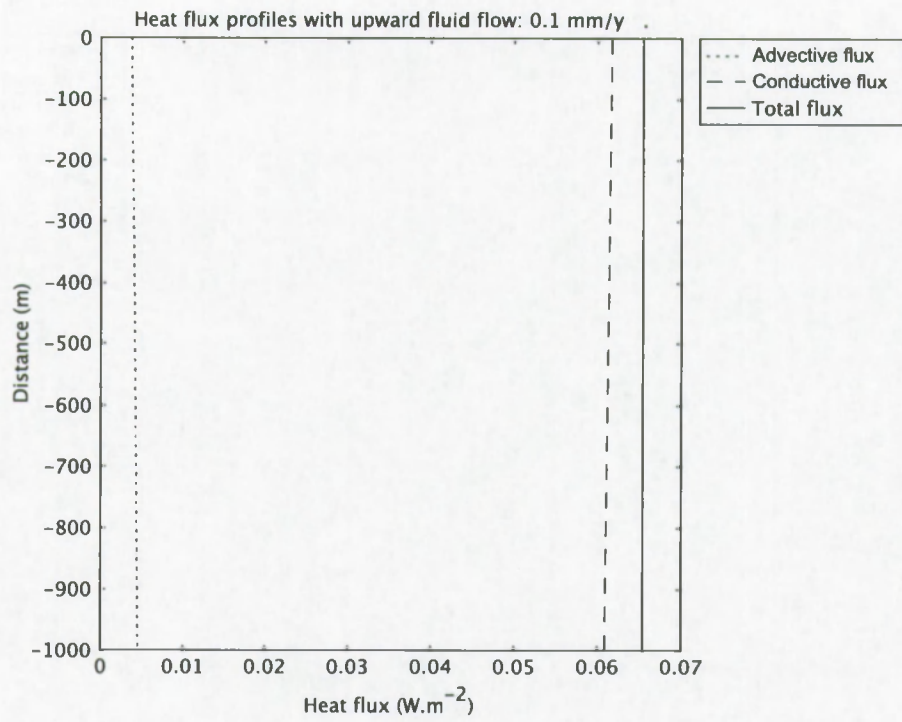
(a)
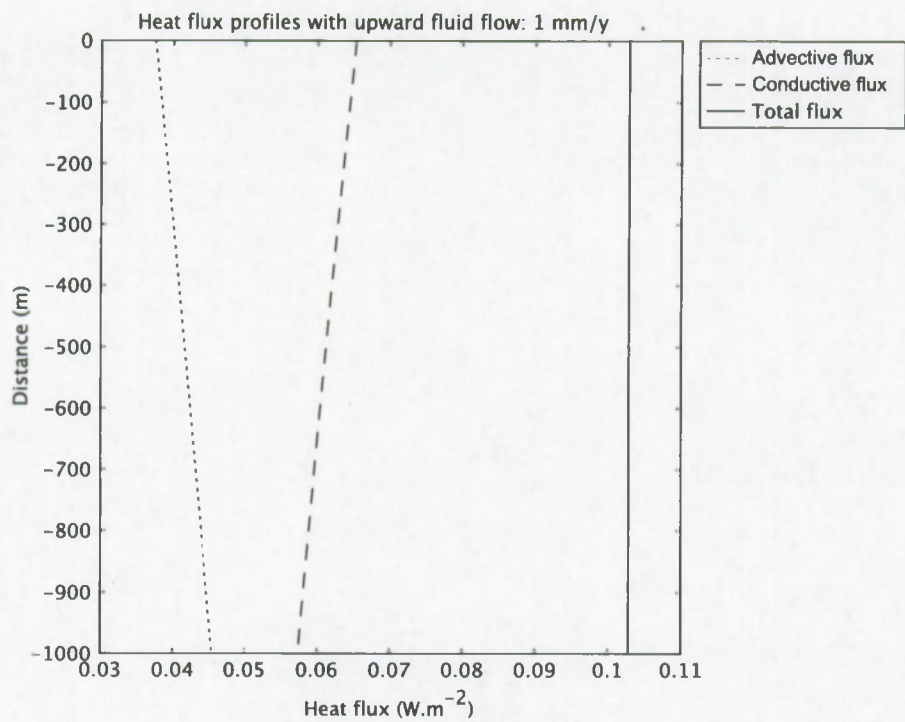
(b)

Figure 6.5: Heat flux profiles for different fluid flow velocities to illustrate the relative importance of convective and diffusive heat transfer.
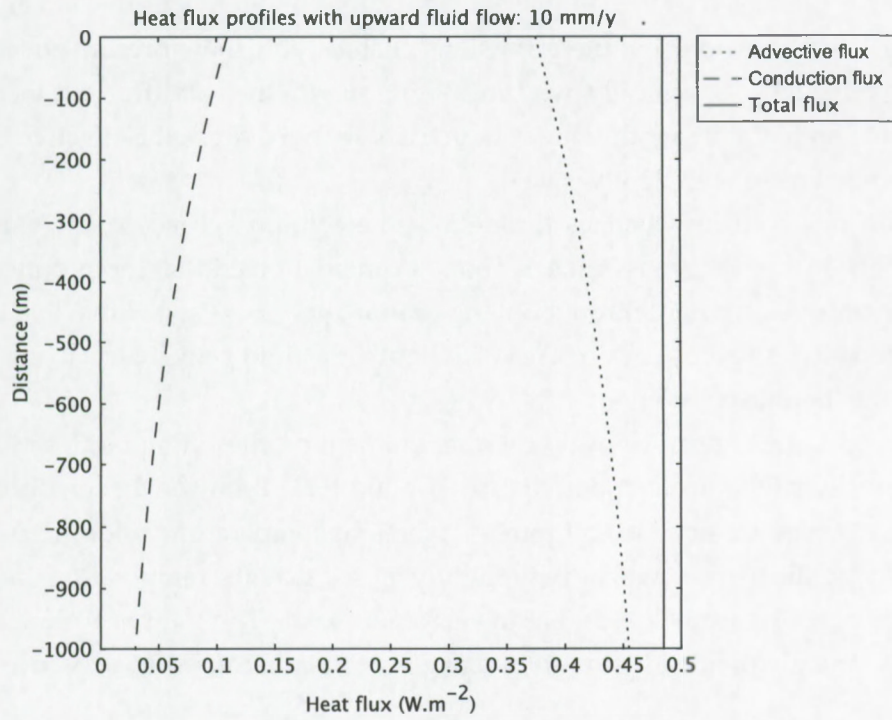
(a)
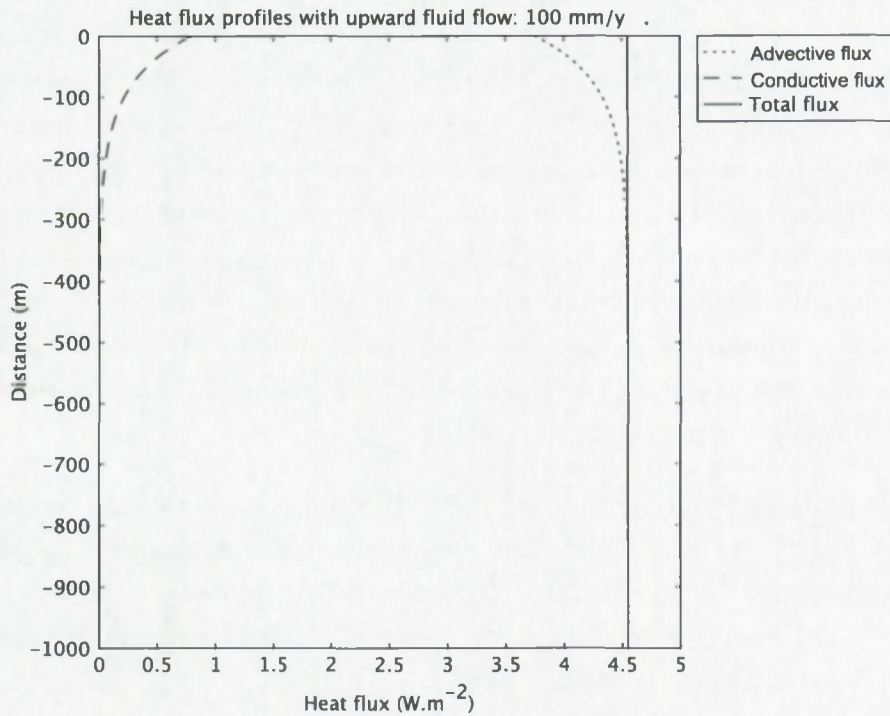
(b)

Figure 6.6: Heat flux profiles for different fluid flow velocities to illustrate the relative importance of convective and diffusive heat transfer.

conductivity is calculated as the volume average of the conductivities of solid and fluid fractions. With changing porosity, these fractions change, and therefore the effective thermal conductivity changes. Specifically, with increasing depth, the solid fraction increases; since the solid fraction has a higher thermal conductivity than the fluid, the effective thermal conductivity will increase with depth as well.

The fluid flow velocity changes throughout the column because conservation of mass must be obeyed. From the mass conservation, it can be derived that the product of porosity and velocity must be constant throughout the column, or $v_1 = \frac{\theta_2}{\theta_1} \cdot v_2$ with v the fluid velocity and θ the porosity. As porosity decreases with depth, the fluid velocity has to increase, which influences the thermal convection.

At first sight, the temperature and thermal gradient profiles do not differ much between the two porosity situations (compare figures 6.4 and 6.7). If no convection occurs, or if the fluid flow velocities are small ($v < 1$ mm.y^{-1}) then the temperature modeled using the variable porosity profile (eq. 6.4) will be only slightly higher than the temperature calculated with the constant porosity profile (0.75) (Figures 6.8a and 6.9a). The total heat flux (Figures 6.8b and 6.9b) is strongly defined by the conductive heat flux (because the advective flux is very small).

The lower porosity will however effect the total heat flux because the effective thermal conductivity increases with decreasing porosity. This even occurs if no fluid flow is present (Figure 6.8b).

Under faster fluid flow conditions, the observations show different patterns. The porosity difference between the two situations indicate a strong control on the total heat flux. The reason for this is that in the case of a decreasing porosity with depth, the fluid flow is much stronger, and the net effect is that the heat flow is higher at depth – heat is transported quicker towards a more shallow position (Figure 6.10). Closer to the surface, these porosity controlled effects become much less strong because the porosity difference is becoming smaller. With decreasing porosity, conductive processes become more important. The temperature difference between the two porosity models in the upper part therefore is a direct consequence of the difference in heat flow at greater depth.

The importance of the porosity model on heat flux clearly depends on what is being observed. The temperature profiles are very similar for both porosity models. Therefore the porosity model is not so critical for the temperature profile itself. However, strong differences occur however in the heat flux calculations. Therefore, a suitable porosity model should be used in thermal modeling exercises.
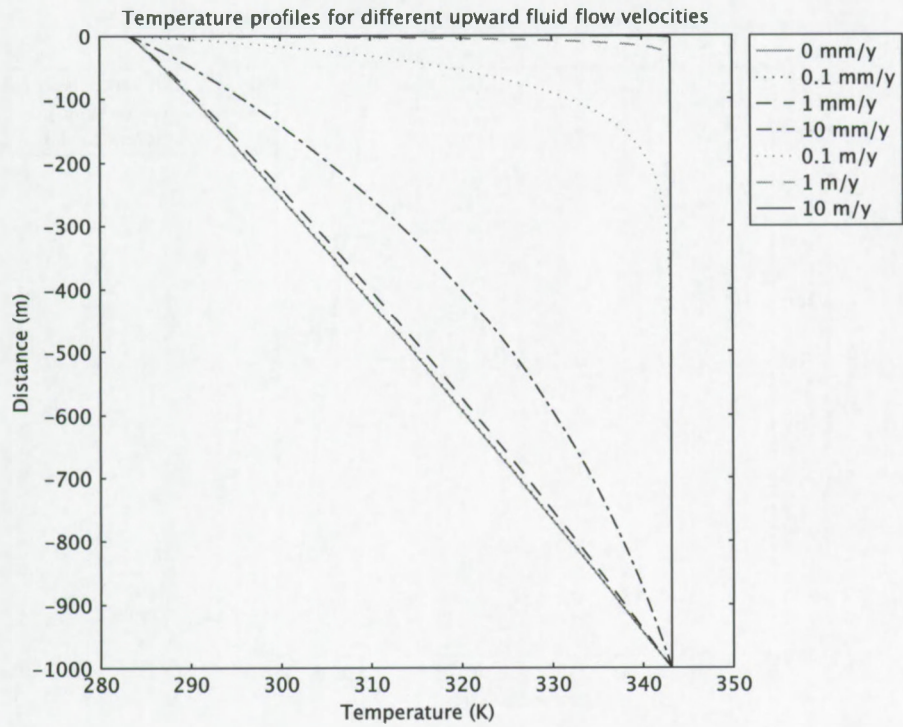
(a)
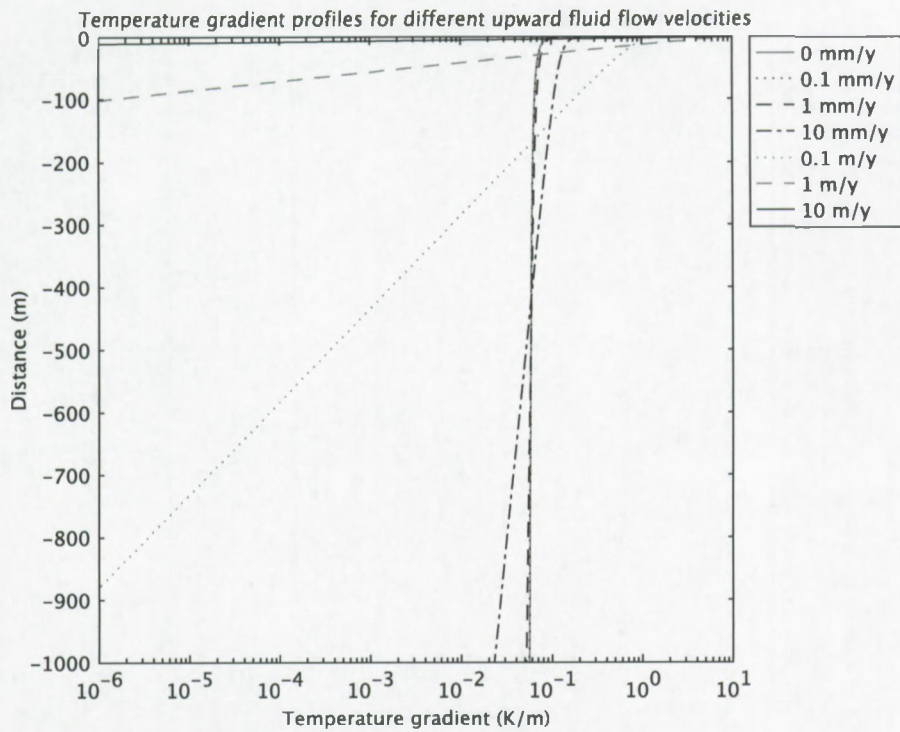
(b)

Figure 6.7: Temperature (a) and thermal gradient (b) profiles under different fluid flow velocities for a variable porosity profile (equation 6.4).

Temperature profiles for different porosity functions. Fluid flow: 0 mm/y

(a)

Heat flux profiles with upward fluid flow: 0 mm/y
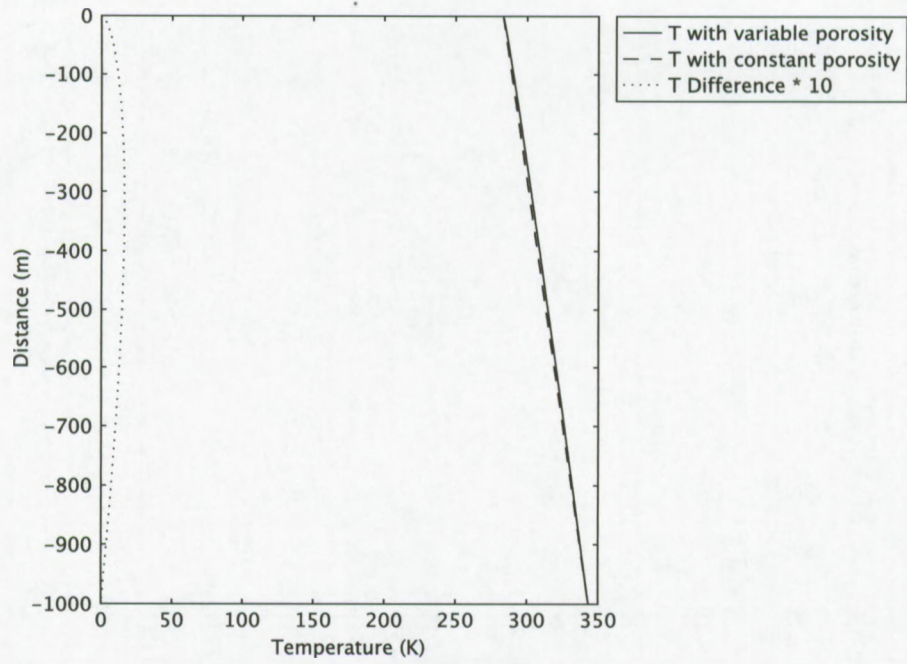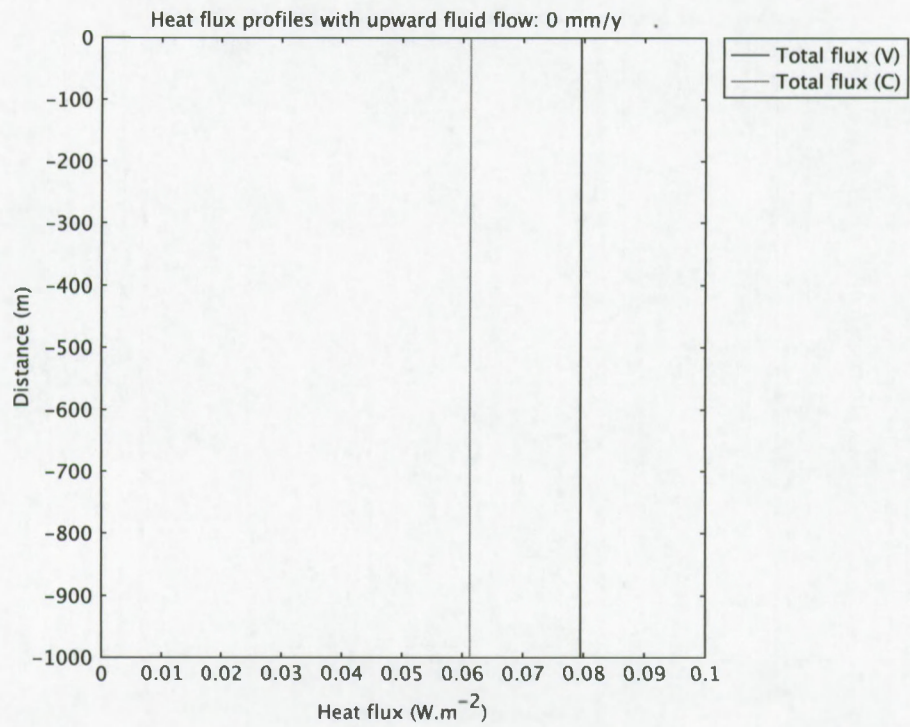
(b)

Figure 6.8: *Temperature and heat flux profiles to compare the effect of the porosity difference at fluid flow velocity 0 mm/y. (C) indicates a constant porosity profile (0.75) and (V) indicates the variable porosity profile as given in eq. 6.4. Temperature differences are multiplied by 10.*

Temperature profiles for different porosity functions. Fluid flow: 1 mm/y

(a)

Heat flux profiles with upward fluid flow: 1 mm/y
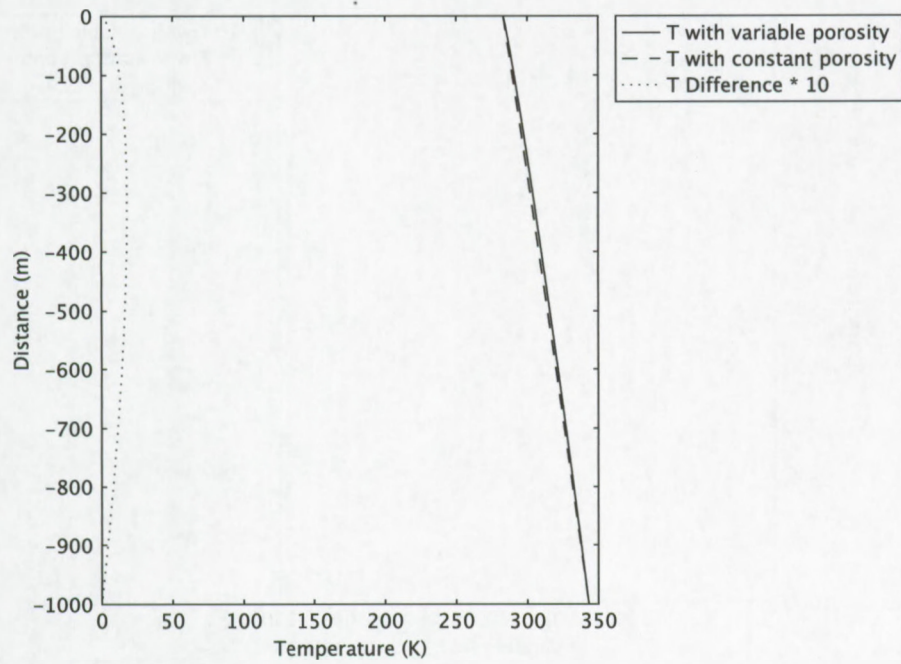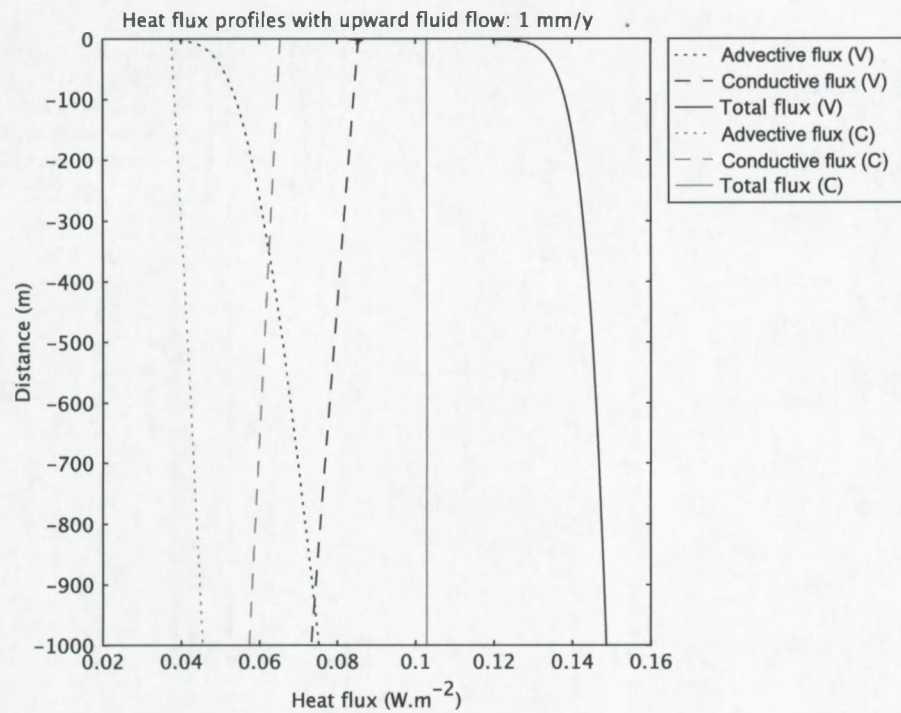
(b)

Figure 6.9: *Temperature and heat flux profiles to compare the effect of the porosity difference at fluid flow velocity 1 mm/y. (C) indicates a constant porosity profile (0.75) and (V) indicates the variable porosity profile as given in eq. 6.4. Temperature differences are multiplied by 10.*

Temperature profiles for different porosity functions. Fluid flow: 100 mm/y
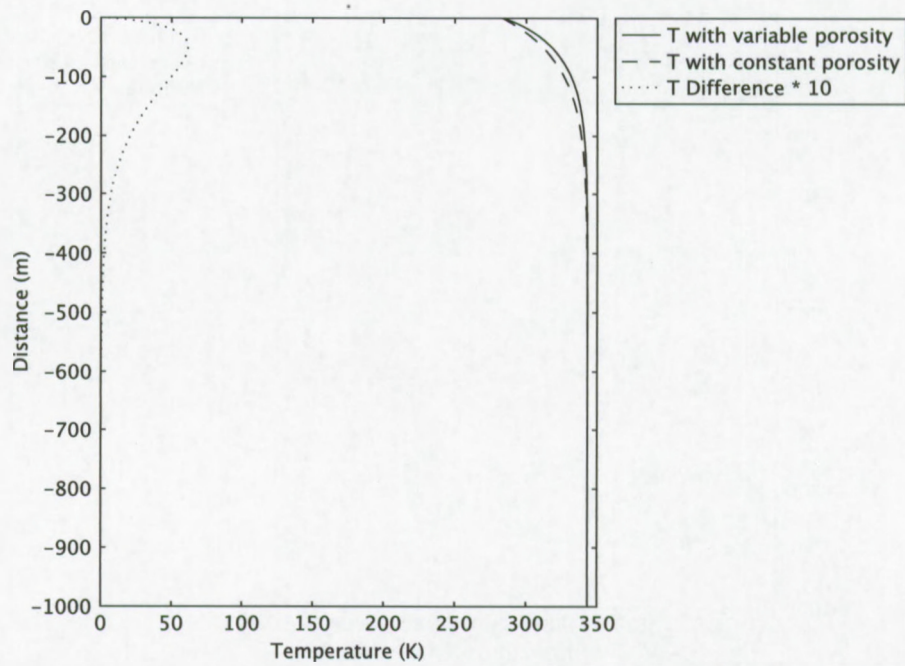
(a)
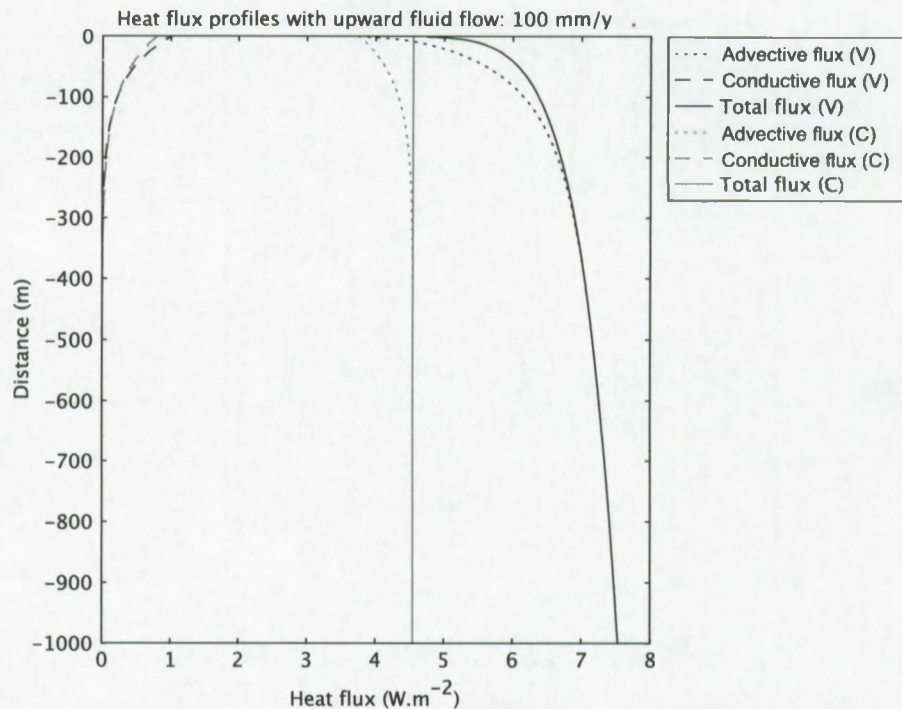
(b)

Figure 6.10: *Temperature and heat flux profiles to compare the effect of the porosity difference at fluid flow velocity 100 mm/y. (C) indicates a constant porosity profile (0.75) and (V) indicates the variable porosity profile as given in eq. 6.4. Temperature differences are multiplied by 10.*

Transient effects   In the scope of this work, it is interesting to evaluate how fast a sediment will cool down after it has been heated over the full column. This situation is an equivalent for what would be observed after a very strong eruptive event would have taken place in a mud volcano crater. During such an event, warm sediment and fluids have been transported over the full sedimentary column towards the surface. Therefore, instantaneously after the eruption (t_0) the temperature over the whole column would be equal to the temperature of the source layer. This source layer temperature is assumed equal to the temperature defined by the surface temperature and the pre-existing (before the eruptive event) geothermal gradient alone. Furthermore, it is assumed that there is an upward residual fluid flow through the mobilized sediment column after the eruptive event has happened. The goal is to evaluate how effective fluid flow is in retarding the cooling down of a sediment column[3]. The model has been run for upward residual fluid velocities ranging from 0 to 10000 mm per year; the source depth of the mobilized sediments was 1000 m. The results are shown graphically in figures 6.11, 6.12, 6.13 and 6.14.

In each graph, the initial state (0 years, or t_0) is represented by a vertical line at 345 K for all depths. After a given time, as heat will dissipate at the seafloor, the temperature will lower near the seafloor. As time progresses, the cooling will be observed at deeper position and finally coincide with the steady state situation, or, as if no eruptive event had taken place.

If no residual fluid flow is present (figure 6.11a) the steady state situation is reached after a time of more than 1000 but less than 10000 years. For small fluid flow velocities (figures 6.11b, 6.12a) there is no significant difference with the no-flow situation. For stronger fluid flows (10 mm per year or more, figures 6.12b, 6.13a,b) the steady state temperature profile is curved upwards. The seafloor is effectively kept at a constant temperature and because the maximum temperature is located at a shallower depth than when fluid flow velocity is low, the diffusive flux is stronger. Consequently the time needed for equilibration will be shorter: after less than 10000 years for an upward flow of 100 mm/y and in less than 1000 years for an upward flow of 1000 mm per year.

Of course, fluid flow does have an impact on the speed of equilibration. The greatest temperature decrease will occur in sediments where the fluid flow velocity is smallest. This is illustrated in the different plots in figure 6.14. After 1 year of equilibration, not much cooling can be observed, except in the upper meters for the situation where fluid flow velocity is small ($v < 100$ mm/y). After 10 years, cooling has progressed down to a few tens of meters in the sediments, except for the highest fluid flow velocities modeled. In the subsequent model stages, the temperature profiles separate more distinctly. For the highest residual fluid flow, at no time, a significant cooling can be observed. For the lowest fluid velocities, it takes a very long time to be discriminated from a no-flow situation.

---

[3]An important simplification has been imposed since this is a 1-dimensional model: cooling only happens at the seafloor. In reality, heat will dissipate to the surroundings of the mud volcano feeder pipe. The longer the path of the pipe, the more significant this effect will be.
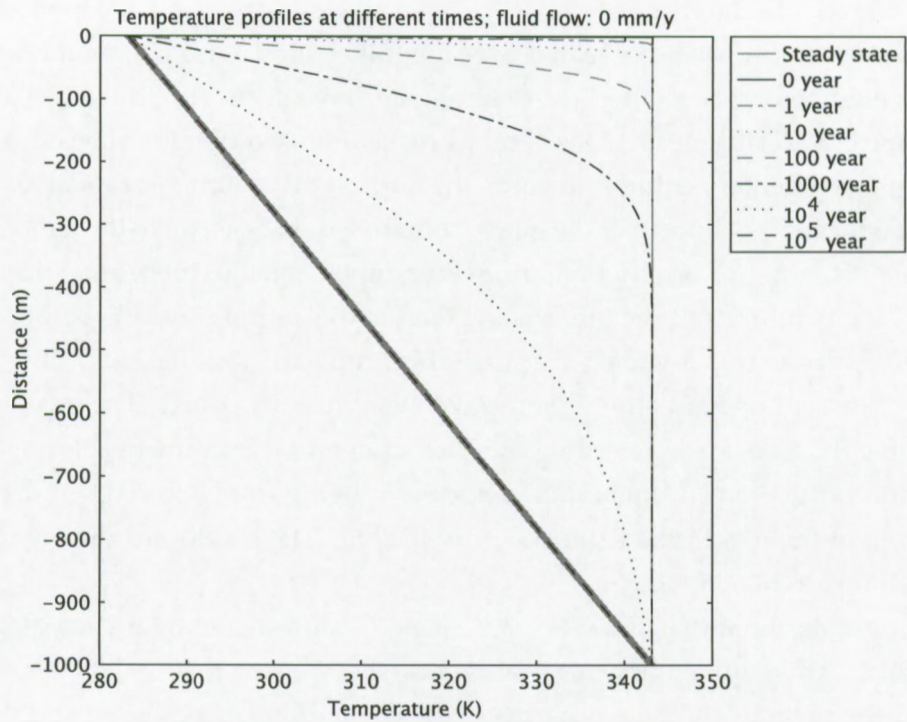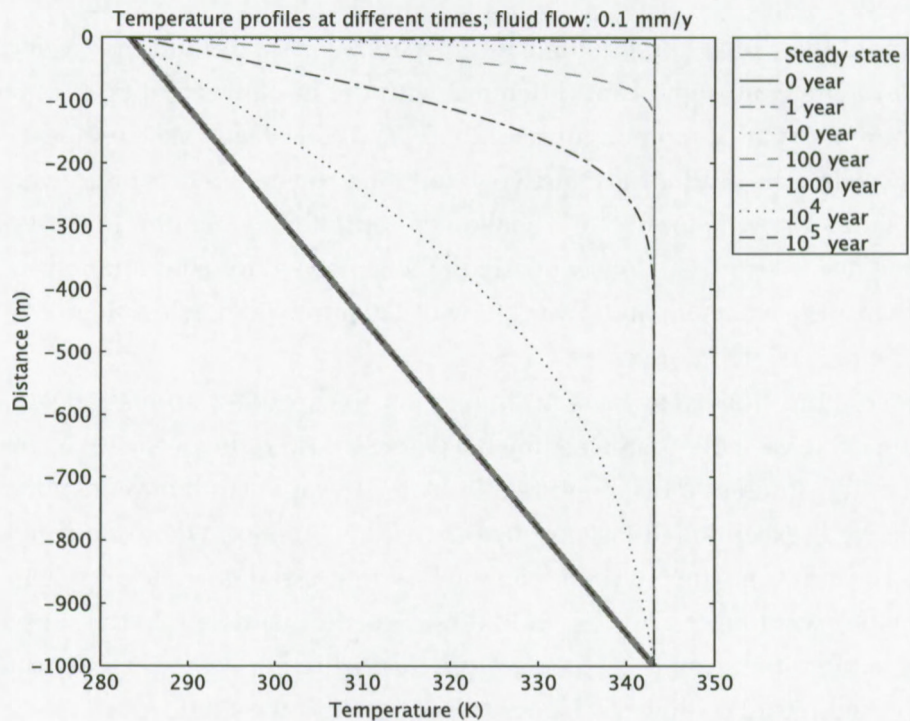
Figure 6.11: *Temperature evolution through time after a hypothetical fluid flow event (e.g. mud volcano activity) which resulted in an initial situation where the temperature is constant with depth. Temperature will become in equilibrium again after a given time. The rate at which this happens depends on the (residual) fluid flow velocity (0 mm/y; 0.1 mm/y). "Steady state" in the legend refers to the situation if no event would have occurred, thus representing the normal geothermal gradient.*
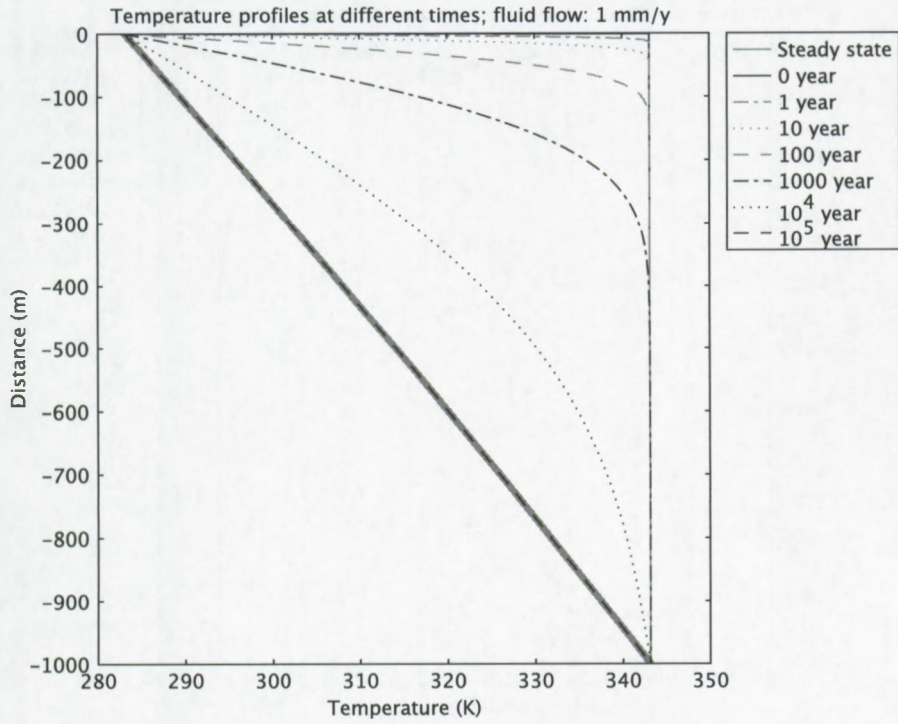
(a)
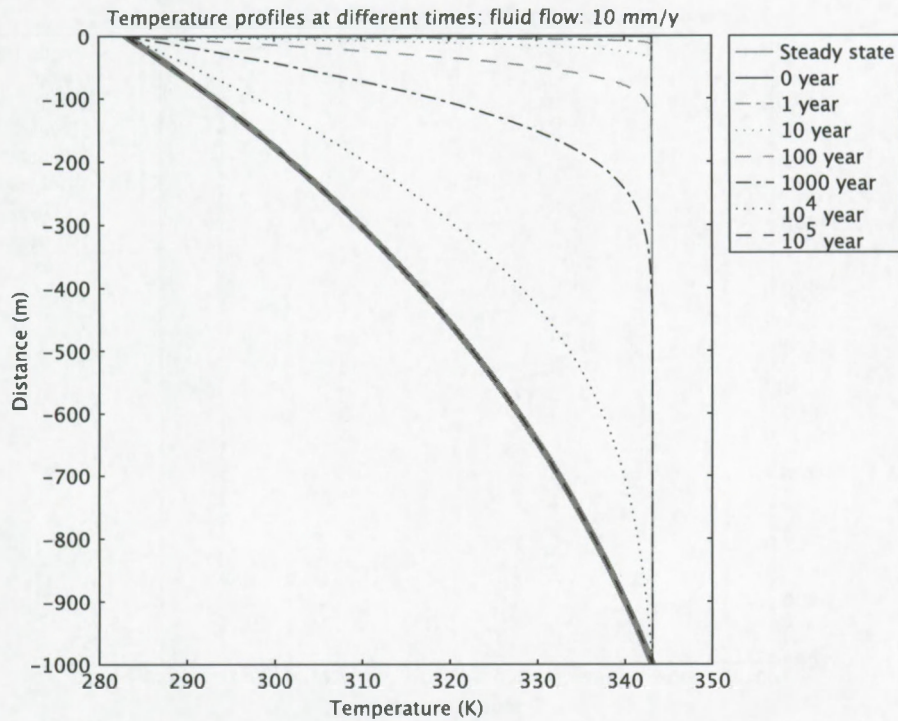
(b)

Figure 6.12: *Continued from figure 6.11; residual fluid flow velocity 1 mm/y; 10 mm/y.*
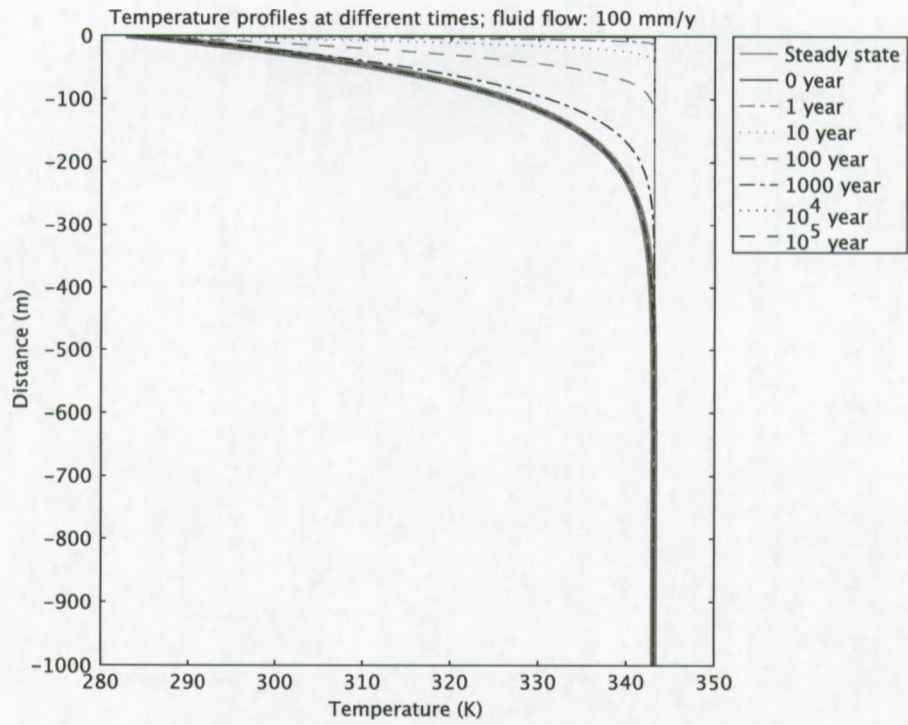
(a)
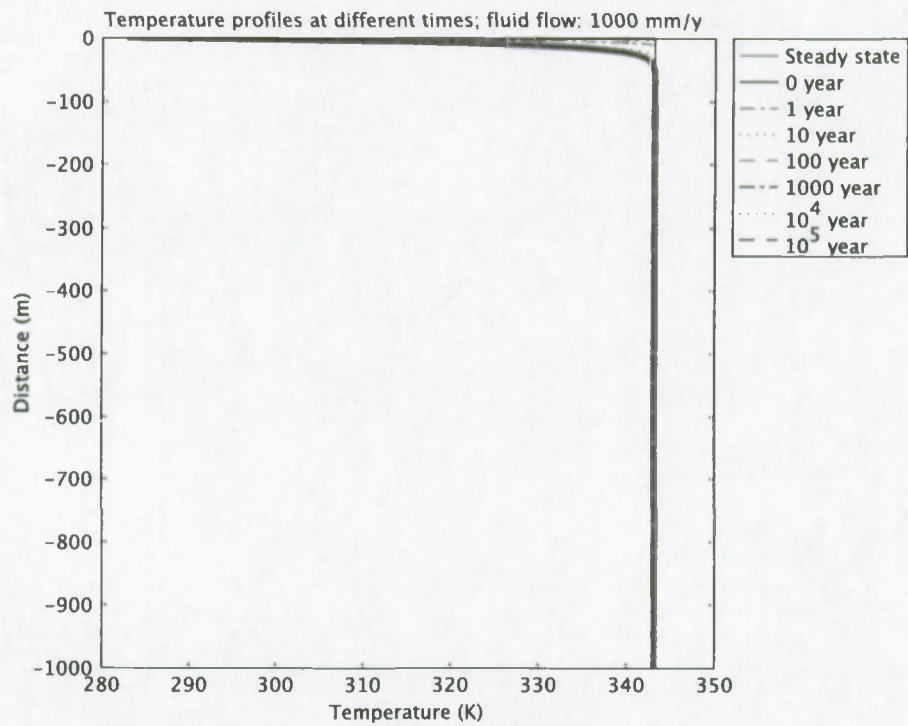
(b)

Figure 6.13: *Continued from figure 6.11; residual fluid flow velocity 100 mm/y; 1000 mm/y.*
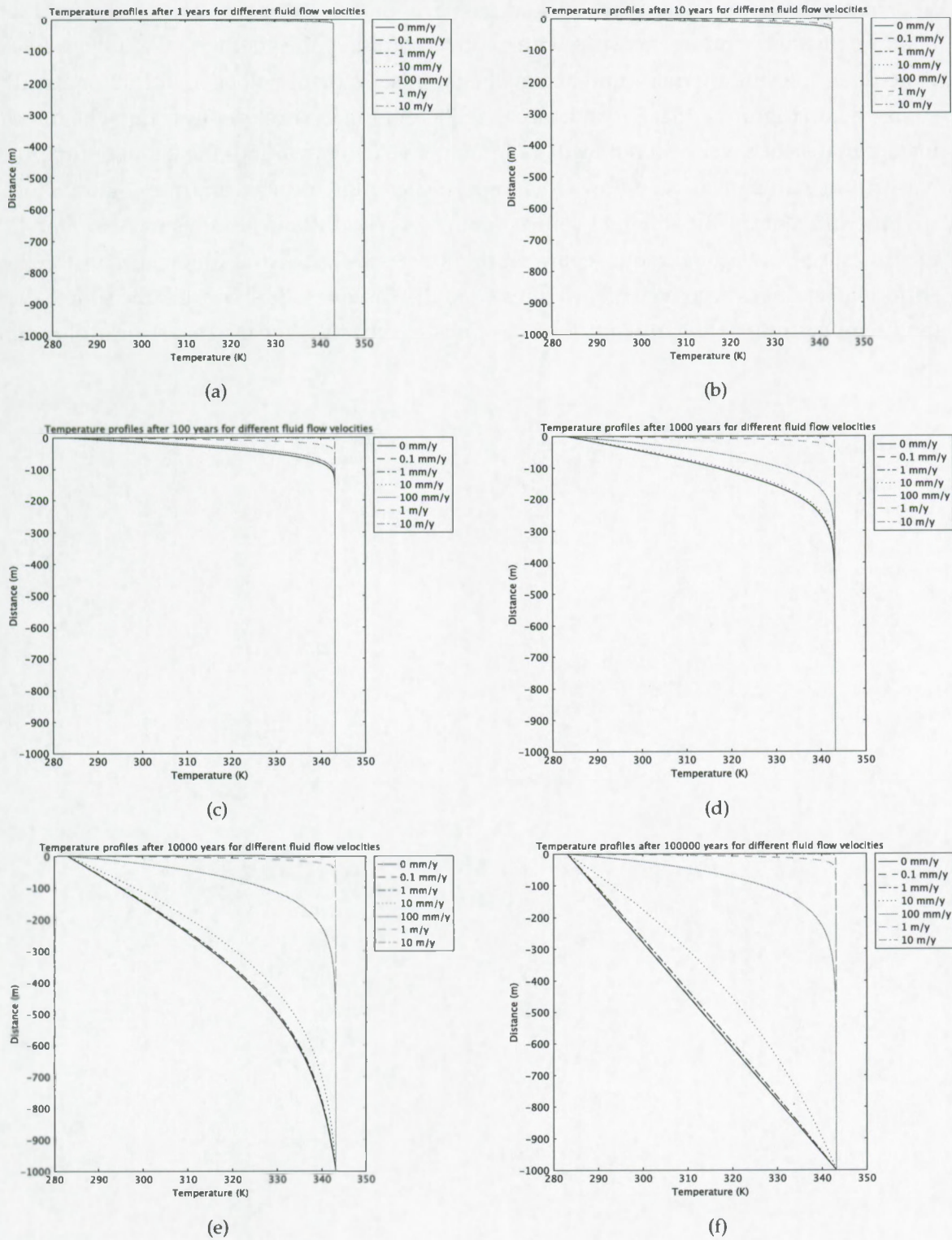
Figure 6.14: *The same hypothetical event as in figure 6.11 is assumed. Here, the temperature evolution is plotted in function of time for different fluid flow velocities. It appears that at any given time, the cooling of the sediments will be strongest when the upward fluid flow is weakest.*

Source depth effects   The depth of fluid mobilization has a direct impact on the fluid temperature; the temperature increases with depth accordingly the geothermal gradient. In case of no fluid flow and thermal equilibrium, the thermal gradient will be identical for any fluid source depth (figures 6.15a, 6.16a), hence the different fluid source depths cannot be discriminated. In case of a weak fluid flow (0.1 - 1 mm per year, figure 6.15b) the temperature profile has little deviation from a no-flow situation. The heat flow near the surface (figure 6.16b) is slightly different for the different source depths. As fluid flow velocities increase, the temperature profiles become more separated (figures 6.15c-f), and the differences in the (near surface) heat fluxes become larger (figures 6.16c-d). These results show that the source depth (and temperature) of the upward flowing fluids effectively alter the (near surface) thermal field.
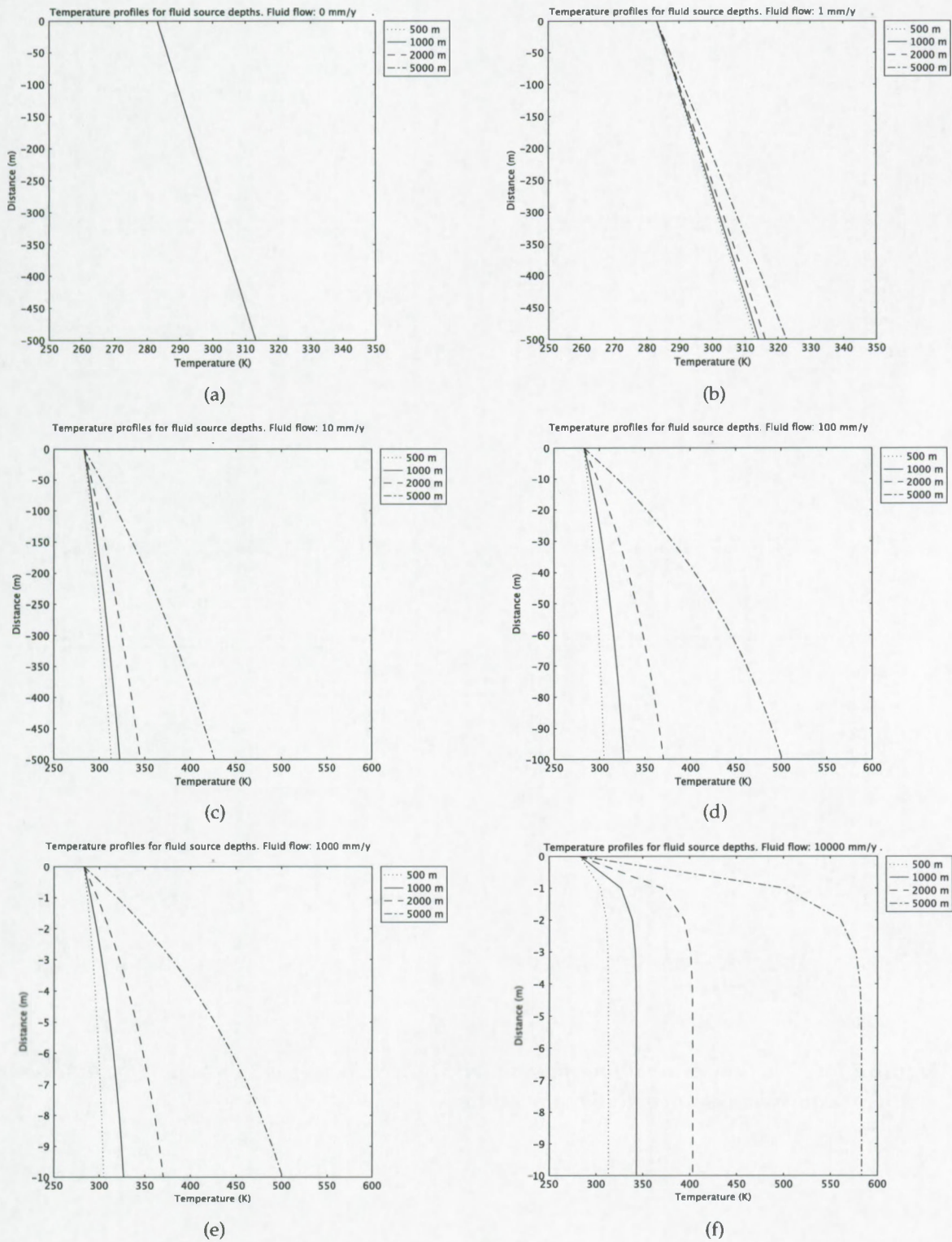
Figure 6.15: *Temperature profiles for different fluid flow velocities in function of the fluid source depth (or equivalent, source fluid temperature).*
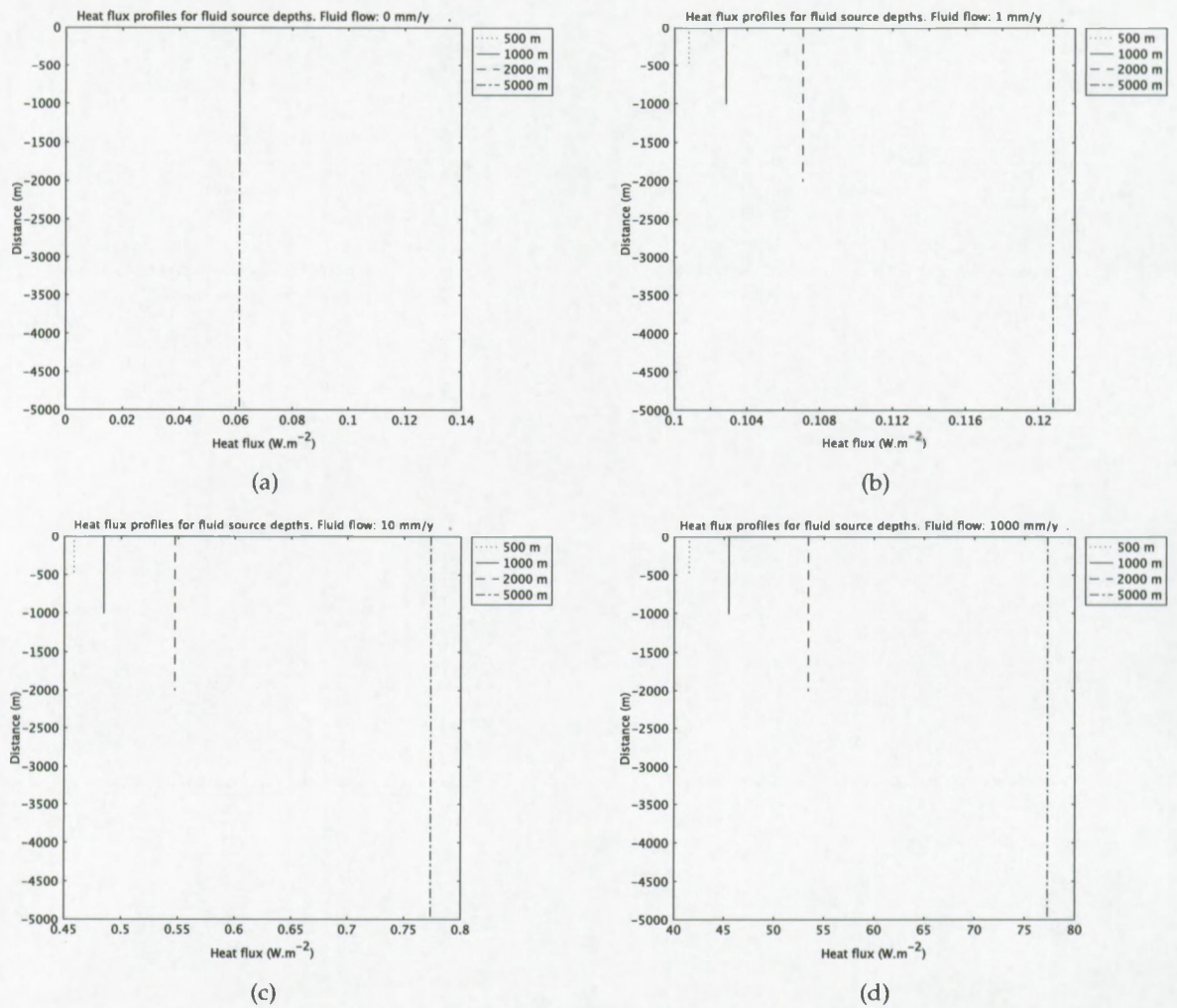
Figure 6.16: *Heat flow profiles for different fluid flow velocities in function of the fluid source depth (or equivalent, source fluid temperature).*

6.4.2 Geochemical effects

For this work, the most relevant geochemical effect of fluid flow is the formation of carbonates related to the anaerobic oxidation of methane (AOM), coupled to sulphate reduction (SR). At several sites in the study area, carbonates with (partial) AOM signatures were sampled at or close to the seafloor, while others where formed at greater depth. The formation of methane derived carbonates, and their relevance, was elaborated in chapter 5, and the numerical approach used in this section in chapter 3. In this section, the depth of AOM will be analyzed in function of upward fluid flow velocity.

The effect of the convective transport on the subsurface geochemistry is modeled through the second order transport reaction model (chapter 3) in one dimension (a vertical profile). As upper boundary condition, the sulfate concentration was set to 30 mol.m^{-3}. This is approximately the concentration of sulphate in the oceans. As a lower boundary, a constant upward flux of methane of 10^{-9} mol m^2 s^{-1} was imposed, in order to ensure that the column length does not play a role in the effective methane concentration at the base. Diffusion coefficients for sulfate and methane are based on Lerman (1979) and corrected for tortuosity (Bear, 1972; Berner, 1980; Boudreau, 1997) (see chapter 3). The porosity model used is derived from Spinelli et al. (2004), and equal to the one used above. The fluid flow velocity varies from 0 to 10 meters per year. The temperature is calculated based on a geothermal gradient of 0.06 K per meter (in case of no fluid flow). The diffusion coefficients are temperature dependent, and for methane it is defined as $D_0 = 3.3 \times 10^{-9}T^2 - 1.5 \times 10^{-6}T + 1.7 \times 10^{-4}$ (T in K), D_0 expressed in $[1 \times 10^{-5}$ cm^2.sec$^{-1}]$. For sulfate, this is $D_0 = 1.6 \times 10^{-9}T^2 - 7 \times 10^{-7}T + 7.5 \times 10^{-5}$. Both functions are based upon data in Lerman (1979). The Soret effect (thermophoresis[4]) is neglected because it is small in comparison to the other effects (Lerman, 1979, p. 98-100).

The model has been calculated with two different lower boundary conditions for methane: a) the methane concentration at -200 m is constant, with 50 mmol per liter, b) the methane flux is defined as 10^{-10} (mol/(m^2. sec)) + v (m/sec) * 10 (mmol.L^{-1})). The first term in this equation is entered because otherwise, at a velocity of 0 meter per second, the flux would be zero, and a trivial solution would be obtained. At zero velocity, the yielded concentration is about 30 mmol/L at 200 m depth. The latter term of the equation defines an inflow at the given velocity of a liquid containing 10 mmol/L methane. As the concentration at a depth is always lower than 50 mmol/L (case a), the reaction depth will be deeper in case b. At the same time, for each velocity, this allows to evaluate the effect of a changing methane concentration as well.

The resulting profiles are shown in figure 6.17. The model indicates, as expected, that the AOM reaction zone shallows with increasing upward fluid flow velocity. At zero velocity (Figure 6.17a), the AOM depth is about 50 m, resp. 70 m for the two cases of the model.

---

[4]The Soret effect is a process that drives heavy molecules preferentially move towards a lower temperature, and light molecules move towards a higher temperature.

At a very light upward fluid flow (less than 1 mm per year), the depth shallows already significantly, to depths of 30 m, resp. 40 m (Figure 6.17b). At a fluid flow velocity of 1 mm per year, the depths are about 5 m, resp. 10 m (Figure 6.17c). At velocities above 100 mm/y, the AOM reaction zone is very close, if not at the seafloor ($z=0$) which means that the methane does not get consumed before it reaches the seafloor.

Under circumstances of upward fluid flow with significant amounts of methane, the AOM zone is quickly pushed towards the seafloor. As the formation of authigenic carbonates can be linked to AOM coupled to SR (see Chapter 5), the formation depth is strongly controlled by the strength of the upward fluid flow in sediments. Precipitation of chimneys and crusts from the different mud volcano craters from which results were reported, can indeed only occur near the seafloor if there is an active upward fluid flow. If not, AOM would take place at a much deeper place in the sediments and not easily accessed for sampling.

At an other site (MOA, Mediterranean Outflow Area), there were indications that the carbonate precipitates had formed deeper in the sediments but exhumed by erosion. Therefore, it may be suggested that the carbonate crusts and chimneys were formed in an area with weaker fluid flow than the other sampled areas. In this case, the chimney morphology might be related to sedimentary heterogeneities leading to preferential fluid flow pathways, rather than to a strong and focused fluid flow. The carbonate specimens from Pen Duick Escarpment would be an intermediate, with moderate fluid flow strengths yielding precipitation not at the seafloor, nor very deep, but at a shallow subsurface position.
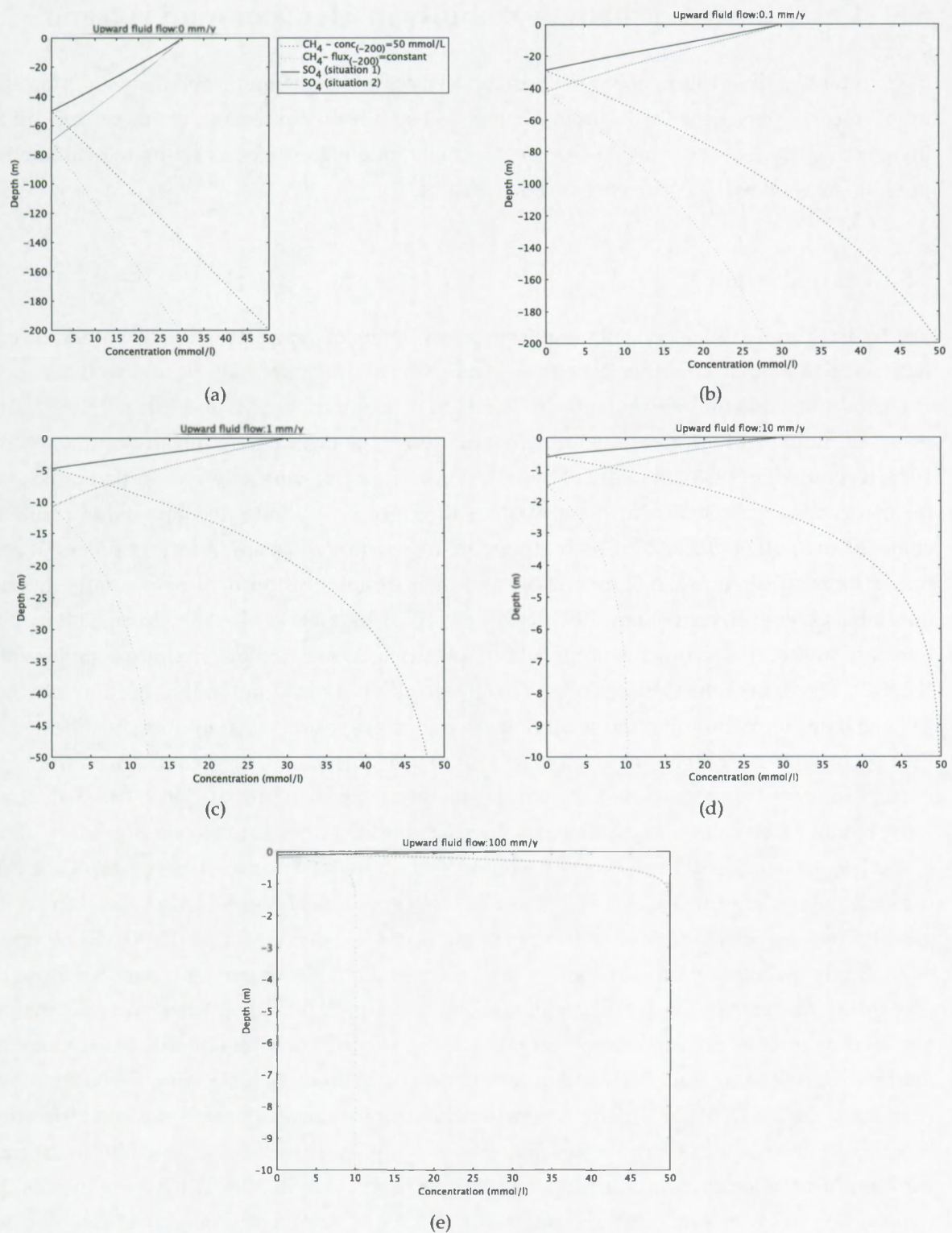
Figure 6.17: *Concentration profiles of CH_4 and SO_4^{2-} under increasing upward fluid flow conditions, with different lower boundary conditions. For each fluid flow velocity case, two CH_4 boundary conditions are imposed: one where the concentration of methane at -200 m is constant at 50 $mmol.L^{-1}$ and one where the concentration is a function of the fluid flow velocity, yielding a methane flux of 10^{-9} $mol.m^2.s^{-1}$. (a) No-flow situation.*

6.5   Case study: Gas hydrate stability in Mercator mud volcano

In Chapter 4, a description of anomalous subsurface reflections under the flanks of Mercator mud volcano were described. In an attempt to explain this reflection, characterized by an inverse polarity (see section 4.2.1.6), a geothermal modeling exercise is set up to evaluate the possible relation to the occurrence of gas hydrates.

6.5.1   Introduction

Gas hydrate is an ice-like crystalline substance, consisting of a cage structure of water molecules with trapped methane or other light gases inside. Gas hydrates are stable under well-described P-T conditions (Sloan, 1998a,b) and adequate gas concentrations (Xu and Ruppel, 1999). The distribution of gas hydrates on continental margins is widespread (Ginsburg and Soloviev, 1998; Kvenvolden, 1998). Stability of hydrates on margins is a very actively studied topic with regard to triggering sediment mass wasting through gas hydrate decomposition (Bouriak et al., 2000; Paull et al., 2003). Gas hydrates are also regarded as an important potential economic target (Collett, 2002; Gupta, 2004) and their destabilization may have a large impact on global change (Kvenvolden, 1993; Jacobsen, 2001; Kennett et al., 2000; Kopf, 2003). Gas hydrates in seafloor sediments occur within a restricted zone, the gas hydrate stability zone (GHSZ). The base of the GHSZ is often recognized as a bottom simulating reflection (BSR) on seismic data, since it mimics the seafloor in areas of a stable and constant local heat flow. The BSR is characterized by an inverse polarity of the seismic signal, originating from the presence of free gas trapped below the hydrate stability zone (Bangs et al., 1993; MacKay et al., 1994; Holbrook et al., 1996, e.g.). Since the thermal gradient defines the lower boundary of the GHSZ, an elevated local heat flow will thin the GHSZ. In that case, the base of the GHSZ, expressed as a crosscutting reflection, can locally intercept the seafloor reflection, for example, in gas hydrates associated to mud volcanoes or gas seeps (De Batist et al., 2002; Van Rensbergen et al., 2002). Submarine mud volcanoes (MVs) are seafloor structures with positive topography from which mud, fluid, and gas emanate (Hedberg, 1974). Their distribution is mainly confined to areas with compressive tectonic activity, vertical compression due to sedimentary loading (burial) and generation and accumulation of hydrocarbons leading to overpressure (Dimitrov, 2002b; Kopf, 2003). The general mechanism for their formation is related to a combination of the rise of overpressured liquefied clays toward the surface and the hydrofracturation of the overburden which opens a feeder pipe. The mobilized material pierces the overburden to expel a mixture of mud, fluids and gases along with brecciated rock derived from the overburden, the mud breccia. Gas hydrates inside mud volcanoes have been observed in several locations (Dimitrov, 2002b), but are generally found at water depths of 1000 m and deeper, e.g., on the Norwegian-Barents-Svalbard margin (Ginsburg et al., 1999), the Gulf of Cadiz and on the Moroccan margin (Gardner, 2001; Mazurenko et al., 2002), the east-

ern Mediterranean ridge (Robertson and the Ocean Drilling Program Leg 160 Scientific Party, 1996), the Black Sea (Soloviev and Ginsburg, 1994; Dimitrov, 2002a; Bohrmann et al., 2003), the Caspian Sea (Huseynov and Guliyev, 2004) and on the Barbados accretionary wedge (Aloisi et al., 2002).

6.5.2 Gas Hydrates in the Gulf of Cadiz

Gas hydrates on the Moroccan margin and in the Gulf of Cadiz have only been reported from a small number of deep-water mud volcanoes: Ginsburg mud volcano (1100 m bsl) (Gardner, 2001; Mazurenko et al., 2002, 2003), Bonjardim mud volcano (2200 m bsl) (Kenyon et al., 2003; Pinheiro et al., 2003) and Capt. Arutyunov mud volcano (1800 m bsl) (Kenyon et al., 2003). Casas et al. (2003) observed possible BSR features at a subbottom depth of 150 ms two-way travel time (TWTT), associated with mud volcanoes and diapirs at a water depth of 388 m on the Gulf of Cadiz slope. They attributed the hydrate stability to elevated pore pressure conditions caused by the diapiric intrusions. Reports of a widespread regional BSR are not yet made.

6.5.3 Results

6.5.3.1 Event Observation

The hypothesis is given that the H event observation (see section 4.2.1.6) is the base of a gas hydrate stability zone. The hypothesis is tested by modeling the gas hydrate occurrence and deriving the H-event inferred heat flow in the mud volcano.

6.5.3.2 Modeling Gas Hydrate Occurrence

Modeling the hydrate stability zone requires information on the composition of the hydrate gas, on the bottom water temperature and geothermal gradient as well as the pore space salinity. Gas hydrates recovered from the nearby Ginsburg mud volcano, which is located at a water depth of 1100 m, had a composition of 81% of CH_4 and 19% of C_{2+} hydrocarbons (Mazurenko et al., 2002). From CTD data it is known that the seafloor temperature in the area is 10°C which is unfavorable for gas hydrate stability. Pore water salinity estimates are derived from mud volcanoes from the Moroccan margin. Bileva and Blinova (2003) reported an average chlorinity of 500 mmol/L. According to equation 6.5, this can be converted to 3.2% salinity, which is comparable to ocean water salinity.

$$S = 1.80655 * [Cl^-] \tag{6.5}$$
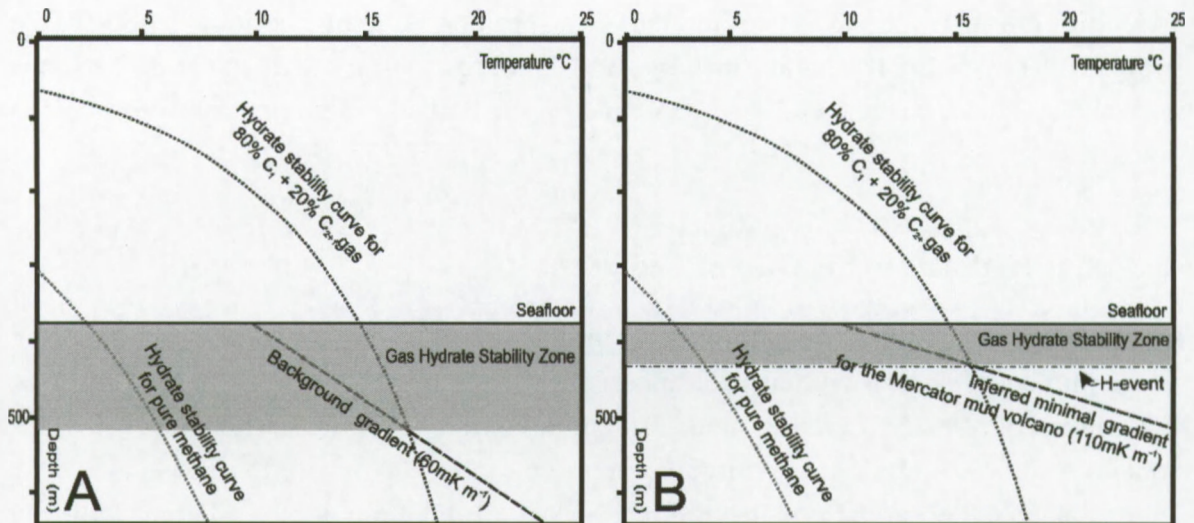
Figure 6.18: *Theoretical gas hydrate stability graphs for gas composition measured at Ginsburg mud volcano (Mazurenko et al., 2002) and pure methane for comparison. Pure methane hydrates are unstable in either case. (a) Situation with a background gradient curve of 60 mK.m^{-1} m and a bottom water temperature of 10°C. Gas hydrates are stable to 140 m below seafloor if gas contains higher-order hydrocarbons. (b) Situation for lowest inferred thermal gradient (110 mK.m^{-1}) in Mercator mud volcano, where hydrates with higher-order hydrocarbons are stable up to 60 m bsf.*

Equation 6.5 expresses a conversion from salinity to chlorinity, with S the salinity and [Cl$^-$] the chlorinity, both in parts per million (ppm) (Wooster et al., 1969).

The gas hydrate equilibrium conditions were determined using the program CSMHYD (Sloan, 1998b) for the given composition of the gas hydrates and salinity of the pore waters. This resulted in the polynomial regression equation

$$logP = a + bT + cT^2 \tag{6.6}$$

with parameters $a = 0.1929$, $b = 0.0395$ and $c = 0.0009$, P in MPa and T in degrees Celsius, and the regression coefficient $R^2 = 0.998$. In Figure 6.18a, the resulting hydrate stability curve is plotted with a seafloor depth of 380 m. The hydrate stability curve for pure methane is plotted for comparison. This result shows that at this water depth and for the given gas composition and seafloor temperature, gas hydrates can be stable. For a thermal gradient of 60mK.m^{-1}, which is a normal background value for the North Atlantic Ocean (Sclater et al., 1980), the depth of the base of the GHSZ is almost 100 m deeper than the present observed H event (Figure 6.18a, with H event in Figure 6.18b). Since thermogenic gas hydrates can theoretically occur at this location, this supports our hypothesis that the H event is the base of a GHSZ. This horizon was mapped and infer the thermal gradient and heat flow from it.

6.5.3.3 Inferred Heat Flow

Bottom simulating reflections have often been used to estimate thermal gradients or heat flow (Yamano et al., 1982). The calculation assumes that the BSR coincides with the three-phase gas hydrate-water-gas vapour boundary, and consists of the following steps (Vanneste et al., 2002): (1) conversion from TWTT to subbottom depth based on a velocity model, (2) calculation of in situ hydrostatic and lithostatic pressure, (3) derivation of the equivalent three-phase gas hydrate equilibrium temperature for these pressure values at the inferred BSR depth, and (4) determination of the geothermal gradient and heat flow.

A relation between pressure, depth, and time is needed for the conversion from two-way travel times to depth and pressure values, which are needed for thermal gradient and heat flow calculations. Data from Ocean Drilling Program Leg 160 (eastern Mediterranean) Site 970 (Milano Dome) and 971 (Napoli Dome), Robertson and the Ocean Drilling Program Leg 160 Scientific Party (1996) shows that pebbly mud (holes 970A, 970B, 970D and 971A, 971B, 971D, 971E) has p-wave velocities from 1500 to 2000 m.s^{-1}. When averaging over depth for these holes, values around 1800 m.s^{-1} are retrieved. For nanofossil ooze with sapropels (hole 970B), the velocity average is about 1600 m.s^{-1}. All values refer to the first tens of meters; therefore an average velocity for the deposits of the top of the Mercator mud volcano of 1800 m.s^{-1} is assumed. Then, on the basis of a p wave velocity 1.5 km.s^{-1} in water and 1.8 km.s^{-1} in the sediment and with a density of water $\rho_w = 1030$ kg.m^{-3} and sediment $\rho_c = 2300$ kg.m^{-3} (based on a $\rho_s = 2650$ kg.m^{-3} for the sediment and $\rho_h = 900$ kg.m^{-3} for the hydrates (Gei and Carcione, 2003), in a 80% sediment to 20% hydrate mixture), the two-way travel time of the seismic sections was converted to depth (Figure 6.19a) and pressure (Figure 6.19b). The calculated pressure field at the H event reflector displays a nearly concentric pattern around the crater of the mud volcano and pressure increases from the crater (3500 kPa) to the deepest point (6000 kPa).

On the basis of the thickness of the layer between the seafloor and the H event, the thermal gradient field and the heat flow pattern in the mud volcano is reconstructed. Inside the crater, no H event is observed, so the thickness is set to 0. The calculation of the thermal gradient field, based on the distribution of a BSR, is derived from equation 6.6 as

$$G_t = \frac{T - T_{sf}}{d_{bsr}} \tag{6.7}$$

with

$$T = \frac{-b + \sqrt{b^2 + 4c(logP - a)}}{2c} \tag{6.8}$$

where G_t is the temperature gradient, T is the temperature ($^\circ C$) defined by equation 6.8, T_{sf} is the temperature at the seafloor ($^\circ C$), d_{bsr} is the depth of the BSR in meters below seafloor,
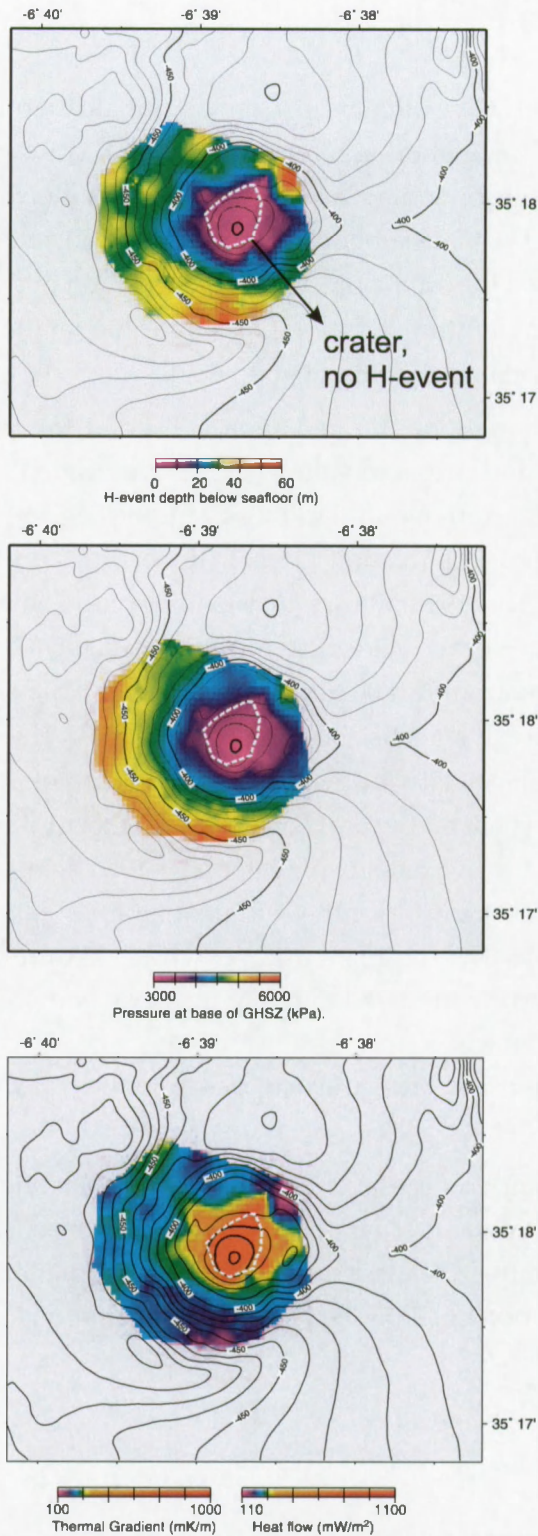
Figure 6.19: (a) Depth of the H event in meters in the Mercator mud volcano. (b) Calculated pressure at the depth of the H event. (c) Calculated thermal gradient and heat flow inferred from the occurrence of the H event. The thermal gradient and heat flow display a quasi-radial pattern around the mud volcano crater, increasing toward it. In the crater area, no H event was observed.

and P is the in situ pressure at the BSR in MPa. For the conversion from the thermal gradient field to the heat flow Φ_Q according equation 6.9, a thermal conductivity k_t of 1.1 W.m^{-2}, with

$$\Phi_Q = k_t G_t \tag{6.9}$$

and Φ_Q in mW.m^{-2} and G_t in mK.m^{-1} is supposed. This value for k_t is used since it is a typical value for this kind of sediments: Grevemeyer et al. (2004) report k_t =1.17W.K^{-1}.m^{-1} for sediments at the Mound Culebra mud dome offshore Nicoya Peninsula, Costa Rica). The thermal gradient and heat flow values calculated on the mud volcano are cut off at 1 K.m^{-1} or 1.1 W.m^{-2} near the edge of the crater because at that location, values move asymptotically to infinite since d_{bsr} approaches zero in equation 6.7.

The inferred heat flow and thermal gradient fields show a more or less concentric pattern around the crater of the Mercator mud volcano (Figure 6.19c). The local minimal value of the heat flow in the Mercator mud volcano is 110 mW.m^{-2} and increases to about 250 mW.m^{-2} craterward. Near the edge of the crater, the heat flow quickly rises to 600 mW.m^{-2} and then increases quickly to 1100 mW.m^{-2} at the crater edge. Within the crater, the heat flow cannot be extrapolated because of the asymptotic rise of the calculated values toward infinity. All that can be inferred here is that heat flow inside the crater is higher than 1100 mW.m^{-2}

6.5.3.4   Accuracy Estimate

Each of the steps to calculate the heat flow from a BSR occurrence is a source of errors. The error on the pressure field at the depth of the H event depends on changes in p wave velocity and density of the mud breccia. If we vary the p wave velocity between 1500 and 2000 m.s^{-1} and the density between 1800 and 2300 kg.m^{-3}, relative errors for the pressure vary between about -6.5 and 2%. It is unlikely that density will be higher than the value we used for the calculations, since porosity, which we assumed to be zero and all pores filled by hydrate, will have a bulk density decreasing effect. However, because of the logarithmic function in the temperature calculation, this error is strongly reduced. The most important factor for the thermal gradient is the p wave velocity since it appears in the denominator of equation 6.7. All together, the varying p wave velocity and bulk density induces an overall error on the thermal gradient of +16.3% for a p wave velocity of 1500 m.s^{-1} and -8.2% for a p wave of 2000 m.s^{-1}. The influence of a variable density is less, and the error values above are the overall extremes. An error for k_t will further affect the heat flow values. If k_t is 0.9 W.m^{-1}.K^{-1}, a value typical for normal hemipelagic sediments, this induces an error of about 18%. Long-term bottom water changes will affect the heat flow pattern according to equation 6.7. More importantly, they can influence the hydrate stability field with bottom water warming causing gas hydrate dissociation. Nevertheless, we rely on the CTD data and assume that temporal fluctuations are small. The overall error on the H event inferred thermal gradient is assumed to be no larger than 15% and the error on the heat flow no larger than 25%. Another source

of uncertainty is the gas hydrate composition since the values we used were not obtained from in situ sampling. However, we assume that source fluids and gases are comparable throughout the region and fluctuations are low.

6.5.4   Interpretation and Discussion

The H event is recognized as a coherent reflector with negative polarity under the seafloor below the Mercator mud volcano's slope. The H event shallows toward the mud volcano's center and disappears in the crater. We interpret the H event as the base of a gas hydrate stability zone, which is affected in the center of the mud volcano by focused fluid flow. We modeled the gas hydrate stability zone in this very shallow area by using a gas hydrate composition reported for the region. The seismic interpretation is supported by the model. Alternative interpretations of this seismic event are possible but can be rejected based on several issues. First, the H event may have been covered by a layer of rocks and clasts, extruded by the mud volcano. This is deemed unlikely since so far, no observations indicate that a complete mud volcano surface would be covered with extruded clasts or rocks. This suggestion can be rejected since it cannot explain the morphology of the seismic event (i.e., the shallowing toward the crater) since different mud extrusion types as described by Van Rensbergen et al. (2005a) cannot produce such a morphology. Second, the event might represent a transition to sedimentary deposits created during a period of inactivity of the mud volcano. This is unlikely as a sedimentary layer would drape the whole mud volcano, therefore also the crater area. Third, a diagenetic boundary may produce a seismic event in a mud volcano. Again, the morphology of such a boundary is hard to explain. For all of these propositions, the inverse polarity of the seismic signal is also not explained. Thus we conclude that the interpretation of the H event as the base of a gas hydrate stability zone is the most reliable.

6.5.4.1   Focused Fluid Flow in Mud Volcanoes

The Mercator mud volcano exactly shows what Ginsburg and Soloviev (1998) proposed in a model concerning hydrate stability in mud volcanoes. Therefore, although the Mercator MV is not visibly active in a sense that it extrudes mudflows, it is inferred to be active as a fluid vent. The concentric pattern of the heat flow distribution is a consequence of lateral heat diffusion away from the feeder pipe (Poort and Klerkx, 2004). Diffusion of gas away from the feeder pipe is the source of hydrocarbon gas hydrates. Hydrates generally occur at continental margins where conversion of high inputs of organic carbon or focusing of methane bearing fluids supply the hydrocarbon gases required for hydrate formation (Davie et al., 2004). The absence of any regional BSR or H event in the surrounding hemipelagic sediments could be explained by an insufficient methane flux which would be needed for gas hydrate formation. A methane flux lower than the theoretical methane solubility would also imply the absence of free gas. The lack of an acoustic impedance inversion at the interface between

gas-free and gas-bearing sediments, may explain the absence of a widespread regional BSR. This would mean that the degassing and dewatering of the accretionary wedge in the Gulf of Cadiz mainly happens through focused flow along faults associated fluid expulsion seafloor structures, and only partly by widespread diffusive processes. The inferred heat flow in the mud volcano, and especially in and near the crater, is very high. However, literature reports indicate that the calculated result is not abnormal for mud volcanoes. Heat flow in active mud volcanoes is known to easily rise above 1 $W.m^{-2}$. The best know case-study is the Hakon Mosby MV on the Norwegian Margin. The crater of the mud volcano has also thermal gradient values of over 1000 $mK.m^{-1}$ (Eldholm et al., 1999) and even values of over 10000 $mK.m^{-1}$ have been estimated by Vogt et al. (1999) in the mud volcano crater. In Lake Baikal, both in situ measured and BSR-derived heat flow evidenced elevated heat flow values compared to background at the Malenki mud crater (Vanneste et al., 2002). Henry et al. (1996) report a steady state surface heat flow of 5000$mW.m^{-2}$ on average in the center of the Atalante mud volcano in the Barbados Trough.

6.5.4.2   Very Shallow Gas Hydrate Occurrence and Significance

Theoretically, gas hydrate occurrence up to 250 m is possible when thermogenic gases are involved. In the Gulf of Mexico, gas hydrate occurrence has been reported up to about 440 m (Sassen et al., 1999). Here we now observe gas hydrates at a water depth up to nearly 350 m. Many shallow hydrate accumulations have been found at water depths below 500 m because the hydrates mainly consist of methane. The uppermost limit for methane hydrate occurrence is about 500 m (Sloan, 1998b). The result in this paper gives an indication that the volume of gas trapped as gas hydrate may be much larger than formerly thought, since many estimates of gas hydrates only account for methane hydrates. An estimate of the quantity of gas hydrate in the Mercator mud volcano was calculated based on the seismic data and a gas hydrate volume percentage of 5%. Volume percentage estimates for Ginsburg mud volcano were 4 – 19% (Mazurenko et al., 2003) and at the Hydrate Ridge, Trehu et al. (2004) conclude gas hydrates contents up to 26 vol % at the summit of the ridge and an average of about 3 – 6 vol % in the upper tens of meters of sediments in the GHSZ. We also used a gas hydrate density of 900 $kg.m^{-3}$ and the same velocity estimates as above. This model leads to a hydrate quantity between 2.5 Mt hydrate stored in this single mud volcano, or with the estimate that 1 m^3 contains 160 m^3 of methane, a quantity of 40×10^8 m^3 methane is obtained.

6.5.5   Case study conclusion

An anomalous reflection (H event) has been observed in shallow mud volcanoes on the Moroccan margin. The H event was mapped in the Mercator mud volcano and was interpreted as the base of a gas hydrate stability zone, based on its inverse polarity and the fact that it mimics the seafloor away from the mud volcano's crater. Inside the crater, the H event is

absent. This was supported by the fact that gas hydrate stability modeling with reported thermogenic gas compositions, indicated that gas hydrates can be stable at this shallow location. BSR inferred heat flow showed a concentric heat flow pattern around the crater, with a very sharp rise in heat flow near the crater, consistent with the interpretation that the gas hydrate layer is affected by a focused flow of warm fluid in the crater. Modeled heat flow values near the crater edge run-up to 1100 mW.m^{-2} and must be still higher inside the crater. Although this is very high compared to background heat flow values, it is not abnormal for mud volcanoes. The absence of a bottom simulating reflection in the surrounding sediments may be explained by a low regional methane flux through the sediments. Consequently, dewatering of the accretionary wedge complex is mainly focused along fault surfaces and through seafloor structures, such as mud volcanoes.

As a future work, the concentric heat flow pattern could be further developed in a fluid flow model. If the temperature in the crater area would be known exactly, one can model a fluid flow distribution taken into account heat advection and all related processes shown earlier in this chapter. As a simple exercise, one could calculate a theoretical fluid flow velocity if the temperature of the expelled fluid would be 15°C.

Take the inferred heat flow of 1100 mW.m^{-2} or 1.1 J.m^{-2}.s^{-1} and divide this by the energy content of water at 15°C, which is 4.1813 kJ.L^{-1}.K^{-1} × 283.15 K = 1.2 MJ.L^{-1} (supposing that 1 kg of water equals 1 L of water). This division results in a volume of water that is extruded at the rate of 28 L.m^{-2}.y or 2.8 cm.y^{-1}. This is in the middle of the range of fluid flow velocities indicated by Hensen et al. (2007) (0.3 to 6 cm.y^{-1}).

6.6   Effects of internal fluid flow drivers

In this chapter, the geothermal and geochemical effects of internal fluid flow drivers were modeled. All fluid flow was modeled as if it were driven upwards due to overpressure.

For the geothermal effects, a range of parameters were varied to see how they influence the geothermal profiles. The largest impact on the temperature profile was found to be the fluid flow velocity itself. The upward advection of heat along with the (warm) fluid significantly raises the temperature at shallower positions. Because the upper part of the sediments is still subject to cooling at the seafloor, very high thermal gradients will be measured near the surface, although that these gradients do not remain constant with depth. As a consequence, the effect of fluid flow should always be considered when interpreting geothermal gradient data measured at shallow position in the sediments, since this does not reflect the deeper gradient.

The porosity profile used in the model also lead to small differences in the model result, albeit less important for temperature profiles than for heat fluxes (this is due to the fact that with decreasing porosity, mass conservation demands higher fluid flow velocities, and thus

higher fluxes). So, the importance of the porosity model used, depends on the questions asked in the model itself.

The factor time is of great importance for heat flow modeling. Cooling of a mud volcano feeder pipe through the seafloor would take more than 1000 but less than 10000 years if no residual fluid flow is left. However, with a residual flow remaining, the cooling will extend less deep, although a stable situation will be reached earlier.

Finally, the source depth from which fluids are mobilized is also important in defining the geothermal field, especially for high fluid flow velocities because in this case, advective transport becomes much greater than conductive transport.

As a case study, the stability of gas hydrates in a shallow mud volcano crater was analyzed. Gas hydrate stability modeling with reported thermogenic gas compositions, indicated that gas hydrates can be stable at this shallow location. BSR inferred heat flow showed a concentric heat flow pattern around the crater, with a very sharp rise in heat flow near the crater, consistent with the interpretation that the gas hydrate layer is affected by a focused flow of warm fluid in the crater.

It was also shown that upward fluid flow with significant amounts of methane is capable of pushing the AOM zone quickly towards the seafloor. The depth of authigenic carbonate formation, as a product of AOM, will thus strongly depend on the strength of upward fluid (and methane) flow. Precipitation of chimneys and crusts from the different mud volcano craters from which results were reported, can indeed only occur near the seafloor if there is an active upward fluid flow. If not, AOM would take place at a much deeper place in the sediments and not easily accessed for sampling, except when erosion of the host sediment results in an exhumation of the previously formed carbonate crusts and chimneys.

In the next chapter, external processes driving fluid flow will be regarded, together with the effects on the geothermal and geochemical field.

Chapter 7

Effects of external drivers of fluid flow

External forces can drive fluid flow in sedimentary environments. In this chapter, sea level fluctuations and seafloor currents will be modeled to reveal their influence of subsurface fluid flow and their effect on the triggering of mud volcanism and the consequences for the geochemical environment in the sediments.

7.1   Introduction

External drivers of fluid flow are defined here as drivers depending on a process essentially acting outside the sedimentary environment, thus in the submarine environment. To drive fluid flow, the process needs to create a pressure gradient (force) in the subsurface.

A first type of driver is formed by tidal sea level changes (section 7.2) which act at (semi)diurnal time scales and have smaller magnitudes – the M_2 tidal constituent[1] has a maximum amplitude of about 1.5 meters along ocean margins (a M2 constituent map can be downloaded from the NASA Godard Space Flight Center website[2]). Effective tidal amplitudes are somewhat larger. Maximum tidal amplitudes recorded worldwide are over 15 meters, although not in oceanic environment (e.g., see the reviews about the tides of the Bay of Fundy by Desplanque and Mossman, 1998, 2001).

A second type of external drivers is related to the change in total pressure at the seafloor over time due to a change in sea level (section 7.3). Sea level fluctuations act at long time scales (e.g., glacial - interglacial) and reach magnitudes of several 10's of meters (Miller et al., 2005).

A third type of external drivers is based on pressure (and related velocity) effects of a water current over a seafloor obstacle (section 7.4). This effect has been explored at small scale (e.g. sand ripples; Thibodeaux and Boyle (1987); Huettel et al. (1998); Huettel and Rusch (2000); Huettel et al. (2003); Reimers et al. (2004); Roy et al. (2005)), an application of this effect to larger scales has not been found in literature. The process is related to a fluid passing over an obstacle with positive topography, yielding acceleration of the fluid at the top and deceleration of a fluid at the base of the obstacle. This acceleration implies a negative pressure anomaly at or near the top, and positive pressure anomalies at the base of the structure. This leads to a fluid flow inside the sediments: at the top, fluid will be driven out of the sediments, while at the base, fluid will be pushed into the sediments. Depending on the shape and scale of the obstacle, fluid recirculation cells can be formed in the sediments. The fluid flow direction is inverted when regarding an obstacle with a negative topography.

In the next sections, these drivers will be discussed, and their impact on subsurface fluid flow will be evaluated.

---

[1]The M_2 tidal constituent, or the principal lunar semi-diurnal constituent, is the part of the tide with a frequency of half a tidal lunar day, or 12 hours and 25 minutes. In most places, this constituent is responsible for most of the tidal amplitude.

[2]http://svs.gsfc.nasa.gov/stories/topex/tides.html

7.2 Tidal sea-level fluctuations

7.2.1 General

Tidal sea-level fluctuations create a pattern of cyclic pressure variations at the seafloor because the height of the water column changes over time. The pressure at the seafloor is given by $P(t) = \rho_w g h(t)$ [Pa] with ρ_w [kg.m^{-3}] the density of water, g [m.s^{-2}] the gravitational acceleration and $h(t)$ [m] the height of the water column as a function of time. In case of a semi-diurnal oscillation with amplitude Δh, this can be expanded to

$$P(t) = \rho_w g(h_0 + \Delta h \cdot \sin(\omega t)) \tag{7.1}$$

with h_0 [m] the average water column height and $\Delta h \cdot \sin(\omega t)$ the oscillation with a frequency of $\omega = 2\pi/T$ [Hz] with T [sec] the period of the oscillation, equal to 12 hours.

If (pore) fluids and sediments would be incompressible, then the pressure difference between high and low tide would be transferred instantaneously into the sediments down to 'infinite' depth, thus no depth-dependent pressure gradient would occur. Hence, in such a situation, no fluid flow would result.

However, (pore) fluids and sediments are effectively compressible. As a consequence, the pressure variation created at the seafloor is not instantaneously transferred into the sediments. Rather, the pressure travels as a wave into the sediment while it is attenuated; the travel depth will depend on the magnitude of the initial pressure difference, the sediment and fluid compressibilities and the period of the oscillation (although in this case, the period is treated as a constant). The resulting fluid flow will further depend on the hydraulic conductivity of the sediment. For highly compressible sediments, e.g. plastic clay, the pressure variations will not travel deep into the sediments, or in other words, the attenuation is strong. For more 'rigid' sediments, e.g. dense, sandy gravel, the pressure variation is less attenuated and thus the effect will be observed deeper in the sediments. The governing equation for describing this effect is given by equation 3.23 on page 42.

As the pressure fluctuations migrate into the sediments, alternating from positive to negative and back every 12 hours, a situation is created where the pressure difference varies with depth. Pore fluids will migrate towards zones with local pressure minima, away from local pressure maxima. The velocity of this fluid flow depends on the hydraulic conductivity of the sediment. Depending on the positions of these local extrema, the pore fluids can flow up- or downwards, or even in both directions at different depths at the same time.

In figure 7.1, these effects are illustrated. Figure 7.1a is a representation of the pressure difference in the sediments (relative to the stable hydrostatic pressure) in function of the compressibility of the host sediment. The model has been run with a semi-diurnal sea-level fluctuation with an amplitude of 2 m. The profiles represent the pressure difference situation after the model has run for 5 periods or 2.5 days in model time. It shows that the pressure difference

travels deeper when the compressibility is smaller. The magnitude of pressure effect remains the same however. Consequently, the pressure gradient is largest when the compressibility of the sediment is largest. The highest pressure gradient corresponds to the highest fluid flow velocities, as shown in figure 7.1b (the hydraulic conductivity corresponds to silty sediments, $K = 10^{-7}$ m.s^{-1}). Figure 7.1c illustrates the pressure difference every 3 hours during one tidal period for a sediment compressibility of 10^{-7} Pa^{-1}. Figure 7.1d illustrates the corresponding fluid flow velocity in silty sediments. This shows indeed that during a single tidal cycle, fluid flow can alternate between upward and downward flow, and that up- and downward flow can co-exist at a single time at different depths.

(a)

(b)

(c)

(d)
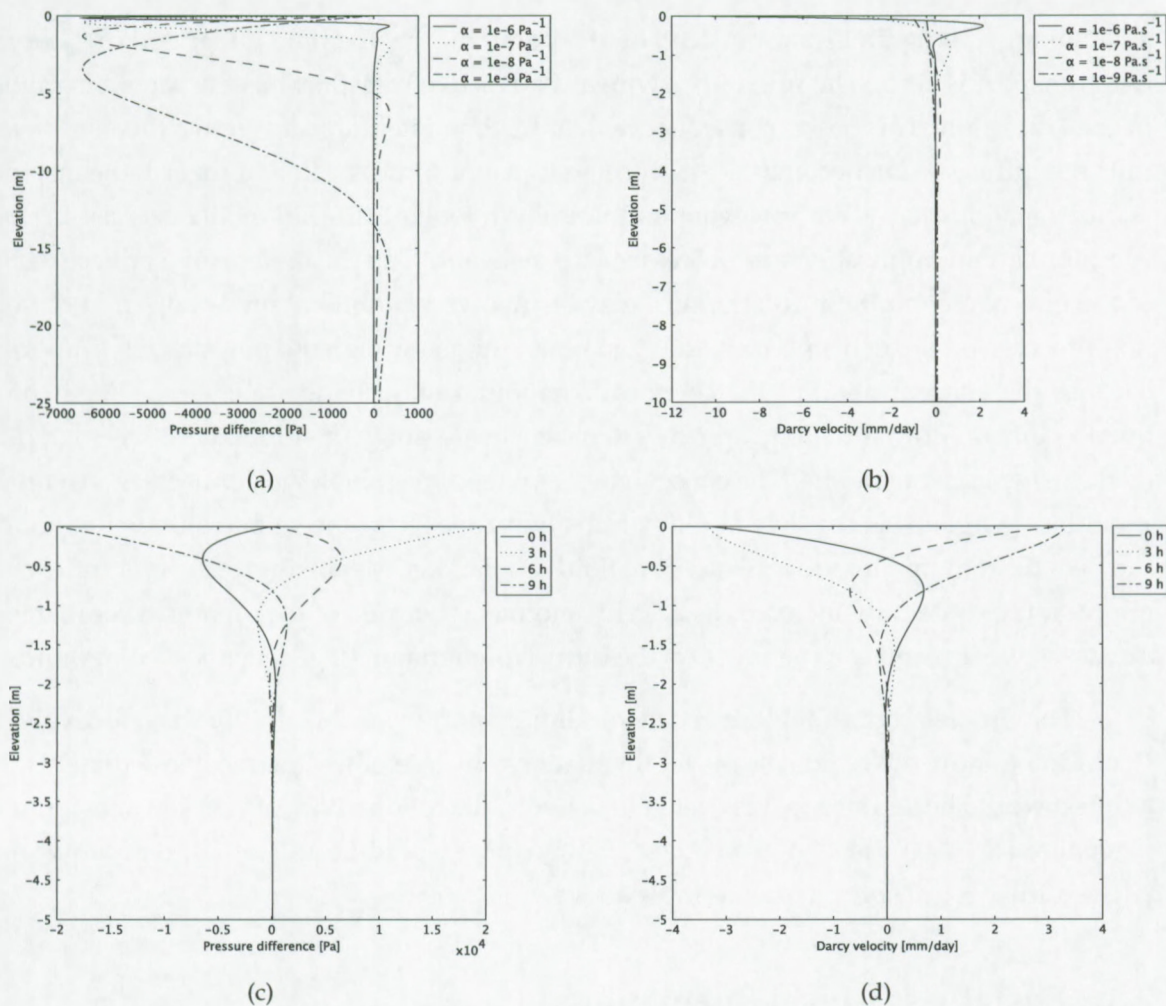
Figure 7.1: *Differential pressure variations in the subsurface and subsurface fluid flow velocity, driven by tidal sea-level fluctuations. See text.*

7.2.2   The significance of pore fluid pumping

The example shown above (Figure 7.1d) leads to maximum instantaneous up- and downward fluid flow velocities of over 3 mm per day in rather permeable sediments. In geochemical terms, this is a strong fluid flow, hence this process must affect the geochemical environment in the subsurface.

If we suppose a sulfate gradient in the upper meters of the sediment of 1 mmol. $m^{-1}.L^{-1}$ and a diffusivity of $3\times10^{-10}m^2.s^{-1}$, then the instantaneous diffusive flux is $3\times10^{-10}mol.s^{-1}.m^{-2}$. For a fluid flow velocity of 3 mm per day and an actual sulfate concentration of 10 mmol $.L^{-1}$ at a certain depth, the instantaneous advective flux is about $3.5 \times 10^{-7}mol.\ s^{-1}.m^{-2}$. Thus, the instantaneous advective flux is three orders of magnitude larger than the instantaneous diffusive flux.

Looking at long timespans, instead of at a point in time, the time-integrated (net) advective transport is zero. The up- and downward advective transport has the same magnitude in each direction. This has as consequence that the time-integrated advective flux is zero and thus the diffusive flux becomes the governing transport process. In that regard, the instantaneous transport may seem irrelevant and not worth looking after in model exercises. However, for certain applications or processes, it is relevant. The (instantaneous) advective flux of a chemical compound through pores may be involved in mineral precipitation or dissolution processes. For such a process, the flushing of fluids through the pores is very important because the concentration of the chemical compound may change over time. As a consequence, in a no-flow situation, a process may be slowed down or stopped if it has to depend on diffusive transport alone. The consequences for (geo)microbiological processes are equally important. Organisms that live at redox transition zones (e.g. the sulfate-sulfide boundary), can benefit from up- and downward pore fluid oscillations. Maybe this process is sufficiently important to drastically increase the activity and metabolic rate of the organism compared to a state where it is solely depending on the diffusive migration of geochemical compounds.

> The process controlling the geochemical transport in such conditions is effectively the pumping induced by tidal sea-level fluctuations. In case of less permeable sediments, the effect would be less strong, yet even with a hydraulic conductivity of 2 orders of magnitude smaller ($K = 10^{-9}m.s^{-1}$), the convective transport would be still equal to or larger than the diffusive transport in the example above.

7.3   Eustatic sea-level fluctuations

In the previous section, it was shown how tidal sea-level fluctuations can influence the subsurface pressure field. If we expand the time-scale from (semi-)diurnal to thousands of years, and the sea-level fluctuations from meters to tens of meters, different effects will appear at different timescales and spatial scales.

One of the most important factors in driving subsurface fluid flow induced by tidal oscillations was the pressure difference in function of time, or in other words, the rate at which the sea-level changes. A tidal sea-level change of 4 meters in the six hour transition from high to low tide equals a sea-level change rate of 1 meter per 1.5 hours. A global eustatic sea-level change of 50 meters in 10000 years has a rate of only 1 meter per 200 years or 1.7 million hours... a difference of over 5 orders of magnitude. The direct consequence of this is that the left term in the governing equation for subsurface fluid flow (equation 3.23 on page 42) is negligibly small compared to the right term. As a consequence, the pressure field will approach a steady state situation at any given time. Therefore, eustatic sea-level fluctuations will not drive fluid flow processes in the shallow subsurface in a similar way to tidal oscillations. However, large-scale fluid flow mechanisms may appear, based on different processes.

Overpressure generation in confined source layers In the (deep) subsurface, the hydraulic conductivity of sediments is variable. If a deposit with very low permeability (a seal) covers permeable sediments, a (relative) sea-level fall can create excess pore pressure below the seal. Suppose a succession of a permeable unit, a low permeability unit and a permeable unit. The height if the sea level is h [m]. The initial pressure state in the whole succession is hydrostatic as shown in Figure 7.2a. The pore pressure p [Pa] at depth z [m] below the sea surface will be $p(z) = p_h(z) = \rho_w g z$ (the subscript h indicates hydrostatic conditions), with g [m.s^{-1}] the gravitational acceleration and ρ_w [kg.m^{-3}] the density of the fluid. A new sea level h' is reached after a sea level drop $dh = h - h'$. Consequently, the pressure in the zone above the seal will decrease and become hydrostatic again, or $p'(z) = p'_h(z) = \rho_w g(z - dh)$. However, the zone under the seal cannot equilibrate as fast as the upper zone because the low permeability sediments slow down the fluid flow from the lower to the upper sediments. The total pore pressure in this zone is now $p'(z) = p'_h(z) + p_e(z) =$, with p_h the hydrostatic pressure as defined before and p_e the excess pressure, or overpressure (the subscript e indicates excess pressure).

As a consequence of the sea level drop, the total stress σ, defined by the total overburden has decreased. In the upper permeable zone, the effective stress $\sigma_e = \sigma - p$ does not change, but in the lower permeable zone, the effective stress will decrease. This pressure situation is cartooned in figure 7.2b. The decrease in effective stress will initially be equal to the hydrostatic pressure difference. In most cases however, this will be insufficient to induce hydrofracturing because the hydrostatic pressure difference is small compared to the initial effective stress. If, however, the initial pressure state already includes overpressure below the seal, e.g. due to the presence of gas or oil, the initial effective stress will be smaller. The hydrostatic pressure difference caused by a sea level fall will then be relatively more important, and further reduce effective stress to such a level that the yield strength of the sediments could be reached. Hydrofracturing, or reactivation of pre-existing fluid pathways may occur. The conditions for fracturing will be dealt with later in this chapter.
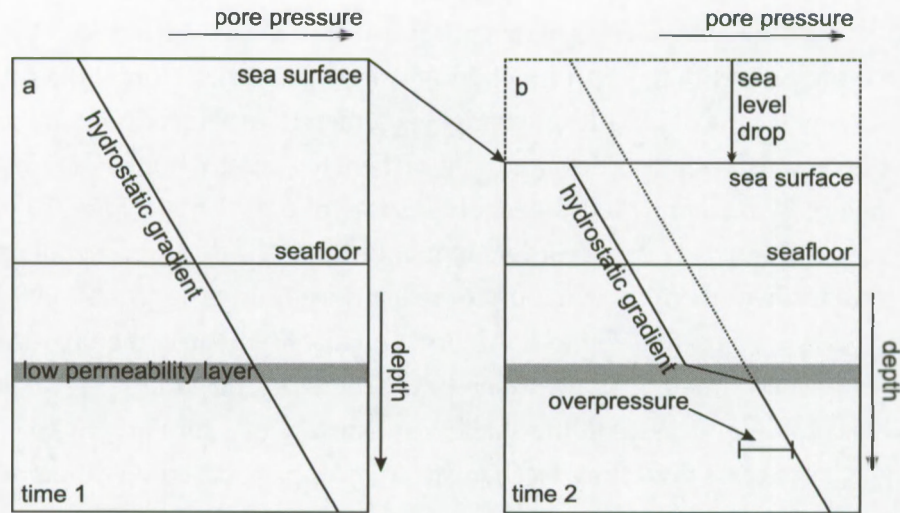
Figure 7.2: The effect on subsurface pore pressure below an layer with low permeability after a sea level drop. a) Initial situation, b) after sea level drop: the pressure below the seal cannot (instantaneously) reach equilibrium and is in a situation of overpressure.

Methane exsolution in mud volcano pipes A second mechanism influenced by a relative sea level fall is the exsolution of gas, e.g. methane, in sediments. Gas exsolution is well-known from eruptions of magmatic volcanoes, driven by the exsolution of dissolved water from the magma in the volcano pipe. Water vapour is formed when a certain confining pressure is released – leading to a considerable volume increase which leads to the violent eruptions characterizing Plinian eruptions. In the feeder pipe of a pre-existing mud volcano, we may expect the presence of large amounts of methane dissolved in the pore waters – at least in cases where thermogenic gas production is (one of) the main cause(s) of the overpressure production at great depth. Let us suppose that the pore waters in the mud column of the feeder pipe is saturated with dissolved methane, and that no gaseous methane is present yet. The solubility of a gas is a function of pressure and temperature, which can be expressed by Henry's Law, or

$$c_a = k_H p_g \tag{7.2}$$

or the concentration c_a [M] of gas compound a in the pore fluid depends on the partial pressure of the gas phase, $p_g [atm]$, with $k_H [M/atm]$ the temperature dependent Henry constant for a given gas. This also signifies that at a given pressure p, the gas must reach concentration c_a before exsolution takes place. A different formulation of the Henry constant is $k_{H,inv}^{px} [MPa]$, an inverse notation where pressure is represented in MPa and concentration as mole fractions

(mol gas / mol H_2O). Then Henry's Law becomes

$$\frac{P}{k_{H,inv}^{px}} = c_a \tag{7.3}$$

The formulation of $k_{H,inv}^{px}$ is obtained from data given by Lekvam and Bishnoi (1997), who experimentally defined the dissolution of methane in water at low temperatures and intermediate pressures (lower than 100 bar, or 10 MPa), below gas hydrate forming conditions. The equation used here will be

$$k_{H,inv}^{px} = 2176 + 83,34(T - 273,15) \tag{7.4}$$

This will only be applied below hydrate forming conditions because the introduction of a third phase greatly complicates the thermodynamics, hence also the methane solubility. Equation 7.4 was compared with experimental data available in literature and yielded fairly good correspondence. For low temperatures (0 and 5 °C) at low to intermediate pressures (0.1 to 10 MPa), the data presented by Handa (1990) corresponds quite well at lower pressures (< 50 MPa), but the difference increases with pressure: about 50% at 100 MPa. At low pressure (3.45 MPa) and low temperatures (0 to 15 °C), equation 7.4 corresponds very well at 10 to 15 °C to data supplied by Song et al. (1997), with less than 25% difference at 15 °C. With decreasing temperature, the difference increases because Song et al. (1997) demonstrate a sorption effect, which they attribute to the onset of gas trapping in water molecules that leads to gas hydrate formation. Yang et al. (2001) present methane solubilities at 25 °C over a broad range of pressure (2.33 to 12.68 MPa) and it appears that at this temperature, equation 7.4 corresponds rather well for pressures up to 10 MPa.

As an example, let the initial water depth be 500 m, and the mud column length 500 m as well. The sea floor temperature is 10 °C and temperature increases with depth, along a gradient of 0.05 K.m^{-1}. Lowering the sea level by 50 m will decrease methane solubility, leading to a gas volume creation of 1.3 to 4.6 $\times 10^{-3}$L per L of pore fluid, depending on depth (Figure 7.3). A sea level drop of 100 m has a slightly higher volume increase, with 1.4 to 5.2 $\times 10^{-3}$L L of pore fluid. It must be noted that these volumes are calculated at in situ pressure and temperature at any depth. At standard conditions, these volumes are much higher. The increase in pore water pressure related to this volume increase depends on the compressibility of the medium, accordingly

$$\frac{dV}{V_p} = \kappa dP_{ex} \tag{7.5}$$

with dV the volume increase per unit of original pore fluid volume V_p, $\kappa[Pa^{-1}]$ the bulk compressibility and dP_{ex} the excess pore pressure created. With compressibillities ranging from 1×10^{-7} for very compressible materials, to 4.4×10^{-10} for water (very little compressible),

the excess pore water pressure results in 50 kPa to 44 MPa. Thus the result is strongly depending on the material compressibility. It can be expected, however, that for shallow depths where overburden pressure (and thus yield strength) is smallest, the volume increase (which directly results in a density decrease) will be able to cause a pressure- and density-driven upward migration of the gas-bearing matrix.

Once this process has started, the gas exsolution process will accelerate because the methane solubility in the uprising mud and fluid will further decrease. This in turn, decreases the confining pressure on the buried and potentially overpressured source system, which can result in increased mud volcano activity due to depressurization of the mud and fluid reservoir.
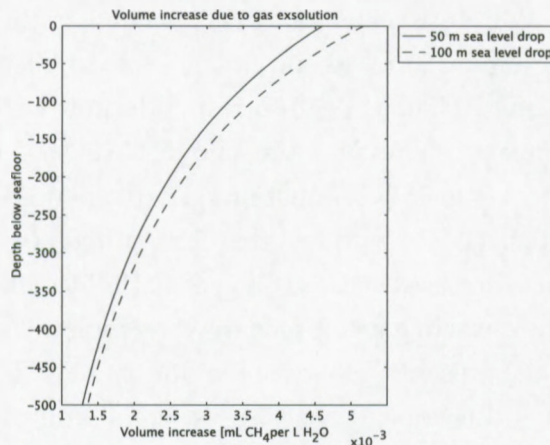
Figure 7.3: Volume increase in mL gas per L of pore fluid in function of depth. Dense line: 50 m sea-level drop. Dashed line: 100 m sea level drop.

7.3.1   Mud flows and mud volcano activity: a eustatic trigger?

The question must now be asked whether large-scale (eustatic) sealevel fluctuations can be the cause of the proven recurrent mud volcano activity on the Moroccan margin (and elsewhere). Hydrofracturation and/or re-activation of pre-existing mud and fluid mobilization pathways must be regarded: it is essentially the breaking up of overburden strata that will allow the migration of fluid and mud towards the surface. Important concepts in this view are the failure criteria of the buried sediments, the stress patterns at great depth, including overpressure. First the case of overburden (hydro)fracturation will be regarded, and second reactivation.

7.3.1.1   Genesis of fractures

The mode of failure in a given rock depends on the differential stress ($\sigma_1 - \sigma_3$) and the rock tensile strength[3] T (Secor, 1965). Furthermore, the fluid pressure P_f is important since it decreases the total stress σ to an effective stress $\sigma' = \sigma - P_f$. The different failure types are illustrated in Fig. 7.4 for an intact rock failure envelope and a cohesionless reactivation.

Three types of failure can be discriminated. For low differential stress, i.e. when $(\sigma_1 - \sigma_3) < 4T$, extension fractures form in accordance with the hydraulic fracture criterion

$$P_f = \sigma_3 + T \tag{7.6}$$

or,

$$\sigma_3' = -T \tag{7.7}$$

This means that faulting will occur if the minimum effective stress equals tensile strength (the minus indicates extension). Because $2\alpha = 0$, failure will occur along planes perpendicular to the least compressive stress σ_3 (Sibson and Scott, 1998).

Under high differential stress, i.e. when $(\sigma_1 - \sigma_3) > 6T$, compressive shear failure may occur in accordance with the linear Coulomb criterion:

$$\tau = C + \mu_i(\sigma_n - P_f) \tag{7.8}$$

where $C \approx 2T$ is the cohesive strength, μ_i the internal friction, and τ and σ_n are the components of shear and normal stress on the failure plane. This can be written in function of the principle stresses (Sibson and Scott, 1998):

$$P_f = \sigma_3 + \frac{4T\sqrt{K} - (\sigma_1 - \sigma_3)}{(K - 1)} \tag{7.9}$$

with $K = \left(\sqrt{(1 + \mu_i^2)} + \mu_i\right)^2$.

Where $4T < (\sigma_1 - \sigma_3) < 6T$, hybrid extensional-shear fractures may be generated. Sibson and Scott (1998) also show that in an extensional regime ($\sigma_v = \sigma_1$), the vertical permeability will be enhanced whereas in a compressional regime ($\sigma_v = \sigma_3$), the horizontal permeability increases. The result is that (sub)vertical extension fractures and steep normal faults in extensional regimes facilitate vertical flow. In strike-slip regimes ($\sigma_v = \sigma_2$), vertical flow is also enhanced through the association of subvertical faults and extension fractures. In compressional regimes, subhorizontal extension fractures and low-dipping thrusts will rather enhance horizontal fluid flow; which makes it easier to sustain fluid overpressure without fluid escape

---

[3]Tensile strength can be defined as the stress at which a rock breaks.
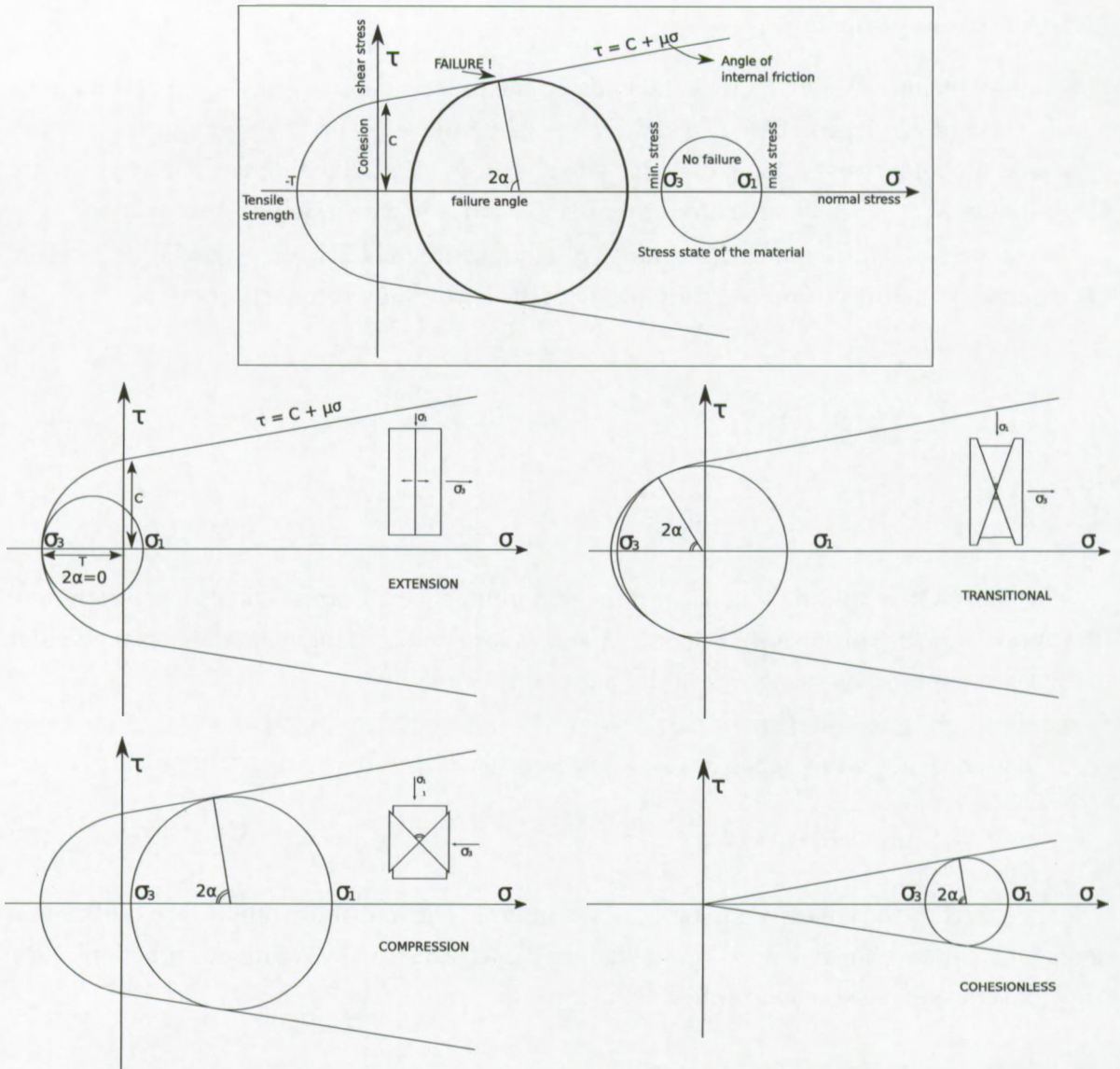
Figure 7.4: *Mohr's Circle representation of stress patterns and failure angles for extensional, transitional and compressional regimes. When no cohesion (C=0) is present, extension will always invoke failure and under compression, smaller deviatoric stress is required to induce failure.*

towards the surface. With this information, it is possible to estimate the amount of overpressure needed to create failure or reactivation in general at any given depth. More specifically, and with interest for mud volcano activity, it is the situation where subvertical extension fractures facilitate vertical flow.

In a situation where no tectonic forces are present, the stress field is controlled by the

overburden. The vertical stress is given by

$$\sigma_v(z) = \int_0^z \rho_b(z) g dz,$$ (7.10)

and the corresponding horizontal stress is

$$\sigma_h(z) = \left(\frac{\nu}{1-\nu}\right) \sigma_v(z)$$ (7.11)

with ν the Poisson ratio for the rock (i.e. a material property that describes the ratio of the transverse strain divided by the relative axial strain when a load is applied to it). A more advanced description of the horizontal stress takes into account the pore pressure increase in a laterally confined basin (Hornbach, 2004):

$$\sigma_h = \left(\frac{\nu}{1-\nu}\right) \sigma_v + \alpha \left(\frac{1-2\nu}{1-\nu}\right) P_f.$$ (7.12)

Since no tectonic forces act, σ_v will be the greatest stress, and thus be defined as σ_1. The horizontal stress σ_h equals the minimum principle stress σ_3.

The normal and shear stress corresponding with the principal stresses are

$$\sigma_n = \left(\frac{\sigma_1 + \sigma_3}{2}\right) - \left(\frac{\sigma_1 - \sigma_3}{2}\right) \cos(2\theta) \qquad \tau = \left(\frac{\sigma_1 - \sigma_3}{2}\right) \sin(2\theta)$$ (7.13)

Taking into account the pore pressure, this leads to

$$\sigma'_n = \sigma_n - P_f \qquad\qquad\qquad \tau' = \tau$$ (7.14)

Now, the potential of a sea level fall as trigger for mud volcano (re)activation will be calculated. The goal is to obtain an equation that describes which sediment- and waterdepth is needed to induce failure. Then, this can be compared to natural examples.

The first case is where no pre-existing overpressure is present in a confined layer, or in other words the pore pressure is hydrostatic. The depth of the top of this confined layer will be varied from 0 meter below the seafloor to 5000 meter below the seafloor; the depth of the sea water column will also be varied from 0 to 2000 m. The density of the buried sediment is taken constant and set to 2000 kg.m^{-3}. The water density is set to 1000 kg.m^{-3} and the gravitational acceleration to 10 m.s^{-2}. These values are chosen in order to obtain an idea about the order of magnitude rather than a 'exact' value with large deviations. Further constants include the tensile strength $T = 10^6$ Pa, Poisson's ratio $\nu = 0.45$ and friction factor $\mu = 0.55$ which gives $K = 2.8604$.

Tensile extensional failure may occur when

$$\sigma_1 - \sigma_3 < 4T.$$

As the vertical stress is the highest stress, this leads to

$$\sigma_v - \sigma_h < 4T$$

which develops, after taking into account equation 7.11, to

$$\sigma_v \left(1 - \frac{\nu}{1 - \nu} \right) < 4T.$$

Reordering and substituting equation 7.10 into the last equation, yields

$$(h_w \rho_w + h_s \rho_b) < \left(\frac{4T}{g} \right) \left(\frac{1 - \nu}{1 - 2\nu} \right) = 3.3 \times 10^6$$

or finally

$$h_w + 2h_s < 2200 \tag{7.15}$$

which means that tensile extensional failure may occur where the height of the overburden water column and two times the sedimentary column is less than 2200 for the given tensile strength of 1 MPa.

For failure actually to occur, the hydraulic fracture criteria (equation 7.6) must be met. This means that the stability is preserved as long as

$$P_f < \sigma_3 + T$$

which can be developed as

$$\begin{aligned} P_f &< \sigma_h + T \\ P_f &< \left(\frac{\nu}{1 - \nu} \right) \sigma_v + T \end{aligned}$$

$$g\rho_w(h_s + h_w) \; < \; \left(\frac{\nu}{1-\nu}\right) g(\rho_b h_s + \rho_w h_w) + T$$

$$h_w\left[g\rho_w - \left(\frac{\nu}{1-\nu}\right)g\rho_w\right] + h_s\left[g\rho_w - \left(\frac{\nu}{1-\nu}\right)g\rho_b\right] \; < \; T$$

$$h_w\rho_w\left(\frac{1-2\nu}{1-\nu}\right) + h_s\left[\rho_w - \left(\frac{\nu}{1-\nu}\right)\rho_b\right] \; < \; \frac{T}{g}$$

$$181.8h_w - 636.4h_s \; < \; 10^5$$

and finally

$$h_w - 3.5h_s < 550. \tag{7.16}$$

This inequality, together with equation 7.15, define the field where stability is maintained (Figure 7.5). As soon as $h_w - 3.5h_s = 550$, extensional failure should occur. This means that extension fractures will only start occurring in water depths over 550 m.

Normal shear failure may occur when

$$\sigma_v - \sigma_h > 6T$$

and taking into account equation 7.11 this leads to

$$\sigma_v\left(1 - \frac{\nu}{1-\nu}\right) > 6T$$

$$\sigma_v > \frac{6T}{\left(\frac{1-2\nu}{1-\nu}\right)}$$

and after substitution of equation 7.10

$$(h_w\rho_w + h_s\rho_b) > \left(\frac{6T}{g}\right)\left(\frac{1-\nu}{1-2\nu}\right) = 3.3 \times 10^6$$

or finally

$$h_w + 2h_s > 3300 \tag{7.17}$$

which means that in order to create failure the sum of the water depth and two times the sediment depth must be larger than 3300 m.

The failure criterion for this situation, as given in equation 7.9, expresses the (minimum) pore pressure needed to effectively create shear fractures. The equation can be further devel-

oped to

$$(h_w + h_s)\,\rho_w g = \left(\frac{\nu}{1-\nu}\right)(h_w\rho_w + h_s\rho_b)g + \frac{\left[4T\sqrt{K} - (h_w\rho_w + h_s\rho_b)g\left(\frac{1-2\nu}{1-\nu}\right)\right]}{(K-1)}$$

which ultimately, after reordering and substituting the constants by their values, leads to

$$h_w = 1.577h_s + 1300. \tag{7.18}$$

Thus, equations 7.17 and 7.18 define minimum water-sediment depths at which normal shear faults will occur solely due to the overburden stress under conditions where pore pressure is hydrostatic.

Now, the four equations 7.15, 7.16, 7.17, 7.18 can be plotted in a graph in function of water depth h_w and sediment depth h_s. Figure 7.5 represents the situation calculated above, i.e. with a tensile strength $T = 1MPa$ corresponding to compacted sediments. The figure illustrates the fact that in extensional regimes both hydraulic extension fractures and normal shear fractures can develop 'near' the seafloor under hydrostatic conditions (indicated as 'Unstable' in Figure 7.5). At deeper levels, this is not possible and fluid pressures higher than hydrostatic pressure are required to invoke failure.

A comment must be made concerning the tensile strength of the sediments. Muds close to the seafloor have a very low tensile strength ($\ll 1$ MPa). However, some tensile strength is needed for tensile cracks to form. If there is no or very low tensile strength, then the requirement in equation 7.15 will never be met because the differential stress will always be too great and correspond to the situation of normal shear (equation 7.17). However, with increasing depth, sediments get more compacted and thus gain strength (e.g. Nichols, 1995; Jolly and Lonergan, 2002). So apart from a lower limit to tensile fracture formation, there is also an upper limit although it is hard to precise the position of that limit. Jolly and Lonergan (2002) report that in this upper zone, where normal shear failure occurs, the injection of fluidized sands manifests itself in the form of pipes rather than dykes or sills.

The amount of overpressure needed to create failure at deeper levels can easily be calculated from equations 7.6 and 7.9 (corresponding to tensile extension fractures and normal shear fracture), but where the pore fluid pressure P_f is augmented with the overpressure p_e, or

$$P_f + p_e = \sigma_3 + T \tag{7.19}$$

$$P_f + p_e = \sigma_3 + \frac{4T\sqrt{K} - (\sigma_1 - \sigma_3)}{(K-1)} \tag{7.20}$$

In other words, the effective stress is further decreased, and failure will occur over a broader
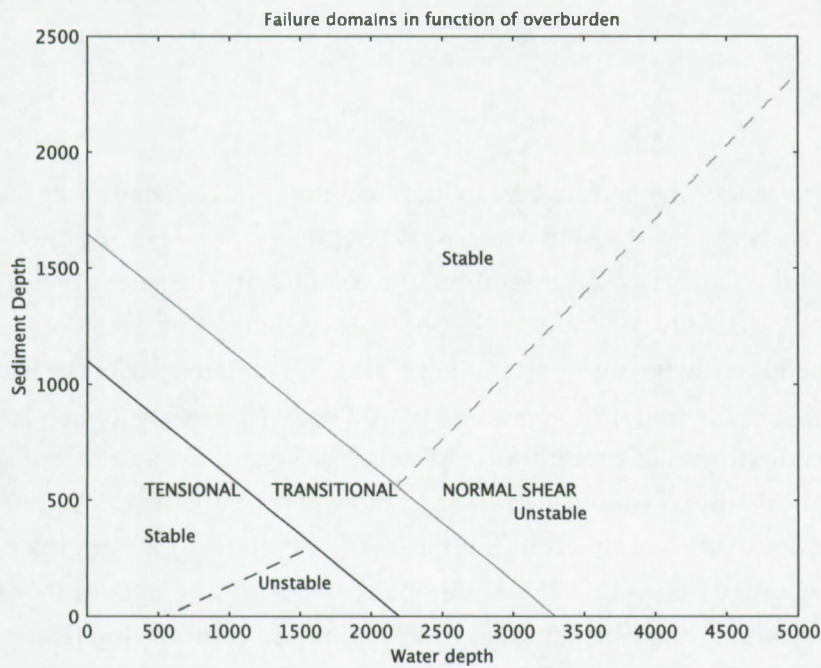
Figure 7.5: Extensional failure domain for a tensile strength of 1 MPa.

field. The two failure criterion equations can be written similarly as before as

$$g\rho_w(h_s + h_w) + p_e = \left(\frac{\nu}{1-\nu}\right)g(\rho_b h_s + \rho_w h_w) + T$$

$$(h_w + h_s)\rho_w g + p_e = \left(\frac{\nu}{1-\nu}\right)(h_w\rho_w + h_s\rho_b)g + \frac{\left[4T\sqrt{K} - (h_w\rho_w + h_s\rho_b)g\left(\frac{1-2\nu}{1-\nu}\right)\right]}{(K-1)}$$

which will lead to

$$h_w = 3.5h_s + 550 - p_e/10000$$

for tensile extension fault creation and

$$h_w = 1.577h_s + 1300.8 - p_e/2795.5$$

for normal shear fault creation.

In case of a sea level fall of e.g. 100 meter, the excess pressure below any layer with low

permeability will be $p_e = \rho_w g \Delta h \approx 1$ MPa. In such a case, the previous equations become, depending on the regime,

$$h_w = 3.5h_s + 450$$
$$h_w = 1.577h_s + 943$$

for the sediments below the layer with low permeability, which means that the unstable domains (figure 7.5) move to the shallower water depths and deeper sediment depths. The presence of a fault will allow fluid migration to re-equilibrate the pressure field. This will be expressed as escape of fluid, possibly with mud entrainment, at the seafloor surface.

In case of the El Arraiche mud volcano field, which is situated at depths between 150 and 850 m, the only possible fractures generated would be tensile extensional fractures (supposing that the sediment tensile strength of 1 MPa is justified). Furthermore, as can be seen in figure 7.5, the mud source should be rather shallow. However, this does not at all explain the presence of rock clasts sampled in the mud volcano craters that originate from kilometers deep (Ovsyannikov et al., 2003). Additionally, the high amounts of thermogenic gases in some mud volcanoes (Stadnitskaia et al., 2006) and fluid composition (Hensen et al., 2007) also indicate deeper fluid sources, and thus will require deeper fluid migration pathways.

Therefore, we can exclude that the origin of the mud volcanoes is due to the genesis of shallow fractures combined with a sea level drop.

7.3.1.2   Fracture reactivation

If a pre-existing fluid flow pathway (a fault, or a mud volcano feeder pipe, for instance) exists, then the tensile strength and cohesion would be much smaller because previous fracturation processes have already taken away the strength of the rock if it has not been cemented. The tensional extension fracture would normally not occur because normal shear fractures would preferentially occur at a higher effective stress (see the last case in figure 7.4). In a theoretical cohesionless case with $C \approx 2T = 0$, equation 7.20 simplifies to

$$P_f + p_e = \sigma_3 + \frac{-(\sigma_1 - \sigma_3)}{(K-1)} \tag{7.21}$$

which can be developed as

$$\rho_w g(h_s + h_w) + p_e = \frac{1}{K-1}\left[K\left(\frac{\nu}{1-\nu}\right) - 1\right]g(\rho_w h_w + \rho_b h_s)$$

or

$$h_w = 1.577h_s - p_e/2796. \tag{7.22}$$

If an overpressure of 1 MPa exists at a certain level, then the depth equation would become

$$h_w = 1.577 h_s - 358.$$

In other words, an overpressure of 1 MPa would allow fluids to break a seal and migrate upwards from a greater depth.

The cohesionless situation also applies to the near-surface sediments, as already discussed in previous section. However, the significance for fluid flow is small if not nonexistent because at very shallow levels, overpressure cannot easily be generated because hydrostatic equilibrium is better retained through the high porosity/permeability.

Let the Mercator mud volcano now serve as an example: its crater is situated at a depth of about 350 m below sea level. If the mud volcano feeder pipe has a low permeability (packed with mud breccia) and therefore acts as a seal, which allows for overpressure to be built up, a 100 m sea level drop would lead to a shear failure and mobilization of the overpressured mud from a depth of 450 m.

> The same comment can be made as in the previous part: mobilization of deep-sourced clasts and thermogenic gases cannot be explained by a mobilization from a few hundred meters.

7.3.1.3   Sea-level fluctuations as a driving mechanism of mud volcano activity?

It seems unlikely that a sea level change as sole cause of subsurface overpressure will be the only driver of mud volcano activity. First of all, the hypothetical source depth would have to be very shallow and this is not observed in the case of the Moroccan margin and Gulf of Cadiz mud volcanoes. The remobilisation process of muds from a shallow depth cannot be excluded however, and might be responsible for some of the extrusive events observed in the study area.

Additionally, a two-stage scenario could be hypothesised, including a mobilisation of fluids, rocks and mud from deeply buried layers to a near-surface position in a mud chamber (similar to a magma chamber in magmatic volcanism). The migration could be controlled by deep tectonic forces related to the accretionary wedge. Mud chambers are known from mud volcanoes elsewhere although there is no proof that such structures would exist in the study area. The second stage would include a transfer of the mud breccia present in the mud chamber towards the surface. Further geophysical and modeling studies should be done to test this hypothesis.

Finally, if a shallow-sourced mud volcanism (stage two) would indeed be driven by sea level fluctuations, other evidence should be found for this in the (seismic) stratigraphic record (erosional events, e.g.).

7.3.1.4   A note about tectonic compression

In the past exercises, the highest stress was the vertical stress or overburden stress: $\sigma_1 = \sigma_v$. This regime actually occurs in deltaic or passive margin environments. In strike slip environments ($\sigma_2 = \sigma_v$; transpressive regime) or thrust fault environments ($\sigma_3 = \sigma_v$; compressive regime), the failure domains defined by equations 7.15 and 7.17 will have to be calculated differently since the Poisson effect is not valid. Furthermore, as the fractures have a certain angle with regard to σ_1, their direction or angle of the fracture will be different as well.

In terms of failure criteria, ultimately the difference between P_f and σ_3 is most important (e.g., Grauls, 1997): in a compressive regime, $\sigma_3 = \sigma_v$, which is higher than in the extensional regime, $\sigma_3 = \sigma_v \nu / (1-\nu)$, and therefore higher fluid pressure will be maintained before failure occurs.

7.4   Seafloor current driven subsurface fluid flow (steady state effect)

7.4.1   Introduction

In this section, an externally driven subsurface fluid flow process that acts on a much smaller scale than in previous sections will be discussed.

Bedform-generated convective transport in sediments (Thibodeaux and Boyle, 1987) is a well-known small-scale process created by imbalances in pressure over distance. Huettel et al. (1996) and related following studies (Huettel et al., 1998; Huettel and Rusch, 2000; Huettel et al., 2003; Reimers et al., 2004; Roy et al., 2005) demonstrated particle transport driven by small pressure gradients when bottom flows are deflected by small surface structures. In their 1996 paper, the ripple topography enhanced interfacial particle flux by a factor 2.3 compared to a control and thus is of importance for organic matter uptake in permeable shelf sediments. Reimers et al. (2004) showed an association of episodic fluid pumping with the greatest 5% of wave heights and current speeds recorded in a rippled continental shelf sand deposit; the distance-time averaged vertical fluid flow velocity varied from 6 to 53 cm h^{-1}. In their study, Reimers et al. emphasize the enhancement of benthic oxygen consumption in pore-water flow-through ripples. These studies thus show that convective transport is a very significant process for the biological and geochemical environment in permeable sediments.

The process of bedform-generated convective transport in sediments is here projected to a larger scale: seafloor obstructions such as carbonate mounds, steep seafloor 'cliffs', etc. will affect the local current patterns in terms of pressure and velocity. Near-seafloor pressure imbalances will, analogous to small scale structures like sand ripples, produce subseafloor fluid convection. Because the pressure effects are active on a larger scale, the advective transport

will be felt down to a greater depth. We will assess the importance of the advective process by modeling what its effect on the sulfate-methane transition zone (SMTZ) is.

7.4.2   The model in general

The model is made up of 3 parts: the flow of water over an obstacle resulting in a pressure field; the effect of this pressure field on the subsurface fluid flow (Darcian model) and finally the transport-reaction in result of this fluid flow. All mathematics and numerics were discussed in chapter 3.

7.4.2.1   Current over a seafloor obstacle

The model geometry is made up by a 2-D box as presented in fig 7.6. The turbulent fluid flow model ($Re = 10^6 - 10^9 \ggg 1$) is based on the Navier-Stokes equations 3.26, describing the motion in incompressible fluids, expanded with equations for turbulence kinetic energy and dissipation rate of turbulence energy (k-epsilon model, valid at high Reynolds numbers, see equations 3.31) (Wilcox, 1998).

The model comprises the steady inflow of a fluid at the left boundary, a no-slip boundary wall condition at the lower boundary, a continuous boundary at the top (no friction) and a neutral boundary at the outflow side of the box. The obstacle in the flow will locally accelerate the flow and hence create low pressure fields at or near the top of the structure. Simultaneously, high pressure fields are created at the foot of the structure (figure 7.7). For different input stream velocities, the resulting vertical velocity profile and the differential pressure profile at the crest and base of the obstacle is shown in figure 7.8. The differential pressure field is calculated for different inflow velocities, ranging from 1 to 100 cm s^{-1}, yielding pressure fields of variable magnitude.

The differential pressure at the bottom is used as upper boundary condition for the subsurface part of the model.

7.4.2.2   Subsurface fluid flow

The second part of the model calculates the flow pattern using a steady state Darcian fluid flow model (see section 3.3.2 for the relevant mathematics). The geometry used (figure 7.9) is a 200 m by 200 m box representing a homogeneous stack of sediments with hydraulic conductivity K. The controlled experiment by Huettel et al. (1996) used sandy sediments, with permeability $k > 2.10^{-11}$ m^2 (equivalent to a hydraulic conductivity $K > 2.10^{-4}$ m.s^{-1}). We will use this as an upper limit for the K range 2×10^{-4} to 1×10^{-13} m.s^{-1}. The differential pressure is imposed as upper boundary, all other boundaries are no-flow boundaries. The model result gives us a differential pressure distribution in the sediments from which we can calculate the fluid flow velocities (equation 3.7), using the differential pressure gradient. Figure 7.10 represents streamlines and direction and magnitude of the flow. Seawater is pulled
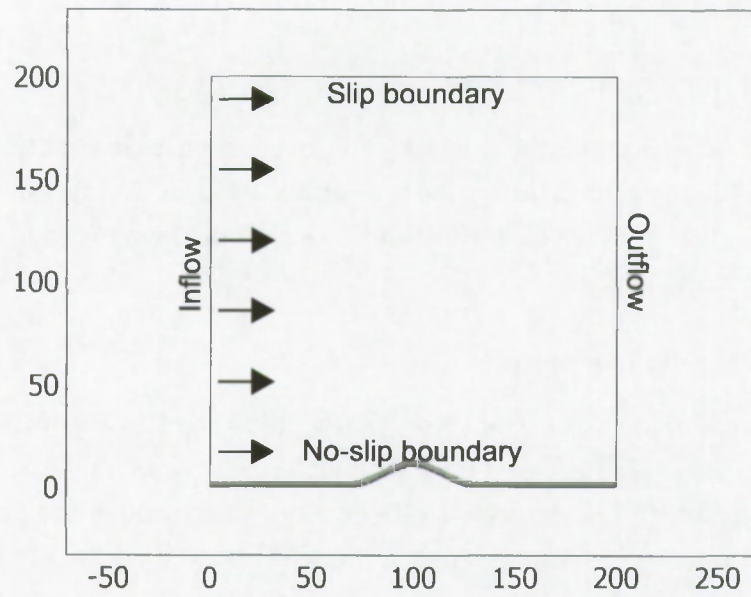
Figure 7.6: *General geometry used for the numerical model involving a current over a seafloor obstacle. Axes units: meters.*
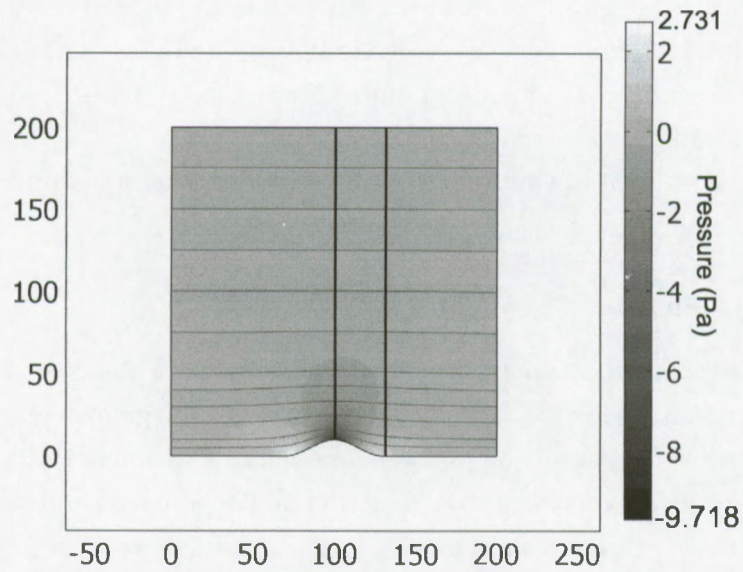
Figure 7.7: *The effect created by an obstacle at the seafloor on the velocity field of the water column. Axes units: meters.*
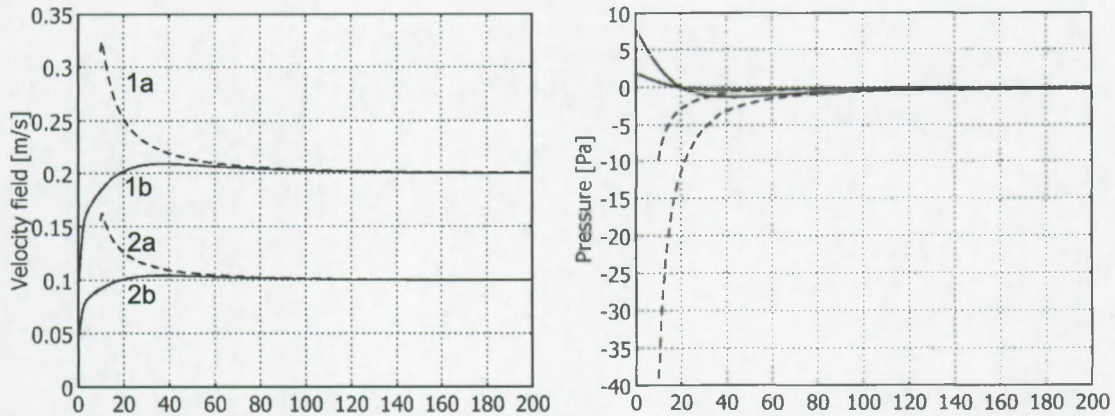
Figure 7.8: Vertical velocity (left) profiles and differential pressure (right) profiles. Curve 1a is a velocity resp. pressure profile at the crest of the obstacle for a input velocity of 10 cm.s^{-1}; curve 1b is situated at the foot of the obstacle. Curves 2a and 2b are analogous for input velocity 20 cm.s^{-1}. Horizontal axis units: meters.

into the sediments near the base up- and downstream of the obstacle, and pore water is extruded near the crest of the obstacle, slightly down the downstream side. The strongest fluid flow is present near the seafloor and quickly weakens with increasing depth.

The fluid flow velocity field is subsequently used as the advective component in a transport-reaction model.

7.4.2.3   Transport-reaction model

The effect of the advective transport on the subsurface geochemistry is modeled through a second order transport reaction model applied to the same geometry as the above darcy model. The change of depth of the sulfate-methane transition zone (SMTZ) is simulated in order to quantify the significance of the process of bedform-generated fluid advection on large structures.

The transport-reaction model comprises (1) diffusive transport of sulfate and methane with diffusion constants 1×10^{-9} resp. 3×10^{-10} m^2.s^{-1} (Lerman, 1979), (2) advective transport driven, with velocities determined in the above darcy model, and (3) reaction of methane and sulfate at their interface, simulating anaerobic methane oxidation (Hinrichs et al., 1999), through the second-order reaction equation 3.41.

A constant concentration of 30 mol.m^{-3} is set as boundary condition for sulfate [SO$_4$] at the seafloor, and for methane [CH$_4$] a constant upward flux of 1×10^{-9} mol.m^{-2}.s^{-1} was imposed at the lower boundary to generate a SMTZ at a depth of 10-15 meter below the seafloor. This value is within the range of methane fluxes reported in seep-related areas: Dale et al. (2009) report fluxes of 1 to 4×10^{-9} mol.m^{-2}.s^{-1} in Aarhus Bay while Lapham et al.
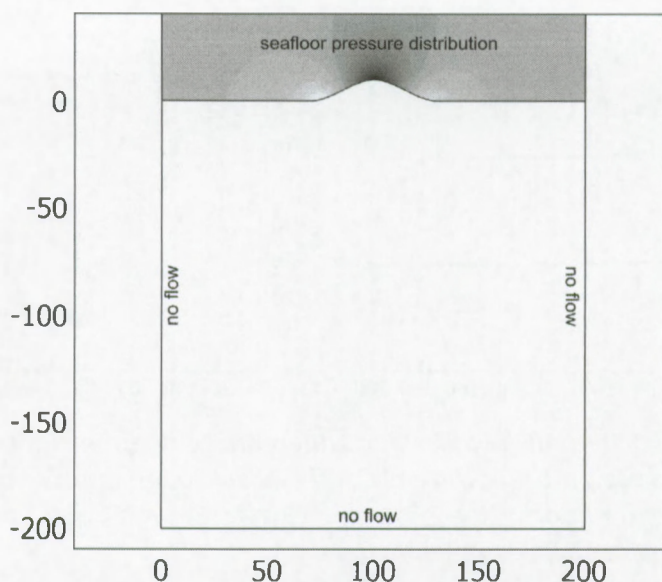
Figure 7.9: *General geometry used for the numerical model involving a subseafloor fluid flow. Dark gray shades indicate low pressure fields, light gray shades indicate high pressure fields. Axis units in meter.*

(2008) measured methane fluxes around brine seeps in the Gulf of Mexico between 6×10^{-8} $mol.m^{-2}.s^{-1}$ and 2×10^{-6} $mol.m^{-2}.s^{-1}$. Sediments around and on Porangahau Ridge on the Hikurangi Margin were characterized by fluxes between 1.33×10^{-10} $mol.m^{-2}.s^{-1}$ and 6.6×10^{-9} $mol.m^{-2}.s^{-1}$ (Coffin et al., 2007).

Depending on the strength of the flow and the geometry, the SMTZ will be pulled upwards or pushed downwards beneath the crest of the structure and pushed downwards beneath the base of the seafloor structure. The effect can also depend on the depth below the seafloor as illustrated in figure 7.11. In this example, the location is below the top of the obstacle and bottom water current velocity is 20 cm s^{-1}. The sulfate profile is pulled upwards near the seafloor due to upward fluid flow (in other words, the concentration is decreased with respect to the no-flow situation; figure 7.12(left)). However, the SMTZ, where the sulfate meets the methane, is pushed downwards due to the relatively strong advection of sulfate from sidewards within the structure. The net effect is that there is a relative increase in sulfate concentration. At lower speeds, vertical sulfate profiles are entirely pulled upwards within the structure. At the top of the obstacle, there is a convex up profile due to the upward flow and near the foot of the obstacle, there is a concave down profile due to the downward flow 7.12.
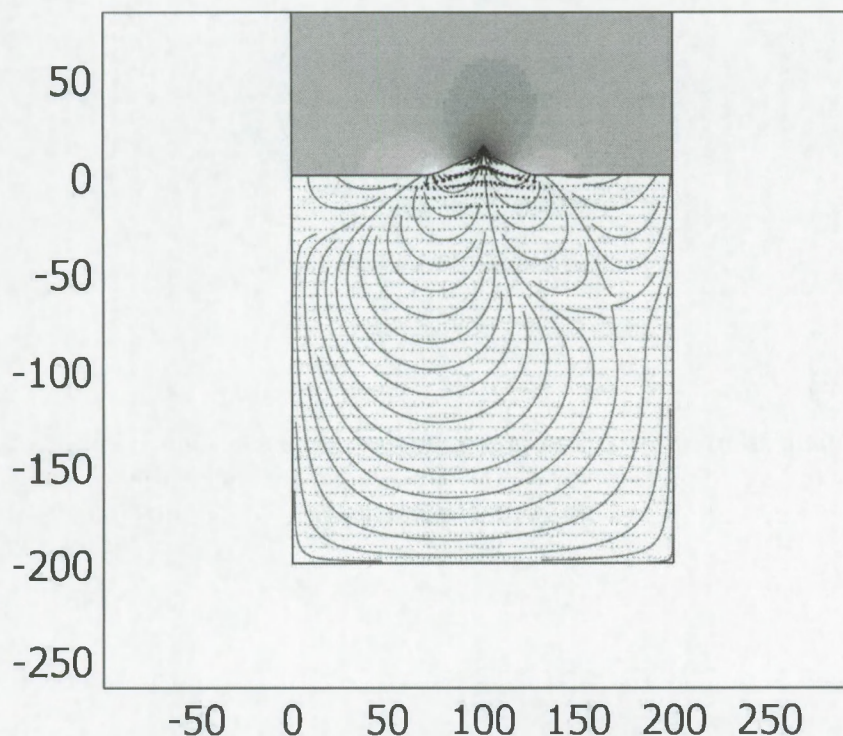
Figure 7.10: *Streamline plot illustrating the subsurface fluid velocity field. Fluids enter the sediment at the foot of the obstacle (on both sides) and fluids leave the sediment at the crest of the obstacle. Axis units in meter.*

7.4.3 Model results and interpretation

Different parameters will be varied in the model: the obstacle geometry, the seafloor current velocity and the sediment hydraulic conductivity.

7.4.3.1 Model geometry

It is evident that the shape of a seafloor obstacle will control the bottom current velocity changes, and thus pressure changes. The width, height and thus steepness of an obstacle slope will be varied for a fixed bottom current velocity $[v = 0.1 \text{ m s}^{-1}]$ and hydraulic conductivity $(K = 1 \times 10^{-6} \text{ m.s}^{-1})$ of the sediments, to assess their impact on the sulfate-methane transition zone (SMTZ) depth and sulphate profile shape. The results are summarized in table 7.1.

The differential pressure field is stronger when the seafloor obstacle is larger. However, it is the pressure gradient that will determine the subsurface fluid flow velocity. The differential
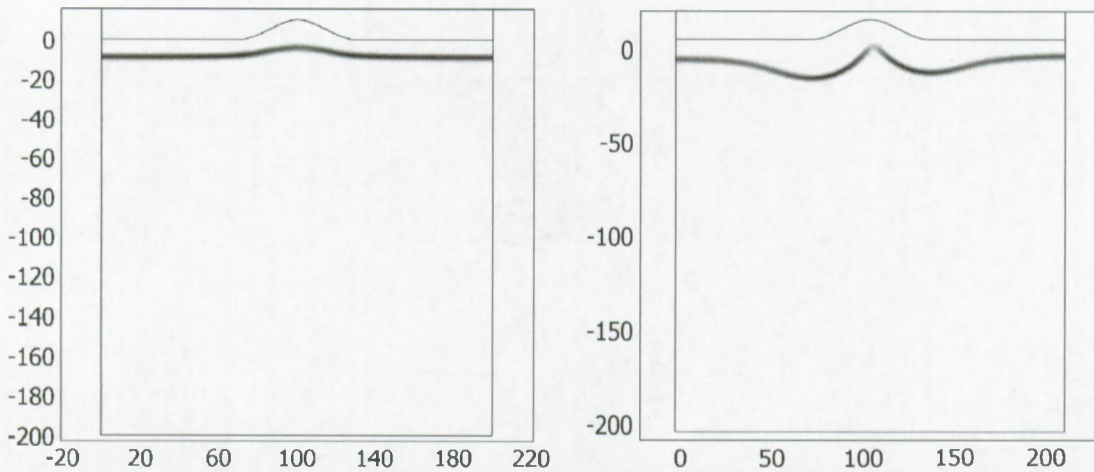
Figure 7.11: *Visualization of the sulfate-methane reaction zone. Left: without advective process; right: with advective process; the SMTZ is pushed down beneath the feet of the obstacle while it is dragged upward below the center of the obstacle. Axis units in meters.*
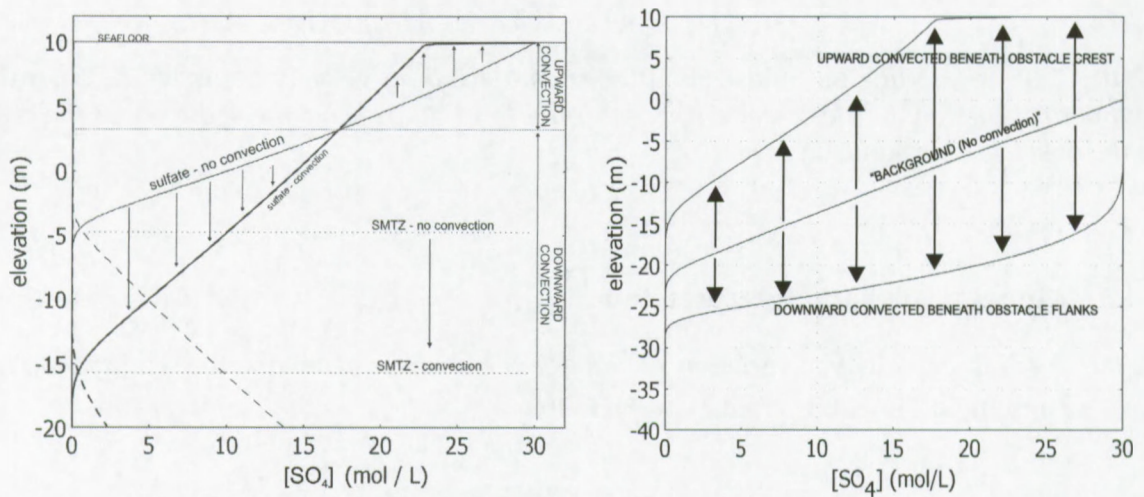
Figure 7.12: *Left: effect of convective processes in figure 7.11 on the sulfate profile below the obstacle crest: near the seafloor, the sulfate concentration is decreased; deeper the sulfate concentration is increased due to sidewards inflow. Right: Effect of the flow direction on the sulfate profile shape: an upward flow yields a convex up profile, a downward flow yields a concave down profile. The former situation occurs below the crest of the obstacle; the latter situation occurs below the flanks and feet of the obstacle.*

pressure gradient decreases with decreasing obstacle height for a fixed width, but increases with decreasing structure width. The reason for this is that for a less wide structure, the differential pressure changes over a shorter distance along the outside of the structure, than for a wide structure. Hence, the pressure gradient is higher in the less wide structure. Or in other words, the differential pressure is focused on a smaller area.

The generated subsurface fluid flow velocities are highest near the seafloor and quickly decreasing with depth; hence, advective transport will be strongest in the upper sediments. The velocity near the seafloor is in the order of 15 mm/y (corresponding with a structure width of 25 meters and a height of 5 meters) to 0.25 mm/y (corresponding with a structure width of 100 meters and a height of 2.5 meters) for the specific bottom water velocity and hydraulic conductivity.

The change in SMTZ depth below the crest of the obstacle is significant for geochemical processes. Depth differences range from about half a meter to more than 5 meters. The depth change has a linear correlation with the slope and height of the structure for a given width (e.g. R^2=99.9% resp. 99.8% for the correlation between the structure slope and height versus the SMTZ depth difference for a structure width of 100 m). For the structure with a width of 25 meters, the results rather show an increase of SMTZ depth change with decreasing structure height. This is due to lateral effects which become relatively more important as the width of the structure decreases.

Apart from the SMTZ depth change, an equally important consequence is that the shape of the sulfate profile changes. Due to the upward advection, the profile gets a concave up shape, instead of a nearly linear shape. The amount of shape change depends on the strength of the upward fluid flow, hence on the geometry of the the obstacle as discussed above (and also other parameters discussed in the next section).

The SMTZ depth change and sulfate profile change at the foot of the structure are much smaller than below the crest, and thus will be of lesser importance for the subsurface geochemical environment.

7.4.3.2 Bottom water current strength and sediment hydraulic conductivity

In this section, we will evaluate the effect of different bottom water current velocities and sediment hydraulic conductivities for a specific obstacle geometry. The used geometry has a height of 10 meters and a width of 50 meters. The bottom water current velocity will be varied from 0.01 m.s^{-1} to 1 m.s^{-1}. The sediment hydraulic conductivity will be varied from 1×10^{-13} m.s^{-1} to 1×10^{-5} m.s^{-1}.

The seafloor differential pressure, its gradient and the subsurface fluid flow velocity will be evaluated at the crest and foot of the structure, as well as the depth change of the SMTZ. Figure 7.13 shows the situation with no advective transport is occurring.

		Width: meters								
		100				**50**			**25**	
	Height: meters	20	10	5	2.5	10	5	2.5	5	2.5
	Slope: degrees	31	16.7	8.5	4.3	31	16.7	8.5	31	16.7
Crest	SMTZ No convection (m)	16.82	12.2	10.44	9.68	14.75	11.53	10.18	12.71	10.73
	SMTZ Convection (m)	11.33	9.74	9.37	9.19	12.72	10.11	9.44	12.29	10.21
	SMTZ Height Difference (m)	5.49	2.46	1.07	0.49	2.03	1.42	0.74	0.42	0.52
	Seafloor diff. pressure (Pa)	-14.3	-5.4	-2.3	-1.1	-12.6	-5	-2.2	-11.9	-4.8
	Seafloor diff. pressure grad (Pa/m)	1.28	0.44	0.19	0.08	2.22	0.8	0.34	3.96	1.43
	Max. velocity (mm/a)	4.3	1.43	0.62	0.25	7.87	2.82	1.13	15	5.16
Foot	SMTZ No convection (m)	8.5	8.69	8.83	8.91	8.75	8.85	8.92	8.81	8.88
	SMTZ Convection (m)	8.4	8.73	8.87	8.93	8.93	8.96	8.98	9.1	9.03
	SMTZ Height Difference (m)	0.1	-0.04	-0.04	0.02	-0.18	-0.11	-0.06	-0.29	-0.15

Table 7.1: Results of model runs in function of obstacle geometry for a supposed fixed bottom current velocity $[v = 0.1 \text{ m s}^{-1}]$ and hydraulic conductivity $(K = 1 \times 10^{-6} \text{ m.s}^{-1})$ of the sediments. Row 1: width of the obstacle. Row 2: Height of the obstacle. Row 3: maximum slope of the obstacle. Rows 4 to 9: values related to the crest of the obstacle. Row 4: depth of the SMTZ when no convective transport occurs. Row 5: depth of the SMTZ when convective transport occurs. Row 6: difference between row 4 and 5 indicating depth change. Row 7: differential pressure (deviation from hydrostatic due to velocity effect) at seafloor. Row 8: pressure gradient at seafloor. Row 9: maximum outward fluid velocity. Row 9-12: values related to the upstream foot of the obstacle, analogous to row 4-6. See text for more information.
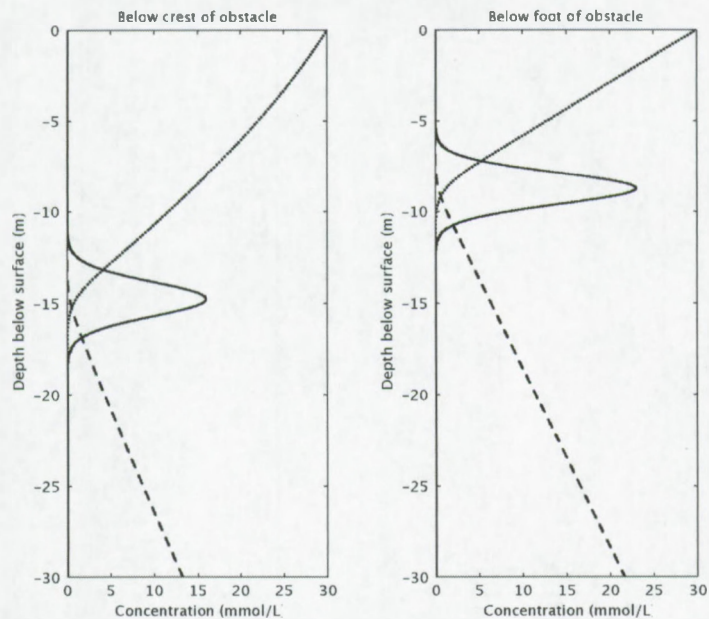
Figure 7.13: *SMTZ when no convective transport is active. The SMTZ depth is 15 m below the crest of the obstacle and 9 meter below the foot of the obstacle. The dotted lines represent the sulfate concentration profile, the dashed line the methane concentration profile and the solid line the reaction of sulfate and methane.*

From the results in table 7.2, it appears that the SMTZ depth can change position in both up- or downward direction. Below the feet of the obstacle, the SMTZ is always pushed downwards due to inflow of seawater (and sulfate) (figures 7.14 and 7.15). The magnitude of the deepening ranges from a few centimeters to multiple meters, the latter especially in permeable sediments with high hydraulic conductivity (10^{-6} - 10^{-5} m s^{-1}). Below the crest of the obstacle, for low hydraulic conductivities or bottom current velocities, the SMTZ is pulled upwards for a few centimeters to meters (figure 7.14). This is an expected situation since the low pressure field at the obstacle crest will effectively promote upward pore fluid flow (table 7.3). However, when high hydraulic conductivity is combined with a high bottom water fluid velocity, the SMTZ gets pushed downwards significantly, due to the strong sidewards inflow of fluids and advecting sulfate (figure 7.15): the structure is being flushed with sulfate-rich seawater. This process of sideward flow actually shuts the seafloor obstacle from the methane supply from below. Figure 7.16 illustrates the different effects in 2 dimensions.

Another important consequence of the subsurface fluid flow is the shape change of the sulfate profile. Three different situations can be identified.

(A) In absence of a significant fluid flow, advective transport is close to zero, hence the only important processes are diffusion and reaction. There is no change in profile shape, nor depth of the SMTZ (figure 7.13).

(B) The fluid flow below the surface is sufficiently strong to give the sulfate profile a
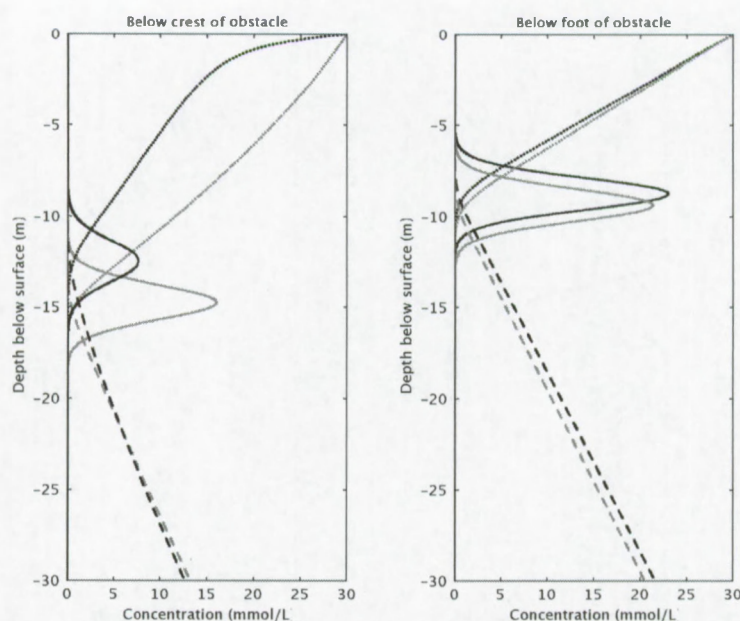
Figure 7.14: SMTZ when moderate convective transport is active. The gray profiles indicate the situation as shown in figure 7.13. The black profiles represent the new situation, with advection. Due to the advective processes, the SMTZ is pulled upwards to about 12.5 m below the crest of the obstacle. Below the feet of the obstacle, the depth does not change much.

concave-up shape and effectively pull the SMTZ upwards below the obstacle crest. Below the feet of the structure, the SMTZ is pushed down to some extent (figure 7.14).

(C) In case of a strong inflow of sulfate at the feet of the structure, the upward flow is insufficiently strong to pull the SMTZ upwards, and the seafloor structure gets shut off from the methane flux from below because the sidewards transported sulfate reacts with the methane before it enters the structure. The net result is that the SMTZ gets pushed down below the crest of the structure, despite the net upward flow of fluids, as is apparent from the concave-up shape of the sulfate profile (figure 7.15).

7.5   Case study: The geochemical environment in carbonate mound settings

Along the Pen Duick Escarpment and other sites on the Renard Ridge and Vernadsky Rigde, small mounded deep-water coral build-ups have been observed and sampled. The origin and evolution of such deep-water coral carbonate mounds is strongly debated (Hovland, 1989; Henriet et al., 2002; Freiwald, 2002; De Mol et al., 2002; Hovland and Risk, 2003), especially concerning the driving genetic mechanisms of such biogenic structures. Either, it is regarded as a biological response to suitable environmental factors (nutrition, currents, temperature,
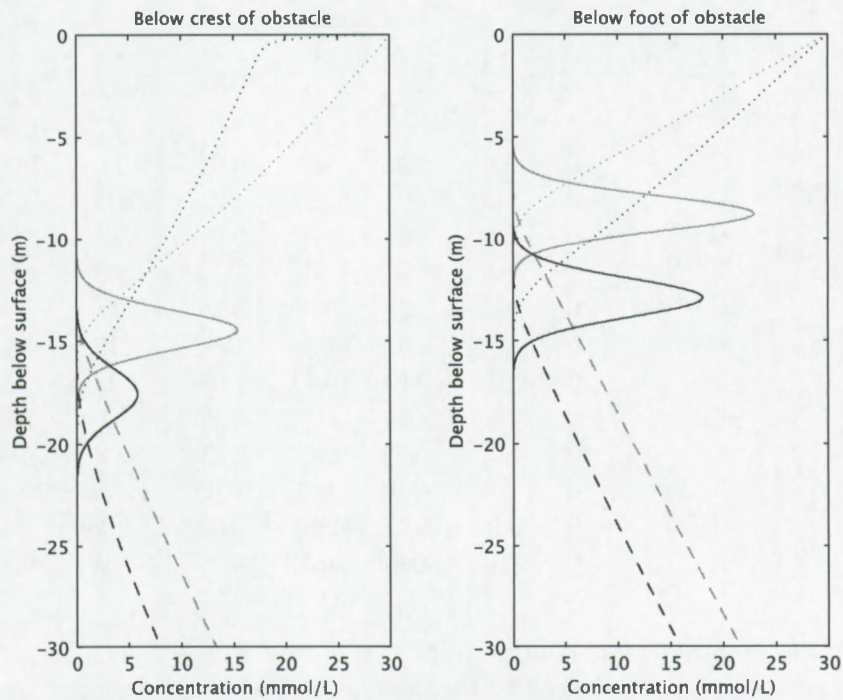
Figure 7.15: *SMTZ when moderate convective transport is active. The gray profiles indicate the situation as shown in figure 7.13. The black profiles represent the new situation, with advection. When the advective process becomes stronger, the SMTZ is pushed downward beneath feet and crest of the mound obstacle. In this situation, the amount of sulfate flushed into the mound is so high that methane reacts away before it can enter the mound structure.*
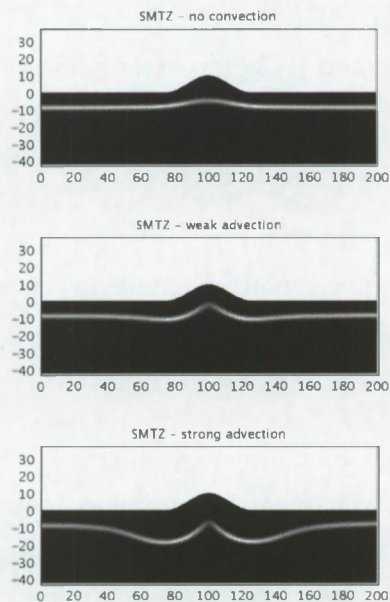
Figure 7.16: *2D representation of subsurface SMTZ of the profiles presented in figures 7.13, 7.14 and 7.15.*

			-log(K)						
		Position	11	10	9	8	7	6	5
Bottom current velocity (m.s^{-1})	0.01	C	0	0	0	0	0	0.02	0.28
		F	0	0	0	0	0	-0.01	-0.02
	0.02	C	0	0	0	0	0.01	0.11	1.03
		F	0	0	0	0	0	-0.01	-0.06
	0.05	C	0	0	0	0	0.07	0.67	2.24
		F	0	0	0	0	-0.01	-0.03	-0.62
	0.10	C	0	0	0	0.02	0.28	2.03	-2.84
		F	0	0	0	-0.01	-0.02	-0.18	-4.17
	0.2	C	0	0	0.01	0.11	1.03	1.2	-13.13
		F	0	0	0	-0.01	-0.06	-1.2	-19.2
	0.5	C	0	0	0.07	0.67	2.21	-9.08	N.S.
		F	0	0	-0.01	-0.03	-0.63	-12.71	N.S.
	1	C	0	0.02	0.28	2.03	-2.92	-23.06	N.S.
		F	0	-0.01	-0.02	-0.18	-4.19	-33.17	N.S.

Table 7.2: *Effect of the hydraulic conductivity and bottom current velocity on the position of the SMTZ below the crest and foot of the obstacle. Bold printed values indicate an upward shift of the SMTZ (in m); normal print indicates a downward shift of the SMTZ (in m). N.S.: No solution, because the whole model domain is flushed with seawater, due to the high hydraulic conductivity.*

salinity), or it is related to geological factors such as methane escape yielding carbonate hardgrounds which serve as settling grounds for corals.

Based on hypotheses by Hovland (1989) and Henriet et al. (1998) and supported by fluid flow modeling (Naeth et al., 2005) and their semblance to Phanerozoic mud mounds, it was deemed possible that enhanced fluid flow and microbial activity, or remnants thereof, would be encountered inside the mound body. The study of the carbonate mounds in the NE Atlantic culminated through drilling the Mound Challenger during IODP Expedition 307 during which 4 sites were visited. Dissolved methane concentrations were found to be low (below 0.2 μM) from the seafloor down to the mound base. Below this point, concentrations increase steeply up to values over 6 mM at 266 meters depth (IODP Expedition 307 Scientists, 2006). This observation is interpreted as a consequence of methane diffusion from deeper Miocene sediments and anaerobic methane oxidation near the mound base (IODP Expedition 307 Scientists, 2006). Furthermore, the microbial cell numbers is lower than average observations (IODP Expedition 307 Scientists, 2006; Parkes et al., 2000) in the upper 30 m of the mound designating this part of the mound as a low-activity site. With increasing depth, cell numbers and dividing cells increase slightly. At the level of the mound base, the cell count increases more rapidly and the rise in dividing cell numbers indicate active populations and suggest methane oxidation and/or methanogenesis occurring in the underlying Miocene silt and sandstones

Bottom current velocity		-log(K)								
		5	6	7	8	9	10	11	12	13
0.01	ΔP					-0.13				
	v	0.75	7.15×10^{-2}	7.15×10^{-3}	7.15×10^{-4}	7.15×10^{-5}	7.15×10^{-6}	7.15×10^{-7}	7.15×10^{-8}	7.15×10^{9}
0.02	ΔP					-0.5				
	v	3.11	0.3	2.86×10^{-2}	2.86×10^{-3}	2.86×10^{-4}	2.86×10^{-5}	2.86×10^{-6}	2.86×10^{-7}	2.86×10^{-8}
0.05	ΔP					-3.15				
	v	20.5	1.87	1.78×10^{-1}	1.78×10^{-2}	1.78×10^{-3}	1.78×10^{-4}	1.78×10^{-5}	1.78×10^{-6}	1.78×10^{-7}
0.1	ΔP					-12.61				
	v	84.39	7.87	7.50×10^{-1}	7.13×10^{-2}	7.13×10^{-3}	7.13×10^{-4}	7.13×10^{-5}	7.13×10^{-6}	7.13×10^{-7}
0.2	ΔP					-50.47				
	v	327.38	33.21	3.09	2.85×10^{-1}	2.85×10^{-2}	2.85×10^{-3}	2.85×10^{-4}	2.85×10^{-5}	2.85×10^{-6}
0.5	ΔP					-315.78				
	v	1778.04	208.91	20.35	1.87	1.78×10^{-1}	1.78×10^{-2}	1.78×10^{-3}	1.78×10^{-4}	1.78×10^{-5}
1	ΔP					-1263.88				
	v	5821.27	816.95	83.64	7.81	7.10×10^{-1}	7.10×10^{-2}	7.10×10^{-3}	7.10×10^{-4}	7.10×10^{-5}

Table 7.3: Effect of the hydraulic conductivity and bottom current velocity on the differential pressure [Pa] and outward fluid velocity on the differential pressure [Pa] and outward fluid velocity at the crest of the obstacle [m.s^{-1}].

(IODP Expedition 307 Scientists, 2006; Webster et al., 2008). Further interpretation of these data lead to the suggestion that 'hydrocarbon seepage is not a necessary condition for the development of a coral mound and very likely not for the Belgica mound province in general' (Ferdelman et al., 2006), although sulfur isotope data indicates the possibility of changes in depth of the sulfate-methane transition zone (SMTZ) (Ferdelman and Boettcher, 2007).

The observations have thus been used to rule out internal (or geological) processes as drivers of mound growth and bring the external (or ecological) factors forward as the main drivers, the oceanographic setting in this case. However, care must be taken to the observations when they are put in the perspective of an active system in which fluid flow is a major player. As it was shown in section 7.4, it is possible for methane seepage to be cut off at the base of a structure due to pore water convection cells within the structure.

The existence of such a situation is here tested. A situation is modeled in similarity to the Challenger Mound in the Porcupine Seabight, albeit strongly simplified. A mound shaped body (figure 7.17), 150 m high and 400 m wide at the base, is put onto a gently sloped surface and partly covered by a younger, gently sloped sedimentary unit. The lower unit consists of siltstone with a hydraulic conductivity of 1×10^{-8} m.s^{-1}. The upper unit consists of hemipelagic sediments with a hydraulic conductivity of 1×10^{-11} m.s^{-1}. Actual parameters are not known but these numbers were chosen to reflect the lithology (Bear, 1972). Although the mound contains large amounts of clay and silt, in this model a higher hydraulic conductivity was chosen because it is known that coral frameworks, coral rubble and moldic and vuggy porosity yield a much higher effective hydraulic conductivity compared to the sediment in which they are buried. Also, because the mound features a layered internal structure, the effect of hydraulic anisotropy (favouring horizontal flow) is tested for a factor of 5 to 1 (horizontal to vertical). The isotropic hydraulic conductivity is set to 1×10^{-7} m.s^{-1} and 1×10^{-6} m.s^{-1}. The subsurface fluid flow is driven by the effect described in section 7.4 (seafloor current driven convection). Seafloor currents were reported at another mound in the Porcupine Seabight (Galway MoundDorschel et al. (2007)) and indicated average speeds up to 20 cm/s with peak velocities of 50 cm/s. the seafloor current is set to 0.2 and 0.5 m.s^{-1}. To model the geochemical profiles, the lower edge at 300-500 m was imposed a methane concentration of 50 mmol.L^{-1}. The seafloor served as a boundary with a sulfate concentration of 30 mmol.L^{-1}.

When no seafloor current is acting, the SMTZ is present well within the mound structure. At a seafloor current speed of 0.2 m.s^{-1}, it was observed that the SMTZ was somewhat deepened below the flanks of the mound and shallowed below it's top. To invoke a shut-off of the mound from methane inflow (SMTZ at the base of the mound), it was needed to increase hydraulic conductivity to 1×10^{-5} m.s^{-1}. At a current speed of 0.5 m.s^{-1}, shut-off was reached at hydraulic conductivities of 1×10^{-6} m.s^{-1} and even strongly enhanced when the horizontal hydraulic conductivity was set to 5×10^{-5} m.s^{-1}.

This modeling exercise shows that either at rather strong seafloor currents or at high effec-
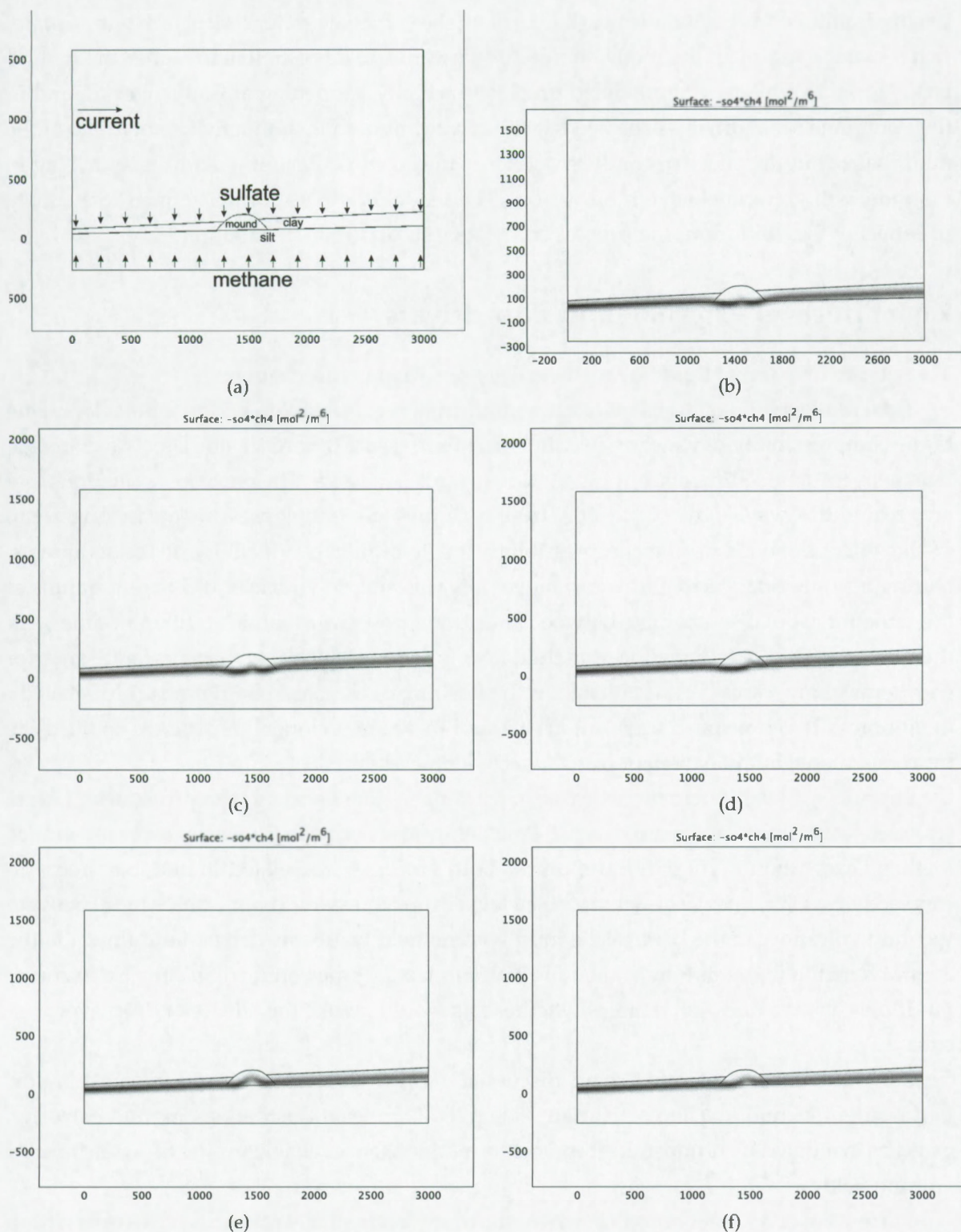
Figure 7.17: *Position of sulfate-methane transition zone under a carbonate mound at different environmental and hydraulic conditions. a) No advective sulfate or methane transport. b) seafloor current speed: $0.2 \ m.s^{-1}$; hydraulic conductivity: $1 \times 10^{-5} \ m.s^{-1}$. c-f) Seafloor current speed: $0.2 \ m.s^{-1}$; hydraulic conductivity: (c-d) $1 \times 10^{-6} \ m.s^{-1}$, (e-f) $1 \times 10^{-7} \ m.s^{-1}$. c) & e) isotropic hydraulic conductivity, d) & f) anisotropic hydraulic conductivity. See text for more information.*

tive hydraulic conductivity it is possible to flush the carbonate mound structure with sulfate-rich seawater and push the methane front downwards, to a position at or under the mound base. To know whether the modeled process is actually happening at Challenger mound in the Porcupine Seabight, it will be needed to know the hydraulic conductivity, not (only) of the mud matrix but the effective conductivity. Only future work, including additional drilling in mounds, will give conclusive information. The model has to be further refined to evaluate the effect of the fluid pumping process on the genesis of carbonate mounds.

7.6   Effects of external fluid flow drivers

Three types of external fluid flow drivers were regarded in this chapter.

Tidal sea-level fluctuations invoke a semi-diurnal pressure difference on the seafloor. Due to the compressibility of water and sediments, this pressure difference does not travel instantaneously into the sediments, but travels downwards as a wave. The pressure oscillations that are created this way, invoke fluid flow from high pressure to low pressure areas. The depth of this effect depends on the compressibility and hydraulic conductivity of the sediments. During a single tidal cycle, fluids can move upwards and downwards at different depths at the same time, but also alternate between an up- and downward mode at different times. Although integrated over time, the total fluid flow is zero, this effect can have a significance for geochemical processes because it enables the flushing of chemical compounds through sediment pores. This can speed up reactions because these are no longer depending on diffusive processes alone, but may benefit from advective processes.

Eustatic sea-level fluctuations act at much longer time and larger depth scales. Large-scale sea-level drops can create overpressure below low permeability layers and may induce methane exsolution in mud volcano pipes. Both processes are related to possible mud volcano activity. First, it was shown that a sea level drop alone would not be able to (re)activate the mud volcanoes in the El Arraiche mud volcano field by deeply driven fluid flow. On the contrary, methane exsolution in the mud volcano feeder pipe could trigger the extrusion of mudflows, yet the question remains whether this would invoke the release of deep overpressure.

Consequently, the internal drivers discussed in previous chapter remain the most important factors for mud volcano activation. The role of sea level fluctuations in mud extrusion could be evaluated if chronostratigraphic information were available for the El Arraiche mud volcano field.

Currents over a seafloor obstacle where shown to create small-scale convective cells within the obstacle. Depending on geometric and hydrogeological parameters, such a process is capable of flushing the obstacle with seawater. In areas where methane is present in the pore fluids and relatively close to the seafloor, it was shown that the sulfate-methane transition zone can actually be pushed downwards. A case study considering the Mound Challenger

showed that the absence of observed methane within the mound could be explained by such a fluid pumping model, although a better hydrogeological understanding of such a mound structure is needed to evaluate how realistic this scenario is. The flushing of sediments with sulfate and the control on the SMTZ depth will also regulate the depth where carbonate crusts are formed. In the future, more detailed modeling should be done to evaluate this process in other settings where carbonate crusts are formed, e.g. the Pen Duick Escarpment.

Part IV

Conclusions

Chapter 8

Conclusions

The El Arraiche mud volcano field is a prime area to study a large number of mud volcanoes, fluid flow processes and the geological environment in which these fluid flow features occur. The area is located on the continental slope of the city of Larache (El Arraiche) in NW Morocco. In a broader sense, the study area is part of the Gulf of Cadiz (Atlantic Ocean). The area had been charted in detail for the first time in 2002 during the Cadipor campagne onboard R/V Belgica. A few months later, extensive seafloor sampling was done with the R/V Professor Logachev (Unesco Training Through Research Programme; TTR-12). Since these initial efforts, the site has evolved into a research ground involving a multidisciplinary approach, combining geophysical, sedimentological, microbiological, numerical and other studies.

- Initially, on the basis of multibeam bathymetric data, side-scan sonar data and high-resolution seismic profiling data, a description of the surface and shallow subsurface morphologies, structures and stratigraphy of the El Arraiche mud volcano field, was made.

  The largest and shallowest mud volcano, Al Idrisi mud volcano, is nearly 250 m high, with the top at only 200 meters water depth. On the slopes of the structures, mud lobes extending from the crater area are recognized and evidence past events during which mud is being extruded from the crater. Mud flows that once deposited at the foot of a mud volcano, also appear in the subsurface on seismic profiles. These bodies are characterized by a chaotic signal because no internal structure is present. This indicates that the mud volcanism is a long-lived and recurring process

  Other mud volcanoes in the area also bear witness of recent and past activity. At the surface, the expression can somewhat differ: Mercator mud volcano has a dome-shaped crater and a stepped terrace morphology, and one mud lobe running down the flank. Fiuza mud volcano is also characterized by different mud lobes at the surface. In the subsurface, all mud volcanoes show buried mud flows. Correlation of the mud flow events between the different mud volcanoes showed that mud extrusion events did not occur exactly simultaneously, however, on a larger time scale (at the level of stratigraphic subunits), the mud volcano activity in the region was strikingly in concert. The onset of the mud volcano activity in absolute terms is uncertain, although it is possible that the first activity appeared shortly after the event responsible for the Quaternary Discontinuity.

  Around the mud volcanoes, large moats are observed, both at the surface as well as buried in the subsurface. The orientation of these moats was observed to be dominantly E-W, which is believed to indicate a strong E-W oriented seafloor current. This was confirmed by near-seafloor current meter observations

  Large ridges, running in a NW-SE direction over tens of kilometers, stand out at the

seafloor by tens of meters and thus draw attention. The two westernmost ridges have been named Renard Ridge (south) and Vernadsky Ridge (north). A third buried seafloor ridge occurs east of Al Idrisi mud volcano. All ridges plunge towards the W or NW. The crests of the ridges all show collapse features to a variable degree. On seismic profiles, normal faults can be observed beneath the ridge crests. Along these faults, many bright spots and areas with accoustic blanking indicate the presence of shallow gas which also adds evidence for fluid migration in the sediments.

The ridge structures consist of a low amplitude seismic facies and is topped by a seismic unconformity. On top of that, mostly parallel seismic units occur with small internal unconformities; these units are believed to be of Plio-Pleistocene age. On the basis of these unconformities, 9 (sub)units were identified. The age of the deepest unconformity is unconstrained at this moment, disallowing a reliable chronostratigraphy.

At several places along the ridges, small mounded seafloor elevations were observed on seismic and bathymetric data. Seafloor sampling showed that in many cases, these small mounds corresponded to patches of mostly dead deepwater corals. The largest examples are found at the top of a seafloor cliff called Pen Duick Escarpment: the cliff is topped by a series of coral buildups of more than ten meter high, as a relic of a past, more viable period. The corals have been found between depths from 700 meters (the deepest part of Vernadsky Ridge) to 200 meters (east of Al Idrisi mud volcano). It is striking that all these mounded features occur near or on a culmination. Circumstances must be, or have been, such that certain current patterns encouraged deepwater coral growth in these spots.

Based on a few observations and morphological similarities, it is suggested that salt sheets exist deep beneath the Plio-Pleistocene units. The morphology of the seafloor ridges (with anastomizing substructures), as well as the subsurface structure known from line-drawings based on industrial-type data, which resembles salt rollers known from the Gulf of Mexico; the presence of salt and gypsum crystals and brines in the crater of Mercator mud volcano, plead for a mechanism that drives the Tertiary tectonic history but also influences the mud volcanism: the process of halokinesis.

- Carbonate crusts and chimney samples were retrieved from several sites in the Gulf of Cadiz, spanning different environments (mud volcanoes and sedimentary environments). Insight in the parental fluids and genetic processes of the different samples were to be revealed using geochemical and mineralogical analyses.

Lithified mud breccia crusts sampled from Kidd mud volcano on the Moroccan margin have been formed in two modes: an aerobic mode during which aragonite is precipitated in voids and fractures, and an anaerobic mode, linked to sulfate reduction during which pyrite and microdolomite formed. These two modes alternated, which

is evidenced by different phases of fracturing and (re)cementing. The parental fluid is thought to be deep-sourced because of the mud volcano setting and isotopic indications for the oxidation of thermogenic methane. Heavy oxygen is interpreted as derived from gas hydrate destabilization or clay dehydration.

Nodular crusts from Meknes mud volcano have a high-Mg calcite mineralogy, and microdolomite and pyrite is present. All this suggests a formation under reducing conditions, within the sulfate reduction zone. Geochemical and isotopic data bear evidence of similar fluids involved as for the Kidd mud volcano.

Dolomitic crusts from Pen Duick Escarpment are pieces of lithified host sediment with variable inclusion of allochems and bioclasts. The formation of the crusts is linked to the seepage and oxidation of thermogenic methane, coupled to sulfate reduction, as evidenced by pyrite (and iron oxihydroxide) occurrence. Bioclast dissolution is thought to be a late product of pyrite oxidation which creates acidity.

Carbonate crusts and chimneys from the Mediterranean Outflow Area are Fe-dolomite / ankerite micrite cemented sandstones with evidence of multiple episodes of carbonate precipitation in small bioclasts, fine fractures and around allochems, after an initial cementation event that lithified the sediment. Recrystallization of bioclasts and other components did not take place, however. The precipitation of these samples must have taken place under slightly elevated temperatures, or influenced by the destabilization of gas hydrates.

Carbonate crusts and chimneys from the Hesperides mud volcano on the Iberian margin are mostly Fe-dolomite / ankerite cemented mud- to wackestones, stained by iron oxides that likely are derived from the oxidation of pyrite. High-Mg calcite crusts also occur. There is evidence of different phases of carbonate precipitation. The samples from this site are the only ones in which microbial methane is inferred as one of the dominant carbon sources, apart from other sources. Here also, heavy oxygen isotope compositions can only be explained by inferring gas hydrate stabilization or clay dehydration.

From the geochemical observations, it is difficult to propose conclusive evidence about the growth mode of carbonate chimneys. However, indications exist that the carbon isotope composition of the parental fluid is changing over time. In radial sense, we have not observed petrographic differences in the matrix cement of the chimneys. This might indicate that the main lithification or cementation probably takes place in one phase, during which the elemental geochemical characteristics of the parental fluid does not change much over time.

The results indicate a high variability in environments of carbonate precipitation in the Gulf of Cadiz: mud volcanoes, carbonate mound and fault-related environments and

sedimentary environments. Carbonate chimneys versus carbonate crusts bear evidence of precipitation in a focused fluid flow versus a more diffuse gas-charged fluid. Differences in mineralogy have provided indications about the relative speed of precipitation and the position with regard to the subsurface geochemical zonation. Carbon and oxygen isotopic data has revealed the existence of different types of parental fluid components that are involved in the formation of these crusts and chimneys: seawater versus fluids derived from gas hydrate destabilization or clay dehydration as oxygen sources; thermogenic versus biogenic methane, but also possibly organic matter and marine dissolved inorganic carbon as carbon sources.

After obtaining these geophysical, geochemical and mineralogical evidences of past and present fluid flow occurring at different scales and under different conditions, it is worth looking at how these fluid flow processes take place, and at what time scales. Part of this can be achieved through numerical modeling.

The fluid flow processes have been divided in two large classes: internal fluid flow drivers versus external fluid flow drivers. Internal drivers are defined as a force or pressure gradient that is created inside the sediment body while external drivers invoke fluid flow processes inside the sediments from outside the sedimentary environment.

- **Internal fluid** flow drivers generate a pressure gradient inside a sediment body and can have different origins. The most important however are density differences and overpressure. Density driven fluid flow is based upon the fact that heavier fluids sink while lighter fluids will rise in sediments. Changing the density of a fluid can be achieved in two ways: either the mass of a unit volume of fluid is changed (e.g. by dissolving a small amount of salt in a volume of water), or by changing the volume of a certain mass of water (e.g. by thermally expanding a fluid through heating). Density driven fluid flow is known from diapiric processes (mud diapirism, salt diapirism), bubbling of gas and oil droplets at the seafloor, ...

  Overpressure in sediments is created when fluid removal from sediments is ineffective upon compaction (undercompaction, disequilibrium compaction). This typically happens under conditions of rapid sedimentation or tectonic compression. An alternative process is the inflow of oil or gas in a sealed permeable layer which increases pressure in the pores due to its lower density.

- The occurrence of large mud volcanoes on the northwest Moroccan margin conveys of the presence of overpressure in the subsurface. On the Moroccan margin, at least two important factors can be identified that play a role in the generation of overpressure: thermal cracking of hydrocarbons leading to oil and gas generation and dehydration of clays. The overpressured mud is piercing the overburden, at least partly controlled by structural features (related to the top of the accretionary wedge). This process is driving

the mud volcano formation and long-lived activity. Given the evidence for a halokinetic influence in the region, salt diapiric processes cannot be excluded.

• The upward fluid flow along faults and in mud volcano feeder pipes will have consequences for the thermal and geochemical environment in the sediments. For the geothermal field, the effect of fluid flow velocity, porosity, time source depth was taken into account.

Modeling of the fluid flow velocity showed that the upward fluid flow in sediments has a major impact on the geothermal profile near the seafloor: in this area the conductive heat flux is more important at low fluid flow velocities than the advective heat flux; at high fluid flow velocities, advective heat flux becomes more important. Geothermal measurements over a short depth profile near the seafloor will therefore not resolve the geothermal situation deeper in the sediments. Such measurements can thus lead to overestimation of the geothermal gradient. Therefore, the effect of fluid flow should always be considered during the interpretation of such data.

The importance of the porosity model on heat flux clearly depends on what is being aimed at. The temperature profiles were very similar for two different porosity models (a compacting model with decreasing porosity with depth and a constant porosity model). Therefore, the porosity model is not so critical for the temperature profile itself. However, for the heat flux calculations, porosity plays a more important role and should be taken into account.

The simple transient cooling model of a mud volcano feeder pipe indicated that if no or a small residual fluid flow is present, a steady state temperature profile is reached in less than 10000 years over a depth of 1000 meters. At high residual fluid flow velocities (or continued activity), high temperatures remain constant throughout the mud volcano feeder pipe; only in the shallowest portions of the sediment (in the order of meters to tens of meters), cooling can be observed.

The depth of fluid mobilization has a direct consequence for the geothermal field if we suppose that in a no-flow situation temperature increases linearly with depth (the geothermal gradient). Thus, the depth of the source fluid will impact the temperature of the rising fluid, and thus the advective heat flux. However, at low fluid velocities, this effect is rather small.

• In this work, the most relevant geochemical process is the formation of carbonates related to the anaerobic oxidation of methane coupled to sulfate reduction. Model results indicated that the anaerobic methane oxidation zone shallows with increasing upward fluid flow velocity, as expected. When the advected methane is highly concentrated, the reaction zone very quickly travels towards the seafloor. The depth of the formation of carbonate crusts is thus strongly controlled by the strength of the upward fluid

flow in the sediments. Precipitation of chimneys and crusts from the different mud volcano craters from which results were reported, can indeed only occur near the seafloor if there is an active upward fluid flow. If not, the process would take place at much deeper sites in the sediments and not easily be accessed in sampling efforts. Carbonate crusts and chimneys from an exhumed site formed at deeper positions must thus have formed under slower fluid flow conditions. Therefore, it could be suggested that chimney formation is rather an expression of preferential fluid flow pathways rather than strong and focussed fluid flow.

In model exercises, it was shown that fluid flow velocities caused by tidal sea-level fluctuations can reach 3 mm per day. The effect on the subsurface geochemical environment are important because it flushes pore waters up and down and thus will facilitate mixing. This may be beneficial for micro-organisms living at specific redox-boundaries in the sediments.

- An application of thermal field calculations in a mud volcano crater was done by calculating a gas hydrate stability field in Mercator mud volcano. An anomalous reflection (H event) has been observed in shallow mud volcanoes on the Moroccan margin. The H event was mapped in the Mercator mud volcano and was interpreted as the base of a gas hydrate stability zone, based on its inverse polarity and the fact that it mimics the seafloor away from the mud volcano's crater. Inside the crater, the H event is absent. This was supported by the fact that gas hydrate stability modeling with reported thermogenic gas compositions, indicated that gas hydrates can be stable at this shallow location. BSR inferred heat flow showed a concentric heat flow pattern around the crater, with a very sharp rise in heat flow near the crater, consistent with the interpretation that the gas hydrate layer is affected by a focused flow of warm fluid in the crater. Modeled heat flow values near the crater edge run up to $1100 mWm^{-2}$ and must be still higher inside the crater. Although this is very high compared to background heat flow values, it is not abnormal for mud volcanoes. The absence of a bottom simulating reflection in the surrounding sediments may be explained by a low regional methane flux through the sediments. Consequently, dewatering of the accretionary wedge complex is mainly focused along fault surfaces and through seafloor structures, such as mud volcanoes.

- **External fluid flow drivers** are defined as drivers essentially acting outside the sedimentary environment, even though these drivers create a subsurface pressure gradient in the subsurface – which drives fluid flow. Three types of external fluid flow drives were regarded: tidal sea level changes (short time span and low amplitude), eustatic sea level changes (long time span and high amplitude) and water currents over seafloor obstacles and the thereby induced pressure effects.

- For tidal sea-level fluctiations to drive subsurface fluid flow, the compressibility of wa-

ter and sediments must be taken into account. If no compressibility would exist, all pressure changes due to the sea level change would occur instantaneously and thus no pressure differences over depth would be generated. A stable pressure does not invoke fluid flow. Howeer, with compressibility taken into account, subsurface fluid flow will be generated. Modeling a 2 m tidal sea level fluctuation showed that fluid flow can alternate between upward and downward fluid flow, and that up- and downward flow can co-exist at a single time at different depths in the sediment. It can be shown that in a permeable environment, geochemical advective transport near the surface is effective. In low-permeable sediments, the advective flux is still equal in magnitude as diffusive fluxes.

- Large-scale sea level fluctuations over long time spans, such as eustatic sea level changes, will invoke completely different fluid flow related processes.

  A (relative) sea level fall can create excess pore pressure in sealed sediments. The reason is that the seal prevents pressure re-equilibration. As a consequence, effective stress decreases below the seal. If effective stress was low already due to pre-existing overpressure (e.g. with presence of gas), then the sea level fall could trigger hydrofracturing processes.

  Based on this, the question whether eustacy can be a trigger of mud volcano activity in the region. Hydrofracturation and/or reactivation of pre-existing mud an fluid mobilization pathways had to be regarded. It was shown that in extensional regimes, both hydraulic extension fractures and normal shear fractures can develop in the shallow subsurface under hydrostatic conditions. Deeper in the sediments, this is not possible without overpressure. For cracks to form, near the seafloor, a certain tensile strength is needed and since loose sediments lack this strength, the requirements for fracture formation will never be met. A compact 'strong' seal however may break up due to overpressure generated below it. In case of the El Arraiche mud volcano field, the potential mud source should be shallow. In combination with deep-sourced rock clasts, it is unlikely that a sea level drop alone will start mud volcano activity and should therefore be assisted by other processes, e.g. the production of gas.

  An other mechanism influenced by a sea level fall is the exsolution of gasses. In a mud volcano feeder pipe, where large amounts of dissolved methane may be expected, the sea level fall may induce the creation of gass bubbles. This leads to a volume increase or pressure increase and it can be expected that this will be able to cause a pressure and density driven upward migration of the gas bearing matrix. Once this process has started, the gas exsolution will actually accellerate while the gas bearing mud is rising in the feeder pipe. Thus, a sea level drop may trigger mud flow extrusion at the seafloor.

- A last external fluid flow driver is a seafloor current over a seafloor obstacle. The process

of bed-form generated convective transport in sediments is projected to a larger scale than what is known from literatures: seafloor obstructions such as carbonate mounds, steep seafloor 'cliffs', etc. will affect the local current patterns in terms of pressure and velocity. Near-seafloor pressure imbalances will, analogous to small scale structures like sand ripples, produce subseafloor fluid convection. Because the pressure effects are active on a larger scale, the advective transport will be felt down to a greater depth. The importance of the advective process was assessed by modeling the effect on the sulfate-methane transition zone (SMTZ).

The numerical model for this exercise was built up by a velocity-pressure model (including turbulence) over a seafloor obstacle, coupled to a subsurface darcian fluid flow model with transport-reaction equations to model the geochemical environment.

Over a hill-shaped obstacle, seawater is pulled into the sediments near the foot of the obstacle and extruded near the crest of the obstacle. This convective cell can influence the sulfate-methane transition zone below the obstacle. Depending on the strength of the flow and the geometry of the obstacle, the SMTZ will be pulled upwards or pushed downwards beneath the crest of the structure and pushed downwards beneath the foot of the structure.

The model has been applied to carbonate mound settings in general and to the Challenger mound off Ireland specifically. The modeling exercice showed that either at rather strong seafloor currents or at high effective hydraulic conductivity it is possible to flush the carbonate mound structure with sulfate-rich seawater and push the methane front downwards, to a position at or under the mound base. This result may be of importance for understanding the geochemical observations that were made during the IODP Expedition 307 inside and below the Challenger mound

Chapter 9

Samenvatting

Deel 1: Algemeenheden

Hoofdstuk 1 : Inleiding

1.1 Vloeistofstromingen doorheen de zeebodem en moddervulkanen

De zeebodem vormt de grens tussen het oceanische milieu en het sedimentaire milieu. Deze twee omgevingen worden gekenmerkt door specifieke chemische en fysische evenwichten en processen. De zeebodem vormt dus niet enkel een grens, maar vooral een overgang van het oceanische naar het sedimentaire milieu.

Vloeistofstroming doorheen de zeebodem is een proces waarbij vloeistoffen van het oceanische milieu in het sedimentaire milieu terechtkomen, en omgekeerd. Aangezien vloeistoffen chemische stoffen bevatten en een bepaalde warmte meedragen, zal vloeistofstroming doorheen de zeebodem zorgen voor transport van chemische stoffen en warmte tussen de oceanische en sedimentaire milieus.

De voornaamste oorzaak van vloeistofstroming doorheen de zeebodem is het voorkomen van een ondergrondse verschil in densiteit van vloeistoffen of het voorkomen van drukverschillen. Voorbeelden hiervan zijn temperatuursverschillen, productie van gas, differentiÃñle belasting van een begraven sedimentlichaam, saliniteitsverschillen tussen twee vloeistoffen,...

Een specifiek type van vloeistofstroming doorheen de zeebodem wordt waargenomen ter hoogte van moddervulkanen. Moddervulkanen worden gevormd als gevolg van de uitstoot van vloeistoffen, modder en stukken gesteente aan het oppervlak (hetzij op land, hetzij onder water). Het uitgestoten materiaal wordt modder breccia genoemd en stroomt typisch uit de krater van de moddervulkaan. Vooraleer het materiaal uitgestoten wordt, komt het aan het oppervlak na getransporteerd te zijn vanuit diepere sedimentlagen doorheen de aanvoerpijp. De reden voor dit transport is het bestaan van overdruk in de diepere sedimentlagen. De uitgestoten modder breccia vormt na verloop van tijd een kegelvormige structuur die zeer grote afmetingen kan aannemen.

De geografische verspreiding van moddervulkanen is voornamelijk verbonden met geologische situaties waarbij de vorming van overdruk of ondercompactie in de begraven sedimenten optreedt; dit is in gebieden met actieve tektoniek of waar orogenese aan de gang is, waar hoge sedimentatiesnelheden voorkomen en waar gasproductie voorkomt. Op dit ogenblik zijn wereldwijd ongeveer 900 moddervulkanen op land en 800 moddervulkanen onder water gekend. Langs de volledige Alpijnse gordel komen moddervulkanen voor: in het westen in de Golf van Cadiz, in de Alboran Zee, in de Adriatische Zee, in en om Griekenland (deels gerelateerd aan de hydrothermale uitstoot in de regio), langsheen de Mediterrane Rug in het oosten van de Middellandse Zee, op de Nijl Delta, in de Zwarte Zee... Verder oostelijk worden moddervulkanen gevonden langs de Iraans-Pakistaanse kusten, India, de Zuid-Chinese Zee, voor de kusten van Brunei en Vietnam, Hongkong en Taiwan. Ter hoogte van de Banda Boog (zuid-oost AziÃñ) en de Timor Zee, alsook voor de kust van Nieuw Zeeland werden moddervulkanen en gasuitsijpelingen waargenomen. In de Atlantische Oceaan is een veelvuldig bestudeerde moddervulkaan de Håkon Mosby voor de kust van Noorwegen. Langs de Afrikaanse kust zijn moddervulkanen onder andere geobseveerd ter hoogte van de Niger Delta. In andere delen van de wereld zijn vloeistofstromingsprocessen even goed gekend; de Westelijke Stille Oceaan, Alaska, de westkust van de Verenigde Staten, ... Een regio die tevens zeer veel moddervulkanisme kent is de Golf van Mexico. Bijgevolg kan gemakkelijk gesteld worden dat het proces van moddervulkanisme een wereldwijd fenomeen is.

1.2 Doel en kader

Het algemene doel van dit werk is een bijdrage te leveren tot de studie van de migratie en expulsie van fluïda aan de zeebodem, meer specifiek in relatie tot moddervulkanisme.

Het studiegebied in dit werk is de Golf van Cadiz. Dit gebied wordt gekenmerkt door het voorkomen van een accretiewig-achtig sedimentlichaam ten westen van de Straat van Gibraltar. Bovenop deze sedimentwig komen vele vloeistofexpulsie structuren voor: gasuitsijpelingen, korsten van verharde sedimenten, moddervulkanen,... De aanwezigheid van metaangas in de sedimenten uit moddervulkanen wijst erop dat er recente activiteit is geweest. Een seismische studie van een provincie van grote moddervulkanen op de Marokkaanse continentale rand kan inzichten leveren in de dynamiek en ontstaan van moddervulkanen in de regio.

Verharde sedimenten zijn gevonden in zones waar ondiep methaangas en vloeistofstromingen doorheen de zeebodem voorkomen; het onstaan van de verhardingen lijkt dus verbonden met het voorkomen van het gas en vloeistofstromingen. Een vergelijkende studie van verharde sedimenten van verschillende locaties kan inzichten leveren in de verschillende types vloeistoffen die aan de basis van het ontstaan van de verhardingen liggen.

Tenslotte worden de observaties en resultaten in een meer algemeen kader geplaatst door

numerieke simulatie-oefeningen uit te voeren die ertoe dienen het potentieel van de vloeistofmigratie oorzaken op thermisch en geochemisch vlak te evalueren.

1.3 Projectkader

Het werk dat hier wordt voorgesteld kadert in verschillende internationale projecten: EC FP5 Research and Training Network EURODOM (2002 - 2005), EC FP6 Integrated Project HERMES (2005 - 2009), ESF EUROMARGINS MoundForce (2003-2006), ESF EUROMARGINS MVSeis (2003 - 2006), ESF EURODIVERSITY Microsystems (2006 - 2008), FWO GeNesis (2003 - 2008).

Hoofdstuk 2 : Geologische achtergrond van het Ibero-Maghrebijns Domein

2.1 Geografie

Het studiegebied van dit werk beslaat de Golf van Cadiz, een deel van de oostelijke Atlantische Oceaan, tussen Spanje en Marokko, ten westen van de Straat van Gibraltar. Langs de Spaanse continentale rand komen canyons voor. In het centrale deel van de Golf komen lobvormige topografische structuren voor met onregelmatige, geaccidenteerde oppervlakken die gekenmerkt worden door breuklijnen – de geomorfologie op zich verraadt al een complexe geologische geschiedenis en structuur. Het zuidelijk deel van de Golf van Cadiz wordt gekenmerkt door een grote depressie – de canyon van de Rharb Vallei.

Het meest opvallende kenmerk van de regio is de boogvormige gebergtegordel die het zuiden van Spanje en het noorden van Marokko beslaat: de Betiden - Rif Boog. Hoogtes van meer dan 1000 m worden slechts enkele tientallen kilometers landinwaarts gevonden. Ten noorden en ten zuiden van de gebertegordel komen grote bekkens voor : het bekken van de Guadalquivir in Spanje en het Rharb bekken in Marokko.

2.2 Oceanografie

De oceanografische situatie in de Golf van Cadiz is relevant voor het begrijpen van sedimentatiepatronen in het studiegebied. De meeste oceanografische studies zijn echter in het noorden van de Golf gedaan langs de Spaanse continentale rand.

Een van de belangrijkste factoren in het stromingspatroon in de Golf van Cadiz is de uitwisseling van waters tussen de Middellandse Zee en de Atlantische Oceaan langs de Straat van Gibraltar. Warm en zout water stroomt uit de Middellandse Zee naar de Atlantische Oceaan, terwijl koud en minder zout water de MIddellandse Zee instroomt.

Een tak van de Golfstroom loopt langs de westkust van het Iberisch schiereiland zuidwaarts naar de Canarische eilanden. Een aftakking hiervan stroomt echter de Golf van Cadiz binnen. Een deel hiervan stroomt de Straat van Gibraltar in, terwijl een ander deel langs de Marokkaanse rand stroomt. Deze stromingen komen voor aan het oppervlak.

Onder deze oppervlaktestromingen stroomt warm en zout water uit de Middellandse Zee en splitst in verschillende takken, hoofdzakelijk in drie grote takken: naar het noorden langs de Spaanse continentale rand, centraal in de Golf van Cadiz en naar het zuidwesten tot aan de Canarische eilanden. Verder is er nog het Noord-Atlantisch Diep Water; het is een koude stroming die uit het noorden van de Atlantische Oceaan komt en deels mengt met het warme water dat uit de Middellandse Zee komt gestroomd. In het zuidelijk deel van de Golf van Cadiz komen sterke seizoenale stromingen voor en zorgen voor opstuwing van koude nutriÃńntrijke waters.

In 2005 werden tijdens de 'Moundforce 2004' campagne aan boord van de R/V Pelagia in het studiegebied op de Marokkaanse continentale rand stromingssnelheden opgemeten tot 25 centimer per seconde aan de zeebodem.

2.3 Geologie

De Golf van Cadiz bevindt zich aan het westelijke uiteinde van het Alpijns vervormings-front tussen EuraziÃń en Afrika. Daarnaast werd de geologie ook beÃŕnvloed door riftings-en spreidingsprocessen die in verband stonden met het openen van de Atlantische Oceaan. Verdere complexiteit wordt toegevoegd door de aanwezigheid van een accretiewig-achtig lichaam, massabewegingen en vermeende subductie onder de Straat van Gibraltar.

Het ontstaan en de evolutie van de Atlantische Oceaan, alsook de convergentie van Eu-raziÃń en Afrika zijn belangrijk voor het begrip van de geologie van de Golf van Cadiz. Zeebodemspreiding trad op vanaf 180 miljoen jaar (Ma) geleden in de Centrale Atlantische Oceaan en rond 140 Ma in het zuiden van de Noordelijke Atlantische Oceaan. De spreiding van de westelijke Tethys Oceaan had tegen het begin van het Jura gezorgd voor de spreid-ing van Africa en Iberia. Een *triple junction* in de buurt van de Gorringe Bank zorgde voor de scheiding van Noord Amerika, Afrika en Iberia. Het duurde echter tot het begin van het Tertiair om de scheiding van de continentale korsten volledig te voltrekken en te resul-teren in voornamelijk passieve continentale randen. Vervolgens zorgde de noordwaartse drift van Afrika voor het sluiten van de oceanische bekkens van de westelijke en centrale Tethys Oceaan en het Alpijns deformatie front bereikte de regio van de huidige Golf van Cadiz. Rond het Eoceen-Oligoceen werden dan ook de interne zones van de Betische - Rif gordel gevormd. Verdere compressie zorgde voor een verkorting van 200 km. In het Pleistoceen gebeurde een belangrijke opheffing in het gebied van de Straat van Gibraltar, terwijl subsidentie voorkwam ter hoogte van het Rharb bekken. Huidige spanningspatronen tonen een N-Z tot NW-ZO gerichte compressie aan, wat correspondeert met een verdergaande convergentie van Afrika en EuraziÃń.

In de laatste decennia zijn twee benaderingswijzen gevolgd om de structuur en geschiede-nis van de Golf van Cadiz te verklaren; een stratigrafisch-structurele benadering (op land) een een geofische benadering (op zee). Dit heeft geleid tot verschillende, zelfs tegengestelde

inzichten van het gebied.

De structuur van de Betische-Rif gebergteketen en de bijhorende voorlandbekkens (Guadalquivir en Rharb bekkens) worden door verscheidene modellen verklaard, gaande van botsings-gebergten, over subductieprocessen tot de aanwezigheid van microcontinenten. Michard et al. (2002) stellen een geÃ¯ntegreerd model voor waarbij het gebogen gebergte bestaat uit een exotisch blok (het Alboran blok, voordien deel van het Alkapeca microcontinent) dat op de Iberische en Afrikaanse plaat werd geduwd en nu de meest interne zones van de gebergteketen vormen. Hierbij traden subductieprocessen op van zowel de Iberische als Afrikaanse plaat, wat ook in tomografische studies wordt aangetoond. Aan de externe zij-de van de gebergteketen werd hierbij een accretiewig gevormd en op het flexurale voorland geschoven. Finaal wordt gesteld (Chalouan and Michard, 2004) dat de Golf van Cadiz een *triple junction* vormt van het type subductie-subductie-transformbreuk door de twee subduc-tiezones ten westen van het Alboran blok te verenigen in de Azoren-Gibraltar transform-breuk. De accretiewig (de externe zone van de Betische - Rif gordel) werd gevormd tot het Laat Tortoniaan, waarna zowel gravitationele instorting van het accretielichaam voorkwam (met vorming van de *olistostroom van de Golf van Cadiz* als subsidentie en milde extensie door flexurale buiging.

Seismische studies tonen ook aan dat het *offshore* gedeelte van de Golf van Cadiz het resul-taat is van drie belangrijke processen: extensie vanaf het Trias tot Laat Krijt; de westwaartse beweging van het Alboran Blok (zie hierboven) en tenslotte de vorming van de chaotische nappe tijdens het Tortoniaan. Latere studies hebben meer details over deze chaotische nappe naar voor gebracht. Het noordelijk en centraal deel van de Golf van Cadiz kan in drie stukken opgedeeld worden: a) in het oosten komen zout en klei lagen waarop extensionele inzakking is gebeurd. Dit komt overeen met de zeewaartse verderzetting van de externe delen van de Betische-Rif gordel. b) Het centrale gebied bestaat uit allochtone eenheden (massabewegin-gen) die tijdens het Tortoniaan gevormd werden. c) In het westen komen overschuivingen voor, die met het front van de accretiewig overeenstemmen. Aan de Marokkaanse kant van de Golf van Cadiz zijn minder gegevens gekend. Echter, Flinch et al. (1996) interpreteren de algemene structuur van de Marokkaanse continentale rand als die van een accretiewig als gevolg van een westwaartse beweging van het Alboran domein.

Hoofdstuk 3: Methodologie

3.1 Geofysische gegevens

De ondergrond wordt met seismiek in beeld op een wijze die relevant is voor de herken-ning van hoge-resolutie stratigrafie en structuren. De methode steunt op het uitsturen van een akoestische impuls en de opname van de echo hiervan. De puls wordt gereflecteerd op verscheidene geologische oppervlakken, bijvoorbeeld lithologische grenzen. De voornaam-ste akoestische bron die in dit werk werd toegepast is een *multi-electrode sparker*, waarbij de

akoestische puls wordt opgewekt door een sterke elektrische ontlading. Na opname van de ruwe gegevens, dienen een reeks filters toegepast te worden om de de gegevens klaar te maken voor interpretatie: compensatie voor de golfbeweging van het zee-oppervlak, *bandpass* filtering om laag- en hoogfrequente ruis te verwijderen, deconvolutie en versterking.

Andere geofysische gegevens omvatten zgn. multibeam dieptebepalingen voor het maken van 3-dimensionele dieptekaarten; side scan sonar metingen waarbij een akoestisch beeld van de zeebodem zelf wordt gemaakt.

3.2 Mineralogische en geochemische gegevens

De carbonaatgesteenten werden op verscheidene wijzen geanalyseerd. X-straal diffractometrie werd gebruikt voor de identificatie van de meest aanwezige mineralen in de stalen. Bulk analyse van verpulverde stalen werden geochemisch geanalyseerd met behulp van Atom-air Absorptie Spectrometrie (AAS). De elementen die bepaald werden waren Ca, Mg, Fe, Al, Mn, Sr, Na, K, Zn en Pb. Stabiele isotopen van koolstof en zuurstof werden bepaald op kleine stalen die uit de stalen genomen werden met een tandartsboor. Deze metingen laten toe de herkomst van de vloeistoffen die betrokken zijn bij de vorming van de carbonaten, te bepalen. Tenslotte werden slijpplaatjes gemaakt om de stalen ook microscopisch te analyseren. Dit gebeurde zowel met gewoon doorvallen en opvallend licht, met koude-cathodeluminescentie. De stalen werden ingebed in epoxyhars en de slijpplaatjes deels gekleurd met een Alizarin Red S - K-ferricyanide mengsel.

3.3 Numerieke methodes

De meeste, zoniet alle fysische processen kunnen uitgedrukt worden als (partiële) differentiaalvergelijkingen. Dit soort vergelijking drukken de wijziging van grootheden uit in de tijd en ruimte. De oplossing van deze vergelijkingen vormen een tak van de wiskunde op zich; ondanks dit kunnen de meeste vergelijkingen niet exact opgelost worden. Daarom worden numerieke benaderingsmethodes toegepast. In dit werk wordt hiertoe de Eindige-Elementen Methode (Finite Element Method) toegepast. In deze methode wordt het gebied waarover de oplossing dient berekend te worden, opgedeeld in een eindig aantal elementen. Op de knooppunten (nodes) van die elementen worden door een zgn. Galerkin discretizatie, functies bekomen voor het berekenen van de oplossing van de vergelijking op dat ene punt. Door alle functies te koppelen aan een groep van randvoorwaarden wordt het mogelijk om een precies resultaat te berekenen in alle knooppunten van de elementen, en bij benadering dus voor het hele continue gebied waarop de (partiële) differentiaalvergelijking van toepassing is. Er werd gebruik gemaakt van de Comsol Multiphysics software voor het uitvoeren van numerieke simulaties.

De numerieke simulaties werden in verschillende onderwerpen toegepast: de modelering van ondergrondse vloeistofstroming (wet van Darcy), turbulente stromingen van vloeistof-

fen over een obstakel (K-Epsilon turbulentiemodel), een transportvergelijkingen. De transportvergelijkingen hadden betrekking op het transport (en reactie) van chemische stoffen in grondwater en op het transport van warmte.

Deel 2: Bewijzen voor vloeistofstromingen in verleden en heden

Hoofdstuk 4: Geofysische bewijzen voor vloeistofstroming: het El Arraiche moddervulkaan veld

4.1 Structuur van het oppervlak en de ondiepe ondergrond.

De oppervlaktemorfologie en -structuur van het El Arraiche moddervulkaan veld wordt best beschreven aan de hand van multibeam bathymetrische gegevens en side scan sonar gegevens. De meest prominente zeevloerstructuren zijn de grote cirkelvormige heuvels die 25 tot 250 meter uitsteken boven de zeebodem. Op basis van sedimentologische gegevens, werden deze structuren geÃ¯dentificeerd als moddervulkanen.

De grootste moddervulkaan is de Al Idrisi moddervulkaan; deze beslaat met een diameter van 4.5 tot 6 kilometer een gebied van meer dan 20 vierkante kilometer en is ongeveer 250 meter hoog. Bovenaan bevindt zich een krater met een diamter van 1.35 kilometer. De flanken zijn 4 tot 10 graden steil. Aan het oppervlak kunnen verscheidene modderstromen geÃ¯dentificeerd worden; deze lopen radiaal van de krater weg eindigen aan of tegen de voet van de flank als een lobvormig lichaam.

De Mercator moddervulkaan bevindt zich op de zuidelijke flank van een NW-ZO gerichte rugstructuur (de Vernadsky Rug). De Mercator moddervulkaan is 140 meter hoog en bedekt een gebied van 5 vierkante kilometer. Er is aan de top geen krater aanwezig, maar wel een koepelvormige structuur. De flanken van de moddervulkaan hebben een terras-morfologie, quasi concentrisch rond het centrum van de moddervulkaan. Aan de westkant is ook een modderstroom zichtbaar. Ten noordwesten van de Mercator moddervulkaan bevindt zich de Kidd moddervulkaan. De Kidd moddervulkaan ligt op de noordelijke flank van de Vernadsky Rug. De hoogste flank van de Kidd moddervulkaan is meer dan 180 meter hoog. De bathymetrische gegevens onthullen verder niet veel meer over de morfologie.

Ten zuiden van de Kidd moddervulkaan ligt de Adamastor moddervulkaan met een typische kegelstructuur. De moddervulkaan heeft een oppervlakte van ongeveer 5 vierkante kilometer en een hoogte van 160 meter. Er zijn ook modderstromen aanwezig op de flanken. Een krater lijkt afwezig te zijn.

Verder zuidwaarts bevindt zich de Renard Rug: een NW-ZO gerichte rugstructuur op de zeebodem. Met deze rug zijn verscheidene moddervulkanen geassocieerd: de Fiuza moddervulkaan (140 meter hoog), Gemini moddervulkaan (een tweeledige moddervulkaan met twee kegelvormige culminaties met een totale oppervlakte van 11 vierkante kilometer en een

hoogte tot 250 meter). Verder komen ook nog kleinere structuurtjes voor: de Lazarillo de Tormes moddervulkaan en de Don Quichote moddervulkaan.

De reeds vermelde rugstructuren (Vernadsky Rug, Renard Rug) zijn structuren die over een afstand van 30 km tot 150 meter boven de zeebodem uisteken; de breedte ervan is 5 tot 10 kilometer. De toppen van de ruggen duiken naar het noordwesten. De noordelijke rug is de Vernadsky Rug. In het westen zijn kleine heuvelachtige structuurtjes (100-400 m diameter, 10 meter hoog) aanwezig bovenop de rug. Op basis van videogegevens is geweten dat dit culminaties zijn die bestaan uit dode diepwaterkoralen. De zuidelijke rug is de Renard Rug. Halfweg de rug komt een 7 kilometer lange klif voor waarop kleine heuvelstructuurtjes staan. De klif wordt de Pen Duick Escarpment genoemd. De heuvelstructuurtjes bestaan uit voornamelijk dode diepwaterkoralen. In een aantal van deze heuvels is ondiep metaan waargenomen.

Ook ten oosten van de Al Idrisi moddervulkaan, in het meest ondiepe deel van het studiegebied, komt een rugstructuur aan het oppervlak. De topografie is er onregelmatig en ook hier werden diepwaterkoralen bemonsterd van wat kleine culminaties lijken te zijn.

Verspreid in het gebied komen depressies voor: rond moddervulkanen en langsheen de ruggen. De meeste van deze depressies zijn W-O tot NW-ZO gericht. Deze dominante richting van de depressies kan erop wijzen dat deze depressies erosiegeulen zijn gevormd door een sterke W-O tot NW-ZO gerichte stromingscomponent.

De gegevens van oppervlaktewaarnemingen zijn gecompileerd in figuur 4.8.

De seismische gegevens laten toe ondiepe breuken, scheuren, plooi- en andere structuren te herkenen. Verder brengen deze gegevens de ondiepe stratigrafie in beeld.

Vooreerst is een regionale onconformiteit gekozen als basisreflector als referentieniveau in het gebied. Op veel plaatsen wordt deze reflectie gekenmerkt door een matig tot hoge amplitude met een lokaal erosief karakter. Onlap structuren worden er soms bovenop waargenomen. Om deze redenen lijkt de reflectie een grens met enige geologische betekenis te vormen, vermoedelijk in termen van relatieve zeespiegelveranderingen. De dieptekaart van deze basisreflector laat toe de grootschalige structurele kenmerken te onderscheiden: de rugstructuren worden gescheiden door diepe bekkens (figuur 4.10).

Op basis van de assocatiatie van de meeste moddervulkanen met de rugstructuren lijkt er een genetische relatie te bestaan tussen de structuur van de ruggen en het voorkomen van de moddervulkanen: de uiteindes van de kleine boogvormige rug- of klifstructuurtjes die binnen de grote Renard Rug worden waargenomen kunnen zones van verhoogde permeabiliteit vormen en/of structureel zwakke zones waar fluÃ¯da preferentieel opwaarts migreren: de Gemini moddervulkaan komt voor op het uiteinde van een dergelijke boogvormige klif (Pen Duick Escarpment), en ten zuiden van een tweede boogvormige klif. Op het oostelijk einde van deze tweede klif komt Don Quichote moddervulkaan voor. Ook Al Idrisi moddervulkaan komt voor op het westelijk uiteinde van een begraven rug. Op het einde van de Pen Duick Escarpment werden ook ondiepe methaanfronten waargenomen onder de koraalheuvels, ter-

wijl centraal langsheen deze structuur het methaanfront beduidend dieper voorkwam.

Op de kruin van de ruggen vertonen zeer veel normale breuken met kleine tot zeer grote verplaatsingen (meer dan 300 ter hoogte van de Kidd moddervulkaan). Het lijkt er op dat de centrale delen van de ruggen zijn ingestort, wat een compensatie kan zijn voor het sediment dat werd verwijderd door moddervulkaanactiviteit, of als gevolg van buiging van de ruggen (flexurale extensie).

Op welke manier de rugstructuren in verbinding staan met dieper gelegen structuren, kan niet achterhaald worden op basis van de in dit werk beschikbare gegevens. Echter, in het werk van Flinch (1993) worden onder het studiegebied de aanwezigheid van begraven geroteerde blokken aangetoond, in een kader van lokale extensionele tektoniek. Deze blokken worden begrensd door diepe lystrische breuken. De posities van de kruinen van deze blokken lijken overeen te komen met de posities ruggen aan de zeebodem. De aanvoer van fluïda langs de lystrische breuken kan het voorkomen van de moddervulkanen verklaren. Dit hypothetisch verband beantwoordt echter niet alle vragen: het model van Flinch verklaart de kleine boogvorme kliffen niet en het voorkomen van quasi-cirkelvormige structuren aan de westelijke uiteinden van de Renard en Vernadsky Ruggen wordt niet verklaard. Deze laatste structuren zouden echter diapirische structuren kunnen zijn. Niet enkel klei- maar ook zoutdiapirsme zou in aanmerkingen kunnen komen. Immers, grote gipskristallen en pekels zijn teruggevonden in de krater van de Mercator moddervulkaan, wat er op wijst dat zout in de ondergrond aanwezig is. Kleine boogvormige ruggen en kliffen worden ook typisch gevormd in een setting waar diapirisme optreedt, maar dan niet in circulaire lichamen, maar onder de vorm van bladstructuren. Ook de profielen in het werk van Flinch (1993) lijken sterk op profielen van gebieden waar extensionele tektoniek samen met halokinese en moddermobilisatie voorkomt. Een dergelijk tektonisch scenario voor het studiegebied zou verder onderzocht dienen te worden.

Ondiepe seismo- en chronostratigrafie Op basis van de seismische gegevens werden 3 grote sedimentaire eenheden herkend, telkens opgedeeld in sub-eenheden. In andere stratigrafische interpretaties in de Golf van Cadiz Cadiz (hoofdzakelijk op de Spaanse shelf) werden dergelijke eenheden gerelateerd aan 3e en 4e orde zeespiegelschommelingen. Het is echter niet mogelijk gebleken om de enige bron van chronostratigrafische informatie (LAR-1 boring, een tiental kilometer landwaarts) te verbinden met de dataset.

Echter, de kleine onconformiteiten in de seismische data zouden kunnen de grenzen van verschillende prograderende clinoformen voorstellen en aggraderende lagen van een of meer stratigrafische sequenties gerelateerd aan de 3e en 4e orde zeespiegelschommelingen. Van de in totaal tien sub-eenheden zouden er negen passen in een model met de 100000-jarige cyclus van na de Mid-Pleistocene Revolutie. In dit geval zou een sedimentatiesnelheid nodig geweest zijn tot 25 cm per 1000 jaar, wat onrealistisch hoog is.

Om sluitende informatie hieromtrent te bekomen, is een chronostratigrafische studie voorgesteld in het IODP boorproject IODP Pre-692 "Mud volcanoes as a window into the deep biosphere" (Depreiter et al., 2006) waarbij geboord zal worden in en om de Mercator moddervulkaan.

4.2 Ondiepe stratigrafie.

Op seismische profielen zijn modderstromen zichtbaar die doorheen de geschienis werden afgezet en vervolgens bedekt door jongere sedimenten. De positie van deze modderstromen in de stratigrafische sequentie liet toe te bepalen wanneer (in relatieve termen) elke moddervulkaan actief was geweest. Door correlatie van de modderstromen tussen de verschillende moddervulkanen bleek dat de extrusie-gebeurtenissen niet precies gelijktijdig liepen; maar, op een grotere tijdsschaal (op het niveau van de sub-eenheden) bleek de activiteit van de verschillende moddervulkanen opvallend overeen te komen. Verder in dit werk worden hypotheses opgesteld over processen die moddervulkaan activiteit kunnen aansturen.

Vanuit de seismische gegevens blijken erosiegeulen steeds diepst te zijn wanneer modderstromen voorkomen en dat ze veel ondieper zijn in tijden van gewone sedimentatie. Verder werd ook de evolutie van de erosiegeulen rond de moddervulkanen bekeken. Het blijkt dat de meeste erosiegeulen oost-west gericht zijn wat kan wijzen op een sterke oost-west gerichte stromingen. Ook nu zijn sterke oost-west gerichte getijdenstromingen verantwoordelijk voor de vorming van erosiegeulen.

Hoofdstuk 5: Geochemische en petrologische bewijzen van vloeistofstroming: carbonaatkorsten en -schouwen

5.1 Inleiding: authigene carbonaten

Authigene carbonaten worden gevormd in sedimenten waar opgelost carbonaat oververzadigd is, en de alkaliniteit voldoende hoog. Dit kan veroorzaakt worden door de anaerobe oxidatie van methaan; een microbieel proces dat gekoppeld is aan sulfaatreductie. De producten van dit proces zijn meestal korstvormige stukken geconsolideerd gastgesteente.

In dit werk worden de stabiele isotopensamenstelling van koolstof en zuurstof gebruikt om de bron van de koolstof en zuurstof aanwezig in de carbonaatmineralen, te achterhalen. Verder worden petrografische en mineralogishe technieken gebruikt om het type carbonaten te identificeren.

5.2 Bemonsteringsplaatsen

Carbonaatkorsten en -schouwen (verwijzend naar de vorm) werden op vier plaatsen bemonsterd. Deze plaatsen zijn 1) moddervulkanen op de Marokkaanse continentale rand (Kidd MV en Meknes MV), 2) een steile helling (Pen Duick Escarpment) die gerelateerd is aan de rugstructuren, aanwezig aan de zeebodem in het studiegebied, 3) een erosief sedimentaire

omgeving ten westen van Tanger en 4) een moddervulkaan op de Spaanse continentale rand (Hesperides MV).

5.3 Resultaten

Petrografie en XRD   De korsten die bemonsterd werden op Kidd moddervulkaan hebben variabele afmetingen en onregelmatige vormen. De korsten bestaan uit versteende modderbreccie (een mengsel van modder en stukken gesteente uitgestoten door de moddervulkaan) met een lichtbruine tot grijze kleur. De korsten worden gekenmerkt door vele openingen, scheuren en barsten die gevuld zijn met sedimenten en cementen. De korsten die bemonsterd werden op Meknes moddervulkaan zijn broze grijze nodulaire korstjes tot 10 cm groot. In doorschijnend licht bestaan de korsten van Kidd moddervulkaan uit een chaotische textuur van modderige aragoniet micriet met daarin drijvend een kleine hoeveelheid micritische peloiden en bioclasten. Van belang is ook de waarneming van pyriet en wolken van ijzer oxihydroxiden die het gesteente roestbruin kleuren. In breuken komen o.a. naaldvormige aragonietwaaiers voor. Onder cathodeluminescentie vallen een aantal kleine rode kristallen op (microdolomiet). De algemene aragonietmineralogie wordt bevestigd door XRD metingen. De gesteenten kunnen algemeen geclassificeerd worden als fossielhoudende intrapelmicrieten. De korsten vanop Meknes moddervulkaan bestaan uit een fijne grijze microsparitische matrix met weinig micritische peloiden, bioclasten en gesteentefragmenten). De porositeit van de korsten is zeer hoog. Kleine hoeveelheden microdolomiet komen ook hier voor.

De korsten vanop 'Pen Duick Escarpment' bestaan uit grijze tot bruine versteende siltige modder met een variërende hoeveelheid bioclasten. De korsten zijn matrixgedragen, fossielhoudende micritische kalkstenen. Ijzer oxihydroxiden kleuren het gesteente bruin; deze zijn een resultaat van pyrietoxidatie. De algemene mineralogie betreft laag- en hoog-Mg calciet en dolomiet.

De korsten en schouwen van ten westen van Tanger ('Mediterranean Outflow Area') zijn gevormd door cementatie van zanden. De gesteenten zijn zeer hard en kleuren geel-bruin. De textuur betreft micritische matrix-gedragen fossielhoudende gecementeerde zand en siltstenen met een aantal accessorische mineralen. De carbonaatmineralen bestaan uit dolomietankeriet micriet die zwak oranje-bruine luminescentie vertoont. In fossielen zijn verschillende fasen van carbonaatcementen waargenomen.

De carbonaatkorsten en -schouwen vanop Hesperides moddervulkaan zijn zeer divers in vorm en grootte. De meeste stalen hebben een 1 mm dikke buitenste donkerbruine rand, bestaande uit ijzer oxihydroxiden. De stalen bestaan uit oranje-bruine micritische tot microsparitisch carbonaat matrix met drijvende sedimentkorrels en bioclasten. De luminescentie van de matrix is zwak oranje. Vele breuken doorsnijden de stalen; deze zijn vaak gevuld met gelijkaardig materiaal als de gesteenten zelf. Fijnkorrelig pyriet komt frequent voor, soms deels geoxideerd. Microdolomiet is eveneens waargenomen. Over het algemeen bestaat de

carbonaatfase in deze stalen uit dolomiet-ankeriet.

Geochemie (AAS)   De resultaten van de geochemische bulk-analyse staan vermeld in tabel 5.1.

De stalen van op de Marokaanse moddervulkanen hebben de hoogste Ca en Sr gehaltes en laagste Mg en Fe gehaltes. De Mg/Ca verhouding is laag, terwijl de Sr/Ca hoog is; dit is in overeenstemming met de aragonietmineralogie.

De stalen van 'Pen Duick Escarpment' hebben hoge Ca en lage tot matig hoge Mg gehaltes en weinig Fe. De Sr/Ca verhoudingen zijn laag, en de Mg/Ca intermediair tot hoog.

De stalen van de 'Mediterranean Outflow Area' hebben lage Ca en Sr gehaltes en eerder hoge Mg en Fe gehaltes. De Mg/Ca zijn intermediair tot hoog, de Sr/Ca verhoudingen laag.

De stalen van de Hesperides moddervulkaan hebben eveneens lage Ca en Sr gehaltes maar hoge Mg en Fe gehaltes. Net als de hoge Mg/Ca en lage Sr/Ca verhouding, is dit in overeenstemming met de mineralogische verschillen tussen de stalen van de verschillende gebieden.

Stabiele isotopen (koolstof, zuurstof)   De $\delta^{13}C$ van de korsten van de Marokkaanse moddervulkanen liggen tussen -30 en -19 ‰. De $\delta^{18}O$ waarden liggen tussen +2 en +5 ‰. De stalen van 'Pen Duick Escarpment' vallen ook binnen deze waarden. De stalen van de 'Mediterranean Outflow Area' hebben een gelijkaardige $\delta^{18}O$ signatuur, maar de $\delta^{13}C$ is iets minder laag: -5 tot -25 ‰.

De stalen van Hesperides moddervulkaan hebben een $\delta^{18}O$ signatuur tussen +4.3 en +7 ‰een een zeer brede waaier aan $\delta^{13}C$ waarden : tussen -15 en -50 ‰.

5.4 Interpretatie en bespreking

De versteende modderbreccie korsten van Kidd moddervulkaan werden gevormd in twee modi: een aerobe modus waarbij aragoniet neersloeg in poriën, holtes en scheuren, en een anaerobe modus gekoppeld aan sulfaatreductie waarbij pyriet en microdolomiet werd gevormd. De bron van koolstof is te vinden in methaan, meest waarschijnlijk thermogeen van oorsprong alhoewel een biogene component niet kan uitgesloten worden. De zuurstof aanwezig in de carbonaten wijst op destabilisatie van gashydraten of dehydratatie van diep begraven kleien.

De nodulaire korsten van de Meknes moddervulkaan suggereren eerder een vorming onder gereduceerde omstandigheden binnen de sulfaatreductiezone. De vloeistofbronnen zijn gelijkaardig aan deze in de Kidd moddervulkaan.

De dolomitische korsten van 'Pen Duick Escarpment' zijn gevormd onder invloed van oxidatie van vermoedelijk thermogeen methaan, gekoppeld aan sulfaatreductie.

De carbonaatkorsten en schouwen uit de 'Mediterranean Outflow Area' zijn ijzerdolomiet of ankeriet micriet gecementeerde zandstenen die verschillende fasen van precipitatie aan-

tonen. De vorming moet onder licht verhoogde temperatuur plaatsgevonden, of onder de invloed van de destabilizatie van gashydraten.

De korsten en schouwen van op Hesperides moddervulkaan zijn de enige stalen waar een invloed van microbieel methaan met zekerheid kan aangetoond worden. De zware zuurstofisotopische samenstelling kan enkel verklaard worden door gashydraatdestabilisatie of klei dehydratatie.

Deze resulaten tonen aan dat in de Golf van Cadiz een hoge variabilitiet in omgevingen bestaat waar carbonaten neerslaan. Carbonaatschouwen geven een blijken van een eerder gefocuste vloeistofstroming, terwijl de korsten eerder lijken gevormd uit diffuus methaan. De isotopische gegevens hebben verschillende vloeistoftypes aangeduid die betrokken zijn in de vorming van deze gesteenten: zeewater tegenover water afkomstig uit gashydraatdestabilisatie of kleidehydratatie; thermogeen tegenover biogeen methaan, maar eveneens organisch materiaal en marien opgelost anorganisch koolstof.

Deel III: Gevolgen van vloeistofstromingen

Hoofdstuk 6: Interne bronnen van vloeistofstromingen

6.1 Inleiding

Een vloeistof stroomt als gevolg van een drukverschil in de vloeistof zelf. De vloeistof stroomt van gebieden van hoge druk naar gebieden van lage druk.

De oorzaken van deze drukverschillen kunnen opgesplitst worden in twee types: 1) interne oorzaken, en 2) externe oorzaken. Interne bronnen van drukverschillen worden hier gedefinieerd als bronnen die zich in de sedimentaire omgeving zelf bevinden, zoals gasvorming, dehydratatie van kleien of andere mineralen,... Externe bronnen van drukverschillen zijn dan die bronnen die buiten de sedimentaire omgeving liggen: zeespiegelbewegingen, stromingen over de zeebodem, ... De gevolgen van deze verschillende oorzaken van vloeistofstromingen zullen in dit en volgend hoofdstuk gemodeleerd worden.

6.2 Interne bronnen van vloeistofstromingen: een overzicht

Er zijn twee belangrijke interne bronnen van vloeistofstromingen: dichtheidsverschillen en overdruk. Dichtheidsverschillen in een vloeistof kunnen veroorzaakt worden door verandering in volume of een verandering in massa van een hoeveelheid vloeistof. Als voorbeeld van een massaverandering kan het oplossen van zout in water gegeven worden; het volume verandert niet of weinig terwijl de massa van het volume water duidelijk toeneemt. Een volumeverandering kan bijvoorbeeld veroorzaakt worden door thermische expansie.

Overdruk ontstaat bij begraving van sedimenten waarbij de poriënvloeistoffen niet vol-
doende snel kunnen ontsnappen terwijl het sediment compacteert. Hierbij kan een situatie
ontstaan waarbij een vloeistof opgesloten wordt in het sediment en het gewicht van boven-
liggende lagen moet dragen. Dit proces wordt ondercompactie genoemd.

6.3 Overdruk op de NW Marokkaanse continentale rand

Het voorkomen van moddervulkanen op de NW Marokkaanse rand toont aan dat er over-
druk bestaat in de diepe ondergrond. Er kunnen in dit gebied twee belangrijke factoren
aangeduid worden die leiden tot overdruk vorming.

Het thermisch kraken van koolwaterstoffen waarbij gas en olie gevormd worden, leiden
tot overdruk. Uit seismische data weten we dat gas aanwezig is in de sedimenten in de buurt
van de moddervulkanen, en uit de analyse van de carbonaatkorsten blijkt dat methaan aan
de basis ligt van de vorming van deze gesteenten. Verder wordt in de literatuur ook bewijs
gevoerd voor de vorming van olie en gas.

Een tweede factor is de dehydratatie van kleien. Literatuurstudie toont aan dat in mod-
dervulkanen in de buurt, dehydratatie de voornaamste bron van vloeistofproductie is. Dit
proces vindt plaats op een diepte van ongeveer 5 km.

Deze twee processen hebben samen een groot potentieel voor overdrukvorming. De pre-
cieze bronlaag kan echter door de structuur van de accretiewig niet vastgelegd worden.

6.4 Modeleren van de gevolgen van interne bronnen van vloeistofstromingen

Geothermische gevolgen Er werd nagegaan op welke wijze opwaartse vloeistofstromingen
het thermisch veld in een moddervulkaan zullen beÃfnvloeden. Verschillende parameters
werden aan modelering onderworpen en leidt tot verscheidene conclusies:

De resultaten tonen aan dat bij vloeistofstromingen sneller dan 1 mm per jaar, advectief
warmtetransport belangrijker wordt dan conductief transport en dat hierdoor het geother-
misch profiel vervormd wordt. De opwaartse fluïdamigratie in sedimenten heeft een grote
impact op het thermisch profiel nabij de zeebodem. Geothermische metingen over een ondiep
profiel zullen niet representatief zijn voor de situatie dieper in de sedimenten. Dergelijke
metingen zullen dus de geothermische gradient overschatten indien geen rekening wordt
gehouden met vloeistofstromingen wanneer dergelijke data geïnterpreteerd worden.

De invloed van een gedetailleerd porositeitsmodel is minder belangrijk voor e berekening
en interpretatie van een temperatuursmodel. Echter, voor berekeningen met de warmteflux,
dient er toch aandacht aan geschonken te worden.

Er werd ook nagegaan wat het effect van een residuele vloeistofstroming is na een sterke
uitstoot van vloeistoffen op het opnieuw in temperatuursevenwicht komen van de sedimenten.
Als vergelijkingspunt werd die situatie genomen waarbij geen residuele vloeistofstroming is:
het blijkt dat er tussen 1000 en 10000 jaar nodig zijn om een nieuw thermisch evenwicht te

bereiken. Bij kleine vloeistofstromingen is er geen groot verschil met deze situatie. Bij sterke stroming zal het stabiele temperatuursprofiel op zich al vervormd zijn, en dus wordt deze evenwichtssituatie sneller bereikt (in minder dan 1000 jaar als er nog een stroming aanwezig is van 1 m per jaar.

Tenslotte werd ook aangetoond dat de brondiepte van de vloeistofmigratie zelf ook van groot belang is, aangezien met toenemende diepte de temperatuur stijgt.

Geochemische gevolgen   De invloed van opwaartse vloeistofstromingen op de diepte van de sulfaat-methaan transitie zone (SMTZ) werd nagegaan. In het kader van dit werk is dit belangrijk aangezien anaerobe oxidatie van methaan plaats vindt in deze zone. Anaerobe oxidatie van methaan is een van de processen die leidt tot de vorming van carbonaatkorsten.

De modeloefeningen tonen aan dat als gevolg van opwaartse vloeistofstromingen de SMTZ mee naar boven beweegt. Een zwakke vloeistofstroming van 1 mm per jaar is al in staat om een SMTZ die zich aanvankelijk op 50 m diep bevond, te verplaatsen naar een diepte van 30 m. Bij stroomsnelheden van 10 cm per jaar of hoger komt deze zone vlakbij de zeebodem zelf te liggen, wat betekent dat het methaan niet geconsumeerd wordt voor het aan de zeebodem ontsnapt.

De vorming van carbonaatkorsten nabij de zeebodem, zoals eerder aangehaald, is dus inderdaad mogelijk onder invloed van een opwaarste vloeistofstroming.

6.5 Gevalstudie: gashydraatstabilitiet in Mercator moddervulkaan

Gashydraten in moddervulkanen worden klassiek waargenomen in sedimenten op water-dieptes van 1000 m en dieper. In deze gevalstudie werd de observatie van een seismische anomalie onder de flanken van de Mercator moddervulkaan, belicht. De anomalie werd geïnterpreteerd als de basis van een gashydraat stabiliteitszone om wille van de inverse po-lareit van het akoestisch signaal. Modelering van de druk-temperatuur omstandigheden, met specifieke gassamenstellingen, toonde aan dat gashydraten de diepte van minder dan 500 m eveneens stabiel kunnen zijn. Het model levert een beeld van het thermisch veld in en om de krater van de moddervulkaan en suggereert door diens hoge waarden een effectieve vloeistofmigratie doorheen de krater van de moddervulkaan.

6.4 Gevolgen van interne bronnen van vloeistofstromingen

In dit hoofdstuk werden de geothermische en geochemische effecten van interne vloeistof-stromingsbronnen gemodeleerd. Alle vloeistofmigratie werd gemodeleerd als ware het ges-tuwd door diepe overdruk.

Om de geothermische effecten in kaart te brengen, werden een aantal parameters gevarieerd. De belangrijkste impact bleek veroorzaakt te zijn door de snelheid van de vloeistofstroming zelf.

Er werd ook aangetoond dat opwaartse vloeistofstroming geladen met methaan inderdaad in staat is om de SMTZ naar de zeebodem te duwen. Carbonaatkorsten, als gevolg van anaerobe oxidatie van methaan, kunnen dus inderdaad aan de zeebodem zelf gevormd worden onder invloed van een dergelijke opwaartse stroming.

Hoofdstuk 7:

7.1 Inleiding

Externe vloeistofmigratiebronnen worden gedefinieerd als processen die actief zijn in de waterkolom, maar leiden tot drukverschillen in de sedimenten. De gevolgen van drie verschillende processes zullen gemodeleerd worden: getijden, eustatische zeespiegelbewegingen en zeebodemstromingen.

7.2 Getijden

Getijden zijn zeespiegelbewegingen met een kleine amplitude en korte periode (ongeveer 12 uur). Het op en neer bewegen van de waterkolom zorgt voor kleine drukvariaties aan de zeebodem. Indien water en sedimenten niet samendrukbaar zouden zijn, zouden deze kleine drukvariaties onmiddellijk in de sedimenten doorgegeven worden en zou er nergens drukonevenwicht ontstaan. Echter, sedimenten en water zijn effectief samendrukbaar. Het gevolg hiervan is dat een drukverandering aan de zeebodem geleidelijk wordt doorgegeven in de sedimenten – er ontstaat als het ware een drukgolf. Doorheen de tijd beweegt de zeespiegel op en neer, wat zal leiden tot het ontstaan van een reeks van drukgolven die neerwaarts, in de sedimenten voortbewegen. Het gevolg van de kleine drukvariaties op verschillende dieptes is dat er kleine vloeistofstromingen zullen ontstaan. Met de getijdenbewegingen zullen de vloeistoffen nu eens opwaarts, dan weer neerwaarts bewegen. Het netto resultaat van de vloeistofstroming is dan op zich wel nul, de beweging op zich kan wel van belang zijn voor chemische en microbiologische processen. Immers, de vloeistofbeweging advectief transport in gang zet en daarmee processen die normaal afhangen van diffusie alleen, aanzienlijk kan versnellen.

7.3 Eustatische zeespiegelbewegingen

Als de zeespiegelbewegingen nu groter worden gemaakt, en de periodes veel langer, dan komen we in het domein van de eustatische zeespiegelbewegingen terecht. Deze bewegingen kunnen hoogteverschillen meebrengen van 50 meter in 10000 jaar. De beweging is dus veel trager, maar tevens veel groter dan die van getijden. De gevolgen zijn van een heel andere aard. Ten eerste speelt de samendrukbaarheid van water en sedimenten hier geen rol meer omdat het over een traag proces gaat. Echter, een significante zeespiegeldaling is wel in staat om (bijkomende) overdruk te creëren in afgesloten lagen. Een gevolg van deze overdruk is

dat de effectieve spanning in het gesteente van die laag zal afnemen en daardoor kan leiden tot hydrofracturatie, het opbreken van de gesteenten. Er wordt verder nagegaan of dit proces kan leiden tot het ontstaan of heractiveren van moddervulkanen.

Een bijkomend effect van een sterke zeespiegeldaling is zogenaamde methaanexsolutie. Er kan verwacht worden dat in een moddervulkaanpijp veel opgelost methaan aanwezig is in de poriënwaters. Omdat de oplosbaarheid van gassen afhankelijk is van druk, kan een drukdaling ertoe leiden dat opgelost methaan wordt omgezet in gasvormig, vrij methaan. Hiermee gaat een aanzienlijke volumetoename gepaard, wat gaat leiden tot het uitstuwen van gas, water en modder uit de moddervulkaan krater.

Modderstromen en moddervulkaan activeit: een eustatische oorzaak? De vraag of moddervulkanen actief kunnen worden als gevolg van een significante zeespiegeldaling werd bestudeerd. Berekeningen tonen aan dat in het geval van het El Arraiche moddervulkaan veld, enkel extensiebreuken zouden kunnen gegenereerd worden in een ondiepe bronlaag. Dit resultaat is problematisch ten aanzien van verschillende waarnemingen weergegeven in de literatuur, waardoor een dergelijke situatie als onwaarschijnlijk kan bestempeld worden. Het ontstaan van moddervulkanen kan niet alleen aan een zeespiegeldaling te wijten zijn. Ook heractivatie van moddervulkanen kan in een dergelijk model niet verklaard worden. Overdruk als gevolg van dehydratatie en thermische kraakprocessen blijft daarmee de meest waarschijnlijke oorzaak van moddervulkanisme in het studiegebied.

7.4 Zeebodemstromingen

De stroming van een vloeistof langs een obstakel zal aanleiding geven tot het ontstaan van snelheids- en drukvariaties langsheen dat obstakel. De stroming van zeewater over een heuvel aan de zeebodem zal leiden tot een lagedrukgebied ter hoogte van de top van de heuvel en hogedrukgebieden ter hoogte van de basis van de heuvel. Deze drukvariaties zullen overgedragen worden naar de sedimentaire omgeving. Als gevolg hiervan, zal zeewater in de voet van de heuvel gepompt worden en zal poriënwater uit het sediment getrokken worden aan de top de heuvel. Een dergelijk principe werd gemodeleerd en verder gekoppeld aan het voorkomen van de sulfaat-methaan transitie zone. De instroom van zeewater, met daarin opgelost sulfaat, aan de voet van een heuvel zal de SMTZ op die plaats neerwaarts duwen. Onder de top van de heuvel hangt het resultaat af van de sterke van de vloeistofstromingen: bij zwakke tot matige stroming zal de SMTZ lichtjes omhoog bewegen. Bij sterke stroming zal de SMTZ eveneens naar beneden geduwd worden omdat de instroom van sulfaat aan de voet van de heuvel zo sterk is dat de hele heuvel doorspoeld wordt met sulfaat. De grootte van deze effecten hangt ook af van de hydraulische parameters van de heuvel en de sedimenten.

7.5 Gevalstudie: het geochemisch milieu in carbonaatheuvel omgevingen

Het principe uit sectie 7.4 werd toegepast op carbonaatheuvels, bouwwerken van koralen en sedimenten die veelvuldig voorkomen in de Atlantische Oceaan. Omdat er discussie bestaat over het ontstaan en de groei van een dergelijke structuur, werd het model toegepast op een carbonaatheuvel met uitgebreide gekende gegevens: Challenger Mound op de Ierse continetale rand. De resultaten kunnen echter terug geprojecteerd worden naar de heuvels die voorkomen boven op de Pen Duick Escarpment en andere plaasten in het studiegebied.

Een recente boring heeft aangetoond dat in die carbonaatheuvel geen methaan aanwezig is; een overwachte observatie. De toepassing van hoger vermeld model toont echter aan dat een eerder sterke zeebodemstroming (0.2 tot 0.5 m per seconde) in staat is om de carbonaatheuvel te doorspoelen met sulfaat en het methaanfront tot een positie aan de basis van of onder de heuvel te brengen. Een kritische factor hierbij is dat de hydraulische conductiviteit voldoende hoog is; deze zou dus in de toekomst zeker op schaal van de volledige heuvel bepaald moeten kunnen worden.

7.6 Gevolgen van externe bronnen van vloeistofstromingen

Drie types van externe vloeistofstromingsbronnen werden in dit hoofdstuk belicht. Er werd aangetoond dat getijden in staat zijn om kleine vloeistofstromingen in de sedimenten te genereren die doorheen de tijd eens opwaarts, dan neerwaarts kunnen bewegen. Dit proces zou van belang kunnen zijn voor bepaalde chemische of microbiologische processen.

Een eustatische zeespiegeldaling is een trager en omvangrijker fenomeen. Methaanexsolutie in moddervulkaanpijpen kan hierdoor optreden en leiden tot uitstoot van modderstromen. Echter, het (her)activeren van een moddervulkaan kan door de zeespiegeldaling alleen niet verklaard worden.

Tenslotte werd het verband tussen zeebodemstromingen en ondergrondse stromingen, en de mogelijke geochemische gevolgen hiervan in beeld gebracht. In een gevalstudie werd aangetoond dat een dergelijk model eerder onverwachte observaties kan verklaren.

Appendices

Appendix A

Processing of seismic data

A.1   SEG-Y data format and preprocessing

The seismic data is recorded in the ELICS format under Delph Seismic (v. 2.0.1). The ELICS formatted data is exported to 16-bit (2 byte integer) SEG-Y format. Navigation is exported seperately.

The SEG-Y data format is a standard published by the Society of Exploration Geophysicists (SEG). The SEG-Y data format contains 1) a 3200-byte file identification record with general information, encoded in EBCDIC; 2) a 400-byte binary record with acquisition and data information (record length, number of channels, sampling rate, ...); and 3) a 240 byte trace header preceding each trace containing information relevant to the trace (trace number, time, date, coordinates, channel number, ...). The subsequent trace data can be 16-bit integer or 32-bit real formatted. The full datasheet can be downloaded from the SEG website[1].

A.2   Swell filtering

Swell filtering is done using software developed in-house by P. Staelens and available through the swellfilter website[2]. The software reads SEG-Y files as input. As a first step, it performs an automated seafloor picking procedure which can be corrected manually. The selected seafloor horizon is then smoothed by use of a bandpass filter. The residual is then applied as static shift to the individual traces and the result is again exported as SEG-Y file.

---

[1] http://www.seg.org
[2] http://www.swellfilter.com

A.3 Signal processing procedure

A.3.1 Data transfer and input in Promax

The swell filtered data is transferred to a Unix system for further processing in Promax 2D (latest version used was v. 2003.12.1) by Landmark Graphics Corp.

SEG-Y data files are read and transferred to the internal Promax format. Below, the settings of this processing flow are shown.

SEG-Y Input

Type of SEG-Y	Std. Fixed Length
Type of Storage	Disk
Select...	Disk Image
Path	/path/swellfilt.sgy
Update LIN db	Yes
Override interval	No
Samples per trace	0 (= no override)
Store reel header	Yes
Input AUX traces	Yes
Get CHAN from header	Yes
Input trace Format	Get from header
	or 2 byte integer
Apply trace weight	Yes
Display ensemble inf	No
Max TIME to input	0. (= whole trace)
Stacked data	No
MAX trace/ensemble	120
Primary SORT	SHOT
Input PRIMARY	FFID
Specify PRIMARY list	*/ (= all traces)
Input SECONDARY	None
Input Global XY	No
Use coordinate scalar	Yes
Scan range	Yes
Use SEG-Y Rev 1	Autodetect
Remap SEG-Y header	No

Disk Data Output → swellfiltered

Output Dataset Filename	swellfiltered
New, or Esisting, File	New
Record length to output	0. (= all)
Trace sample format	16 bit
Skip primary disk storage?	No

A.3.2   Visualisation of signal spectrum

The signal spectrum is visualized to decide how the final band pass filter should be designed, using following processing flow.

Disk Data Input ← **swellfiltered**

Read data from other	No
Select dataset	swellfiltered
Propagate input file history	Yes
Trace read option	Sort
Interactive data access	No
Select primary header entry	FFID
Select secondary header entry	None
Sort order	*/
Presort	Memory
Read data multiple times	No
Process headers only	No
Override input sample interval	No

Interactive Spectral Analysis

Data selection method	Simple
Display data by	Traces
Number of traces per analysis	* or as needed
Number of traces between loc	0
Primary header for sorting	FFID
Scondary header for sorting	None
Display average power spectrum	Yes
Type of scaling for power	dB Power
Type of mapping for power	Linear
Reference power	-1
Display average phase spectrum	Yes
Phase shift?	None
Unwrap phase spectrum	No
Display selected trace data	Yes
Display the FX power spectrum	Yes
Display the pre-FFT time window	No
Pre-FFT time window taper type	Hanning
Percent flat	80
Set freq display range auto	Yes
Set power display range auto	Yes
Set phase display range auto	Yes

A.3.3   Signal processing

In the next steps, a wide bandpass will be applied to the data before the predictive devon-volution step. This is followed by a narrow banpass. After an AGC gain, the final data is obtained.

Disk Data Input ← swellfiltered

parameters	see above

Bandpass Filter

TYPE	Single Filter
TYPE specification	Butterworth
PHASE of filter	Zero
Domain	Frequency
Zero padding	25.
Notch filter?	No
Freq-slope values	150-24-1500-24
Re-apply trace mute?	Yes

Spiking/Predictive Decon

TYPE	Minimum phase pred
Decon operator length	20
Operator prediction	2
Water relative?	No
Filter corretion?	No
Apply specif. taper?	No
White Noise level	0.1
Window rejection fct.	2
Time gate reference	Time 0
Get gates from DB	No
SELECT PRIMARY word	FFID
SELECT SECONDARY word	None
SPECIFY parameters	time as required
Output	Normal output
Apply bandpass?	No
Re-apply trace mute?	Yes

Bandpass Filter

Similar as above but	
Freq-slope values	250-24-1200-24

Automatic Gain Control

Application mode	APPPLY
Type of AGC scalar	RMS
AGC operator length	50.
BASIS	Trailing
Exclude hard zeroes?	Yes
Robust scaling?	No

Ensemble Redefine (optional, only if Trace Display follows)

Mode of application	Entire
Max. traces per ens.	500 (for display)

Trace Display Label (optional)

Trace label	as required

Trace Display (optional–check quality visually)

Device	This screen
Start time	as required
End time	as required
Max traces per screen	500 or as required
Overlap	0 or as required
Number of Ensembles	1 or as required
Variable spacing?	No
Output mode	When done
Trace display mode	As required
Header plot param	None
Direction	Left to right
Polarity	Normal
Primary Label	FFID
Secondary Label	None
Trace scaling	Conventional
Excursion clip	2
Scalar for multipl.	1
Scaling option	individual
Trace orientation	Vertical

Ensemble Redefine (optional–only if Trace Display preceded)

Mode of application	Entire
Max. traces per ens.	1

Disk Data Output → processed

Output Dataset	processed
New,or Existing,File	New
Record length	0. (= all)
Trace sample format	16 bit
Skip primary disk str	No

A.3.4   SEG-Y Output

Finally, 16-bit SEG-Y data is written to the harddisk and copied for storage.

Disk Data Input ← processed

Read data from other	No
Select dataset	processed
Propagate input file history	Yes
Trace read option	Sort
Interactive data access	No
Select primary header entry	FFID
Select secondary header entry	None
Sort order	*/
Presort	Memory
Read data multiple times	No
Process headers only	No
Override input sample interval	No

SEG-Y Output

Type of SEG-Y	Standard
Type of storage to use	Disk Image
Enter DISK file path	/path/filtered.sgy
Polarity	NORMAL
EBCDIC Reel Header Gen.	Derived from hist
Display information option	None
JOB ID ♯ for bin header	9999
Line ♯ for bin header	9999
Desired trace format	2 byte Integer
Maximum time to output	0.
Remap SEGY header values	No

Appendix B

Seismic velocity model for the El Arraiche mud volcano field.

During the campagnes of the R/V Belgica (Cadipor II) and R/V Pelagia (Moundforce II) in May 2005, a wide-angle seismic experiment was conducted to obtain a seismic velocity model for the sedimentary environment in the El Arraiche mud volcano field. The main reason to obtain a reliable velocity model are the running IODP Proposals 673 and 689, which aim to drill the carbonate mound environment on the Pen Duick Escarpment (Henriet et al.) respectively the Mercator mud volcano environment (Depreiter et al.).

Because no long streamers were available for this experiment, the R/V Pelagia was used as a gunning vessel, firing an array of 4 airguns. At the same time, the R/V Belgica was used as recording vessel, on which the acoustic data was recorded. The geometry of the experiment was set up as follows: R/V Belgica and R/V Pelagia were directed on parallel lines 50 m apart in opposite directions. Efforts were made to sail towards each other at such a speed that the mid point between the ships, thus between source and receiver, was constant. This common mid point (CMP) was located be in the proximinty MOMA-03A point, one of the drilling targets in the IODP-673 drilling proposals in the vicinity of Pen Duick Escarpment and Gemini MV. The direction of sailing was parralel to the average strike of the Renard Ride / Pen Duick Escarpment. Figure B.1 represents the positioning of R/V Belgica, R/V Pelagia and the CMPs. The CMP of shot point 106 (orange) is 500 m south of MOMA-03A. The coordinates of CMP 106 are W6.7933276 / N35.2695145.
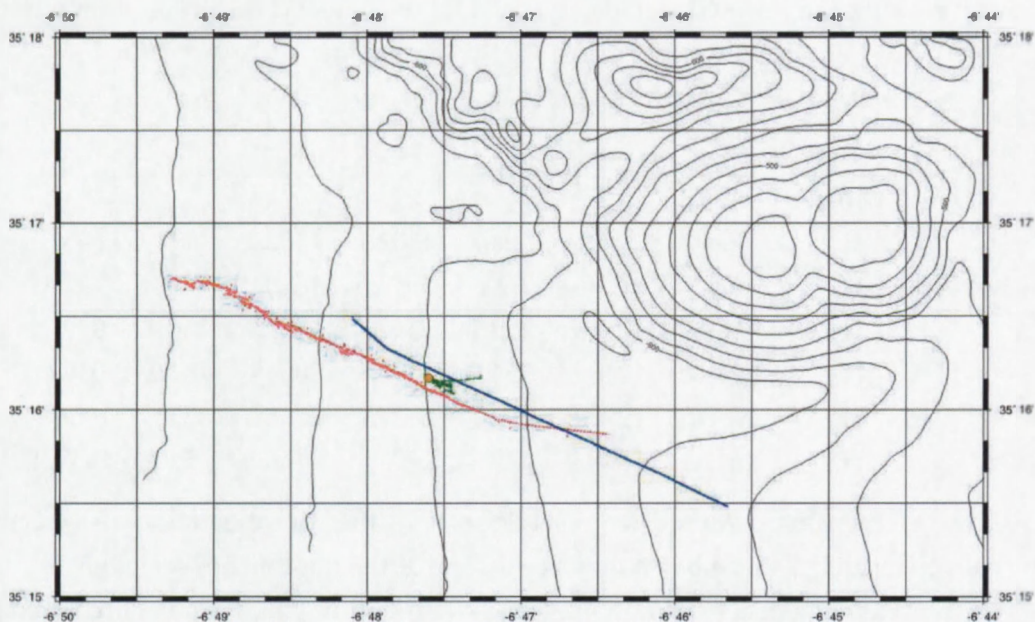

Figure B.1: Navigation during wide angle seismic experiment. Blue dots represent R/V Belgica navigation. Red dots represent R/V Pelagia navigation. Green dots represent Common Mid Points (CMP). Orange dot is CMP of shotpoint 106. Background: bathymetric contour with Gemini MV on the right side.

Including the direct wave, seven horizons have been picked (Figure B.2) for which the seismic velocity was calculated using

$$t^2 = t_0^2 + fracx^2v_{rms}^2 \tag{B.1}$$

. t is the two-way travel time of the signal, x the horizontal distance, v the unknown RMS velocity and t_0 is the vertical two-way travel time component of the signal, calculated as

$$t_0^2 = t^2 - t_{direct}^2 \tag{B.2}$$

with t_{direct}^2 the horizontal two-way travel time component of the signal. The RMS velocity is the velocity calculated over the entire signal, i.e. from source to receiver and is a root-mean-square average of the velocities in the water column and all sediment above the specified reflector. To obtain the velocity of a specific layer between two selected horizons, a conversion from RMS velocity to interval velocity is calculated through Dix equation:

$$V_{int} = \sqrt{\frac{t_{(i+1)}V_{(rms,i+1)}^2 - t_i V_{(rms,i)}^2}{t_{(i+1)} - t_i}} \tag{B.3}$$

For the actual velocity component, only shots 150 to 257 of the raw data because the earlier shots had a too large lateral offset distance, which yielded errors.

After picking the selected signals, the calculations yielded results as shown in the following table:

Horizon	t	t_0	t_{ssf}	V_{rms}	V_{int}	Z_{ssf}	Z
Direct	140.62	0					
H_0	868.0	856.5	0.0	1502.1	1502.1	0	643.3
H_1	965.9	955.6	99.1	1513.3	1610.0	75.0	723.1
H_2	1080.7	1071.6	215.1	1547.5	1829.1	166.4	829.1
H_3	1218.6	1210.5	354.0	1599.9	2004.4	283.2	938.4
H_4	1298.5	1290.8	434.3	1637.6	2204.5	355.6	1056.9
H_5	1612.1	1605.9	749.4	1792.4	2426.8	671.6	1439.2

with t_{ssf} the time recorded from seafloor, V_{rms} the root mean square velocity, V_{int} the interval velocity, Z_{ssf} the sub-seafloor depth, and Z the depth from sealevel.

The interval velocities gradually increases with depth which can be attributed to increasing compaction of the hemipelagic sediments.
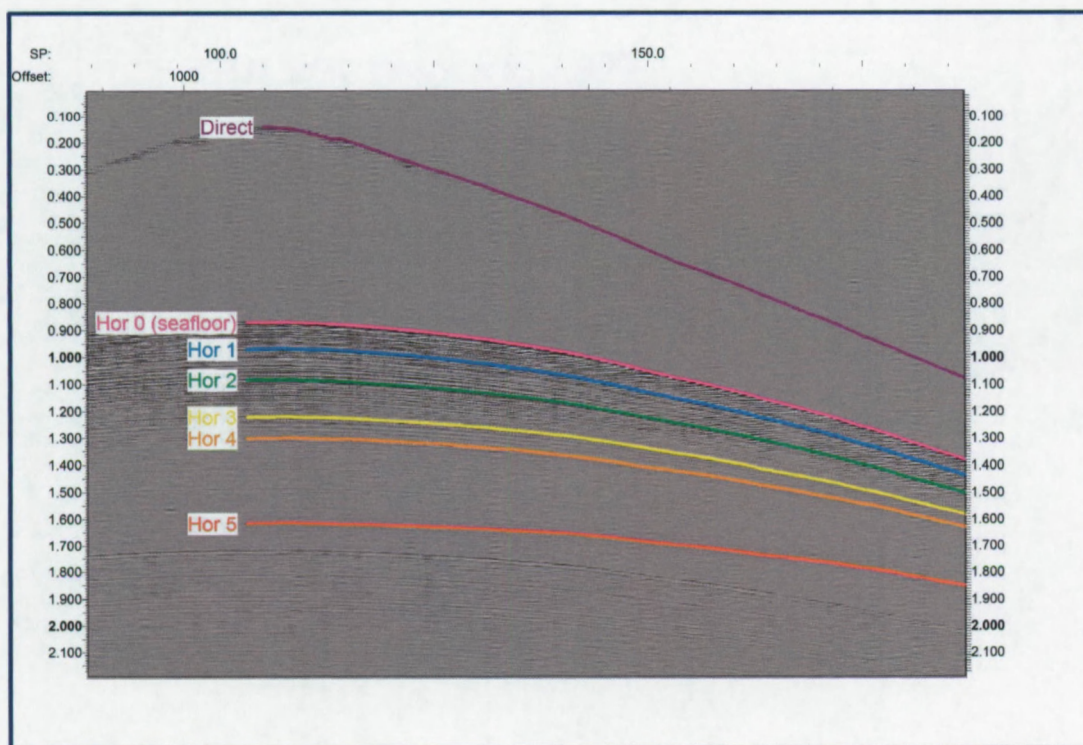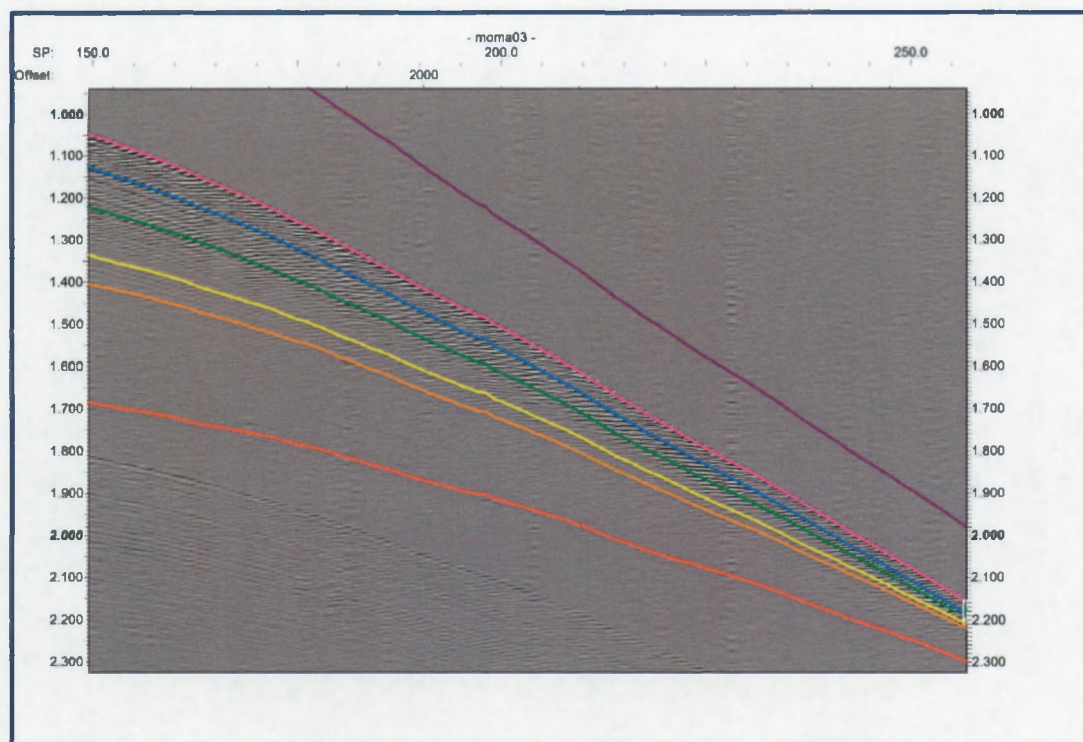
Figure B.2: CMP gather of wide angle seismic experiment. Purple horizon is direct wave. Pink horizon is seafloor.

Appendix C

Publications

The El Arraiche mud volcano field at the Moroccan Atlantic slope, Gulf of Cadiz

Pieter Van Rensbergen[a,*], Davy Depreiter[a], Bart Pannemans[a], Geert Moerkerke[a],
David Van Rooij[a], Bruno Marsset[b], Grigorii Akhmanov[c], Valentina Blinova[c],
Michael Ivanov[c], Merouane Rachidi[d], Vitor Magalhaes[e],
Luis Pinheiro[e], Marinha Cunha[f], Jean-Pierre Henriet[a]

[a]Renard Centre of Marine Geology, Ghent University, Krijgslaan 281-S8, 9000 Ghent, Belgium
[b]IFREMER, Brest, France
[c]UNESCO-MSU Centre for Marine Geoscience, Moscow State University, Moscow, Russia
[d]Mohamed V University, Rabat, Morocco
[e]Departamento de Geociências, Universidade de Aveiro, Aveiro, Portugal
[f]Departamento de Biologia, Universidade de Aveiro, Aveiro, Portugal

Abstract

The El Arraiche field is a new mud volcano field discovered near the Moroccan shelf edge in the Gulf of Cadiz that consists of 8 mud volcanoes in water depths from 200 to 700 m. The largest mud volcano in the field (Al Idrissi mud volcano) is 255 m high and 5.4 km wide. The cluster was discovered during a survey with the RV Belgica and studied further during Leg 2 of the TTR 12 survey onboard the R/V Prof Logachev. The 2002 surveys yielded detailed multibeam bathymetry over a 700 km^2 study area, dense grids of high-resolution seismic data, deep-tow sub bottom profiles, sidescan sonar mosaics over the major structures. Selected video imagery lines, video guided grab samples, dredge samples, gravity cores, and box cores were collected for groundtruthing purposes. Eight mud volcanoes in water depths from 200 to 700 m cluster around two, sub-parallel anticlines and associated active extensional faults. Rock clasts and regional seismic data locate the El Arraiche field over a Late Miocene–Pliocene extensional basin. The onset of mud volcanic activity is estimated at about 2.4 Ma and probably roots in the Cretaceous–Miocene accretionary wedge. Stacked outflows are visible up to a depth of about 500 m below the sea floor. The occurrence of long-lived mud volcanoes bear witness to continued overpressure generation at depth, either by in situ oil and gas generation or by focussed flow and accumulation in the area. Geochemical analyses of pore water from cores demonstrate the presence of thermogenic hydrocarbon processes. The activity of the mud volcanoes is indicated by the thickness of hemi-pelagic sediments covering extruded mud breccia, the

occurrence of seep-typical fauna, the degree of mixing between thermogenic and biogenic hydrocarbon processes, or the depth to the base of the sulphate reduction zone. Given its structural setting and the evidence of thermogenic and biogenic hydrocarbons, the area has promising hydrocarbon potential but remains untested.

1. Introduction

Since the first mud volcano was discovered in the Gulf of Cadiz in 1999 (Gardner, 2000, 2001), 30 or more mud volcanoes were identified in the span of three years (Pinheiro et al., 2002; Somoza et al., 2003), together with vast fields of hydrocarbon-derived pockmarks and other features related to fluid escape (Barazza and Ercilla, 1996). As such, the Gulf of Cadiz (Fig. 1) has, in a very short time, become one of the prime targets to study these submarine features and the associated sedimentary, biological and biochemical processes.

In May 2002 a new mud volcano cluster was discovered (Fig. 2) near the Moroccan shelf edge offshore of the city of Larache during a survey with RV Belgica and studied further during Leg 2 of the TTR 12 survey on board of RV Prof Logachev. The El Arraiche mud volcano cluster (Fig. 2) consists of 8 mud volcanoes in water depths from 200 to 700 m. The largest mud volcano in the field (Al Idrissi mud volcano) is 255 m high and 5.4 km wide and the smallest mud volcanoes (Lazarillo de Tormes and Don Quichote mud volcanoes) are only 500 m wide and 25 m high. The surveys yielded detailed multibeam bathymetry over the entire area, dense grids of high-resolution seismic
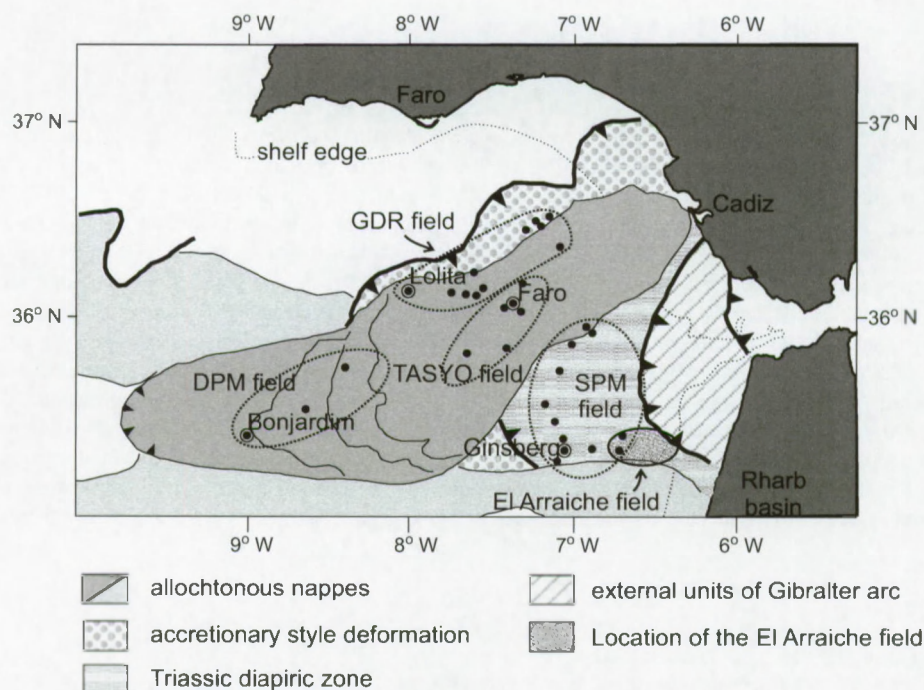

Fig. 1. Mud volcano provinces of the Gulf of Cadiz in their structural setting (based on Maldonado et al., 1999; Somoza et al., 2003). GDR=Guadalquivir ridge, DPM=Deep Portuguese margin, SPM=Spanish Morrocan margin.
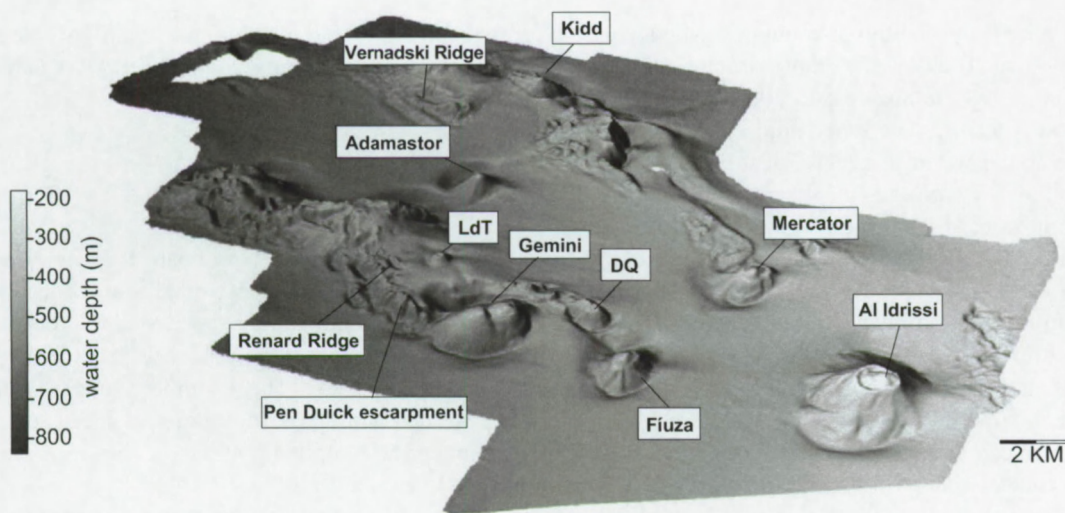
Fig. 2. 3D morphology of the El Arraiche mud volcano field at the Morroccan Atlantic margin derived from multibeam bathymetry. Al Idrissi is the largest mud volcano, 255 m high and 5.4 km in diameter. Don Quichote (DQ) and Lazarillo de Tormes (LdT), the smallest mud volcanoes, are only about 25 m high.

data, a few very high-resolution deep-towed sub-bottom profiles, side scan sonar data over the major structures, selected video imagery, video guided grab samples, dredge samples and gravity cores. Integration of data sets allows studying these long-lived mud volcanoes in detail, and moreover, macro as well as micro level studies over selected places from the regional scales down to microscopic scales.

Mud volcanoes in the Gulf of Cadiz are closely associated with accretionary wedge-type setting related to the convergence of the African and Eurasian plate boundaries and gravitational thin-skinned tectonics over a Triassic salt decollement, also commonly known as the olistostrome unit (Somoza et al., 2003). The newly discovered El Arraiche field is part of a larger cluster of mud volcanoes (the Spanish Moroccan Field, Gardner, 2001) that lies within the accretionary realm but outside the active olistostrome units (Fig. 1). Like other mud volcanoes in the Gulf of Cadiz (Somoza et al., 2002), the El Arraiche mud volcanoes evidence episodic expulsion of liquidized sediment thought to be related to the episodic migration of hydrocarbons. This paper describes the main characteristics of the mud volcanoes in the El Arraiche field and discusses their origin, structural setting and the implications for the hydrocarbon potential of this area offshore Morocco.

2. Geological setting

The Gulf of Cadiz is situated between 9° W to 6° 45′ W and 34° N to 37.15′ N enclosed by the Iberian peninsula and Morocco, west of Gibraltar. The bathymetry is steadily increasing from 200 m at the shelf edge to depths of over 4 km in the Horseshoe and Seine abyssal plains. Geologically, the setting of the Gulf of Cadiz is extremely complex and still under debate (Sartori et al., 1994; Maldonado et al., 1999; Gutscher et al., 2002). One of the most important structures is the large olistostrome complex (or allochthonous nappes) that were emplaced in the Tortonian in an accretionary wedge-type environment (Maldonado et al., 1999; Medialdea et al., 2004). The main part of the olistostrome unit occupies the central part of the Gulf of Cadiz as a lobe-shaped structure that extends over 300 km into the ocean (Fig. 1, Maldonado et al., 1999), its extent seems not yet well defined (Maldonado et al., 1999; Somoza et al., 1999; Medialdea et al., 2004; Maestro et al., 2003). The study area is situated south of the main olistostrome unit where thick Late Miocene–Pliocene sedimentary series were deposited in extensional basins at the back of advancing allochthonous sheets (Medialdea et al., 2004). Mio–Pliocene depocentres are bordered by shallow ridges characterized by large and active normal faults (Flinch, 1993), probably super-

posed on relict Miocene thrust anticlines (Maldonado et al., 1999) or Triassic salt diapir structures (Berástegui et al., 1998; Somoza et al., 2003).

All mud volcanoes and other fluid escape features have been found within the realm of the accretionary prism units. They cluster in several mud volcano fields (Somoza et al., 2003, Fig. 1): the Guadalquivir Diapir Ridge (GDR) mud volcano field is located at the north-western side of the Guadalquivir Ridge at the margin of the Tortonian olistostrome unit and at the main thrust belt in this area. It is a dense field with 11 identified mud volcanoes, mud cones and large fluid escape structures in water depths from 380 to 1560 m (Somoza et al., 2003). The term "mud cone" refers to conical shaped hills without proof of mud breccia (Somoza et al., 2003) but is further used here to indicate the mud volcanic hill. The largest structure, the Lolita mud cone, occurs in a water depth of 1560 m and is 316 m high and 5.7 km wide. The Tasyo mud volcano field is separated from the GDR mud volcano field by the Cadiz undercurrent channel. It lies over the north-central part of the main olistostrome unit and consists of 8 mud volcanoes or mud cones amidst many other unidentified circular sea floor structures. The largest structure, the Faro mud volcano, is 190 m high and 2.6 km wide and set in a water depth of 795 m. The Deep Portuguese Margin (DPM) mud volcano field occupies the distal part of the main olistostrome unit in water depths between about 2 to 3.2 km. Only three mud volcanoes have been discovered in this large area but many other features that resemble mud volcanoes or mud cones still need to be studied. The largest in this mud volcano field is probably the Bonjardim mud volcano that was encountered in a water depth of about 3060 m. It is about 100 m high and about 1 km in diameter (Pinheiro et al., 2002). The Spanish-Moroccan (SPM) mud volcano field lies within the "Triassic Diapiric" structural zone (Somoza et al., 2003), south of the main olistostrome unit, in a water depth of about 600 to 1200 m. The largest structure in this area is probably the Ginsburg mud volcano that is over 200 m high and about 4 km in diameter in a water depth of about 1200 m (Gardner, 2000, 2001).

The El Arraiche mud volcano field is located at the south-eastern continuation of the Spanish-Moroccan mud volcano field, offshore the city of Larache. The mud volcano field is located within the accretionary prism structure but outside the realm of the main olistostrome units. Exploration well LAR-1 is located about 8 km east of the study area.

3. Data

The multibeam survey on board R/V Belgica used a Kongsberg EM 1002, extended with a deep water module. Maximum sailing speed was 6 knots, with a swath width of 750 m in shallow water (<500 m) and 500 m in deep water. The acquired data was corrected and cleaned with the Kongsberg packages Merlin and Neptune. The footprint at 400 m is 15 × 15 m. In total 700 km^2 was covered.

A total of 62 high-resolution seismic profiles (Fig. 3) were acquired in three dense grids with a line spacing of about 1 km centred on the Mercator, Al Idrissi and Gemini mud volcanoes. The seismic acquisition used a SIG sparker (80 electrodes) with an energy of 500 J and a SIG surface single channel streamer. In some cases a water gun (15 in.^{3}) or a GI-gun (SODERA 35 in.^{3} generator and 35 in.^{3} injector) were used. Along 5 lines the IFREMER deep-tow Chirp source (650–2000 Hz) was tested with the IFREMER deep-tow 2-channel streamer (of which only one channel was used during this campaign), with excellent results in terms of penetration and resolution. Seismic profiles were digitally recorded using the Elics Delph system. Data processing (swell-filter, band pass filter, deconvolution and signal amplification) used the Landmark Promax processing software. Interpretation and mapping was done using Seismic Microsystems' Kingdom Suite.

During the TTR 12 survey side scan sonar imagery over the main features (Fig. 3) was acquired using the deep-towed hydro-acoustic complex Mak-1, with an operating frequency of 30 kHz, and a sub bottom profiler operating at 5 kHz. The Vernadsky Ridge, the deeper part of the Renard Ridge and the Mercator mud volcano were surveyed with one sidescan sonar line each, Al Idrissi and Gemini mud volcanoes and the upper Renard Ridge were each covered by a mosaic of three lines. Based on the side scan sonar data, 6 transects were chosen for a deep-towed TV-line, for a total of 15 h. Based on the TV-lines, TV-guided grab samples were taken (Fig. 3). Dredge samples of mud breccia at the sea floor were taken on Mercator and Al
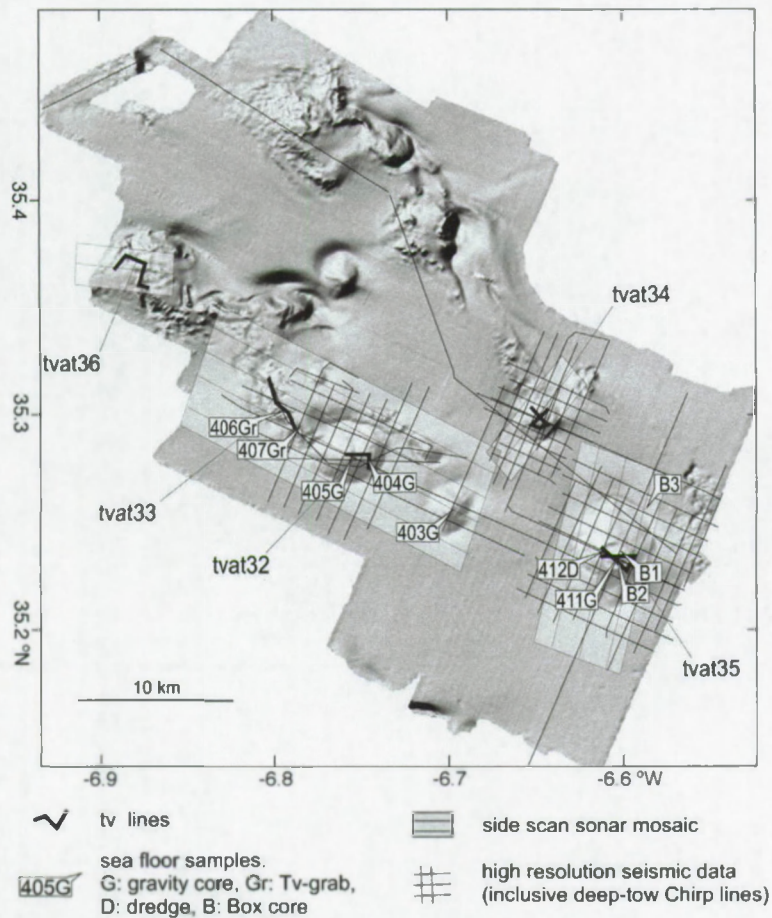
Fig. 3. Shaded bathymetry map of the El Arraiche mud volcano field with localisation of the available seismic data, side scan sonar mosaics, TV-lines, and sea floor samples.

Idrissi mud volcanoes. In the craters of the main mud volcanoes (Mercator, Al Idrissi, Gemini, and Fiúza) the subsurface was sampled by gravity cores. Four additional box cores are also available from the R/V Belgica survey. The technical details of the equipment and core analysis strategies during TTR12 survey are listed in the cruise report Kenyon et al. (2003). Geochemical sampling was performed on all gravity cores within the El Arraiche mud volcano field at irregular intervals of about 10 to 30 cm, depending on the lithology. Geochemical sampling and analysis procedures are described by De Mol et al. (1998) and Stadnitskaia et al. (2002). This paper uses measurements of methane concentrations and the ratio between methane concentration and the concentration in high hydrocarbons (C_1 / C_{2+}).

4. Data description and interpretation

The El Arraiche mud volcano field (Fig. 2) consists of at least 8 mud volcanoes of varying size that are clustered around two sub-parallel sea floor ridges, the Vernadsky and Renard ridges, both with steep fault escarpments. The ridges rise up in water depths of about 700 m and stretch to the shelf edge. Most mud volcanoes occur on top of the Renard ridge (Lazarillo de Tormes mud volcano, Gemini mud volcano, Don Quichote mud volcano and Fiúza mud volcano). The Kidd mud volcano is situated on top of the Vernadsky Ridge. Isolated mud volcanoes occur between the ridges (Adamastor mud volcano, Mercator mud volcano, Al Idrissi mud volcano).
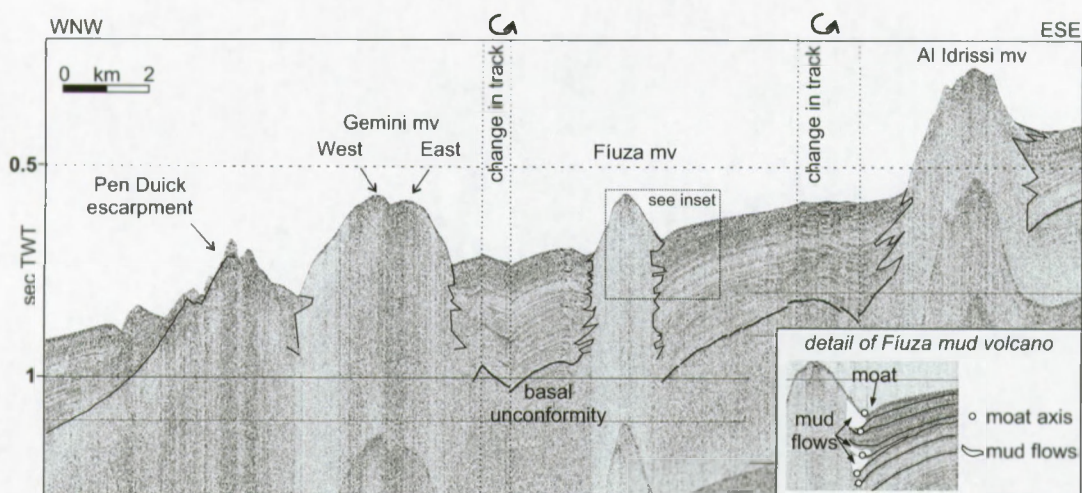
Fig. 4. General high-resolution seismic line (sparker source) over Al Idrissi, Fiúza and Gemini mud volcanoes. The mud volcanoes are characterized by a reflection-free seismic facies that shows stacked outflow lenses within a stratified series of hemi-pelagic sediments above a regional unconformity. The inset shows a detail of interfingering mud flows that accumulate in moats at the base of the Fiúza mud volcano cone.
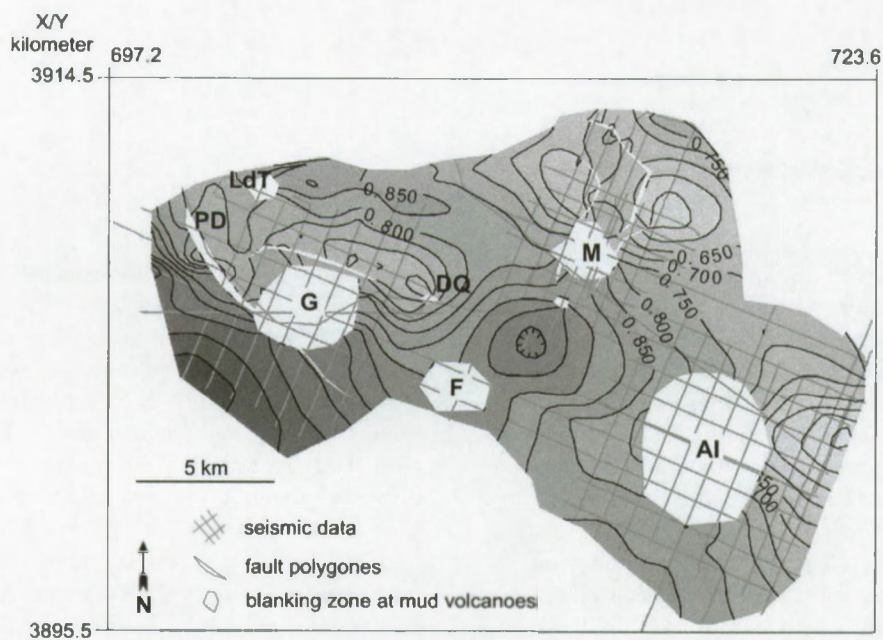
Fig. 5. Time–structure map of the basal unconformity (Fig. 4) mapped on basis of the high-resolution seismic data. The age of the basal unconformity is estimated 2.4 Ma, an upper estimate for the onset of mud volcanism. Indicated abreviations are AI=Al Idrissi, M=Mercator, G=Gemini, F=Fiúza, DQ=Don Quichote, LdT=Lazarillo de Tormes, PD=Pen Duick escarpment. Contouring is in milliseconds TWT below sea level.

Table 1
General morphological characteristics of the main mud volcanoes of the El Arraiche field

Name	Water depth top (m)	Height (m)	Slope			Crater	Slope		Moat		Quadrant
			Width base (km)	Width top (km)	Overall angle (°)	Max depth (m)	Height (m)	Diameter (km)	Max depth (m)	Radius (km)	
Al Idrissi	197	111–255	4.3–5.4	1.2–1.5	5–8	17	14–42	1.9–2.3	2.85	16	
Mercator	350	51–141	2.45–1.82	0.98–1.1	5.5–10	2	22–38	0.65–0.8	1.3	9	
Gemini W	423	170–252	4.1–2.3	1.1	5.5–8.5	No crater	23–27	0.52–0.87	1.5–1.9	12	
Gemini E	423	117–169	4.1–2.3	0.95–1.3	5–10.5	No crater	13–23	0.7–0.87	0.95–1.25	3	
Fiúza	393	97–143	2.9–2.1	0.75–0.8	6–10	No crater	27	0.5–0.7	1.1–1.6	36	

The mud volcanoes stand out as conical hills on the sea floor with varying slope profiles (Van Rensbergen et al., 2005), mud breccia deposits were found at their top. On the seismic data, the mud volcanoes are characterized by a reflection-free seismic facies that shows stacked outflow lenses within a stratified series of hemi-pelagic sediments above a regional unconformity (Fig. 4). This basal unconformity is mapped in Fig. 5 and is used to document the structural setting of the mud volcanoes. The following paragraphs will describe each of the mud volcanoes. Statistical and descriptive information on the mud volcanoes can be found in Table 1.

4.1. Al Idrissi mud volcano

Al Idrissi mud volcano is the largest and shallowest mud volcano in the field, situated just below the shelf edge in water depths of about 420 m (Fig. 2). It appears to be located on a westward plunging anticline (Fig. 5), visible in the bathymetry and on seismic data at the eastern side of the Al Idrissi mud volcano but almost entirely disappears at its western side. Deep moats at the base occur at the northern and southern side of the mud cone but they are absent over the plunging anticline at the western and eastern sides. The mud volcano is 225 m high, up to 5.4 km wide at its base and 1.5 km wide at the top (Table 1). It is almost circular at the base and has an eye-shaped crater at the top. The crater is up to 17 m deep at the western side, the eastern part is occupied by a central dome-shaped elevation, maximum 42 m above the crater floor. The flanks of the mud volcano are dominated by down slope mud flows. On the side scan sonar mosaic (Fig. 6), mud flows have an even texture but return high backscatter in contrast to the pelagic slope sediments. Backscatter contrast is lower on the southern and eastern flanks probably where pelagic sediments drape the mud extrusions. Core 411G (Fig. 7) and box cores B1 and B2 at the top and at the northern flank of the central dome reveal a sandy layer at the surface of 3–5 cm thick with a sharp and irregular limit separating it from a mud breccia. In core 411G (Fig. 7) this mud breccia is a stiff structureless clay with claystone clasts up to 1 cm. The small clasts encountered at the central dome is in contrast with rock clasts found at the crater floor. Here, up to 0.5 m large rocks were dredged. They
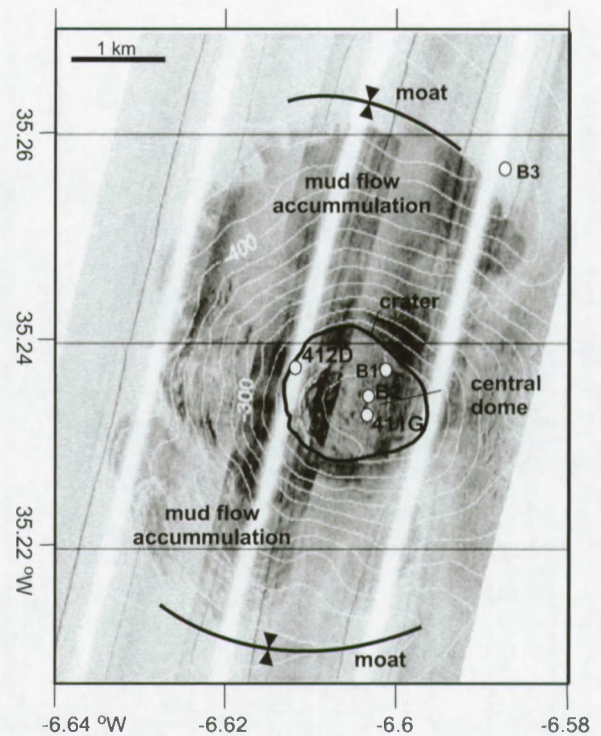

Fig. 6. Side scan sonar mosaic over the Al Idrissi mud volcano with superimposed bathymetry. This mud volcano is 225 m high, 5.4 km wide at its base and 1.5 km wide at the top. The flanks of the mud volcano are dominated by down slope mud flows with high backscatter that contrast with pelagic slope sediments with low backscatter.

are mainly of Upper Miocene and Pliocene age and composed of coarse to fine grained sandstones and siltstones, some with biodetritus in a calcite cement (Akhmanov et al., 2002).

4.2. Mercator mud volcano

The Mercator mud volcano is set at the southern flank of the Vernadsky Ridge within a 2 km wide, N–S oriented, collapse zone. This collapse zone is L-shaped and turns 90 degrees west, north of the Mercator mud volcano (Figs. 2 and 5). The mud volcano is an asymmetric mud volcano (Fig. 8) with a moat along its southern and western side. It is 141 m high at the southern side, 90 m high at the northern side and only 51 m high at its eastern side (Table 1). It has a maximum diameter of 2.45 km at the base and 1.1 km at its top. Side scan sonar data show a semi-concentric pattern related to the fronts of mud flow lobes, rather
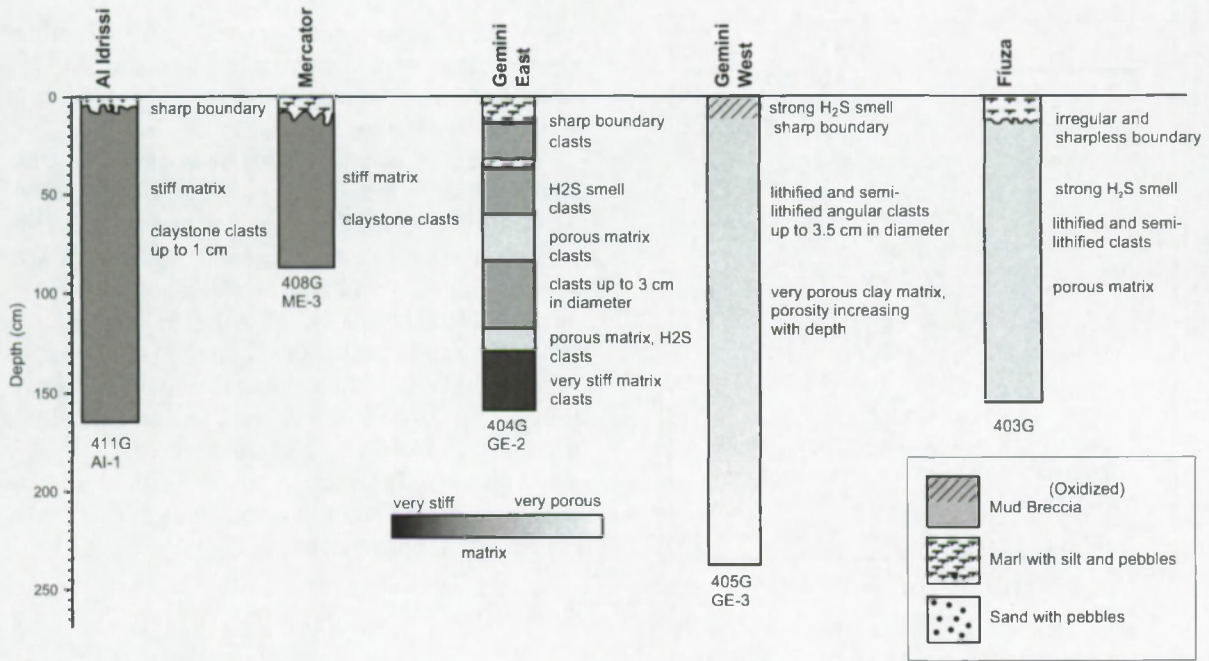
Fig. 7. Description of gravity cores located at the crests of the main mud volcanoes. The localisation of the cores is indicated on Fig. 3. Cores have widely varying fluid contents. Inactive mud volcanoes are covered by a hemi-pelagic drape.

than a radial outward mud flow pattern. A 2 m deep rimmed crater occurs at the northern side but is absent at the southern side. The top of the mud volcano consists of a crater and a 38 m high central dome. Solitary blocks ($\pm$ 10 cm in diameter) occur. Core 408 (Fig. 7) yielded a grey, structureless, slightly silty clay with clay stone clasts, covered by 8 cm of oxidized marl. The seismic data (Fig. 9) show a smaller buried structure, interpreted as a buried mud volcano occurs south of Mercator mud volcano within the same collapse zone.

4.3. Gemini mud volcano

The Gemini mud volcano occurs south of the large fault escarpments at the sea floor that bound the southern flank of the Renard Ridge (Fig. 2). It consists of two mud volcanoes in one large oval-shaped mud cone (Fig. 10). The entire mud volcano is up to 252 m high, 4.1 km long to 2.3 km wide at the base, the maximum diameter at the top of the eastern part (Gemini East) is 1.3 km and the maximum diameter of the western part (Gemini West) is 0.9 km (Table 1). The summits of both Gemini East and Gemini West consist of a flat crater area with a central dome of respectively

23 and 27 m above the flat crater area. Core 404G at the eastern summit (Fig. 7) reveals 12 cm of bio-turbated marl (hemi-pelagic mud), on top of different layers of mud breccia. Another marl layer with a thickness of 4 cm occurs at 32 cm depth. The mud breccia is gray and very gas-saturated, with randomly distributed rock clasts. At the western summit is no hemi-pelagic sediment. Core 405G (Fig. 7) shows a gray mud breccia with a strong H_2S smell. The surface layer (11cm) is an oxidized, heavily bioturbated mud breccia. Moats are present parallel to the long axis of the mud volcano.

4.4. Other mud volcanoes

Fiúza mud volcano is a smaller mud volcano east of Gemini (Fig. 10). It is located at the western termination of the Renard Ridge and possibly at the southern continuation of the collapse depression that host the Mercator mud volcano but no faults could be traced in either direction to its location. The mud volcano is maximum 143 m high, 2.2 km wide at the base and has a flat top of up to 0.75 km wide with a central dome of 27 m high and maximum 0.7 km wide (Table 1). Core 403G (Fig. 7) at the top of the mud volcano retrieved a
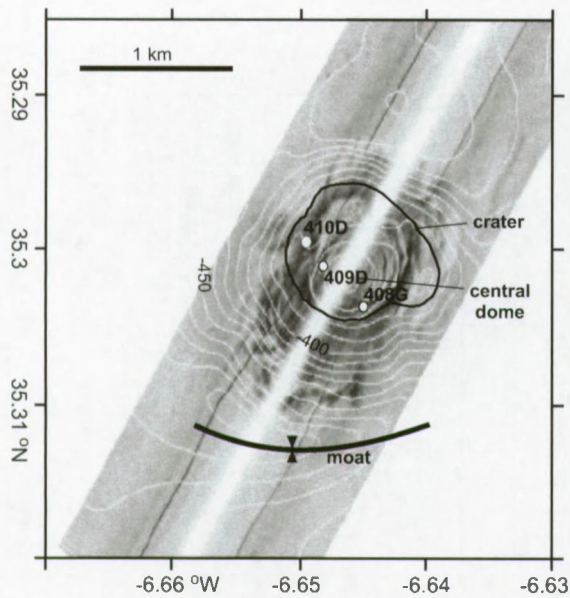
Fig. 8. Side scan sonar image of the Mercator mud volcano with superimposed bathymetry. This asymmetric mud volcano is 140 m high at the southern side but only 90 m high at the northern side. It has a diameter of 1.84 km at the base and 0.5 km at its top. Side scan sonar data show a semi-concentric pattern of mud flow lobe fronts in the crater and on the slope, different from radial outward mud flow pattern at Al Idrissi mud volcano.

homogeneous mud breccia covered by 12 cm of pelagic marl. A semi-circular moat occurs around the base of the mud volcano. Moats are also prominent at deeper levels on seismic data.

Kidd and Adamastor mud volcanoes have been described earlier by Gardner and Shashkin (2000). Adamstor is 2 km wide at the base and about 160 m high. Kidd is sitting on the edge of a fault escarpment, it is about 4 km wide but its height is difficult to measure (between 60 to 160 m). The smaller Don Quichote and Lazarillo de Tormes mud volcanoes occur at the crest of fault blocks on top of the Renard Ridge. Lazarillo de Tormes mud volcano, is 500 m wide and 25 m high. No cores were taken at these mud volcanoes. In general, both mud volcano setting seem associated with extensional faults at the crest of the Renard Ridge anticline.

4.5. Interpretation

On seismic sections, the mud volcanoes consist of a columnar zone without coherent acoustic information, about the width of the mud volcanic cone (Fig. 4). Large mud flows emerging from this central zone are also free of reflections, but show a sharp transi-
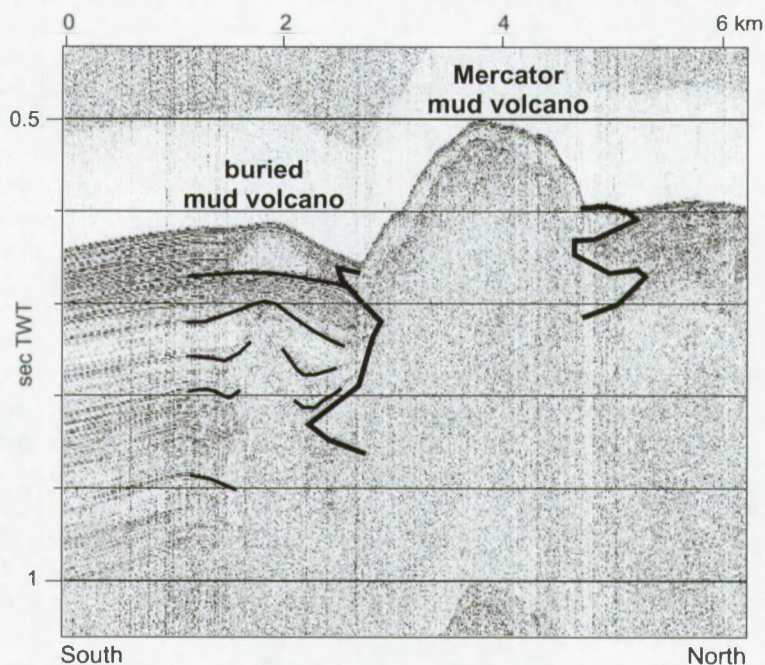

Fig. 9. Seismic line through the Mercator mud volcano and a smaller buried mud volcano just south of it.
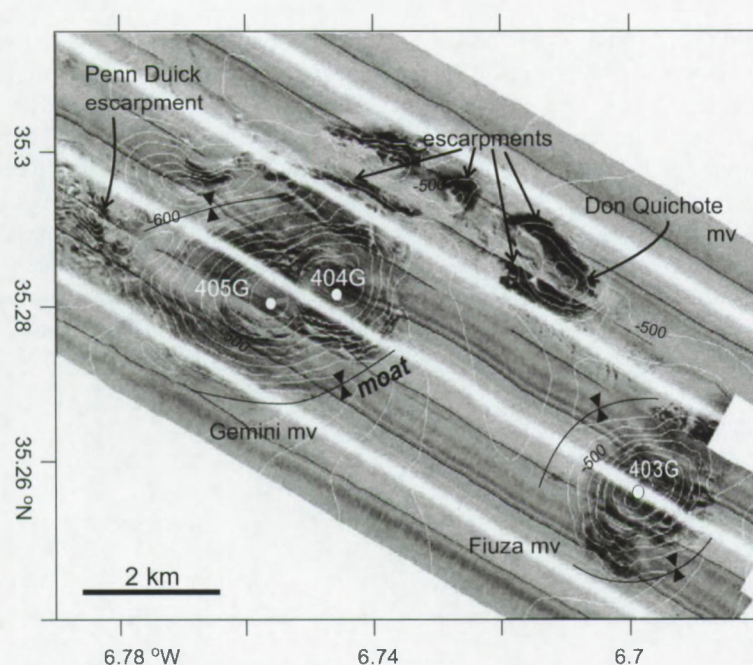
Fig. 10. Side scan sonar mosaic over the Gemini and Fiúza mud volcanoes with superimposed bathymetry. The entire mud volcano is about 200 m high, 4.88 km long to 2.5 km wide at the base, the diameter at the top of the eastern part is 0.9 km and the diameter of the western part is 0.6 km. The summits consist of a flat area with a central dome of respectively 20 and 30 m above the flat top. Fiúza mud volcano is 60 m high, 2.2 km wide at the base and has a flat top of about 600 m wide with a central dome of 10–18 m high and about 300 m wide.

tion to the surrounding sediments. The mud flow deposits are typically lens-shaped, convex at the top and often fill a moat at the base of the mud volcano. In the subsurface, the same pattern returns at several levels bounded by local unconformities (Fig. 4). Stacked outflow lenses produce the typical Christmas-tree morphology of long-lived mud volcanoes, similar to other mud volcanoes in the Gulf of Cadiz (Somoza et al., 2002). On the seismic data only the tips of the largest outflow deposits are visible and probably represent only the largest extrusion events. The lateral dimensions of feeder channel and outflow deposits in the subsurface cannot be measured due to acoustic blanking under almost the entire width of the present-day mud volcano. 3D seismic data in other mud volcanic provinces have demonstrated that the width of the feeder channel is probably much smaller than the zone affected by acoustic blanking or by chaotic reflections (Van Rensbergen et al., 1999).

Moats at the base of mud volcanoes are mostly interpreted as subsidence rims related to volume reduc-

tion caused by degassing and sediment removal (Prior et al., 1989; Camerlenghi et al. 1995). However, high-resolution seismic profiles across these moats show the details of a cut-and-fill facies, indicating erosion by currents. Somoza et al. (2002) also suggest that the moats are caused by erosional currents deflected by the mud volcano cone. For the El Arraiche mud volcano field, Van Rensbergen et al. (2005) suggest erosion in combination with subsidence; subsidence rims can be deepened by current or smoothed by sediment fill. The subsidence rims do not evolve into sediment withdrawal synclines but are filled by mud flows and layered hemi-pelagic sediments and re-appear higher in the section at a slightly different position.

Episodic mud extrusion created vertical columns of remoulded mud up to 500 m below the top of the mud volcanoes. The deepest observed occurrence of mud extrusion deposits is underlain by a regional unconformity. The unconformity, between 450 and 1250 ms TWT (or about 350 and 900 m below sea level), bears witness to a wide-spread erosional event and is the base for a seemingly continuous succession of deep

water sediments. This basal unconformity is interpreted to correspond to an important sea level low stand at 2.4 Ma (Hernández-Molina et al., 2002). This estimated date is well within the age limits obtained by correlation with a near-by industrial well LAR-1 (Flinch et al., 1996), and yields a reasonable sedimentation rate of about 10 cm/ka. The interpreted age (2.4 Ma) of the regional unconformity can be regarded as an upper estimate for the duration of the mud volcano activity in the El Arraiche field.

The time–structure map of this basal unconformity (Fig. 5) shows the structural highs and younger normal faults at the crests. Fault interpretation from the seismic sections is difficult due to the fact that data quality at the mud volcanoes and ridges is not optimal. The bathymetry data show much better the geometry of active faults. Steep escarpments are drawn from sea floor dip maps on the shaded relief map of the study area together with structural information from the seismic

data in Fig. 11. Numerous extentional faults create steep escarpments, in places more than 100 m high, with rapidly varying strike. They are interpreted as collapse faults related to the uplift of the anticlines. Also the Vernadsky Ridge and Renard Ridge anticlines are not continuous structures but appear almost as an 'en-echellon' succession of curved sections, disrupted by 2–3 km wide NW–SE trending deformation zones. From the seismic data, it appears that these deformation zones are associated with increased subsidence and collapse of the anticlines.

5. Discussion

5.1. Origin of El Arraiche mud volcano field

There is little information about the deep-seated feeder system of the El Arraiche field. High-resolution
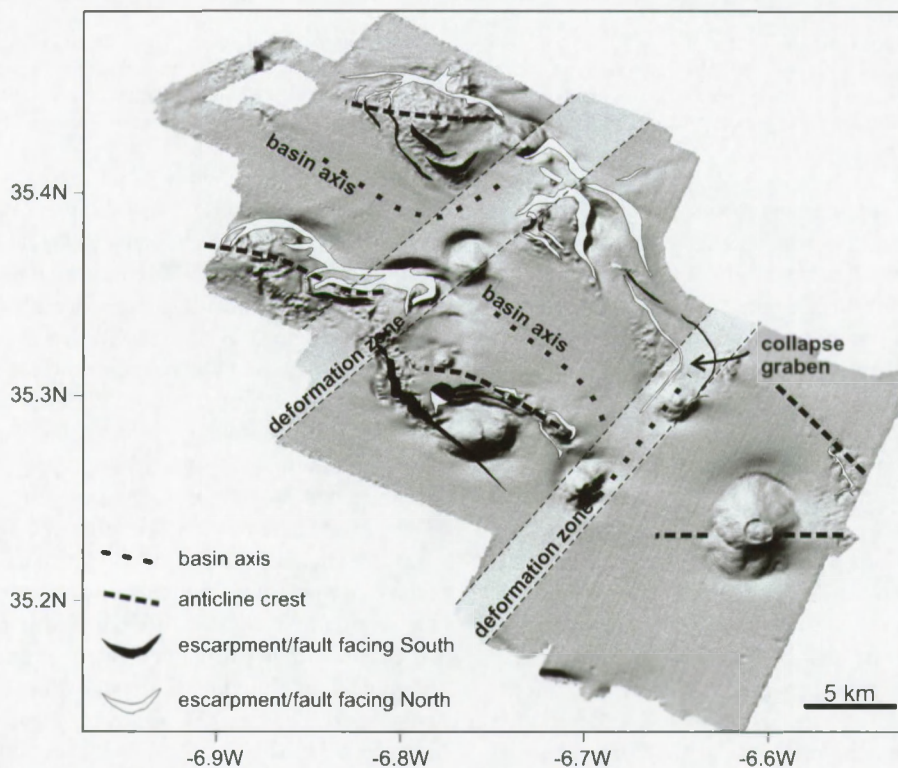
Fig. 11. The localisation of anticlines, basins, and faults from the time–structure map in Fig. 5 drawn on a shaded illumination map of the sea floor at the El Arraiche mud volcano field. In the western part of the study area, good seismic coverage is missing and structures are interpreted from detailed sea floor analysis. Faults have rapidly varying strike and throw, anticlines are discontinuous, and seem compartmentalized by NE–SW trending collapse zones.

seismic profiles only penetrate the upper 500 m and in this case only image the extrusive part of the mud volcano system. Moreover, the subsurface immediately below the mud volcanoes is almost entirely blanked. Only mud breccia clasts from the mud volcanoes bear witness of the stratigraphy that was traversed by the mud volcano feeder system. Petrographic studies of mud breccia clasts retrieved from Al Idrissi and Mercator mud volcanoes by Akhmanov et al. (2002) situate the mud volcano field over an Upper Miocene–Pliocene sedimentary basin. Smaller limestone clasts indicate that the mud volcano feeder system probably roots in or below Upper Cretaceous–Miocene rocks, similar to the other mud volcano fields in the Gulf of Cadiz (Akhmanov et al., 2002; Ovsyannikov et al., 2003).

Upper Miocene–Pliocene clasts were of exceptionally large size, which indicates the shallow position of Upper Miocene–Pliocene rocks in this area. On basis of the near-by exploration well LAR-1 and its correlation with industrial 2D seismic lines (Flinch, 1993), the top Pliocene and top Miocene at the Al Idrissi mud volcano are estimated to occur respectively at about 150 and 900 m below the sea floor. The base of the Upper Miocene was not encountered in the 2400 m deep LAR-1 drill hole. Hence, the distance of vertical transport of the large blocks ranges from 370 m (the depth to top Pliocene plus the height of the mud volcano) to over a kilometre.

The source of overpressure seems to be, at least partly, related to pore fluid volume expansion during thermogenic gas generation (Barker, 1990). The large mud volcanoes (Al Idrissi, Gemini, Mercator and Fiúza) bears witness of repetitive sediment extrusion

and growth since they appeared about 2.4 Ma ago. Gas generation in Mesozoic source rocks and focussed fluid flow along the basal detachment of the accretionary wedge both provide possible sources for sustained and repeated fluid injection into the overburden sediments, probably increased by periods of tectonic compression. Geochemical analysis of gravity cores on the mud volcanoes (Table 2) yielded hydrocarbon gasses from thermogenic origin in the crater of Gemini West and gasses from mixed thermogenic/biogenic in the craters of Fiúza and Gemini East mud volcanoes, the latter was interpreted by Bileva and Blinova (2002) as evidence for a longer period of inactivity. Hydrocarbon gasses with thermogenic signature were also retrieved from Ginsberg mud volcano, down slope of the El Arraiche field (Mazurenko et al., 2002).

5.2. Mud volcano activity

The notion of present-day activity of mud volcanoes depends on whether fluid or sediment expulsion is considered. Both processes occur at mud volcanoes and they are closely related given that fluid flow is the main cause of subsurface sediment mobilisation (see discussion by Van Rensbergen et al., 2003). But both fluid seepage and sediment extrusion activity are difficult to assess and conclusions can diverge as is illustrated below. Table 2 summarizes the indications of mud volcano activity for the main mud volcanoes in the El Arraiche field. The time since the last sediment extrusion is indicated by the thickness of hemi-pelagic sediments that cover mud breccia at the crater. Our observations indicate that most recent

Table 2

Overview of indicators of mud volcanic activity. Average C_1/C_{2+} ratio is calculated for the measurements below the sulphate reduction zone (SRZ)

	Thickness pelagic drape	Thickness SRZ	Maximum methane concentration	C_1/C_{2+} ratio (average)	Seep fauna	Interpretation
Al Idrissi	No	55 cm	564 (ml/l) (at 161 cm)	1700	No seep fauna observed	Large flux of biogenic gas
Mercator	8 cm	≫ 80 cm	0.6 (ml/l) (at 61 cm)	–	Pogonophora	Very low flux
Gemini east	11 cm	90 cm	504 (ml/l) (at 153 cm)	888	Pogonophora	Low gas flux of mixed origin
Gemini west	No	45 cm	875 (ml/l) (at 201 cm)	27	Pogonophora	Large flux of thermogenic gas
Fiúza	12	35 cm	109 (ml/l) (at 71 cm)	803	No seep fauna observed	Moderate gas flux of mixed origin

crater-wide sediment extrusion occurred at Al Idrissi and Gemini West mud volcanoes. At Mercator mud volcano, recent extrusion seems to have occurred only in a narrow zone at the crest of the central dome (Van Rensbergen et al., 2005). The activity of gas seepage can be deduced from the depth of the sulfate reduction zone (SRZ) and by the occurrence of typical seep fauna. Al Idrissi and Gemini West are the most active mud volcanoes; there is no or little pelagic drape, the SRZ is shallowest and the methane concentrations in the sediments are high. It is remarkable that the C_1/C_{2+} ratio at Al Idrissi is typical for biogenic methane whereas Gemini West has C_1/C_{2+} ratio typical for thermogenic methane.

5.3. Structural control on mud volcano occurrences and its implications for hydrocarbon exploration

The Vernadsky Ridge anticline and the anticline below Al Idrissi mud volcano continue into the shelf area where they were mapped by Flinch (1993) on basis of regional seismic lines. Flinch et al. (1996) mapped listric faults over Miocene thrust anticlines that bound large Pliocene extensional basins (Fig. 12). Similar Pliocene extensional basins have been identified on regional seismic lines in the central Gulf of Cadiz (IAM-T3 line in Gracia et al., 2003 and in Medialdea et al., 2004). They formed at the back of the advancing sheets (Medialdea et al., 2004), probably facilitated by the mobilisation of Triassic evaporites and Miocene shales (Maestro et al., 2003).

The structural setting of the El Arraiche field is thus very different from the GDR, Tasyo and DPM mud volcano fields in the Gulf of Cadiz and the geographical division in mud volcano fields also has geological relevance. A generalized line drawing along a NW–SE transect illustrates the structural setting of the different mud volcano fields (Fig. 12). The GDR mud volcano field is located at the north-western margin of the Tortonian olistostrome and at the major fold and thrust belt in this area (Gracia et al., 2003). Large thrusts faults are known to focus fluid flow at the base of the accretionary system. These fluids are likely to move upwards along stacked steep inverse faults at the front thrust zone (GDR field) or at thrust anticlines within the olistostrome unit (TASYO field en DPM field). At places, mud volcanoes are interpreted to overlie diapirs of Miocene plastic marly clays of the olistostrome unit (Maldonado et al., 1999; Somoza et al., 2003). The olistostrome unit is densely fractured, thrust anticlines are not continuous and very irregular, hence mud volcano distribution seems random. Pinheiro et al. (2002) indicate that mud volcanoes seemed aligned along a conjugate fault system with NW–SE and NE–SW direction, probably strike-slip faults. In any case, the influence of the intensely deformed allochthonous units on the distribution of mud volcanoes and fluid escape features is dominant. The SPM mud volcano field and the El Arraiche field are located outside the main olistostrome unit. Here, most compressional structures are buried below a thick, continuous, Plio–Pleistocene sequence that
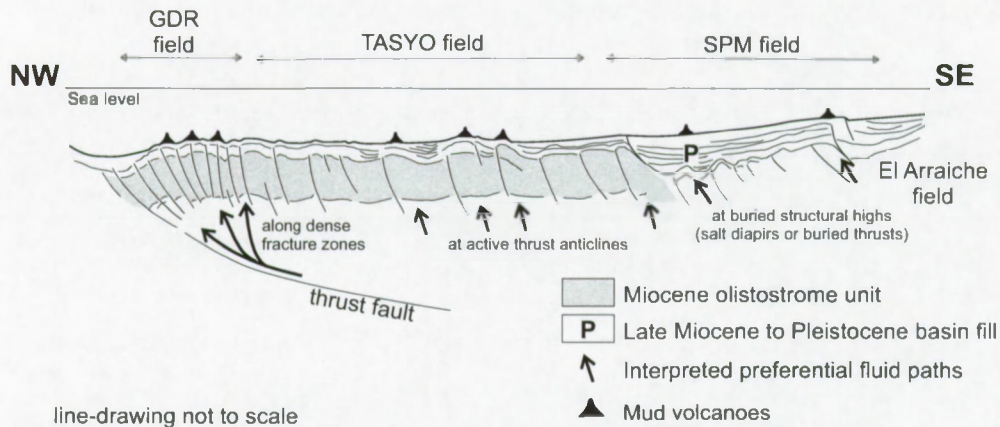

Fig. 12. General structural cross section of the Gulf of Cadiz showing the main mud volcano fields in their structural setting (based on Gracia et al., 2003; Flinch, 1993).

seals accretionary complex structures of Miocene age (Gracia et al., 2003).

The mud volcanoes seem to be located within extensional fault zones, which facilitate vertical upward fluid and sediment injections. The exact location of the mud volcanoes depends on the local and regional stress directions. Mercator mud volcano, the buried mud volcano south of Mercator mud volcano, and Fiúza mud volcano seem to occur within a NE–SW trending deformation zone. Kidd and Adamastor mud volcanoes, and probably a smaller one just south of Adamastor, also appear to occur within a NE–SW oriented deformation zone, almost parallel to the collapse depression that host the Mercator mud volcano (Fig. 11). Sediment injections will occur along fault sections or fractures perpendicular to the direction of minimum horizontal stress (Tingay et al., 2003). Since the anticlines are most likely compressional structures, sediment injections are expected to occur along fault zones perpendicular to the anticline.

Hydrocarbon exploitation in the Gulf of Cadiz only occurs at the Spanish shelf where Spain's largest gas field, the Poseidon field, produced >500 million Nm³ of natural gas in 2002 (Mineco, 2003). The Moroccan and Portuguese margins are largely under explored, only 5 wildcats were drilled at the Portuguese margin in the Algarve basin (IGM, 2003) and 1 at the Moroccan shelf offshore the city of Larache (ONAREP, 2003). In the entire Gulf of Cadiz only 7 exploration wells were drilled at water depths >200 m. The main hydrocarbon source rock is Early to Middle Jurassic oil and gas prone shale. Oil generation was estimated to occur since Toarcian times (ONAREP, 2003). The most important reservoir rocks are Jurassic reefal build-ups and Cretaceous deltaic sands. In the deep water areas Tertiairy turbidites and carbonates are considered to be possible reservoir rocks (ONAREP, 2003). Hydrocarbon exploration in the Gulf of Cadiz is hampered by the intense deformation and nappes emplacement since the Tortonian. Mud volcanoes in the entire Gulf of Cadiz seem to root in Cretacous to Miocene rocks (Akhmanov et al., 2002), below or within the olistostrome units. Somoza et al. (1999) suggest large possible hydrocarbon accumulations below the salt-floored olistostrome units. In the central part of the Gulf of Cadiz the structural deformation extends up to the sediment surface and controls the distribution of mud volcanoes in the GDR, Tasyo

and DPM mud volcano fields. This may indicate a redistribution of hydrocarbon fluids from deeper sources along several fault-controlled pathways through the allochthonous complex. In the SPM and the El Arraiche mud volcanoes fields, most of accretionary wedge thrust anticlines are sealed by a thick Pliocene section and may host considerable hydrocabon accummulations. The area offshore El Arraiche remains poorly tested for hydrocarbon accummulations but seems to have very good potential.

6. Conclusions

The newly discovered El Arraiche field at the Moroccan Atlantic margin, Gulf of Cadiz, consists of 8 mud volcanoes of varying size and shape just below the Moroccan shelf edge. The largest mud volcano, Al Idrissi mud volcano, is 225 m high and 5.3 km in diameter, the smallest observed mud volcano is only 25 m high and 500 m wide. The mud volcanoes seem to be associated with extensional faults with quickly varying throw and strike that compartmentalize anticlinal ridges. The anticlines can be traced regionally and bound extensional basins that formed during the Late Miocene.

The El Arraiche mud volcano field is part of a larger cluster of mud volcanoes (the Spanish Moroccan Field, Gardner, 2001) that lie within the accretionary realm but outside the active olistostrome units. This distinction is clear on regional seismic lines (Gracia et al., 2003; Medialdea et al., 2004) but it also has bearings on the composition and the size of rock clasts in the mud volcanoes (Akhmanov et al., 2002). As other mud volcanoes in the Gulf of Cadiz (Somoza et al., 2002), the El Arraiche mud volcanoes are long-lived structures thought to be related to the episodic migration of hydrocarbons. Onset of mud volcanic activity in the El Arraiche field is estimated at about 2.4 Ma. Since the Upper Pliocene, episodic expulsion of liquidized sediment created vertical piles of extruded mud of up to 500 m thick.

The occurrence of large mud volcanoes bears witness of continued overpressure generation at depth, either by in situ oil and gas generation or by focussed flow and accumulation in the area. The activity of the mud volcanoes is indicated by the thickness of hemipelagic sediments covering extruded mud breccia, the

occurrence of seep-typical fauna, the degree of mixing between thermogenic and biogenic hydrocarbons, or the depth of the sulphate reduction zone. These indications give variable results. Gemini West and Al Idrissi mud volcanoes are most active, as they lack a hemipelagic sediment drape, feature a shallow sulphate reduction zone, high concentrations of methane, and living Pogonophora worms. The ratio of methane concentration over the concentration of higher homologues gives a biogenic gas source in case of the Al Idrissi mud volcano and a thermogenic signature for the Gemini West crater. The eastern twin crater, Gemini East, was the least active, covered by 12 cm of hemi-pelagic mud. Given its structural setting and the evidence of thermogenic hydrocarbons, the area has promising hydrocarbon potential but remains untested.

Acknowledgement

References

Akhmanov, G.G., Ivanoc, M.K., Henriet, J.P., Sarantzev, E.S., 2002. The El Arraiche diapiric field and its "exotic" mud volcanic deposits recovered during the TTR-12 cruise in the Gulf of Cadiz, IOC Workshop Report, vol. 187, p. 9.

Barazza, J., Ercilla, G., 1996. Gas-charged sediments and large pockmark features on the Gulf of Cadiz slope (SW Spain). Mar. Pet. Geol. 13 (2), 253–261.

Barker, C., 1990. Calculated volume and pressure changes during the thermal cracking of oil to gas in reservoirs. AAPG Bull. 74, 1404–1413.

Berástegui, X., Banks, C.J., Puig, C., Taberner, C., Waltham, D., Fernández, M., 1998. Lateral diapiric emplacement of Triassic evaporites at the southern margin of the Guadalquivir Basin, Spain. In: Mascle, A., Puigdefábregas, C., Luterbacher, H., Fernandez, M. (Eds.), Cenozoic Foreland Basins of Western Europe, Geol. Soc. Spec. Publ., vol. 134, pp. 49–68.

Bileva, E., Blinova, V., 2002. Geochemical characteristics of hydrocarbon gasses from mud volcanoes of the Gulf of Cadiz. IOC Workshop Report, vol. 187, p. 12.

Camerlenghi, A., Cita, M.B., Dellavedova, B., Fusi, N., Mirabile, L., Pellis, G., 1995. Geophysical evidence of mud volcanism on the Mediterranean Ridge. Mar. Geophys. Res. 17 (2), 115–141.

De Mol, B., Stadnitskaya, A., Swennen, R., Belenkaya, I., Cave, R., 1998. Geochemical sampling. In: Kenyon, N.H., Ivanov, M.K., Akhmetzhanov, A.M. (Eds.), Cold Water Carbonate Mounds and Sediment Transport on the Northeast Atlantic Margin: Preliminary Results of Geological and Geophysical Investigations During the TTR-7 Cruise of R/V Professor Logachev in Co-operation with the CORSAIRES and ENAM 2 Programmes, July–Aug. 1997, IOC Technical Series, vol. 52. UNESCO, pp. 15–20.

Flinch, J.A. 1993. Tectonic evolution of the Gibraltar Arc. Unpublished PhD thesis, Rice University, Houston.

Flinch, J.A., Bally, A.W., Wu, S., 1996. Emplacement of a passive margin evaporitic allochton in the Betic Cordillera of Spain. Geology 24, 67–70.

Gardner, J.M., 2000. Gulf of Cadiz/Moroccan margin, mud diapirism and mud volcanism study, introduction and geological setting. In: Kenyon, N.H., Ivanov, M.K., Akhmetzhanov, A.M., Akhmanov, G.G. (Eds.), Multidisciplinary Study of Geological Processes on the North East Atlantic and Western Mediterranean Margins, UNESCO Intergovernmental Oceanographic Commission Technical Series, vol. 56, p. 56.

Gardner, J.M., 2001. Mud volcanoes revealed and sampled on the Western Moroccan continental margin. Geophys. Res. Lett. 28 (2), 339–342.

Gardner, J.M., Shashkin, P., 2000. Gulf of Cadiz/Moroccan margin (leg 2). Mud diapirism and mud volcanism study. Side scan sonar. In: Kenyon, N.H., Ivanov, M.K., Akhmetzhanov, A.M., Akhmanov, G.G. (Eds.), Multidisciplinary Study of Geological Processes on the North East Atlantic and Western Mediterranean Margins, IOC Technical Series, vol. 56.

Gracia, E., Danobeitia, J., Verges, J., Bartolome, R., Cordoba, D., 2003. Crustal architecture and tectonic evolution of the Gulf of Cadiz (SW Iberian margin) at the convergence of the Eurasian and African plates. Tectonics 22 (4), 1033.

Gutscher, M.A., Malod, J., Rehault, J.P., Contrucci, I., Klingelhoefer, F., Mendes-Victor, L., Spakman, W., 2002. Evidence for active subduction beneath Gibraltar. Geology 30 (12), 1071–1074.

Hernández-Molina, F.J., Somoza, L., Vazquez, J.T., Lobo, F., Fernández-Puga, M.C., Llave, E., Daíz-del Río, V., 2002. Quaternary stratigraphic stacking patterns on the continental shelves of the southern Iberian Peninsula: their relationship with global climate and palaeoceanographic changes. Quat. Int. 92, 5–23.

IGM 2003. http://www.igm.ineti.pt/departam/npep/default.htm.

Kenyon, N.H., Ivanov, M.K., Akhmetzhanov, A.M., Akhmanov, G.G., (Eds.), 2003. Interdisciplinary Geoscience Research on the North East Atlantic Margin, Mediterranean Sea, and Mid Atlantic Ridge During the TTR-12 Cruise of RV Professor

Logachev, June–August 2002, IOC Technical Series, vol. 67. UNESCO (156 pp.).

Maestro, A., Somoza, L., Medialdea, T., Talbot, C.J., Lowrie, A., Vazquez, J.T., Diaz-del-Rio, V., 2003. Large-scale slope failure involving Triassic and Middle Miocene salt and shale in the Gulf of Cadiz (Atlantic Iberian Margin). Terra Nova 15, 380–391.

Maldonado, A., Somoza, L., Pallarés, L., 1999. The betic orogen and the Iberian–African boundary in the Gulf of Cadiz: geological evolution. Mar. Geol. 155, 9–43.

Mazurenko, L.L., Soloviev, V.A., Belenkaya, I., Ivanov, M.K., Pinheiro, L.M., 2002. Mud volcano gas hydrates in the Gulf of Cadiz. Terra Nova 14, 321–329.

Medialdea, T., Vegas, R., Somoza, L., Va zquez, J.T., Maldonado, A., Diaz-del-Rio, V., Maestro, A., Cordoba, D., Fernandez-Puga, M.C., 2004. Structure and evolution of the "Olistostrome" complex of the Gibraltar Arc in the Gulf of Cádiz (eastern Central Atlantic): evidence from two long seismic cross-sections. Mar. Geol. 209, 173–198.

Mineco 2003. http://www.cne.es/documentos/petroleo/estadisticas/.

ONAREP 2003. http://www.onhym.com/onarep/.

Ovsyannikov, D.O., Sadekov, A.Yu., Kozlova, E., 2003. Rock fragments from mud volcanic deposits of the Gulf of Cadiz: an insight into the Eocene–Pliocene sedimentary succession of the basin. Mar. Geol. 3273, 1–11.

Pinheiro, L.M., Ivanov, M.K., Sautkin, A., Akhmanov, G., Magalhães, V.H., Volkonskaya, A., Monteiro, J.H., Somoza, L., Gardner, J., Hamouni, N., Cunha, M.R., 2002. Mud volcanism in the Gulf of Cadiz: results from the TTR-10 cruise. Mar. Geol. 3269, 1–21.

Prior, D.B., Doyle, E.H., Kaluza, M.J., 1989. Evidence for sediment eruption on deep-sea floor, Gulf of Mexico. Science 243, 517–519.

Sartori, R., Torelli, L., Zitellini, N., Peis, D., Lodolo, E., 1994. Eastern segment of the Azores–Gibraltar line (central-eastern Atlantic): an oceanic plate boundary with diffuse compressional deformation. Geology 22, 555–558.

Somoza, L., Maestro, A., Lowrie, A., 1999. Allochtonous Blocks as Hydrocarbon Traps in the Gulf of Cadiz. Offshore Technology Conf. Proc. OTC-12202, pp. 571–577.

Somoza, L., Gardner, J.M., Diaz-del-Rio, V., Vazquez, J.T., Pinheiro, L.M., Hernàndez-Molina, F.J.the TASYO/Anastasya shipboard parties, 2002. Numerous methane gas-related sea floor structures identified in the Gulf of Cádiz. EOS, p. 541.

Somoza, L., Díaz-del-Río, V., León, R., Ivanov, M., Fernández-Puga, M.C., Gardner, J.M., Hernández-Molina, F.J., Pinheiro, L.M., Rodero, J., Lobato, A., Maestro, A., Vázquez, J.T., Medialdea, T., Fernández-Salas, L.M., 2003. Seabed morphology and hydrocarbon seepage in the Gulf of Cádiz mud volcano area: acoustic imagery, multibeam and ultra-high resolution seismic data. Mar. Geol. 195, 153–176.

Stadnitskaia, A., Blinova, V., Poludetkina, E., 2002. Hydrocarbon gas sampling. In: Kenyon, N.H., Ivanov, M.K., Akhmetzhanov, A.M., Akhmanov, G.G. (Eds.), Geological Processes in the Mediterranean and Black Seas and North East Atlantic; Preliminary Results of Investigations during the 11th Training-Through-Research (TTR-11) Cruise of RV Professor Logachev, July–September, 2001, IOC Technical Series, vol. 62. UNESCO, pp. 34–39.

Tingay, M.R.P., Hillis, R.R., Morley, C.K., Swarbrick, R.E., Okpere, E.C., 2003. Pore pressure/stress coupling in Brunei Darussalam—implications for shale injection. In: Van Rensbergen, P., Hillis, R.R., Maltman, J., Morley, C.K. (Eds.), Subsurface Sediment Mobilisation, Special Publication of the Geological Society of London, vol. 216, pp. 369–379.

Van Rensbergen, P., Morley, C.K., Ang, D.W., Hoan, T.Q., Lam, N.T., 1999. Structural evolution of shale diapirs from reactive rise to mud volcanism: 3D seismic data from the Baram delta, offshore Brunei Darussalam. J. Geol. Soc. Lond. 156, 633–650.

Van Rensbergen, P., Hillis, R.R., Maltman, J., Morley, C.K., 2003. Subsurface sediment mobilization, introduction. In: Van Rensbergen, P., Hillis, R.R., Maltman, J., Morley, C.K. (Eds.), Subsurface Sediment Mobilisation, Special Publication of the Geological Society of London, vol. 216, pp. 1–8.

Van Rensbergen, P., Depreiter, D., Pannemans, B., Henriet, J.P., 2005. Seafloor expression of sediment extrusion and intrusion at the El Arraiche mud volcano field, Gulf of Cadiz. J. Geophys. Res. 110 (F2), F02010. (24 May).

Seafloor expression of sediment extrusion and intrusion at the El Arraiche mud volcano field, Gulf of Cadiz

Pieter Van Rensbergen, Davy Depreiter, Bart Pannemans, and Jean-Pierre Henriet

Renard Centre of Marine Geology, Ghent University, Gent, Belgium

[1] The El Arraiche mud volcano field consists of eight mud volcanoes up to 255 m high and 5.4 km wide, located in the Moroccan margin of the Gulf of Cadiz at water depths between 700 and 200 m. Available data include detailed swath bathymetry over the entire area, dense grids of high-resolution seismic data, very high resolution deep tow subbottom profiles, side scan sonar mosaics over the major structures, selected underwater video lines, and sediment samples. The main morphological aspects of the mud volcanoes are, from the margin toward the center, a subsidence rim or moat, the mud volcano slope, in some cases a deep crater, and a recent central mud dome at the top. The slope is characterized by radial outward sediment flow deposits or by a concentric pattern of terraces and steps. The sediment flow deposits can be divided into elongate outflows that accumulate at the base of the slope and short bulky outflow deposits that freeze on the steep slope. The crater hosts extruded sediment ranging from fluidized sand to mud breccia with centimeter- to meter-sized rock clasts issued from several vents within the crater. The concentric slope terraces and the central mud dome are interpreted to result from several phases of uplift caused by sediment intrusion or shallow diapirism. The mud volcano growth is thus interpreted to result from a combination of extrusive and intrusive processes.

1. Introduction

[2] The El Arraiche mud volcano field (Figure 1) was discovered in May 2002 in the Moroccan Atlantic margin in the Gulf of Cadiz [*Van Rensbergen et al.*, 2005]. It consists of eight mud volcanoes of varying size and shape just below the shelf edge (Figure 2). The largest mud volcano in the field (Al Idrissi mud volcano) is 255 m high and 5.4 km wide. The 2002 surveys by the RV *Belgica* and the RV *Logachev* yielded detailed swath bathymetry over the entire area, dense grids of high-resolution seismic data, very high resolution deep tow subbottom profiles, side scan sonar mosaics over the major structures, selected video lines, TV grabs, dredge samples and gravity cores.

[3] The large amount of sea floor data and the clear shape of the larger mud volcanoes prompted this paper to focus on the morphology of the mud volcano cones. Although mud volcanoes are prominent features in the submarine seascape [see *Kopf and Behrman*, 2000, and references therein], little attention has yet been given to their small-scale morphology. Morphological mapping using high-resolution multibeam bathymetry offshore, or satellite altimetry onshore, has only become widely available during the past decade. Previously, submarine

mud volcanoes were imaged using side scan sonar mosaics and single beam bathymetry. The imaging resolution of deep towed side scan sonar systems is often an order of magnitude better than that of a hull-mounted multibeam system, but the impact of acoustic properties of the sediment and of the acquisition direction on the imaging makes it often difficult to interpret morphological information.

[4] Mud volcanoes in their broadest sense refer to any extrusion of mobilized sediment. Included are (1) mud volcanoes sensu strictu that are cone shaped with central vents, (2) mud mounds or ridges that are positive features without vent structure, and (3) mud pools that are negative features [*Brown*, 1990]. This morphological variation is related to the variation of fluid content [*Shih*, 1967], sediment properties and the width of the feeder system [*Kopf and Behrman*, 2000]. The feeder system may vary from narrow feeder pipes (diatremes) [*Brown*, 1990] that channel fluids and fluidized sediment to wide areas with bulk movement of plastic mud [*Deville et al.*, 2003]. Mud volcanoes sensu strictu are often considered as a sedimentary analog of stratovolcanoes, built by stacked sediment flows issued from a central crater or subsidiary vents at the flanks [e.g., *Dimitrov*, 2002]. In that case, outflow lenses accumulate as wedge-shaped deposits, thinning away from the feeder area, and build a mud volcano cone. The crater area is a low-relief area formed by collapse after expulsion of fluids and possibly
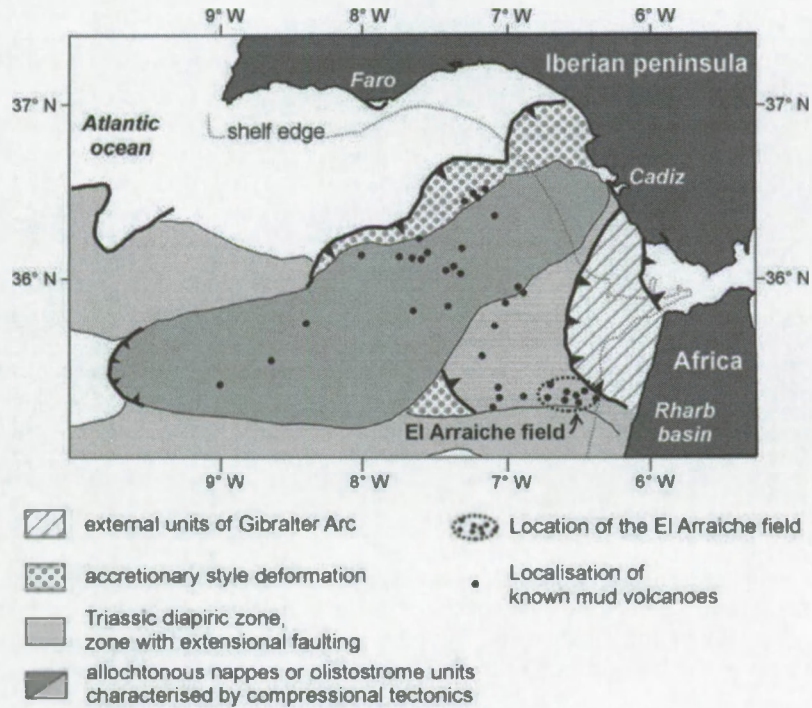
Figure 1. Geological setting of the El Arraiche mud volcano field, south in the Gulf of Cadiz (modified after *Maldonado et al.* [1999], *Somoza et al.* [2003], and *Pinheiro et al.* [2003]).

by subsidence because of sediment removal. As in the case for magmatic volcanoes [*Annen et al.*, 2001], the morphology of mud volcanoes sensu stricto is largely attributed to extrusion processes whereas the effect of intrusive processes remains unclear. High-resolution seismic profiles provide little information about the internal structure of a large mud cone, due to acoustic blanking.

We can in this case only deduce formation processes from the information available at the surface.

2. Geological Background

[5] In the Gulf of Cadiz, over 30 mud volcanoes have been sampled since they were first discovered in 1999
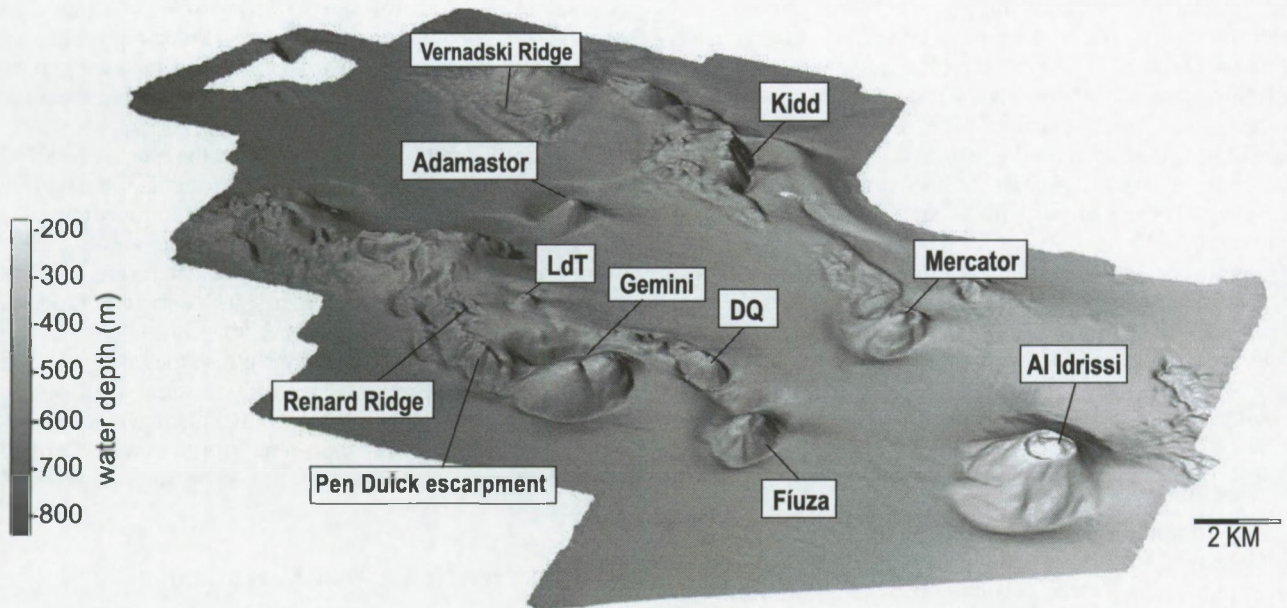
Figure 2. Three-dimensional morphology of the El Arraiche mud volcano field derived from multibeam bathymetry. Al Idrissi is the largest mud volcano, 255 m high and 5.4 km in diameter. Don Quichote (DQ) and Lazarillo de Tormes (LdT), the smallest mud volcanoes, are only about 25 m high.
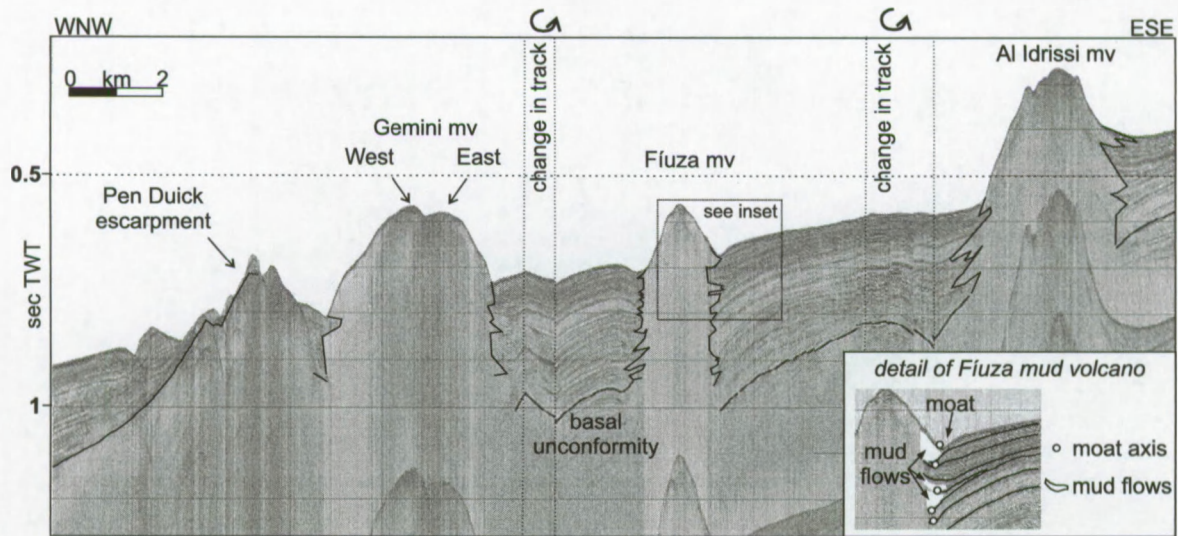
Figure 3. General high-resolution seismic line (sparker source) over Al Idrissi, Fíuza, and Gemini mud volcanoes. On the seismic sections the mud volcanoes are reflection-free zones. At their flanks, mud flow deposits interfinger with stratified sediments. The inset shows a detail of interfingering mud flows that accumulate in moats at the base of the Fíuza mud volcano cone.

[*Gardner*, 2001; *National Geographic*, 2002]. Most occur in the central part (Figure 1) [*Somoza et al.*, 2003; *Pinheiro et al.*, 2003] where large Miocene, densely faulted olistostrome units occur close to the sediment surface [*Maldonado et al.*, 1999]. The El Arraiche mud volcano field is located in the Moroccan Atlantic continental slope in water depths ranging from 200 m to 700 m. In contrast to the central mud volcano fields, the El Arraiche field is located over a large extensional Pliocene basin between regions of olistostrome emplacement (Figure 1) [*Flinch*, 1993; *Flinch et al.*, 1996; *Gràcia et al.*, 2003]. Within the Pliocene basin, the El Arraiche mud volcanoes occur over anticlinal ridges where the Pliocene plumbing system is thinnest and extensional faulting facilitates fluid and sediment injection into the overburden [*Van Rensbergen et al.*, 2005]. On seismic sections (Figure 3), the mud volcanoes are imaged as a columnar zone without acoustic penetration, about the width of the mud volcanic cone. Large sediment flows emerging from this central zone are also free of reflections, but show a sharp transition to the stratified hemipelagic sediment. These sediment flows are typically lens shaped, convex at the top and often fill a moat at the base of the mud volcano. The earliest sediment flows occur just above a regional unconformity, about 350 m and 900 m below sea level, attributed to a sea level low at 2.4 ma [*Hernández-Molina et al.*, 2002; *Van Rensbergen et al.*, 2005]. Since this time successive episodes of mud volcanism created a pile of remolded mud of over 400 m thick.

3. Data and Methods

[6] The multibeam survey on board R/V *Belgica* used a Kongsberg EM 1002, extended with a deep water module. Maximum sailing speed was 6 knots, with a swath width of 750 m in shallow water (<500 m) and limited to 500 m in deep water to reduce signal deterioration and noise. The acquired data were corrected and cleaned with the Kongsberg packages Merlin and Neptune. The footprint at 400 m

is 15 m × 15 m. In total, 700 km^2 were covered. In addition, a total of 62 high-resolution seismic profiles were acquired in three dense grids with a line spacing of about 1 km centered on the Mercator, Al Idrissi and Gemini mud volcanoes [*Van Rensbergen et al.*, 2005].

[7] During the TTR 12 survey, side scan sonar imagery over the main features was acquired using the deep-towed hydroacoustic complex Mak-1, with an operating frequency of 30 kHz, and a subbottom profiler operating at 5 kHz. On the basis of the side scan sonar data, six transects were chosen for a deep-towed video line, for a total of 15 hours. On the basis of the video lines, TV-guided grab samples were taken. Dredge samples of mud breccias at the surface were taken on Mercator and Al Idrissi mud volcanoes. In the craters of the main mud volcanoes (Mercator, Al Idrissi, Gemini, and Fíuza) the subsurface was sampled by gravity cores. Four additional box cores are also available from the R/V *Belgica* survey.

[8] From the eight mud volcanoes in the cluster, four (Al Idrissi, Mercator, Gemini and Fíuza) are studied in detail by combining multibeam, side scan sonar and sedimentological data. For a better visualization, slope angle and curvature (second derivative of z in x and y) were calculated on basis of the three-dimensional bathymetry. The curvature function calculates isobath curvature on a map view and distinguishes between convex and concave shapes. It is a good tool to map sediment flow deposits as they stand out as elevations (convex) on the slope. The sedimentary facies within the crater and on the upper slopes were described from underwater video lines calibrated by core, dredge and grab samples.

4. Data Description and Interpretation

[9] The morphology of the mud volcanoes in the El Arraiche field consist of, from base to top: a moat around part of the base of the mud volcano cone, an irregular slope characterized by radial outward sediment flows,

name	Water depth top (m)	Height (m)	Slope			Crater	Crater's central dome		Moat		Quadrant
			Width base (km)	Width top (km)	Overall angle (°)	max depth (m)	Height (m)	Diameter (km)	Radius (km)	Max depth (m)	
Al Idrissi	197	111 - 255	4.3 - 5.4	1.2 - 1.5	5 - 8	17	14 – 42	1.9 – 2.3	2.85	16	
Mercator	350	51 – 141	2.45 – 1.82	0.98 – 1.1	5.5 - 10	2	22 – 38	0.65 – 0.8	1.3	9	
Gemini W	423	170 - 252	4.1 – 2.3	1.1	5.5 - 8.5	No crater	23 - 27	0.52 – 0.87	1.5 – 1.9	12	
Gemini E	423	117 – 169		0.95 – 1.3	5 - 10.5	No crater	13 – 23	0.7 – 0.87	0.95 – 1.25	3	
Fíuza	393	97 - 143	2.9 – 2.1	0.75 – 0.8	6 - 10	No crater	27	0.5 – 0.7	1.1 – 1.6	36	

Figure 4. General morphological characteristics of the main mud volcanoes of the El Arraiche field.

terraces and/or depositional sediment flow escarpments (lobe fronts), a crater depression or a flat top, and a central dome. Figure 4 gives an overview of the measures of these main morphological aspects for the mud volcanoes discussed in this paper. More detailed measurements are listed in Table 1 to avoid lengthy descriptions in the next paragraphs.

4.1. Al Idrissi Mud Volcano

[10] Al Idrissi mud volcano is the largest and shallowest mud volcano in the field, situated just below the shelf edge (Figure 5). It is up to 255 m high and 5.4 km in diameter. It has a well-developed crater (−17 m) and large central dome (42 m) within the crater. Numerous sediment flow deposits characterize the flanks of the mud volcano (Figure 5a) and extend from the crater to the moat at the base. The moat is up to 16 m deep and has a radius of about 2.85 km. On side scan sonar data, high-backscatter sediment flow deposits contrast sharply with the low-backscatter sea floor (Figure 5b), except at the southeastern side of the volcano where the backscatter intensity weakens probably due to a thickening hemipelagic cover. The contrast in backscatter distinguishes erupted sediment from the hemipelagic slope sediments. Sediment extrusion is well constrained to the semicircular cone. There are no distant outrunners observed. The radial pattern of down slope sediment flows is clearly visualized by the curvature function (Figure 5c).

[11] Two types of sediment flow deposits can be distinguished: elongated sediment flow deposits that extend to the foot of the slope (type I) and short bulky sediment flow deposits that occur on the steeper parts of the slope (type II). Type I sediment flow deposits are up to 2.5 km long and accumulate at the foot of the slope in a fan or drop-shaped termination. Their distal part is often captured and deflected by the erosional moat. They have an even texture on side scan sonar indicating a smooth surface without flow fronts. The slope has a concave profile with an increasing slope angle of 0.5°–7° at the base to 12°–14° near the top (Figure 5d). Type II sediment flow deposits occur mainly at the western slope in a somewhat tongue-shaped area with irregular relief. They do not extend downward to the base of the slope. The depositional lobes have a very steep and high depositional fronts (<14°). The

resulting slope is irregular but with a constant overall angle of about 8°.

[12] The crater and the top of the slope of Al Idrissi mud volcano (Figure 6) were surveyed with underwater video lines and sampled by gravity cores, box cores and dredges. Within this area two sedimentary facies can be identified; AI-1 and AI-2. Facies AI-1 is a coarse, pebbly sand with some patches of small stones (<10 cm) that covers most of the crescent-shaped crater depression and the central cone within the crater (Figure 5e). Core 411G and box cores B1 and B2 (location in Figure 6b) at the top and at the northern flank of the central dome reveal that the sandy layer is only 3–5 cm thick with a sharp and irregular limit separating it from mud breccias. In core 411G (Figure 7) this mud breccia is a stiff, structureless clay with clay stone clasts up to 1 cm. Facies AI-2 is the main facies on the slopes within and around the crater and is very heterogeneous. Stones litter the surface, with sizes ranging from 1–2 cm to more than 50 cm. Clast distribution ranges from areas featuring virtually no stones, strongly resembling AI-1, to true piles of blocks. A dredge over AI-2 at the upper western slope showed that the stones have a wide variety of lithologies, from cemented limestone to sandstone. On the southeast slope, prominent features of facies AI-2 are smoothed by a drape of dark green mud. Facies AI-2 and AI-1 are interpreted as material that was brought to the surface by mud volcanic extrusion, with possible reworking and redistribution of sediment within the crater. The crater sedimentology contrasts strongly with the background sediment, which was retrieved in box core B3 (Figure 5e), north of Al Idrissi at 415 m water depth and consists of a homogenous light brownish oxidized mud (silty clay).

[13] Sediment extrusion in the crater is imaged in detail using the curvature function in combination with side scan sonar (Figure 6a) and sedimentological data from video lines and sea floor samples (Figure 6b). Sediment flows within the crater were erupted from at least three individual vents. Vents are interpreted to be present at the common origin of radial sediment flow deposits, often a rounded elevation. Sediment flows from vent A and B are associated with the rocky sediment facies AI-2 and display a series of flow fronts on side scan sonar images that are below the resolution of the multibeam system. The sandy facies AI-1 is associated with flows from vent C at the top of the central

Table 1. Detailed Measurements of the Main Morphological Elements of the Mud Volcanoes

Interpreted Extrusion Types	Slope Profile	Overall Slope Angle, deg	Steepest Depositional Slope Angle, deg	Lowest Depositional Slope Angle, deg	Lobe Fronts and Terraces		
					Maximum Height, m	Maximum Width	Distance From Crater Rim, km
Al Idrissi							
Type I elongate mud flows	steepening concave-up	5 (incl. by-pass zone)	8.5	0.5	~20	~800	0.9–2.5
Type II short mud flows	straight with undulations	8	14	4	~40	~700	0.45–1.4
Crater's central dome	terraced	3	7.5	0 at top	~10	~700	within crater
Mercator							
Type I elongate mud flows	steepening concave-up	5.5	8	1.5	no lobe fronts	~600	0.9–1.3
Diapiric uplift?	terraced	8	12.5	2.5	~45	~1500	0–1
Crater's central dome	convex -up	5	11	0 at top	~25	~500	within crater
Gemini							
Type I elongate mud flows	steepening concave-up	5	10	1	no lobe fronts	~600	0.8–1.2
Type II short mud flows	terraced, convex-up	8.5	15.5	5.5	~45	~600	0.25–0.9
Diapiric uplift?	terraced	10.5	17	6	~35	~1400	0–1.1
Crater's central dome	convex -up	3	9.5	0 at top	~20	~500	within crater
Fiuza							
Type I elongate mud flow	steepening concave-up	6	10	5	~15	~600	0.6–0.9
Type II short mud flows	terraced, convex-up	10	18	6	~50	~400	0.3–0.7
Diapiric uplift?	terraced	8	13	3.5	~30	~400	0–0.8
Crater's central dome	convex -up	2.5	6	0 at top	~10	~200	within crater

dome. Most likely, fluidized sand spread out from the top to the deepest part of the crater depression. The sand layer is only 3–4 cm thick and it is unlikely that it formed the observed convex sediment flow deposits, which has meter-scale relief. Therefore it is interpreted to postdate earlier mud breccia extrusion at vent C.

4.2. Mercator Mud Volcano

[14] Mercator mud volcano is an asymmetric mud volcano (Figure 8), about 140 m high at the southern side but only 90 m high at the northern side and only 50 m high at the eastern side. The crater is very shallow (−2 m) but the central dome is large (38 m). In this case, the slope is characterized by concentric steps rather then by radial sediment flow deposits.

[15] The concentric pattern is mainly caused by two terraces at the southern flank of the mud volcano (Figure 8). These terraces are almost horizontal (slope 2°–3°) separated by high steps that continue laterally for up to 1.5 km. The overall slope of the southern flank is about 7°. The upper slope has a high backscatter on side scan sonar data that is not related to the step-like morphology but probably caused by lithology or surface roughness. Flow fronts on the side scan sonar image coincide with short convex deposits that may be attributed to type II sediment flows. These sediment flow deposits are difficult to distinguish and do not seem to have a large effect on the overall slope morphology.

[16] Type I sediment flow deposits fan out at the base of the western slope (Figure 8). They extend 1300 m from the crater edge and accumulated in a base-of-slope deposit. Depositional lobes (on the scale of the available resolution) have a width of 500–600 m. The depositional slope is very low (1°–2°) and there are no steep flow fronts observed. On side scan sonar data (Figure 8b), these sediment flow deposits have a smooth surface and a low backscatter that blends in with the surrounding sea floor. The northern flank is a steep regular and smooth surface with a slope of about 10°–13°. An escarpment at the eastern flank could be related to a WNW-ESE oriented fault, which would help to explain the asymmetry in the morphology. No such fault was observed on the subsurface data. The escarpment may be due to gravitational instability of the southern mud volcano flank (G. Ernst, personal communication, 2004), but no such indications were observed on the subsurface data.

[17] The top of the Mercator mud volcano (Figure 9) consists of a shallow crater (−2 m) and high central dome (38 m). At the southern side the crater is absent and only a break in slope occurs. The central dome is flat topped with an overall slope of about 5°. Mud breccia with up to 10 cm large clasts crops out at the sea floor at the top of the central dome. On the basis of underwater observations and sediment samples, a generally decreasing thickness of the hemipelagic mud overlying the mud breccia is observed from the flanks toward the top. The hemipelagic sediment cover has a thickness of 8 cm at core 408G (Figure 7). At the top of the central dome a single vent was identified at the origin of radial sediment flow deposits within the crater. The sediment flow deposits are characterized by concentric flow fronts on side scan sonar data that seem to culminate in steep slope at the front of the depositional
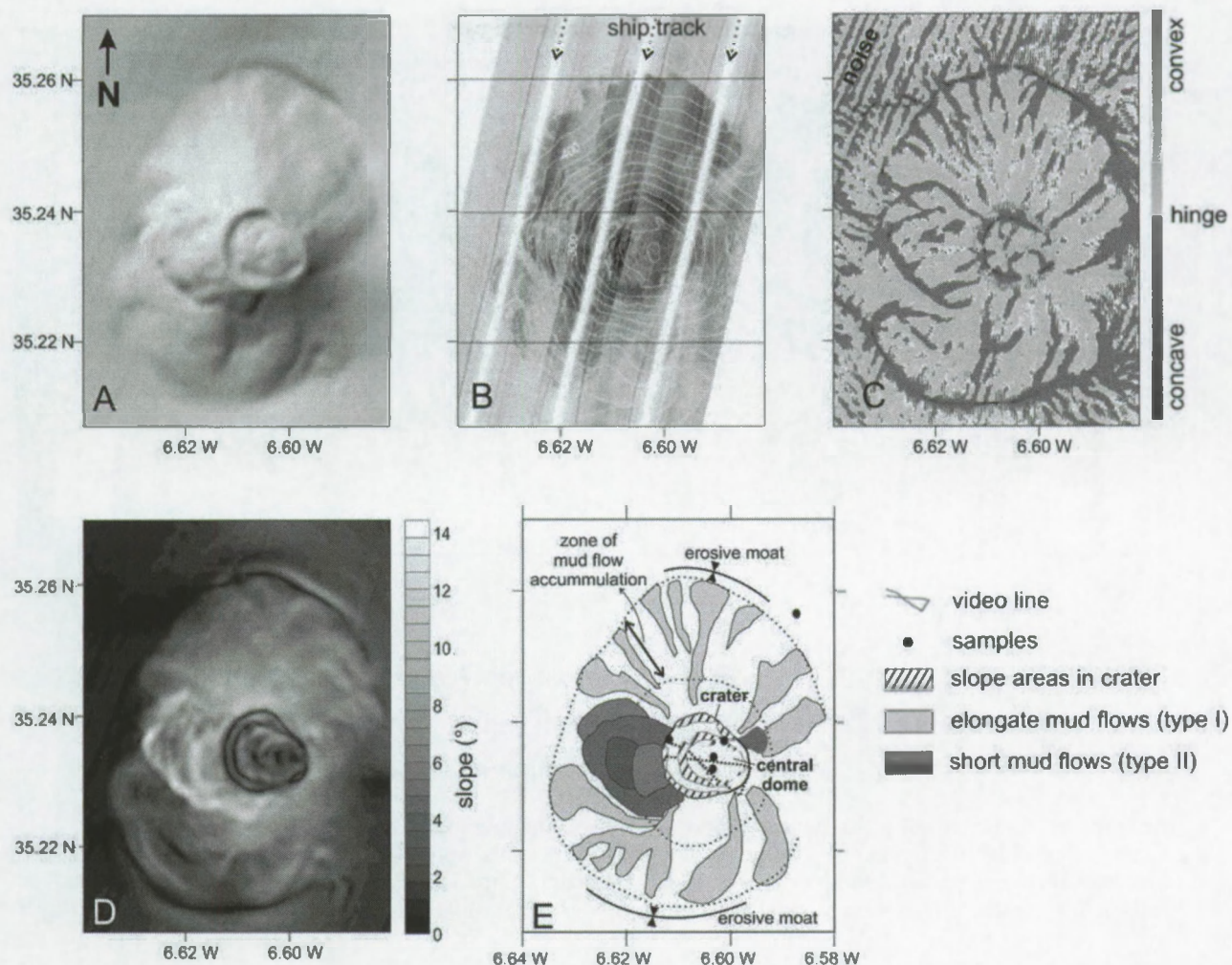
Figure 5. Morphology of the Al Idrissi mud volcano. (a) Shaded relief map. (b) Side scan sonar mosaic with bathymetry contours. (c) Curvature of mud volcano isobaths. (d) Slope map with bathymetry contours. (e) Interpretation map. Numerous sediment flow deposits, characterized by high backscatter and convex morphologies, are distinguished on the slopes. They occur in a radial pattern away from the crater and accumulate at the base of the volcanic cone (type I sediment flows), which results in a steepening, concave slope profile. On the western slope, sediment flow deposits accummulated at the slope (type II sediment flows) and created a steeper irregular slope profile. See color version of this figure at back of this issue.

lobe. These extrusive deposits are also covered by hemi-pelagic mud, except at the top of the central dome. The most recent extrusion was restricted to the crest of the central dome, which indicates that extrusive activity has been decreasing. This is confirmed by low hydrocarbon seepage activity assessed by *Van Rensbergen et al.* [2005].

4.3. Gemini and Fíuza Mud Volcanoes

[18] Gemini mud volcano consists of two summits in one large oval-shaped mud volcano (Figure 10). The Gemini mud volcano is about 250 m high, 4.88 km long to 2.5 km wide at the base, the diameter at the top of the eastern part is 0.9 km and the diameter of the western part is 0.6 km. The summits consist of a flat area with central domes of 23 m and 27 m, respectively, above the flat top. The differentiation between the two summits is visible from about 80 m below the top of the mud volcano as a 400 m long and 20 m deep crease.

[19] The morphology of the slopes involves semiconcentric terraces at southern and northwestern flanks, type I sediment flow deposits at the eastern and western sides, and, less distinguishable, type II sediment flow deposits at the northern slope of Gemini East. The semiconcentric steps are about 20 m high, have a maximum slope of 17°, and continue laterally for about 1–1.4 km. At the northern flank of Gemini East, the steps are only 500 m wide and may also be attributed to type II sediment flow deposits. The side scan sonar data show high backscatter and irregular texture, similar to the upper slopes of the Mercator mud volcano. Type I sediment flow deposits are only visible at the eastern and western sides of the mud volcano. They are characterized by the fan-shaped deposit at the base of the slope, and their smooth texture and low-backscatter values on side scan sonar data.

[20] The sedimentology of the top of the mud volcano is similar to that of the Mercator mud volcano and consists of
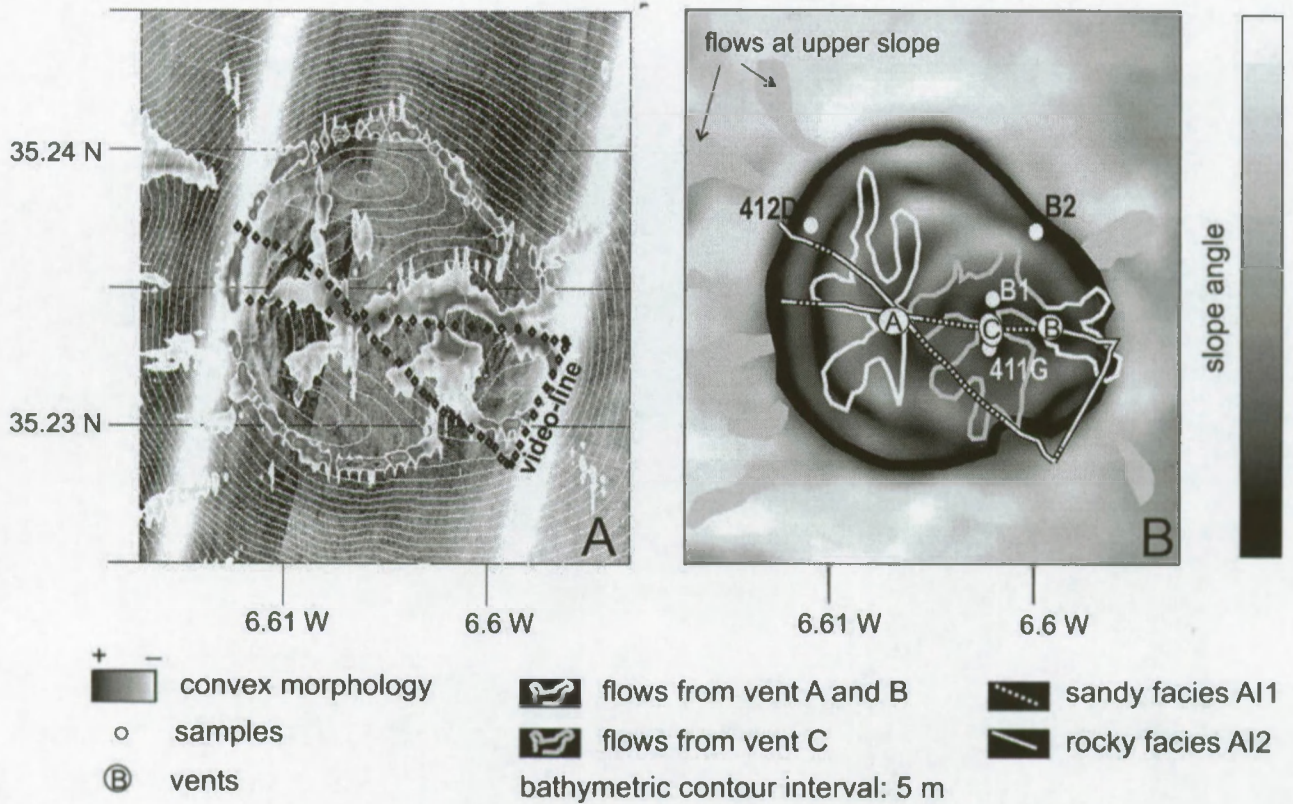
Figure 6. Crater of Al idrissi mud volcano. (a) Convex morphologies mapped over side scan sonar image shows the distribution of small mud flows issued by vents within the crater. (b) Slope map with indication of interpreted sediment flow deposits and sedimentary facies from underwater video lines distinguishing the different outflow events. See color version of this figure at back of this issue.
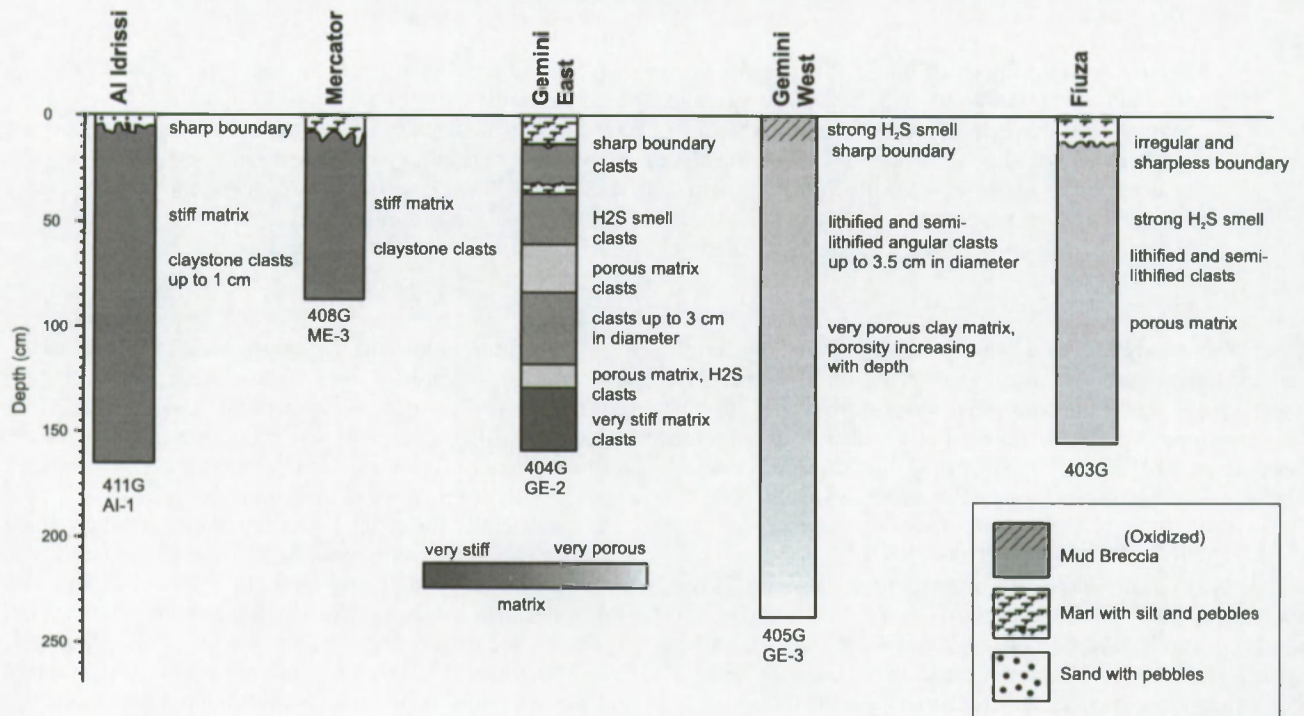
**Figure 7.** Description of gravity cores located at the crests of the main mud volcanoes. The localization of the cores is indicated in Figure 6 (crater of Al Idrissi mud volcano), Figure 9 (crater of Mercator mud volcano), Figure 10 (for Fíuza mud volcano), and Figure 11 (top of Gemini mud volcano). Cores have widely varying fluid contents. Inactive mud volcanoes are covered by a hemipelagic drape.

Figure 8. Morphology of the Mercator mud volcano. (a) Shaded relief map. (b) Side scan sonar mosaic with bathymetry contours. (c) Curvature of mud volcano isobaths. (d) Slope map with bathymetry contours. (e) Interpretation map. Mercator mud volcano is an assymetric mud volcano with a smooth northern slope and concentric steps at the southern slope. Only at the western slope, type I sediment flow deposits, here characterized by a low backscatter, fan out at the base of the cone. See color version of this figure at back of this issue.

mud breccia overlain by hemipelagic mud of varying thickness. Core 404G at the eastern summit (Figure 7) reveals 12 cm of bioturbated marl (hemipelagic mud), on top of different layers of mud breccias. Core 405G at the western summit (Figures 7 and 10e) shows a gray mud breccia with a heavy H_2S smell without hemipelagic sediment. The surface layer is an oxidized, heavily bioturbated mud breccia with centimeter-sized clasts. Figure 11 shows the detail of the top of the mud volcano. Sediment flow deposits issued from at least six vents distributed over the crestal area were identified. A remarkable observation is that the gully that separates both crests is not filled in by the extrusive sediment flows.

[21] Fiuza mud volcano is a smaller mud volcano east of Gemini (Figure 10). It is 143 m high, up to 2.9 km wide at the base and has a flat top of about 800 m wide with a central dome of 27 m high and 500–700 m wide. The flanks of the Fiuza mud volcano mainly consist of radial outward type I sediment flows with an overall slope of about 6°. At the northern flank (overall slope about 9.5°), a 400 m wide step with a slope of 18° may be attributed to a type II sediment flow. At the southern flank (overall slope 6.5°) a series of steps with a slope of about 11° resemble the

morphology that typified the Mercator mud volcano. Core 403G (Figures 7 and 10e) at the top of the mud volcano retrieved a homogeneous mud breccia covered by 12 cm of pelagic marl. The Fiuza mud volcano is encircled by a moat with a maximum depth of 27 m below the surrounding sea floor. The Fiuza mud volcano is too small for its summit to image successfully.

5. Synthesis and Discussion

5.1. Extrusion Deposits

[22] In a synthesis of our observations (Figure 12) four types of sediment extrusion deposits could be distinguished. Table 2 is a synthesis of Table 1 and gives the measured minimum and maximum values for each morphological element.

[23] 1. Type I sediment flows form elongate concave deposits that spread out at the base of the slope. The smooth, even texture stands out on side scan sonar data, also when the backscatter is high. They are characterized by low depositional slopes, gentle lobe fronts (if any) and a long down slope length. As they accumulate at the base of the slope they tend to reduce the overall slope angle and
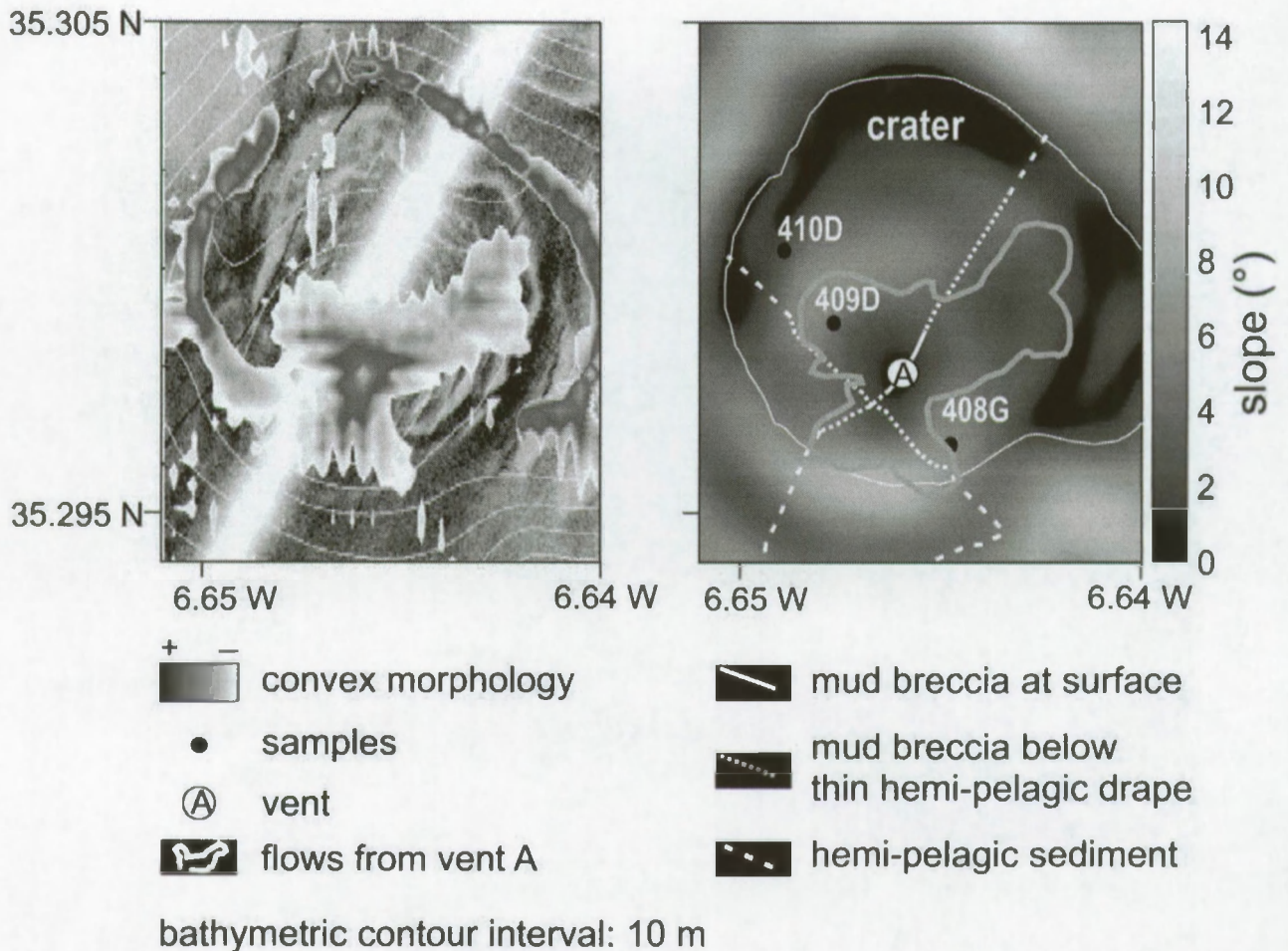
Figure 9. Crater of Mercator mud volcano. (a) Convex morphology mapped over side scan sonar image shows the distribution of small mud flows within the crater around a single vent at the summit. (b) Slope map with indication of interpreted sediment flow deposits and sedimentary facies from underwater video lines. See color version of this figure at back of this issue.

create a typical steepening concave slope profile. They can be interpreted as debris flows with low yield strength [*Mulder and Cochonat*, 1996].

[24] 2. Type II sediment flows form short irregular flow deposits that accumulate on the mud volcano slopes. Semiconcentric flow fronts, variable backscatter and irregular texture characterize type II flow deposits on side scan sonar data. The depositional slopes are considerably steeper and lobe fronts are high. The resulting slope profile is irregular with a linear to convex profile. They can be interpreted as debris flows with high yield strength [*Mulder and Cochonat*, 1996].

[25] 3. A third type of debris flows is restricted to the crater area. Several vents at the top and the flanks of the central dome issue small-scale debris flows but do not evolve into large eruptions feeding large down slope sediment flows. This is the most recent extrusion activity at the mud volcanoes [*Van Rensbergen et al.*, 2005]. They consist of mud breccia with centimeter- to meter-sized clasts. It is not possible to determine whether they are the equivalent of type I or type II sediment flows.

[26] 4. A fourth type of sediment extrusion is fluidized sand ejection. Fluidization only occurs in cohesionless sediments and is different from the cohesive mud breccia flows. Extrusion of fluidized sand may account for the sand layer at the top of the Al Idrissi mud volcano. Sand layers were also encountered at the top of the Kidd mud volcano (Gulf of Cadiz) [*Gardner*, 2001] and in the crater of the Granada mud volcano [*Kenyon et al.*, 2000].

[27] The above four types are sediment extrusion features that shape the surface of the mud volcanic cone. The processes of sediment extrusion and some geomechanical aspects have been discussed by *Henry et al.* [1996] and *Kopf and Behrman* [2000] for mud volcanoes respectively offshore Barbados and at the Mediterranean Ridge. Both manuscripts describe the ascending mud as a low-viscosity fluid that is injected along narrow diatremes or conduits. The size of the clasts it carries to the surface is thought to depend on the velocity of the liquid mud. Nevertheless, our observations provide evidence for the variability in extruded sediment (sand to mud breccia with centimeter- to meter-sized clasts and varying porosity) within one mud volcano. Subsequently, differences in debris flow accumulation cause variations in the growth processes from widening and flattening of the cone (type I flows) to

Figure 10. Morphology of Gemini and Fíuza mud volcanoes. (a) Shaded relief map. (b) Side scan sonar mosaic with bathymetry contours. (c) Curvature of mud volcano isobaths. (d) Slope map with bathymetry contours. (e) Interpretation map. Gemini mud volcano is a large oval-shaped mud volcano with two summits and an overall convex slope profile. The northern and southern flanks are steep with semiconcentric terraces. Type I sediment flow deposits at the base of the eastern and western slopes locally decrease the steep slope gradient. The flanks of the Fíuza mud volcano mainly consist of radial outward type I sediment flows that appear to mask a series of steps at the southern flank. See color version of this figure at back of this issue.
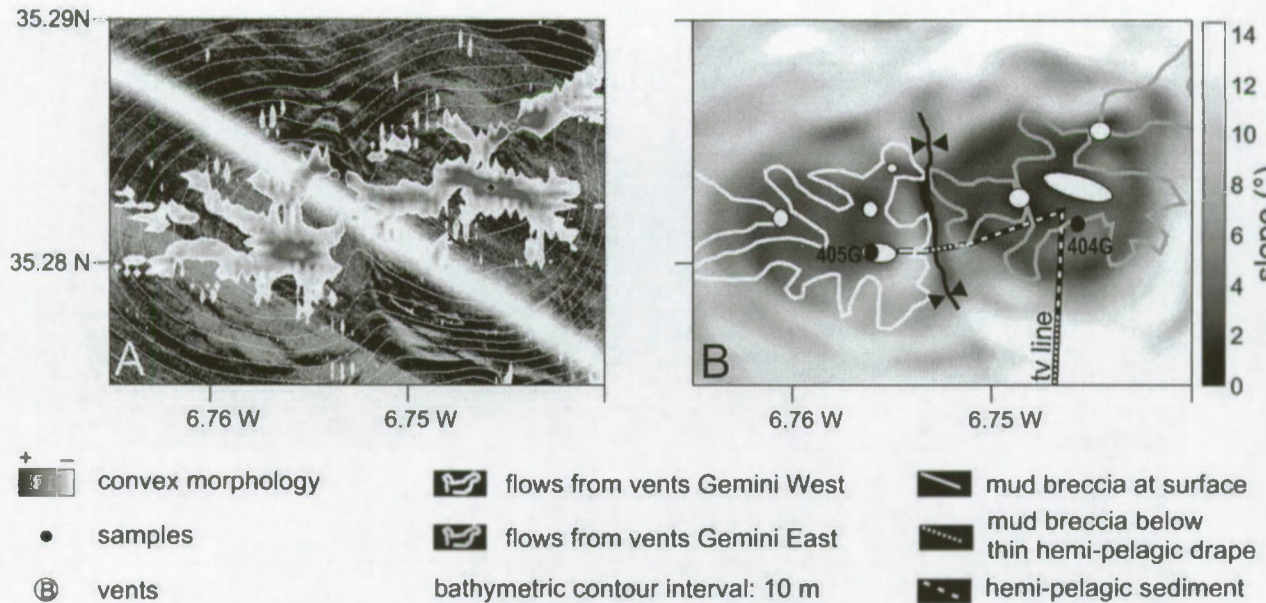
Figure 11. Crater of Gemini mud volcano. (a) Convex morphology mapped over side scan sonar image. (b) Slope map with indication of interpreted sediment flow deposits and sedimentary facies from underwater video lines. Up to seven vents have been identified at both summits. At the western summit, mud flow extrusion occurred recently. See color version of this figure at back of this issue.

steepening of the slopes by cohesive debris flows (type II flows).

5.2. Endogenic Processes

[28] Mud volcano growth is not only controlled by the obvious exogenic processes but also by less conspicuous endogenic processes. According to *Brown* [1990] and *Camerlenghi et al.* [1995], mud volcano cones are formed during last phase mud volcano activity by intrusion of mobilized sediment, after an episode of mainly fluid and gas expulsion in mud pools. In this study we also observe morphological elements that do not appear to correspond solely to extruded sediment deposits and may partly result from endogenic growth processes.

[29] 1. The elevation of the central dome in the crater hosts several vents extruding small sediment flows. The overall slope of the central dome is much less steep than the slope of the mud volcano flanks. The central domes consist of mud breccia with varying matrix density. In all mud volcanoes of the El Arraiche field, the central dome is the youngest morphological feature, postdating sediment flows on the slopes.

[30] 2. A concentric pattern of terraces and steps is observed at Mercator, Gemini and Fíuza mud volcanoes. The terraces and steps have a large along slope continuity. The steps are less high and less steep then the lobe fronts created by type II sediment flows. The resultant slope has a step-like, concave profile. The typical step-like slope may be obliterated later by extrusive sediment flows and may evolve into a linear (type II flows) or steepening concave (type I flows) slope profile.

[31] The central dome, the concentric terraces and steps are most likely not formed by lobes of extruded debris flows but are attributed here to diapiric phases, possibly followed by collapse. Uplift of the sedimentary overburden by diapirism may occur by vertical pressure exerted by a buoyant diapiric body and/or by the injection of sedimentary dykes and sills [*Annen et al.*, 2001]. Mud diapirism driven by density reequilibration is likely to occur within the mud volcano edifice. Variations in gas and fluid content can create large density differences in the mud. For example, *Kopf and Behrman* [2000] measured mud breccia densities of mud volcanoes at the Mediterranean Ridge ranging between 1200 and 1400 kg m^{-3} for mousse-like silty and sandy clays to 1700–2300 kg m^{-3} for matrix supported mud debris flow deposits. A simple calculation of the possible gravitational compensation using the above values indicates that a central dome of 40 m height has an isostatic compensation depth of maximum 90 m below the top of the mud volcano. In other words, buoyancy effects within the mud cone can cause internal diapirism, even without taking into account the effect of elevated fluid pressure. Shallow-seated diapirism that extruded mud cones at the sediment surface without much sediment fluidization (small fluid and gas flux) was documented in Lake Baikal and contrasted sharply with neighboring gas and fluid expulsion craters caused by a large gas flux [*Van Rensbergen et al.*, 2003].

[32] On a larger scale, the same process may occur within the 400-m-thick pile of remolded sediment that accumulated since the onset of mud volcanism about 2.4 ma ago [*Van Rensbergen et al.*, 2005]. The concentric pattern of terraces and steps may be caused by successive diapiric phases with decreasing diameter, each possibly followed by collapse and crater formation due to degassing or dewatering. Similar terraces on the slope of the Ginsburg mud volcano, west of the El Arraiche mud volcano field, were interpreted by *Gardner* [2000] as a diapiric feature.

[33] The occurrence of uplift and diapirism in mud volcanoes seems contradictory to their common association
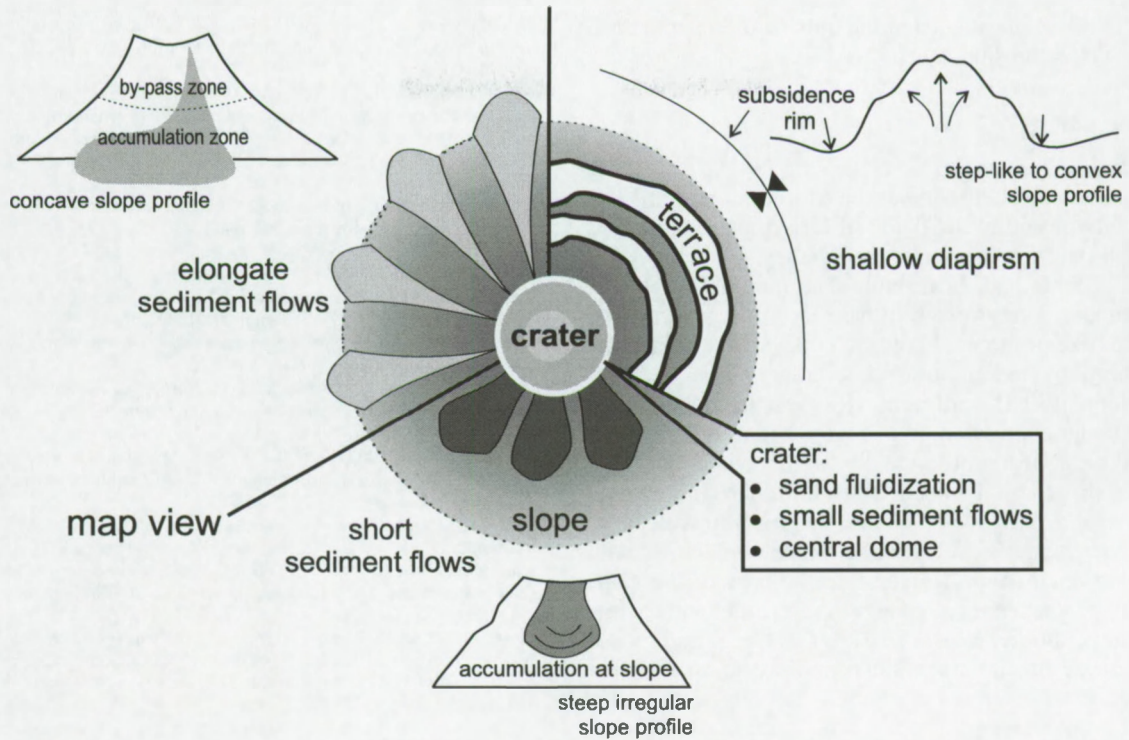
Figure 12. Interpretation drawing indicating the main sediment extrusion and intrusion processes and their resulting morphology. The slope morphology is shaped by different types of sediment flows and by uplift caused by sediment intrusion and diapirism. Within the crater the central dome is attributed to diapirism of low-density mud within the volcanic cone, whereas recent sediment extrusion created small debris flows, and fluidized sand flows were issued from secondary vents.

with subsidence rims. Subsidence rims around large mud volcanoes are a common feature at the Mediterranean ridge [*Camerlenghi et al.*, 1995], in the Gulf of Mexico [*Prior et al.*, 1989], at the Niger delta [*Graue*, 2000], and in the Gulf of Cadiz [*Somoza et al.*, 2002]. They are mostly attributed to collapse related to volume reduction caused by degassing, sediment removal or salt dissolution. However, also diapirs are often associated with a rim of synformal folding [e.g., *Weinberg and Podladchikov*, 1995; *Harrison and Maltman*, 2003] related to sediment withdrawal. However, more important subsidence probably takes place after mud volcano or mud diapir activity has ceased and dewatering occurs. Well-developed collapse depressions are found over abandoned mud volcanoes [*Graue*, 2000] and "deflated" diapirs [*Morley and Guerin*, 1996]. *Somoza et al.* [2002] on the other hand suggest that the moats are caused by erosional currents deflected by the mud volcano cone. In the El Arraiche field, the seismic data indeed indicate erosion in combination with subsidence. The subsidence rims do not evolve into sediment withdrawal synclines but are filled by

mud flows and layered hemipelagic sediments and reappear higher in the section at a slightly different position.

[34] Mud volcano feeder pipes were described as a network of sedimentary dykes by *Morley* [2003] and *Van Rensbergen et al.* [1999]. Dyke intrusions that reach the surface create vents. At present, vents seem to be restricted to the crater area. At Gemini mud volcano, at least 6 vents could be identified over a larger crestal area along an ENE-WSW orientation. It remains unclear whether large debris flows on the slopes were issued by vents within or outside the crater depressions. The observations at Gemini mud volcano seem to suggest the latter. Large flows occur at the eastern and western flanks in the continuation of the alignment of vents at the crest, and parallel to the mud volcano's long axis, although the eastern and western slopes are not the directions of highest slope gradient. At the Mercator mud volcano, a single large mud flow seems to originate directly from the single vent at the crest of the central dome. At Al Idrissi mud volcano the crater is 17 m deep, yet the slopes are entirely covered by sediment flow

Table 2. Synthesis of the Measurements of the Main Morphological Elements of the Mud Volcanoes

	Overall Slope, deg	Steepest Slope, deg	Lowest Slope, deg	Max. Height Steps, m	Max. Width (Slope Parallel), m	Max. Length (Down Slope), m
Type I elongate mud flow	5–6	8–10	0.5–5	0–20	600–800	900–2500
Type II short mud flows	8–10	14–18	4–6	40–50	400–700	700–1400
Diapiric uplift?	8.2–10.5	12.5–13	2.5–6	30–45	400–1500	entire slope
Crater's central dome	2.5–5	6–11	0	10–25	200–700	within crater
Sand fluidization			sand sheet within crater			

deposits. Were vents situated at the outside of the crater rim or did the crater subside later?

6. Conclusions

[35] The El Arraiche field is a cluster of 8 mud volcanoes situated below the shelf edge at the Moroccan margin. The largest mud volcano in the field (Al Idrissi mud volcano) is 255 m high and 5.4 km wide, the smallest we observed is only 500 m wide and 25 m high. The morphology of the mud volcanoes consist of, from base to top: a moat around part of the base of the mud volcano cone, an irregular slope characterized by radial outward sediment flows, terraces and/or depositional sediment flow escarpments (lobe fronts), a crater depression or a flat top, and a central dome.

[36] On basis of the observations we conclude that these large cone-shaped mud volcanoes result from a combination of intrusive and extrusive processes. Sediment flow deposits on the slopes range between two end-members. Flows with low yield strength (type I) extend to the base of the slope and create a steepening convex slope profile with a low overall slope angle ($5°-6°$). Flows with a high yield strength freeze on the steep slope and create an irregular slope profile with almost constant slope angle ($8°-10°$). Within the crater, several vents issue fluidized sand and small debris flows that consist of mud breccia with centimeter- to meter-sized clasts in a mud matrix. The extrusive sediment flows shape the surface of the mud volcano but in this study we also observe morphological elements that do not appear to correspond solely to extruded sediment deposits and may be partly result from sediment intrusion processes. The flat-topped central dome and the concentric pattern of continuous terraces and steps on the slope are interpreted to result from different phases of uplift by sediment intrusion, each possibly followed by collapse due to degassing or dewatering. Intrusive processes may involve shallow-seated diapirism caused by density reequilibration within the thick pile of remolded mud volcano sediments or uplift and volumetric expansion by injection of sedimentary dykes.

References

Annen, C., J.-F. Lénat, and A. Provost (2001), The long-term growth of volcanic edifices: Numerical modeling of the role of dyke intrusion and lava-flow emplacement, *J. Volcanol. Geotherm. Res.*, *105*, 263–289.

Brown, K. M. (1990), Nature and hydrogeological significance of mud diapirs and diatremes for accretionary systems, *J. Geophys. Res.*, *95*, 8969–8982.

Camerlenghi, A., M. B. Cita, B. Dellavedova, N. Fusi, L. Mirabile, and G. Pellis (1995), Geophysical evidence of mud volcanism on the Mediterranean Ridge, *Mar. Geophys. Res.*, *17*, 115–141.

Deville, E., A. Battani, R. Griboulard, S. Guerlais, J. P. Herbin, J. P. Houzay, C. Muller, and A. Prinzhofer (2003), The origin and processes of mud volcanism: New insights from Trinidad, *Spec. Publ. Geol. Soc. London*, *216*, 381–394.

Dimitrov, L. (2002), Mud volcanoes—The most important pathway for degassing deeply buried sediments, *Earth Sci. Rev.*, *59*, 49–76.

Flinch, J. A. (1993), Tectonic evolution of the Gibraltar Arc, Ph.D. thesis, Rice Univ., Houston, Tex.

Flinch, J. A., A. W. Bally, and S. Wu (1996), Emplacement of a passive margin evaporitic allochton in the Betic Cordillera of Spain, *Geology*, *24*, 67–70.

Gardner, J. M. (2000), Gulf of Cadiz/Moroccan margin: Mud diapirism and mud volcanism study, in *Multidisciplinary Study of Geological Processes on the North East Atlantic and Western Mediterranean Margins, IOC Tech. Ser.*, vol. 56, edited by N. H. Kenyon et al., pp. 56–79, UNESCO, Paris.

Gardner, J. M. (2001), Mud volcanoes revealed and sampled on the western Moroccan continental margin, *Geophys. Res. Lett.*, *28*, 339–342.

Gràcia, E., J. Dañobeitia, J. Vergés, R. Bartolomé, and D. Cordoba (2003), Crustal architecture and tectonic evolution of the Gulf of Cadiz (SW Iberian margin) at the convergence of the Eurasian and African plates, *Tectonics*, *22*(4), 1033, doi:10.1029/2001TC901045.

Graue, K. (2000), Mud volcanoes in deepwater Nigeria, *Mar. Petrol. Geol.*, *17*, 959–974.

Harrison, P., and A. J. Maltman (2003), Numerical modelling of reverse-density structures in soft non-Newtonian sediments, *Spec. Publ. Geol. Soc. London*, *216*, 35–50.

Henry, P., et al. (1996), Fluid flow in and around a mud volcano field seaward of the Barbados accretionary wedge: Results from Manon cruise, *J. Geophys. Res.*, *101*, 20,297–20,323.

Hernández-Molina, F. J., L. Somoza, J. T. Vazquez, F. Lobo, M. C. Fernández-Puga, E. Llave, and V. Díaz-del Río (2002), Quaternary stratigraphic stacking patterns on the continental shelves of the souther Iberian Peninsula: Their relationship with global climate and palaeoceanographic changes, *Quat. Int.*, *92*, 5–23.

Kenyon, N. H., M. K. Ivanov, A. M. Akhmetzhanov, and G. G. Akhmanov (Eds.) (2000), *Multidisciplinary Study of Geological processes on the North East Atlantic and Western Mediterranean Margins, IOC Tech. Ser.*, vol. 56, 20 pp., UNESCO, Paris.

Kopf, A., and J. H. Behrman (2000), Extgrusion dynamics of mud volcanoes on the Mediterranean Ridge accretionary complex, *Spec. Publ. Geol. Soc. London*, *174*, 169–204.

Maldonado, A., L. Somoza, and L. Pallarés (1999), The betic orogen and the Iberian-African boundary in the Gulf of Cadiz: Geological evolution, *Mar. Geol.*, *155*, 9–43.

Morley, C. K. (2003), Outcrop examples of mudstone intrusions from the Jerudong anticline, Brunei Darussalam and inferences for hydrocarbon reservoirs, *Spec. Publ. Geol. Soc. London*, *216*, 381–394.

Morley, C. K., and G. Guerin (1996), Comparison of gravity-driven deformation styles and behaviour associated with mobile shales and salt, *Tectonics*, *15*, 1154–1170.

Mulder, T., and P. Cochonat (1996), Classification of offshore mass movements, *J. Sediment. Res.*, *66*, 43–57.

National Geographic (Portuguese ed.) (2002), Combustível do Futuro? Margem sul nacional rica em vulcões de lama, Portuguese ed., *21*(1), 30.

Pinheiro, L. M., et al. (2003), Mud volcanism in the Gulf of Cadiz: Results from the TTR-10 cruise, *Mar. Geol.*, *195*, 131–151.

Prior, D. B., E. H. Doyle, and M. J. Kaluza (1989), Evidence for sediment eruption on deep-sea floor, Gulf of Mexico, *Science*, *243*, 517–519.

Shih, T. T. (1967), A survey of the active mud volcanoes in Taiwan and a study of their types and the character of the mud, *Petrol. Geol. Taiwan*, *5*, 259–311.

Somoza, L., V. Diaz-del-Rio, J. T. Vàzquez, L. M. Pinheiro, F. J. Hernàndez-Molina, and the TASYO/Anastasya Shipboard Parties (2002), Numerous methane gas–related sea floor structures identified in the Gulf of Cádiz, *Eos Trans. AGU*, *83*, 541.

Somoza, L., et al. (2003), Seabed morphology and hydrocarbon seepage in the Gulf of Cádiz mud volcano area: Acoustic imagery, multi-beam and ultra-high resolution seismic data, *Mar. Geol.*, *195*, 153–176.

Van Rensbergen, P., C. K. Morley, D. W. Ang, T. Q. Hoan, and N. T. Lam (1999), Structural evolution of shale diapirs from reactive rise to mud volcanism: 3D seismic data from the Baram delta, offshore Brunei Darussalam, *J. Geol. Soc. London*, *156*, 633–650.

Van Rensbergen, P., J. Poort, R. Kipfer, M. De Batist, M. Vanneste, J. Klerkx, N. Granin, O. Khlystov, and P. Krinitsky (2003), Near-surface sediment mobilization and methane venting in relation to hydrate destabilization in Southern Lake Baikal, Siberia, *Spec. Publ. Geol. Soc. London*, *216*, 207–221.

Van Rensbergen, P., et al. (2005), The El Arraiche mud volcano field at the Moroccan Atlantic slope, Gulf of Cadiz, *Mar. Geol.*, in press.

Weinberg, R. F., and Y. Y. Podladchikov (1995), The rise of solid state diapirs, *J. Struct. Geol.*, *17*, 1183–1195.

D. Depreiter, J.-P. Henriet, B. Pannemans, and P. Van Rensbergen, Renard Centre of Marine Geology, Ghent University, Krijgslaan 281-S8, 9000 Gent, Belgium. (davy.depreiter@ugent.be; jeanpierre.henriet@ugent.be; happybappa@hotmail.com; pieter_vanrensbergen@yahoo.com)
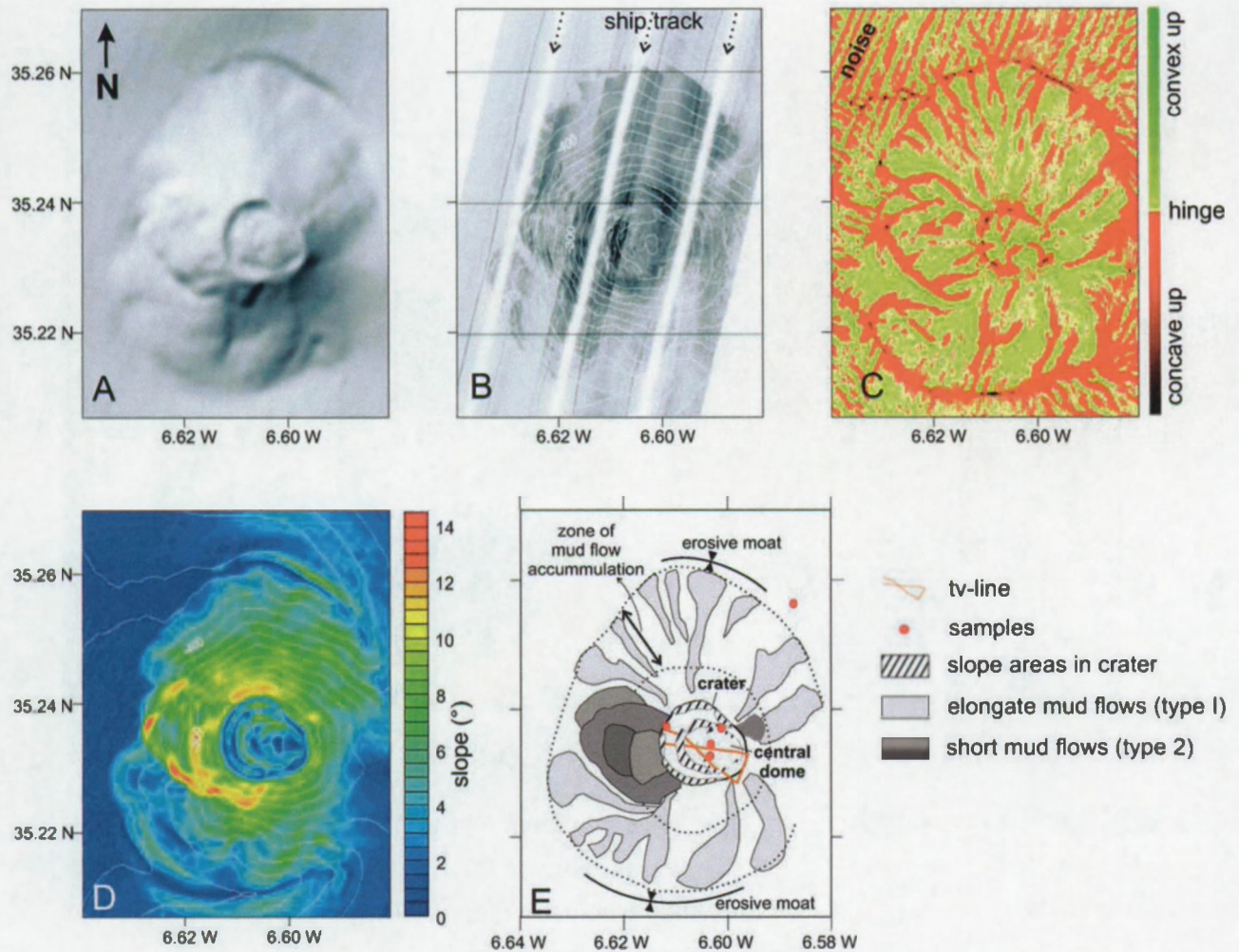
Figure 5. Morphology of the Al Idrissi mud volcano. (a) Shaded relief map. (b) Side scan sonar mosaic with bathymetry contours. (c) Curvature of mud volcano isobaths. (d) Slope map with bathymetry contours. (e) Interpretation map. Numerous sediment flow deposits, characterized by high backscatter and convex morphologies, are distinguished on the slopes. They occur in a radial pattern away from the crater and accumulate at the base of the volcanic cone (type I sediment flows), which results in a steepening, concave slope profile. On the western slope, sediment flow deposits accummulated at the slope (type II sediment flows) and created a steeper irregular slope profile.

Figure 6. Crater of Al idrissi mud volcano. (a) Convex morphologies mapped over side scan sonar image shows the distribution of small mud flows issued by vents within the crater. (b) Slope map with indication of interpreted sediment flow deposits and sedimentary facies from underwater video lines distinguishing the different outflow events.

Figure 8. Morphology of the Mercator mud volcano. (a) Shaded relief map. (b) Side scan sonar mosaic with bathymetry contours. (c) Curvature of mud volcano isobaths. (d) Slope map with bathymetry contours. (e) Interpretation map. Mercator mud volcano is an assymetric mud volcano with a smooth northern slope and concentric steps at the southern slope. Only at the western slope, type I sediment flow deposits, here characterized by a low backscatter, fan out at the base of the cone.

Figure 9. Crater of Mercator mud volcano. (a) Convex morphology mapped over side scan sonar image shows the distribution of small mud flows within the crater around a single vent at the summit. (b) Slope map with indication of interpreted sediment flow deposits and sedimentary facies from underwater video lines.

Figure 10. Morphology of Gemini and Fíuza mud volcanoes. (a) Shaded relief map. (b) Side scan sonar mosaic with bathymetry contours. (c) Curvature of mud volcano isobaths. (d) Slope map with bathymetry contours. (e) Interpretation map. Gemini mud volcano is a large oval-shaped mud volcano with two summits and an overall convex slope profile. The northern and southern flanks are steep with semiconcentric terraces. Type I sediment flow deposits at the base of the eastern and western slopes locally decrease the steep slope gradient. The flanks of the Fíuza mud volcano mainly consist of radial outward type I sediment flows that appear to mask a series of steps at the southern flank.

Figure 11. Crater of Gemini mud volcano. (a) Convex morphology mapped over side scan sonar image. (b) Slope map with indication of interpreted sediment flow deposits and sedimentary facies from underwater video lines. Up to seven vents have been identified at both summits. At the western summit, mud flow extrusion occurred recently.

Geophysical evidence of gas hydrates in shallow submarine mud volcanoes on the Moroccan margin

D. Depreiter, J. Poort, P. Van Rensbergen, and J. P. Henriet

Renard Centre of Marine Geology, Ghent University, Ghent, Belgium

[1] Gas hydrates inside mud volcanoes have been observed in several locations but are generally found at water depths of 1000 m and deeper. We present the first observation of the base of a gas hydrate stability zone within a shallow mud volcano in the El Arraiche mud volcano field on the Moroccan Atlantic margin. The mud volcano base is located at about 475 m and is over 125 m high. On high-resolution seismics we observed an anomalous but coherent reflection under the slopes of the mud volcano. The event was interpreted as the base of a gas hydrate stability zone because of its inverse polarity and its morphology. Far from the crater, the event is nearly parallel to the seafloor. Closer toward the crater, the event shallows. Inside the mud volcano crater, no event is observed. A stability model using thermogenic gas compositions is applied to local P-T conditions, indicating that thermogenic gas hydrates can be stable at this depth. The high modeled heat flow in the crater of the mud volcano indicates a focused flow of warm fluids. Below the slopes of the mud volcano, the inferred heat flow is also elevated but less high. In areas of thermogenic gas production, gas hydrates can occur at shallow water depths, even in areas with high heat flow. This also suggests that dewatering of the accretionary wedge complex is mainly focused along fault surfaces and through seafloor structures, such as mud volcanoes.

Citation: Depreiter, D., J. Poort, P. Van Rensbergen, and J. P. Henriet (2005), Geophysical evidence of gas hydrates in shallow submarine mud volcanoes on the Moroccan margin, *J. Geophys. Res.*, *110*, B10103, doi:10.1029/2005JB003622.

1. Introduction

[2] Gas hydrate is an ice-like crystalline substance, consisting of a cage structure of water molecules with trapped methane or other light gases inside. Gas hydrates are stable under well-described *P-T* conditions [*Sloan*, 1998a, 1998b] and adequate gas concentrations [*Xu and Ruppel*, 1999]. The distribution of gas hydrates on continental margins is widespread [*Ginsburg and Soloviev*, 1998; *Kvenvolden*, 1998]. Stability of hydrates on margins is a very actively studied topic in regard to triggering sediment mass wasting through gas hydrate decomposition [*Bouriak et al.*, 2000; *Paull et al.*, 2003]. Gas hydrates are also regarded as an important potential economic target [*Collett*, 2002; *Gupta*, 2004] and their destabilization may have a large impact on global change [*Kvenvolden*, 1993; *Jacobsen*, 2001; *Kennett et al.*, 2000; *Kopf*, 2003].

[3] Gas hydrates in seafloor sediments occur within a restricted zone, the gas hydrate stability zone (GHSZ). The base of the GHSZ is often recognized as a bottom simulating reflection (BSR) on seismic data, since it mimics the seafloor in areas of a stable and constant local heat flow. The BSR is characterized by an inverse polarity of the seismic signal, originating from the presence of free gas trapped below the hydrate stability zone [e.g., *Bangs et al.*,

1993; *MacKay et al.*, 1994; *Holbrook et al.*, 1996]. Since the thermal gradient defines the lower boundary of the GHSZ, an elevated local heat flow will thin the GHSZ. In that case, the base of the GHSZ, expressed as a crosscutting reflection, can locally intercept with the seafloor reflection, for example, in gas hydrates associated to mud volcanoes or gas seeps [*De Batist et al.*, 2002; *Van Rensbergen et al.*, 2002].

[4] Submarine mud volcanoes (MVs) are seafloor structures with positive topography from which mud, fluid, and gas emanate [*Hedberg*, 1974]. Their distribution is mainly confined to areas with compressive tectonic activity, vertical compression due to sedimentary loading (burial) and generation and accumulation of hydrocarbons leading to overpressure [*Dimitrov*, 2002a; *Kopf*, 2003]. The general mechanism for their formation is related to a combination of the rise of overpressured liquefied clays toward the surface and the hydrofracturing of the overburden which opens a feeder pipe. The mobilized material pierces the overburden to expel a mixture of mud, fluids and gases along with brecciated rock derived from the overburden, the mud breccia.

[5] Gas hydrates inside mud volcanoes have been observed in several locations [*Dimitrov*, 2002a], but are generally found at water depths of 1000 m and deeper, e.g., on the Norwegian-Barents-Svalbard margin [*Ginsburg et al.*, 1999], the Gulf of Cadiz and on the Moroccan margin [*Gardner*, 2001; *Mazurenko et al.*, 2002], the eastern
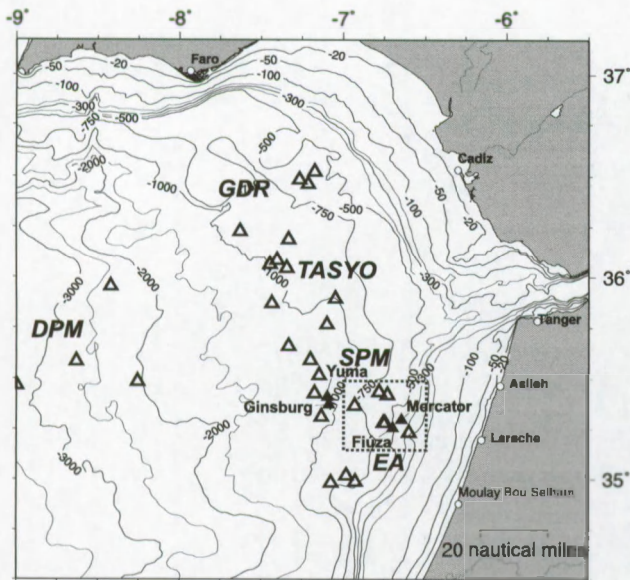
Figure 1. Gulf of Cadiz and NW Moroccan margin. Mud volcanoes and diapiric structures are indicated by triangles. Solid triangles are mud volcanoes mentioned in the text. DPM (Deep Portugese Margin) [*Pinheiro et al.*, 2003], TASYO and GDR (Guadalquivir Diapiric Ridge) [*Somoza et al.*, 2003], SPM (Spanish-Moroccan Field) [*Gardner*, 2001], EA (El Arraiche field) [*Van Rensbergen et al.*, 2005a]. The location of Figure 2 is indicated by the dotted box.

Mediterranean ridge [*Robertson et al.*, 1996], the Black Sea [*Soloviev and Ginsburg*, 1994; *Dimitrov*, 2002b; *Bohrmann et al.*, 2003], the Caspian Sea [*Huseynov and Guliyev*, 2004] and on the Barbados accretionary wedge [*Aloisi et al.*, 2002].

[6] In this paper, we present a reflection event within a mud volcano found in the El Arraiche mud volcano field on the Moroccan margin. The mud volcano is about 125 m high and its crater is situated at a depth of about 350 m below sea level (bsl). We will map the distribution of this event and calculate the local heat flow pattern, the results of which plead for the occurrence of hydrates of thermogenic hydrocarbon gases in this shallow location and the event to be the base of a GHSZ.

2. Regional Setting

[7] The Gulf of Cadiz is situated between 9°W to 6°45′W and 34°N to 37°15′N (Figure 1), bounded by the Iberian peninsula and Morocco, west of the Gibraltar area. The geological setting of the Gulf of Cadiz is extremely complex and still under debate [*Sartori et al.*, 1994; *Maldonado et al.*, 1999; *Gutscher et al.*, 2002]. The area is characterized by the presence of an accretionary wedge formed by westward motion of the front of the Gibraltar Arc (the Betic-Rif mountain chain) during middle Miocene. Formation of the allochthonous nappes took place during the Tortonian, as a consequence of increased subsidence [*Maldonado et al.*, 1999]. The African-Eurasian convergence since the Cenozoic yields a compressional-transpressional tectonic regime, reactivating many normal faults and causing widespread

diapirism in the north of the Gulf of Cadiz [*Berastegui et al.*, 1998; *Somoza et al.*, 2003]. Mud volcanoes in the Gulf of Cadiz are associated with these diapiric structures [*Somoza et al.*, 2003; *Pinheiro et al.*, 2003]. The main part of the olistostrome unit occupies the central part of the Gulf of Cadiz as a lobe-shaped structure that extends over 300 km into the Atlantic Ocean, its extent seems not well defined yet [*Maldonado et al.*, 1999; *Somoza et al.*, 2003; *Medialdea et al.*, 2004; *Maestro et al.*, 2003].

[8] The El Arraiche mud volcano field is located on top of the accretionary wedge of the Gulf of Cadiz, at depths between 200 and 800 m at the NW Moroccan continental slope [*Van Rensbergen et al.*, 2005a] (Figures 1 and 2). The local structure of the study area is characterized by extensional tectonics, in contrast to the main part of the Gulf of Cadiz. This is expressed as large rotated blocks bound by lystric faults that created Plio-Pleistocene depocenters [*Flinch*, 1993, 1996]. The extension might be a response to the advancement of the allochthonous sheets as was reported for the northern Gulf of Cadiz by *Medialdea et al.* [2004].

[9] The mud volcanoes of the El Arraiche mud volcano field are positioned above large normal faults that bound the rotated blocks and serve as fluid migration pathways, fuelling the mud volcanoes [*Van Rensbergen et al.*, 2005a]. The normal faults are probably superposed on relict thrust anticlines [*Maldonado et al.*, 1999] or Triassic salt diapiric structures [*Berastegui et al.*, 1998; *Somoza et al.*, 2003]. The source of the overpressured fluids is believed to be located at the base of the accretionary wedge body since rock clasts in the mud breccia are reported to be of an age up to early Eocene [*Ovsyannikov et al.*, 2003].

[10] Gas hydrates on the Moroccan margin and in the Gulf of Cadiz have only been reported from a small number of deep-water mud volcanoes: Ginsburg mud volcano (1100 m bsl) [*Gardner*, 2001; *Mazurenko et al.*, 2002, 2003], Bonjardim mud volcano (2200 m bsl) [*Kenyon et al.*, 2001; *Pinheiro et al.*, 2003] and Capt. Arutyunov mud volcano (1800 m bsl) [*Kenyon et al.*, 2003]. *Casas et al.* [2003] observed possible BSR features at a subbottom depth of 150 ms two-way travel time (TWTT), associated with mud volcanoes and diapirs at a water depth of 388 m on the Gulf of Cadiz slope. They attributed the hydrate stability to elevated pore pressure conditions caused by the diapiric intrusions. Reports of a widespread regional BSR are not yet made.

[11] The Mercator and Fiúza mud volcanoes are situated in the El Arraiche mud volcano field (Figure 2). The Mercator mud volcano's top is at a water depth of 350 m, the deepest part of the surrounding moat is about 475 m deep. Its diameter is nearly 2.5 km. There is a crater present, with a dome form extrusion in the center. The flanks of the mud volcano are characterized by a stepped or terrace-like morphology. The Fiúza MV is located deeper, with its top at 400 m and its base around 525 m. All morphological details are reported by *Van Rensbergen et al.* [2005b].

3. Methods and Results

3.1. Seismic Reflection Profiling

[12] The El Arraiche mud volcano field was covered with detailed multibeam bathymetry (Kongsberg EM1002) and
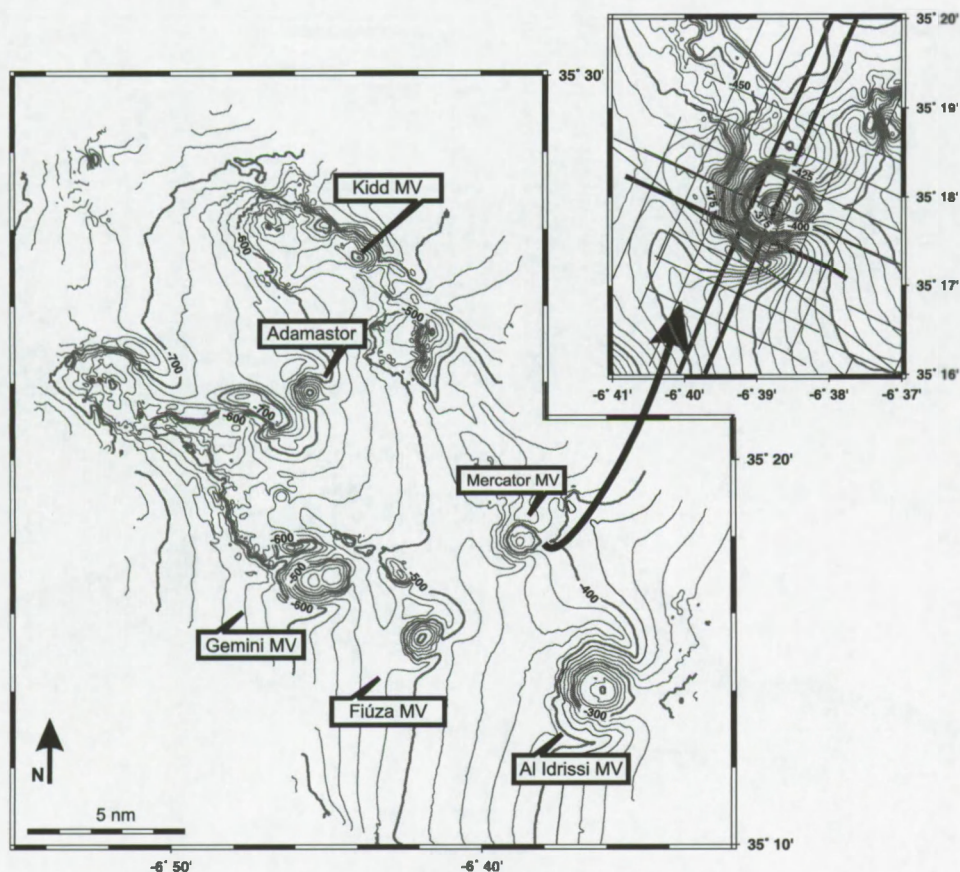
Figure 2. Bathymetric map of the El Arraiche mud volcano field with indication of major mud volcanoes. Inset shows a detail of the Mercator mud volcano with 2-D seismic track lines; bold lines are profiles displayed in Figure 3.

high-resolution seismics (80 electrode 500J sparker, 35 cubic inch Sodera GI gun and the Ifremer Deeptow Chirp Sonar system). The seismic data were acquired in three narrowly spaced orthogonal grids over three large mud volcanoes: Al Idrissi, Mercator, and Gemini MVs. Interpretation was executed in the Kingdom Suite seismic interpretation software package (Seismic Micro-Technology, Inc.) and further handling with the GMT mapping tools [*Wessel and Smith*, 1991].

3.2. Event Observation

[13] The Mercator and Fiúza mud volcanoes both show an anomalous but coherent subbottom reflection, which we name the H event (Figure 3). The depth of the H event varies from 0 m near the mud volcano crater to over 50 ms further away. The presence of any coherent signal is unexpected since mud volcanoes are mainly built up by an extruded mud-supported breccia, hence lacking any internal structure and only a chaotic seismic facies is expected. The depth of this event was mapped over the Mercator mud volcano, a seismic grid over the Fiúza MV is not present.

[14] The seismic signal shows that the H event has an inverse polarity in regard to the seafloor reflection (Figure 4). The H event only occurs within the mud volcano body and does not extend into the layered hemipelagic sedimentary environment around the mud volcanoes. Hence it is not a crosscutting reflection. Away from the crater, the reflection is

parallel to the seafloor, where it forms a bottom simulating reflector (BSR) at a depth of about 50 milliseconds below the seafloor. The H event shallows toward the center of the mud volcano and intercepts with the seafloor reflection at the edge of the crater (Figures 3 and 5).

[15] We introduce the hypothesis that the H event is the base of a gas hydrate stability zone. We test this hypothesis by modeling the gas hydrate occurrence and deriving the H event inferred heat flow in the mud volcano.

3.3. Modeling Gas Hydrate Occurrence

[16] Modeling the hydrate stability zone requires information on the composition of the hydrate gas, on the bottom water temperature and geothermal gradient as well as the pore space salinity. Gas hydrates recovered from the nearby Ginsburg mud volcano, which is located at a water depth of 1100 m, had a composition of 81% of CH_4 and 19% of C_{2+} hydrocarbons [*Mazurenko et al.*, 2002]. From CTD data we know that the seafloor temperature in the area is 10°C which is unfavorable for gas hydrate stability. Pore water salinity estimates are derived from mud volcanoes from the Moroccan margin. [*Blinova and Bileva*, 2003] reported an average chlorinity of 500 mmol L^{-1}. According to equation (1), this can be converted to 3.2% salinity, which is comparable to ocean water salinity.

$$S = 1.80655[Cl^-] \qquad (1)$$
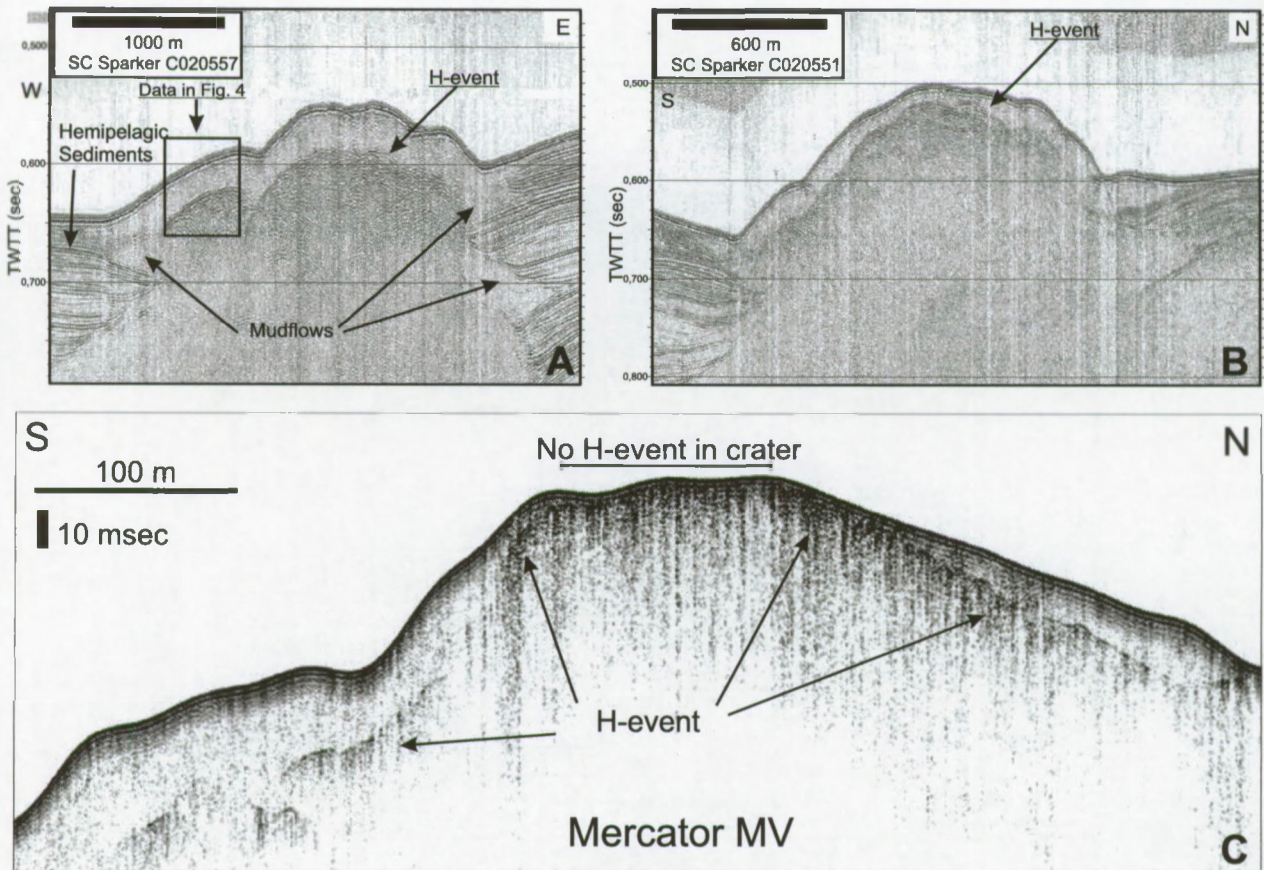
Figure 3. (a and b) High-resolution sparker and (c) very high resolution chirp sonar (courtesy Ifremer) seismic lines over Mercator MV. The stratified seismic facies at the sides of Mercator MV (Figures 3a and 3b) represents hemipelagic sediments. The mud volcano itself has no internal structure; therefore a chaotic to transparent facies is observed. The unexpected H event reflector is visible on all profiles, Figure 3a is a profile far away from the crater and therefore the event occurs deepest. Figure 3b is a profile that passes next to the crater; therefore the H event is shallower near the crater than elsewhere. Figure 3c line crosses the crater and shows the H event intercepting the seafloor reflection.

Equation (1) expresses a conversion from salinity to chlorinity, with S the salinity and [Cl$^-$] the chlorinity, both in parts per million (ppm) [*Wooster et al.*, 1969].

[17] The gas hydrate equilibrium conditions were determined using the program CSMHYD [*Sloan*, 1998a] for the given composition of the gas hydrates and salinity of the pore waters. This resulted in the polynomial regression equation

$$\log P = a + bT + cT^2 \qquad (2)$$

with parameters $a = -0.1929$, $b = 0.0395$ and $c = 0.0009$, P in MPa and T in degrees Celsius, and the regression coefficient $R^2 = 0.998$. In Figure 6a, the resulting hydrate stability curve is plotted with a seafloor depth of 380 m. The hydrate stability curve for pure methane is plotted for comparison. This result shows that at this water depth and for the given gas composition and seafloor temperature, gas hydrates can be stable. For a thermal gradient of 60 mK m^{-1}, which is a normal background value for the North Atlantic Ocean [*Sclater et al.*, 1980], the depth of the base of the GHSZ is almost 100 m deeper than the present observed H event (Figure 6a, with H event in Figure 6b).
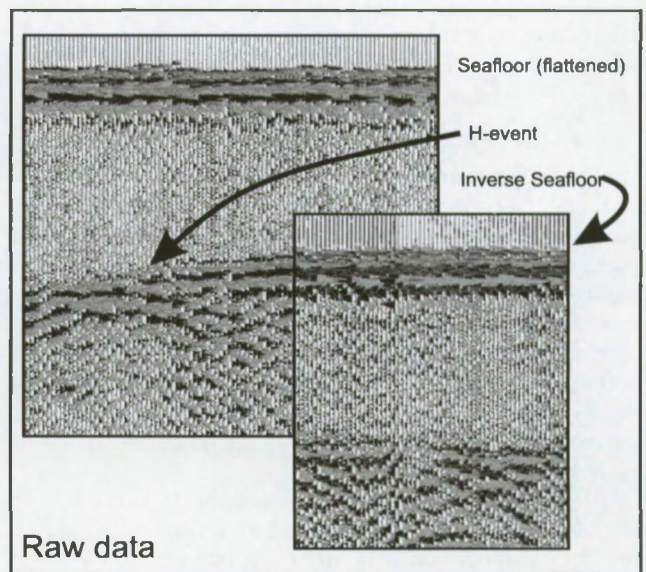

Figure 4. Inverse seismic polarity of the H event with regard to the seafloor reflector.
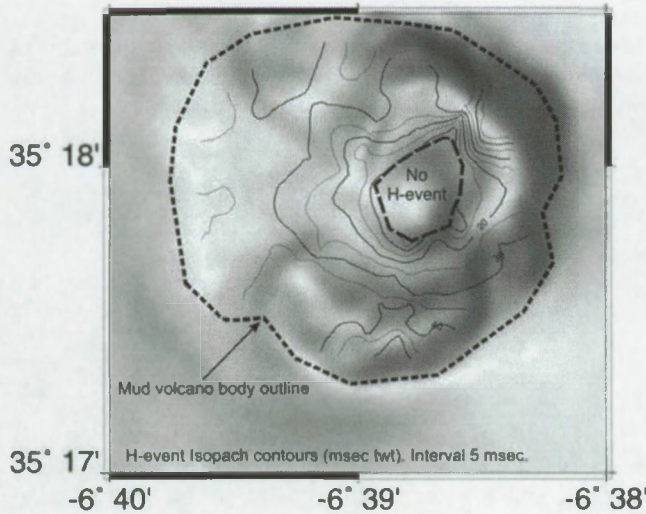
Figure 5. Subbottom depth of the H event in the Mercator mud volcano in two-way travel time. The concentric shallowing of the H event toward the crater is shown by the contours. Background figure is a shaded relief map of the Mercator mud volcano (illuminated from west).

[18] Since thermogenic gas hydrates can theoretically occur at this location, this supports our hypothesis that the H event is the base of a GHSZ. We will map this horizon and infer the thermal gradient and heat flow from it.

3.4. Inferred Heat Flow

[19] Bottom simulating reflections have often been used to estimate thermal gradients or heat flow [*Yamano et al.*, 1982]. The calculation assumes that the BSR coincides with the three-phase gas hydrate-water-gas vapor boundary, and

consists of the following steps [*Vanneste et al.*, 2003]: (1) conversion from TWTT to subbottom depth based on a velocity model, (2) calculation of in situ hydrostatic and lithostatic pressure, (3) derivation of the equivalent three-phase gas hydrate equilibrium temperature for these pressure values at the inferred BSR depth, and (4) determination of the geothermal gradient and heat flow.

[20] A relation between pressure, depth, and time is needed for the conversion from two-way travel times to depth and pressure values, which are needed for thermal gradient and heat flow calculations. Data from Ocean Drilling Program Leg 160 (eastern Mediterranean) Site 970 (Milano Dome) and 971 (Napoli Dome) [*Robertson et al.*, 1996] shows that pebbly mud (holes 970A, 970B, 970D and 971A, 971B, 971D, 971E) has p wave velocities from 1500 to 2000 m s^{-1}. When averaging over depth for these holes, values around 1800 m s^{-1} are retrieved. For nanofossil ooze with sapropels (hole 970B), the velocity average is about 1600 m s^{-1}. All values refer to the first tens of meters; therefore we assume an average velocity for the deposits of the top of the Mercator mud volcano of 1800 m s^{-1}. Then, on the basis of a p wave velocity 1.5 km s^{-1} in water and 1.8 km s^{-1} in the sediment and with a density of water $\rho_w = 1030$ kg m^{-3} and sediment $\rho_c = 2300$ kg m^{-3} (based on a $\rho_s = 2650$ kg m^{-3} for the sediment and $\rho_h = 900$ kg m^{-3} for the hydrates [*Gei and Carcione*, 2003], in a 80% sediment to 20% hydrate mixture), the two-way travel time of the seismic sections was converted to depth (Figure 7a) and pressure (Figure 7b). The calculated pressure field at the H event reflector displays a nearly concentric pattern around the crater of the mud volcano and pressure increases from the crater (3500 kPa) to the deepest point (6000 kPa).

[21] On the basis of the thickness of the layer between the seafloor and the H event, we reconstructed the thermal
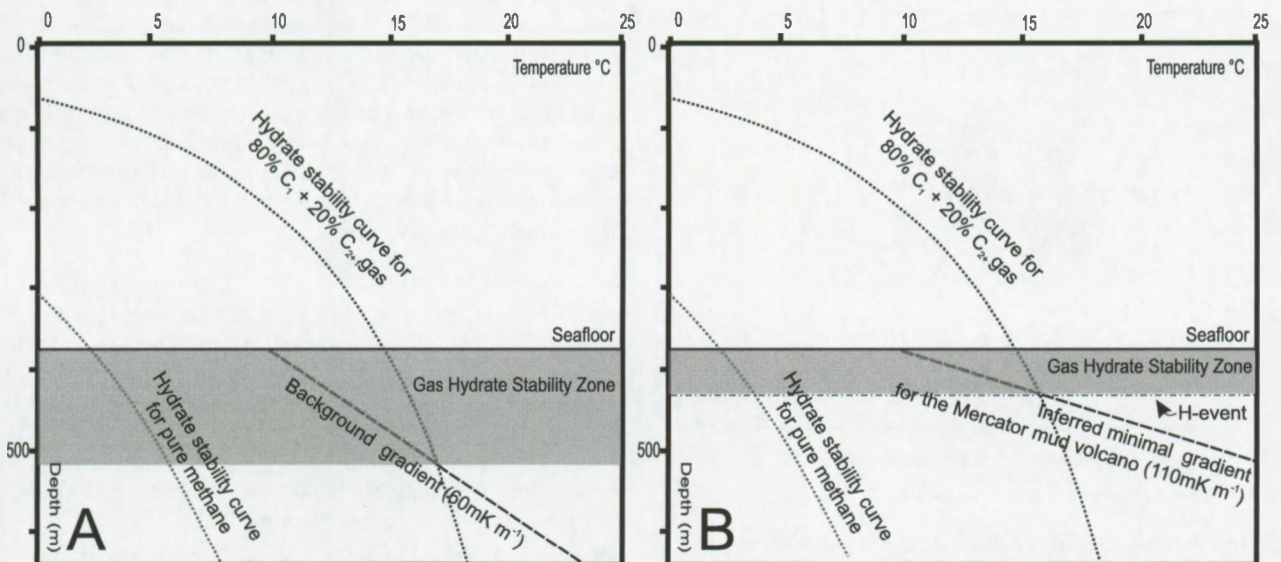
Figure 6. Theoretical gas hydrate stability graphs for gas composition measured at Ginsburg mud volcano [*Mazurenko et al.*, 2002] and pure methane for comparison. Pure methane hydrates are unstable in either case. (a) Situation with a background gradient curve of 60 mK m^{-1} and a bottom water temperature of 10°C. Gas hydrates are stable to 140 m below seafloor if gas contains higher-order hydrocarbons. (b) Situation for lowest inferred thermal gradient (110 mK m^{-1}) in Mercator mud volcano, where hydrates with higher-order hydrocarbons are stable up to 60 m bsf.
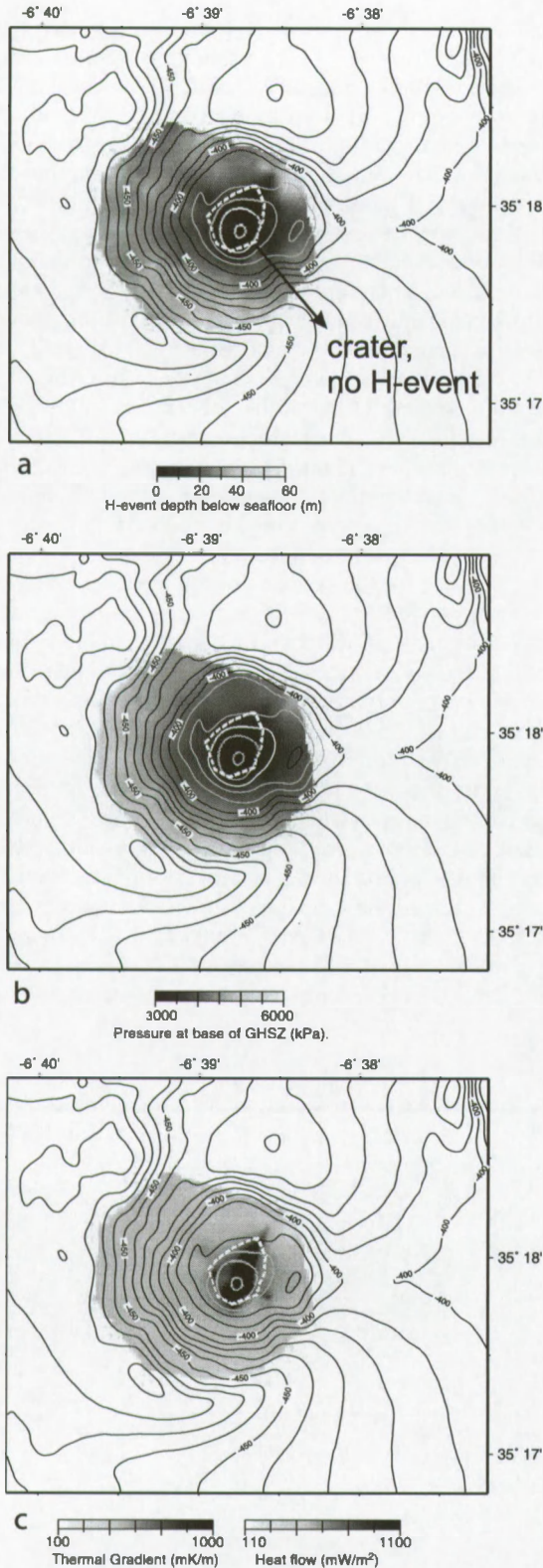
Figure 7. (a) Depth of the H event in meters in the Mercator mud volcano. (b) Calculated pressure at the depth of the H event. (c) Calculated thermal gradient and heat flow inferred from the occurrence of the H event. The thermal gradient and heat flow display a quasi-radial pattern around the mud volcano crater, increasing toward it. In the crater area, no H event was observed. See color version of this figure at back of this issue.

gradient field and the heat flow pattern in the mud volcano. Inside the crater, no H event is observed, so the thickness is set to 0. The calculation of the thermal gradient field, based on the distribution of a BSR, is derived from equation (2) as

$$G_t = \frac{T - T_{sf}}{d_{bsr}} \qquad (3)$$

with

$$T = \frac{-b + \sqrt{b^2 + 4c(\log P - a)}}{2c} \qquad (4)$$

where G_t is the temperature gradient, T is the temperature (°C) defined by equation (4), T_{sf} is the temperature at the seafloor (C), d_{bsr} is the depth of the BSR in meters below seafloor, and P is the in situ pressure at the BSR in MPa. For the conversion from the thermal gradient field to the heat flow Φ_Q according equation (5), we supposed a thermal conductivity k_t of 1.1 W K^{-1} m^{-1}, with

$$\Phi_Q = k_t G_t \qquad (5)$$

and Φ_Q in mW m^{-2} and G_t in mK m^{-1}. This value for k_t is used since it is a typical value for this kind of sediments [e.g., *Grevemeyer et al.*, 2004] report $k_t = 1.17$ W K^{-1} m^{-1} for sediments at the Mound Culebra mud dome offshore Nicoya Peninsula, Costa Rica). The thermal gradient and heat flow values calculated on the mud volcano are cut off at 1 K m^{-1} or 1.1 W m^{-2} near the edge of the crater because at that location, values move asymptotically to infinite since d_{bsr} approaches zero in equation (3).

[22] The inferred heat flow and thermal gradient fields show a more or less concentric pattern around the crater of the Mercator mud volcano (Figure 7c). The local minimal value of the heat flow in the Mercator mud volcano is 110 mW m^{-2} (Figure 6b) and increases to about 250 mW m^{-2} craterward. Near the edge of the crater, the heat flow quickly rises to 600 mW m^{-2} and then increases quickly to 1100 mW m^{-2} at the crater edge. Within the crater, the heat flow cannot be extrapolated because of the asymptotical rise of the calculated values toward infinity. All we can infer here is that heat flow inside the crater is higher than 1100 mW m^{-2}.

3.5. Accuracy Estimate

[23] Each of the steps to calculate the heat flow from a BSR occurrence is a source of errors. The error on the pressure field at the depth of the H event depends on changes in p wave velocity and density of the mud breccia. If we vary the p wave velocity between 1500 and 2000 m s^{-1} and the density between 1800 and 2300 kg m^{-3}, relative errors for the pressure vary between about −6.5 and 2%. It is unlikely that density will be higher than the value we used for the calculations, since porosity, which we assumed to be zero and all pores filled by hydrate, will have a bulk density decreasing effect. However, because of the logarithmic function in the temperature calculation, this error is strongly reduced. The most important factor for the thermal gradient is the p wave velocity since it appears in the denominator of equation (3). All together, the varying p wave velocity and bulk density induces an overall error on the thermal gradient

of +16.3% for a p wave velocity of 1500 m s^{-1} and −8.2% for a p wave of 2000 m s^{-1}. The influence of a variable density is less, and the error values above are the overall extremes. An error for k_t will further affect the heat flow values. If k_t is 0.9 W m^{-1} K^{-1}, a value typical for normal hemipelagic sediments, this induces an error of about 18%. Long-term bottom water changes will affect the heat flow pattern according to equation (3). More importantly, they can influence the hydrate stability field with bottom water warming causing gas hydrate dissociation. Nevertheless, we rely on the CTD data and assume that temporal fluctuations are small. The overall error on the H event inferred thermal gradient is assumed to be no larger than 15% and the error on the heat flow no larger than 25%. Another source of uncertainty is the gas hydrate composition since the values we used were not obtained from in situ sampling. However, we assume that source fluids and gases are comparable throughout the region and fluctuations are low.

4. Interpretation and Discussion

[24] The H event is recognized as a coherent reflector with negative polarity under the seafloor below the Mercator mud volcano's slope. The H event shallows toward the mud volcano's center and disappears in the crater. We interpret the H event as the base of a gas hydrate stability zone, which is affected in the center of the mud volcano by focused fluid flow. We modeled the gas hydrate stability zone in this very shallow area by using a gas hydrate composition reported for the region. The seismic interpretation is supported by the model. Alternative interpretations of this seismic event are possible but can be rejected based on several issues.

[25] First, the H event may have been covered by a layer of rocks and clasts, extruded by the mud volcano. This is deemed unlikely since so far, no observations indicate that a complete mud volcano surface would be covered with extruded clasts or rocks. This suggestion can be rejected since it cannot explain the morphology of the seismic event (i.e., the shallowing toward the crater) since different mud extrusion types as described by *Van Rensbergen et al.* [2005b] cannot produce such a morphology. Second, the event might represent a transition to sedimentary deposits created during a period of inactivity of the mud volcano. This is unlikely as a sedimentary layer would drape the whole mud volcano, therefore also the crater area. Third, a diagenetic boundary may produce a seismic event in a mud volcano. Again, the morphology of such a boundary is hard to explain. For all of these propositions, the inverse polarity of the seismic signal is also not explained. Thus we conclude that the interpretation of the H event as the base of a gas hydrate stability zone is the most reliable.

4.1. Focused Fluid Flow in Mud Volcanoes

[26] The Mercator mud volcano exactly shows what *Ginsburg* [1998] proposed in a model concerning hydrate stability in mud volcanoes. Therefore, although the Mercator MV is not visibly active in a sense that it extrudes mudflows, it is inferred to be active as a fluid vent. The concentric pattern of the heat flow distribution is a consequence of lateral heat diffusion away from the feeder pipe [*Poort and Klerkx*, 2004]. Diffusion of gas away from the

feeder pipe is the source of hydrocarbon gases hydrate. Hydrates generally occur at continental margins where conversion of high inputs of organic carbon or focusing of methane bearing fluids supply the hydrocarbon gases required for hydrate formation [*Davie et al.*, 2004]. The absence of any regional BSR or H event in the surrounding hemipelagic sediments could be explained by an insufficient methane flux which would be needed for gas hydrate formation. A methane flux lower than the theoretical methane solubility would also imply the absence of free gas. The lack of an acoustic impedance inversion at the interface between gas-free and gas-bearing sediments, may explain the absence of a widespread regional BSR. This would mean that the degassing and dewatering of the accretionary wedge in the Gulf of Cadiz mainly happens through focused flow along faults associated fluid expulsion seafloor structures, and only partly by widespread diffusive processes.

[27] The inferred heat flow in the mud volcano, and especially in and near the crater, is very high. However, literature reports indicate that the calculated result is not abnormal for mud volcanoes. Heat flow in active mud volcanoes is known to easily rise above 1 W m^{-2}. The best know case-study is the Håkon Mosby MV on the Norwegian Margin. The crater of the mud volcano has also thermal gradient values of over 1000 mK m^{-1} [*Eldholm et al.*, 1999] and even values of over 10,000 mK m^{-1} have been estimated by *Vogt et al.* [1999] in the mud volcano crater. In Lake Baikal, both in situ measured and BSR-derived heat flow evidenced elevated heat flow values compared to background at the Malenki mud crater [*Vanneste et al.*, 2003]. *Henry et al.* [1996] report a steady state surface heat flow of 5000 mW m^{-2} on average in the center of the Atalante mud volcano in the Barbados Trough.

4.2. Very Shallow Gas Hydrate Occurrence and Significance

[28] Theoretically, gas hydrate occurrence up to 250 m is possible when thermogenic gases are involved. In the Gulf of Mexico, gas hydrate occurrence has been reported up to about 440 m [*Sassen et al.*, 1999]. Here we now observe gas hydrates at a water depth up to nearly 350 m (Figure 5). Many shallow hydrate accumulations have been found at water depths below 500 m because the hydrates mainly consist of methane. The uppermost limit for methane hydrate occurrence is about 500 m [*Sloan*, 1998a]. The result in this paper gives an indication that the volume of gas trapped as gas hydrate may be much larger than formerly thought, since many estimates of gas hydrates only account for methane hydrates.

[29] An estimate of the quantity of gas hydrate in the Mercator mud volcano was calculated based on the seismic data and a gas hydrate volume percentage of 5%. Volume percentage estimates for Ginsburg mud volcano were 4–19% [*Mazurenko et al.*, 2003] and at the Hydrate Ridge [*Trehu et al.*, 2004] conclude gas hydrates contents up to 26 vol % at the summit of the ridge and an average of about 3–6 vol % in the upper tens of meters of sediments in the GHSZ. We also used a gas hydrate density of 900 kg^{-3} and the same velocity estimates as above. This model leads to a hydrate quantity between 2.5 Mt hydrate stored in this single mud volcano, or with the estimate that 1 m^3 contains

160 m^3 of methane, a quantity of 40×10^8 m^3 methane is obtained.

5. Conclusion

[30] An anomalous reflection (H event) has been observed in shallow mud volcanoes on the Moroccan margin. The H event was mapped in the Mercator mud volcano and was interpreted as the base of a gas hydrate stability zone, based on its inverse polarity and the fact that it mimics the seafloor away from the mud volcano's crater. Inside the crater, the H event is absent. This was supported by the fact that gas hydrate stability modeling with reported thermogenic gas compositions, indicated that gas hydrates can be stable at this shallow location. BSR inferred heat flow showed a concentric heat flow pattern around the crater, with a very sharp rise in heat flow near the crater, consistent with our interpretation that the gas hydrate layer is affected by a focused flow of warm fluid in the crater. Modeled heat flow values near the crater edge run-up to 1100 mW m^{-2} and must be still higher inside the crater. Although this is very high compared to background heat flow values, it is not abnormal for mud volcanoes. The absence of a bottom simulating reflection in the surrounding sediments may be explained by a low regional methane flux through the sediments. Consequently, dewatering of the accretionary wedge complex is mainly focused along fault surfaces and through seafloor structures, such as mud volcanoes.

References

Aloisi, G., C. Pierre, J. M. Rouchy, and J. C. Faugeres (2002), Isotopic evidence of methane-related diagenesis in the mud volcanic sediments of the Barbados accretionary prism, *Cont. Shelf Res.*, 22(16), 2355–2372.

Bangs, N., D. Sawyer, and X. Golovchenko (1993), Free gas at the base of the gas hydrate zone in the vicinity of the Chile triple junction, *Geology*, 21, 905–908.

Berastegui, X., C. J. Banks, C. Puig, C. Taberner, D. Waltham, and M. Fernandez (1998), Lateral diapiric emplacement of Triassic evaporites at the southern margin of the Guadalquivir Basin, Spain, in *Cenozoic Foreland Basins of Western Europe*, edited by A. Mascle et al., *Geol. Soc. Spec. Publ.*, 143, 49–68.

Blinova, V., and E. Bileva (2003), Some geochemical characteristics of relatively active and passive mud volcanoes (Gulf of Cadiz and Alboran Sea), in *Geological and Biological Processes at Deep-Sea European Margins and Oceanic Basins*, *IOC Workshop Rep.*, vol. 187, edited by M. Marani, G. Akhmanov, and A. Suzyumov, p. 17, UNESCO, Paris.

Bohrmann, G., et al. (2003), Mud volcanoes and gas hydrates in the Black Sea: New data from Dvurechenskii and Odessa mud volcanoes, *Geo Mar. Lett.*, 23(3–4), 239–249.

Bouriak, S., M. Vanneste, and A. Saoutkine (2000), Inferred gas hydrates and clay diapirs near the Storegga slide on the southern edge of the Voring Plateau, offshore Norway, *Mar. Geol.*, 163, 124–148.

Casas, D., G. Ercilla, and J. Baraza (2003), Acoustic evidences of gas in the continental slope sediments of the Gulf of Cadiz (E Atlantic), *Geo Mar. Lett.*, 23(3–4), 300–310.

Collett, T. (2002), Energy resource potential of natural gas hydrates, *AAPG Bull.*, 86(11), 1971–1992.

Davie, M. K., O. Y. Zatsepina, and B. A. Buffett (2004), Methane solubility in marine hydrate environments, *Mar. Geol.*, 203(1–2), 177–184.

De Batist, M., J. Klerkx, P. Van Rensbergen, M. Vanneste, J. Poort, A. Y. Golmshtok, A. A. Kremlev, O. M. Khlystov, and P. Krinitsky (2002),

Active hydrate destabilization in Lake Baikal, Siberia?, *Terra Nova*, 14(6), 436–442.

Dimitrov, L. I. (2002a), Mud volcanoes: The most important pathway for degassing deeply buried sediments, *Earth Sci. Rev.*, 59(1–4), 49–76.

Dimitrov, L. (2002b), Contribution to atmospheric methane by natural seepages on the Bulgarian continental shelf, *Cont. Shelf Res.*, 22(16), 2429–2442.

Eldholm, O., E. Sundvor, P. R. Vogt, B. O. Hjelstuen, K. Crane, A. K. Nilsen, and T. P. Gladczenko (1999), SW Barents Sea continental margin heat flow and Håkon Mosby mud volcano, *Geo Mar. Lett.*, 19(1–2), 29–37.

Flinch, J. (1993), Tectonic evolution of the Gibraltar Arc, Ph.D. thesis, 381 pp., Rice Univ., Houston, Tex., Aug.

Flinch, J. F. (1996), Accretion and extensional collapse of the external Western Rif (northern Morocco), in *Peri-Tethys Memoir 2: Structure and Prospects of Alpine Basins and Forelands.*, *Mem.*, vol. 170, edited by P. A. Ziegler and F. Horvath, pp. 61–86, Mus. Natl. d'Hist. Nat., Paris.

Gardner, J. M. (2001), Mud volcanoes revealed and sampled on the Western Moroccan continental margin, *Geophys. Res. Lett.*, 28(2), 339–342.

Gei, D., and J. M. Carcione (2003), Acoustic properties of sediments saturated with gas hydrate, free gas and water, *Geophys. Prospect.*, 51(2), 141–157.

Ginsburg, G. D. (1998), Gas hydrate accumulation in deep-water marine sediments, in *Gas Hydrates: Relevance to World Margin Stability and Climatic Change*, edited by J. Henriet and J. Mienert, *Geol. Soc. Spec. Publ.*, 137, 51–62.

Ginsburg, G., and V. Soloviev (1998), *Submarine Gas Hydrates*, 216 pp., VNIIOkeangeologia, Saint Petersburg, Russia.

Ginsburg, G. D., A. V. Milkov, V. A. Soloviev, A. V. Egorov, G. A. Cherkashev, P. R. Vogt, K. Crane, T. D. Lorenson, and M. D. Khutorskoy (1999), Gas hydrate accumulation at the Håkon Mosby mud volcano, *Geo Mar. Lett.*, 19(1–2), 57–67.

Grevemeyer, I., et al. (2004), Fluid flow through active mud dome Mound Culebra offshore Nicoya peninsula, Costa Rica: Evidence from heat flow surveying, *Mar. Geol.*, 207(1–4), 145–157.

Gupta, A. (2004), Marine gas hydrates: Their economic and environmental importance, *Curr. Sci.*, 86(9), 1198–1199.

Gutscher, M. A., J. Malod, J. P. Rehault, I. Contrucci, F. Klingelhoefer, L. Mendes-Victor, and W. Spakman (2002), Evidence for active subduction beneath Gibraltar, *Geology*, 30, 1071–1074.

Hedberg, H. D. (1974), Relation of methane generation to undercompacted shales, shale diapirs, and mud volcanos, *AAPG Bull.*, 58(4), 661–673.

Henry, P., et al. (1996), Fluid flow in and around a mud volcano field seaward of the Barbados accretionary wedge: Results from Manon cruise, *J. Geophys. Res.*, 101(B9), 20,297–20,323.

Holbrook, W., H. Hoskins, W. Wood, R. Stephen, and D. Lizarralde (1996), Methane hydrate and free gas on the Blake Ridge from vertical seismic profiling, *Science*, 273, 1840–1843.

Huseynov, D. A., and I. S. Guliyev (2004), Mud volcanic natural phenomena in the South Caspian basin: Geology, fluid dynamics and environmental impact, *Environ. Geol.*, 46(8), 1012–1023.

Jacobsen, S. (2001), Gas hydrates and deglaciations, *Nature*, 412, 691–693.

Kennett, J., K. Cannariato, I. Hendy, and R. Behl (2000), Carbon isotopic evidence for methane hydrate instability during quaternary interstadials, *Science*, 288, 128–133.

Kenyon, N., M. Ivanov, A. Akhmetzhanov, and G. Akhmanov (2001), Interdisciplinary geoscience research on the north east Atlantic margin and Mid-Atlantic Ridge, *IOC UNESCO Tech. Ser.* 60, 76 pp., UNESCO, Paris.

Kenyon, N., M. Ivanov, A. Akhmetzhanov, and G. Akhmanov (2003), Interdisciplinary geoscience research on the north east Atlantic margin, Mediterranean Sea and Mid-Atlantic Ridge, *IOC UNESCO Tech. Ser.*, 67, 32 pp., UNESCO, Paris.

Kopf, A. J. (2003), Global methane emission through mud volcanoes and its past and present impact on the Earth's climate, *Int. J. Earth Sci.*, 92(5), 806–816.

Kvenvolden, K. (1993), Gas hydrates: Geological perspective and global change, *Rev. Geophys.*, 31(2), 173–187.

Kvenvolden, K. (1998), A primer on the geological occurrence of gas hydrate, in *Gas Hydrates: Relevance to World Margin Stability and Climatic Change*, edited by J. Henriet and J. Mienert, *Geol. Soc. Spec. Publ.*, 137, 9–30.

MacKay, M., R. Jarrard, G. Westbrook, and R. Hyndman (1994), Origin of bottom simulating reflectors: geophysical evidence from the Cascadia accretionary prism, *Geology*, 22, 459–462.

Maestro, A., L. Somoza, T. Medialdea, C. J. Talbot, A. Lowrie, J. T. Vazquez, and V. Diaz-Del-Rio (2003), Large-scale slope failure involving triassic and middle miocene salt and shale in the Gulf of Cadiz (Atlantic Iberian margin), *Terra Nova*, 15(6), 380–391.

Maldonado, A., L. Somoza, and L. Pallares (1999), The Betic orogen and the Iberian-African boundary in the Gulf of Cadiz: Geological evolution (central North Atlantic), *Mar. Geol.*, *155*(1–2), 9–43.

Mazurenko, L. L., V. A. Soloviev, I. Belenkaya, M. K. Ivanov, and L. M. Pinheiro (2002), Mud volcano gas hydrates in the Gulf of Cadiz, *Terra Nova*, *14*(5), 321–329.

Mazurenko, L. L., V. A. Soloviev, J. M. Gardner, and M. K. Ivanov (2003), Gas hydrates in the Ginsburg and Yuma mud volcano sediments (Moroccan margin): Results of chemical and isotopic studies of pore water, *Mar. Geol.*, *195*(1–4), 201–210.

Medialdea, T., R. Vegas, L. Somoza, J. T. Vazquez, A. Maldonado, V. Diaz-Del-Rio, A. Maestro, D. Cordoba, and M. C. Fernandez-Puga (2004), Structure and evolution of the 'olistostrome' complex of the Gibraltar Arc in the Gulf of Cadiz (eastern central Atlantic): Evidence from two long seismic cross-sections, *Mar. Geol.*, *209*(1–4), 173–198.

Ovsyannikov, D. O., A. Y. Sadekov, and E. V. Kozlova (2003), Rock fragments from mud volcanic deposits of the Gulf of Cadiz: An insight into the Eocene-Pliocene sedimentary succession of the basin, *Mar. Geol.*, *195*(1–4), 211–221.

Paull, C. K., P. G. Brewer, W. Ussler, E. T. Peltzer, G. Rehder, and D. Clague (2003), An experiment demonstrating that marine slumping is a mechanism to transfer methane from seafloor gas-hydrate deposits into the upper ocean and atmosphere, *Geo Mar. Lett.*, *22*(4), 198–203.

Pinheiro, L. M., et al. (2003), Mud volcanism in the Gulf of Cadiz: Results from the TTR-10 cruise, *Mar. Geol.*, *195*(1–4), 131–151.

Poort, J., and J. Klerkx (2004), Absence of a regional surface thermal high in the Baikal rift: New insights from detailed contouring of heat flow anomalies, *Tectonophysics*, *383*, 217–241.

Robertson, A., et al. (1996), Mud volcanism on the Mediterranean Ridge: Initial results of Ocean Drilling Program Leg 160, *Geology*, *24*, 239–242.

Sartori, R., L. Torelli, N. Zitellini, D. Peis, and E. Lodolo (1994), Eastern segment of the Azores-Gibraltar line (central-eastern Atlantic): An oceanic plate boundary with diffuse compressional deformation, *Geology*, *22*, 555–558.

Sassen, R., S. Joye, S. T. Sweet, D. A. Defreitas, A. V. Milkov, and I. R. Macdonald (1999), Thermogenic gas hydrates and hydrocarbon gases in complex chemosynthetic communities, Gulf of Mexico continental slope, *Org. Geochem.*, *30*(7), 485–497.

Sclater, J. G., C. Jaupart, and D. Galson (1980), The heat flow through oceanic and continental crust and the heat loss of the Earth, *Rev. Geophys.*, *18*(1), 269–311.

Sloan, E. (1998a), *Clathrate hydrates of natural gases*, 705 pp., CRC Press, Boca Raton, Fla.

Sloan, E. (1998b), Physical/chemical properties of gas hydrates and application to world margin stability and climatic change, in *Gas Hydrates: Relevance to World Margin Stability and Climatic Change*, edited by J. Henriet and J. Mienert, *Geol. Soc. Spec. Publ.*, *137*, 31–50.

Soloviev, V., and G. Ginsburg (1994), Formation of submarine gas hydrates, *Bull. Geol. Soc. Denmark*, *41*, 86–94.

Somoza, L., et al. (2003), Seabed morphology and hydrocarbon seepage in the Gulf of Cadiz mud volcano area: Acoustic imagery, multibeam and ultra-high resolution seismic data, *Mar. Geol.*, *195*(1–4), 153–176.

Trehu, A. M., et al. (2004), Three-dimensional distribution of gas hydrate beneath southern Hydrate Ridge: Constraints from ODP Leg 204, *Earth Planet. Sci. Lett.*, *227*(3–4), 557–558.

Vanneste, M., J. Poort, M. De Batist, and J. Klerkx (2003), Atypical heat-flow near gas hydrate irregularities and cold seeps in the Baikal Rift zone, *Mar. Pet. Geol.*, *19*(10), 1257–1274.

Van Rensbergen, P., M. De Batist, J. Klerkx, R. Hus, J. Poort, M. Vanneste, N. Granin, O. Khlystov, and P. Krinitsky (2002), Sublacustrine mud volcanoes and methane seeps caused by dissociation of gas hydrates in Lake Baikal, *Geology*, *30*, 631–634.

Van Rensbergen, P., et al. (2005a), The El Arraiche mud volcano field at the Moroccan Atlantic slope, Gulf of Cadiz, *Mar. Geol.*, *219*(1), 1–17.

Van Rensbergen, P., D. Depreiter, B. Pannemans, and J. Henriet (2005b), Seafloor expression of sediment extrusion and intrusion at the El Arraiche mud volcano field, Gulf of Cadiz, *J. Geophys. Res.*, *110*, F02010, doi:10.1029/2004JF000165.

Vogt, P. R., J. Gardner, and K. Crane (1999), The Norwegian-Barents-Svalbard (NBS) continental margin: Introducing a natural laboratory of mass wasting, hydrates, and ascent of sediment, pore water, and methane, *Geo Mar. Lett.*, *19*(1–2), 2–21.

Wessel, P., and W. Smith (1991), Free software helps map and display data, *Eos Trans. AGU*, *72*, 441, 445–446.

Wooster, W., A. Lee, and G. Dietrich (1969), Redefinition of salinity, *Deep Sea Res. Oceanogr. Abstr.*, *16*(3), 321–322.

Xu, W., and C. Ruppel (1999), Predicting the occurrence, distribution, and evolution of methane gas hydrates in porous marine sediments, *J. Geophys. Res.*, *104*(B3), 5081–5095.

Yamano, M., S. Uyeda, Y. Aoki, and T. H. Shipley (1982), Estimates of heat-flow derived from gas hydrates, *Geology*, *10*(7), 339–342.

————————————

D. Depreiter, J. P. Henriet, J. Poort, and P. Van Rensbergen, Renard Centre of Marine Geology, Ghent University, Krijgslaan 281 S8, B-9000 Ghent, Belgium. (davy.depreiter@ugent.be)
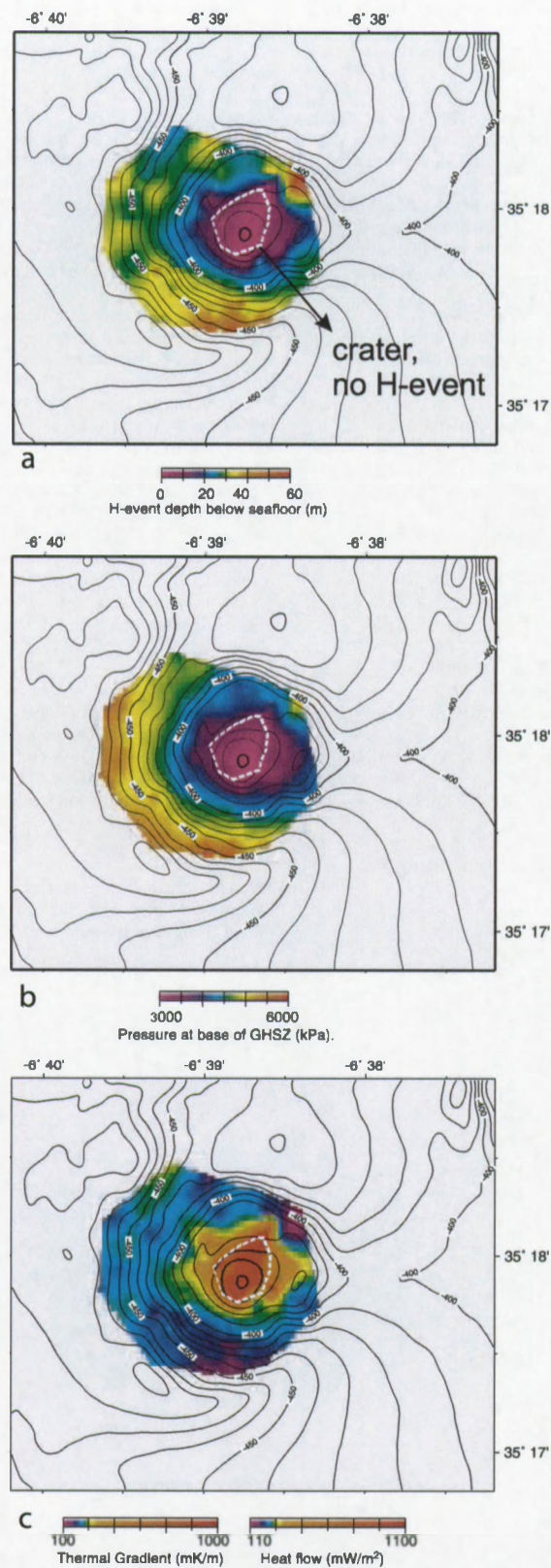
Figure 7. (a) Depth of the H event in meters in the Mercator mud volcano. (b) Calculated pressure at the depth of the H event. (c) Calculated thermal gradient and heat flow inferred from the occurrence of the H event. The thermal gradient and heat flow display a quasi-radial pattern around the mud volcano crater, increasing toward it. In the crater area, no H event was observed.

Carbonate mounds in a mud volcano province off north-west Morocco: Key to processes and controls

Anneleen Foubert [a,*], Davy Depreiter [a], Tim Beck [b], Loïs Maignien [a,c], Bart Pannemans [a], Norbert Frank [d], Dominique Blamart [d], Jean-Pierre Henriet [a]

[a] Renard Centre of Marine Geology, University Gent, Krijgslaan 281-S8, B-9000 Gent, Belgium
[b] Institute of Palaeontology, University of Erlangen/Nuremberg, Loewenichstrasse 28, D-91054 Erlangen, Germany
[c] LABMET, University Gent, Coupure Links 653, B-9000 Gent, Belgium
[d] Laboratoire des Sciences de Climat et de l Environnement, Laboratoire mixte CNRS/CEA, avenue de la Terrasse, F-91198 Gif-sur-Yvette, France

Abstract

This paper presents a new cluster of carbonate mounds discovered in 2002 in the Gulf of Cadiz off Morocco (R/V Belgica 2002) in water depths of 500 to 600 m amidst a field of giant mud volcanoes. Multibeam bathymetry, side scan sonar imagery and 2D seismics are analyzed to present four mound provinces: (1) the Pen Duick Mound Province on the Pen Duick Escarpment, (2) the Renard Mound Province on the Renard Ridge, (3) the Vernadsky Mound Province on the Vernadsky Ridge and the Al Idrisi Mound Province on the gas-blanked sediments above the buried Al Idrisi Ridge. Video imagery and surface samples are described to ground-truth the different mound areas.

The paradox is that nearly no live corals are presently being observed at the surface of the mounds, while the mound cores display throughout a high number of reef-forming cold-water coral fragments (scleractinians) in association with numerous associated fauna formerly inhabiting the econiches provided by the coral framework. Environmental and oceanographic conditions during the recent past (glacials/stadials) were probably more favourable for cold-water coral growth.

Pore water analyses in on-mound cores at the south-eastern edge of Pen Duick Escarpment give evidence of focused, higher methane fluxes and sulphate reduction rates on mounds than in the surrounding sediments. Cores from several mounds display horizons of strong corrosion and dissolution of the coral fragments.

A three-phase model for carbonate mound evolution in these settings is proposed. (1) In a first stage external controls (positive oceanographic and environmental conditions, the presence of an active planktonic food chain, based on a high primary production, and a suitable substrate) are responsible for the initiation of cold-water coral growth. (2) Once the cold-water corals established an initial framework, sedimentation becomes an important factor controlling mound growth: the cold-water corals baffle the sediments. (3) Throughout mound growth, the mound may episodically be affected by diagenetic processes responsible for aragonite dissolution and probably carbonate precipitation.
© 2007 Elsevier B.V. All rights reserved.

Keywords: carbonate mounds; cold-water corals; Gulf of Cadiz (Moroccan margin); early diagenesis

* Corresponding author. Present address: TOTAL - DGEP/GSR/TG/ISS/CARBBA2022 - CSTJF - Avenue Larribau 64018 Pau Cedex - France.
Tel.: +33 (0)5 59 83 42 66; fax: +33 (0)5 59 83 66 92.
E-mail address: anneleen.foubert@total.com (A. Foubert).

1. Introduction

The presence of cold-water corals with their associated ecosystems is widespread along the whole European continental margin (Roberts et al., 2006). However, the association of these cold-water corals with the build-up of recent carbonate mounds was until four years ago only well studied in some delineated provinces W of Ireland (Henriet et al., 1998; Kenyon et al., 1998; De Mol et al., 2002; Huvenne et al., 2002). A milestone in the study of the role of cold-water corals in mound build-up was IODP Expedition 307, which drilled in May 2005 "Challenger Mound" in the Belgica Mound Province off western Ireland. The mound body consisted of a 155-m-thick sequence with cold-water coral-bearing sediments of Plio-Pleistocene age (Expedition Scientists, 2005). The success of Expedition 307 paved the way for the further exploration of the diverse world of carbonate mounds.

An exploratory cruise of *R/V Belgica* in 2002 off Larache (Morocco) has led to the discovery of small mounds topping ridges and structural heights, respectively on Pen Duick Escarpment, Renard Ridge, Vernadsky Ridge and Al Idrisi Ridge (Fig. 1). These mounds are found amidst 9 giant mud volcanoes: the El Arraiche mud volcano field (Van Rensbergen et al., 2005a) (Fig. 1). They occur in a setting where focused fluid seepage is observed (Baraza and Ercilla, 1996; Pinheiro et al., 2003; Somoza et al., 2003; Van Rooij et al., 2005). Because of its unique setting, the carbonate mound site on the Moroccan margin became rapidly involved in a developing stage of focused multidisciplinary research. The high amount of data, acquired recently in these new mound settings on the Moroccan margin, asks for a comprehensive review which will be presented in this paper.

In this paper an overview will be given of the co-occurrence of cold-water corals and carbonate mounds with mud volcanoes (El Arraiche mud volcano field) and active fluid seepage in the Gulf of Cadiz on the Moroccan margin. Attention will be paid to the wide-spread extinction of healthy cold-water coral frameworks observed nowadays on the Moroccan margin. A three-phase model for carbonate mound development will be proposed. This paper can form the stepping stone for a comparative study between the mounds on the Moroccan margin and global mound occurrences, including the mound provinces in Porcupine Seabight,
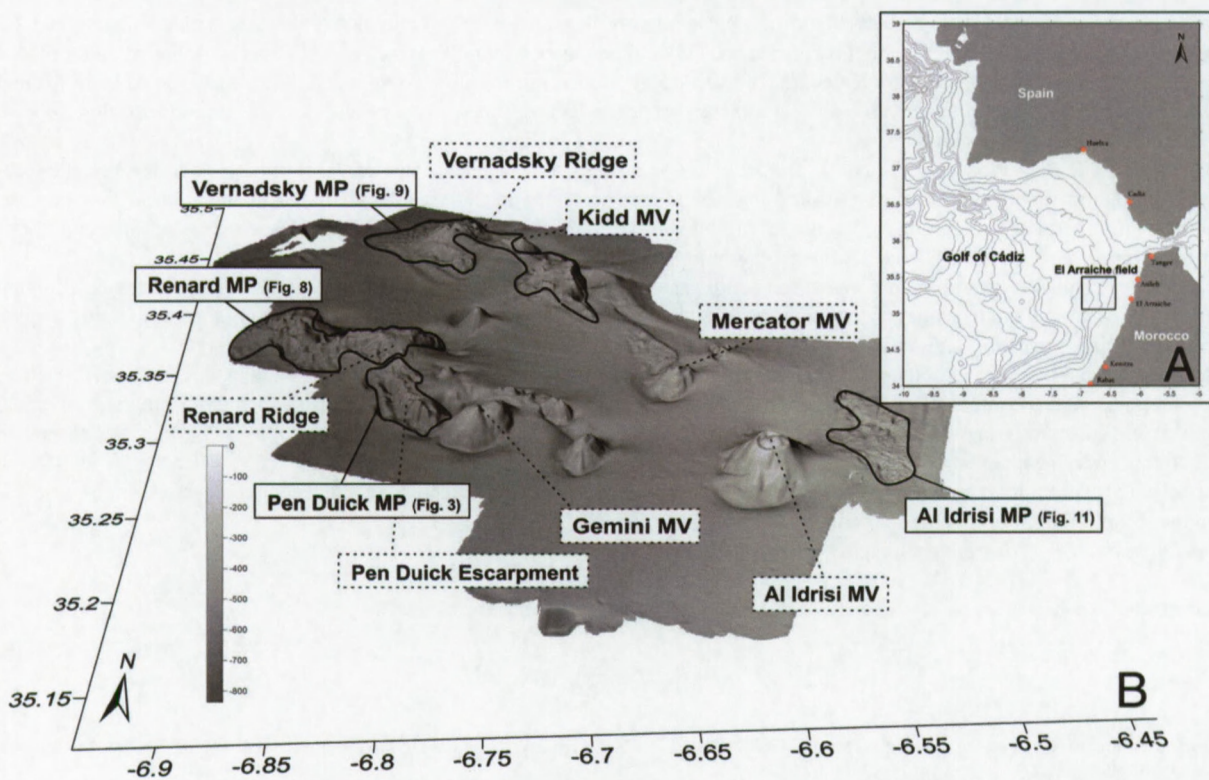

Fig. 1. (A) Location of the study area "El Arraiche mud volcano field" (rectangle) on the Moroccan margin. (B) 3D bathymetric map of the study area. The dashed lines represent the mud volcanoes (MV) and the geomorphological structures. The solid lines indicate the presence of the mound provinces (MP).

off Angola and Congo, Mauritania, Brazil, Florida Strait, Blake Plateau, Orphan Knoll and many more to be unveiled.

2. General setting

2.1. Geological setting

The Gulf of Cadiz is situated west of Gibraltar between 9°W to 6°45′W and 34°N to 37°15′N, enclosed by the Iberian Peninsula and Morocco (Fig. 1A). The geological setting of the Gulf of Cadiz is complex and still under debate (Sartori et al., 1994; Maldonado et al., 1999; Gutscher et al., 2002). The area is characterized by the presence of an accretionary wedge formed by a westward motion of the front of the Gibraltar Arc (the Betic–Rif mountain chain) during the Middle Miocene. Formation of a large olistostrome complex (allochthonous nappes) took place during the Tortonian, as a consequence of increased subsidence (Maldonado et al., 1999). The African–Eurasian convergence since the Cenozoic yields a compressional–transpressional tectonic regime, reactivating many normal faults and causing wide-spread diapirism in the north of the Gulf of Cadiz (Berastegui et al., 1998; Somoza et al., 2003). The main part of the olistostrome unit occupies the central part of the Gulf of Cadiz as a lobe-shaped structure, extending over 300 km into the Atlantic Ocean (Maldonado et al., 1999; Maestro et al., 2003; Somoza et al., 2003; Medialdea et al., 2004).

The study area, El Arraiche mud volcano field, is situated 35 km offshore the north-western Moroccan margin, on top of the accretionary wedge of the Gulf of Cadiz (Van Rensbergen et al., 2005a). The bathymetry is increasing from 200 m to 800 m at the north-western Moroccan continental slope. The study area is characterized by extensional tectonics, in contrast to the main part of the Gulf of Cadiz. This is expressed as large rotated blocks bound by lystric faults that created Plio-Pleistocene depocentres (Flinch, 1993, 1996). In the El Arraiche mud volcano field these rotated blocks are expressed at the seafloor as two subparallel ridges, Vernadsky and Renard Ridges, both with steep fault escarpments, as exemplified by Pen Duick Escarpment (PDE) on Renard Ridge (Fig. 1B). The ridges rise up in water depths of about 700 m and stretch to the shelf edge. Eight mud volcanoes are clustered around these ridges, positioned above large normal faults that bound the rotated blocks and serve as fluid migration pathways fuelling the mud volcanoes (Van Rensbergen et al., 2005a) (Fig. 1B). The source of the overpressured fluids is believed to be located at the base of the accretionary

wedge body since rock clasts in the mud breccia are reported to be of an age up to early Eocene (Ovsyannikov et al., 2003). The onset of mud volcano activity in the El Arraiche mud volcano field is estimated at about 2.4 Ma. Since the Upper Pliocene, episodic expulsion of liquidized sediment created vertical piles of extruded mud up to 500 m thick (Van Rensbergen et al., 2005a).

Geophysical evidence of shallow gas and subsurface fluid flow has been reported in the Gulf of Cadiz (e.g. Baraza and Ercilla, 1996; Pinheiro et al., 2003; Somoza et al., 2003; Depreiter et al., 2005b). Gas hydrates on the Moroccan margin and in the Gulf of Cadiz have only been reported from a small number of deep-water mud volcanoes (Gardner, 2001; Kenyon et al., 2001, 2003; Mazurenko et al., 2003; Pinheiro et al., 2003). Depreiter et al. (2005b) observed anomalous reflections in the Mercator mud volcano and interpreted this as the base of a gas hydrate stability zone. Video imagery visualized the presence of an active 'brown smoker' chimney on Mercator mud volcano in a water depth of about 400 m (Depreiter et al., 2005b; Van Rooij et al., 2005).

2.2. Oceanographic setting

The present-day oceanographic circulation in the Gulf of Cadiz is controlled by the exchange of water masses through the strait of Gibraltar and by the interaction of Mediterranean Outflow Water (MOW) with the Atlantic circulation. The highly saline and warm near-bottom MOW flows into the Atlantic Ocean below the less saline, surficial Atlantic Inflow Water (AI) that enters the Mediterranean Sea (Madelain, 1970; Thorpe, 1976; Ochoa and Bray, 1991; Baringer and Price, 1999) (Fig. 2A).

The AI is composed of North Atlantic Superficial Water (NASW) flowing between the surface and a water depth around 100 m and North Atlantic Central Water (NACW) extending between 100 and 700 m (Caralp, 1988) (Fig. 2A). The general surface circulation in the Gulf of Cadiz is anticyclonic with short-term, meteorologically induced variations in the upper layer. It must be considered in relation to the north-eastern Atlantic circulation and could be understood as the last meander of the Azores current. The presence of upwelling regions off the northern margin (Ruiz and Navarro, 2006) (Fig. 2A), can be explained as the direct result of local wind forcing (Garcia-Lafuente et al., 2006).

Below NACW, Mediterranean Water is present. After having passed the Strait of Gibraltar, the MOW undergoes a decrease in temperature, salinity and velocity caused by its rapid mixing with NACW. It then divides into two main cores west of 6°20′W: a Mediterranean
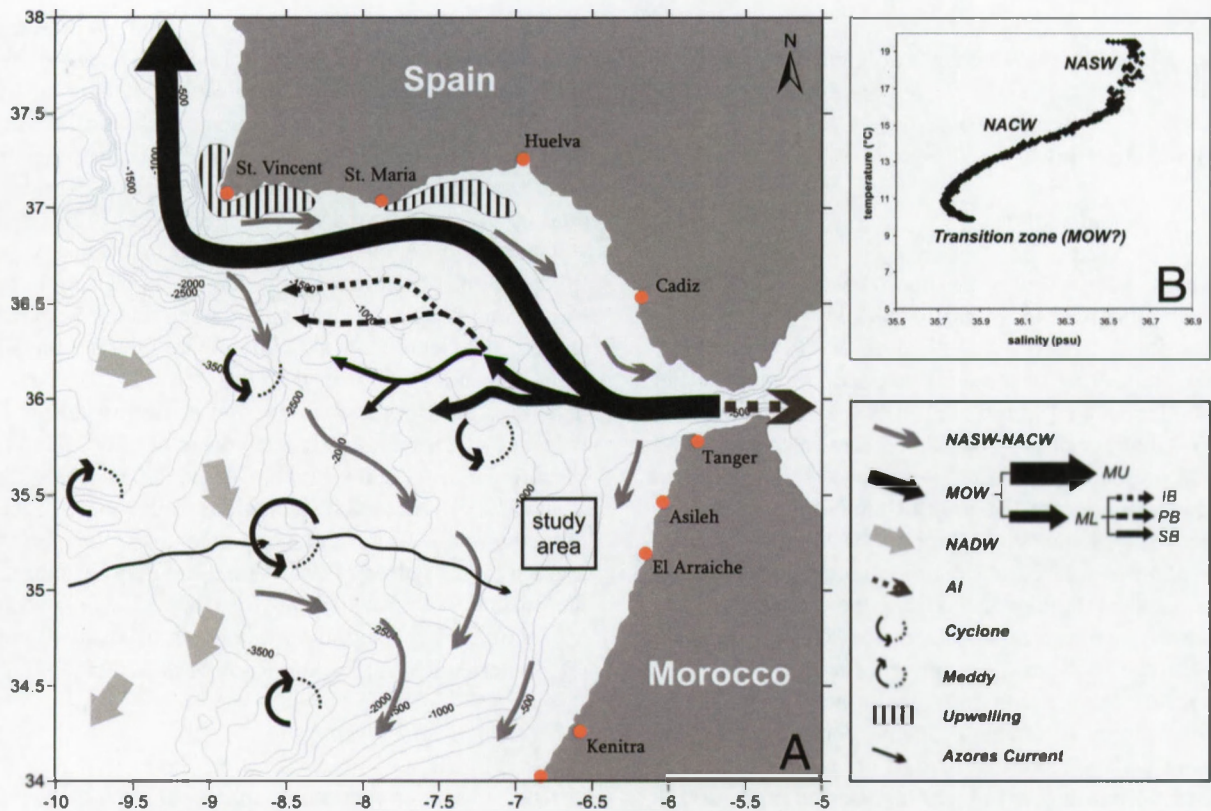
Fig. 2. (A) General circulation pattern in the Gulf of Cadiz (figure modified after Thomson et al., 1999; Schönfeld and Zahn, 2000; Carton et al., 2002; Hernandez-Molina et al., 2003; Vanney and Ménanteau, 2004; Llave et al., 2006; Ruiz and Navarro, 2006) with visualization of North Atlantic Surface Water (NASW), North Atlantic Central Water (NACW), Mediterranean Outflow Water (MOW), North Atlantic Deep Water (NADW), Azores Current, meddies, cyclones and upwelling regions. (B) CTD-profile (temperature versus salinity) characterizing the different water masses in the study area.

Upper Core (MU) and a Mediterranean Lower Core (ML). The upper core is a geostrophically steered current following a northward path along the Spanish and Portuguese continental margin between 400 and 800 m water depth. The lower core is a more ageostrophical current flowing at depths between 800 and 1300 m (Zenk and Armi, 1990; Baringer, 1993; Bower et al., 1997). This lower core is influenced by the morphology of the slope and divided in three minor branches between the Cadiz and the Huelva meridians (6°20′–7°) (Kenyon and Belderson, 1973; Melieres, 1974; Nelson et al., 1999; Hernandez-Molina et al., 2003): (a) Intermediate Branch (IB), (b) Principal Branch (PB) and a (c) Southern Branch (SB) (Fig. 2A). It has to be mentioned that at Cape St. Vincent the undercurrents veer northwards and become unstable enough to often produce deep anticyclones, called meddies (Bower et al., 1995; Sadoux et al., 2000). Hydrological measurements in 1999 revealed three eddies in the Gulf of Cadiz, displaying substantial interactions: two meddies (meddy Christine, S of Cape St. Vincent and meddy

Isabelle close to the Moroccan margin) and a deep cyclone, which is coupled with meddy Isabelle as a baroclinic dipole (N of meddy Isabelle and SE of meddy Christine) (Carton et al., 2002) (Fig. 2A).

North Atlantic Deep Water (NADW) is present below the MOW at depths >1500 m (Fig. 2A) (Ambar et al., 2002). It flows from the Greenland–Norwegian Sea region towards the south.

Recent CTD-measurements and current measurements showed that El Arraiche Mud Volcano Field along the Moroccan margin is mainly influenced by NACW (with temperatures between 11 and 16 °C and salinities between 35.6 and 36.5 psu) (Fig. 2B). The typical signature of MOW is not clearly recorded in the study area but the temporarily influence of MOW by meddies cannot be excluded (Fig. 2B). Recent measurements with a BOBO-Lander of the Netherlands Institute of Sea Research (NIOZ), deployed on top of Pen Duick Escarpment, showed the relatively weak effect of internal waves and tidal currents compared to other mound provinces (SE and SW Rockall Trough) (Mienis et al., 2005).

3. Material and methods

The multibeam bathymetry was acquired with a SIMRAD Kongsberg EM1002, installed on board of *R/V Belgica* during the CADIPOR I and II cruises ("Gulf of CADiz — PORcupine Seabight Comparative Study") in 2002 and 2005, respectively. The data were recorded with a sailing speed of 6 to 7 knots and swath widths ranging from ca. 500 m in deep water to 700 m in shallow water. The beam angles were generally chosen quite narrow (20 to 30°), in order to focus the acoustic energy towards the relatively large depth below the vessel. A spike filter of weak to medium strength was switched on during acquisition. The data were corrected and cleaned with the Kongsberg packages Merlin and Neptune. The footprint at 400 m is 15 × 15 m. In total 725 km^2 was covered.

High-resolution seismic data were acquired during the CADIPOR I and II campaigns (*R/V Belgica* 2002, 2005) with an 80 electrode 500 J sparker, 35 in^3 Sodera GI gun and the Ifremer Deeptow Chirp Sonar System. The seismic profiles were digitally recorded using the Elics Delph system. Data processing (swell-filter, band pass filter, deconvolution and signal amplification) was done using Landmark Promax processing software. Interpretation and mapping was executed in the Kingdom Suite seismic interpretation software package (Seismic Micro-Technology, Inc.).

Sidescan sonar imagery (SSS) was collected with the MAK-1M deep-towed hydro-acoustic complex on board of the *R/V Logachev* during the TTR-12, TTR-14 and TTR-15 cruises in 2002, 2004 and 2005. The MAK-1M deep-towed hydro-acoustic system contains a high-resolution sidescan sonar operating at a frequency of 30 kHz, with a total swath range of 2 km (1 km per side) and a subbottom profiler, operating at a frequency of 5 kHz. The fish was towed at a constant altitude of about 100 m above the seafloor with a speed of 1.5–2 knots. The positioning of the tow-fish was archived by using a short-based underwater navigation system. The data were recorded digitally and stored in SEG-Y format. A time-variant gain control was applied during the acquisition of the data. The processing of the collected data (slant-range-to-ground-range (SLT) correction, geometrical correction and smoothing average filtering) was carried out on board.

Video imagery was collected during the TTR12 cruise with *R/V Logachev* (TVAT33 and TVAT36) and during the CADIPOR II campaign with *R/V Belgica* (c0505-video06) by using a deep-towed frame mounted camera. The imagery was recorded on analog tapes, converted in digital format and imported in a GIS-system (Adélie-GIS 8.3).

6 Hammon grabs (B05-1212, B05-1211, B05-1209, B05-1208, B05-1214 and B05-1215), 2 TV-guided grabs (AT407Gr, AT406Gr) and 1 dredge (AT574D) are used in this study to ground-truth the video material, sidescan sonar imagery and multibeam. The samples were collected respectively during the CADIPOR II cruise (*R/V Belgica* 2005) and the TTR-12 and TTR-15 campaigns (*R/V Logachev* 2002, 2005). One Kasten core (MD04-2804) was collected during the CADICOR cruise in 2004 on board of the *R/V Marion Dufresne* to give insight into the mound structures on PDE. The Kasten core was opened and described in detail. Bulk samples were taken each 20 cm for macrofaunal analysis. Six coral species from the top of the core were sampled for U/Th dating. ^{230}Th/U datings were measured in the Laboratoire des Sciences du Climat et de l'Environnement (LSCE) in Gif-sur-Yvette with a thermal ionization mass spectrometer (Finnigan MAT262). Five cores (AT564G, AT534G, AT570G, AT571G and AT572G) were acquired during respectively the TTR14 and TTR15 cruises with the gravity corer on board of *R/V Logachev*. The cores were opened and described in detail.

4. Data description and interpretation

4.1. Pen Duick Mound Province

4.1.1. Geomorphology

Extensive multibeam bathymetry and seismics along the top of PDE, a fault-bounded cliff, revealed a series of elongated mounds and mound clusters (Fig. 3). The mounds occur in water depths between 500 and 600 m and can measure up to 60 m in height. They are elongated in E–W direction, with a length of about a half a kilometer. At the base of the cliff smaller mound patches are found, again characterized by an E–W orientation. A NW–SE oriented moat delineates the base of the escarpment. Based on the integration of bathymetry, seismic data and side scan sonar imagery, so far 15 mound structures along the top of the cliff have been identified. The south-west facing part of the cliff has a height of 65 m above the sediments and an average slope gradient varying between 15 and 20°. The eastern edge of the cliff reaches slope gradients up to 25°.

4.1.2. Seismics

A very high-resolution deep-tow chirp seismic profile along the crest of PDE (Fig. 4) shows the mounds as rounded cone shaped features, with a height up to 60 m. No internal structures are observed. On some parts of the profile, mostly between 1500 and 4000 m along the
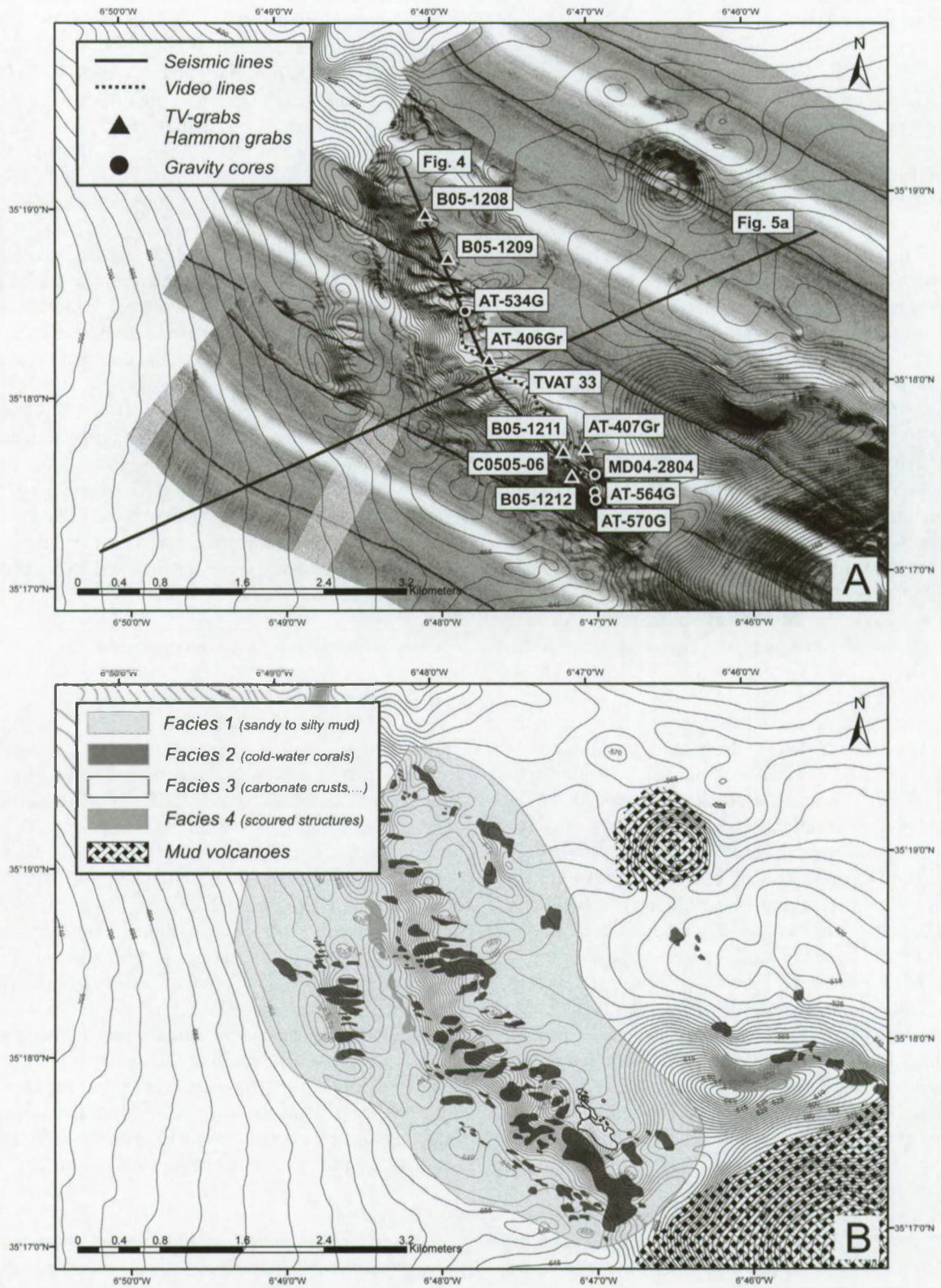
Fig. 3. (A) Bathymetry (contour spacing is 5 m), side scan sonar imagery and location of the seismic profiles, core material and video lines in the Pen Duick Mound Province. (B) Interpretation of sidescan sonar imagery (MAKAT 66-68), representing the four described facies.
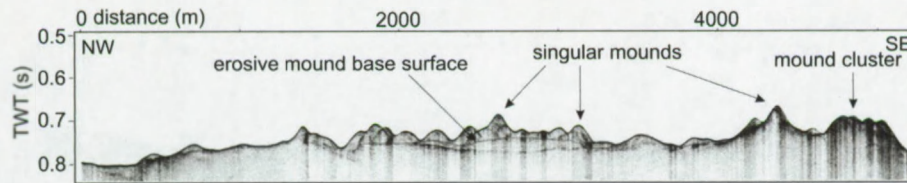
Fig. 4. CHIRP seismic profile (IFREMER) over Pen Duick Escarpment indicating the singular mounds topping the cliff and the erosive mound base surface (location: see Fig. 3A).

distance axis, subsurface reflections are recorded. Generally, the subsurface has a low amplitude. The widely U-shaped geometry of the reflections is caused by directional changes during the acquisition of the data (Fig. 3A). An erosive surface below the mounds can be observed and is interpreted as the mound base.

A profile perpendicular to the PDE shows medium to high amplitude sequences, covering a low-amplitude unit (Fig. 5A). The low-amplitude body has a very steep SW dipping slope beneath the escarpment. Northwards, NE dipping reflections are observed in the low-amplitude unit. The low-amplitude structural acoustic basement, which is part of Renard Ridge, is eroded and crops out at the seafloor. Diffractions at and above the outcropping basement are indicative for the occurrence of elevated mound structures.

A small mound-like low-amplitude body occurs in the high amplitude sequences that cover the basement. Other profiles near the PDE also indicated the presence of small mound-like features in the sedimentary sequences (inset Fig. 5A). Reflections are draping the features, indicating that they are real physical structures. The small mounded features only occur upslope a set of small normal faults associated with gas blanking and bright spots. A direct relation between the two observations is speculative. The features may be interpreted as small buried mounds and could be an indication of the onset of mound growth in the area.

4.1.3. Video imagery and SSS

The integrated analysis of sidescan sonar (MAKAT 66–68), video imagery (TVAT 33 and c0505-video06) and ground truthing by surface coring (AT407Gr, AT406Gr, B05-1212, B05-1211, B05-1209 and B05-1208) revealed four distinctive facies (Fig. 3).

Facies 1 corresponds with sandy to silty clays (Figs. 3 and 6C), characterized by an even surface with some well-delineated patches of cobble to boulder-sized stones. This facies presents the surface sediments in between the different mounds and mound patches. On sidescan sonar imagery it shows low backscatter strength with a very smooth surface. These fine-grained deposits are associated with typical soft-bottom communities (spiral an-

thipatharians, isidiid gorgonians (*Isidella elongata*) and hexactinellid sponges), as well as characterized by a high amount of burrows.

Facies 2 reveals cold-water corals, lying at the surface of the mounds and mound patches along the crest of PDE. Most of the mounds are covered with dead coral fragments and sediment-clogged dead coral rubble, surrounded and overlain by a layer of brownish silty mud (Fig. 6D). The most common observed cold-water coral fragments are classified as *Dendrophyllia* spp. (*D. alternata*, *D. cornucopia* and *D.* sp.), *Lophelia pertusa*, *Madrepora oculata*, *Desmophyllum cristagalli*, and *Caryophyllia calveri*. At the south-eastern edge of PDE the surface units are dominated by *Dendrophyllia* spp. (*D.* sp. and *D. cornucopia*) and some small fragments of *Stenocyathus vermiformis*, as identified in boxcores B05-1212 and B05-1211. Gravity coring (see below) shows that these upper units, built up by mainly *Dendrophyllia* spp., are further down-core replaced by *L. pertusa* and *M. oculata*, associated with *D. cristagalli* and *Caryophyllia* spp. Boxcores B05-1209, B05-1208 and grab AT406Gr learn that more west on Pen Duick Escarpment, the dominating coral species are *L. pertusa*, *M. oculata* and *D. alternata*. A high amount of macrofaunal and microfaunal life is associated with the cold-water coral fragments (crinoids, bryozoans, ophiuroids, gastropods, molluscs, hydroids, serpulids, gorgonians, foraminifers). Mass occurrences of crinoids are observed, using the dead skeletons of cold-water corals as substrate. The cold-water coral patches are characterized by a high backscatter strength and a clear acoustic shadow on sidescan sonar imagery.

Facies 3 consists of carbonate crusts, boulders or hard rock covered by a fine layer of hemipelagic mud (Fig. 6E). Boulder fields, rock outcrops and outcropping carbonate crusts are a common feature in between the mounds. Two distinct patches of carbonate slabs are observed in the eastern part of the TV-line TVAT33, respectively with a length of 11 m and 20 m (Fig. 3B). Solemyid shells, brachiopods (*Megerlia truncata*), dendrophyllid corals, anthipatharians, sponges and calcareous tube worms (Serpulidae) were observed attached on the carbonate crusts (Fig. 6B). It should be noted that the dominating
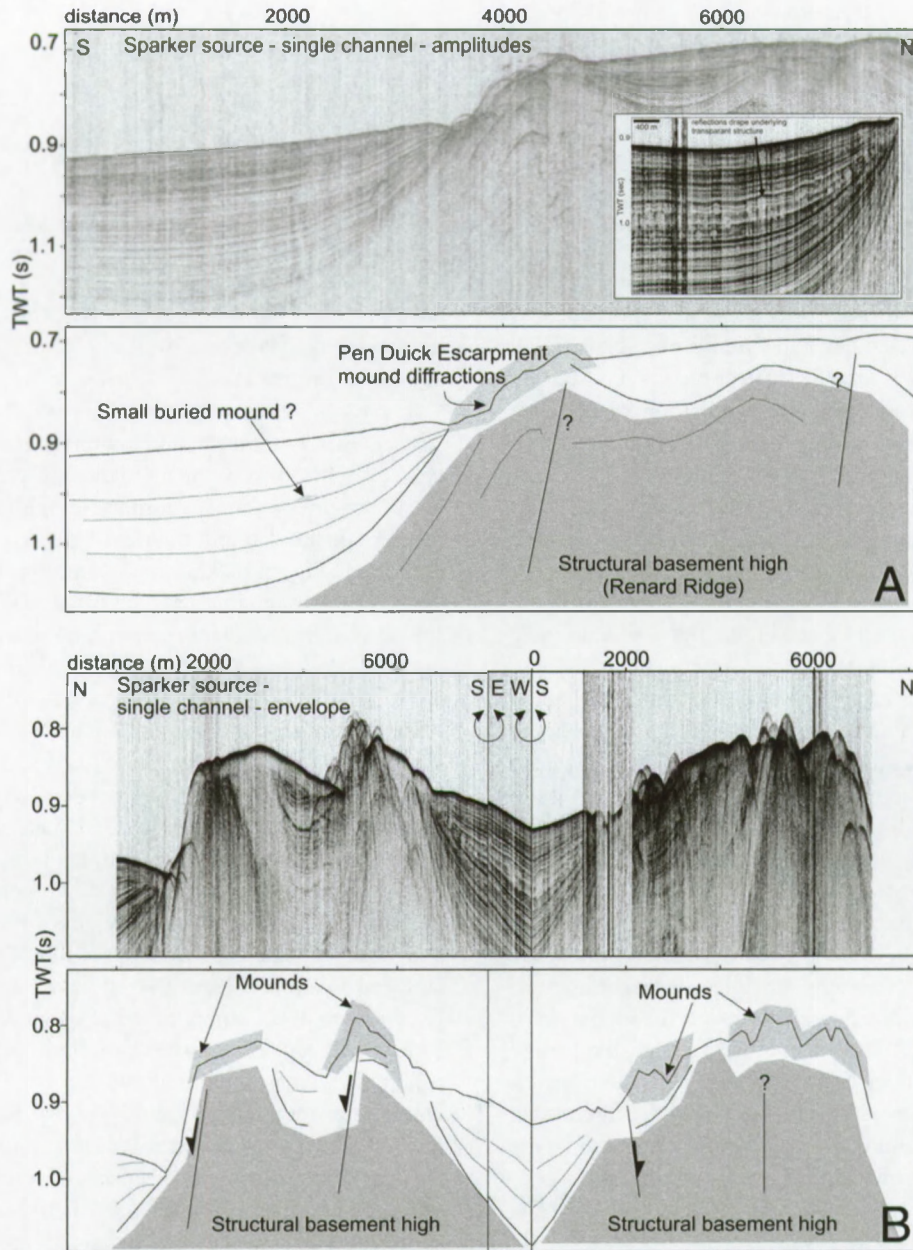
Fig. 5. (A) Sparker seismic profile perpendicular to the PDE, showing the mound diffractions on the escarpment, the structural basement high (location: see Fig. 3). The inset represents some small buried mounds occurring in the sediments at the foot of the escarpment. (B) Set of Sparker seismic profiles over Renard Ridge (location: see Fig. 7). The structural basement, two faults and mound structures can be recognized on the profiles.

cold-water corals associated with these carbonate crusts are mainly *Dendrophyllia* spp. using fossil coral framework and carbonate crusts as substrate. The bivalve *Spondylus gussoni* is often co-occurring with these species on hard substrates.

Facies 4 is recognized on sidescan sonar imagery by its strong backscatter (Fig. 3). It corresponds with the scoured moat at the foot of the escarpment or with a steep bank or slope, probably created by strong erosive along-slope currents leaving behind a lag deposit of coarser material or dead cold-water coral fragments.

4.1.4. Coring

Four cores, respectively a Kasten core MD04-2804 and three gravity cores AT564G, AT534G and AT570G have been collected on PDE to give insight into the
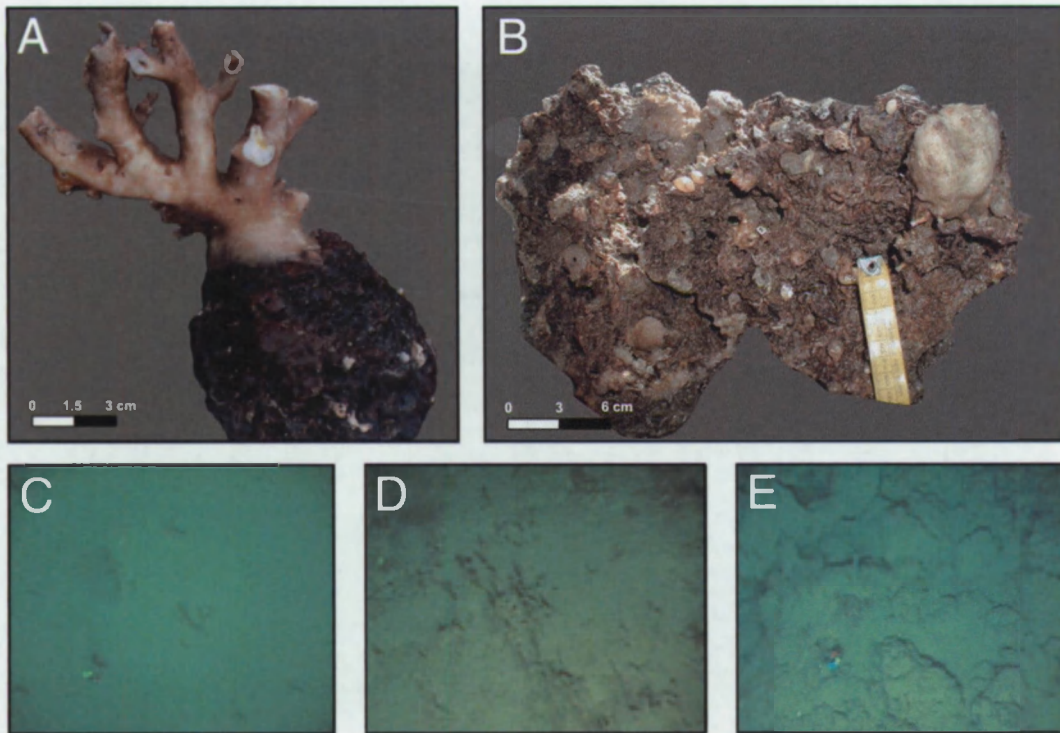
Fig. 6. (A) Cold-water coral *Dendrophyllia alternata* attached on carbonate chimney (station AT574D). (B) Benthic epifauna (bivalves (*Spondylus gussoni*), brachiopods (*Megerlia truncata*), sponges and calcareous tube worms (Serpulidae) attached on carbonate crust (station AT407Gr). (C) Video image representing silty mud colonized by spiral anthipatharians and isidiid gorgonians (~ facies 1). (D) Sediment-clogged dead cold-water coral fragments (~ facies 2). (E) Video image showing outcropping carbonate crusts, covered with a thin layer of silty mud (~ facies 3).

mound structures (Fig. 3A). The mound cores display throughout all their penetration depth a high number of reef-forming cold-water scleractinians like *L. pertusa*, *M. oculata*, *D. cristagalli*, *Dendrophyllia* spp. and *Caryophyllia* spp. In association with the cold-water coral fragments numerous shell-bearing invertebrates are determined formerly inhabiting the econiches provided by the coral framework. Based on these observations, every single mound structure on PDE can be interpreted as a cold-water coral mound.

The Kasten core MD04-2804, with a core penetration of 594 cm, is located on the mound cluster at the eastern edge of PDE at a water depth of 505 m (Fig. 3A). The whole core is characterized by cold-water coral fragments embedded in brownish oxidized sandy silt to very fine sand in the top 10 cm grading downwards in silty clays to clayey silts (Fig. 7). The most common colonial cold-water coral species, *L. pertusa*, *M. oculata* and *Dendrophyllia* spp., representing 90% of the total coral content, are alternating in distinctive zones. The upper part, between 0 and 60 cm, is dominated by *Dendrophyllia* spp. (*D. cornucopia* and *D.* sp.) in association with *S. vermiformis* (forming small well-preserved (fossil) specimens up to 2 cm long and 1 to 2 mm wide). Less common in the upper part are *L. pertusa*

and *M. oculata*. *D. cristagalli* occurs as big fragments (up to 5–6 cm) in between the previously described species. Down-core, *L. pertusa* and *M. oculata* are predominating, associated with some specimens of *D. cristagalli* and *Caryophyllia* sp. *Dendrophyllia* spp. is disappearing. As a result of bioerosion and chemical dissolution, the preservation of the coral fragments is rather poor in certain units. In between 215 and 330 cm the cold-water coral fragments are in a very bad stage of preservation mainly due to chemical dissolution (Fig. 7). The density of the coral fragments is changing throughout the core.

Among the cold-water coral fragments, other invertebrate species could be identified. Most of the reported species are known to live in association with cold-water corals. Frequently occurring species were the bivalves *Lima marioni*, *Acesta excavata*, *Asperarca nodulosa*, *Delectopecten vitreus*, *Pseudamussium sulcatum*, *S. gussoni* and *Heteranomia squamula*, the gastropods *Calliostoma* cf. *maurolici*, *Bursa ranelloides*, *Alvania tomentosa*, *Alvania cimicoides* and *Amphissa acutecostata*, the brachiopod species *M. truncata* and *Terebratulina* spp. as well as several echinoderms, e.g. the echinoid *Cidaris cidaris* and mass occurrences of unidentified crinoids. A specific group of bivalves and
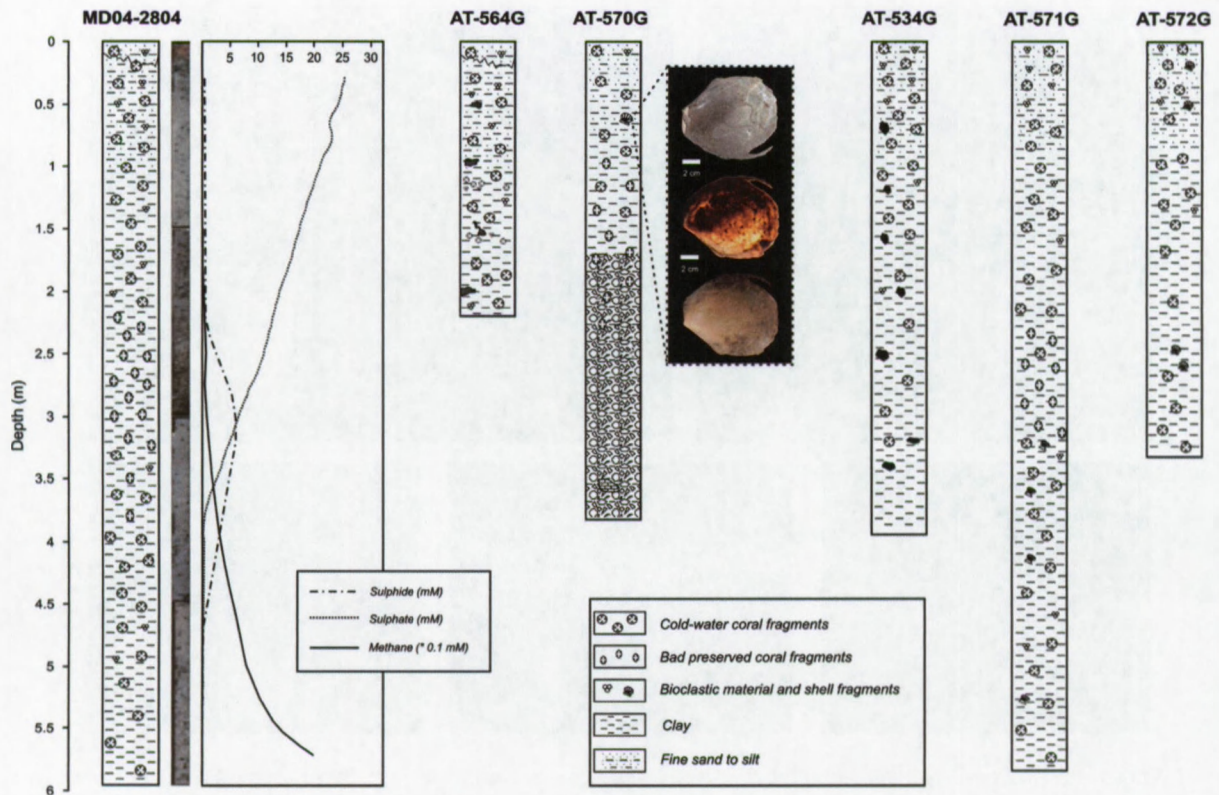
Fig. 7. Description of Kasten core MD04-2804 and gravity cores AT564G, AT570G and AT534G located in the Pen Duick Mound Province and gravity cores AT571G and AT572G, located in the Renard Mound Province. Pore water analysis (sulphate, sulphide and methane) and core images are shown for core MD04-2804. The picture represents an altered bivalve species (*Acesta excavata*), recovered from core AT570G.

gastropods occurring as associates in the cold-water coral environments of the study area are noteworthy as representatives of a local fauna not present in other cold-water coral environments further north. These species are either restricted to the Moroccan margin, at least restricted to the Gulf of Cadiz area (e.g. the gastropod species *A. tomentosa*, *Neptunea contraria*, *Pseudosetia amydralox*, *Crisilla amphiglypha* and *Bittium watsoni*) or are part of a fauna not extending further north than the southernmost Bay of Biscay (e.g. *Limopsis angusta*, *B. ranelloides*). These species are of high importance for palaeoenvironmental or oceanographic reconstructions as they are not reported from any other cold-water coral site along the European continental margin. The large bivalve *A. excavata*, on the other hand, implies a clearly boreal influence, nowadays known to be a common and abundant associate to cold-water coral reefs along the Norwegian margin (see López Correa et al., 2005).

Pore water analysis evidences a sharp sulphate-methane transition (SMT) zone at 3.5 m below the mound top, whereas the depth of no sulphate is much deeper in the surrounding sediments (Fig. 7). The horizon characterized by a strong corrosion of the coral

fragments is just lying above and at the front of the recent location of the zone of anaerobic methane oxidation (AOM). Due to the alteration of the cold-water coral fragments, absolute U/Th dating should be questioned (U-series open system behaviour). However, two U/Th datings at 10 and 50 cm core depth yielded confident ages of respectively 290 ± 20 ka and 320 ± 36 ka. Radiocarbon dating on the bivalve *A. excavata*, recovered from the top of the core, yielded ages from more than 50,000 yr BP (Matthias López Correa, pers. com.).

Gravity core AT564G is localized on the same mound cluster as core MD04-2804 at a water depth of 538 m and has a recovery length of 219 cm (Fig. 3). The top of the sediments (0–15 cm) consists of brownish water-saturated very fine sand with coral fragments (Fig. 7), dominated by *Dendrophyllia* spp. in association with *L. pertusa* and *M. oculata*. As in core MD04-2804, also *S. vermiformis*, well-preserved *D. cristagalli* and some *Caryophyllia* spp. fragments are reported in the upper part. The remaining part of the core is represented by a 200-cm-thick horizon of silty clay to clayey silt, with a high amount of *L. pertusa* in alternation with *M. oculata*. *Dendrophyllia* spp. are missing again, while *D. cristagalli*

and *Caryophyllia* spp. are still present in minor quantities. The density of the coral fragments is changing throughout the core. The preservation of the coral fragments is only fair but a well-delineated zone of very badly preserved coral fragments could not be detected. Throughout the succession bioturbations and burrows filled with (soupy) water-saturated clays are observed. Between 116–125 cm and 154–165 cm, an accumulation of smaller coral fragments is noted.

Another core, situated at the south-eastern flank of the same mound cluster as described before and at a water depth of 580 m, is gravity core AT570G. It has a recovery length of 385 cm (Fig. 3). The upper 30 cm are characterized by cold-water coral fragments (dominated by *Dendrophyllia* spp.) embedded in a brownish silty matrix (Fig. 7). Between 0 and 93 cm the brownish silty sediments are grading into grayish silty clays, while the embedded cold-water coral fragments become dominated by the species *L. pertusa* and *M. oculata*. The amount of coral debris is denser at respectively 15–25 cm and 41–80 cm. At 63 cm, a 10 cm large bivalve *A. excavata* was recovered. From 93 cm to 174 cm, cold-water coral fragments embedded in a gray clayey matrix become more and more dissolved (especially between 147 and 174 cm). A remarkable observation is the presence of mud breccia and mud clasts between 174 and 385 cm. From 174 to 231 cm, some coral fragments are still present between the mud breccia and the clay but they disappear completely below this zone.

Gravity core AT534G is retrieved from a mound at the western edge of PDE at a water depth of 550 m (Fig. 3). It has a total length of 395 cm. The presence of large cold-water coral fragments, mainly *L. pertusa* associated with *M. oculata* and big fragments of *D. cristagalli* (up to 3 cm length) in a grayish brown silty matrix are characterizing the uppermost 10 cm of the core (Fig. 7). *Dendrophyllia* spp. (*D. cornucopia* and *D.* sp.) are not present anymore, as observed in AT564G and MD04-2804. Some fragments of *D. alternata* could be identified. Between 10 and 37 cm the silty sediments turn to silty clay. This silty clay is present through the whole core unit until the base, whereas the amount of coral fragments (mainly *L. pertusa*) is decreasing downwards. The bottom part of the core (from 330 cm to bottom) is free of coral fragments. The preservation of the coral fragments throughout the core is rather good.

4.2. Renard Mound Province

4.2.1. Geomorphology

The western edge of Renard Ridge forms a structural high where cold-water corals probably started to build up mound-like structures (Fig. 8). The western part of the ridge has a height of 100 m above the seafloor. The top of the ridge is covered with mound clusters and single mounds occurring in water depths between 550 and 700 m. Single mounds are reaching a height up to 30 m. The mounds are smaller than the mounds reported along the PDE. Cold-water coral patches are present on the sediments flanking the western and south-western sides of the ridge. The total amount of mounds and cold-water coral patches can be estimated at 65. As observed on PDE, the mounds and patches are elongated. A clear E–W oriented moat is present at the north-eastern part of the ridge which shows a slope inclination of 23°.

4.2.2. Seismics

A set of seismic profiles, jointly shown in Fig. 5B, shows the occurrence of many mounded features at the culminations of the low-amplitude acoustic (and structural) basement. The two sides of the profile are mirrored sections of the ridge — the ends of the profile are located north, the central part of the profile south (Fig. 8). The presence of at least two large normal faults can be inferred from the data. A first fault occurs at the northern side of the ridge and dips towards the north. At the surface, the basement crops out. Along the ridge, elevated features are indicating the presence of mound structures. Further southwards, a second normal fault with a large offset again disrupts the seafloor. A large set of diffractions is again interpreted as the presence of mounds on top of the outcropping basement. The height of the mounds reaches several tens of meters.

4.2.3. Video imagery and SSS

The combination of sidescan sonar imagery (MAKAT 75) and ROV video imagery (TVAT 36) made it possible to delineate the different patches and mounds covered with mainly dead cold-water coral fragments, identified as *L. pertusa*, *M. oculata* and some *D. alternata*. It corresponds with facies 3 as described on PDE (Figs. 6 and 8). It should be noted that the corals are more densely branched and form higher frameworks in comparison to PDE, where most of the corals are present at the seafloor as smaller fragments and branches. Anthipatharians, large reddish alcyonaceans, sponges and many crinoids use the dead cold-water coral fragments as substrate. Facies 1, consisting of sandy to silty mud, is draped over whole the ridge and forms the main facies between the mounds and cold-water coral patches (Figs. 6 and 8). As on PDE, this mud layer is colonized by typical soft-bottom communities (spiral anthipatharians, isidiid gorgonians and hexactinellid sponges). Bioturbation and burrows are common.
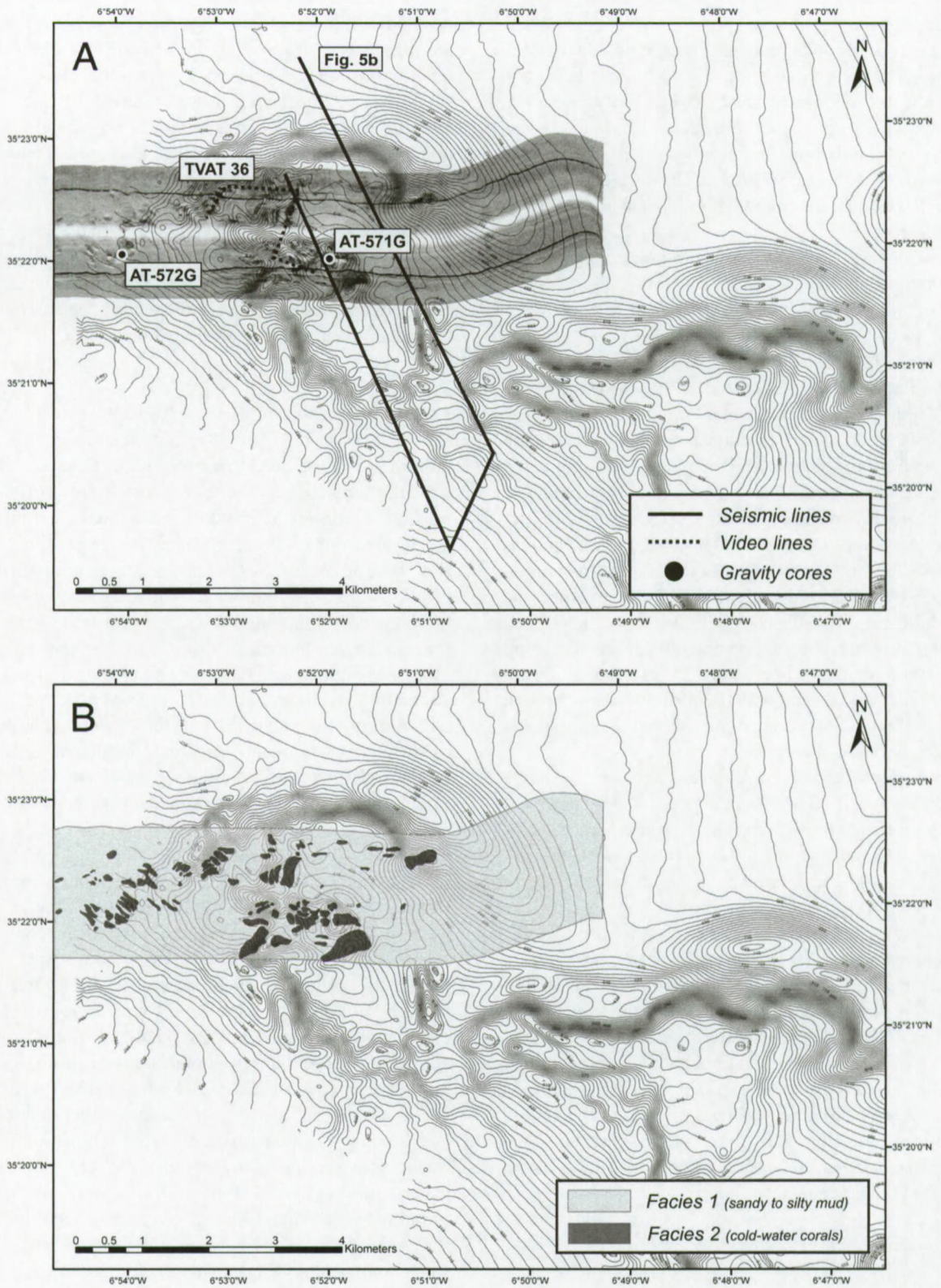
Fig. 8. (A) Bathymetry (contour spacing is 5 m), side scan sonar imagery and location of the seismic profiles, core material and video line in the Renard Mound Province. (B) Interpretation of sidescan sonar imagery (MAKAT 75), representing two distinctive facies.

Some boulders, colonized by benthic epifauna, are present between the mounds.

4.2.4. Coring

Two gravity cores have been collected at the western edge of Renard Ridge, respectively AT571G on top of a small mound on Renard Ridge and AT572G on top of a cold-water coral patch in the sediments flanking Renard Ridge (Fig. 8).

Gravity core AT571G has a recovery length of 581 cm and is localized on top of a small mound at a water depth of 580 m. Coral fragments are present throughout whole the core length but the density of coral fragments changes (Fig. 7). The main coral fragments are identified as *L. pertusa* and *M. oculata*. Less abundant are the species *D. cristagalli*, *D. alternata* and *Caryophyllia* spp. The determined species of the coral fragments are alternating in different zones, whereby in certain units *L. pertusa* seems to dominate, while in other zones *M. oculata* takes the overhand. The matrix in the upper 37 cm consists of brownish sandy silt going over in silty clay becoming more compact towards the bottom. Bioclastic fragments from bivalves, gastropods (including pteropods), echinoids, crinoids, bryozoans, crustaceans and serpulids are present between the coral fragments. Planktonic and benthic foraminifera are common. Badly preserved and heavily dissolved coral fragments are frequently observed between 250 and 300 cm. The colour of the sediments in which the corals are embedded becomes lighter in and especially below this unit.

Core AT572G, with a recovery length of 333 cm, is acquired on top of a cold-water coral patch on the flank of Renard Ridge at a water depth of 712 m. Coral fragments are present in the upper 70 cm but their amount is decreasing by going downwards (Fig. 7). The upper brownish sandy silt (0–70 cm) grades into grayish silty clay to dark clay at the bottom. The most abundant coral species are identified as *M. oculata* and *L. pertusa*. The coral fragments in the upper zone are rather well-preserved.

4.3. Vernadsky Mound Province

4.3.1. Geomorphology

The northern edge of Vernadsky Ridge is densely covered by small mound-like structures while mound-like patches are found on the sediments flanking the ridge (Fig. 9). The mounds on top of the ridge reach heights up to 50 m and widths up to 250 m. The mounds and mound patches are elongated and seem to be lined up, following the structural height. They occur in water depths between 700 and 500 m. The south-western flank

of the Vernadsky Ridge has a gentler slope than the north-eastern flank, reaching maximum slope values of about 23°. A small NW–SE directed moat is present at the south-western flank, while deeper scoured moat structures are observed at the other side of the ridge. The total amount of mounds and cold-water coral patches on this northern edge of the Vernadsky Ridge can be estimated at 130.

The central part of the Vernadsky Ridge consists also of a topographic height, providing substrate for the settlement of benthic organisms. At the edges, mound-like structures are recognized, which can be interpreted as small NW–SE orientated mound patches. They have a similar acoustic signature on seismics and sidescan sonar imagery as the mound-like structures at the northern edge of Vernadsky Ridge (Fig. 9).

4.3.2. Seismics

Seismic profiles over the central part of the Vernadsky Ridge give insight into its structure. Fig. 10A shows the outcropping and eroded low-amplitude acoustic basement being covered by younger sequences. Correlation of the seismic data around the ridge culmination indicated that a large normal fault had been active during the past. This has created an offset of about 400 m at the ridge crest. Northwards of the large normal fault, smaller faults are found, which could either be antithetics from the main fault, or a consequence of sediment removal in the subsurface due to mud volcano activity.

In the vicinity of this structurally active place, acoustic diffractions are observed (Fig. 10B). Some diffractions clearly stand out above the seafloor and thus can be interpreted as mound structures. The seismic data retrieved at the northern part of the Vernadsky Ridge are densely populated by acoustic diffractions (Fig. 10C). Structural basement highs are separating small intraridge basins. These are likely to be fault-controlled. Nearly the whole seafloor reflection is obscured by diffractions. The diffraction height runs up to 50 m and their width up to 200 m. These diffractions are again interpreted as mound diffractions, indicating that nearly the whole seabed is covered with mound build-ups and mound patches.

4.3.3. SSS

Sidescan sonar imagery (MAKAT 107–108) revealed similar acoustic signatures as observed on Renard Ridge and PDE (Fig. 9). The mound structures and mound patches are characterized by a high backscatter strength and a clear acoustic shadow, and can be interpreted as cold-water coral carbonate mounds and/or cold-water coral patches (cf. facies 2 on PDE and Renard Ridge). In between the mound patches, a smooth
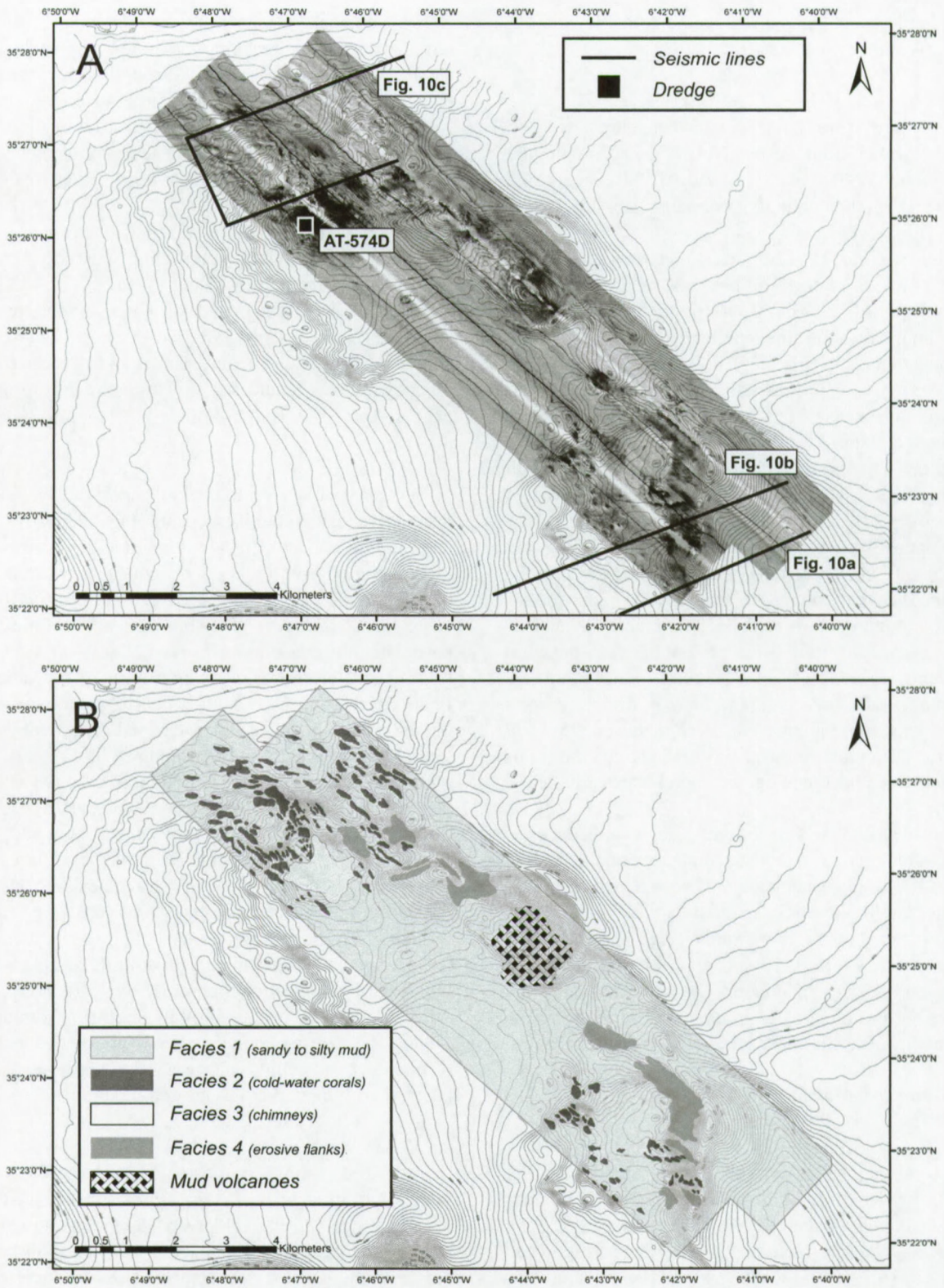
Fig. 9. (A) Bathymetry (contour spacing is 5 m), side scan sonar imagery and location of the seismic profiles and core material in the Vernadsky Mound Province. (B) Interpretation of sidescan sonar imagery (MAKAT 107-108), representing four distinctive facies.
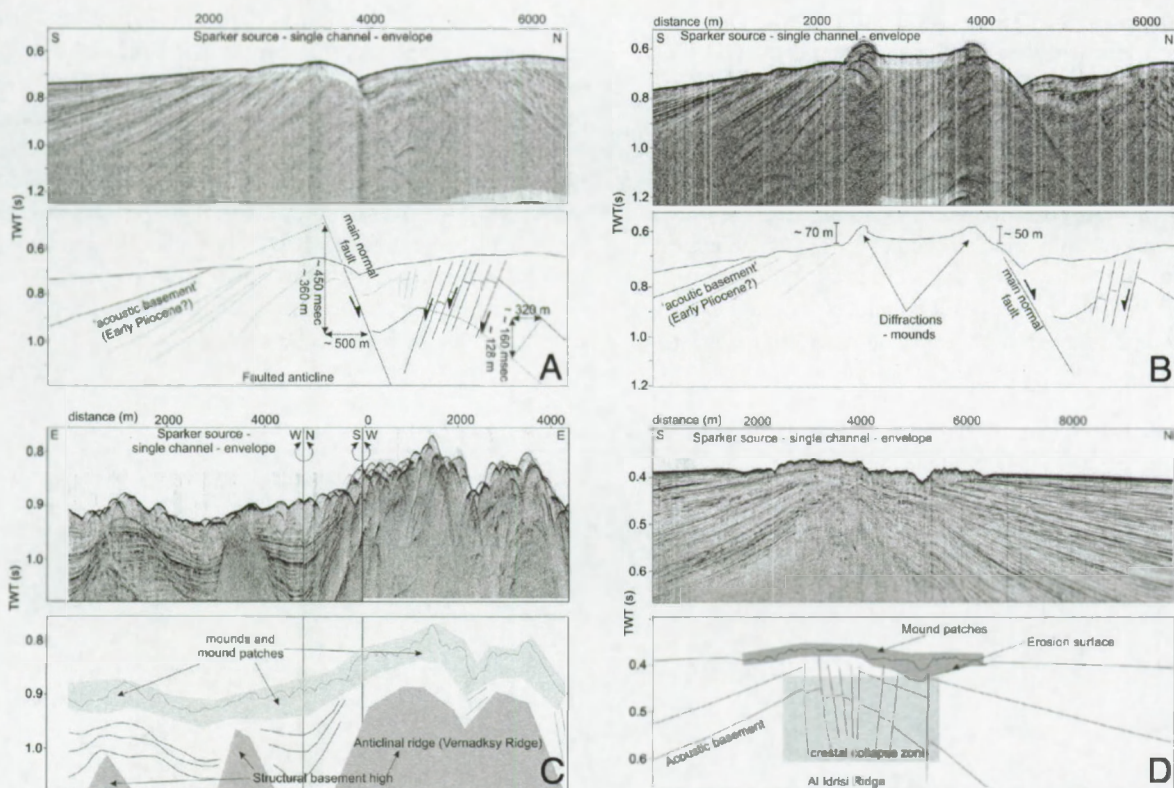
Fig. 10. (A) Sparker seismic profile over the central part of Vernadsky Ridge (location: see Fig. 9), showing the outcropping acoustic basement as well as a normal fault and a set of smaller faults giving insight into the structure of the ridge. (B) Sparker seismic profile over the central part of Vernadsky Ridge (location: see Fig. 9), representing a set of diffractions on top of the basement, which can be interpreted as mound structures. (C) Set of seismic profiles over the northern part of Vernadsky Ridge (location: see Fig. 9), showing the dense population of different mounds and mound patches and the structural basement highs separated by small intraridge basins. (D) Sparker seismic profile in Al Idrisi Mound Province (location: see Fig. 11), representing the Al Idrisi Ridge and a set of small mound-like features on the sediments burying the ridge.

surface with low backscatter intensity is observed, corresponding with sandy to silty clays (facies 1). Kidd mud volcano can be clearly delineated (Fig. 9). Another area with high backscatter intensity is located on top of Vernadsky Ridge. Ground truthing using a dredge (station AT574D), revealed that this area with high backscatter corresponds with the presence of carbonate crusts and chimneys. Serpulids, bivalves (*S. gussoni*), bryozoans, dendrophyllid corals, etc. use the chimneys and crusts as substrate to settle on (e.g. Fig. 6B: *D. alternata* attached on chimney). Also the steep north-eastern flanks with their associated NW–SE orientated scoured moats, are characterized by higher backscatter strengths.

4.4. Al Idrisi Mound Province

4.4.1. Geomorphology and SSS

East of mud volcano Al Idrisi, mound patches on a much smaller scale are observed (Fig. 11). They appear on multibeam bathymetry and sidescan sonar imagery as small E–W aligned mound-like features, not higher than 10 m and in rather shallow water depths (350 to 200 m).

Ground truthing by Hammon grabs (B05-1214 and B05-1215) revealed that the structures are covered with cold-water coral fragments, dominated nearly exclusively by *L. pertusa* and *M. oculata*, embedded in brownish oxidized silty clays, which grade into grayish and stiff silty clays.

4.4.2. Seismics

Below the Al Idrisi mud volcano, an anticline is buried below the sedimentary sequences. The crest of the low-amplitude basement, culminating at less than 100 m below the seafloor, is highly fractured and has collapsed in response to sediment withdrawal by mud volcano activity. Several bright spots indicate the presence of gas in the sediments at shallow positions. Mound-like features with a low-amplitude and chaotic internal facies are topping the anticline culmination area at the seafloor. Below the chaotic facies, an erosive surface is present (Fig. 10D). The chaotic mounded features can be interpreted as small coral patches, what is confirmed by sampling. The erosive surface is interpreted as the base of the mounds.
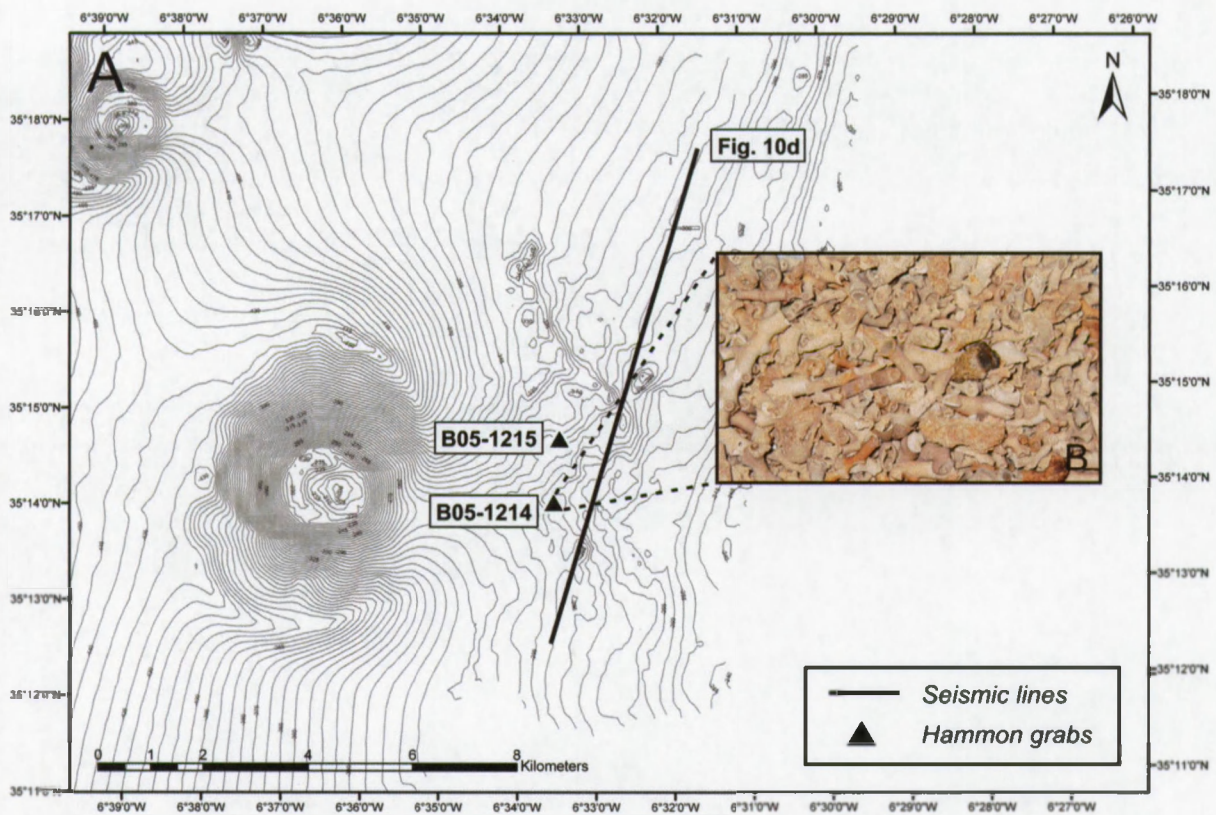

Fig. 11. Bathymetry (contour spacing is 5 m) and location of seismic profile and core material in the Al Idrisi Mound Province. Inset presents the dead cold-water coral fragments (mainly *Lophelia pertusa* and *Madrepora oculata*), recovered from the surface.

5. Discussion

5.1. Initiation of cold-water coral growth

As shown before seismic data reveal a close association between the anticlinal ridges and mound structures. In El Arraiche mud volcano province, cold-water coral mounds show to be closely related to the Renard, Vernadsky and Al Idrisi Ridges. While Renard and Vernadsky Ridges show nowadays outcropping basement, Al Idrisi Ridge is entirely buried, with indications of gas occurrence in the sediments above the ridge. Several explanations for this co-occurrence between mounds and ridges seem to be possible.

The erosive basement surface could have created a prime hard substrate for coral larvae to settle on. The more, by forming seafloor elevations these basement ridges can create enhanced currents and thus a higher food particle flux which forms the base for a highly active planktonic food chain, which is often regarded as an important factor in the process of cold-water coral growth: "the highest on the elevation, the more food" (Mortensen, 2000; Freiwald, 2002; De Mol et al., 2002). Moreover, the effect of tidal waves, as reported on PDE by Mienis et al. (2005), may have enhanced seabed food supply at an initial stage. The external input of nutrients driving cold-water coral growth is not the only factor controlling mound build-up. Sediment input is another important factor for mound growth, whereby cold-water coral colonies on elevated structures are baffling transported sediments to build up mounds (Foubert et al., 2005a; Huvenne et al., 2005; Wheeler et al., 2005a).

As Al Idrisi Ridge does not show a clear topographic elevation that would have favoured cold-water coral growth as explained in scenario 1, the main reason for initial cold-water coral growth might have been the presence of a suitable settling ground. Because Al Idrisi Ridge is clearly buried, with the cold-water coral build-ups not related to the basement, hardgrounds may have been an initial substrate. Hardgrounds could have been created by gas or fluid seepage cementing partly the seafloor.

5.2. Extinction of cold-water corals

Another phenomenon is the wide-spread extinction of cold-water corals on the Moroccan margin, Gulf of Cadiz. So far, no extensive live frame-work building corals could be observed. In contrast, healthy living coral colonies are observed on the Norwegian margins up to the north (e.g. Freiwald et al., 1997, 2002; Hovland and Mortensen, 1999; Fosså et al., 2005), in Rockall Trough and on Rockall Bank (e.g. Akhmetzhanov et al., 2003; Kenyon et al., 2003; van Weering et al., 2003), on Porcupine Bank (e.g. Wheeler et al., 2005b), in Porcupine Seabight (e.g. Foubert et al., 2005a; Huvenne et al., 2005; Wheeler et al., 2005a), and south of the Galicia Bank (Duineveld et al., 2004). The cold-water corals and their associated ecosystems in the Mediterranean Sea are already in a stage of retirement since the onset of the Holocene (Taviani et al., 2005). The coral fragments appearing at the surface in the southern part of the Gulf of Cadiz are rather old, reaching ages older than 300 ka (~ MIS 9) at the south-eastern edge of Pen Duick Escarpment.

However, the presence of clear mound structures built up by cold-water corals evidences that in the recent geological past, environmental and oceanographic conditions were suitable for prolific cold-water coral growth. Before the onset of the recent interglacial conditions, the Gulf of Cadiz was much more influenced by a North Atlantic regime (Vanney, 2002), resulting in a descent of the polar front (until Portugal), decrease in temperatures, lowering of the general sea level (100–120 m), influence of icebergs and their associated ice rafted debris from the north (even up to south of the Gulf of Cadiz) (Heinrich events, Lebreiro et al., 1996). Llave et al. (2006) and Voelker et al. (2006) suggested that the lower Mediterranean branch with a significantly higher salinity and density (Schönfeld, 1997; Zahn et al., 1997; Cacho et al., 2000), enhanced during climatic coolings (glacials/stadials). This lower branch of intensive and deeper MOW (Thomson et al., 1999; Schönfeld and Zahn, 2000; Rogerson, 2002) results in a stronger interaction with the seafloor and higher current velocities (Llave et al., 2006). The enhancement of the lower core of MOW (mainly the Principal and Southern Branches) during previous glacial conditions can have enhanced the formation of meddies (carriers of cells of MOW with their full biological content), which have probably strongly influenced the Moroccan Margin. Several molluscan and foraminiferal species co-occurring with the cold-water corals, as observed in the Kasten core MD04-2804 and the surface boxcores, belong to a Mediterranean fauna, indicating an important influence of MOW in the past. The bivalve species L. marioni and S. gussoni are preferably occurring in areas with a clear influence of MOW. Molluscan species such as the bivalves Microgloma tumidula and Yoldiella wareni or the gastropod species Drilliola emendata and Alvania electa are mainly occurring in areas under the influence of MOW. Moreover, the study of an off-mound core (Vanneste, 2005) between Renard Ridge and Vernadsky Ridge, showed the presence of coarser and more reworked material during colder

periods, indicating higher currents which can be linked with the input of more vigorous meddies and the interaction of these meddies with NACW. These meddies and the interaction of these meddies with NACW, are responsible for a fresh supply and a higher flux of nutrients, which is positive for prolific cold-water coral growth (Freiwald et al., 2002).

Nowadays, all the cold-water coral fragments and mounds are draped by a fine layer of silty mud. The off-mound core between Renard Ridge and Vernadsky Ridge is characterized by finer sediments since the onset of the Holocene and a rather high sedimentation rate (18.5 cm/ka) could be calculated for this period (Foubert et al., 2005b). The deposition of finer sediments since the onset of the Holocene evidences that currents are nowadays probably weaker than during glacial times. It can be postulated that a major change in oceanographic conditions since the onset of the Holocene, together with a decrease in the food particle flux and higher sedimentation rates, are responsible for the dead of most of the cold-water coral colonies. Moreover, large-scale changes in oceanography may have an effect on small-scaled tidal current systems, which might explain the relatively weak tidal currents nowadays reported by Mienis et al. (2005) in the southern Gulf of Cadiz along the Moroccan margin.

It is worth to mention that the environmental and oceanographic situation described for colder periods on the Moroccan margin, can be nowadays observed in well-delineated areas of Porcupine Seabight, where cold-water corals are still alive (De Mol et al., 2002; Foubert et al., 2005a; Huvenne et al., 2005; Wheeler et al., 2005a). Current regimes in Porcupine Seabight and along the Moroccan margin seem to be opposite to each other during glacial and interglacial periods (at least for the most recent ones).

5.3. Cold-water coral dissolution and carbonate precipitation

The growth of cold-water corals and the origin of carbonate mounds was a heavily debated subject during the last decade. Different theories were invoked concerning cold-water coral growth and the development of carbonate (mud) mounds built up by cold-water corals. Cold-water coral reefs on the Norwegian margins and carbonate mounds in Porcupine Seabight were supposed to be related with light hydrocarbon seepage (Hovland, 1990; Hovland et al., 1998; Henriet et al., 1998, 2002). Hovland and Mortensen (1999) suggested a new hydraulic theory relying on the assumption that there is a stable local input of nutrients through the seabed at or

near the location where the reefs are found. Recent research learns that an external flux of nutrients (with optima at boundaries between different water masses) and an active planktonic food chain, based on a higher primary productivity in surface waters and subsequent food transport to the sea floor is the main factor controlling cold-water coral growth (Duineveld et al., 2004; Roberts et al., 2006) and so mound build-up.

In the Gulf of Cadiz, on the Moroccan margin, mounds built up by cold-water corals occur in an area characterized by the presence of gas seepage and subsurface fluid flow. However it should be noted that no direct relationship could be found between cold-water coral growth and fluid or gas seepage. On the other hand, a positive relationship between focused fluid flow and carbonate mound distribution on the south-eastern edge of PDE is observed. This is evidenced by a rather high sulphate gradient, with a methane oxidation front at 3 m below the surface measured on core MD04-2804 (Fig. 7). Three main reasons can be invoked to explain a higher internal methane flux towards the mounds at the south-eastern edge of the ridge. First of all, a mounded feature on a scarp or a hill on the seabed subjected to rather strong peak currents will develop zones of high pressure at the lows of the slopes and low pressure areas at or near the summit (Depreiter et al., 2005a). This pressure effect would create a fluid migration from deeper layers to the top of the structure. This effect will be enhanced at the edges of a ridge, where higher pressure gradients are created. So, in this view, the pumping of fluids in carbonate mound systems is driven by external currents. Another reason is the association of the mounds with the ridges, and thus with the faults co-occurring with the ridges. Indeed, as observed on the seismics, the ridges are partly fault-controlled. The faults can be preferable pathways for fluids, canalizing the fluids towards the mounds on top of the ridges. A third reason can be the influence by the recent eruptive activity of the neighbouring Gemini West mud volcano, focusing the extrusion of fluids towards the mud volcano crater. Van Rensbergen et al. (2005b) has shown that Gemini West mud volcano is one of the most active mud volcanoes in the region, as it lacks a hemipelagic sediment drape of fine mud (as observed over most of the mud volcanoes, mounds, carbonate slabs and covering the seafloor in between the mounds) and it features a shallow sulphate reduction zone (as observed in the Kasten core MD04-2804). The presence of mud breccia and mud clasts in gravity core AT570G (at the south-eastern flanc of a mound at the south-eastern edge of PDE), confirms the influence of the recent activity of mud volcanoes on this south-

eastern edge. The mud breccia and clasts recovered in this core are similar to the mud breccia and clasts recovered from cores on the neighbouring mud volcanoes (Van Rensbergen et al., 2005b).

The cold-water coral fragments embedded in the sediments, as observed in well-delineated parts of the studied cores, are heavily dissolved. This phenomenon is clearly observed in core MD04-2804, whereby the cold-water coral fragments are in a rather bad stage of preservation due to dissolution just above and at the front of the recent zone of anaerobic oxidation of methane. This can be explained by a pure diagenetic process (resulting from the fluxes in pore water transport). Oxidation of organic matter alters the pH and the alkalinity of interstitial water and thus the diagenesis of carbonate minerals (Tribble, 1993). In general, model results indicate that mineral saturation states decrease during oxic respiration (from release of carbonic acid) and increase during sulphate reduction (from increase in alkalinity) (Jørgensen, 1983; Reeburg, 1983). The C:N ratio of the organic matter and the degree to which sulphide precipitates as a mineral phase also affect the saturation state with respect to carbonate minerals. Tribble (1993) suggested that the aragonite saturation state initially drops but becomes oversaturated during extensive sulphate reduction. A pattern of initial aragonite dissolution followed by carbonate precipitation as a function of the extent of sulphate reduction can occur within reefs in a manner similar to that described for sediments (Tribble, 1993). Throughout this process the interstitial waters keep close to equilibrium compositions with aragonite. This buffers the pH of the waters. Because interstitial water in the reef has a short residence time, the observed equilibration suggests rapid kinetics. A similar process is noted in the mounds in Porcupine Seabight SW of Ireland, where no obvious recent methane fluxes or seepage is noted (Foubert et al., 2007). However, when a flux of methane reaches the aerobic zone, aerobic methane oxidation takes the overhand and drops the pH drastically, stimulating a net dissolution of aragonite. During coupled anaerobic methane oxidation and sulphate reduction, HCO_3^- and HS^- are released, increasing the pH and so stimulating a system that becomes oversaturated in respect to aragonite, resulting in carbonate precipitation. Precipitation of sulphides as FeS strongly affects the aragonite saturation state. So, focused and alternating fluxes of methane in time can stimulate dissolution of cold-water corals in the aerobic zone and precipitation of carbonate in the anaerobic zone. However, no distinctive zones of explicit carbonate precipitation are noted in the studied cores, while extensive horizons of coral dissolution are clearly present. More focused geochemical research on the carbonate-rich fractions and the pore fluids have to be carried out in order to understand the processes behind carbonate dissolution and precipitation and the possible effect of alternating fluxes of methane in time. Despite the fact that the exact mechanisms are not yet completely understood, it can be assumed that mounds, built up by the interaction between sediment dynamics and coral framework, can be affected by the dynamics of internally controlled pore water fluxes.

While cold-water coral growth has obviously nothing to do with seepage, the mounds they create by the interaction between sediment dynamics and coral framework can be affected by internally controlled fluid fluxes.

5.4. A "three-phase" model for the development of carbonate mounds

By combining the observations, a three-phase mound development model can be proposed for the mounds on the Moroccan margin:

(1) In a first stage the cold-water corals start to colonize a suitable substrate under specific environmental and oceanographic conditions, positive for cold-water coral growth. The most important factor is the presence of a planktonic food chain, based on a high primary production and an enhanced food particle flux towards the seafloor. Elevated positions (e.g. Renard and Vernadsky Ridges, Pen Duick Escarpment), creating enhanced currents and so a higher nutrient flux, are preferable. Tidal currents may have at this stage an additional positive effect on the availability of planktonic food particles for cold-water corals.

(2) During a second phase, the interaction between sediments, currents and cold-water corals plays an important role. As described in Porcupine Seabight, sedimentation and hydrodynamics regulated by oceanographic and climatic changes are crucial in mound development (De Mol et al., 2005; Dorschel et al., 2005; Foubert et al., 2005a; Frank et al., 2005; Huvenne et al., 2005; Rüggeberg et al., 2005; Wheeler et al., 2005a). The initial cold-water coral frameworks start to baffle sediments under certain current regimes, a crucial phase to build up mounds. In this phase, coral colony development and sediment baffling proceed in harmony. When sedimentation prevails, cold-water corals can be buried. On the contrary, when no sediments are available the polyps can be kept sediment-free and cold-water corals can build healthy reef frameworks (cold-water coral reefs) up to several meters high, as

observed on the Norwegian margins (Freiwald et al., 2002).

(3) In a last phase, when the cold-water corals are embedded in a sediment-rich matrix and when an initial mound structure is already built, fluid seepage and fluxes in pore water transport affects the built structures by diagenetic processes, resulting in for example cold-water coral dissolution (as observed on the mounds on Pen Duick Escarpment and Renard Ridge). It should be mentioned that the last phase can be concurrent with phase 2. A continuous interaction between the different phases is responsible for the final character of the mound structures.

6. Conclusion

The mound and mound patches in El Arraiche mud volcano field can be divided in four well-delineated provinces: Pen Duick Escarpment (Pen Duick Mound Province), western edge of Renard Ridge (Renard Mound Province), Vernadsky Ridge (Vernadsky Mound Province) and Al Idrisi Ridge (Al Idrisi Mound Province). The mounds are highest and most developed on PDE, while the Al Idrisi patches are just characterized by small elevated structures (up to 3 m). The Renard Ridge mounds and Vernadsky Ridge mounds have many similarities, whereby most of the mounds are observed on top of the ridges and fading out mound patches are colonizing the sediments burying the flanks of the ridges. The seismic data confirmed a close association between the anticlinal ridges at or below the seafloor, and the mound structures built up by cold-water corals on the seafloor.

The gravity cores, boxcores and video imagery display a high number of reef-forming cold-water scleractinians like *L. pertusa*, *M. oculata*, *Dendrophyllia* spp., *D. cristagalli* and *Caryophyllia* spp. with numerous faunal associations formerly inhabiting the econiches provided by the coral framework. Temporal and spatial variations are observed in the dominance of the different cold-water coral species. Under present interglacial environmental and oceanographic conditions, no healthy live coral reefs could be observed. However, environmental and oceanographic conditions during colder periods (glacials/stadial) where probably more favourable for cold-water coral growth. Meddies, anticyclonic cells of MOW, and the interaction of these meddies with NACW, could have played hereby a major role.

Fluid seepage can affect the built mound structures by diagenetic processes, resulting in cold-water coral dissolution. However, no obvious relation between cold-water coral growth and seepage is observed.

A three-phase model for the mound development on the Moroccan margin can be proposed. During a first phase the cold-water corals start to colonize suitable substrates under specific environmental and oceanographic conditions positive for cold-water coral growth. In a second stage, the cold-water coral frameworks start to baffle sediments regulated by environmental changes and build up cold-water coral mounds. During the last phase, fluid seepage affects the initial structures by diagenetic processes. The continuous interaction between the last two phases, which may be concurrent, is responsible for the final character of the mounds.

References

Akhmetzhanov, A.M., Kenyon, N.H., Ivanov, M.K., Wheeler, A.J., Shashkin, P.V., van Weering, T.C.E., 2003. Giant carbonate mounds and current-swept seafloors on the slope of the southern Rockall Trough. In: Mienert, J., Weaver, P.P.E. (Eds.), European Margin Sediment Dynamics: Side-Scan Sonar and Seismic Images. Springer-Verlag, Heidelberg, pp. 203–209.

Ambar, I., Serra, N., Brogueira, M.J., Cabecadas, G., Abrantes, F., Freitas, P., Goncalves, C., Gonzalez, N., 2002. Physical, chemical and sedimentological aspects of the Mediterranean outflow off Iberia. Deep-Sea Res. Pt. II 49 (19), 4163–4177.

Baraza, J., Ercilla, G., 1996. Gas-charged sediments and large pockmark-like features on the Gulf of Cadiz slope (SW Spain). Mar. Pet. Geol. 13 (2), 253–261.

Baringer, M.O., 1993. Mixing and Dynamics of the Mediterranean Outflow. Mass. Institute of Technology/Woods Hole Oceanographic Institute Joint Program, Mass. 244 pp.

Baringer, M.O.N., Price, J.F., 1999. A review of the physical oceanography of the Mediterranean outflow. Mar. Geol. 155 (1–2), 63–82.

Berastegui, X., Banks, C.J., Puig, C., Taberner, C., Waltham, D., Fernandez, M., 1998. Lateral diapiric emplacement of Triassic evaporites at the southern margin of the Guadalquivir Basin, Spain. In: Mascle, A. (Ed.), Cenozoic Foreland Basins of Western Europe. Geol. Soc. Spec. Pub., pp. 49–68.

Bower, A.S., Armi, L., Ambar, I., 1995. Direct evidence of meddy formation off the southwestern coast of Portugal. Deep-Sea Res. Pt. 42 (9), 1621–1630.

Bower, A.S., Armi, L., Ambar, I., 1997. Lagrangian observations of meddy formation during a Mediterranean undercurrent seeding experiment. J. Phys. Oceanogr. 27, 2545–2575.

Cacho, I., Grimalt, J.O., Sierro, F.J., Shackleton, N., Canals, M., 2000. Evidence for enhanced Mediterranean thermohaline circulation during rapid climatic coolings. Earth Planet. Sci. Lett. 183 (3–4), 417–429.

Caralp, M.H., 1988. Late Glacial to Recent deep-sea benthic foraminifera from the Northeastern Atlantic (Cadiz Gulf) and Western Mediterranean (Alboran Sea): paleooceanographic results. Mar. Micropaleontol. 13, 265–289.

Carton, X., Cherubin, L., Paillet, J., Morel, Y., Serpette, A., Le Cann, B., 2002. Meddy coupling with a deep cyclone in the Gulf of Cadiz. J. Mar. Syst. 32 (1–3), 13–42.

De Mol, B., Van Rensbergen, P., Pillen, S., Van Herreweghe, K., Van Rooij, D., McDonnell, A., Huvenne, V., Ivanov, M., Swennen, R., Henriet, J.P., 2002. Large deep-water coral banks in the Porcupine Basin, southwest of Ireland. Mar. Geol. 188 (1–2), 193–231.

De Mol, B., Henriet, J.P., Canals, M., 2005. Development of coral banks in Porcupine Seabight: do they have Mediterranean ancestors? In: Freiwald, A., Roberts, J.M. (Eds.), Cold-Water Corals and Ecosystems. Springer-Verlag, Berlin, pp. 515–533.

Depreiter, D., Foubert, A., Henriet, J.P., 2005a. Geofluid pumping in carbonate mound systems: a factor for growth and stabilisation? Geosphere–Biosphere Coupling Processes: The TTR Interdisciplinary Approach Towards Studies of the European and North African Margins. IOC UNESCO Workshop Report 197, pp. 16.

Depreiter, D., Poort, J., Van Rensbergen, P., Henriet, J.P., 2005b. Geophysical evidence of gas hydrates in shallow submarine mud volcanoes on the Moroccan margin. J. Geophys. Res. 110, B10103.

Dorschel, B., Hebbeln, D., Ruggeberg, A., Dullo, W.C., Freiwald, A., 2005. Growth and erosion of a cold-water coral covered carbonate mound in the Northeast Atlantic during the Late Pleistocene and Holocene. Earth Planet. Sci. Lett. 233 (1–2), 33–44.

Duineveld, G.C.A., Lavaleye, M.S.S., Berghuis, E.M., 2004. Particle flux and food supply to a seamount cold-water coral community (Galicia Bank, NW Spain). Mar. Ecol-Prog. Ser. 277, 13–23.

Expedition Scientists, 2005. Modern carbonate mounds: porcupine drilling. IODP Prel. Rep. 307. doi:10.2204/iodp.pr.307.2005.

Flinch, J., 1993. Tectonic Evolution of the Gibraltar Arc. Rice University, Houston, Texas. 381 pp.

Flinch, J., 1996. Accretion and extensional collapse of the external Western Rif (northern Morocco). In: Ziegler, P.A., Horvath, F. (Eds.), Peri-Tethys Memoir 2: Structure and Prospects of Alpine Basins and Forelands. Mem. Mus. Natl. d'hist. Nat., Paris, pp. 61–86.

Fosså, J.H., Lindberg, B., Christensen, O., Lundälv, T., Svellingen, I., Mortensen, P.B., Alvsvåg, J., 2005. Mapping of Lophelia reefs in Norway: experiences and survey methods. In: Freiwald, A., Roberts, J.M. (Eds.), Cold-Water Corals and Ecosystems. Springer-Verlag, Berlin, pp. 359–391.

Foubert, A., Beck, T., Wheeler, A.J., Opderbecke, J., Grehan, A., Klages, M., Thiede, J., Henriet, J.P., Polarstern ARK-XIX/3a Party, 2005a. New view of the Belgica Mounds, Porcupine Seabight, NE Atlantic: preliminary results from the Polarstern ARK-XIX/3a ROV cruise. In: Freiwald, A., Roberts, J.M. (Eds.), Cold-Water Corals and Ecosystems. Springer-Verlag, Berlin, pp. 403–415.

Foubert, A., Maignien, L., Beck, T., Depreiter, D., Blamart, D., Henriet, J.P., 2005b. Pen Duick Escarpment on the Moroccan margin: a new mound lab? Geosphere–Biosphere Coupling Processes: The TTR Interdisciplinary Approach Towards Studies of the European and North African Margins. IOC UNESCO Workshop Report 197, pp. 17.

Foubert, A., Van Rooij, D., Blamart, D., Henriet, J.P., 2007. X-ray imagery and physical core logging as a proxy of the content of sediment cores in cold-water coral mound provinces: a case study from Porcupine Seabight, SW of Ireland. Int. J. Earth Sci. 96, 141–158.

Frank, N., Lutringer, A., Paterne, M., Blamart, D., Henriet, J.-P., Van Rooij, D., van Weering, T.C.E., 2005. Deep-water corals of the northeastern Atlantic margin: carbonate mound evolution and upper intermediate water ventilation during the upper Holocene. In: Freiwald, A., Roberts, J.M (Eds.), Cold-Water Corals and Ecosystems. Springer-Verlag, Berlin, pp. 113–133.

Freiwald, A., 2002. Reef-forming cold-water corals. In: Wefer, G., Billett, D., Hebbeln, D., Jørgensen, B.B., Schlüter, M., Van Weering, T. (Eds.), Ocean Margin Systems. Springer-Verlag, Berlin Heidelberg, pp. 365–385.

Freiwald, A., Henrich, R., Patzold, J., 1997. Anatomy of a deep-water coral reef mound from Stjernsund West Finnmark, northern Norway. In: James, N.P., Clarke, J.A.D. (Eds.), Cool-Water Carbonates. SEPM Spec. Pub., p. 441–162.

Freiwald, A., Hühnerbach, V., Lindberg, B., Wilson, J.B., Campbell, J., 2002. The Sula Reef Complex, Norwegian shelf. Facies 47, 179–200.

Garcia-Lafuente, J., Delgado, J., Criado-Aldeanueva, F., Bruno, M., del Rio, J., Miguel Vargas, J., 2006. Water mass circulation on the continental shelf of the Gulf of Cadiz. Deep-Sea Res. Pt. II 53 (11–13), 1182–1197.

Gardner, J.M., 2001. Mud volcanoes revealed and sampled on the Western Moroccan continental margin. Geophys. Res. Lett. 28 (2), 339–342.

Gutscher, M.A., Malod, J., Rehault, J.P., Contrucci, I., Klingelhoefer, F., Mendes-Victor, L., Spakman, W., 2002. Evidence for active subduction beneath Gibraltar. Geology 30, 1071–1074.

Henriet, J.P., Guidard, S., ODP "Proposal 573" Team, 2002. Carbonate mounds as a possible example for microbial activity in geological processes. In: Wefer, G., Billett, D., Jørgensen, B.B., Schlüter, M., van Weering, T. (Eds.), Ocean Margin Systems. Springer-Verlag, Berlin, pp. 439–455.

Henriet, J.P., De Mol, B., Pillen, S., Vanneste, M., Van Rooij, D., Versteeg, W., Croker, P.F., Shannon, P.M., Unnithan, V., Bouriak, S., Chachkine, P., Porcupine-Belgica 97 Shipboard Party, 1998. Gas hydrate crystals may help build reefs. Nature 391 (6668), 648–649.

Hernandez-Molina, F.J., Llave, E., Somoza, L., Fernandez, M., Maestro, A., Leon, R., Medialdea, T., Barnolas, A., Garcia, M., Diaz del Rio, V., Fernandez-Salas, L.M., Gardner, J., 2003. Looking for clues to palaeoceanographic imprints: a diagnosis of the Gulf of Cadiz contourite depositional systems. Geology 31 (1), 19–22.

Hovland, M., 1990. Do carbonate reefs form due to fluid seepage? Terra Nova 2, 8–18.

Hovland, M., Mortensen, P.B., 1999. Norske korallrev og prosesser i havbunnen (Norwegian coral reefs and seabed processes). John Grieg, Bergen. 167 pp.

Hovland, M., Mortensen, P.B., Brattegard, T., Strass, P., Rokoengen, K., 1998. Ahermatypic coral banks off Mid-Norway: evidence for a link with seepage of light hydrocarbons. Palaios 13 (2), 189–200.

Huvenne, V.A.I., Blondel, P., Henriet, J.P., 2002. Textural analyses of sidescan sonar imagery from two mound provinces in the Porcupine Seabight. Mar. Geol. 189 (3–4), 323–341.

Huvenne, V.A.I., Beyer, A., de Haas, H., Dekindt, K., Henriet, J.-P., Kozachenko, M., Olu-Le Roy, K., Wheeler, A.J., TOBI/Pelagia, CARACOLE cruise participants, 2005. The seabed appearance of different coral bank provinces in the Porcupine Seabight, NE Atlantic: results from sidescan sonar and ROV seabed mapping. In: Freiwald, A., Roberts, J.M. (Eds.), Cold-Water Corals and Ecosystems. Springer-Verlag, Berlin, pp. 535–569.

Jørgensen, B.B., 1983. Processes at the sediment–water interface. In: Bolin, B., Cook, R.B. (Eds.), The Major Biogeochemical Cycles and Their Interactions. J. Wiley and Sons, pp. 477–509.

Kenyon, N., Ivanov, M., Akhmetzanov, A., Akhmanov, G., 2001. Interdisciplinary Geoscience Research on the North East Atlantic Margin. IOC UNESCO Tech. Ser. 76.

Kenyon, N.H., Belderson, R.H., 1973. Bed forms of the Mediterranean undercurrent observed with side-scan sonar. Sediment. Geol. 9, 77–79.

Kenyon, N.H., Ivanov, M.K., Akhmetzhanov, A.M., 1998. Cold-Water Carbonate Mounds and Sediment Transport on the Northeast Atlantic Margin. IOC UNESCO Tech. Ser. 52.

Kenyon, N.H., Akhmetzanov, A.M., Wheeler, A.J., van Weering, T.C.E., de Haas, H., Ivanov, M.K., 2003. Giant carbonate mud mounds in the southern Rockall Trough. Mar. Geol. 195, 5–30.

Lebreiro, S.M., Moreno, J.C., McCave, I.N., Weaver, P.P.E., 1996. Evidence for Heinrich layers off Portugal (Tore Seamount: 39°N, 12°W). Mar. Geol. 131 (1–2), 47–56.

Llave, E., Schönfeld, J., Hernandez-Molina, F.J., Mulder, T., Somoza, L., Diaz del Rio, V., Sanchez-Almazo, I., 2006. High-resolution stratigraphy of the Mediterranean outflow contourite system in the Gulf of Cadiz during the late Pleistocene: the impact of Heinrich events. Mar. Geol. 227 (3–4), 241–262.

López Correa, M., Freiwald, A., Hall-Spencer, J., Taviani, M., 2005. Distribution and habitats of Acesta excavata (Bivalvia: Limidae) with new data on its shell ultrastructure. In: Freiwald, A., Roberts, J.M. (Eds.), Cold-Water Corals and Ecosystems. Springer-Verlag, Berlin, pp. 173–205.

Maestro, A., Somoza, L., Medialdea, T., Talbot, C.J., Lowrie, A., Vazquez, J.T., Diaz-del-Rio, V., 2003. Large-scale slope failure involving Triassic and Middle Miocene salt and shale in the Gulf of Cadiz (Atlantic Iberian Margin). Terra Nova 15, 380–391.

Madelain, F., 1970. Influence de la topographie du fond sur l'ecoulement méditerranéen entre le Détroit de Gibraltar et le Cap Saint-Vincent. Cah. Oceanogr. 22, 43–61.

Maldonado, A., Somoza, L., Pallares, L., 1999. The Betic orogen and the Iberian–African boundary in the Gulf of Cadiz: geological evolution (central North Atlantic). Mar. Geol. 155 (1–2), 9–43.

Mazurenko, L.L., Soloviev, V.A., Gardner, J.M., Ivanov, M.K., 2003. Gas hydrates in the Ginsburg and Yuma mud volcano sediments (Moroccan Margin): results of chemical and isotopic studies of pore water. Mar. Geol. 195 (1–4), 201–210.

Medialdea, T., Vegas, R., Somoza, L., Vazquez, J.T., Maldonado, A., Diaz-del-Rio, V., Maestro, A., Cordoba, D., Fernandez-Puga, M.C., 2004. Structure and evolution of the "Olistostrome" complex of the Gibraltar Arc in the Gulf of Cadiz (eastern Central Atlantic): evidence from two long seismic cross-sections. Mar. Geol. 209, 173–198.

Melieres, 1974. Recherches sur la dynamique sédimentaire du Golfe de Cadiz (Espagne). Univ. Paris A. 235 pp.

Mienis, F., Van Weering, T.C.E., de Stigter, H., de Haas, H., Richter, T., 2005. Near bed hydrodynamic conditions of carbonate mounds in the Northeast Atlantic Ocean, European Geosciences Union. Geophys. Res. Abstr. 04902.

Mortensen, P.B., 2000. Lophelia pertusa (Scleractinia) in Norwegian Waters. Distribution, Growth, and Associated Fauna. University of Bergen, Bergen, Norway.

Nelson, C.H., Baraza, J., Maldonado, A., Rodero, J., Escutia, C., Barber, J.H., 1999. Influence of the Atlantic inflow and Mediterranean outflow currents on Late Quaternary sedimentary facies of the Gulf of Cadiz continental margin. Mar. Geol. 155 (1–2), 99–129.

Ochoa, J., Bray, N.A., 1991. Water mass exchange in the Gulf of Cadiz. Deep-Sea Res. 38 (1), S465–S503.

Ovsyannikov, D.O., Sadekov, A.Y., Kozlova, E.V., 2003. Rock fragments from mud volcanic deposits of the Gulf of Cadiz: an insight into the Eocene–Pliocene sedimentary succession of the basin. Mar. Geol. 195 (1–4), 211–221.

Pinheiro, L.M., Ivanov, M.K., Sautkin, A., Akhmanov, G., Magalhaes, V.H., Volkonskaya, A., Monteiro, J.H., Somoza, L., Gardner, J., Hamouni, N., Cunha, M.R., 2003. Mud volcanism in the Gulf of Cadiz: results from the TTR-10 cruise. Mar. Geol. 195 (1–4), 131–151.

Reeburg, W.S., 1983. Rates of biogeochemical processes in anoxic sediments. Ann. Rev. Earth Planet. Sci. 11, 269–298.

Roberts, J.M., Wheeler, A.J., Freiwald, A., 2006. Reefs of the deep: the biology and geology of cold-water coral ecosystems. Science 312, 543–547.

Rogerson, M., 2002. Climatic influence on sediment transport in the Mediterranean outflow current (Gulf of Cadiz, Spain). Newsl. Micropalaeontol. 66, 16–17.

Rüggeberg, A., Dorschel, B., Dullo, W.C., Hebbeln, D., 2005. Sedimentary patterns in the vicinity of a carbonate mound in the Hovland Mound Province, northern Porcupine Seabight. In: Freiwald, A., Roberts, J.M. (Eds.), Cold-Water Corals and Ecosystems. Springer-Verlag, Berlin, pp. 87–112.

Ruiz, J., Navarro, G., 2006. Upwelling spots and vertical velocities in the Gulf of Cadiz: an approach for their diagnose by combining temperature and ocean colour remote sensing. Deep-Sea Res. Pt. II 53 (11–13), 1282–1293.

Sadoux, S., Baey, J.M., Fincham, A., Renouard, D., 2000. Experimental study of the stability of an intermediate current and its interaction with a cape. Dyn. Atmos. Ocean. 31, 165–192.

Sartori, R., Torelli, N., Zitellini, D., Peis, D., Lodolo, E., 1994. Eastern segment of the Azores–Gibraltar line (central-eastern Atlantic): an oceanic plate boundary with diffuse compressional deformation. Geology 22, 555–558.

Schönfeld, J., 1997. The impact of the Mediterranean Outflow Water (MOW) on the benthic foraminiferal assemblages and surface sediments at the southern Portuguese continental margin. Mar. Micropaleontol. 29, 211–236.

Schönfeld, J., Zahn, R., 2000. Late Glacial to Holocene history of the Mediterranean Outflow. Evidence from benthic foraminiferal assemblages and stable isotopes at the Portuguese margin. Palaeogeogr. Palaeoclimatol. Palaeoecol. 159, 85–111.

Somoza, L., Diaz-del-Rio, V., Leon, R., Ivanov, M., Fernandez-Puga, M.C., Gardner, J.M., Hernandez-Molina, F.J., Pinheiro, L.M., Rodero, J., Lobato, A., 2003. Seabed morphology and hydrocarbon seepage in the Gulf of Cadiz mud volcano area: acoustic imagery, multibeam and ultra-high resolution seismic data. Mar. Geol. 195 (1–4), 153–176.

Taviani, M., Freiwald, A., Zibrowius, H., 2005. Deep coral growth in the Mediterranean Sea: an overview. In: Freiwald, A., Roberts, J.M.

(Eds.), Cold-Water Corals and Ecosystems. Springer-Verlag, Berlin, pp. 137–156.

Thomson, J., Nixon, S., Summerhayes, C.P., Schönfeld, J., Zahn, R., Grootes, P., 1999. Implications for sedimentation changes on the Iberian margin over the last two glacial/interglacial transitions from $(^{230}Th_{excess})_0$ systematics. Earth Planet. Sci. Lett. 165 (3–4), 255–270.

Thorpe, S.A., 1976. Variability of the Mediterranean undercurrent in the Gulf of Cadiz. Deep-Sea Res. 23, 711–727.

Tribble, G.W., 1993. Organic matter oxidation and aragonite diagenesis in a coral reef. J. Sediment. Petrol. 63 (3), 523–527.

Van Rensbergen, P., Depreiter, D., Pannemans, B., Moerkerke, G., Van Rooij, D., Marsset, B., Akhmanov, G., Blinova, V., Ivanov, M., Rachidi, M., Magalhaes, V., Pinheiro, L., Cunha, M., Henriet, J.P., 2005a. The El Arraiche mud volcano field at the Moroccan Atlantic slope, Gulf of Cadiz. Mar. Geol. 219 (1), 1–17.

Van Rensbergen, P., Depreiter, D., Pannemans, B., Henriet, J.-P., 2005b. Seafloor expression of sediment extrusion and intrusion at the El Arraiche mud volcano field, Gulf of Cadiz. J. Geophys. Res. 110, F02010.

Van Rooij, D., Depreiter, D., Bouimetarhan, I., De Boever, E., De Rycker, K., Foubert, A., Huvenne, V., Réveillaud, J., Staelens, P., Vercruysse, J., Versteeg, W., Henriet, J.-P., 2005. First sighting of active fluid venting in the Gulf of Cadiz. EOS 86 (49), 509–511.

van Weering, T.C.E., de Haas, H., de Stigter, H.C., Lykke-Andersen, H., Kouvaev, I., 2003. Structure and development of giant carbonate mounds at the SW and SE Rockall Trough margins, NE Atlantic Ocean. Mar. Geol. 198, 67–81.

Vanneste, H., 2005. Een paleo-oceanografische studie van Laat-Quartaire sedimenten aan de hand van coccolieten en kleiminer-alogie langsheen de Marokkaanse continentale rand, Golf van Cadiz. University Gent. 114 pp.

Vanney, J.-R., 2002. Géographie de l'océon Global. Gordon & Breach, Paris. 350 pp.

Vanney, J.R., Ménanteau, L., 2004. Géographie du golfe ibéro-marocain. Instituto Hidrografico, Lisboa — Portugal.

Voelker, A.H.L., Lebreiro, S.M., Schönfeld, J., Cacho, I., Erlenkeuser, H., Abrantes, F., 2006. Mediterranean outflow strengthening during northern hemisphere coolings: a salt source for the glacial Atlantic? Earth Planet. Sci. Lett. 245 (1–2), 39–55.

Wheeler, A.J., Kozachenko, M., Beyer, A., Foubert, A., Huvenne, V.A.I., Klages, M., Masson, D.G., Olu-Le Roy, K., Thiede, J., 2005a. Sedimentary processes and carbonate mounds in the Belgica mound province, Porcupine Seabight, NE Atlantic. In: Freiwald, A., Roberts, J.M. (Eds.), Cold-Water Corals and Ecosystems. Springer-Verlag, Berlin, pp. 571–603.

Wheeler, A.J., Beck, T., Thiede, J., Klages, M., Grehan, A., Monteys, F.X., the Polarstern ARK XIX/3a Shipboard Party, 2005b. Deep-water coral mounds on the Porcupine Bank, Irish margin: preliminary results from the Polarstern ARK-XIX/3a ROV cruise. In: Freiwald, A., Roberts, J.M. (Eds.), Cold-Water Corals and Ecosystems. Springer-Verlag, Berlin, pp. 393–402.

Zahn, R., Schönfeld, J., Kudrass, H.-R., Park, M.-H., Erlenkeuser, H., Grootes, P., 1997. Thermohaline instability in the North Atlantic during meltwater events: stable isotope and ice-rafted detritus records from core SO75-26KL, Portuguese margin. Paleoceanography 12 (5), 696–710.

Zenk, W., Armi, L., 1990. The complex spreading pattern of Mediterranean Water off the Portuguese continental slope. Deep-Sea Res. 37 (12), 1805–1823.

ORIGINAL

Numerical simulation of upwelling currents in pockmarks, and data from the Inner Oslofjord, Norway

Øyvind Hammer · Karen E. Webb · Davy Depreiter

Abstract The deflection of oceanic or tidal currents into pockmarks has been studied by both general three-dimensional computational fluid dynamics simulations and acoustic measurements in a number of pockmarks in the Inner Oslofjord, Norway. The modeling demonstrates upstream convergence of flow lines, followed by upwelling over the pockmark. This upwelling is an effect of deflected regional currents, not of expulsion of fluids or gas from the seafloor, and is sufficiently strong to prevent the settling of fine particles. The field measurements, although noisy at low vertical velocities, are consistent with the hypothesis of upwelling. The reduction in sedimentation rate inferred over the pockmarks (relative to that of the flat surrounding seabed) can explain the maintenance, or even deepening of pockmarks in the absence of fluid or gas seepage. The current pattern may also have consequences for the marine biology of pockmarks.

Introduction

Pockmarks are circular to elongated depressions in the seafloor, ubiquitous especially on the continental shelf throughout the world (Hovland and Judd 1988; Hovland et al. 2002). Ranging from less than 1 m to more than 1 km

Ø. Hammer (✉) · K. E. Webb
Physics of Geological Processes, University of Oslo,
P.O. Box 1048, Blindern,
0316 Oslo, Norway
e-mail: ohammer@nhm.uio.no

D. Depreiter
Renard Centre of Marine Geology, University of Gent,
9000 Gent, Belgium

in diameter, these features are considered to form mainly as a result of sudden or gradual release of gas (usually methane; Scanlon and Knebel 1989), meteoric groundwater (Khandriche and Werner 1995), or overpressured pore water (Harrington 1985).

Deflection of oceanic currents in pockmarks is a critical issue for a number of reasons. A fundamental problem in pockmark research is age estimation, usually involving consideration of relative rates of sedimentation or erosion inside and outside the pockmark. Does the pockmark act as a sediment trap, or do currents keep the pockmark open long after fluid expulsion or seepage has ceased? Elongated pockmarks are often aligned along prevailing current directions, which may indicate that the pockmarks were initially circular, but have been deformed by sediment transport, deposition, and erosion (Josenhans et al. 1978; Hovland 1983; Bøe et al. 1998).

Coarse sediment is often found in the center of pockmarks (Manley et al. 2004; Webb et al. 2009). In some cases, this is due to authigenic carbonate in methane seep settings, or may be explained as a winnowed lag deposit caused by the expulsion or seepage of fluids. However, such lag deposits can also be due to currents, as well as to the accumulation of anthropogenic and other debris, as sometimes observed in pockmarks (e.g., Manley et al. 2004; Webb et al. 2009).

Currents are known to influence the distribution of benthic organisms, both by affecting larval settlement, and by controlling the transport of nutrients to suspension feeders such as corals, sea anemones, and crinoids. The distribution of benthic organisms around a pockmark may therefore reflect hydrodynamic patterns affected by the pockmark's geometry (Webb et al. unpublished data; Wildish et al. 2008). Furthermore, the frequently observed

association between pockmarks and high densities of fish (Hovland and Judd 1988; Dando et al. 1991) may partly be connected with current patterns.

Although long-term measurements of physical parameters such as pressure and temperature in pockmarks are available (e.g., Marinaro et al. 2006), pockmark currents have been measured directly only rarely. In fact, to our knowledge there is only one published study on current measurements in pockmarks. Manley et al. (2004) carried out long-term ADCP measurements from a moored instrument in a pockmark in Lake Champlain, USA/Canada, and also provide an interesting discussion of possible effects of currents on pockmark sedimentation. They suggest that a cyclo-stropic rotational flow may be induced as the water column is stretched vertically when advected across the pockmark, and furthermore that an inward and downward flow may be set up around the perimeter. This could bring particles to the center of the pockmark, where the fines could get resuspended.

This paper presents numerical modeling of currents as deflected by a generic pockmark. We have also attempted to validate the modeling results using current measurements in pockmarks in the Inner Oslofjord, Norway. The morphology and sedimentology of these pockmarks have been described by Webb et al. (2009). No direct evidence of gas seepage from Oslofjord pockmarks has so far been detected, but there are weak indications of freshwater flux (Hammer and Webb, personal observation). The aim of this paper is not to address the formation or maintenance of the Inner Oslofjord pockmarks in particular, but rather to use these as convenient structures for validating the numerical modeling. Many of these pockmarks are near-perfectly circular, large, and in areas of relatively strong tidal current.

Materials and methods

Hydrodynamic conditions (the pressure and flow velocity fields) in a synthetic, generic pockmark geometry were simulated in three dimensions using the SAGE adaptive mesh Navier-Stokes solver (Science Applications International Corporation, San Diego, CA, 2005). The code was run using 32 processor nodes on an HP BL 460c cluster provided by the NOTUR network in Norway. Horizontal domain size was 100×100 m. Water depth outside the model pockmark was set at 60 m, typical of the Inner Oslofjord pockmarks (Webb et al. 2009). The mesh was automatically adapting down to a minimum cell size of 63 × 63×63 cm near the seafloor. The pockmark was modeled

using a rotated cosine function, giving a diameter of 40 m and a maximum depth of 7 m. These dimensions are typical for pockmarks in general (Hovland and Judd 1988), and for the Inner Oslofjord pockmarks in particular (Webb et al. 2009). Inflow from the southern edge, and outflow from the northern edge of the model pockmark were based on a parabolic velocity profile approximating the steady-state flow inside the domain. The exact form of this profile was uncritical, because the model pockmark was placed at considerable distance (30 m) from the inflow and outflow boundaries. Surface current velocity was set at 20 cm/s, which is high but not uncommon for the tidal currents of the Inner Oslofjord (cf. during the measurements in multiple pockmarks mentioned below, we observed surface current speeds varying between ca. 10 cm/s and 30 cm/s). The program run was terminated at 30 s simulated time (roughly 10,000 CPU h), when the flow field had reached steady state.

The pockmarks investigated in this paper are shown in Fig. 1 and Table 1. In pockmark 186, current velocity profiles were measured using a Nortek Aquadopp acoustic Doppler current profiler (ADCP) with 1-MHz transducers. The instrument was mounted on an aluminum frame, raising the transducers 25 cm above the seafloor, and set up to collect data through a vertical column with 0.5-m cells starting at 45 cm above the seafloor. The range was 8 m, and each measurement was averaged over 8 min. The instrument was deployed at six sites within pockmark 186 (Fig. 2), at 56 m water depth north of Nesodden in the Inner Oslofjord (Webb et al. 2009). This pockmark was selected because of its regular circular shape, substantial depth (5.8 m) relative to its diameter (31 m), and flat surrounding seafloor. The complete operation took slightly less than 4 h (11:10 A.M. to 3:00 P.M. on 29 April 2008). In this time period, tidal current speed remained fairly constant (around 20 cm/s at the surface), but the current rotated from SSE to ESE.

For comparison of upwelling inside and outside of pockmarks, the vertical current component was measured in the center of nine other pockmarks in the Oslofjord, as well as at adjacent control sites situated on flat seafloor 100–150 m outside each pockmark (Table 1). The measurements were made from aboard the RV *Trygve Braarud*, by means of a ship-mounted Nortek Continental ADCP with 190-kHz transducers and 2-m cell size. We selected pockmarks in relatively shallow water (less than 50 m), in order to minimize the measurement area encompassed by the three divergent beams of the ADCP. Surface current velocities were less than 20 cm/s at all sites. Measurements from a cell ca. 4 m above the seafloor were averaged over 5 min. Vertical currents inside and outside of pockmarks were compared by means of a paired t test, using the software PAST (Hammer et al. 2001).

Fig. 1 Locations of the Inner Oslofjord pockmarks listed in Table 1
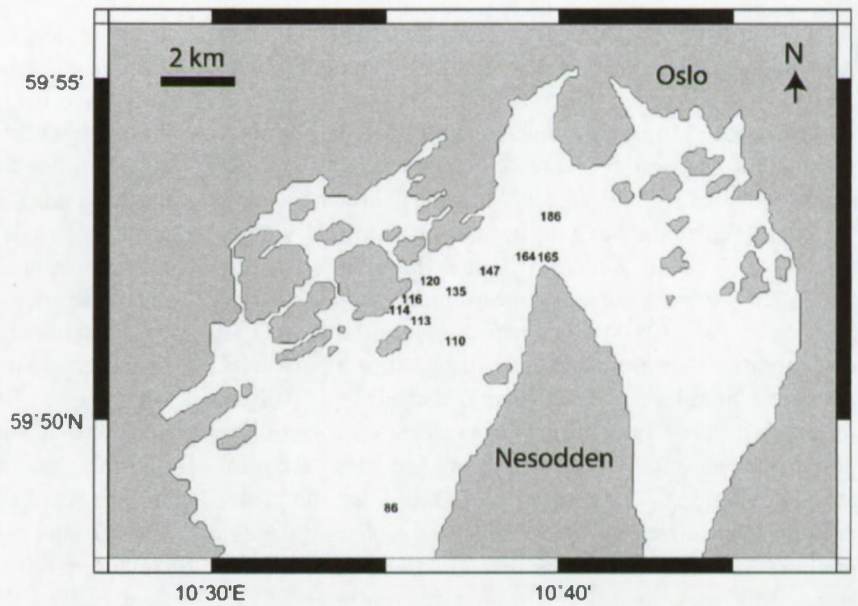
Results

The results of the hydrodynamic modeling are shown in Figs. 3, 4, 5, and 6, revealing several interesting phenomena. As expected, overall current velocities decrease substantially in the sheltered area inside the model pockmark. There is no clear flow separation or formation of an eddy—the dominant mode is laminar flow subparallel to the seafloor (Fig. 3), with water masses first flowing down into the pockmark, and then escaping up.

In a top view (Fig. 4), however, currents are clearly deflected in the horizontal plane above the model pockmark, showing marked convergence upstream and divergence downstream. The velocity field 1.5 m above seafloor

(Fig. 5) shows the low velocity down in the pockmark, and high velocities around the rim. The converging water masses escape partly through an updraft, with its focus inside the pockmark, but displaced slightly downstream. The vertical component of current velocity, v_z, reaches 0.5 cm/s near the bottom of the model pockmark, but minor upwelling can be traced high into the water column, nearly to the surface (Fig. 6).

In pockmark 186, the horizontal components of measured current profiles generally align along the regional tidal current direction, which varied through the measurement period as the tide was turning (data not shown). The vertical component was positive at all six measurement sites, but varied depending on location within the pockmark. In positions to the left

Table 1 Pockmarks in the Inner Oslofjord, Norway, investigated in the present study

Pockmark	Lat. N	Long. E	Water depth (m)	Pockmark depth (m)	Observed vertical current (m/s)	
					Inside	Outside (control)
86	59°48.736'	10°35.212'	45.4	7.1	-	-
110	59°51.167'	10°37.079'	46.8	8.1	0.23	0.20
113	59°51.466'	10°36.081'	40.6	5.5	0.18	0.08
114	59°51.699'	10°35.472'	27.8	5.3	0.08	0.06
116	59°51.753'	10°35.751'	34.4	5.2	0.15	0.10
120	59°52.060'	10°36.341'	40.5	4.5	0.17	0.08
135	59°51.901'	10°37.092'	31.9	5.9	0.05	0.02
147	59°52.199'	10°38.082'	31.3	5.8	0.09	0.06
164	59°52.413'	10°39.312'	26.8	5.4	0.08	0.04
165	59°52.403'	10°39.521'	28.1	4.1	0.07	0.05
186	59°52.990'	10°39.830'	56.3	5.8	-	-

Pockmark 86 was used only for Fig. 8. Pockmark 186 was studied by multiple ADCP measurements inside the structure. The vertical currents in the remaining pockmarks were measured by ADCP inside and outside each pockmark
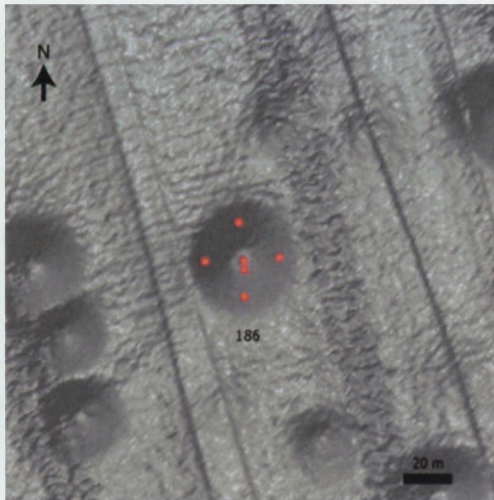
Fig. 2 Sonar bathymetry in the vicinity of pockmark 186 (data provided by the Norwegian Geological Survey). *Red dots* ADCP deployment sites. The surrounding pockmarks are not among those mentioned in this paper. *Smaller ripples* and *straight lines* are surveying artifacts. Depth of seafloor outside pockmarks ca. 56 m. Depth of pockmark 186 is 5.8 m


Fig. 4 Current speed and vectors from numerical simulation, in a horizontal plane (i.e., not parallel to the seafloor) immediately above and in the vicinity of the model pockmark. Scale bar at *lower left* refers to vector lengths. Note convergence of flow upstream (*left*), and divergence downstream (*right*) of the pockmark

(Fig. 7a), upstream (Fig. 7b), and upstream right (Fig. 7c) of the pockmark (relative to the current direction), upwelling was generally less than 2 cm/s, except very close to the seafloor. The smallest overall upwelling, less than 1 cm/s above 2 m from the seafloor, was observed in the upstream position (Fig. 7b). Maximum upwelling (>3 cm/s) was recorded at the center and downstream sites (Fig. 7d, e). The center downstream location (Fig. 7f) showed intermediate upwelling.

The results of ship-mounted ADCP measurements over other pockmarks and control sites (Table 1) reveal that the vertical component was positive in all cases, but significantly stronger inside the pockmarks (average 174%; paired t test $p<0.01$). Both sets of ADCP measurements were, however, noisy relative to the small vertical velocities. There was correlation between water depth and vertical

velocities at control sites (Spearman's rank correlation r_S= 0.75, p=0.02).

Discussion

The main result of this study is the considerable upwelling reconstructed over the model pockmark, potentially affecting sedimentation. The field measurements were noisy, and the deeper water at pockmark locations relative to outside may have contributed to

Fig. 3 Current vectors from numerical simulation of the model pockmark (lateral view). The overall current direction is from *left to right*. Scale bar at *lower left* refers to vector lengths
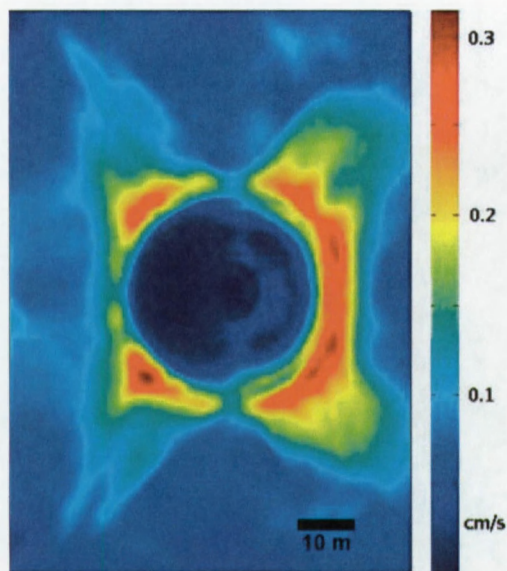
Fig. 5 Current speed from numerical simulation, 1.5 m above the seafloor in and around the model pockmark. Orientation as in Fig. 4. Note localized areas of strong current (*red*) around the rim

higher measured velocities inside pockmarks through the observed correlation between water depth and vertical velocity (the reason for this effect is unknown). The detailed measurements in pockmark 186 are in general accordance with the upwelling hypothesis, except that the upwelling in the center downstream position (Fig. 7f) is somewhat smaller than expected from the modeling results. We therefore consider the ADCP results to be consistent with, rather than confirming, the upwelling hypothesis.
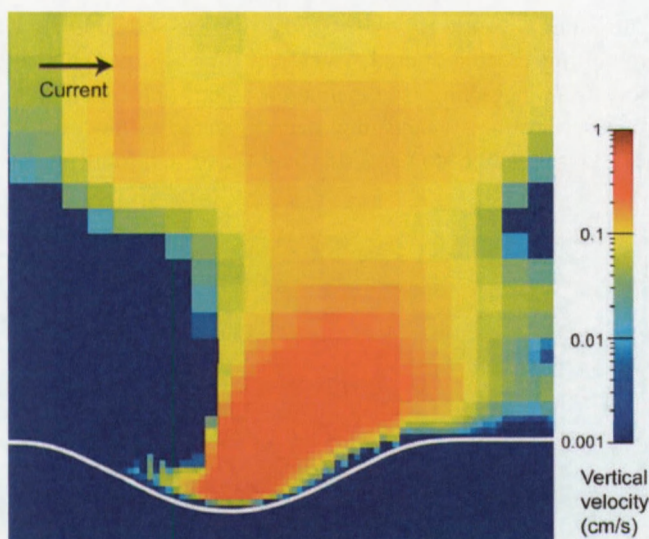

Fig. 6 Vertical component (v_z) of current velocity (cm/s) from numerical modeling, showing upwelling (lateral view). Seabed indicated by *white line*

Stokes' law (Lamb 1994) gives the terminal settling velocity V_s for a particle of diameter D:

$$V_s = \frac{\left(\rho_p - \rho_f\right)gD^2}{18\mu}$$

Using a particle density $\rho_p = 2.65$ g/cm^3, fluid density $\rho_f = 1.03$ g/cm^3, dynamic viscosity $\mu = 0.01308$ g/cm per second (in water at 10°C), and a vertical current velocity of 0.5 cm/s, as seen in the simulation, we find that spherical particles with a diameter less than about $D = 85$ μm (that is, clay, silt, and even very fine sand) would be unable to settle through the water column near the center of the pockmark. This effect could produce a lag deposit consisting of coarser sediment, in accordance with observations by Manley et al. (2004) in Lake Champlain, and Webb et al. (2009) in the Inner Oslofjord. However, some proportion of fine particles could still settle by flocculation (e.g., Kranck 1975).

Clearly, the overall reduction in horizontal current velocity inside the pockmark will lead to higher sedimentation rates, especially from bed load. This will, however, be counteracted by the updraft in the center of the pockmark. The net sedimentation rate will be controlled by the balance of these two processes, and is therefore likely to vary depending on particular conditions controlled by, for example, pockmark shape, regional current velocity, grain size distribution of bed load and suspended sediments, and cohesiveness of the sediment.

The lack of flow separation (Fig. 3) may be ascribed to the very smoothly curving edge of the model pockmark.

The convergence of flow upstream of the pockmark (Fig. 4) is another interesting result from the simulation. This effect is due to the increase in depth, causing a vertical elongation of the water column resulting in a pressure drop. Any natural water current will have a small net angular momentum. As water masses converge upstream of the pockmark, it could be theorized that the preservation of angular momentum would dictate acceleration in the rotational flow, and the formation of a vortex (cf. Manley et al. 2004). Because no angular momentum was imposed, the phenomenon could not arise in the simulations shown here, but pockmark vortices in nature remains a possibility.

Current patterns are also of interest because they have profound effects on the distributions of many marine organisms, both direct and indirect—for example, by affecting larval settlement, and the supply of nutrients and oxygen (e.g., Rosenberg 1995). From the results presented above (cf. Fig. 5), we would predict higher densities of benthic suspension feeders (e.g., corals, sea anemones, and crinoids) in and around the high-velocity areas of a pockmark, i.e., on the rims and slopes, rather than in the center. However, the nature of the substrate is probably

Fig. 7 Vertical component (v_z) of ADCP measurements at various locations within pockmark 186 (cf. *red dots* in Fig. 2). The positions in the pockmark relative to the background current direction at the time of measurement are as follows: **a** left, **b** upstream, **c** upstream right, **d** downstream right, **e** center, **f** downstream center (*sf* seafloor)
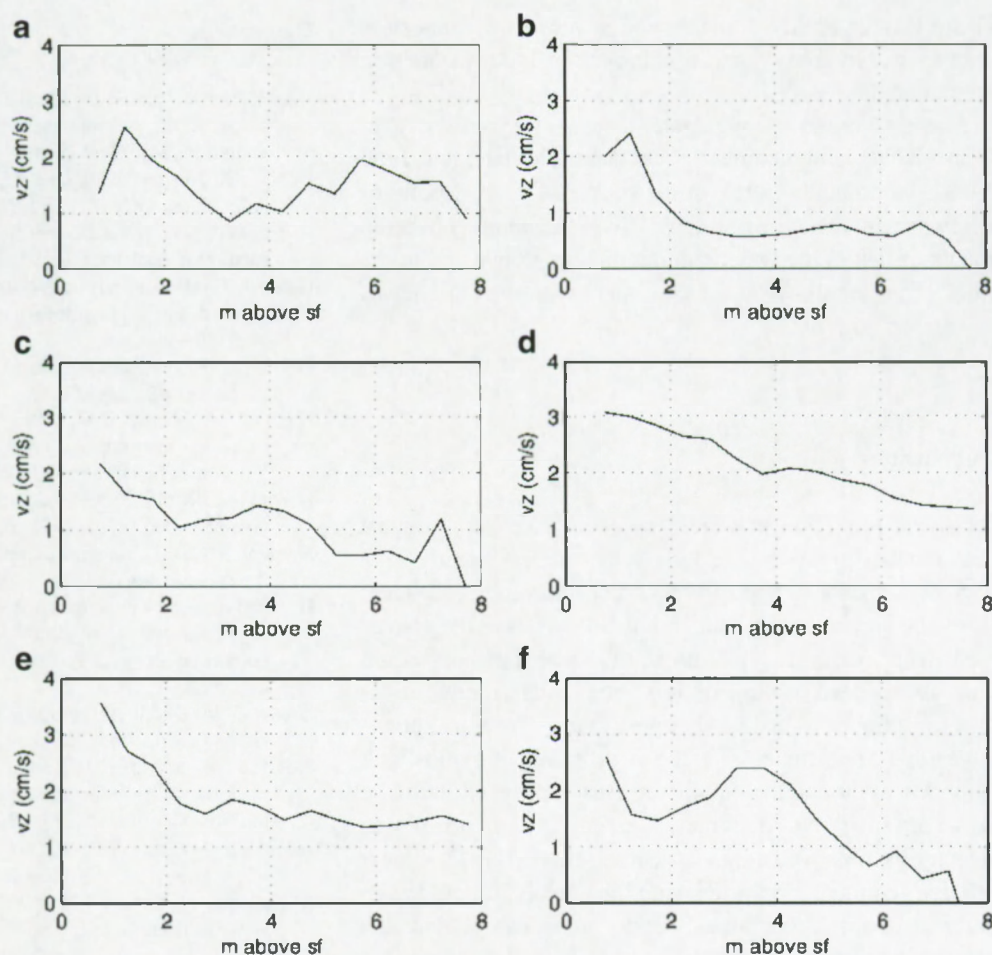
another key factor determining the distribution of organisms within pockmarks (e.g., Gray 1974). In the center, carbonate rocks and anthropogenic debris often provide a hard surface for organisms to encrust or attach to. Such objects are also likely to increase the complexity of current flow patterns. If we exclude the centre, compared to

Fig. 8 Accumulation of fish above the downstream edge of pockmark 86, Inner Oslofjord, as revealed by subbottom profiling (6 kHz). *P* Pockmark, *F* fish

the surrounding seabed we still see much higher abundances of fauna, especially suspension feeders, on the rims and slopes of pockmarks in the Troll Field, North Sea (Webb et al., unpublished data). As the substrate in these habitats is comparably soft sediments, these differences in faunal abundances are most likely to be a result of altered current flow patterns in pockmarks. The pockmarks studied in the Troll Field showed an increase in the abundance of fauna inside, including high abundances of suspension-feeding anemones on the slopes. One pockmark had large colonies of the tree-like soft coral *Paragorgia arborea* in its center, this being one of the key habitat-forming "bubblegum" corals worldwide. The presence of corals in the center of pockmarks could be due to the nature of the substrate, or possibly to the upwelling current. Hovland (2005) also reported that 33 pockmarks in the Kristin field off the coast of mid-Norway had coral reefs in their center or along their inside rim. These coral species are typically found at locations exposed to currents, implying that the pockmarks are associated with increased flow. Wildish et al. (2008) reported high densities of holothurians in some pockmarks

in the Bay of Fundy, Canada, and suggested a connection with special hydrodynamic conditions causing resuspension of sediment.

Fish are known to congregate in areas of upwelling (e.g., Genin 2004), and also near pockmarks (Hovland and Judd 1988; Dando et al. 1991). In the course of several years of fieldwork in the Oslofjord, we have frequently observed shoals of fish in the water column directly above and to the sides of pockmarks (Fig. 8), consistent with the presence of an updraft current.

Conclusions

From the modeling and field evidence, we here suggest that currents may be deflected by the pockmark in a way that produces a positive vertical current component from the pockmark, possibly but not necessarily associated with rotation. This upwelling phenomenon could lead to reduced sedimentation rate, and winnowing of the fine fraction inside the pockmark. To our knowledge, this scenario has not been proposed previously. It provides a model that could at least partly explain the lack of infill in pockmarks even where no active seepage is observed (e.g., Ussler et al. 2003). The lower relative sedimentation rate inside the pockmark could even make it deepen over time. We do not consider that this effect could initiate a pockmark, but it could explain the lack of infill in old, inactive pockmarks.

Future modeling work should include the simulation of flow patterns in pockmarks with other types of geometry, most notably elongate and trench pockmarks (Hovland 1983; Bøe et al. 1998; Webb et al. 2009). Also, a more complete model simulating current flow and sediment transport, deposition, and erosion in a changing geometry is necessary in order to understand the development of pockmarks over time, including elongation in the direction of current flow (Josenhans et al. 1978; Hovland 1983; Bøe et al. 1998). Such simulation is, however, extremely computer intensive. More accurate field measurement is also necessary. Hovland et al. (2002) made a plea for long-term monitoring of temperature, pressure, and fluid flow in pockmarks (cf. Marinaro et al. 2006). Such studies should ideally also include measuring of current patterns and sedimentation rates.

References

Bøe R, Rise L, Ottesen D (1998) Elongate depressions on the southern slope of the Norwegian Trench (Skagerrak): morphology and evolution. Mar Geol 146:191–203

Dando PR, Austen MC, Burke RJ, Kendall MA, Kennicutt MC, Judd AG, Moore DC, O'Hara SCM, Schmaljohann R, Southward AJ (1991) Ecology of a North Sea pockmark with an active methane seep. Mar Ecol Prog Ser 70:49–63

Genin A (2004) Bio-physical coupling in the formation of zooplankton and fish aggregations over abrupt topographies. J Mar Syst 50:3–20

Gray JS (1974) Animal-sediment relationships. Oceanogr Mar Biol Annu Rev 12:223–261

Hammer Ø, Harper DAT, Ryan PD (2001) PAST: paleontological statistics software package for education and data analysis. Palaeontol Electronica 4(1)

Harrington PK (1985) Formation of pockmarks by pore-water escape. Geo-Mar Lett 5:193–197. doi:10.1007/BF02281638

Hovland M (1983) Elongate depressions associated with pockmarks in the western slope of the Norwegian Trench. Mar Geol 51:35–46

Hovland M (2005) Pockmark-associated coral reefs at the Kristin field off Mid-Norway. In: Freiwald A, Roberts JM (eds) Cold-water corals and ecosystems. Springer, Berlin Heidelberg New York, pp 623–632

Hovland M, Judd AG (1988) Seabed pockmarks and seepages. Graham & Trotman, London

Hovland M, Gardner JV, Judd AG (2002) The significance of pockmarks to understanding fluid flow processes and geohazards. Geofluids 2:127–136

Josenhans HW, King LH, Fader GB (1978) A side-scan sonar mosaic of pockmarks on the Scotian Shelf. Can J Earth Sci 15:831–840

Khandriche A, Werner F (1995) Freshwater induced pockmarks in Bay of Eckernfoerde, Western Baltic. In: Mojski JE (ed) Proc 3rd Marine Geological Conf The Baltic. Panstwowy Instytut Geologiczny, Warzawa, pp 155–164

Kranck K (1975) Sediment deposition from flocculated suspensions. Sedimentology 22:111–123

Lamb H (1994) Hydrodynamics, 6th edn. Cambridge University Press, Cambridge

Manley PL, Manley TO, Watzin MC, Gutierrez J (2004) Lakebed pockmarks in Burlington Bay, Lake Champlain: I. Hydrodynamics and implications of origin. In: Manley TO, Manley PL, Mihuc TB (eds) Lake Champlain: Partnerships and research in the new millennium. Springer, Berlin Heidelberg New York, pp 299–330

Marinaro G, Etiope G, Bue NL, Favali P, Papatheodorou G, Christodoulou D, Furlan F, Gasparoni F, Ferentinos G, Masson M, Rolin J-F (2006) Monitoring of a methane-seeping pockmark by cabled benthic observatory (Patras Gulf, Greece). Geo-Mar Lett 26:297–302. doi:10.1007/s00367-006-0040-4

Rosenberg R (1995) Benthic marine fauna structured by hydrodynamic processes and food availability. Neth J Sea Res 34:303–317

Scanlon KM, Knebel HJ (1989) Pockmarks in the floor of Penobscot Bay, Maine. Geo-Mar Lett 9:53–58. doi:10.1007/BF02262818

Ussler W, Paull CK, Boucher J, Friederich GE, Thomas DJ (2003) Submarine pockmarks: a case study from Belfast Bay, Maine. Mar Geol 202:175–192

Webb KE, Hammer Ø, Lepland A, Gray JS (2009) Pockmarks in the Inner Oslofjord, Norway. Geo-Mar Lett 29:111–124. doi:10.1007/s00367-008-0127-1

Wildish DJ, Akagi HM, McKeown DL, Pohle GW (2008) Pockmarks influence benthic communities in Passamaquoddy Bay, Bay of Fundy, Canada. Mar Ecol Prog Ser 357:51–66

Bibliography

P. Aharon and B. Fu. Microbial sulfate reduction rates and sulfur and oxygen isotope fractionations at oil and gas seeps in deepwater Gulf of Mexico. *Geochimica et Cosmochimica Acta*, 64(2):233–246, 2000.

G. Akhmanov, M. Ivanov, J. P. Henriet, and E. Sarantzev. The Al Araiche diapiric field and its exotic mud volcanic deposits recovered during the TTR12 cruise in the Gulf of Cadiz. In *Geological and biological processes at deep-sea European margins and oceanic basins. TTR12 post-cruise meeting and international conference*, 2003. Bolgona, Italy, February 2-6.

J. Allouc. Quaternary Crusts on Slopes of the Mediterranean-Sea - a Tentative Explanation for Their Genesis. *Marine Geology*, 94(3):205–238, 1990.

G. Aloisi, C. Pierre, J. M. Rouchy, and J. C. Faugeres. Isotopic evidence of methane-related diagenesis in the mud volcanic sediments of the Barbados Accretionary Prism. *Continental Shelf Research*, 22 (16):2355–2372, nov 2002.

J. Auzende, J. Olivet, and L. Pastouret. Implication structurales et paleogeographiques de la presence de Messinien a l'ouest de Gibraltar. *Marine Geology*, 43:9âĂŞ18., 1981.

A. Bally. Thoughts on the tectonics of folded belts. In K. McClay and N. Price, editors, *Thrust and nappe tectonics*, page 13âĂŞ32. Geological Society of London, Oxford, England, 1981.

N. L. Bangs, D. S. Sawyer, and X. Golovchenko. Free gas at the base of the gas hydrate zone in the vicinity of the Chile Triple Junction. *Geology*, 21:905–908, 1993.

J. Baraza and G. Ercilla. Gas-charged sediments and large pockmark-like features on the Gulf of Cadiz slope (SW Spain). *Marine and Petroleum Geology*, 13(2):253–261, 1996.

A. Barber, S. Tjokrosapoetro, and T. Charlton. Mud volcano, shale diapirs, wrench faults and melanges in accretionary complexes, eastern Indonesia. *American Association of Petroleum Geology Bulletin*, 70: 1729–1741, 1986.

P. M. Barnes, G. Lamarche, J. Bialas, S. Henrys, I. Pecher, G. L. Netzeband, J. Greinert, J. J. Mountjoy, K. Pedley, and G. Crutchley. Tectonic and geological framework for gas hydrates and cold seeps on the hikurangi subduction margin, New Zealand. *Marine Geology*, In Press, Accepted Manuscript:–, 2009. ISSN 0025-3227.

J. Bear. *Dynamics of Fluids in Porous Media*. New York: Dover Publications, Inc;., 1972.

R. Beck. The oceans, the new frontier in exploration. *Journal of the Australian Petroleum Exploration Association*, 12:1–21, 1972.

R. Berner. *Early Diagenesis: A Theoretical Approach*. Princeton Univ. Press, 1980.

T. Bickert and G. Wefer. South Atlantic and benthic foraminifer delta C-13 deviations: implications for reconstructing the Late Quaternary deep-water circulation. *Deep-Sea Research Part II: Topical Studies in Oceanography*, 46(1-2):437–452, 1999.

E. Bileva and V. Blinova. Geochemical characteristics of hydrocarbon gases from mud volcanoes of the Gulf of Cadiz. In M. Marani, G. Akhmanov, and A. Suzyumov, editors, *Geological and biological processes at deep-sea European margins and oceanic basins*, volume 187 of *Intergovernmental Oceanographic Commission Workshop Report No. 187*, page 17, 2003.

A. Boetius, K. Ravenschlag, C. Schubert, D. Rickert, F. Widdel, A. Gieseke, R. Amann, B. Joergensen, and O. Witte, U. andPfannkuche. A marine microbial consortium apparently mediating anaerobic oxidation of methane. *Nature*, 407:623–626, 2000.

G. Bohrmann, M. Ivanov, J. P. Foucher, V. Spiess, J. Bialas, J. Greinert, W. Weinrebe, F. Abegg, G. Aloisi, Y. Artemov, V. Blinova, M. Drews, F. Heidersdorf, A. Krabbenhoft, I. Klaucke, S. Krastel, T. Leder, I. Polikarpov, M. Saburova, O. Schmale, R. Seifert, A. Volkonskaya, and M. Zillmer. Mud Volcanoes and Gas Hydrates in the Black Sea: New Data From Dvurechenskii and Odessa Mud Volcanoes. *Geo-Marine Letters*, 23(3-4):239–249, 2003.

J. Bonnin, J. Olivet, and J. Auzende. Structure en nappe a l'ouest de Gibraltar. *Comptes Rendus de l'Académie des sciences*, 280:559âĂŞ562, 1975.

B. Boudreau. *Diagenetic Models and their Implementation*. Springer-Verlag, 1997.

J. Bouillin, M. Durand-Delga, and P. Olivier. *Betic-Rifian and Tyrrhenian Arcs: distinctive features, genesis and development stages*, pages 281–303. Elsevier, Amsterdam, 1986.

S. Bouriak, M. Vanneste, and A. Saoutkine. Inferred gas hydrates and clay diapirs near the Storegga Slide on the southern edge of the Voring Plateau, offshore Norway. *Marine Geology*, 163:124–148, 2000.

E. Buforn, C. Sanz de Galdeano, and A. Udias. Seismotectonics of the Ibero-Maghrebian region. *Tectonophysics*, 248:247–261, 1995.

E. A. Burton. Controls On Marine Carbonate Cement Mineralogyreview And Reassessment. *Chemical Geology*, 105(1-3):163–179, mar 1993.

J. Cadet, J. Fourniget, M. Gigout, M. Guillemin, and G. Pierre. La néotectonique des littoraux. *Bulletin de la Société Géologique de France*, 3:600–605, 1977.

A. Camerlenghi, M. B. Cita, W. Hieke, and T. Ricchiuto. Geological Evidence for Mud Diapirism on the Mediterranean Ridge Accretionary Complex. *Earth and Planetary Science Letters*, 109(3-4):493–504, 1992.

A. Camerlenghi, M. B. Cita, B. Dellavedova, N. Fusi, L. Mirabile, and G. Pellis. Geophysical Evidence of Mud Diapirism on the Mediterranean Ridge Accretionary Complex. *Marine Geophysical Researches*, 17(2):115–141, 1995.

X. Carton, L. Cherubin, J. Paillet, Y. More, A. Serpette, and B. Le Cann. Meddy coupling with a deep cyclone in the Gulf of Cadiz. *Journal of Marine Systems*, 32(1-3):13–42, 2002.

D. Casas, G. Ercilla, and J. Baraza. Acoustic Evidences of Gas in the Continental Slope Sediments of the Gulf of Cadiz (E Atlantic). *Geo-Marine Letters*, 23(3-4):300–310, 2003.

W. Cavazza, F. Roure, W. Spakman, G. Stampfli, and P. Ziegler, editors. *The TRANSMED Atlas. The Mediterranean Region from Crust to Mantle*. Springer-Verlag, 2004.

A. Chalouan and A. Michard. The Alpine Rif Belt (Morocco): a case of mountain building in a subduction-subduction-transform fault triple junction. *Pure and Applied Geophysics*, 161:489–519, 2004.

A. Chalouan, A. Michard, H. Feinberg, R. Montigny, and O. Saddiqi. The Rif mountain building (Morocco): a new tectonic scenario. *Bulletin de la Société Géologique de France*, 172:603–616, 2001.

J. Chow, J. S. Lee, C. S. Liu, B. D. Lee, and J. S. Watkins. A submarine canyon as the cause of a mud volcanoLiuchieuyu Island in Taiwan. *Marine Geology*, 176(1-4):55–63, jun 2001.

P. Cirac, M. Frappa, and E. Jaaid. Evolution morpho-structurale récente de la plateforme continentale ouest-rifaine (Maroc nord-atlantique). *Oceanologica Acta*, 16:1–19, 1993.

R. Coffin, L. Hamdan, W. Wood, J. Phlman, J. Smith, S. Henrys, and I. Pecher. Estimates of Vertical Methane Fluxes in Porangahau Ridge Sediment on the Hikurangi Margin, New Zealand. In *AGU Fall Meeting Proceedings*, 2007.

P. Colantoni, G. Gabbianelli, C. Ceffa, and C. Ceccolini. Bottom features and gas seepages in the Adriatic Sea. In *Abstracts and guidbook, fifth international conference on gas in marine sediments*, pages 28–31, 1998. Bologna, 9-12 September.

T. S. Collett. Energy resource potential of natural gas hydrates. *American Association of Petroleum Geology Bulletin*, 86(11):1971–1992, 2002.

A. Crespo-Blanc and D. Frizon de Lamotte. Structural evolution of the external zones derived from the Flysch trough and the South Iberian and Maghrebian paleomargins around the Gibraltar arc: a comparative study. *Bulletin de la Société Géologique de France*, 177:267–282, 2006.

P. Curzi. Sedimentation, subsidence and tectonics affecting gas charged sediments in central Adriatic Sea. In *Abstracts and guidbook, fifth international conference on gas in marine sediments*, pages 182–184, 1998. Bologna, 9-12.

A. Dale, P. Regnier, P. Van Cappellen, H. Fossing, J. Jensen, and B. Joergensen. Remote quantification of methane flux in gassy marine sediments trhough seismic survey. *Geology*, 37:235–238, 2009.

P. Dando, D. Stuben, and S. Varnavas. Hydrothermalism in the Mediterranean Sea). *Progress in Oceanography*, 44:333–67, 1999.

D. Davidson, D. Leaist, and R. Hesse. Oxygen-18 enrichment in the water of a clathrate hydrate. *Geochimica et Cosmochimica Acta*, 47:2293–2295, 1983.

M. K. Davie, O. Y. Zatsepina, and B. A. Buffett. Methane Solubility in Marine Hydrate Environments. *Marine Geology*, 203(1-2):177–184, 2004.

M. De Batist, J. Klerkx, P. Van Rensbergen, M. Vanneste, J. Poort, A. Y. Golmshtok, A. A. Kremlev, O. M. Khlystov, and P. Krinitsky. Active Hydrate Destabilization in Lake Baikal, Siberia? *Terra Nova*, 14 (6):436–442, 2002.

B. De Mol, P. Van Rensbergen, S. Pillen, K. Van Herreweghe, D. Van Rooij, A. McDonnell, V. Huvenne, M. Ivanov, R. Swennen, and J. P. Henriet. Large deep-water coral banks in the Porcupine Basin, southwest of Ireland. *Marine Geology*, 188(1-2):193–231, aug 2002.

D. Depreiter, J. Poort, P. Van Rensbergen, and J. P. Henriet. Geophysical evidence of gas hydrates in shallow submarine mud volcanoes on the Moroccan Margin. *Journal of Geophysical Research*, 110: –10103, 2005.

D. Depreiter, J. Henriet, J. Poort, A. Foubert, P. V. Rensbergen, R. Parkes, A. Weightman, H. Sass, J. Sas, W. Verstraete, L. Maignien, N. Boon, K. Hinrichs, K. Mangelsdorf, K. Zink, J. S. Damsté, H. Cypionka, R. Amils, R. Swennen, S. Kasten, N. Holm, G. Ori, L. Pinheiro, W. BrÃijckmann, S. Louwye, and S. Spezzaferri. Mud volcanoes as a window into the deep biosphere: IODP Proposal 689, 2006. http://www.iodp.org/index.php?option=com_docman&task=doc_download&gid=819.

C. Desplanque and D. J. Mossman. A review of ice and tide observations in the Bay of Fundy. *Atlantic Geology*, 34(3):195–209, Nov. 1998.

C. Desplanque and D. J. Mossman. Bay of Fundy tides. *Geoscience Canada*, 28(1):1–11, Mar. 2001.

J. Dewey, M. Helman, E. Torco, D. Hutton, and S. Knott. *Alpine Tectonics*, volume 45 of *Geological Society Special Publication*, chapter Kinematics of the western Mediterranean, page 265âĂŞ283. Geological Society London, 1989.

V. Diaz-del Rio, L. Somoza, J. Martinez-Frias, M. P. Mata, A. Delgado, F. J. Hernandez-Molina, R. Lunar, J. A. Martin-Rubi, A. Maestro, M. C. Fernandez-Puga, R. Leon, E. Llave, T. Medialdea, and J. T. Vazquez. Vast fields of hydrocarbon-derived carbonate chimneys related to the accretionary wedge/olistostrome of the Gulf of Cadiz. *Marine Geology*, 195(1-4):177–200, mar 2003.

J. Dickson. Carbonate identification and genesis as revealed by staining. *Journal of Sedimentary Petrology*, 36:491âĂŞ505., 1966.

L. Dimitrov. Contribution to Atmospheric Methane by Natural Seepages on the Bulgarian Continental Shelf. *Continental Shelf Research*, 22(16):2429–2442, 2002a.

L. I. Dimitrov. Mud Volcanoes - the Most Important Pathway for Degassing Deeply Buried Sediments. *Earth-Science Reviews*, 59(1-4):49–76, 2002b.

P. Domenico and M. Mifflin. Water from low-permeability sediments and land subsidence. *Water Resources Research*, 1:563–&, 1965.

B. Dorschel, D. Hebbeln, A. Foubert, and A. Wheeler. Hydrodynamics and cold-water coral facies distribution related to recent sedimentary processes at Galway Mound west of Ireland. *Marine Geology*, 224:184–195, 2007.

S. Dupre, J. Woodside, J.-P. Foucher, G. de Lange, J. Mascle, A. Boetius, V. Mastalerz, A. Stadnitskaia, H. Ondreas, C. Huguen, F. Harmegnies, S. Gontharet, L. Loncke, E. Deville, H. Niemann, E. Omoregie, K. O.-L. Roy, A. Fiala-Medioni, A. Dahlmann, J.-C. Caprais, A. Prinzhofer, M. Sibuet, C. Pierre, J. S. S. Jaap Sinninghe Damste, and the NAUTINIL Scientific Party. Seafloor geological studies above active gas chimneys off Egypt (Central Nile Deep Sea Fan). *Deep Sea Research Part I: Oceanographic Research Papers*, 54:1146–1172, 2007.

M. Durand-Delga. La courbure de Gibraltar, extrémité occidentale des chaÃŏnes alpines, unit l'Europe et l'Afrique. *Eclogae Geologicae Helvetiae*, 65:267–278, 1972.

M. Durand-Delga. La Méditerranée occidentale, étapes de sa genÃİse et problÃİmes structuraux liés Ãă celle-ci. *Mémoires de la Société Géologique de France*, 10:203–224, 1980.

B. Duval, C. Cramez, and M. Jackson. Raft Tectonics In The Kwanza Basin, Angola. *Marine and Petroleum Geology*, 9(4):389–404, AUG 1992. ISSN 0264-8172.

O. Eldholm, E. Sundvor, P. R. Vogt, B. O. Hjelstuen, K. Crane, A. K. Nilsen, and T. P. Gladczenko. Sw Barents Sea Continental Margin Heat Flow and Hakon Mosby Mud Volcano. *Geo-Marine Letters*, 19(1-2):29–37, 1999.

T. E. Faber. *Fluid Dynamics for Physicists*. New York: Cambridge University Press, 1995.

S. Farlow. *Partial Differential Equations for Scientists and Engineers*. Dover Publications, NY, 1993.

G. Faure. *Principles of isotope geology*. John Wiley & Sons, Inc., New York, 1986. 2nd Edition.

T. Ferdelman and M. Boettcher. Isotope Biogeochemistry of Sulfur in a Cold-Water Carbonate Mound (IODP Site 1317). In *Eos Trans. AGU*, volume 88, 2007. Fall Meet. Suppl., Abstract B22A-07.

T. Ferdelman, A. Kano, T. Williams, and the IODP Expedition 307 Scientists. IODP Expedition 307 drills cold-water coral mound along the Irish continental margin. *Scientific Drilling*, 2:11–16, 2006.

M. Fernandez-Puga, J. Vazquez, L. Somoza, V. Diaz-del Rio, T. Medialdea, and R. Mata, M.P.and Leon. Gas-related morphologies and diapirism in the Gulf of Cadiz. *Geo-Marine Letters*, 27(2-4):213–221, 2007.

J. Flinch and P. Vail. *Plio-Pleistocene sequence stratigraphy and tectonics of the Gibraltar Arc*, volume Mesozoic and Cenozoic Sequence Stratigraphy of European Basins of *SEPM Spec. Publ.*, pages 199–208. SEPM, 1998.

J. F. Flinch. *Tectonic Evolution of the Gibraltar Arc*. PhD thesis, Rice University, 1993.

J. F. Flinch, A. W. Bally, and S. G. Wu. Emplacement of a Passive-Margin Evaporitic Allochthon in the Betic Cordillera of Spain. *Geology*, 24(1):67–70, 1996.

R. Folk. Practical classification of limestones. *American Association of Petroleum Geology Bulletin*, 43: 1–38, 1959.

A. M. Folkard, P. A. Davies, A. F. G. Fiúza, and I. Ambar. Remotely sensed sea surface thermal patterns in the Gulf of Cadiz and the Strait of Gibraltar: Variability, correlations and relationships with the surface wind field. *Journal of Geophysical Research*, 102(C3):5669–5683, 1997.

B. Fonseca. The source of the Lisbon Earthquake. *Science*, 308:50, 2005.

A. Foubert, D. Depreiter, T. Beck, L. Maignien, B. Pannemans, N. Frank, D. Blamart, and J. Henriet. Carbonate mounds in a mud volcano province off north-west Morocco: key to processes and controls. *Marine Geology*, 248:74–96, 2008.

R. Freeze and J. Cherry. *Groundwater*. Prentice-Hall, Inc., Englewood Clifs, NJ, USA, 1979.

A. Freiwald. Reef-forming Cold-Water Corals. In G. Wefer, D. Billett, D. Hebbeln, B. B. Joergensson, M. Schluter, and T. van Weering, editors, *Ocean Margin Systems*, pages 365–385. Springer-Verlag Berlin Heidelberg, 2002.

I. Friedman and J. O'Neill. Compilation of stable isotope fractionation factors of geochemical interest. In M. Fleischer, editor, *Data of Geochemistry, 6th edition*, USGS Professional Paper, pages 440–KK, 1977.

D. Frizon de Lamotte. La structure du rif externe (Maroc): mise au point sur le role des decrochements des chevauchements et des glissements gravitaires. *Journal of African Earth Sciences*, 6(5):755–766, 1987.

J. Gardner. Mud volcanoes on the Moroccan continental margin. *EOS, Transactions of the American Geophysical Union*, 80:46, 1999.

J. Gardner. Morphology of seafloor mud volcanoes on the Moroccan Margin. In *IOC Workshop Report No. 168, Geological Processes on European Continental Margins*, page 12, 2000.

J. M. Gardner. Mud Volcanoes Revealed and Sampled on the Western Moroccan Continental Margin. *Geophysical Research Letters*, 28(2):339–342, 2001.

D. Gei and J. M. Carcione. Acoustic Properties of Sediments Saturated With Gas Hydrate, Free Gas and Water. *Geophysical Prospecting*, 51(2):141–157, 2003.

G. D. Ginsburg and V. A. Soloviev. *Submarine gas hydrates*. VNIIOkeangeologia, Saint-Petersburg, 1998.

G. D. Ginsburg, A. V. Milkov, V. A. Soloviev, A. V. Egorov, G. A. Cherkashev, P. R. Vogt, K. Crane, T. D. Lorenson, and M. D. Khutorskoy. Gas Hydrate Accumulation at the Hakon Mosby Mud Volcano. *Geo-Marine Letters*, 19(1-2):57–67, 1999.

R. K. Given and B. H. Wilkinson. Kinetic Control Of Morphology, Composition, And Mineralogy Of Abiotic Sedimentary Carbonates. *Journal Of Sedimentary Petrology*, 55(1):109–119, 1985.

A. Gonzalez-Ferrnandez, D. Cordoba, L. Matias, and M. Torne. Seismic crustal structure in the Gulf of Cadiz (SW Iberian Peninsula). *Marine Geophysical Researches*, 22:207–223, 2001.

S. Gradmann, C. Hubscher, Z. Ben-Avraham, D. Gajewski, and G. Netzeband. Salt tectonics off northern Israel. *Marine and Petroleum Geology*, 22(5):597–611, MAY 2005. ISSN 0264-8172. doi: 10.1016/j.marpetgeo.2005.02.001.

K. Graue. Mud volcanoes in deepwater Nigeria. *Marine and Petroleum Geology*, 17(8):959–974, sep 2000.

D. Grauls. Minimum principal stress as a control of overpressures ni sedimentary basins. In J. Hendry, P. Carey, P. Parnell, A. Ruffell, and R. Worden, editors, *Proceedings of Geofluids II '97 (Queens University, Belfast)*, number ISBN 1-897799-83-7, pages 219–223, 1997.

I. Grevemeyer, A. J. Kopf, N. Fekete, N. Kaul, H. W. Villinger, M. Heesemann, K. Wallmann, V. Spiess, H. H. Gennerich, M. Muller, and W. Weinrebe. Fluid Flow Through Active Mud Dome Mound Culebra Offshore Nicoya Peninsula, Costa Rica: Evidence From Heat Flow Surveying. *Marine Geology*, 207(1-4):145–157, 2004.

E. Grossman and T. Ku. Carbon and oxygen carbon isotope fractionation in biogenic aragonite: temperature effects. Chemical Geology (Isotope Geoscience). *Chemical Geology (Isotope Geoscience)*, 59: 59–74, 1986.

A. K. Gupta. Marine gas hydrates: their economic and environmental importance. *Current Science*, 86 (9):1198–1199, 2004.

M. A. Gutscher, J. Malod, J. P. Rehault, I. Contrucci, F. Klingelhoefer, L. Mendes-Victor, and W. Spakman. Evidence for Active Subduction Beneath Gibraltar. *Geology*, 30(12):1071–1074, 2002.

M. Haeckel, C. Berndt, V. Liebetrau, P. Linke, A. Reitzi, J. Schonfeld, and H. Vanneste. Genesis and rates of fluid flow at the Mercator mud volcano, Gulf of Cadiz. *Geochimica et Cosmochimica Acta*, 71 (15):A367–A367, Aug. 2007.

Y. P. Handa. Effect Of Hydrostatic-Pressure And Salinity On The Stability Of Gas Hydrates. *Journal of Physical Chemistry*, 94(6):2652–2657, Mar. 1990.

H. D. Hedberg. Relation of Methane Generation to Undercompacted Shales, Shale Diapirs, and Mud Volcanos. *American Association of Petroleum Geology Bulletin*, 58(4):661–673, 1974.

J. Henriet, B. De Mol, S. Pillen, M. Vanneste, V. R. D., W. Versteeg, P. Croker, P. Shannon, V. Unnithan, S. Bouriak, P. Chachkine, and P.-B. . S. Party. Gas hydrate crystals may help build reefs. *Nature*, 391: 648–649, 1998.

J. P. Henriet, S. Guidard, and the ODP "Proposal 753" Team. Carbonate Mounds as a Possible Example for Microbial Activity in Geological Processes. In G. Wefer, D. Billett, D. Hebbeln, B. B. Joergensson, M. Schluter, and T. van Weering, editors, *Ocean Margin Systems*, pages 439–455. Springer-Verlag Berlin Heidelberg, 2002.

P. Henry, X. Lepichon, S. Lallemant, S. Lance, J. B. Martin, J. P. Foucher, A. Fialamedioni, F. Rostek, N. Guilhaumou, V. Pranal, and M. Castrec. Fluid Flow in and Around a Mud Volcano Field Seaward of the Barbados Accretionary Wedge: Results From Manon Cruise. *Journal of Geophysical Research-Solid Earth*, 101(B9):20297–20323, 1996.

C. Hensen, M. Nuzzo, E. Hornibrook, L. Pinheiro, B. Bock, V. MagalhÃČes, and W. BrÃijckmann. Sources of mud volcano fluids in the Gulf of Cadiz - indications for hydrothermal imprint. *Geochimica et Cosmochimica Acta*, 71(5):1232–1248, 2007.

F. J. Hernandez-Molina, E. Llave, D. Stow, M. Garcia, L. Somoza, J. T. Vazquez, F. Lobo, A. Maestro, V. Diaz de Rio, R. Leon, T. Medialdea, and J. Gardner. The contourite depositional system of the Gulf of Cadiz: A sedimentary model related to the bottom current activity of the Mediterranean outflow water and its interaction with the continental margin. *Deep-Sea Research Part II: Topical Studies in Oceanography*, 53:1420–1463, 2006.

J. Hernandez-Molina, E. Llave, L. Somoza, M. C. Fernandez-Puga, A. Maestro, R. Leon, T. Medialdea, A. Barnolas, M. Garcia, V. D. del Rio, L. M. Fernandez-Salas, J. T. Vazquez, F. Lobo, J. M. A. Dias, J. Rodero, and J. Gardner. Looking for clues to paleoceanographic imprints: A diagnosis of the Gulf of Cadiz contourite depositional systems. *Geology*, 31(1):19–22, 2003.

K.-U. Hinrichs, J. M. Hayes, S. P. Sylva, P. G. Brewer, and E. F. DeLong. Methane-consuming archaebacteria in marine sediments. *Nature*, 398(6730):802–805, Apr. 1999. ISSN 0028-0836.

W. S. Holbrook, H. Hoskins, W. T. Wood, R. A. Stephen, and D. Lizarralde. Methane hydrate and free gas on the Blake Ridge from vertical seismic profiling. *Science*, 273:1840–1843, 1996.

M. Hornbach. Critically pressured free-gas reservoirs gelow gas-hydrate provinces. *Nature*, 427:142–145, 2004.

M. Hovland. Do carbonate reeffs form due to fluid seepage? *Terra Nova*, 2:8–18, 1989.

M. Hovland and M. Risk. Do Norwegian deep-water coral reefs rely on seeping fluids? *Marine Geology*, 198(1-2):83–96, jun 2003.

M. Hovland, M. Talbot, H. Qvale, S. Olaussen, and L. Aasberg. Methane-related carbonate cements in pockmarks of the North Sea. J. Sed. Petrol.,. *Journal of Sedimentary Petrology*, 57:881–892, 1987.

M. Hovland, J. W. Gallagher, M. B. Clennell, and K. Lekvam. Gas Hydrate and Free Gas Volumes in Marine Sediments: Example From the Niger Delta Front. *Marine and Petroleum Geology*, 14(3): 245–255, 1997.

M. Hudec and M. Jackson. Advance of allochtonous salt sheets in passive margins and orogens. *American Association of Petroleum Geology Bulletin*, 90:1535–1564, 2006.

M. Huettel and A. Rusch. Transport and degradation of phytoplankton in permeable sediment. *Limnology and Oceanography*, 45(3):534–549, 2000.

M. Huettel, W. Ziebis, and S. Forster. Flow-induced uptake of particulate matter in permeable sediments. *Limnology and Oceanography*, 41(2):309–322., 1996.

M. Huettel, W. Ziebis, S. Forster, and G. W. Luther III. Advective transport affecting metal and nutrient distributions and interfacial fluxes in permeable sediments. *Geochimica et Cosmochimica Acta*, 62(4): 613–631, 1998.

M. Huettel, H. Roy, E. Precht, and S. Ehrenhauss. Hydrodynamical impact on biogeochemical processes in aquatic sediments. *Hydrobiologia*, 494:231–236, 2003.

D. A. Huseynov and I. S. Guliyev. Mud Volcanic Natural Phenomena in the South Caspian Basin: Geology, Fluid Dynamics and Environmental Impact. *Environmental Geology*, 46(8):1012–1023, 2004.

IODP Expedition 307 Scientists. Site U1317. In T. Ferdelman, A. Kano, T. Williams, J. Henriet, and the Expedition 307 scientists., editors, *Modern Carbonate Mounds: Porcupine Drilling*, volume 307 of *Proceedings of the Integrated Ocean Drilling Program*. Washington, DC (Integrated Ocean Drilling Program Management International, Inc.), 2006.

S. B. Jacobsen. Gas hydrates and deglaciations. *Nature*, 412:691–693, 2001.

R. Jolly and L. Lonergan. Mechanisms and controls on the formation of sand intrusions. *Journal of the Geological Society*, 159:605–617, 2002.

A. Jones, J. Greinert, D. Bowden, I. Klaucke, J. Petersen, G. Netzeband, and W. Weinrebe. Acoustic and visual characterisation of methane-rich seabed seeps at Omakere Ridge on the Hikurangi Margin, New Zealand. *Marine Geology*, In Press, Accepted Manuscript:–, 2009. ISSN 0025-3227.

A. Judd and M. Hovland. *Seabed Fluid Flow*. Cambridge University Press, 2007.

J. P. Kennett, K. G. Cannariato, I. L. Hendy, and R. J. Behl. Carbon isotopic evidence for methane hydrate instability during quaternary interstadials. *Science*, 288(5463):128–133, 2000. doi: 10.1126/science.288.5463.128.

N. Kenyon, R. Belderson, and A. Stride. Detailed tectonic trends on the central part of the Hellenic Outer Ridge and in the Hellenic Trench System. In *Trench-Forearc Geology*, volume Special Publication 10. Geological Society of London, 1982.

N. H. Kenyon, M. K. Ivanov, A. M. Akhmetzhanov, and G. G. Akhmanov, editors. *Multidisiplinary Study of Geological Processes on the North East Atlantic and Western Mediterranean Margins*, volume 56 of *UNESCO/IOC Technical Series*, 1999.

N. H. Kenyon, M. K. Ivanov, A. M. Akhmetzhanov, and G. G. Akhmanov, editors. *Interdisciplinary Geoscience Research on the North East Atlantic Margin Mid-Atlantic Ridge.*, volume 60 of *IOC/UNESCO Technical Series*, 2000.

N. H. Kenyon, M. K. Ivanov, A. M. Akhmetzhanov, and G. G. Akhmanov, editors. *Interdisciplinary Geoscience Research on the North East Atlantic Margin, Mediterranean Sea and Mid-Atlantic Ridge.*, volume 67 of *IOC/UNESCO Technical Series*, 2003.

I. Klaucke, W. Weinrebe, C. J. Petersen, and D. Bowden. Temporal variability of gas seeps offshore New Zealand: Multi-frequency geoacoustic imaging of the Wairarapa area, Hikurangi margin. *Marine Geology*, In Press, Corrected Proof:–, 2009. ISSN 0025-3227.

A. Kopf. Significance of mud volcanism. *Reviews Of Geophysics*, 40(2):52, 2002.

A. Kopf, A. H. F. Robertson, and N. Volkmann. Origin of mud breccia from the Mediterranean Ridge accretionary complex based on evidence of the maturity of organic matter and related petrographic and regional tectonic evidence. *Marine Geology*, 166(1-4):65–82, may 2000.

A. J. Kopf. Global Methane Emission Through Mud Volcanoes and Its Past and Present Impact on the Earth's Climate. *International Journal of Earth Sciences*, 92(5):806–816, 2003.

E. V. Kozlova, M. Ivanov, and V. Blinova. Organic matter from the rock clasts in the mud volcanoes of the Gulf of Cadiz. *Geophysical Research Abstracts*, 10:A08834, 2008.

K. A. Kvenvolden. Gas hydrates - geological perspective and global change. *Reviews of Geophysics*, 31 (2):173–187, 1993.

K. A. Kvenvolden. A primer on the geological occurrence of gas hydrate. In J. P. Henriet and J. Mienert, editors, *Gas Hydrates: Relevance to world margin stability and climatic change*, volume 137, chapter Special Publication, pages 9–30. The Geological Society, London, 1998.

P. La Violette and H. Lacombe. Tidal-induced pulses in the flow through the Strait of Gibraltar. *Oceanologica Acta*, Special Issue:13–27, 1988.

L. Lapham, M. Alperin, J. Chanton, and C. Martens. Upward advection rates and methane fluxes, oxidation, and sources at two Gulf of Mexico brine seeps. *Marine Chemistry*, 112:65–71, 2008.

H. J. Lee and J. Baraza. Geotechnical characteristics and slope stability in the Gulf of Cadiz. *Marine Geology*, 155:173–190, 1999.

K. Lekvam and P. R. Bishnoi. Dissolution of methane in water at low temperatures and intermediate pressures. *Fluid Phase Equilibria*, 131(1-2):297–309, 1997.

R. Leon, L. Somoza, T. Medialdea, A. Maestro, V. Diaz de Rio, and M. Fernandez-Puga. Classification of sea-floor features associated with methane seeps along the Gulf of Cadiz continental margin. *Deep-Sea Research Part II: Topical Studies in Oceanography*, 53:1464–1481, 2006.

A. Lerman. *Geochemical Processes: Water and Sediment Environments*. Wiley, 1979.

K. Lewis and B. Marshall. Seep faunas and other indictors of methane-rich dewatering on the New Zealand convergent margins. *New Zealand Journal of Geology and Geophysics*, 39:181âĂŞ200., 1996.

A. Limonov, J. Woodside, M. Cita, and M. Ivanov. The Mediterranean Ridge and related mud diaprirsm: a background. *Marine Geology*, 132:7–19, 1996.

E. Llave, F. HernÃạndez-Molina, L. Somoza, V. Diaz-del Rio, D. Stow, and A. Maestro. Seismic stacking patterns of the FaroâĂŞAlbufeira contourite system (Gulf of Cadiz): a Quaternary record of paleogeographic and tectonic influences. *Marine Geophysical Researches*, 22:487–508, 2001.

M. Longman. Carbonate diagenetic textures from nearsurface diagenetic environments. *American Association of Petroleum Geology Bulletin*, 64:461âĂŞ487, 1980.

D. Lumsden. Discrepancy between thin-section and x-ray estimates of dolomite in limestone. *Journal of Sedimentary Petrology*, 49:429–436, 1979.

E. Lundin. Thin-Skinned Extensional Tectonics On A Salt Detachment, Northern Kwanza Basin, Angola. *Marine and Petroleum Geology*, 9(4):405–411, AUG 1992. ISSN 0264-8172.

F. Machin, J. L. Pelegri, A. Marrero-Diaz, I. Laiz, and A. Ratsimandresy. Near-surface circulation in the southern Gulf of Cadiz. *Deep-Sea Research Part II: Topical Studies in Oceanography*, 63:1161–1181, 2006.

M. E. MacKay, R. D. Jarrard, G. K. Westbrook, and R. D. Hyndman. Origin of bottom simulating reflectors: geophysical evidence from the Cascadia accretionary prism. *Geology*, 22:459–462, 1994.

A. Maestro, L. Somoza, T. Medialdea, C. J. Talbot, A. Lowrie, J. T. Vazquez, and V. Diaz-Del-Rio. Large-Scale Slope Failure Involving Triassic and Middle Miocene Salt and Shale in the Gulf of Cadiz (Atlantic Iberian Margin). *Terra Nova*, 15(6):380–391, 2003.

L. Maignien, D. Depreiter, A. Foubert, W. Boon, N. andVerstraete, and J. Henriet. Biogeochemistry of Carbonate mounds from the Pen Duick Escarpment in the Gulf of Cadiz. In *Geoph. Res. Abstracts*, volume 9, page A08287, 2007.

A. Maldonado, L. Somoza, and L. Pallares. The Betic Orogen and the Iberian-African Boundary in the Gulf of Cadiz: Geological Evolution (Central North Atlantic). *Marine Geology*, 155(1-2):9–43, 1999.

J. Mascle, C. Huguen, and J. Benkhelil. Images may show start of European-African plate collision. *EOS, Transactions of the American Geophysical Union*, 80:421, 425, 428, 1999.

R. Matsumoto. Vuggy carbonate crust formed by hydrocarbon seep- age on the continental shelf of Baffin Island, northeast Canada. *Geochemical Journal*, 24:143âĂŞ158, 1990.

R. Matsumoto and W. Borowski. Gas Hydrate Estimates From Newly Determined Oxygen Isotopic Fractionation (Gh-Iw) And δ18O Anomalies Of The Interstitial Waters: Leg 164, Blake Ridge. In C. Paull and R. Matsumoto, editors, *Proceedings of the Ocean Drilling Program, Scientific Results*, volume 164, College Station, TX, 2000. Ocean Drilling Program.

L. L. Mazurenko, V. A. Soloviev, I. Belenkaya, M. K. Ivanov, and L. M. Pinheiro. Mud volcano gas hydrates in the Gulf of Cadiz. *Terra Nova*, 14(5):321–329, 2002.

L. L. Mazurenko, V. A. Soloviev, J. M. Gardner, and M. K. Ivanov. Gas Hydrates in the Ginsburg and Yuma Mud Volcano Sediments (Moroccan Margin): Results of Chemical and Isotopic Studies of Pore Water. *Marine Geology*, 195(1-4):201–210, 2003.

K. McClay, J. Munoz, and J. Garcia-Senz. Extensional salt tectonics in a contractional orogen: A newly identified tectonic event in the Spanish Pyrenees. *Geology*, 32(9):737–740, SEP 2004. ISSN 0091-7613. doi: 10.1130/G20565.1.

L. McNeill, K. Piper, C. Goldfinger, L. Kulm, and R. Yeats. Listric normal faulting on the Cascadia continental margin. *Journal of Geophysical Research-Solid Earth*, 102(B6):12123–12138, JUN 10 1997.

T. Medialdea, R. Vegas, L. Somoza, J. T. Vazquez, A. Maldonado, V. Diaz-Del-Rio, A. Maestro, D. Cordoba, and M. C. Fernandez-Puga. Structure and Evolution of the 'Olistostrome' Complex of the Gibraltar Arc in the Gulf of Cadiz (Eastern Central Atlantic): Evidence From Two Long Seismic Cross-Sections. *Marine Geology*, 209(1-4):173–198, 2004.

A. Michard, A. Chalouan, H. Feinberg, B. Goffé, and R. Montigny. How does the Alpine belt end between Spain and Morocco? *Bulletin de la Société Géologique de France*, 173:3–15, 2002.

F. Mienis, H. de Haas, and shipboard scientific party. Report of cruise 'Moundforce 2004', cruise 64PE229 - The distribution, morphology, sedimentology and watermass characteristics of and around mounds in the Gulf of Cadiz and at the SW Rockall Trough Margin. Technical report, Royal Netherlands Institute for Sea Research, Texel, NL, 2004.

A. V. Milkov. Worldwide Distribution of Submarine Mud Volcanoes and Associated Gas Hydrates. *Marine Geology*, 167(1-2):29–42, 2000.

K. Miller, M. Kominz, J. Browning, J. Wright, G. Mountain, M. Katz, P. Sugerman, B. Cramer, N. Christie-Blick, and S. Pekar. The Phanerozoic Record of Global Sea-Level Change. *Science*, 310 (5752):1293–1298, 2005.

C. K. Morley. Tectonic and sedimentary evidence for synchronous and out-of-sequence thrusting, Larache-Acilah area, Western Moroccan Rif. *Journal of the Geological Society*, 149:39–49, 1992.

C. Mulder. *Tectonic framework and distribution of Miocene chemical sediments with emphasis on the Eastern Mediterranean*, pages 44–59. New-Holland Publishing Company, Amsterdam, 1973.

T. Mulder, M. Voisset, P. Lecroart, E. Le Drezen, E. Gonthier, V. Hanquiez, J. C. Faugeres, E. Habgood, F. J. Hernandez-Molina, F. Estrada, E. Llave-Barranco, D. Poirier, C. Gorini, Y. Fuchey, A. Voelker, P. Freitas, F. Lobo Sanchez, L. Fernandez, N. Kenyon, and J. Morel. The Gulf of Cadiz: an unstable giant contouritic levee. *Geo-Marine Letters*, 23:7–18, 2003.

H. Mullins, S. W. Wise, A. F. Gardulski, E. J. Hinchey, P. M. Masters, and D. I. Siegel. Shallow Subsurface Diagenesis of Pleistocene Periplatform Ooze - Northern Bahamas. *Sedimentology*, 32(4):473–467, 1985.

T. Naehr, R. N.M., G. Bohrmann, C. Paull, and R. Botz. Methane-derived authigenic carbonates associated with gas hydrate decomposition and fluid venting above the Blake Ridge Diapir. In C. Paull, R. Matsumoto, P. Wallace, , and W. Dillon, editors, *Proceedings of the Ocean Drilling Program, Scientific Results*, volume 164, pages 285–300, College Station, TX, 2000. Ocean Drilling Program.

J. Naeth, R. di Primio, B. Horsfield, R. Schaefer, P. Shannon, W. Bailey, , and J. Henriet. Hydrocarbon seepage and carbonate mound formation: a basin modelling study from the Porcupine Basin (offshore Ireland). *Journal of Petroleum Geology*, 28(2):43–62, 2005.

C. Nelson, J. Baraza, A. Maldonado, J. Rodero, C. Escutia, and J. Barber. Influence of the Atlantic inflow and Mediterranean outflow currents on Late Quaternary sedimentary facies of the Gulf of Cadiz continental margin. *Marine Geology*, 155:99–129, 1999.

R. Nichols. The liquification and remobilization of sandy sediments. In A. Hartley and D. Prosser, editors, *Characterisation of Deep Marine Clastic Systems*, volume 94, pages 63–76. Geological Society, London, 1995.

H. Niemann, J. Duarte, C. Hensen, E. Omoregie, V. Magalhaes, M. Elvert, L. Pinheiro, A. Kopf, and A. Boetius. Microbial methane turnover at mud volcanoes of the Gulf of Cadiz. *Geochimica et Cosmochimica Acta*, 70:5336–5355, 2006.

D. O. Ovsyannikov, A. Y. Sadekov, and E. V. Kozlova. Rock Fragments From Mud Volcanic Deposits of the Gulf of Cadiz: an-Insight Into the Eocene-Pliocene Sedimentary Succession of the Basin. *Marine Geology*, 195(1-4):211–221, 2003.

R. J. Parkes, B. A. Cragg, and P. Wellsbury. Recent studies on bacterial populations and processes in marine sediments: a review. *Hydrogeological Review*, 8:11–28, 2000.

C. K. Paull, P. G. Brewer, W. Ussler, E. T. Peltzer, G. Rehder, and D. Clague. An Experiment Demonstrating That Marine Slumping Is a Mechanism to Transfer Methane From Seafloor Gas-Hydrate Deposits Into the Upper Ocean and Atmosphere. *Geo-Marine Letters*, 22(4):198–203, 2003.

I. Pecher, S. Henrys, and H. Zhu. Methane focussing on the Hikurangi Margin, New Zealand - inferences from the reflection strength of BSRs. In *EGS-AGU-EUG Joint Assembly*, page A8018, 2003. Nice, April 6-11.

J. Peckmann and V. Thiel. Carbon cycling at ancient methane-seeps. *Chemical Geology*, 205(3-4):443–467, may 2004.

J. L. Pelegri, J. Aristegui, L. Cana, M. Gonzalez-Davila, A. Hernandez-Guerra, S. Hernandez-Leon, A. Marrero-Diaz, M. F. Montero, P. Sangra, and M. Santana-Casiano. Coupling between the open ocean and the coastal upwelling region off northwest Africa: water recirculation and offshore pumping of organic matter. *Journal of Marine Systems*, 54(1-4):3–37, 2005.

L. M. Pinheiro, M. K. Ivanov, A. Sautkin, G. Akhmanov, V. H. Magalhaes, A. Volkonskaya, J. H. Monteiro, L. Somoza, J. Gardner, N. Hamouni, and M. R. Cunha. Mud Volcanism in the Gulf of Cadiz: Results From the Ttr-10 Cruise. *Marine Geology*, 195(1-4):131–151, 2003.

A. Pique and E. Laville. The central Atlantic rifting: reactivation of Palaeozoic structures? *Journal of Geodynamics*, 21:235–255, 1996.

J. Platt, S. Allerton, A. Kirker, C. Mandeville, A. Mayfield, E. Platzman, and A. Rimi. The ultimate arc: differential displacement, oroclinal bending and vertical axis rotation in the External Betic-Rif Arc. *Tectonics*, 22:doi:10.1029/2001TC001321, 2003.

J. Poort and J. Klerkx. Absence of a regional surface thermal high in the Baikal rift; new insights from detailed contouring of heat flow anomalies. *Tectonophysics*, 383:217–241, 2004.

U. v. Rad, R. H., and B. U. Authigenic carbonates derived from oxidized methane vented from the Makran accretionary prism off Pakistan. *Marine Geology*, 136:55–77, 1996.

Y. Rao, C. Subrahmanyam, A. Rastogi, and B. Deka. Anomalous seismic reflections related to gas/gas hydrate occurrences along the western continental margin of India. *Geo-Marine Letters*, 21:1–8, 2001.

C. E. Reimers, H. A. Stecher III, G. L. Taghon, C. M. Fuller, M. Huettel, A. Rusch, N. Ryckelynck, and C. Wild. In situ measurements of advective solute transport in permeable shelf sands. *Continental Shelf Research*, 24:183–201, 2004.

S. Ritger, B. Carson, and E. Suess. Methane-Derived Authigenic Carbonates Formed By Subduction Induced Pore-Water Expulsion Along The Oregon Washington Margin. *Geological Society Of America Bulletin*, 98(2):147–156, feb 1987. Comes with discussion and reply.

H. Roberts and P. Aharon. Hydrocarbon-derived carbonate buildups of the northern Gulf of Mexico continental slope: A review of submersible investigations. *Geo-Marine Letters*, 14:135–148, 1994.

A. Robertson and the Ocean Drilling Program Leg 160 Scientific Party. Mud volcanism on the Mediterranean Ridge: Initial results of Ocean Drilling Program Leg 160. *Geology*, 24(3):239–242, 1996.

J. Rodero, L. Pallares, and A. Maldonado. Late Quaternary seismic facies of the Gulf of Cadiz Spanish margin: depositional processes influenced by sea-level change and tectonic controls. *Marine Geology*, 155:131–156, 1999.

H. Roy, M. Huettel, and B. B. Jorgensen. The influence of topography on the functional exchange surface of marine soft sediments, assessed from sediment topography measured in situ. *Linology and Oceanography*, 50(1):106–112, 2005.

R. Sassen, S. Joye, S. T. Sweet, D. A. Defreitas, A. V. Milkov, and I. R. Macdonald. Thermogenic Gas Hydrates and Hydrocarbon Gases in Complex Chemosynthetic Communities, Gulf of Mexico Continental Slope. *Organic Geochemistry*, 30(7):485–497, 1999.

R. Sassen, A. V. Milkov, H. H. Roberts, S. T. Sweet, and D. A. Defreitas. Geochemical Evidence of Rapid Hydrocarbon Venting From a Seafloor-Piercing Mud Diapir, Gulf of Mexico Continental Shelf. *Marine Geology*, 198(3-4):319–329, 2003.

A. Sautkin, A. R. Talukder, M. C. Comas, J. I. Soto, and A. Alekseev. Mud volcanoes in the Alboran Sea: evidence from micropaleontological and geophysical data. *Marine Geology*, 195(1-4):237–261, mar 2003.

H. U. Schluter, A. Prexl, C. Gaedicke, H. Roeser, C. Reichert, H. Meyer, and C. von Daniels. The Makran accretionary wedge: sediment thicknesses and ages and the origin of mud volcanoes. *Marine Geology*, 185(3-4):219–232, jun 2002.

F. Schwartz and H. Zhang. *Fundamentals of Groundwater*. Wiley, Chichester, UK,, 2003.

J. G. Sclater, C. Jaupart, and D. Galson. The Heat-Flow Through Oceanic and Continental-Crust and the Heat-Loss of the Earth. *Reviews of Geophysics*, 18(1):269–313, 1980.

D. Seber, M. Barazangi, B. A. Tadili, M. Ramdani, A. Ibenbrahim, and B. S. D. . Three-dimensional upper mantle structure beneath the intraplate Atlas and interplate Rif mountains of Morocco. *Journal of Geophysical Research*, 101(B2):3125–3138, 1996.

D. Secor. The role of fluid pressure in jointing. *American Journal of Science*, 263:633–646, 1965.

S. Seni. Evolution Of Salt Structures During Burial Of Salt Sheets On The Slope, Northern Gulf Of Mexico. *Marine and Petroleum Geology*, 9(4):452–468, AUG 1992. ISSN 0264-8172.

S. Sheppard and H. Gilg. Stable isotope geochemistry of clay minerals. *Clay Minerals*, 31:1–24, 1996.

R. Sibson and J. Scott. Stress/fault controls on the containment and release of overpressured fluids: examples from gold-quartz vein systems in Juneau, Alaska, Victoria, Australia, and Otago, New Zealand. *Ore Geology Reviews*, 13:293–306, 1998.

E. D. Sloan. *Clathrate hydrates of natural gases*. Marcel Dekker Inc., New York, 1998a.

E. D. Sloan. Physical/chemical properties of gas hydrates and application to world margin stability and climatic change. In J. P. Henriet and J. Mienert, editors, *Gas Hydrates: Relevance to world margin stability and climatic change*, volume 137, chapter Special Publication, pages 31–50. The Geological Society, London, 1998b.

I. Smith and D. Griffiths. *Programming the Finite Element Method*. Wiley, Chichester, UK, 2004.

V. A. Soloviev and G. D. Ginsburg. Formation of submarine gas hydrates. *Bulletin of the Geological Society of Denmark*, 41:86–94, 1994.

L. Somoza, F. HernÃ\u0105ndez-Molina, J. de Andrés, and J. Rey. Continental shelf architecture and sea-level cycles: Late Quaternary high-resolution stratigraphy of the gulf of cadiz (Spain). *Geo-Marine Letters*, 17:133–139, 1997.

L. Somoza, V. Diaz-Del-Rio, R. Leon, M. Ivanov, M. C. Fernandez-Puga, J. M. Gardner, F. J. Hernandez-Molina, L. M. Pinheiro, J. Rodero, A. Lobato, A. Maestro, J. T. Vazquez, T. Medialdea, and L. M. Fernandez-Salas. Seabed Morphology and Hydrocarbon Seepage in the Gulf of Cadiz Mud Volcano Area: Acoustic Imagery, Multibeam and Ultra-High Resolution Seismic Data. *Marine Geology*, 195 (1-4):153–176, 2003.

K. Y. Song, G. Feneyrou, F. Fleyfel, R. Martin, J. Lievois, and R. Kobayashi. Solubility measurements of methane and ethane in water at and near hydrate conditions. *Fluid Phase Equilibria*, 128(1-2):249–259, Feb. 1997.

G. Spinelli, E. Giambalvo, and A. Fisher. Sediment permeability, distribution, and influence on fluxes in oceanic basement. In E. Davis and H. Elderfield, editors, *Hydrogeology of the Oceanic Lithospherenae*, pages 151–188. Cambridge University Press, 2004.

A. Stadnitskaia, M. Ivanov, V. Blinova, R. Kreulen, and T. Van Weering. Molecular and carbon isotopic variability of hydrocarbon gases from mud volcanoes in the Gulf of Cadiz, NE Atlantic. *Marine and Petroleum Geology*, 23:281–296, 2006.

A. Stadnitskaia, D. Nadezhkin, B. Abbas, V. Blinova, M. Ivanov, and J. Sinnighe Damsté. Carbonate form by anaerobic oxidation of methane: Evidence from lipid biomarker and fossil 16S rDNA. *Geochimica et Cosmochimica Acta*, 72:1824–1836, 2008.

R. Stevenson. Huelva Front and Malaga, Spain, Eddy Chain as defined by Satellite and Oceanographic Data. *Deutsche Hydrographische Zeitschrift*, 2:52–57, 1977.

R. H. Sumner and G. K. Westbrook. Mud Diapirism in Front of the Barbados Accretionary Wedge: the Influence of Fracture Zones and North America-South America Plate Motions. *Marine and Petroleum Geology*, 18(5):591–613, 2001.

L. J. Thibodeaux and J. D. Boyle. Bedform-Generated Convective-Transport In Bottom Sediment. *Nature*, 325(6102):341–343, Jan. 1987.

L. Torelli, R. Sartori, and N. Zitellini. The giant chaotic body in the Atlantic Ocean off Gibraltar: new results from a deep seismic surveys. *Marine and Petroleum Geology*, 14:125–138, 1997.

D. Tortella, M. Torne, and Perez-Estaun. Geodynamic evolution of the Eastern segment of the Azores-Gibraltar Zone: The Gorringe Bank and the Gulf of Cadiz region. *Marine Geophysical Researches*, 19: 211–230, 1997.

J. Traynor and C. Sladen. Seepage in Vietnam - onshore and offshore examples. *Marine and Petroleum Geology*, 14:345–362, 1997.

A. M. Trehu, M. E. Torres, P. E. Long, G. Bohrmann, F. R. Rack, T. S. Collett, D. S. Goldberg, A. V. Milkov, M. Riedel, P. Schultheiss, N. L. Bangs, S. R. Barr, W. S. Borowski, G. E. Claypool, M. E. Delwiche, G. R. Dickens, E. Gracia, G. Guerin, M. Holland, J. E. Johnson, Y. J. Lee, C. S. Liu, X. Su, B. Teichert, H. Tomaru, M. Vanneste, M. Watanabe, and J. L. Weinberger. Three-Dimensional Distribution of Gas Hydrate Beneath Southern Hydrate Ridge: Constraints From Odp Leg 204 (Vol 222, Pg 845, 2004). *Earth and Planetary Science Letters*, 227(3-4):557–558, 2004.

P. Van Rensbergen and C. Morley. Fluid expulsion from overpressured shale, an alternative for shale diapirism. Expamples from offshore Brunei. In *Conference Proceedings, Subsurface sediment mobilization conference*, 2001. Ghent University, September 11-13.

P. Van Rensbergen, M. De Batist, J. Klerkx, R. Hus, J. Poort, M. Vanneste, N. Granin, O. Khlystov, and P. Krinitsky. Sublacustrine Mud Volcanoes and Methane Seeps Caused by Dissociation of Gas Hydrates in Lake Baikal. *Geology*, 30(7):631–634, 2002.

P. Van Rensbergen, D. Depreiter, B. Pannemans, and J. P. Henriet. Seafloor expression of sediment extrusion and intrusion at the El Arraiche mud volcano field, Gulf of Cadiz. *Journal of Geophysical Research*, 110(F2), 2005a.

P. Van Rensbergen, D. Depreiter, B. Pannemans, G. Moerkerke, D. Van Rooij, B. Marsset, G. Akhmanov, V. Blinova, M. Ivanov, M. Rachidi, V. Magalhaes, L. Pinheiro, M. Cunha, and J. P. Henriet. The El Arraiche mud volcano field at the Moroccan Atlantic slope, Gulf of Cadiz. *Marine Geology*, 219(1): 1–17, 2005b.

M. Vanneste, J. Poort, M. De Batist, and J. Klerkx. Atypical Heat-Flow Near Gas Hydrate Irregularities and Cold Seeps in the Baikal Rift Zone. *Marine and Petroleum Geology*, 19(10):1257–1274, 2002.

B. Vendeville and M. Jackson. The Fall Of Diapirs During Thin-Skinned Extension. *Marine and Petroleum Geology*, 9(4):354–371, AUG 1992. ISSN 0264-8172.

P. Villanueva and J. M. Gutierrezmas. The Hydrodynamics Of The Gulf Of Cadiz And The Exchange Of Water Masses Through The Gibraltar Strait. *International Hydrographic Review*, 71(1):53–65, 1994.

P. R. Vogt, J. Gardner, and K. Crane. The Norwegian-Barents-Svalbard (Nbs) Continental Margin: Introducing a Natural Laboratory of Mass Wasting, Hydrates, and Ascent of Sediment, Pore Water, and Methane. *Geo-Marine Letters*, 19(1-2):2–21, 1999.

E. Wachter and J. Hayes. Exchange of Oxygen Isotopes in Carbon Dioxide-Phosphoric Acid Systems. *Chemical Geology*, 52(3-4):365–374, 1985.

G. Webster, A. Blazejak, B. A. Cragg, A. Schippers, H. Sass, J. Rinna, T. Xiaohong, F. Mathes, T. Ferdelman, J. C. Fry, A. Weightman, and R. J. Parkes. Subsurface microbiology and biogeochemistry of a deep, cold-water carbonate mound from the Porcupine Seabight (IODP Expedition 307). *Environmental Microbiology*, 11:239–257, 2008.

M. Whiticar. Carbon and hydrogen isotope systematics of bacterial formation and oxidation of methane. *Chemical Geology*, 161(1-3):291–314, 1999.

M. Wiedicke, S. Neben, and V. Spiess. Mud volcanoes at the front of the Makran accretionary complex, Pakistan. *Marine Geology*, 172:57–73, 2001.

D. Wilcox. *Turbulence Modeling for CFD*. DCW Industries, Inc., 1998.

W. S. Wooster, A. J. Lee, and G. Dietrich. Redefinition of Salinity. *Deep Sea Research Part*, 16:321–322, 1969.

X. Xie, S. Li, H. He, and X. Liu. Seismic evidence for fluid migration pathways from an overpressured system in the South China Sea. *Geofluids*, 3(4):245–253, nov 2003.

W. Xu and C. Ruppel. Predicting the occurrence, distribution, and evolution of methane gas hydrates in porous marine sediments. *Journal of Geophysical Research*, 104(B3):5081–5095, 1999.

M. Yamano, S. Uyeda, Y. Aoki, and T. H. Shipley. Estimates of heat-flow derived from gas hydrates. *Geology*, 10(7):339–342, 1982.

S. O. Yang, S. H. Cho, H. Lee, and C. S. Lee. Measurement and prediction of phase equilibria for water plus methane in hydrate forming conditions. *Fluid Phase Equilibria*, 185(1-2):53–63, July 2001.

P. Yin, S. Berne, P. Vagner, B. Loubrieu, and Z. Liu. Mud volcanoes at the shelf margin of the East China Sea. *Marine Geology*, 194(3-4):135–149, mar 2003.

H. Zeyen, P. Ayarza, M. Fernandez, and A. Rimi. Lithospheric structure under the western African-European plate boundary: A transect across the Atlas Mountains and the Gulf of Cadiz. *Tectonics*, 24:–2001, 2005. doi: 10.1029/20045C001639.

P. Ziegler and B. van Hoorn. *Extensional Tectonics and Stratigrahy of the North Atlantic Margins*, volume Memoir 46, chapter Evolution of the North Atlantic - An Overview, pages 111–129. American Association of Petroleum Geologists, 1989.

O. Zienkiewicz, R. Taylor, and J. Zhu. *The Finite Element Method - Its basis and Fundamentals*. Elsevier, Amsterdam, 6th edition edition, 2005.

L. Zouhri, C. Lamouroux, D. Vachard, and A. Pique. Evidence of flexural extension of the Rif foreland: The Rharb-Mamora basin (Northern Morocco). *Bulletin de la Société Géologique de France*, 173(6): 509–514, 2002.